

# Ultra-high quantum coherent and scalable superconducting circuit optomechanics, from topological lattices to quantum storage

Présentée le 8 mars 2024

Faculté des sciences et techniques de l'ingénieur  
Laboratoire de photonique et mesures quantiques (STI/SB)  
Programme doctoral en génie électrique

pour l'obtention du grade de Docteur ès Sciences

par

**Amir YOUSSEFI**

Acceptée sur proposition du jury

Prof. R. C. R. Fleury, président du jury  
Prof. T. Kippenberg, directeur de thèse  
Prof. Y. Nakamura, rapporteur  
Prof. A. Safavi-Naeini, rapporteur  
Prof. P. Scarlino, rapporteur





# بِسْمِ اللَّهِ الرَّحْمَنِ الرَّحِيمِ

﴿إِنَّ فِي خَلْقِ السَّمُوتِ وَالْأَرْضِ وَاخْتِلَافِ اللَّيْلِ وَالنَّهَارِ لَآيَاتٍ لِّأُولِي الْأَلْبَابِ،  
الَّذِينَ يَذْكُرُونَ اللَّهَ قِيَمًا وَقُعُودًا وَعَلَىٰ جُنُوبِهِمْ وَيَتَفَكَّرُونَ فِي خَلْقِ السَّمُوتِ وَالْأَرْضِ  
رَبَّنَا مَا خَلَقْتَ هَذَا بَطْلًا سُبْحَنَكَ فَقِنَا عَذَابَ النَّارِ﴾ (آل عمران ۱۹۰-۱۹۱)

آمان که خاک را به نظر کیما کنند،

آیا بود که گوشه چشمی به ما کنند...

با استعانت از مولایمان صاحب العصر والزمان روحی لَدِ الْفِدَاءِ،

تقدیم به مادر عزیزتر از جانم،

تقدیم به همسر همیشه مهربانم



# Acknowledgements

Alhamdulillah, my Ph.D. has reached its conclusion with the publication of this thesis, while, undoubtedly, new journeys are just beginning.

I would like to deeply thank Prof. Tobias J. Kippenberg, my Ph.D. advisor in the laboratory of photonics and quantum measurement (LPQM). During the six years of my Ph.D., he was always supporting, trusting, and guiding me in the right direction. I am proud of having the opportunity to work with him very closely and not only learn science itself but more importantly, learn how to do research and push the boundaries of science.

Within LPQM, I had the unique opportunity to collaborate with brilliant colleagues and friends. I would like to extend my acknowledgments to each of them. I first want to recognize the earlier members of the circuit team, including Alexey Feofanov, Laszlo Daniel Toth, and Nathan Rafaël Bernier. Though our overlap was relatively short, I gleaned valuable insights from their expertise.

Gratitude is also due to the current circuit team members, who played an instrumental role in achieving significant results. Special thanks go to my dear friend Mahdi Chegnizadeh, whose collaboration was invaluable in my thesis projects. The time we spent together, not limited to scientific endeavors, was genuinely enjoyable, and I wish him a productive Ph.D. journey. I extend my appreciation to Shingo Kono (-san) for his substantial contributions to the experiments after joining the project and our intellectually stimulating discussions. Furthermore, I'd like to acknowledge my friend Andrea Bancora; our time together in the lab was highly productive and very funny. Thanks to Yash Joshi and Tatiana Vovk, who collaborated with me on their master's theses, yielding remarkable results. I acknowledge Itay Shomroni for his very professional collaboration on two projects. I enjoyed our collaborative efforts with Marco Scigliuzzo in developing novel ideas over the past two years.

My Iranian friends in LPQM deserve special mention, particularly Amirali Arabmoheghi, with whom I engaged in many interesting afternoon discussions, and Mohammad Bereyhi for helping me to understand how things work in LPQM at the beginning of my Ph.D. I also wish to acknowledge my many good friends at LPQM, including but not limited to Nick Jacob Sauerwein, Nils Engelsens, Arslan Sajid Raja, Sergey Fedorov, Alberto Beccari, Amir Ghadimi,

Anton Lukashchuk, Jahe Pan, Evgenii Guzovskii, Hao Li, Xuxin Wang, Alessio Zicoschi, Liu Qiu, and countless others. I extend my best wishes to each of them. Specific gratitude goes to Antonella Ragnelli, who expertly managed essential yet often hidden aspects of our research and played a pivotal role in my understanding of project management. Last but certainly not least, I express my appreciation to Kathleen Vionnet, whose meticulous efforts behind the scenes were instrumental in resolving administrative matters.

Beyond academic life, I must acknowledge my family, whose unwavering support has been a constant throughout my life's journey, culminating in this point. Words fail to capture the depth of my gratitude to my beloved mother, Mrs. Fatemeh Saatchi Tehrani, who initially planted the seeds of my curiosity and wholeheartedly dedicated herself to nurturing it. She has consistently been a source of confidence and energy, guiding me through each stage of life with her wise advice. I express profound gratitude to my dear wife, Mrs. Seyedeh Sharareh Mirzargar, whose presence has breathed a fresh spirit into my life and supported me unwaveringly during the challenging Ph.D. years. I express my gratitude every day, praying to God for blessing me with all of you in my life.

Lastly, I acknowledge all the individuals who played pivotal roles in my earlier stages of education. I must again thank my mother for reading scientific books to me and igniting my passion for learning. I extend my sincere gratitude to my dear aunt, Mrs. Zohre Saatchi Tehrani, who taught me the fundamentals of numbers and alphabets. My appreciation extends to all the educators at Bahman 21st Primary School in Tehran, Daar-al Tahfeez Al-Quran in Tehran, Allameh Helli 1 Secondary School, Allameh Helli 1 High School, the Iran Physics Olympiad committee, and the Sharif University of Technology. In particular, I express my thanks to Prof. Amin Khavasi and Prof. Seyed Akbar Jafari for their guidance and supervision during my BSc thesis in Sharif's Electrical Engineering and Physics Departments and to Prof. Sina Khorasani who was always offering great advice to me. I wish them all the best.

*Lausanne, September 2023*

Amir Youssefi

# Abstract

Mechanical oscillators can exhibit modes with ultra-low energy dissipation and compact form factors due to the slow velocity of acoustic waves, and are already used in applications ranging from timing to wireless filters. Over the past decade, novel ways in which mechanical systems can be quantum controlled have been developed, based on either coupling to electromagnetic cavities in quantum optomechanics or superconducting qubits. The former route has utilized the coupling to electromagnetic cavities both in the optical and microwave domains, and enabled to reach a regime where the quantum nature of the optomechanical interaction becomes relevant. This allowed numerous advances such as optomechanical ground state cooling, quantum transduction, or entanglement of macroscopic mechanical resonators.

An enduring challenge in constructing such hybrid systems is the dichotomy of engineered coupling to an auxiliary degree of freedom, while being mechanically well isolated from the environment, that is, low quantum decoherence. In this thesis, we show how to overcome this challenge by introducing a superconducting circuit optomechanical platform with an ultra-low quantum decoherence rate. This enabled us to reach 0.07 quanta motional ground state occupation and realize mechanical squeezing of -2.7 dB below zero-point fluctuation. To directly measure the quantum-state lifetime, we observe the free evolution of the phase-sensitive squeezed state for the first time, preserving its non-classical nature over milli-second timescales, substantially longer than conventional superconducting qubits and on par with ion traps.

Furthermore, our novel platform enables us to scale up optomechanical systems to arrays and lattices, realizing non-trivial topological modes in such multimode systems. This has been a long-lasting challenge in the field of optomechanics due to the stringent requirements on identical individual optomechanical sites. We introduce a novel technique to exploit optomechanical interaction and directly measure collective mode shapes in a large-scale superconducting lattice and explore the physics of edge states in optomechanical strained-graphene lattices. Such ultra-low quantum decoherence and reproducible platform not only increases the fidelity of quantum control and measurement of macroscopic mechanical systems but may equally benefit interfacing with qubits, exploring emergent nonlinear dynamics

in complex optomechanical systems, and placing the system in a parameter regime suitable for tests of quantum gravity. Particularly, the long mechanical quantum-state lifetime has applications in quantum sensing and makes this platform a perfect candidate for quantum storage elements in quantum computing and communication systems.

In the last part of this thesis, we report the first proof-of-concept cryogenic electro-optical readout of a superconducting circuit using a lithium niobate modulator to reduce the heat load and address the scaling challenge in future superconducting circuit-based quantum computers. Although the noise level in the electro-optical readout chain is still substantially higher than the conventional electronic methods, we discuss the requirements and envision the parameter regimen that may lead to near-quantum limited optical readout in advanced future platforms.

**Key words:**

Quantum optomechanics, Quantum electromechanical, superconducting circuits, Mechanical squeezing, Topological lattices, Quantum decoherence, Cryogenic electro-optical readout

# Résumé

Les oscillateurs mécaniques peuvent présenter des modes avec une dissipation d'énergie ultra-faible et des facteurs de forme compacts en raison de la vitesse lente des ondes acoustiques, et sont déjà utilisés dans des applications allant de la synchronisation aux filtres sans fil. Au cours de la dernière décennie, de nouvelles méthodes de contrôle quantique des systèmes mécaniques ont été développées, basées soit sur le couplage avec des cavités électromagnétiques en optomécanique quantique, soit sur des qubits supraconducteurs. La première voie a utilisé le couplage avec des cavités électromagnétiques à la fois dans les domaines optique et micro-onde, et a permis d'atteindre un régime où la nature quantique de l'interaction optomécanique devient pertinente. Cela a permis de nombreuses avancées telles que le refroidissement optomécanique à l'état fondamental, la transduction quantique ou l'intrication de résonateurs mécaniques macroscopiques. Un défi persistant dans la construction de tels systèmes hybrides est la dichotomie du couplage conçu à un degré de liberté auxiliaire, tout en étant mécaniquement bien isolé de l'environnement, c'est-à-dire une faible décohérence quantique. Dans cette thèse, nous montrons comment surmonter ce défi en introduisant une plateforme optomécanique à base de circuit supraconducteur avec un taux de décohérence quantique ultra-faible. Cela nous a permis d'atteindre une occupation de l'état fondamental de mouvement de 0,07 quanta et de réaliser une compression mécanique de -2,7 dB en dessous de la fluctuation du point zéro. Pour mesurer directement la durée de vie de l'état quantique, nous observons pour la première fois l'évolution libre de l'état comprimé sensible à la phase, en préservant sa nature non classique sur des échelles de temps de la milliseconde, nettement plus longues que les qubits supraconducteurs conventionnels et de l'ordre des pièges à ions. De plus, notre nouvelle plateforme nous permet d'étendre les systèmes optomécaniques avec des grilles et des réseaux, en réalisant des modes topologiques non triviaux dans de tels systèmes multimodes. Cela a été un défi de longue date dans le domaine de l'optomécanique en raison des exigences strictes imposées par des sites optomécaniques individuels identiques. Nous introduisons une nouvelle technique pour exploiter l'interaction optomécanique et mesurer directement les formes des modes collectifs dans un réseau supraconducteur à grande échelle et explorer la physique des états de bord dans les réseaux optomécaniques de graphène tendu. Cette décohérence quantique ultra-faible et cette plateforme reproductible augmentent non seulement la fidélité du contrôle quantique et de la mesure des systèmes mécaniques macroscopiques, mais peuvent également bénéficier de l'interface avec des qubits,

explorer la dynamique non linéaire émergente dans les systèmes optomécaniques complexes et placer le système dans un régime de paramètres adapté à tests de gravité quantique. En particulier, la longue durée de vie de l'état quantique mécanique a des applications dans la détection quantique et fait de cette plateforme un candidat parfait pour les éléments de stockage quantique dans les systèmes d'informatique et de communication quantiques. Dans la dernière partie de cette thèse, nous présentons la première preuve de concept de la lecture électro-optique cryogénique d'un circuit supraconducteur en utilisant un modulateur au niobate de lithium pour réduire la charge thermique et relever le défi de la mise à l'échelle dans les futurs ordinateurs quantiques basés sur des circuits supraconducteurs. Bien que le niveau de bruit dans la chaîne de lecture électro-optique soit encore nettement supérieur aux méthodes électroniques conventionnelles, nous discutons des exigences et envisageons le régime de paramètres qui pourrait conduire à une lecture optique quasiment limitée quantiquement dans les futures plateformes avancées.

**Mots clefs :**

Optomécanique quantique, Électromécanique quantique, Circuits supraconducteurs, Compression mécanique, Réseaux topologiques, Décohérence quantique, Lecture électro-optique par cryogénique



# Zusammenfassung

Mechanische Oszillatoren können aufgrund der langsamen Geschwindigkeit akustischer Wellen Modi mit extrem geringem Energieverlust und kompakten Formfaktoren aufweisen und werden bereits für Anwendungen von der Zeitmessung bis hin zu Radiofrequenzfiltern für drahtlose Kommunikation eingesetzt. Im letzten Jahrzehnt wurden neuartige Wege zur Kontrolle mechanischer Systeme im Quantenregime entwickelt, die entweder auf der Kopplung an elektromagnetische Resonatoren in der Quantenoptomechanik oder supraleitenden Qubits in der Quantenelektromechanik basieren. Der erstere Weg nutzte die Kopplung an Resonatoren sowohl im optischen als auch im Mikrowellenbereich und ermöglichte es, einen Bereich zu erreichen, in dem die Quantennatur der optomechanischen Wechselwirkung relevant wird.

Dies ermöglichte zahlreiche Fortschritte wie optomechanische Kühlung makroskopischer mechanischer Resonatoren in den quantenmechanischen Grundzustand, die Quantentransduktion oder die Verschränkung mechanischer Schwingungen.

Eine dauerhafte Herausforderung beim Aufbau solcher Hybridsysteme ist die Dichotomie der technischen Kopplung an einen Hilfsfreiheitsgrad bei gleichzeitiger mechanischer guter Isolierung von der Umgebung, d. h. geringer Quantendekohärenz. In dieser Arbeit zeigen wir, wie diese Herausforderung durch die Einführung einer optomechanischen Plattform mit supraleitenden Schaltkreisen und einer extrem niedrigen Quantendekohärenzrate bewältigt werden kann. Dies ermöglichte es uns, eine Quantengrundzustandsbesetzung der Schwingung von 0,07 Phononen zu erreichen und eine mechanische Kompression von -2,7 dB unter der Nullpunktschwankung zu realisieren. Um die Lebensdauer eines Quantenzustands direkt zu messen, beobachteten wir zum ersten Mal die freie Entwicklung des phasenempfindlichen gequetschten Zustands, der seine nichtklassische Natur über Zeitskalen im Millisekundenbereich beibehält, wesentlich länger als bei herkömmlichen supraleitenden Qubits und auf Augenhöhe mit Ionenfallen.

Darüber hinaus ermöglicht uns unsere neuartige Plattform, optomechanische Systeme auf Arrays und Gitter zu skalieren und so nicht-triviale topologische Modi in solchen Multimode-Systemen zu realisieren. Aufgrund der strengen Anforderungen an identische einzelne optomechanische Standorte stellt dies seit langem eine Herausforderung im Bereich der Optome-

chanik dar. Wir stellen eine neuartige Technik vor, um optomechanische Wechselwirkungen zu nutzen und kollektive Modenformen in einem großen supraleitenden Gitter direkt zu messen, und erforschen die Physik von Randzuständen in optomechanischen Gittern aus gespanntem Graphen.

Eine solche ultraniedrige Quantendekohärenz und reproduzierbare Plattform erhöht nicht nur die Genauigkeit der Quantenkontrolle und -messung makroskopischer mechanischer Systeme, sondern kann auch von Nutzen sein für die Anbindung von Qubits, die Erforschung neuer nichtlinearer Dynamiken in komplexen optomechanischen Systemen und die Platzierung des Systems in einem geeigneten Parameterbereich Tests der Quantengravitation. Insbesondere die lange Lebensdauer mechanischer Quantenzustände findet Anwendung in der Quantensensorik und macht diese Plattform zu einem perfekten Kandidaten für Quantenspeicherelemente in Quantencomputer- und Kommunikationssystemen.

Im letzten Teil dieser Arbeit berichten wir zum Ersten mal eine kryogene elektrooptische Auslesung eines supraleitenden Schaltkreises unter Verwendung eines Lithiumniobat-Modulators um die Wärmebelastung zu reduzieren und die Skalierungsherausforderung in zukünftigen Quantencomputern auf der Basis supraleitender Schaltkreise zu bewältigen. Obwohl der Rauschpegel in der elektrooptischen Ausleseketten immer noch wesentlich höher ist als bei herkömmlichen elektronischen Methoden, diskutieren wir die Anforderungen und stellen uns das Parameterschema vor, das zu einer nahezu quantenbegrenzten optischen Auslesung in fortschrittlichen zukünftigen Plattformen führen könnte.

### **Schlüsselwörter:**

Quantenoptomechanik, Quantenelektromechanik, supraleitende Schaltkreise, mechanisches Quetschen, topologische Gitter, Quantendekohärenz, elektrooptische Auslesung durch Kryotechnik

# Publications

- **A. Youssefi**<sup>I\*</sup>, S. Kono\*, M. Chegnizadeh\*, & T. J. Kippenberg, “A squeezed mechanical oscillator with milli-second quantum decoherence”, **Nature Physics** (2023) [↗](#)
- **A. Youssefi**\*, S. Kono\*, A. Bancora\*, M. Chegnizadeh, J. Pan, T. Vovk, & T. J. Kippenberg, “Topological lattices realized in superconducting circuit optomechanics”, **Nature** 612 (2022) [↗](#)
- **A. Youssefi**\*, I. Shomroni\*, Y. J. Joshi, N. R. Bernier, A. Lukashchuk, P. Urich, L. Qiu, & T. J. Kippenberg, “A cryogenic electro-optic interconnect for superconducting devices”, **Nature Electronics** 4 (2021) [↗](#)
- I. Shomroni\*, **A. Youssefi**\*, N. Sauerwein, L. Qiu, P. Seidler, D. Malz, A. Nunnenkamp, & T. J. Kippenberg, “Two-Tone Optomechanical Instability and Its Fundamental Implications for Backaction-Evading Measurements”, **Physical Review X** 9 (2019) [↗](#)
- Y.J. Joshi, N. Sauerwein, **A. Youssefi**, P. Urich, & T. J. Kippenberg, “Automated wide-ranged finely tunable microwave cavity for narrowband phase noise filtering”, **Review of Scientific Instruments** 92 (2021) [↗](#)
- S. Kono, J. Pan, M. Chegnizadeh, X. Wang, **A. Youssefi**, M. Scigliuzzo, & T. J. Kippenberg, “Mechanically Induced Correlated Errors on Superconducting Qubits with Relaxation Times Exceeding 0.4 Milliseconds”, **arXiv (Under review in Nature Comm.)** (2023) [↗](#)

---

<sup>I\*</sup>: These authors have equal contributions.

# Contents

<b>Acknowledgements</b>	<b>i</b>
<b>Abstract (English/Français/Deutsch)</b>	<b>iii</b>
<b>Publications</b>	<b>ix</b>
<b>List of figures</b>	<b>xiv</b>
<b>List of tables</b>	<b>xviii</b>
<b>1 Introduction</b>	<b>1</b>
<b>2 Theory</b>	<b>8</b>
2.1 Basics of optomechanics . . . . .	8
2.2 Multi-tone optomechanical cooling and sideband asymmetry . . . . .	10
2.3 Optomechanical amplification . . . . .	17
2.4 Theory of multimode circuit optomechanics . . . . .	21
2.4.1 Theoretical model . . . . .	21
<b>3 Circuit analysis, design, and simulation</b>	<b>26</b>
3.1 Electrical circuit . . . . .	26
3.1.1 Waveguide coupling to the circuit . . . . .	27
3.1.2 Circuit theory of the dimerized arrays . . . . .	29
3.1.3 Circuit design principles . . . . .	31
3.1.4 Electromagnetic simulations . . . . .	32
3.2 Mechanical properties of the drumhead resonator . . . . .	35
3.2.1 FEM simulation of the mechanical mode . . . . .	37
3.2.2 Mechanical loss analysis . . . . .	39
3.3 Single photon optomechanical coupling rate ( $g_0$ ) . . . . .	40
3.4 Mask programming . . . . .	42
<b>4 Fabrication</b>	<b>45</b>
4.1 History and challenges of the conventional circuit optomechanical platforms . . . . .	45

## CONTENTS

---

4.2	The new nano-fabrication process for ultra-coherent and reproducible circuit optomechanics . . . . .	47
4.2.1	Material selection . . . . .	49
4.2.2	Optical lithography . . . . .	50
4.2.3	Etching trenches in silicon . . . . .	51
4.2.4	Bottom aluminum layer deposition . . . . .	52
4.2.5	Bottom layer patterning and etching . . . . .	53
4.2.6	Sacrificial layer deposition . . . . .	54
4.2.7	Chemical-mechanical polishing . . . . .	55
4.2.8	Ion beam etching . . . . .	61
4.2.9	SiO <sub>2</sub> opening for galvanic connection . . . . .	62
4.2.10	Top aluminum layer deposition . . . . .	65
4.2.11	Dicing . . . . .	67
4.2.12	Release . . . . .	67
4.2.13	Packaging . . . . .	74
<b>5</b>	<b>Experiment</b>	<b>78</b>
5.1	Cryogenics . . . . .	78
5.1.1	Dilution refrigerator . . . . .	79
5.1.2	Helium battery . . . . .	83
5.2	Microwaves and electronics . . . . .	85
5.2.1	Cryogenic wiring . . . . .	85
5.2.2	Cold attenuators . . . . .	85
5.2.3	High Electron Mobility Transistor Amplifiers . . . . .	86
5.2.4	Cryogenic circulators, couplers, and Eccosorb filters . . . . .	86
5.2.5	Electrical spectrum analyzer . . . . .	87
5.2.6	Vector network analyzer . . . . .	89
5.2.7	Other microwave components . . . . .	90
5.2.8	Phase locking and clock distribution . . . . .	91
5.3	Josephson traveling wave parametric amplifier . . . . .	91
5.3.1	Estimation of the JTWPA added noise using SNRI . . . . .	93
5.4	Microwave tone cancellation . . . . .	95
5.5	Microwave filter cavities . . . . .	97
5.6	Instrument control and data acquisition . . . . .	99
<b>6</b>	<b>Characterization</b>	<b>103</b>
6.1	Microwave resonance characterization . . . . .	103
6.1.1	Circle fit in the complex plane . . . . .	104
6.2	Mechanical resonator characterization . . . . .	106
6.2.1	Optomechanical sidebands . . . . .	106
6.2.2	Optomechanically induced transparency . . . . .	107
6.2.3	Ringdown and ring-up . . . . .	109
6.3	$g_0$ characterization . . . . .	111

6.4	Microwave cavity heating . . . . .	115
6.5	HEMT added noise . . . . .	117
<b>7</b>	<b>A squeezed mechanical oscillator with milli-second quantum decoherence</b>	<b>121</b>
7.1	Quantum decoherence . . . . .	122
7.2	Ultra-coherent circuit optomechanical platform . . . . .	124
7.2.1	Fabrication technique . . . . .	125
7.3	High-fidelity optomechanical ground state cooling . . . . .	127
7.3.1	Detailed discussion on the sideband asymmetry calibration . . . . .	129
7.3.2	Experimental details of the sideband asymmetry measurement . . . . .	132
7.4	Measurement of motional heating rate . . . . .	134
7.4.1	Optomechanical amplification measurement and calibration . . . . .	135
7.5	Recording thermalization of squeezed mechanical state . . . . .	137
7.5.1	Generation and calibration of mechanical squeezed states . . . . .	138
7.5.2	Dephasing effect on thermalization of squeezed states . . . . .	140
7.6	Technical information on the experiment . . . . .	142
7.6.1	Experimental setup and wiring . . . . .	142
7.6.2	Full data of chip characterization . . . . .	145
<b>8</b>	<b>Topological lattices realized in superconducting circuit optomechanics</b>	<b>148</b>
8.1	challenges of realizing multi-mode optomechanical systems . . . . .	149
8.2	Multimode optomechanics in lattices . . . . .	150
8.3	Review on SSH model in a 1D bosonic chain . . . . .	152
8.3.1	Band structure . . . . .	152
8.3.2	Bulk-edge correspondence . . . . .	153
8.3.3	Finite-size effect . . . . .	154
8.3.4	Effect of parasitic couplings . . . . .	156
8.4	Circuit optomechanical lattices . . . . .	159
8.4.1	Device design considerations . . . . .	161
8.4.2	Device fabrication . . . . .	161
8.5	Optomechanical modeshape measurement . . . . .	161
8.5.1	Extraction of participation ratio from optomechanical damping rate . . . . .	164
8.5.2	Iterative normalization . . . . .	165
8.5.3	Orthogonalization of modeshapes . . . . .	166
8.5.4	Modeshape extraction methods comparison . . . . .	167
8.5.5	Statistical analysis of orthogonality and measurement error . . . . .	169
8.6	Disorder effect and edge state hybridization in SSH chains . . . . .	169
8.6.1	Observation of edge state localization . . . . .	171
8.7	2D circuit optomechanical lattice . . . . .	172
8.7.1	Extended data for 2D lattice . . . . .	174
8.8	Strained graphene model . . . . .	177
8.8.1	Band structure . . . . .	177
8.8.2	Graphene ribbon . . . . .	180

## CONTENTS

---

8.8.3	Strained graphene ribbon . . . . .	184
8.8.4	Finite-width effect on graphene ribbon . . . . .	186
8.9	24-site honeycomb lattice . . . . .	187
8.9.1	Band structure and modes shapes . . . . .	187
8.9.2	Effect of parasitic couplings . . . . .	188
8.10	Experimental setup and measurement techniques . . . . .	189
8.10.1	Full experimental setup . . . . .	189
8.10.2	Ringdown data analysis and cavity shifts . . . . .	191
8.10.3	Samples parameters . . . . .	192
8.10.4	Measurement of optomechanical coupling rate . . . . .	194
<b>9</b>	<b>Cryogenic electro-optic interconnect for superconducting devices</b>	<b>198</b>
9.1	Principle of Operation of electro-optical transducer . . . . .	200
9.1.1	Quantum mechanical model for a phase modulator. . . . .	202
9.2	Cryogenic Characterization of the optical modulator . . . . .	203
9.3	Optical readout of coherent microwave spectroscopy . . . . .	204
9.4	Optical readout of an incoherent microwave spectrum . . . . .	206
9.5	Experimental details and charachtrization . . . . .	208
9.5.1	Calibration of the transduction gain . . . . .	208
9.5.2	Experimental details and heating measurements. . . . .	209
<b>10</b>	<b>Conclusion and outlook</b>	<b>211</b>
<b>Appendix A</b>	<b>Supplementary discussions on nano-fabrication</b>	<b>216</b>
A.1	Aluminum thin films . . . . .	216
A.1.1	Deposition method . . . . .	216
A.1.2	Low-temperature stress of aluminum films . . . . .	216
A.1.3	High temperature aluminum deposition . . . . .	217
A.1.4	High temperature sputtering and surface roughness . . . . .	217
A.1.5	Effect of evaporation rate on surface roughness . . . . .	217
A.1.6	Effect of annealing cycle on the stress . . . . .	218
A.1.7	Yield stress of aluminum films . . . . .	219
A.2	Non-uniformity tolerance . . . . .	220
A.3	Sapphire substrate processing . . . . .	221
<b>Appendix B</b>	<b>Linear quantum model for electro-optical phase modulators</b>	<b>223</b>
B.1	Quantum model description . . . . .	223
B.2	Computing $V_{zp}$ and $G$ . . . . .	226
	<b>Bibliography</b>	<b>238</b>
	<b>Curriculum Vitae</b>	<b>239</b>

# List of Figures

2.1	Cavity optomechanics. . . . .	8
2.2	Optomechanical sideband cooling and sideband asymmetry. . . . .	10
2.3	Optomechanical amplification. . . . .	18
2.4	Optomechanical arrays and lattices. . . . .	22
3.1	capacitive and inductive circuit electromechanics. . . . .	26
3.2	Micro-strip and co-planar waveguides. . . . .	27
3.3	Waveguide coupling to the circuit. . . . .	28
3.4	Circuit theory of the dimerized arrays. . . . .	29
3.5	Circuit simulation with Sonnet <sup>®</sup> . . . . .	32
3.6	Mutual inductive coupling simulation. . . . .	33
3.7	Coupling to the CPW waveguide. . . . .	34
3.8	Simulation of the full designs . . . . .	35
3.9	Geometrical parameters of the vacuum-gap capacitor. . . . .	36
3.10	Extraction of the aluminum film stress at low temperatures. . . . .	37
3.11	COMSOL <sup>®</sup> FEM simulation of mechanical modes. . . . .	38
3.12	FEM simulation of the loss dilution factor. . . . .	40
3.13	GDSII design programming. . . . .	44
4.1	Examples of circuit optomechanical devices. . . . .	46
4.2	Challenges of the conventional fabrication process. . . . .	47
4.3	Overview on the fabrication technique for the new generation circuit optomechanics . . . . .	48
4.4	Photo-resists cross section . . . . .	50
4.5	Dose text . . . . .	51
4.6	Si etching . . . . .	52
4.7	Bottom Al layer patterning . . . . .	53
4.8	SiO <sub>2</sub> sacrificial layer . . . . .	54
4.9	CMP tool . . . . .	56
4.10	Topography planarization in CMP . . . . .	57
4.11	CMP uniformity . . . . .	58
4.12	CMP planarization . . . . .	59
4.13	IBE etch-back . . . . .	62



## LIST OF FIGURES

---

4.14	Circuits without galvanic connection . . . . .	63
4.15	Problem of galvanic connection with sharp edges. . . . .	63
4.16	Reflow process for smooth SiO <sub>2</sub> opening. . . . .	64
4.17	Removing native aluminum oxide in Plassys . . . . .	66
4.18	Released devices . . . . .	69
4.19	Elements of the final device . . . . .	70
4.20	Collapsed drums. . . . .	71
4.21	Effect of the release holes. . . . .	72
4.22	Effect of top layer thickness on the release. . . . .	72
4.23	Effect of clamps, size, and shape on the release. . . . .	73
4.24	Chip box . . . . .	74
4.25	Wire bonds . . . . .	75
4.26	Detail fabrication process flow . . . . .	76
4.27	Example of wafer and chip layout . . . . .	77
5.1	Dilution fridge. . . . .	79
5.2	Cooldown of dilution fridge. . . . .	82
5.3	Helium battery. . . . .	84
5.4	Microwave wiring in the fridge. . . . .	87
5.5	Fluctuation scaling with averages in ESA. . . . .	89
5.6	Photo of room temperature components and the measurement instruments. . . . .	90
5.7	Josephson traveling wave parametric amplifier. . . . .	92
5.8	JTWPA SNRI and added noise. . . . .	93
5.9	Microwave tone cancellation. . . . .	96
5.10	Motorized microwave filter cavity. . . . .	98
5.11	Frequency stability of the motorized filter cavity. . . . .	99
5.12	Computer control of the measurement flow. . . . .	100
6.1	Searching for microwave resonances. . . . .	104
6.2	Resonance feature in the complex plain and coupling regimes. . . . .	104
6.3	Effect of electric delay and Fanoness on resonance. . . . .	105
6.4	Circle fitting to measured data. . . . .	106
6.5	Optomechanical parametric instability. . . . .	107
6.6	Optomechanical induced transparency. . . . .	108
6.7	Ringdown and amplification rate measurements. . . . .	110
6.8	Temperature sweep of the dilution fridge. . . . .	113
6.9	Temperature dependence of system parameters. . . . .	114
6.10	$g_0$ measurement. . . . .	115
6.11	Microwave cavity heating. . . . .	116
6.12	Cavity heating treatment. . . . .	117
6.13	HEMT noise characterization . . . . .	118
7.1	Mechanical quality factors in circuit optomechanics platforms since 2010. . . . .	122

7.2	Ultra-coherent circuit optomechanics . . . . .	125
7.3	High-fidelity optomechanical ground-state cooling. . . . .	127
7.4	Sideband asymmetry experiment . . . . .	132
7.5	Comparing mechanical linewidth from ringdown and PSD. . . . .	133
7.6	Recording the motional heating rate out of the quantum ground state . . . . .	135
7.7	Optomechanical amplification . . . . .	137
7.8	Tracking the free evolution of a mechanical squeezed state . . . . .	138
7.9	Optomechanical squeezing . . . . .	140
7.10	Measurement of squeezing . . . . .	141
7.11	Dephasing effect on the free evolution of a mechanical squeezed state . . . . .	143
7.12	Detailed experimental setup for ultra-coherent electromechanics project. . . . .	144
7.13	Chip layout of for the ultra-coherent electromechanical samples . . . . .	146
8.1	Optomechanical lattices composed of superconducting circuit optomechanical systems. . . . .	150
8.2	1D SSH model . . . . .	154
8.3	finite-size effect in 1D SSH model . . . . .	155
8.4	Effect of parasitic couplings on the 1D SSH model . . . . .	157
8.5	Superconducting circuit optomechanical chain realizing the 1D SSH model . . . . .	159
8.6	Example of a honeycomb lattice and the galvanic connection in the circuit . . . . .	162
8.7	Optomechanical modeshape measurement and Hamiltonian reconstruction of a topological SSH chain . . . . .	163
8.8	Numerical justification of iterative normalization method. . . . .	167
8.9	Three different modeshape extraction methods comparison . . . . .	168
8.10	Inner products of the measured eigenstates as an indicator for measurement accuracy . . . . .	170
8.11	Disorder effect in SSH chains . . . . .	172
8.12	Disorder effect on hybridization for different chain lengths . . . . .	173
8.13	Experimental evidence of edge state localization . . . . .	174
8.14	Two-dimensional superconducting circuit optomechanical honeycomb lattice realizing the strained graphene model . . . . .	175
8.15	Characterization of 24-site 2D honeycomb lattice . . . . .	176
8.16	Hamiltonian reconstruction of 24-site 2D honeycomb lattice . . . . .	177
8.17	Modeshapes of 24-site 2D honeycomb lattice . . . . .	178
8.18	Honeycomb lattice for a graphene of infinite size . . . . .	179
8.19	Graphene ribbon . . . . .	181
8.20	Strain-free graphene ribbons . . . . .	183
8.21	Strained graphene ribbons with different edges . . . . .	185
8.22	Strained graphene ribbons of finite width . . . . .	187
8.23	Edge states of graphene ribbons overlapping the flake structure . . . . .	188
8.24	24-site honeycomb lattice designed bands . . . . .	189
8.25	Effect of parasitic coupling on the 2D honeycomb lattice . . . . .	189

## LIST OF FIGURES

---

8.26	Experimental setup for optomechanical lattices experiment . . . . .	190
8.27	Data analysis of the ringdown traces . . . . .	192
8.28	Measurement of optomechanical coupling rate in the optomechanical array . .	195
9.1	Principle of a cryogenic electro-optical interconnect for readout of supercon- ducting devices . . . . .	200
9.2	Cryogenic characterization of a LiNbO <sub>3</sub> phase modulator . . . . .	202
9.3	Electro-optic readout of a coherent microwave spectrum of a superconducting electromechanical system . . . . .	205
9.4	Electro-optic readout of an incoherent microwave spectrum of a superconduct- ing electromechanical system . . . . .	207
9.5	Illustration of the gain characterization procedure . . . . .	209
9.6	Schematic signal flow when pre-amplifier is used in electro-optical conversion.	209
9.7	Heat dissipation and temperature gradients . . . . .	210
10.1	Gravitational induced time-shift ambiguity in massive mechanical superposition states . . . . .	212
10.2	Integration of electromechanical device with superconducting qubits . . . . .	213
10.3	Collective dynamics in superconducting circuit optomechanical chains . . . .	214
A.1	High temperature aluminum deposition . . . . .	218
A.2	Effect of annealing on the aluminum stress . . . . .	219
A.3	Broken clamps and yield stress. . . . .	220
A.4	Sapphire substrate processing . . . . .	222
B.1	Added noise in electro-optic phase modulation . . . . .	225

# List of Tables

3.1	Scaling rules in drum-head capacitor based circuit optomechanics. . . . .	42
4.1	CMP optimized parameters . . . . .	61
5.1	Cold attenuation setup . . . . .	86
7.1	The comparison of the longest measured mechanical quantum state lifetime in various platforms. . . . .	123
7.2	System parameters . . . . .	126
7.3	Full characterization data of different resonances in a chip. . . . .	146
8.1	Infidelities between different subsequent normalization methods . . . . .	168
8.2	Infidelities between the measured modes and the theoretical ones . . . . .	169
8.3	1D hybridized cavity modes parameters . . . . .	193
8.4	1D mechanical modes parameters . . . . .	193
8.5	2D hybridized cavity modes parameters . . . . .	193
8.6	2D mechanical modes parameters . . . . .	193
A.1	High temperature aluminum sputtering . . . . .	217

# 1 Introduction

The light-matter interaction has always been a substantial question for scientists for hundreds of years. It has been vastly studied both within the classical framework of electromagnetic fields and the quantum mechanical description of light interacting with a medium. Although the effect of materials on electromagnetic waves such as absorption, scattering, refraction, and nonlinearities had been deeply understood in the 18th and 19th centuries, the action of light on materials, specifically mechanical objects had only been explored in the middle of the 20th century. Scientists explained the momentum transfer from light to mechanical objects (Beth, [1936](#)) and the first experiments showing laser trapping (Ashkin, [1997](#)) and laser cooling of atoms (Hänsch and Schawlow, [1975](#); Wineland and Itano, [1979](#)) have realized in the 1970s. Shortly afterward, the field of laser cooling and trapped ions flourished and resulted in several applications in modern physics and technologies. Concurrently, scientists considered the effect of electromagnetic radiation pressure on macroscopic objects - mainly suspended mirrors of a cavity for the purpose of interferometric gravitational wave detection- and explored the dynamical back-action of light (Cohadon, Heidmann, and Pinard, [1999](#)), measurement-induced noises (Braginsky, Borisovich, and Khalili, [1995](#)), and quantum limits of optomechanical detection (Braginskii and A. B. Manukin, [1977](#)) in such systems.

Mechanical oscillators can exhibit modes with ultra-low mechanical dissipation and compact form factors due to the slow velocity of acoustic waves, and are already used in applications ranging from timing to wireless filters. Over the past two decades, quantum control of mechanical systems has been firmly established, after atoms, molecules, and ions in the first wave of quantum technologies development and superconducting circuits in the second wave. The quantum control has been in particular catalyzed by cavity optomechanics (Aspelmeyer, T. J. Kippenberg, and Marquardt, [2014](#)), that uses radiation pressure coupling of mechanical oscillators to electromagnetic cavities. This coupling, already predicted in 1970 by Braginsky (V. Braginski and A. Manukin, [1967](#)) in the context of gravitational wave detection, has today been established in a host of micro- and nano-scale optomechanical systems. Laser cooling and gravitational wave interferometric detectors may be considered the two ancestors of the field of cavity optomechanics, which substantially improved our understanding of the quantum

nature of mesoscopic mechanical objects by controlling them via electromagnetic radiation pressure both in the optical and microwave domains. Cavity optomechanics emerged in the 1990s first by the theoretical works showing optomechanical feedback cooling (Mancini, Vitali, and Tombesi, 1998), nonclassical mechanical state generation (Fabre et al., 1994; Mancini and Tombesi, 1994), and quantum non-demolition measurements (Jacobs et al., 1994), followed shortly by the first experimental realizations of optical feedback cooling (Cohadon, Heidmann, and Pinard, 1999), radiation pressure self-oscillations (T. Kippenberg et al., 2005), and damping (Schliesser et al., 2006). Since then, Several experimental platforms have developed to realize cavity optomechanics, covering a wide range of length- and mass-scales, from kg scale LIGO mirrors (Whittle et al., 2021) to pico-gram and nano-meter scale optomechanical crystals (Chan, Alegre, et al., 2011). This enabled to reach a regime where the quantum nature of the optomechanical interaction becomes relevant (J. D. Teufel, Donner, Castellanos-Beltran, et al., 2009) and allowed a host of advances, including cooling mechanical systems to the ground state (J. D. Teufel, Donner, D. Li, et al., 2011; Chan, Alegre, et al., 2011), generation of entanglement between electromagnetic fields and mechanical oscillators (Palomaki, J. Teufel, et al., 2013; Barzanjeh, Redchenko, et al., 2019), quantum state transfer (Palomaki, Harlow, et al., 2013), remote entanglement of mechanical oscillators (Riedinger et al., 2018; C. Ockeloen-Korppi et al., 2018; Kotler et al., 2021), generation of squeezed mechanical states via optomechanical reservoir engineering (Wollman et al., 2015), quantum non-demolition measurement of motion (Shomroni, Qiu, et al., 2019), optomechanical induced transparency (Weis et al., 2010), and generation of squeezed light (Purdy et al., 2013). On the applied side, such optomechanical systems have been realized to create novel interfaces that convert microwave to optical fields with minimum added noise (Andrews et al., 2014; R. Delaney et al., 2022), realizing non-reciprocal microwave transmission (Bernier et al., 2017; Barzanjeh, Wulf, et al., 2017), and quantum-limited microwave directional amplification (Lépinay, Damskäg, et al., 2019).

Such mechanical oscillator-based hybrid quantum systems are today envisioned to allow advances in quantum sensing of displacement (Barzanjeh, Xuereb, et al., 2022), force, or magnetic fields, are considered as compact storage elements in quantum computing and communication (Pechal, Arrangoiz-Arriola, and Safavi-Naeini, 2018; A. Reed et al., 2017; Palomaki, Harlow, et al., 2013), and to make fundamental tests of quantum gravity (Y. Liu, Mummery, et al., 2021; Gely and G. A. Steele, 2021b), and even assist in searches for dark matter (Carney et al., 2021; Manley et al., 2021).

Although the field of cavity optomechanics experienced significant advancements in the recent decade, there are still important challenges existing on the path of maturing this platform to be practically used in quantum technologies. All the optomechanical coupling approaches share the dichotomy of using a well-isolated low-dissipation mechanical oscillator, that on the other hand requires to have sufficient coupling to an auxiliary degree of freedom, while at the same time should be coupled very weakly to a cold environment – to minimize the quantum decoherence of mechanical oscillator's state limited by both thermal decoherence and dephasing. Across all optomechanical platforms, ranging from kg-scale mirrors (Whittle

et al., 2021) to trapped particles in ultra-high vacuum (Magrini et al., 2021; Tebbenjohanns et al., 2021), or optomechanical crystals at milli-Kelvin temperatures (MacCabe et al., 2020), an enduring challenge has been to achieve low quantum decoherence. Today's opto and electro-mechanical systems, as well as systems that feature qubits coupled to mechanical oscillators, are compounded by large thermal decoherence that is typically well above 1000's of quanta per second, well above what can be achieved with the vibrations of trapped charged particles (i.e. ion traps) (Gaebler et al., 2016; Leibfried et al., 2003), resulting in much shorter quantum state storage times that can be achieved in superconducting qubits (Kono et al., 2023). One notable exception is optomechanical crystals (MacCabe et al., 2020; Chan, Safavi-Naeini, et al., 2012) – which however, suffer from strong dephasing, thereby posing again a limit on quantum decoherence again.

A particularly promising platform for quantum control is circuit optomechanics (J. D. Teufel, Donner, D. Li, et al., 2011), which operates at mK temperatures, is sideband resolved, and can be interfaced with superconducting qubits (A. Reed et al., 2017; A. Clerk et al., 2020). These circuits have been used for numerous advances including mechanical squeezing (Wollman et al., 2015; Pirkkalainen, Damskäg, et al., 2015; Lecocq, Clark, et al., 2015), entanglement (Kotler et al., 2021; C. Ockeloen-Korppi et al., 2018; Palomaki, J. Teufel, et al., 2013), non-classical state storage (A. Reed et al., 2017; Palomaki, Harlow, et al., 2013), and non-reciprocal circuits (Bernier et al., 2017). However, it has been a challenge to achieve ultra-low thermal decoherence in this platform – state-of-the-art decoherence rates are O (1 kHz) (Palomaki, Harlow, et al., 2013), which is above what e.g., laser-based quantum manipulation of trapped ions can achieve. Enhancing the quantum coherence in such systems improves the fidelity of quantum optomechanical protocols (Wallucks et al., 2020; Pechal, Arrangoiz-Arriola, and Safavi-Naeini, 2018; Gely and G. A. Steele, 2021a) and may equally benefit future tests of quantum mechanics (Fiaschi et al., 2021; Marinković et al., 2018; Gely and G. A. Steele, 2021b; Y. Liu, Mummery, et al., 2021).

In this thesis, we discuss how to meet these challenges and demonstrate a superconducting circuit optomechanical system which simultaneously realizes ultra-low quantum decoherence, while exhibiting large optomechanical coupling rates. We achieved 20 Hz thermal decoherence rate (corresponding to 130 quanta of motional heating per second) and 0.09 Hz dephasing rate, more than 100-fold improvement - and on par with trapped ions (Gaebler et al., 2016; Leibfried et al., 2003)- corresponding to a lifetime of the quantum ground state of 7.7 milli-seconds. Using the exceptionally low thermal decoherence, we showed that it is possible to attain high fidelity ground state preparation of a micro-mechanical oscillator to  $n_m = 0.07$  quanta i.e. a 93% ground state occupation, which is one of the lowest occupations reached for macroscopic mechanical oscillators to date (Whittle et al., 2021). We utilize ultra-low dephasing to prepare the micromechanical oscillator in a squeezed mechanical state (3 dB below the zero-point fluctuation) using reservoir engineering techniques.

The low quantum decoherence enables us to record for the first time the free evolution of the squeezed state, and preserve and monitor the non-classical nature of such state over a 2 ms

period of free evolution. Our measurements provide a direct snapshot of the environmental-induced decoherence of a quantum-squeezed mechanical oscillator.

Scaling optomechanical systems is another important aspect to exploit more applications in this field. Yet all optomechanical experiments -be it the optical or microwave regime, and both covering the classical and quantum regime- have consistently employed only single (or few-mode) optomechanical systems (that use at most two coupled optomechanical systems). Pioneering theoretical studies have predicted that significantly richer physics and novel dynamics can be accessed in optomechanical lattices that coupled many optomechanical systems. Numerous theoretical proposals studied collective (G. Heinrich et al., 2011; Xuereb, Genes, and Dantan, 2012) and quench (Raeisi and Marquardt, 2020) dynamics, Anderson localization (Roque et al., 2017), topological properties (Peano et al., 2015; Ren et al., 2020), quantum many-body dynamics (Ludwig and Marquardt, 2013) and entanglement (Akram et al., 2012), non-reciprocity (Sanavio, Peano, and Xuereb, 2020), reservoir engineering (Tomadin et al., 2012), and soliton generation (Gan et al., 2016) in optomechanical lattices. Viewed more broadly, multi-mode systems enable the realization of condensed matter Hamiltonians using lattice models and have been successfully explored in a variety of fields, including circuit QED, or to realize topologically protected modes (C. W. Peterson et al., 2018).

However, implementing such optomechanical lattices has not been realized to date and is a longstanding challenge. The lumped-element implementation of site-by-site engineerable optomechanical lattices is not yet realized in optical or microwave platforms due to the technical limitations in the reproducible scaling of individual building blocks. Indeed, the coupling of the optomechanical cavities has been compounded by disorder in the optical resonance frequencies or mechanical eigenfrequencies.

In this thesis, we show how to overcome this challenge to achieve large-scale configurable optomechanical lattices in microwave superconducting circuit optomechanics. This is achieved using a novel approach to create ultra-coherent, low disorder vacuum gap capacitors, from which we create both 1D and 2D coupled systems, implementing the topological Su-Schrieffer-Heeger (SSH) model (Asbóth, Oroszlány, and Pályi, 2016; Ozawa et al., 2019) model in both 1D chains and in 2D honeycomb lattices. Our approach achieves remarkably low disorder in both microwave and mechanical degrees of freedom, as evidenced by the observation of fully hybridized edge modes across an SSH chain.

As one of many novel directions, utilizing the embedded optomechanical interaction, we are able to perform direct modeshape measurement and reconstruct the full Hamiltonian, beyond the tight-binding approximations, allowing the extraction disorder and coupling strength to higher-order sites. Such optomechanical mode shape measurements are therefore equally able to overcome the experimental challenge of eigenmode measurement in large-scale multimode superconducting circuits as a platform for quantum simulation and many-body physics studies, where only indirect approaches were performed by near field scanning probes (Underwood et al., 2016), laser scanning microscopy (H. Wang et al., 2019; Morvan



et al., 2021), or dispersive coupling to qubits (Kim et al., 2021).

The last topic we discuss in this thesis is cryogenic electro-optical interconnects. Although quantum control of ions, atoms, and molecules has already been achieved in the '90s, the developments of superconducting circuits have led to a scalable platform for quantum computing that culminated in the first proof-of-principle computation (Arute et al., 2019) that on a classical computer takes many orders of magnitude more time—even on the fastest supercomputers. While technologically there is still a major gap to bridge, and likely decades will have to pass before quantum computing can perform (if ever at all) actual programmed algorithms, the field itself has already captured the interest across a wide range of disciplines. Underlying these advances are Josephson junctions, nature's most profound nonlinear element. In contrast to atoms and ions, these systems can be microfabricated on chip, controlled at the quantum level with electrical control lines, and are actively pursued by all large actors in quantum computing (IBM, Google). They have achieved some of the most remarkable quantum measurements to date, such as resolving single photons of the microwave field (Schuster et al., 2007), or synthesizing arbitrary quantum states (Hofheinz et al., 2009).

Despite these promising virtues however, scaling up those systems in the number of qubits faces unique challenges. Chief among them is the coherence and scaling of superconducting circuits. In this context, one future challenge is becoming progressively obvious: the massive transfer of control signals both into and out of the dilution refrigerator to control hundreds of qubits. Superconducting qubits operate at 10 mK -where only quantum fluctuations of the microwave field dominate the noise- and have to be carefully shielded. Currently, the workhorse to control and readout qubits is dispersive readout via microwave cavities, using copper alloys (CuNi) coaxial cables and cryogenic high electron mobility transistors (HEMTs) as readout amplifiers. These, however, induce a substantial heat load within the cryogenic system. Already today, the most advanced superconducting experiments have many dozens of control lines, each contributing a major thermal load from the room temperature environment. With the increasing number of qubits, this problem poses in the long term a major challenge, as it requires dilution refrigerators with higher cooling power and more space. This problem is compounded by the fact that improvements in qubit coherence make the devices more susceptible to thermal fluctuations and noise from the higher temperature stages.

Such considerations are not new to other fields of technology: e.g. data center optical interconnects. Data centers have seen over the past decades a remarkable development. Initially based on electrical cables to transfer data between server racks, the massive increase in data rates and power consumption (Jones et al., 2018) as well as the sheer size of cables, has led to the deployment of optical fiber transceivers. First developed in the early 2000s, fiber optic interconnects based on silicon photonics are now commercial reality, and used in any data center. While the importance of fiber optical interconnects is both undisputed and omnipresent in data centers, and they are poised in the future to even replace on-board chip to chip communication, the use of fiber optical interconnects in cryogenic superconducting technology has not been considered, and is in its infancy.

In this thesis, we also demonstrate the first proof-of-concept cryogenic electro-optical interconnect experiment that can serve as a blueprint for future development and that clearly demonstrates the potential of the approach. While the noise figures we achieve in our experiment are presently far from those of commercial HEMT amplifiers, the advances in integrated electro-optics that are underway (e.g. thin film LNOI (Zhang et al., 2019)) can significantly improve the required switching voltages to levels where they outperform HEMT. Remarkably, the presently achieved parameters are well within reach, indicating that cryogenic optical interconnects for superconducting circuits can become a reality.

Specifically, we demonstrate that microwave drive lines can be replaced with optical fibers and the HEMT with a commercial Titanium-doped optical  $\text{LiNbO}_3$  phase modulator, thereby implementing an electro-optic interconnect transducing the weak microwave signals from a superconducting system into the optical domain. While modulators are the workhorse of telecommunications—and presently experience rapid advancement with integrated devices that operate at only CMOS voltage levels—there are hardly any experiments that have explored their low-temperature behavior. In our work, we demonstrate that we can operate state-of-the-art  $\text{LiNbO}_3$  phase modulators for the first time at 800mK -a temperature that is below the base temperature for HEMT amplifiers. Specifically, we characterized the phase modulator at 800mK and performed a cryogenic 5 GBaud/s data communication experiment. This operation temperature is below the 3K operational temperature of HEMT amplifiers, and we importantly reveal that heating via laser absorption is marginal.

To illustrate the potential for superconducting circuitry we use the electro-optical cryogenic optical interconnect to read out a superconducting microwave optomechanical system at a base temperature of 15mK. We implement direct optical detection of such systems for the first time. The major advantages of our approach are the substantially smaller heat load due to three orders of magnitude lower thermal conductivity of the fiber, and the possibility to transduce at lower temperature, introducing less thermal noise in the output. We performed coherent spectroscopy of the device, observing optomechanically induced transparency (Weis et al., 2010; Safavi-Naeini, Alegre, et al., 2011), and compared the readout to conventional HEMT. Importantly we are able to resolve fine, Hertz level features of the superconducting device, which are below the linewidth of the laser employed. Equally important, we also performed incoherent spectroscopy of the output signal and investigated the noise figure of this method experimentally. We show that with a half voltage of 10 mV the approach can outcompete HEMT amplifiers in their noise figure—a value that is feasible considering recent advances in the efficiency (half-voltage) of optical modulators using thin film integrated lithium niobate modulator technology<sup>6</sup> or novel materials with very high Pockels coefficient.

The structure of the thesis in the next chapters is as follows. In the second chapter, We review the basic theoretical framework of cavity optomechanics and provide deep theoretical discussions on optomechanical sideband cooling in the presence of additional probes as well as a novel calibration-free mechanical occupation measurement technique. In the same chapter, we introduce multi-mode optomechanics and discuss how to probe collective microwave

mode shapes using optomechanical interaction in arrays and lattices. In Chapter 3, we discuss the design principles and simulations for optomechanical devices. Chapter 4 comprehensively shows the novel nano-fabrication process we developed to fabricate ultra-coherent and scalable circuit optomechanical systems. In the next chapter, we review all experimental techniques including cryogenics and microwave measurements required to conduct the experiments. In Chapter 6, we show how to characterize the mechanical and microwave properties of a circuit optomechanical device. Chapter 7 is focusing on the ultra-coherent optomechanical project, followed by Chapter 8 discussing the multi-mode optomechanical project and the observation of non-trivial topological properties in 1D and 2D lattices. Chapter 9 presents the cryogenic electro-optical project. the last Chapter is concluding the results and provides an overview of potential future projects and the outlook.

## 2 Theory

In this chapter, we briefly review the theoretical background of quantum optomechanics in the first section. In the second section, we discuss in detail the theoretical treatment of multi-tone optomechanical cooling and sideband asymmetry. In the third section, we discuss optomechanical amplification and finally, in section 4, we show the theory of multi-mode optomechanics and optomechanical modeshape measurement.

### 2.1 Basics of optomechanics

The aim of this section is not to comprehensively review the field of optomechanics but to provide the necessary tools to understand the results and discussions in the next two sections of multi-tone optomechanical cooling, optomechanical amplification, and multi-mode optomechanics. However, we refer the readers who are interested in thoroughly step-by-step analyzing the theory of quantum optomechanics and understanding different optomechanical phenomena to the nicely written textbook by W. Bowen and G. Milburn (Bowen and Milburn, 2015). Along with the textbook, the precious review article on cavity optomechanics (Aspelmeyer, T. J. Kippenberg, and Marquardt, 2014) discusses the advancements in the field on both experimental and theoretical aspects at a higher level and introduces different platforms for realizing optomechanical systems. Cavity optomechanics is studying the interaction be-

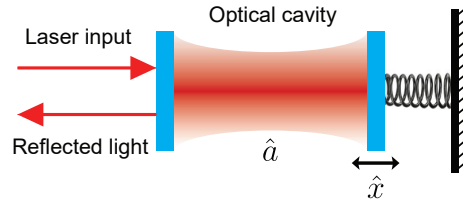


Figure 2.1: **Cavity optomechanics.** A simple example of an optomechanical system consists of an optical Fabry–Pérot cavity with a mechanically compliant mirror that can modify the cavity frequency. The system can be derived through the fixed semi-transparent mirror by an incident laser field.

tween an electromagnetic (Optical or microwave) cavity and a mechanical oscillator. A famous conceptual example of such interaction is a Fabry–Pérot optical cavity consisting of a fixed mirror and a mechanically compliant mirror, which has a mass and is connected to a spring forming a mechanical harmonic oscillator (Fig. 2.1). The optical cavity can be derived by an external laser field coupled through the fixed mirror into the cavity. The mechanical resonator can modulate the resonance frequency of the optical cavity and consequently the output signal. On the other hand, this interaction allows manipulating the mechanical oscillator through incident electromagnetic radiation pressure on the mirror. The Hamiltonian of this system can be written as the sum of the optical energy (photons in the cavity), the mechanical energy (phonons in the oscillator), and the external drive term:

$$\hat{H} = \hbar\omega_c(x)\hat{a}^\dagger\hat{a} + \hbar\Omega_m\hat{b}^\dagger\hat{b} + i\hbar\bar{s}\sqrt{\kappa_{\text{ex}}}\left(e^{i\omega_L t}\hat{a}^\dagger - e^{-i\omega_L t}\hat{a}\right), \quad (2.1)$$

where  $\omega_c(x)$  is the optical cavity frequency as a function of the mirror's position,  $\Omega_m$  is the mechanical frequency of the oscillator,  $\hat{a}$  and  $\hat{b}$  are annihilation operators for optical and mechanical mode,  $\bar{s}$  and  $\omega_L$  are the amplitude and frequency of the drive laser, and  $\kappa_{\text{ex}}$  is the external coupling rate of the optical cavity. Considering the first-order perturbation in the cavity frequency -small vibration amplitudes of the mirror compared with the optical linewidth- we can approximate  $\omega_c(x) = \omega_c - G\hat{x}$ , where  $\hat{x} = x_{\text{ZPF}}(\hat{b} + \hat{b}^\dagger)$  and  $G = -\frac{d\omega_c(x)}{dx}$ . We note that we neglected constant terms corresponding to ground state energies ( $\hbar\omega_c/2$  and  $\hbar\Omega_m/2$ ).

We can re-write Eq. 2.1 in the rotating frame with the drive's frequency by applying a parameter replacement ( $\hat{a} \rightarrow e^{-i\omega_L t}\hat{a}$ ):

$$\hat{H} = -\hbar\Delta\hat{a}^\dagger\hat{a} + \hbar\Omega_m\hat{b}^\dagger\hat{b} + \hbar g_0\hat{a}^\dagger\hat{a}(\hat{b}^\dagger + \hat{b}) + i\hbar\bar{s}\sqrt{\kappa_{\text{ex}}}\left(\hat{a}^\dagger - \hat{a}\right), \quad (2.2)$$

where  $\Delta = \omega_L - \omega_c$  is the drive detuning from the cavity resonance frequency, and  $g_0 = x_{\text{ZPF}}G$  is the optomechanical single-photon coupling rate.

We are often interested in the small signal response of the system therefore we can expand the optical annihilation operator around its steady-state solutions and linearize the Hamiltonian. We decompose the annihilation operator as  $\hat{a} = \bar{a} + \delta\hat{a}$ , where  $|\bar{a}|^2 = n_p$  is the amplitude of the coherent intracavity field induced by pump ( $n_p$  is the intracavity photon number), and  $\delta\hat{a}$  is the annihilation operator of the cavity field fluctuations around the coherent response. Neglecting the zeroth order terms, we achieve the linearized optomechanical interaction Hamiltonian:

$$\hat{H}_{\text{int}} = \hbar g(\delta\hat{a}^\dagger + \delta\hat{a})(\hat{b}^\dagger + \hat{b}), \quad (2.3)$$

where  $g = g_0\sqrt{n_p}$  is the cavity-enhanced optomechanical coupling rate.

Now we can drive Quantum Langevin equations to describe the dynamics of optical field and mechanical motion quadratures. We define two quadratures of optical field as  $\hat{I} = \frac{1}{\sqrt{2}}(\hat{a} + \hat{a}^\dagger)$

and  $\hat{Q} = \frac{1}{\sqrt{2}i}(\hat{a} - \hat{a}^\dagger)$ , and mechanical quadratures as  $\hat{X} = \frac{1}{\sqrt{2}}(\hat{b} + \hat{b}^\dagger)$  and  $\hat{P} = \frac{1}{\sqrt{2}i}(\hat{b} - \hat{b}^\dagger)$ . The Langevin equations are derived as:

$$\begin{aligned}\dot{\hat{I}} &= \Delta \hat{Q} - \kappa/2 \hat{I} + \sqrt{\kappa_{\text{ex}}} \hat{I}_{\text{ex}} + \sqrt{\kappa_0} \hat{I}_0, \\ \dot{\hat{Q}} &= -\Delta \hat{I} - \kappa/2 \hat{Q} - 2g \hat{X} + \sqrt{\kappa_{\text{ex}}} \hat{Q}_{\text{ex}} + \sqrt{\kappa_0} \hat{Q}_0, \\ \dot{\hat{X}} &= \Omega_m \hat{P} - \Gamma_m/2 \hat{X} + \sqrt{\Gamma_m} \hat{X}_0, \\ \dot{\hat{P}} &= -\Omega_m \hat{X} - \Gamma_m/2 \hat{P} - 2g \hat{I} + \sqrt{\Gamma_m} \hat{P}_0,\end{aligned}\tag{2.4}$$

where  $\kappa_0$  is the intrinsic loss rate of the cavity,  $\kappa = \kappa_{\text{ex}} + \kappa_0$  is the total cavity linewidth, and  $I_0$  and  $I_{\text{ex}}$  are the intrinsic thermal bath noise operator and external drive noise operators respectively for quadrature  $I$ . The same notation of noise operators is used for other quadratures. Dynamical equations (Eqs. 2.4) combined with input-output theory can explain basic optomechanical effects such as optomechanical damping, anti-damping, ponderomotive squeezing, etc. In the following we focus on the theoretical derivation of multi-tone optomechanical cooling and multi-mode optomechanics.

## 2.2 Multi-tone optomechanical cooling and sideband asymmetry

In this section, we provide a detailed theory for continuous-wave multi-tone optomechanical cooling and show how optomechanical sideband asymmetry can be used to characterize mechanical occupation.

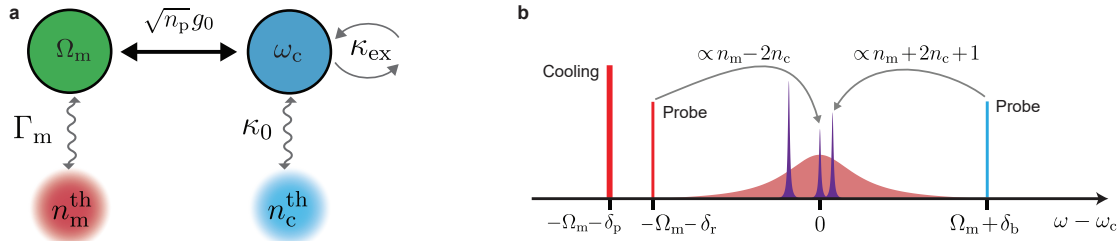


**Figure 2.2: Optomechanical sideband cooling and sideband asymmetry.** **a**, Mode diagram of an optomechanical system when driving the microwave cavity with  $n_p$  intracavity pump photon numbers. Mechanical and microwave modes are coupled to their thermal baths. **b**, Frequency scheme of pumps and probes in a sideband asymmetry and optomechanical cooling experiment.

Here we discuss the theory of optomechanical sideband cooling in the presence of a cooling pump and two additional probes used in a sideband asymmetry experiment. As schematically shown in Fig. 2.2, to extract the mechanical occupation in our experiments, we pump our device with three microwave tones simultaneously: cooling pump, red probe, and blue probe. The cooling pump is red-detuned from the cavity and has relatively higher power compared to those of the red and blue probes. The red and blue probes have a balanced power in a way that their effective dynamical back-actions are canceled out of each other. Although the

expressions for sideband cooling have been already derived in prior works considering one or two tones (Weinstein et al., 2014), the cavity response was considered to be flat around the cavity frequency, and two probes were considered symmetrically detuned from the cavity. In our actual experiment, the pump and probes have asymmetric detuning with respect to the cavity; hence, it is required to derive the full expressions without assuming a flat cavity and by considering arbitrary detunings. Nevertheless, We report the simplified expressions assuming the flat cavity approximation at the end of this section.

The Langevin equations of an optomechanical system in the presence of the three microwave tones are given by

$$\begin{aligned}\frac{d\hat{a}}{dt} &= -\frac{\kappa}{2}\hat{a} - ig_0(\hat{b} + \hat{b}^\dagger)\hat{a} + \sqrt{\kappa_0}\hat{a}_0^{\text{in}}(t) \\ &\quad + \sqrt{\kappa_{\text{ex}}}\left(\alpha_b e^{-i(\Omega_m + \delta_b)t} + \alpha_r e^{+i(\Omega_m + \delta_r)t} + \alpha_p e^{+i(\Omega_m + \delta_p)t} + \hat{a}_{\text{ex}}^{\text{in}}(t)\right), \\ \frac{d\hat{b}}{dt} &= -i\Omega_m\hat{b} - \frac{\Gamma_m}{2}\hat{b} - ig_0\hat{a}^\dagger\hat{a} + \sqrt{\Gamma_m}\hat{b}_0^{\text{in}}(t),\end{aligned}\tag{2.5}$$

where  $\hat{a}(\hat{b})$  is the annihilation operator for the microwave cavity (mechanical oscillator),  $g_0$  is the single photon optomechanical coupling rate,  $\kappa_{\text{ex}(0)}$  is the microwave external coupling (internal loss) rate,  $\Gamma_m$  is the mechanical intrinsic damping rate,  $\hat{a}_0^{\text{in}}(\hat{b}_0^{\text{in}})$  is the noise operator for the intrinsic loss of the microwave cavity (mechanical oscillator), and  $\hat{a}_{\text{ex}}^{\text{in}}$  is the noise operator for the external field. Furthermore,  $\alpha_{p,r,b}$  denotes the coherent amplitude of the cooling pump with a detuning of  $\Delta_p = -\Omega_m - \delta_p$ , the red probe with a detuning of  $\Delta_r = -\Omega_m - \delta_r$ , and the blue probe with a detuning of  $\Delta_b = +\Omega_m + \delta_b$ , respectively. Note that the Langevin equation for the cavity is described in the rotating frame of the cavity frequency ( $\omega_c$ ). The noise operator correlations satisfy the thermal distribution:

$$\begin{aligned}\langle \hat{b}_0^{\text{in}\dagger}(t)\hat{b}_0^{\text{in}}(t') \rangle &= n_m^{\text{th}}\delta(t-t'), \\ \langle \hat{b}_0^{\text{in}}(t)\hat{b}_0^{\text{in}\dagger}(t') \rangle &= (n_m^{\text{th}} + 1)\delta(t-t'), \\ \langle \hat{a}_0^{\text{in}\dagger}(t)\hat{a}_0^{\text{in}}(t') \rangle &= n_c^{\text{th}}\delta(t-t'), \\ \langle \hat{a}_0^{\text{in}}(t)\hat{a}_0^{\text{in}\dagger}(t') \rangle &= (n_c^{\text{th}} + 1)\delta(t-t'), \\ \langle \hat{a}_{\text{ex}}^{\text{in}\dagger}(t)\hat{a}_{\text{ex}}^{\text{in}}(t') \rangle &= 0, \\ \langle \hat{a}_{\text{ex}}^{\text{in}}(t)\hat{a}_{\text{ex}}^{\text{in}\dagger}(t') \rangle &= \delta(t-t'),\end{aligned}\tag{2.6}$$

where  $n_m^{\text{th}}(n_c^{\text{th}})$  is the mechanical (cavity) thermal bath occupation. We can safely assume that the waveguide of the input-output line is in the ground state. This can be experimentally verified and will be discussed in Sec. 6.4 and Sec. 7.3.2.

To solve the equations, we first divide the cavity field into coherent amplitudes and fluctuation, i.e.,  $\hat{a}(t) \rightarrow \bar{a}_b e^{-i(\Omega_m + \delta_b)t} + \bar{a}_r e^{+i(\Omega_m + \delta_r)t} + \bar{a}_p e^{+i(\Omega_m + \delta_p)t} + \hat{a}(t)$ , where  $\bar{a}_{p,r,b}$  is the coherent amplitude induced by the cooling pump, red probe, and blue probe, respectively, and  $\hat{a}(t)$  is

the fluctuation. Considering sufficiently small  $g_0$  compared to the other cavity parameters, we can find approximated solutions for the coherent amplitudes:

$$\begin{aligned}\bar{a}_b &\simeq \frac{\sqrt{\kappa_{\text{ex}}}}{-i(\Omega_m + \delta_b) + \kappa/2} \alpha_b, \\ \bar{a}_{r,p} &\simeq \frac{\sqrt{\kappa_{\text{ex}}}}{+i(\Omega_m + \delta_{r,p}) + \kappa/2} \alpha_{r,p},\end{aligned}\tag{2.7}$$

where we can assume that the coherent amplitudes are real without loss of generality.

By linearizing the nonlinear optomechanical coupling terms in the Langevin equations (Eq. (2.5)) around the coherent amplitudes and going into the rotating frame of the mechanical oscillator ( $\hat{b} \rightarrow \hat{b}e^{-i\Omega_m t}$ ), we have

$$\begin{aligned}-ig_0\hat{a}^\dagger\hat{a} &= -ig_0\left\{\left(\bar{a}_r^*e^{-i(\Omega_m+\delta_r)t} + \bar{a}_p^*e^{-i(\Omega_m+\delta_p)t}\right)\hat{a} + \left(\bar{a}_b e^{-i(\Omega_m+\delta_b)t}\right)\hat{a}^\dagger\right\} \\ &\quad -ig_0\left\{\left(\bar{a}_r e^{+i(\Omega_m+\delta_r)t} + \bar{a}_p e^{+i(\Omega_m+\delta_p)t}\right)\hat{a}^\dagger + \left(\bar{a}_b^* e^{+i(\Omega_m+\delta_b)t}\right)\hat{a}\right\}, \\ -ig_0(\hat{b} + \hat{b}^\dagger)\hat{a} &= -ig_0\left\{\left(\bar{a}_r e^{+i\delta_r t} + \bar{a}_p e^{+i\delta_p t}\right)\hat{b} + \left(\bar{a}_b e^{-i\delta_b t}\right)\hat{b}^\dagger\right\} \\ &\quad -ig_0\left\{\left(\bar{a}_b e^{-i(2\Omega_m+\delta_b)t}\right)\hat{b} + \left(\bar{a}_r e^{+i(2\Omega_m+\delta_r)t} + \bar{a}_p e^{+i(2\Omega_m+\delta_p)t}\right)\hat{b}^\dagger\right\}.\end{aligned}\tag{2.8}$$

By neglecting the fast oscillating terms using the rotating wave approximation, Eq. (2.8) can be simplified as

$$\begin{aligned}-ig_0\hat{a}^\dagger\hat{a} &\simeq -ig_0\left\{\left(\bar{a}_r^*e^{-i(\Omega_m+\delta_r)t} + \bar{a}_p^*e^{-i(\Omega_m+\delta_p)t}\right)\hat{a} + \left(\bar{a}_b e^{-i(\Omega_m+\delta_b)t}\right)\hat{a}^\dagger\right\}, \\ -ig_0(\hat{b} + \hat{b}^\dagger)\hat{a} &\simeq -ig_0\left\{\left(\bar{a}_r e^{+i\delta_r t} + \bar{a}_p e^{+i\delta_p t}\right)\hat{b} + \left(\bar{a}_b e^{-i\delta_b t}\right)\hat{b}^\dagger\right\}.\end{aligned}\tag{2.9}$$

Thus, we have the linearized Langevin equations:

$$\begin{aligned}\frac{d\hat{a}}{dt} &= -\frac{\kappa}{2}\hat{a} - i\left\{\left(g_r e^{+i\delta_r t} + g_p e^{+i\delta_p t}\right)\hat{b} + \left(g_b e^{-i\delta_b t}\right)\hat{b}^\dagger\right\} + \sqrt{\kappa_{\text{ex}}}\hat{a}_{\text{ex}}^{\text{in}}(t) + \sqrt{\kappa_0}\hat{a}_0^{\text{in}}(t), \\ \frac{d\hat{b}}{dt} &= -\frac{\Gamma_m}{2}\hat{b} - i\left\{\left(g_r e^{-i\delta_r t} + g_p e^{-i\delta_p t}\right)\hat{a} + \left(g_b e^{-i\delta_b t}\right)\hat{a}^\dagger\right\} + \sqrt{\Gamma_m}\hat{b}_0^{\text{in}}(t),\end{aligned}\tag{2.10}$$

where  $g_{p,r,b} = g_0\bar{a}_{p,r,b}$  is the linearized optomechanical coupling rate. Then, we take the Fourier transform of the time derivative equations, leading to

$$\begin{aligned}-i\omega\hat{a}(\omega) &= -\frac{\kappa}{2}\hat{a}(\omega) - i\left\{\left(g_r\hat{b}(\omega + \delta_r) + g_p\hat{b}(\omega + \delta_p)\right) + \left(g_b\hat{b}^\dagger(-(\omega - \delta_b))\right)\right\} \\ &\quad + \sqrt{\kappa_{\text{ex}}}\hat{a}_{\text{ex}}^{\text{in}}(\omega) + \sqrt{\kappa_0}\hat{a}_0^{\text{in}}(\omega), \\ -i\omega\hat{b}(\omega) &= -\frac{\Gamma_m}{2}\hat{b}(\omega) - i\left\{\left(g_r\hat{a}(\omega - \delta_r) + g_p\hat{a}(\omega - \delta_p)\right) + \left(g_b\hat{a}^\dagger(-(\omega - \delta_b))\right)\right\} + \sqrt{\Gamma_m}\hat{b}_0^{\text{in}}(\omega),\end{aligned}\tag{2.11}$$



where

$$\begin{aligned}\hat{b}(\omega) &\equiv \mathcal{F}\{\hat{b}(t)\} = \frac{1}{\sqrt{2\pi}} \int_{-\infty}^{+\infty} \hat{b}(t) e^{i\omega t} dt, \\ \hat{b}(t) &= \mathcal{F}^{-1}\{\hat{b}(\omega)\} = \frac{1}{\sqrt{2\pi}} \int_{-\infty}^{+\infty} \hat{b}(\omega) e^{-i\omega t} d\omega, \\ \hat{b}^\dagger(\omega) &= (\mathcal{F}\{\hat{b}(t)\})^\dagger.\end{aligned}\tag{2.12}$$

By substituting  $\hat{a}(\omega)$  into  $\hat{b}(\omega)$  in Eq. (2.11), we obtain

$$\begin{aligned}\frac{\hat{b}(\omega)}{\chi_m} &= -\left(\chi_r g_r^2 + \chi_p g_p^2 - \chi_b g_b^2\right) \hat{b}(\omega) + \\ &\quad -i g_r \sqrt{\kappa_{\text{ex}}} \chi_r \hat{a}_{\text{ex}}^{\text{in}}(\omega - \delta_r) - i g_r \sqrt{\kappa_0} \chi_r \hat{a}_0^{\text{in}}(\omega - \delta_r) \\ &\quad -i g_p \sqrt{\kappa_{\text{ex}}} \chi_p \hat{a}_{\text{ex}}^{\text{in}}(\omega - \delta_p) - i g_p \sqrt{\kappa_0} \chi_p \hat{a}_0^{\text{in}}(\omega - \delta_p) \\ &\quad -i g_b \sqrt{\kappa_{\text{ex}}} \chi_b \hat{a}_{\text{ex}}^{\text{in}\dagger}(-(\omega - \delta_b)) - i g_b \sqrt{\kappa_0} \chi_b \hat{a}_0^{\text{in}\dagger}(-(\omega - \delta_b)) \\ &\quad + \sqrt{\Gamma_m} \hat{b}_0^{\text{in}}(\omega) \\ &\quad - \chi_r \left\{ g_r g_p \hat{b}(\omega + \delta_p - \delta_r) + g_r g_b \hat{b}^\dagger(-\omega + \delta_b + \delta_r) \right\} \\ &\quad - \chi_p \left\{ g_p g_r \hat{b}(\omega + \delta_r - \delta_p) + g_p g_b \hat{b}^\dagger(-\omega + \delta_b + \delta_p) \right\} \\ &\quad + \chi_b \left\{ g_b g_r \hat{b}^\dagger(-\omega + \delta_b + \delta_r) + g_b g_p \hat{b}^\dagger(-\omega + \delta_b + \delta_p) \right\},\end{aligned}\tag{2.13}$$

where  $\chi_p^{-1}(\omega) = -i(\omega - \delta_p) + \kappa/2$ ,  $\chi_r^{-1}(\omega) = -i(\omega - \delta_r) + \kappa/2$ ,  $\chi_b^{-1}(\omega) = -i(\omega - \delta_b) + \kappa/2$ , and  $\chi_m^{-1}(\omega) = -i\omega + \Gamma_m/2$  are optical and mechanical susceptibilities.

As long as the coupling rates are small compared to detuning, i.e.,  $|\chi_i g_i g_{j \neq i}| \simeq \sqrt{\Gamma_{\text{opt}}^i \Gamma_{\text{opt}}^{j \neq i}}/2 \ll |\delta_i \pm \delta_{j \neq i}|$ , where  $\Gamma_{\text{opt}}^k = 4g_k^2/\kappa$  is the optomechanical damping rate induced by each microwave drive and  $i, j, k \in \{r, b, p\}$ , we can safely neglect the terms for the mechanical annihilation operator with the detuning ( $\delta_{p,r,b}$ ) and find a solution with respect to  $\hat{b}(\omega)$ :

$$\begin{aligned}\frac{\hat{b}(\omega)}{\chi_{\text{eff}}} &\simeq -i g_p (\sqrt{\kappa_0} \chi_p \hat{a}_0^{\text{in}}(\omega - \delta_p) + \sqrt{\kappa_{\text{ex}}} \chi_p \hat{a}_{\text{ex}}^{\text{in}}(\omega - \delta_p)) \\ &\quad -i g_r (\sqrt{\kappa_0} \chi_r \hat{a}_0^{\text{in}}(\omega - \delta_r) + \sqrt{\kappa_{\text{ex}}} \chi_r \hat{a}_{\text{ex}}^{\text{in}}(\omega - \delta_r)) \\ &\quad -i g_b (\sqrt{\kappa_0} \chi_b \hat{a}_0^{\text{in}\dagger}(-(\omega - \delta_b)) + \sqrt{\kappa_{\text{ex}}} \chi_b \hat{a}_{\text{ex}}^{\text{in}\dagger}(-(\omega - \delta_b))) \\ &\quad + \sqrt{\Gamma_m} \hat{b}_0^{\text{in}}(\omega)\end{aligned}\tag{2.14}$$

where  $\chi_{\text{eff}}^{-1} = \chi_m^{-1} + \chi_p g_p^2 + \chi_r g_r^2 - \chi_b g_b^2$  is the effective mechanical susceptibility. Using Wiener–Khinchin theorem and correlation relations in Eq. (2.6), the power spectral density of the mechanics is

calculated as

$$\begin{aligned}
 S_{\hat{b}\hat{b}}(\omega) &= |\chi_{\text{eff}}|^2 \left( \left( g_p^2 |\chi_p|^2 (\kappa_0 n_c^{\text{th}}) + \Gamma_m n_m^{\text{th}} \right) + \left( g_r^2 |\chi_r|^2 (\kappa_0 n_c^{\text{th}}) + g_b^2 |\chi_b|^2 (\kappa_0 n_c^{\text{th}} + \kappa) \right) \right) \\
 &\simeq \frac{\Gamma_{\text{tot}}}{|(I_{\text{opt}}^p + I_{\text{opt}}^r - I_{\text{opt}}^b)/2 + (1 - i2\omega/\kappa)(\Gamma_m/2 - i\omega)|^2} \\
 &\quad \times \left( \frac{I_{\text{opt}}^p n_c + \Gamma_m (1 + \frac{4\omega^2}{\kappa^2}) n_m^{\text{th}}}{\Gamma_{\text{tot}}} + \frac{I_{\text{opt}}^r n_c + I_{\text{opt}}^b (n_c + 1)}{\Gamma_{\text{tot}}} \right). \tag{2.15}
 \end{aligned}$$

Here, we approximate  $\chi_p/\chi_0 \simeq \chi_b/\chi_0 \simeq \chi_r/\chi_0 \simeq 1$ , where  $\chi_0^{-1}(\omega) = -i\omega + \kappa/2$ , which is valid as long as the detunings are sufficiently smaller than the cavity linewidth. We also define the total mechanical damping rate as  $\Gamma_{\text{tot}} = I_{\text{opt}}^p + I_{\text{opt}}^r - I_{\text{opt}}^b + \Gamma_m$ , where  $I_{\text{opt}}^{p,r,b} = 4g_{p,r,b}^2/\kappa$  is the optomechanical damping rate induced by each microwave drive. Furthermore, we define the cavity thermal occupation as  $n_c = \kappa_0 n_c^{\text{th}}/\kappa$ , which is derived later in Eq. (2.20).

If we assume a flat cavity response around the sidebands, which is valid in the weak coupling regime  $\Gamma_{\text{tot}} \ll \kappa$ , we obtain a Lorentzian function around  $\omega = 0$  with linewidth  $\Gamma_{\text{tot}}$ , which is expressed by

$$S_{\hat{b}\hat{b}}(\omega) \simeq \frac{\Gamma_{\text{tot}}}{\omega^2 + (\Gamma_{\text{tot}}/2)^2} \left( \frac{I_{\text{opt}}^p n_c + \Gamma_m n_m^{\text{th}}}{\Gamma_{\text{tot}}} + \frac{I_{\text{opt}}^r n_c + I_{\text{opt}}^b (n_c + 1)}{\Gamma_{\text{tot}}} \right). \tag{2.16}$$

By integrating Eq. (2.16), we can calculate the steady-state phonon occupation:

$$n_m \equiv \langle \hat{b}^\dagger \hat{b} \rangle = \frac{I_{\text{opt}}^p n_c + \Gamma_m n_m^{\text{th}}}{\Gamma_{\text{tot}}} + \frac{I_{\text{opt}}^r n_c + I_{\text{opt}}^b (n_c + 1)}{\Gamma_{\text{tot}}}. \tag{2.17}$$

By increasing the cooling power, i.e. increasing  $I_{\text{opt}}^p$ , the mechanical occupation will decrease as long as the system is in the weak coupling regime, and it finally converges to  $n_c$ . We also see spurious effects induced by the blue and red probes, which are negligible as long as  $I_{\text{opt}}^b \ll I_{\text{opt}}^p$  and  $I_{\text{opt}}^{b,r} n_c \ll I_{\text{opt}}^p$ . Note that even if the cavity thermal occupation is zero, the blue probe adds an additional phonon occupation, called by a quantum back-action, which is given by  $I_{\text{opt}}^b/\Gamma_{\text{tot}}$ .

By substituting Eq. (2.14) into the first equation of Eq. (2.11), we find a solution for  $\hat{a}(\omega)$ :

$$\begin{aligned} \frac{\hat{a}(\omega)}{\chi_0} = & \sqrt{\kappa_0} \hat{a}_0^{\text{in}}(\omega) + \sqrt{\kappa_{\text{ex}}} \hat{a}_{\text{ex}}^{\text{in}}(\omega) \\ & - g_p^2 \chi_{\text{eff}}(\omega + \delta_p) \chi_p(\omega + \delta_p) (\sqrt{\kappa_0} \hat{a}_0^{\text{in}}(\omega) + \sqrt{\kappa_{\text{ex}}} \hat{a}_{\text{ex}}^{\text{in}}(\omega)) \\ & - g_r^2 \chi_{\text{eff}}(\omega + \delta_r) \chi_r(\omega + \delta_r) (\sqrt{\kappa_0} \hat{a}_0^{\text{in}}(\omega) + \sqrt{\kappa_{\text{ex}}} \hat{a}_{\text{ex}}^{\text{in}}(\omega)) \\ & + g_b^2 \chi_{\text{eff}}(\omega - \delta_b) \chi_b(\omega - \delta_b) (\sqrt{\kappa_0} \hat{a}_0^{\text{in}}(\omega) + \sqrt{\kappa_{\text{ex}}} \hat{a}_{\text{ex}}^{\text{in}}(\omega)) \\ & - i \sqrt{\Gamma_m} (g_p \chi_{\text{eff}}(\omega + \delta_p) \hat{b}_0^{\text{in}}(\omega + \delta_p) \\ & + g_r \chi_{\text{eff}}(\omega + \delta_r) \hat{b}_0^{\text{in}}(\omega + \delta_r) \\ & + g_b \chi_{\text{eff}}(\omega - \delta_b) \hat{b}_0^{\text{in}\dagger}(-(\omega - \delta_b))). \end{aligned} \quad (2.18)$$

Therefore, we can also obtain the microwave cavity thermal occupation using Eq. (2.18), where the first two terms are multiplied by only the cavity susceptibility, which has the cavity linewidth  $\kappa$ , while the other terms are multiplied by both the cavity and the mechanical susceptibilities, where the latter has a very narrow linewidth ( $\Gamma_{\text{tot}}$ ) compared to  $\kappa$ . Since the terms with the mechanical susceptibility play a minor role in the cavity thermal photon number, the power spectral density of the cavity can be simply calculated as

$$\begin{aligned} S_{\hat{a}\hat{a}}(\omega) & \simeq |\chi_0|^2 \kappa_0 n_c^{\text{th}} \\ & = \frac{\kappa}{\omega^2 + (\kappa/2)^2} \left( \frac{\kappa_0 n_c^{\text{th}}}{\kappa} \right). \end{aligned} \quad (2.19)$$

By taking the integral of the above equation, we obtain the steady-state cavity thermal occupation:

$$n_c \equiv \langle \hat{a}^\dagger \hat{a} \rangle = \frac{\kappa_0 n_c^{\text{th}}}{\kappa}. \quad (2.20)$$

The cavity thermal occupation can be interpreted as the averaged photon occupation of the intrinsic and external baths, weighted with the respective rates, where the temperature of the external bath is assumed to be zero.

Using the input-output relation for the external bath:  $\hat{a}_{\text{ex}}^{\text{out}}(\omega) = \hat{a}_{\text{ex}}^{\text{in}}(\omega) - \sqrt{\kappa_{\text{ex}}} \hat{a}(\omega)$ , we can calculate the symmetrized noise power spectral density of the output microwave field as

$$\bar{S}(\omega) = \frac{1}{2} \int_{-\infty}^{+\infty} \left\langle \hat{a}_{\text{ex}}^{\text{out}\dagger}(\omega') \hat{a}_{\text{ex}}^{\text{out}}(\omega) + \hat{a}_{\text{ex}}^{\text{out}}(\omega') \hat{a}_{\text{ex}}^{\text{out}\dagger}(\omega) \right\rangle d\omega'.$$

For simplicity, we assume that the sideband signals are well separated in the frequency space and that the linewidths of the sidebands are much smaller than the cavity linewidth, which is the case for our experiment. In this case, we can neglect the cross terms between the different

sideband signals, and describe the spectrum as  $\bar{S}(\omega) \simeq \frac{1}{2} + \bar{S}_c(\omega) + \bar{S}_p(\omega) + \bar{S}_r(\omega) + \bar{S}_b(\omega)$ , where

$$\bar{S}_c(\omega) = 4 \frac{\kappa_{\text{ex}}}{\kappa} \frac{n_c}{1 + \frac{4\omega^2}{\kappa^2}}, \quad (2.21)$$

$$\begin{aligned} \bar{S}_p(\omega) = & \frac{\kappa_{\text{ex}}}{\kappa} \frac{I_{\text{opt}}^p \Gamma_{\text{tot}}}{|(I_{\text{opt}}^p + I_{\text{opt}}^r - I_{\text{opt}}^b)/2 + (1 - i2\omega/\kappa)(\Gamma_m/2 - i(\omega + \delta_p))|^2} \left( \frac{1}{1 + \frac{4\omega^2}{\kappa^2}} \right) \left\{ \right. \\ & \frac{I_{\text{opt}}^p n_c + I_{\text{opt}}^r n_c + I_{\text{opt}}^b (n_c + 1) + \Gamma_m \left(1 + \frac{4\omega^2}{\kappa^2}\right) n_m^{\text{th}}}{\Gamma_{\text{tot}}} \\ & - \left( \left(1 - \frac{4\omega(\omega + \delta_p)}{\kappa \Gamma_{\text{tot}}}\right) (2n_c + 1) - \left(1/2 - \frac{4\omega(\omega + \delta_p)}{\kappa \Gamma_{\text{tot}}}\right) \right) \\ & \left. + \frac{I_{\text{opt}}^p + I_{\text{opt}}^r - I_{\text{opt}}^b + \Gamma_m \left(1 + \frac{4\omega^2}{\kappa^2}\right)}{2\Gamma_{\text{tot}}} \right\}, \end{aligned} \quad (2.22)$$

$$\begin{aligned} \bar{S}_r(\omega) = & \frac{\kappa_{\text{ex}}}{\kappa} \frac{I_{\text{opt}}^r \Gamma_{\text{tot}}}{|(I_{\text{opt}}^p + I_{\text{opt}}^r - I_{\text{opt}}^b)/2 + (1 - i2\omega/\kappa)(\Gamma_m/2 - i(\omega + \delta_r))|^2} \left( \frac{1}{1 + \frac{4\omega^2}{\kappa^2}} \right) \left\{ \right. \\ & \frac{I_{\text{opt}}^p n_c + I_{\text{opt}}^r n_c + I_{\text{opt}}^b (n_c + 1) + \Gamma_m \left(1 + \frac{4\omega^2}{\kappa^2}\right) n_m^{\text{th}}}{\Gamma_{\text{tot}}} \\ & - \left( \left(1 - \frac{4\omega(\omega + \delta_r)}{\kappa \Gamma_{\text{tot}}}\right) (2n_c + 1) - \left(1/2 - \frac{4\omega(\omega + \delta_r)}{\kappa \Gamma_{\text{tot}}}\right) \right) \\ & \left. + \frac{I_{\text{opt}}^p + I_{\text{opt}}^r - I_{\text{opt}}^b + \Gamma_m \left(1 + \frac{4\omega^2}{\kappa^2}\right)}{2\Gamma_{\text{tot}}} \right\}, \end{aligned} \quad (2.23)$$

$$\begin{aligned} \bar{S}_b(\omega) = & \frac{\kappa_{\text{ex}}}{\kappa} \frac{I_{\text{opt}}^b \Gamma_{\text{tot}}}{|(I_{\text{opt}}^p + I_{\text{opt}}^r - I_{\text{opt}}^b)/2 + (1 - i2\omega/\kappa)(\Gamma_m/2 - i(\omega - \delta_b))|^2} \left( \frac{1}{1 + \frac{4\omega^2}{\kappa^2}} \right) \left\{ \right. \\ & \frac{I_{\text{opt}}^p n_c + I_{\text{opt}}^r n_c + I_{\text{opt}}^b (n_c + 1) + \Gamma_m \left(1 + \frac{4\omega^2}{\kappa^2}\right) n_m^{\text{th}}}{\Gamma_{\text{tot}}} \\ & + \left( \left(1 - \frac{4\omega(\omega - \delta_b)}{\kappa \Gamma_{\text{tot}}}\right) (2n_c + 1) - \left(1/2 - \frac{4\omega(\omega - \delta_b)}{\kappa \Gamma_{\text{tot}}}\right) \right) \\ & \left. + \frac{I_{\text{opt}}^p + I_{\text{opt}}^r - I_{\text{opt}}^b + \Gamma_m \left(1 + \frac{4\omega^2}{\kappa^2}\right)}{2\Gamma_{\text{tot}}} \right\}, \end{aligned} \quad (2.24)$$

where  $\bar{S}_c$  is the noise power spectral density of the cavity thermal emission and  $\bar{S}_{p,b,r}$  is the noise power spectral density of the sideband generated by the cooling pump, red probe, and blue probe, respectively.

Here, we can further simplify the above equation by assuming a flat cavity response around

the sidebands, i.e.  $\omega/\kappa \simeq 0$ , i.e.,

$$\bar{S}_p(\omega) \simeq \frac{\kappa_{\text{ex}}}{\kappa} \frac{I_{\text{opt}}^p \Gamma_{\text{tot}}}{I_{\text{tot}}^2/4 + (\omega + \delta_p)^2} (n_m - 2n_c) \quad (2.25)$$

$$\bar{S}_r(\omega) \simeq \frac{\kappa_{\text{ex}}}{\kappa} \frac{I_{\text{opt}}^r \Gamma_{\text{tot}}}{I_{\text{tot}}^2/4 + (\omega + \delta_r)^2} (n_m - 2n_c) \quad (2.26)$$

$$\bar{S}_b(\omega) \simeq \frac{\kappa_{\text{ex}}}{\kappa} \frac{I_{\text{opt}}^b \Gamma_{\text{tot}}}{I_{\text{tot}}^2/4 + (\omega - \delta_b)^2} (n_m + 2n_c + 1). \quad (2.27)$$

The full noise power spectral density contains the three Lorentzian peak of the sidebands with a linewidth of  $\Gamma_{\text{tot}}$  with a slight frequency spacing on top of the Lorentzian peak of the cavity thermal emission with a linewidth of  $\kappa$ , which are individually accessible due to the frequency spacing among the sidebands, as well as the large linewidth difference between the sidebands and the cavity emission.

## 2.3 Optomechanical amplification

In chapter 7, to characterize the thermal decoherence of our mechanical oscillator, we use a time-domain protocol where the mechanical oscillator is first prepared in either a vacuum or squeezed state and then measured after a certain free-evolution time. When we measure the mechanical oscillator, we apply a microwave pump blue-detuned by the mechanical frequency to induce a two-mode squeezing process between the mechanical oscillator and the microwave cavity, corresponding to a phase-insensitive amplification of the mechanical quadratures. By measuring the optomechanical sideband signals induced by the pump field, we can obtain both the mechanical quadratures amplified in a nearly quantum-limited manner. This intrinsic optomechanical amplification technique was introduced by Reed *et.al.* (A. Reed et al., 2017; R. D. Delaney et al., 2019). Here, we theoretically describe the quantum measurement of the mechanical quadratures based on optomechanical amplification.

The Langevin equations of the mechanical oscillator and the microwave cavity with the blue-detuned pump are given by

$$\frac{d\hat{a}}{dt} = +i\Omega_m \hat{a} - \frac{\kappa}{2} \hat{a} - i g_b (\hat{b} + \hat{b}^\dagger) + \sqrt{\kappa_{\text{ex}}} \hat{a}_{\text{ex}}^{\text{in}}(t) + \sqrt{\kappa_0} \hat{a}_0^{\text{in}}(t) \quad (2.28)$$

$$\frac{d\hat{b}}{dt} = -i\Omega_m \hat{b} - \frac{\Gamma_m}{2} \hat{b} - i g_b (\hat{a} + \hat{a}^\dagger) + \sqrt{\Gamma_m} \hat{b}_0^{\text{in}}(t), \quad (2.29)$$

where  $g_b$  is the linearized optomechanical coupling rate. Note that the equation for the

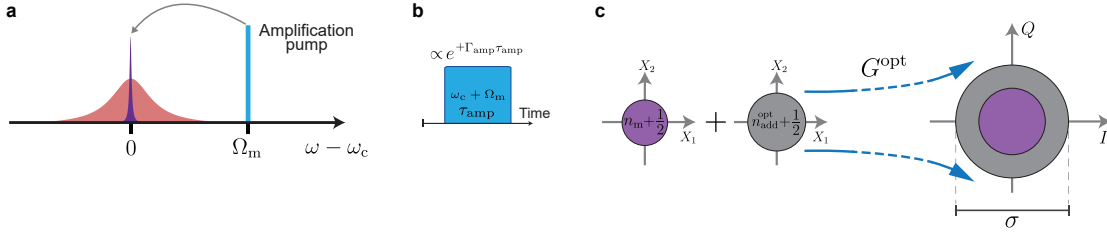


Figure 2.3: **Optomechanical amplification.** **a, b**, Frequency and pulse scheme for optomechanical amplification. **c**, Schematic diagram showing optomechanical amplification process. A desired mechanical mode to be measured is amplified intrinsically in the optomechanical system by activating two-mode-squeezing interaction between mechanics and microwave. During this phase-insensitive amplification, a constant noise is added to the state shown by  $n_{\text{add}} + \frac{1}{2}$  referred to the input.

microwave cavity is described in the rotating frame of the pump frequency. By going to the rotating frames with the respective frequencies, we have

$$\frac{d\hat{a}}{dt} = -\frac{\kappa}{2}\hat{a} - ig_b\hat{b}^\dagger + \sqrt{\kappa_{\text{ex}}}\hat{a}_{\text{ex}}^{\text{in}}(t) + \sqrt{\kappa_0}\hat{a}_0^{\text{in}}(t) \quad (2.30)$$

$$\frac{d\hat{b}}{dt} = -\frac{\Gamma_m}{2}\hat{b} - ig_b\hat{a}^\dagger + \sqrt{\Gamma_m}\hat{b}_0^{\text{in}}(t), \quad (2.31)$$

where the rotating wave approximations are applied for neglecting the fast-oscillating terms. In the parameter regime of our experiment, it can be assumed that the cavity dynamics is much faster than that of the mechanical oscillator. Using Eq. (2.30) under  $\frac{d\hat{a}}{dt} = 0$ , we can therefore obtain a quasi steady state of the microwave cavity as

$$\hat{a} = -i\frac{2g_b}{\kappa}\hat{b}^\dagger + \frac{2\sqrt{\kappa_{\text{ex}}}}{\kappa}\hat{a}_{\text{ex}}^{\text{in}}(t) + \frac{2\sqrt{\kappa_0}}{\kappa}\hat{a}_0^{\text{in}}(t). \quad (2.32)$$

By substituting Eq. (2.32) into Eq. (2.31), we have the Langevin equation of the mechanical oscillator in the optomechanical amplification process, i.e.,

$$\frac{d\hat{b}}{dt} = \frac{\Gamma_{\text{amp}}}{2}\hat{b} + \sqrt{\Gamma_m}\hat{b}_0^{\text{in}}(t) - i\sqrt{\Gamma_{\text{opt}}^b\eta_\kappa}\hat{a}_{\text{ex}}^{\text{in}\dagger}(t) - i\sqrt{\Gamma_{\text{opt}}^b(1-\eta_\kappa)}\hat{a}_0^{\text{in}\dagger}(t), \quad (2.33)$$

where  $\Gamma_{\text{amp}} = \Gamma_{\text{opt}}^b - \Gamma_m$  is the effective amplification rate,  $\Gamma_{\text{opt}}^b = 4g_b^2/\kappa$  is the optomechanical anti-damping rate, and  $\eta_\kappa = \kappa_{\text{ex}}/\kappa$  is the collection efficiency of the cavity. We can solve the derivative equation from the initial time  $t = 0$  when the blue-detuned pump field is applied, i.e.,

$$\hat{b}(t) = e^{\frac{\Gamma_{\text{amp}}t}{2}} \left[ \hat{b}(0) + \int_0^t dt' e^{-\frac{\Gamma_{\text{amp}}t'}{2}} \left( \sqrt{\Gamma_m}\hat{b}_0^{\text{in}}(t') - i\sqrt{\Gamma_{\text{opt}}^b\eta_\kappa}\hat{a}_{\text{ex}}^{\text{in}\dagger}(t') - i\sqrt{\Gamma_{\text{opt}}^b(1-\eta_\kappa)}\hat{a}_0^{\text{in}\dagger}(t') \right) \right], \quad (2.34)$$

where  $\hat{b}(t)$  is the mechanical annihilation operator at time  $t$ . By combining the solution with Eq. (2.32) and the input-output relation of the external microwave field:  $\hat{a}_{\text{ex}}^{\text{out}}(t) = \hat{a}_{\text{ex}}^{\text{in}}(t) - \sqrt{\kappa_{\text{ex}}}\hat{a}$ , we obtain the output microwave field as

$$\begin{aligned} \hat{a}_{\text{ex}}^{\text{out}}(t) = & (1 - 2\eta_{\kappa})\hat{a}_{\text{ex}}^{\text{in}}(t) - 2\sqrt{\eta_{\kappa}(1 - \eta_{\kappa})}\hat{a}_0^{\text{in}}(t) \\ & + i\sqrt{\eta_{\kappa}\Gamma_{\text{opt}}^{\text{b}}}e^{\frac{\Gamma_{\text{amp}}t}{2}} \times \\ & \left[ \hat{b}^{\dagger}(0) + \int_0^t dt' e^{-\frac{\Gamma_{\text{amp}}t'}{2}} \left( \sqrt{\Gamma_{\text{m}}}\hat{b}_0^{\text{in}\dagger}(t') + i\sqrt{\Gamma_{\text{opt}}^{\text{b}}\eta_{\kappa}}\hat{a}_{\text{ex}}^{\text{in}}(t') + i\sqrt{\Gamma_{\text{opt}}^{\text{b}}(1 - \eta_{\kappa})}\hat{a}_0^{\text{in}}(t') \right) \right]. \end{aligned} \quad (2.35)$$

In our experiment, we measure the output microwave field after the phase-insensitive amplifications. The measured microwave field can be effectively described as

$$\hat{a}_{\text{ex}}^{\text{out}'}(t) = \sqrt{G} \left[ \hat{a}_{\text{ex}}^{\text{out}}(t) + \hat{c}^{\text{in}\dagger}(t) \right], \quad (2.36)$$

where  $G$  is the total microwave gain and  $\hat{c}^{\text{in}}(t)$  is the annihilation operator of an ancillary mode describing the effective added noise of the microwave measurement chain, which is normally dominated by the HEMT amplifier noise when no pre-amplifier is used (see Sec. 5.3).

In order to maximize the signal-to-noise ratio in the measurement of the mechanical quadratures, we integrate the measured output microwave signal over a normalized matched filter function defined as  $m(t) = \sqrt{\frac{\Gamma_{\text{amp}}}{\Gamma_{\text{amp}}^{\tau} - 1}} e^{\frac{\Gamma_{\text{amp}}t}{2}}$  ( $0 \leq t \leq \tau$ ), where  $\tau$  is the final time of the integral. Note that the filter function can be complex-valued for a more general case. Namely, the time-independent complex amplitude of the output microwave field is given by

$$\hat{A} = \int_0^{\tau} dt m^*(t) \hat{a}_{\text{ex}}^{\text{out}'}(t). \quad (2.37)$$

In the large gain limit ( $e^{\Gamma_{\text{amp}}\tau} \gg 1$ ), where  $\Gamma_{\text{opt}}^{\text{b}} \gg \Gamma_{\text{m}}$  can be assumed, the microwave complex amplitude is described as

$$\begin{aligned} \hat{A} = & \sqrt{G^{\text{opt}}} \left\{ i\hat{b}^{\dagger}(0) - \sqrt{\eta_{\kappa}}\hat{a}_{\text{ex}}' - \sqrt{(1 - \eta_{\kappa})}\hat{a}_0' \right. \\ & \left. + i\sqrt{\frac{\Gamma_{\text{m}}}{\Gamma_{\text{amp}}}}\hat{b}_0'^{\dagger} + \frac{1}{\sqrt{\eta_{\kappa}e^{\Gamma_{\text{amp}}\tau}}}\hat{c}^{\dagger} + \frac{1}{\sqrt{\eta_{\kappa}e^{\Gamma_{\text{amp}}\tau}}} \left[ (1 - 2\eta_{\kappa})\hat{a}_{\text{ex}} - 2\sqrt{\eta_{\kappa}(1 - \eta_{\kappa})}\hat{a}_0 \right] \right\}, \end{aligned} \quad (2.38)$$

where  $G^{\text{opt}} = G\eta_{\kappa}e^{\Gamma_{\text{amp}}\tau}$  is the total scaling factor in the optomechanical amplification process. Here, we define time-independent convoluted annihilation operators for  $\hat{a}_{\text{ex}}^{\text{in}}$ ,  $\hat{a}_0^{\text{in}}$ ,  $\hat{b}_0^{\text{in}}$ , and  $\hat{c}^{\text{in}}$  respectively, to satisfy the bosonic commutation relations in the large gain limit, i.e.,  $\hat{O} = \int_0^{\tau} dt m^*(t) \hat{O}^{\text{in}}(t)$  and  $\hat{O}' = \frac{\Gamma_{\text{m}}^{\frac{3}{2}}}{e^{\Gamma_{\text{amp}}\tau}} \int_0^{\tau} dt \int_0^t ds e^{\Gamma_{\text{amp}}(t - \frac{s}{2})} \hat{O}^{\text{in}}(s)$ . Moreover, in order to straightforwardly convert the microwave complex amplitude to that of the mechanical oscilla-

tor, we redefine the microwave complex amplitude as  $i\hat{A}^\dagger \rightarrow \hat{A}$ , i.e.,

$$\hat{A} = \sqrt{G^{\text{opt}}} \left( \hat{b}(0) + \hat{c}_{\text{opt}}^\dagger \right), \quad (2.39)$$

where an ancillary mode effectively describing all the contributions of the added noises is defined as

$$\begin{aligned} \hat{c}_{\text{opt}} = & i\sqrt{\eta_\kappa} \hat{a}'_{\text{ex}} + i\sqrt{(1-\eta_\kappa)} \hat{a}'_0 + \sqrt{\frac{\Gamma_m}{\Gamma_{\text{amp}}}} \hat{b}'_m - \frac{i}{\sqrt{\eta_\kappa} e^{\Gamma_{\text{amp}} \tau}} \hat{c}^\dagger \\ & - \frac{i}{\sqrt{\eta_\kappa} e^{\Gamma_{\text{amp}} \tau}} \left[ (1-2\eta_\kappa) \hat{a}_{\text{ex}} - 2\sqrt{\eta_\kappa(1-\eta_\kappa)} \hat{a}_0 \right]. \end{aligned} \quad (2.40)$$

Importantly note that the first and second terms dominate the total added noise. The third term is the added noise due to the thermal decoherence of the mechanical oscillator during the amplification process, which is negligible in the large amplification rate limit, i.e.,  $\Gamma_{\text{amp}} \gg \Gamma_{\text{th}} = \Gamma_m n_m^{\text{th}}$ . The fourth term is the added noise from the microwave measurement noise, dominated by the HEMT amplifier noise for our experiment, which is also negligible when the optomechanical amplification gain is sufficiently large, i.e.  $e^{\Gamma_{\text{amp}} \tau} \gg n_{\text{add}}^{\text{H}}$ , where  $n_{\text{add}}^{\text{H}}$  is the added noise of the HEMT amplifier. The rest terms are the quantum noises for the microwave cavity, which are suppressed by the optomechanical amplification gain, and can be safely neglected. Therefore, the annihilation operator of the ancilla mode is approximated by

$$\hat{c}_{\text{opt}} \approx i\sqrt{\eta_\kappa} \hat{a}'_{\text{ex}} + i\sqrt{1-\eta_\kappa} \hat{a}'_0, \quad (2.41)$$

where the ancilla mode can be understood as the hybridized mode of the convoluted microwave external and internal noise operators.

To characterize the thermalization of mechanical vacuum or squeezed states, we need to measure the variances of the mechanical quadratures at  $t = 0$ , when the blue-detuned pump is turned on. As defined in Eq. (2.39), we are able to directly measure both the quadratures of the output microwave field. Here, the measured microwave quadratures are defined as

$$\begin{aligned} \hat{I} &= \frac{\hat{A} + \hat{A}^\dagger}{\sqrt{2}}, \\ \hat{Q} &= \frac{\hat{A} - \hat{A}^\dagger}{\sqrt{2}i}, \end{aligned} \quad (2.42)$$

while the mechanical quadratures to be measured are defined as

$$\begin{aligned} \hat{X}_1 &= \frac{\hat{b}(0) + \hat{b}^\dagger(0)}{\sqrt{2}}, \\ \hat{X}_2 &= \frac{\hat{b}(0) - \hat{b}^\dagger(0)}{\sqrt{2}i}. \end{aligned} \quad (2.43)$$



Using Eq. (2.39), the expectation value of the variance of the microwave quadratures are described as

$$\begin{aligned}\langle \hat{I}^2 \rangle &= G^{\text{opt}} \left( \langle \hat{X}_1^2 \rangle + n_{\text{add}}^{\text{opt}} + \frac{1}{2} \right), \\ \langle \hat{Q}^2 \rangle &= G^{\text{opt}} \left( \langle \hat{X}_2^2 \rangle + n_{\text{add}}^{\text{opt}} + \frac{1}{2} \right),\end{aligned}\tag{2.44}$$

where it is assumed that the ancilla mode is not initially correlated with the mechanical oscillator, while it is in the thermal state with the effective added noise, given by  $\langle \hat{c}_{\text{opt}}^\dagger \hat{c}_{\text{opt}} \rangle = n_{\text{add}}^{\text{opt}}$ . Note that when the ancilla mode is in the vacuum states, i.e.,  $n_{\text{add}}^{\text{opt}} = 0$ , the added noise becomes 1/2, which corresponds to the ideal simultaneous measurements of both the mechanical quadratures in the quantum limit. Using Eqs. (2.44), we can obtain the variance of the mechanical quadratures as

$$\begin{aligned}\langle \hat{X}_1^2 \rangle &= \frac{\langle \hat{I}^2 \rangle}{G^{\text{opt}}} - n_{\text{add}}^{\text{opt}} - \frac{1}{2}, \\ \langle \hat{X}_2^2 \rangle &= \frac{\langle \hat{Q}^2 \rangle}{G^{\text{opt}}} - n_{\text{add}}^{\text{opt}} - \frac{1}{2}.\end{aligned}\tag{2.45}$$

Furthermore, using Eq. (2.45), we can obtain the phonon occupation as the average of the variances of both the mechanical quadratures, subtracted by the half quanta, i.e.,

$$\begin{aligned}n_{\text{m}} = \langle \hat{b}^\dagger(0) \hat{b}(0) \rangle &= \frac{\langle \hat{X}_1^2 \rangle + \langle \hat{X}_2^2 \rangle}{2} - \frac{1}{2} \\ &= \frac{1}{G^{\text{opt}}} \frac{\langle \hat{I}^2 \rangle + \langle \hat{Q}^2 \rangle}{2} - n_{\text{add}}^{\text{opt}} - 1.\end{aligned}\tag{2.46}$$

## 2.4 Theory of multimode circuit optomechanics

This section provides the theoretical description of a multimode circuit optomechanical system and shows how the collective microwave mode-shapes in optomechanical lattices. The theoretical discussion here is later used in chapter 8 to explain the system.

### 2.4.1 Theoretical model

In our model, each electromechanical element consists of a single microwave mode optomechanically coupled to an individual mechanical mode. In addition, the microwave modes are electromagnetically coupled to each other. The Hamiltonian of the multimode system is in general given by

$$\hat{H}/\hbar = \sum_i \left[ \omega_{\text{c},i} \hat{a}_i^\dagger \hat{a}_i + \Omega_{\text{m},i} \hat{b}_i^\dagger \hat{b}_i + g_{0,i} \hat{a}_i^\dagger \hat{a}_i (\hat{b}_i^\dagger + \hat{b}_i) \right] + \sum_{i \neq j} \left[ J_{ij} \hat{a}_i^\dagger \hat{a}_j + J_{ji} \hat{a}_j^\dagger \hat{a}_i \right], \tag{2.47}$$

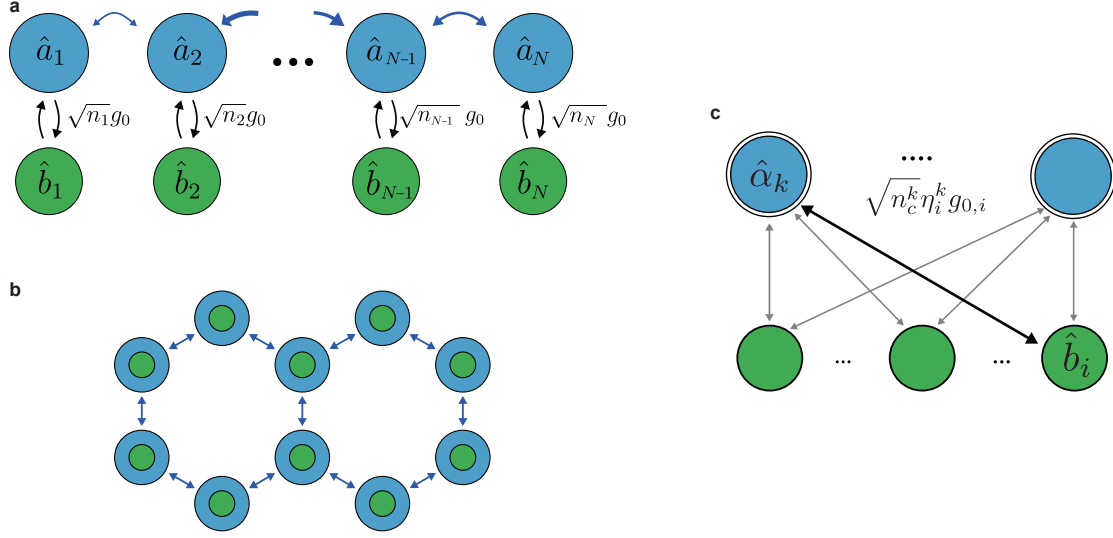


Figure 2.4: **Optomechanical arrays and lattices.** **a**, Mode diagram of a 1-D optomechanical array. Electromagnetic and mechanical modes are shown by blue and green circles correspondingly. Each individual optomechanical building block is coupled to the neighbors with microwave coupling. **b**, Example of a 2-D optomechanical lattice. **c**, Equivalent mode diagram in the collective electromagnetic basis. The collective electromagnetic modes are coupled to all the mechanical resonators by the effective optomechanical coupling rates which are proportional to their energy participation ratio,  $\eta_i^k$ .

where  $\hat{a}_i$  and  $\hat{b}_i$  are annihilation operators for microwave mode  $i$  with a resonance frequency  $\omega_{c,i}$  and mechanical mode  $i$  with a resonance frequency  $\Omega_{m,i}$ ,  $g_{0,i}$  is the single-photon optomechanical coupling rate, and  $J_{ij}$  is the coupling strength between microwave modes  $i$  and  $j$ .

Assuming that the single-photon optomechanical coupling rates are sufficiently smaller than the microwave resonance frequencies and the electromagnetic coupling strengths, collective microwave modes can be well defined regardless of the coupling to the mechanical modes. Thus, we first focus on the Hamiltonian of the coupled microwave modes:

$$\hat{H}_c / \hbar = \sum_i \omega_{c,i} \hat{a}_i^\dagger \hat{a}_i + \sum_{i \neq j} (J_{ij} \hat{a}_i^\dagger \hat{a}_j + J_{ji} \hat{a}_j^\dagger \hat{a}_i). \quad (2.48)$$

In a matrix representation, the quadratic Hamiltonian  $\hat{H}_c$  can be described as

$$\hat{H}_c = \hat{\mathbf{a}}^\dagger \mathbf{H}_c \hat{\mathbf{a}}, \quad (2.49)$$

where

$$\hat{\mathbf{a}} = \begin{bmatrix} \hat{a}_1 \\ \hat{a}_2 \\ \vdots \\ \hat{a}_i \\ \vdots \end{bmatrix}, \quad \hat{\mathbf{a}}^\dagger = [\hat{a}_1^\dagger \ \hat{a}_2^\dagger \ \cdots \ \hat{a}_i^\dagger \ \cdots], \quad \text{and} \quad \mathbf{H}_c/\hbar = \begin{bmatrix} \ddots & & & & \\ & \omega_{c,i} & & J_{ji} & \\ & & \ddots & & \\ & J_{ij} & & \omega_{c,j} & \\ & & & & \ddots \end{bmatrix}. \quad (2.50)$$

Since  $\mathbf{H}_c$  is an hermitian matrix, it can be diagonalized by a unitary matrix  $\mathbf{U}_\psi$  as

$$\mathbf{D}_c = \mathbf{U}_\psi \mathbf{H}_c \mathbf{U}_\psi^\dagger, \quad (2.51)$$

where  $\mathbf{D}_c$  is a diagonal matrix whose diagonal element  $[\mathbf{D}_c]_{k,k}$  corresponds to the eigen-energy  $\hbar\tilde{\omega}_c^k$  of the collective microwave mode  $k$ . On the basis of the collective microwave modes  $\hat{\mathbf{a}} = \mathbf{U}_\psi \hat{\mathbf{a}}$ , Hamiltonian (2.48) is described as

$$\begin{aligned} \hat{H}_c/\hbar &= \hat{\mathbf{a}}^\dagger (\mathbf{D}_c/\hbar) \hat{\mathbf{a}} \\ &= \sum_k \tilde{\omega}_c^k \hat{a}_k^\dagger \hat{a}_k. \end{aligned} \quad (2.52)$$

Note that collective microwave mode  $k$  is explicitly be represented using the bare microwave modes as

$$\hat{a}_k = \sum_i \psi_i^k \hat{a}_i, \quad (2.53)$$

where  $\psi_i^k = [\mathbf{U}_\psi]_{k,i}$  is the complex amplitude of the normalized mode function of collective microwave mode  $k$  at site  $i$ . Thus, we define the participation ratio of bare mode  $i$  to collective mode  $k$  as

$$\eta_i^k = |\psi_i^k|^2. \quad (2.54)$$

As will be discussed in chapter 8, our main goal is to characterize the participation ratio using the optomechanical damping effects in multimode optomechanics.

The property of the unitary transformation gives the normalization conditions of the mode functions:

$$\sum_i \eta_i^k = \sum_i |\psi_i^k|^2 = 1 \quad (2.55)$$

and

$$\sum_k \eta_i^k = \sum_k |\psi_i^k|^2 = 1, \quad (2.56)$$

as well as the orthogonalization condition between different mode functions:

$$\sum_i \psi_i^{k*} \psi_i^l = 0 \quad (\text{if } l \neq k). \quad (2.57)$$

The normalization condition of Eq. (2.55) describes the photon-number conservation in collective mode  $k$  when it is decomposed into the bare modes, while the normalization condition of Eq. (2.56) describes the photon-number conservation in bare mode  $i$  when it is decomposed into the collective modes.

Next, we describe the Hamiltonian of the multimode optomechanical system based on the collective microwave modes. Using the inverse unitary transformation  $\hat{\mathbf{a}} = \mathbf{U}_\psi^\dagger \hat{\mathbf{a}}_b$ , the bare microwave mode  $i$  is represented as

$$\hat{a}_i = \sum_k \psi_i^{k*} \hat{a}_k. \quad (2.58)$$

With this relation, Hamiltonian (8.2) is rewritten as

$$\hat{H}/\hbar = \sum_k \tilde{\omega}_c^k \hat{a}_k^\dagger \hat{a}_k + \sum_i \Omega_{m,i} \hat{b}_i^\dagger \hat{b}_i + \sum_{k,l,i} \left[ g_{0,i} \psi_i^{l*} \psi_i^k \hat{a}_k^\dagger \hat{a}_l (\hat{b}_i^\dagger + \hat{b}_i) \right]. \quad (2.59)$$

Assuming that the frequency detuning  $|\tilde{\omega}_k - \tilde{\omega}_l|$  among the collective microwave modes are sufficiently larger than the single-photon optomechanical coupling rates, the rotating-wave approximation can be valid, and the non-energy conservation term  $\propto \hat{a}_k^\dagger \hat{a}_l$  (if  $k \neq l$ ) can be neglected. Thus, the Hamiltonian can be approximated as

$$\begin{aligned} \hat{H}/\hbar &= \sum_k \tilde{\omega}_c^k \hat{a}_k^\dagger \hat{a}_k + \sum_i \Omega_{m,i} \hat{b}_i^\dagger \hat{b}_i + \sum_{k,i} g_{0,i} \psi_i^{k*} \psi_i^k \hat{a}_k^\dagger \hat{a}_k (\hat{b}_i^\dagger + \hat{b}_i) \\ &= \sum_k \tilde{\omega}_c^k \hat{a}_k^\dagger \hat{a}_k + \sum_i \Omega_{m,i} \hat{b}_i^\dagger \hat{b}_i + \sum_{k,i} \left( \eta_i^k g_{0,i} \right) \hat{a}_k^\dagger \hat{a}_k (\hat{b}_i^\dagger + \hat{b}_i), \end{aligned} \quad (2.60)$$

where  $\psi_i^{k*} \psi_i^k = \eta_i^k$ . In the collective-mode picture, mechanical mode  $i$  is optomechanically coupled to collective microwave mode  $k$  with the single-photon optomechanical coupling rate  $g_{0,i}$  weighted by  $\eta_i^k$ , the participation ratio of bare microwave mode  $i$  to collective microwave mode  $k$ .

In our multimode optomechanical system, it can be assumed that the collective microwave modes and the mechanical modes are well isolated from each other in frequency space and the frequency spacing between the collective microwave modes is much larger than the mechanical frequencies, enabling us to operate the multimode system as a single microwave mode coupled to a single mechanical mode. Furthermore, our multimode system is locally connected to an input line on one side and an output line on the other side, resulting in collective microwave mode  $k$  being coupled to the input line with the external coupling rate  $\kappa_1^k$  and the output line with the external coupling rate  $\kappa_2^k$ , respectively. Note that  $\kappa_1^k$  and  $\kappa_2^k$  depend on the mode function of collective mode  $k$ .

Here, we consider the case when collective microwave mode  $k$  is driven by a coherent field with a frequency  $\omega_i^k$  from the input line to couple mechanical mode  $i$  to collective microwave mode  $k$ . The effective Hamiltonian in the rotating frame of  $\omega_i^k$  is given by

$$\hat{H}_i^k / \hbar = \Delta_i^k \hat{a}_k^\dagger \hat{a}_k + \Omega_{m,i} \hat{b}_i^\dagger \hat{b}_i + \left( \eta_i^k g_{0,i} \right) \hat{a}_k^\dagger \hat{a}_k (\hat{b}_i^\dagger + \hat{b}_i) + \sqrt{\kappa_1^k \dot{n}_d^k} (\hat{a}_k^\dagger + \hat{a}_k), \quad (2.61)$$

where  $\Delta_i^k = \tilde{\omega}_c^k - \omega_i^k$  is the detuning between the collective microwave frequency  $\tilde{\omega}_c^k$  and the drive frequency  $\omega_i^k$  and  $\dot{n}_d^k$  is the photon flux of the cavity drive field. With this Hamiltonian, the quantum Langevin equations of collective microwave mode  $k$  and mechanical mode  $i$  are given by

$$\begin{aligned} \dot{\hat{a}}_k &= \left[ -i\Delta_i^k - \frac{\kappa_{\text{tot}}^k}{2} - i \left( \eta_i^k g_{0,i} \right) (\hat{b}_i^\dagger + \hat{b}_i) \right] \hat{a}_k - i\sqrt{\kappa_1^k \dot{n}_d^k} + \sqrt{\kappa_1^k} \hat{a}_{\text{in},1} + \sqrt{\kappa_2^k} \hat{a}_{\text{in},2} + \sqrt{\kappa_0^k} \hat{a}_{\text{in},0} \\ \dot{\hat{b}}_i &= \left( -i\Omega_{m,i} - \frac{\Gamma_{m,i}}{2} \right) \hat{b}_i - i \left( \eta_i^k g_{0,i} \right) \hat{a}_k^\dagger \hat{a}_k + \sqrt{\Gamma_{m,i}} \hat{b}_{\text{in}}, \end{aligned} \quad (2.62)$$

where  $\kappa_0^k$  and  $\kappa_{\text{tot}}^k = \kappa_0^k + \kappa_1^k + \kappa_2^k$  are the intrinsic loss rate and the total decay rate of the microwave mode, respectively. Moreover,  $\Gamma_{m,i}$  is the intrinsic loss rate of the mechanical mode, and  $\hat{a}_{\text{in},0}$ ,  $\hat{a}_{\text{in},1}$ ,  $\hat{a}_{\text{in},2}$ , are  $\hat{b}_{\text{in}}$  are input quantum and thermal noises from the corresponding baths.

Assuming that the coherent amplitude of the microwave mode is not affected by the optomechanical coupling, the quantum Langevin equation for the microwave mode can be divided into the classical part with  $\langle \hat{a}_k \rangle$  and the quantum part with  $\delta \hat{a}_k$ . By using the linearization  $\hat{a}_k = \langle \hat{a}_k \rangle + \delta \hat{a}_k$ , we therefore have

$$\begin{aligned} \langle \dot{\hat{a}}_k \rangle &= \left( -i\Delta_i^k - \frac{\kappa_{\text{tot}}^k}{2} \right) \langle \hat{a}_k \rangle - i\sqrt{\kappa_1^k \dot{n}_d^k} \\ \delta \dot{\hat{a}}_k &= \left( -i\Delta_i^k - \frac{\kappa_{\text{tot}}^k}{2} \right) \delta \hat{a}_k - i \left( \eta_i^k g_{0,i} \right) \langle \hat{a}_k \rangle (\hat{b}_i^\dagger + \hat{b}_i) + \sqrt{\kappa_1^k} \hat{a}_{\text{in},1} + \sqrt{\kappa_2^k} \hat{a}_{\text{in},2} + \sqrt{\kappa_0^k} \hat{a}_{\text{in},0} \\ \dot{\hat{b}}_i &= \left( -i\Omega_{m,i} - \frac{\Gamma_{m,i}}{2} \right) \hat{b}_i - i \left( \eta_i^k g_{0,i} \right) \left( \langle \hat{a}_k \rangle \hat{a}_k^\dagger + \langle \hat{a}_k \rangle^* \hat{a}_k \right) + \sqrt{\Gamma_{m,i}} \hat{b}_{\text{in}}. \end{aligned} \quad (2.63)$$

Note that the bare optomechanical coupling terms are neglected. The time evolution of the mechanical mode is sufficiently slow for the classical amplitude of the microwave mode to be in the steady state. Using  $\langle \dot{\hat{a}}_k \rangle = 0$ , the classical amplitude is therefore obtained as

$$\langle \hat{a}_k \rangle = \frac{-i\sqrt{\kappa_1^k \dot{n}_d^k}}{i\Delta_i^k + \frac{\kappa_{\text{tot}}^k}{2}}. \quad (2.64)$$

## 3 Circuit analysis, design, and simulation

In this chapter, we discuss the mechanical and electrical properties of the circuit optomechanical devices, calculate the optomechanical coupling rate based on the geometrical and material parameters of the system, and show how a design can be programmed as a digital pattern for fabrication.

### 3.1 Electrical circuit

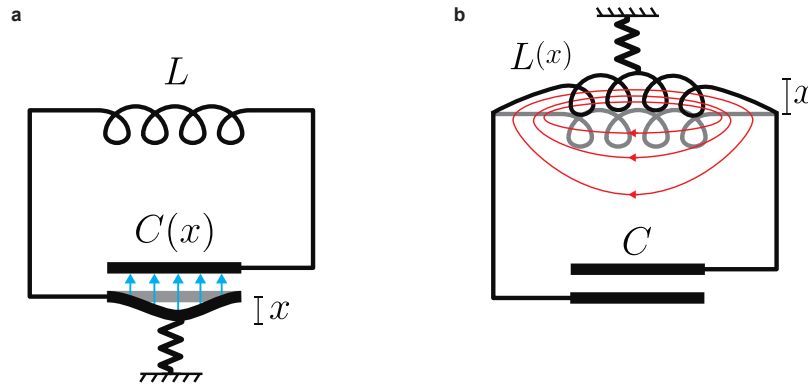


Figure 3.1: **Two possible realizations of circuit electromechanics.** **a**, A mechanically compliant capacitor is manipulating the confined electric field and thus the resonance frequency. **b**, A mechanically compliant inductor is manipulating the magnetic field and thus the resonance frequency.

A lumped element microwave resonator is formed by shunting a capacitor,  $C$ , and an inductor,  $L$ . Each of these elements can in principle be coupled to a mechanical degree of freedom (Fig.3.1). For the case of geometric inductance manipulation, due to the relatively distributed magnetic field and large geometries in standard meander or spiral inductors, position deformation results in a relatively small inductance modulation. Researchers have investigated other approaches for inductive electro-mechanical coupling such as kinetic inductance modulation (Roos et al., 2023) or exploiting Josephson junction's nonlinearity by shunting them

to a mechanical oscillator and applying external magnetic flux (Rodrigues, Bothner, and G. Steele, 2019) and achieving significantly high optomechanical coupling rates, however, these approaches suffer from low mechanical quality factors and lack of scalability. Mechanically compliant capacitors are more conventional in the field of circuit optomechanics. This may be due to the fact that the spatial electric field concentration can be quite high in the vacuum-gap capacitors which results in higher sensitivity to position and geometry change of the element and consequently higher optomechanical coupling rate, for example, a 10 nm change in the gap size of a vacuum-gap capacitor with 100 nm gap results in 10% change of the capacitance and  $\sim 5\%$  change of the resonance frequency. In this case, the microwave resonance frequency can be expanded with respect to the position ( $x$ ) as:

$$\omega(x) = \frac{1}{\sqrt{LC(x)}} = \omega_c - \frac{\omega_c}{2C(0)} \frac{\partial C}{\partial x} x + \mathcal{O}(x^2), \quad (3.1)$$

Where  $\omega_c = 1/\sqrt{LC(0)}$  is the unmodulated frequency of the resonator. In the case of ideal vacuum-gap parallel plate capacitor  $C(x) = \frac{\epsilon_0 A_{\text{cap}}}{d+x}$ , where  $A_{\text{cap}}$  is the effective area of the plates, and  $d$  is the gap size. The optomechanical coupling rate for the ideal LC circuit with an ideal vacuum gap capacitor is derived as:

$$G = \frac{\partial \omega(x)}{\partial x} = + \frac{\omega_c}{2d}. \quad (3.2)$$

As shown, the optomechanical coupling rate only depends on the gap size for a certain microwave frequency. The detailed calculation of the optomechanical single-photon coupling rate for the geometry of drumhead capacitors is provided in Sec. 3.3.

### 3.1.1 Waveguide coupling to the circuit

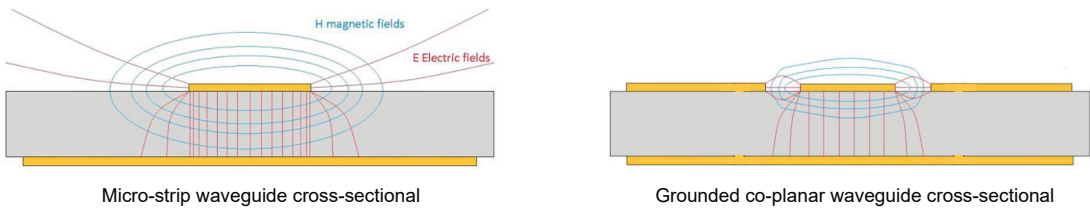


Figure 3.2: **Micro-strip and co-planar waveguides.** The figure shows two types of waveguides employed in the different electromechanical projects. While micro-strip waveguides support a simultaneous non-local coupling to many circuits separated in frequency, CPW offers selective coupling to circuits and less cross-talk thanks to its confined electromagnetic field.

To control and readout the LC circuit we couple it to a waveguide (Fig. 3.2). For projects employing a single electromechanical LC such as mechanical squeezing, we use micro-strip waveguides which are magnetically coupled to the LC circuit - through mutual inductance between the waveguide and the meander or spiral inductor of the LC circuit. When employing

Chapter 3

arrays and lattices of electromechanical circuits, we normally use a coplanar waveguide structure terminated with a loop inductor which offers local coupling to a circuit while reducing the cross-talk and parasitic coupling to far circuits. In both cases, the size of the waveguide should be designed to guarantee the 50-Ohm impedance matching. Considering  $525 \mu\text{m}$  thickness of the wafer and Silicon's dielectric constant of  $\epsilon_r^{(\text{Si})} = 11.8$ , we calculate  $426 \mu\text{m}$  width for the micro-strip waveguide. The same parameters result in  $18 \mu\text{m}$  core width and  $8 \mu\text{m}$  core-ground gap spacing for the CPW. We note that for CPW the ratio of the gap and core widths defines the impedance as long as they are both much smaller than the thickness of the substrate, therefore the actual sizes can scale to higher or lower values. To analyze

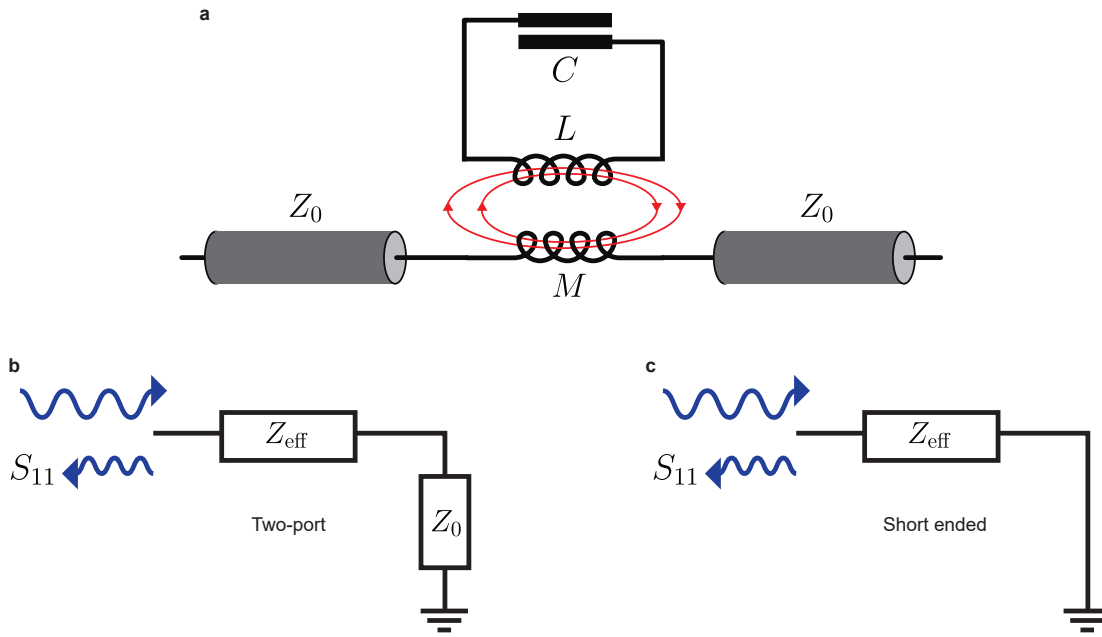


Figure 3.3: **Waveguide coupling to the circuit.** **a**, LC circuit is inductively coupled to a 50-ohm impedance microwave waveguide. The effective lump element impedance of such a coupling in the network analysis is  $Z_{\text{eff}}$ . The scattering matrix parameters can be calculated based on the ratio of  $Z_{\text{eff}}$  and  $Z_0 = 50 \text{ Ohm}$  in two cases of a semi-infinite waveguide **(b)** or the short-ended waveguide **(c)**.

the circuit coupling to a micro-strip waveguide, we consider a lumped element model for the piece of waveguide magnetically coupled to the LC circuit with the mutual inductance of  $M$ . The effective impedance of the mutual inductance coupled with the LC circuit can be calculated as:

$$Z_{\text{eff}} = \frac{M^2 \omega^2}{R + \frac{1}{jC\omega} + jL\omega}, \quad (3.3)$$

Where  $R$  is the effective resistance considered for the LC to model the internal loss. For high- $Q$  microwave resonances where the linewidth of the resonance is much smaller than the



resonance frequency, the impedance can be approximated as:

$$Z_{\text{eff}} = \frac{\frac{M^2 \omega_c^2}{2L}}{\frac{R}{2L} + i(\omega - \omega_c)}, \quad (3.4)$$

With  $\omega_c = 1/\sqrt{LC}$ . In the case of a two-port waveguide, we can calculate the reflection coefficient from the left port - $S_{11}$  of the scattering matrix- by assuming the right port to be in series by a matched load,  $Z_0$ , modeling the semi-infinite waveguide on the right side. The reflection coefficient of a waveguide terminated with  $Z_L$  is given by  $S_{11} = \frac{Z_L - Z_0}{Z_L + Z_0}$  (Pozar, 2011). Assuming  $Z_L = Z_{\text{eff}} + Z_0$  for the two-port case we derive the reflection coefficient as:

$$S_{11} = \frac{\kappa_{\text{ex}}/2}{(\kappa_{\text{ex}} + \kappa_0)/2 + i(\omega - \omega_c)}, \quad \kappa_{\text{ex}} = \frac{M^2 \omega_c^2}{2Z_0 L}, \quad \kappa_0 = R/L, \quad (3.5)$$

Where  $\kappa_{\text{ex}}$  defines the external coupling rate and  $\kappa_0$  defines the intrinsic loss rate of the circuit. The transmission coefficient also can be calculated as:

$$S_{21} = \frac{\kappa_0/2 + i(\omega - \omega_c)}{(\kappa_{\text{ex}} + \kappa_0)/2 + i(\omega - \omega_c)}. \quad (3.6)$$

For the case of the short ended waveguide, the reflection is calculated as:

$$S_{11} = \frac{(\kappa_{\text{ex}}^{(\text{short})} - \kappa_0)/2 - i(\omega - \omega_c)}{(\kappa_{\text{ex}}^{(\text{short})} + \kappa_0)/2 + i(\omega - \omega_c)}, \quad \kappa_{\text{ex}}^{(\text{short})} = 2 \times \kappa_{\text{ex}} = \frac{M^2 \omega_c^2}{Z_0 L}, \quad (3.7)$$

Where the external coupling rate is double of the two-ported case.

### 3.1.2 Circuit theory of the dimerized arrays

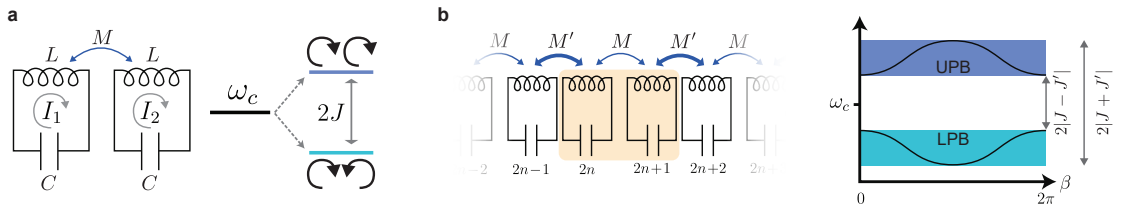


Figure 3.4: **Circuit theory of the dimerized arrays.** **a**, Two coupled LC circuits. The inductive coupling results in energy splitting. The higher frequency mode supports symmetric currents. While the lower frequency mode shows anti-symmetric currents. **b**, Infinite chain of dimerized circuits with alternating couplings. The energy band structure of such a chain consists of two passbands (UPB and LPB) located around the central frequency.

Here we briefly discuss the circuit theory of microwave SSH chains and link the circuit elements of such a system to the Hamiltonian parameters - i.e. the coupling rates. We first consider two coupled identical LC circuits as shown in figure 3.4a. The system can be described by electrical

### Chapter 3

currents,  $I_1(t)$  and  $I_2(t)$ . Kirchhoff's equations result in:

$$L\ddot{I}_1(t) - M\ddot{I}_2(t) + \frac{1}{C}I_1(t) = 0, \quad L\ddot{I}_2(t) - M\ddot{I}_1(t) + \frac{1}{C}I_2(t) = 0 \quad (3.8)$$

Which can be transferred to the frequency domain:

$$(\omega_c^2 - \omega^2)LI_1 = -M\omega^2 I_2, \quad (\omega_c^2 - \omega^2)LI_2 = -M\omega^2 I_1 \quad (3.9)$$

Where  $\omega_c = \sqrt{\frac{1}{LC}}$ . Equation 3.9 results in two eigenfrequencies

$$\omega_c \sqrt{\frac{1}{1 \mp \frac{M}{L}}} \simeq \omega_c (1 \pm \frac{M}{2L}) \quad (3.10)$$

corresponding to two eigen modes of  $I_1 = \pm I_2$  respectively. Based on the energy splitting, the energy coupling rate can be extracted as  $J = \omega_c \frac{M}{2L}$ . It is worth mentioning that the symmetric mode ( $I_1 = I_2$ ) corresponds to the higher resonance frequency and the asymmetric mode to the lower one.

Now we describe the infinite array of coupled dimer LC circuits with the staggered couplings of  $M$  and  $M'$  as shown in figure 3.4b. For each dimer (sites  $2n$  and  $2n+1$ ) we can derive the frequency domain circuit equations:

$$\begin{aligned} (\omega_c^2 - \omega^2)I_{2n} + \frac{M}{L}\omega^2 I_{2n+1} + \frac{M'}{L}\omega^2 I_{2(n-1)+1} &= 0 \\ (\omega_c^2 - \omega^2)I_{2n+1} + \frac{M'}{L}\omega^2 I_{2(n+1)} + \frac{M}{L}\omega^2 I_{2n} &= 0. \end{aligned} \quad (3.11)$$

Considering Bloch's theorem, the propagating mode in such an array can be described by a harmonic function:

$$I_{2n} = I_0 e^{i\beta 2n}, \quad I_{2n+1} = I'_0 \lambda e^{i\beta 2n} \quad (3.12)$$

Where  $\beta \in \mathbb{R}$  is the wave number of the propagating mode,  $\lambda \in \mathbb{C}$  is defining the phase and amplitude difference between circuits in a dimer and  $I_0 \in \mathbb{R}$  is one of the current's amplitudes. Therefore equation 3.11 will be simplified to:

$$\begin{aligned} (\omega_c^2 - \omega^2) + \lambda \frac{M + M' e^{-i\beta}}{L} \omega^2 &= 0 \\ \lambda (\omega_c^2 - \omega^2) + \frac{M + M' e^{i\beta}}{L} \omega^2 &= 0. \end{aligned} \quad (3.13)$$

Solving for  $\omega$  from equations 3.13 will result in the band structure of the infinite chain:

$$\omega = \frac{\omega_c}{\sqrt{1 \pm \frac{\sqrt{M^2 + M'^2 + 2MM' \cos(\beta)}}{L}}} \quad (3.14)$$

As shown in figure 3.4b, the energy spectrum of the infinite chain consists of two passbands. In case of small mutual coupling ( $\frac{M}{L}, \frac{M'}{L} \ll 1$ ) The upper passband (UPB) and lower passband boundaries are:

$$\begin{aligned}\omega_{\pm}^{\text{UPB}} &= \omega_c + |J \pm J'| \\ \omega_{\pm}^{\text{LPB}} &= \omega_c - |J \mp J'|\end{aligned}\quad (3.15)$$

Where  $J = \omega_c \frac{M}{2L}$ ,  $J' = \omega_c \frac{M'}{2L}$  are the mutual coupling rates in the chain. In the finite chains, when  $J < J'$ , two edge states arise in the middle of the band gap due to the truncated boundary condition of the chain. This can be intuitively understood in the extreme case of  $J \ll J'$ , when the first and last LC circuits are fully isolated from the rest of the chain, which consists of strongly coupled circuits.

To probe arrays of electromechanical systems, the specific sites of the chain or lattice can be inductively coupled to coplanar waveguides using two short-circuited inductive loop couplers. The external coupling rate to the outermost sites is typically designed to be comparably smaller than internal microwave couplings in the chain to avoid deviation from the ideal model such as SSH model. The relation between the external coupling rate and the mutual inductance follows the same logic as what has been discussed before for a micro-strip waveguide (Eq. 3.5).

### 3.1.3 Circuit design principles

Here we review design rules and relations between the system parameters and the geometrical parameters of the circuits. First, we consider a single microwave LC resonator. The capacitance of a vacuum-gap capacitor can be approximated by  $C_{\text{VG}} = \frac{\epsilon_0 A_{\text{eff}}}{d}$ , where  $A_{\text{eff}}$  is the effective area of the parallel plate and  $d$  is the gap size. Assuming the wire width of the conductors can be neglected compared to the inductance size, the self-inductance or mutual inductance of inductors can be precisely calculated using Neumann's formula:

$$L_{A,B} = \frac{\mu_0}{4\pi} \oint_A \oint_B \frac{d\mathbf{r}_A \cdot d\mathbf{r}_B}{|\mathbf{r}_A - \mathbf{r}_B|} \quad (3.16)$$

Where the path integral is carried out over the geometrical curve of the inductors. In the case of self-inductance  $A = B$  and in the case of mutual inductance  $A$  and  $B$  refer to the curve functions of the two inductors. Using Neumann's formula we can numerically calculate the inductance having the curve functions, however, two simple approximate scaling rules can be extracted from the formula: The self-inductance of a spiral scales with  $L \propto N_s^2 r_{\text{eff}}$  where  $N_s$  is the number of turns and  $r_{\text{eff}}$  is the effective radius of the spiral. The mutual inductance between two spirals  $A$  and  $B$  with the distance of  $l$  scales with  $M \propto N_{s,A} N_{s,B} r_{\text{eff},A}^2 r_{\text{eff},B}^2 / l^3$  in far distances ( $l \gg r_{\text{eff},A}, r_{\text{eff},B}$ ). To increase microwave coupling rates ( $J = \omega_c \frac{M}{2L}$ ) in a design,  $M$  needs to increase while  $L$  is fixed. This can be achieved by increasing the aspect ratio of spirals to have longer adjacent wires in neighbor sites, like the spirals used in the 10-site 1D chain discussed in Sec. 8.4.

## Chapter 3

### 3.1.4 Electromagnetic simulations

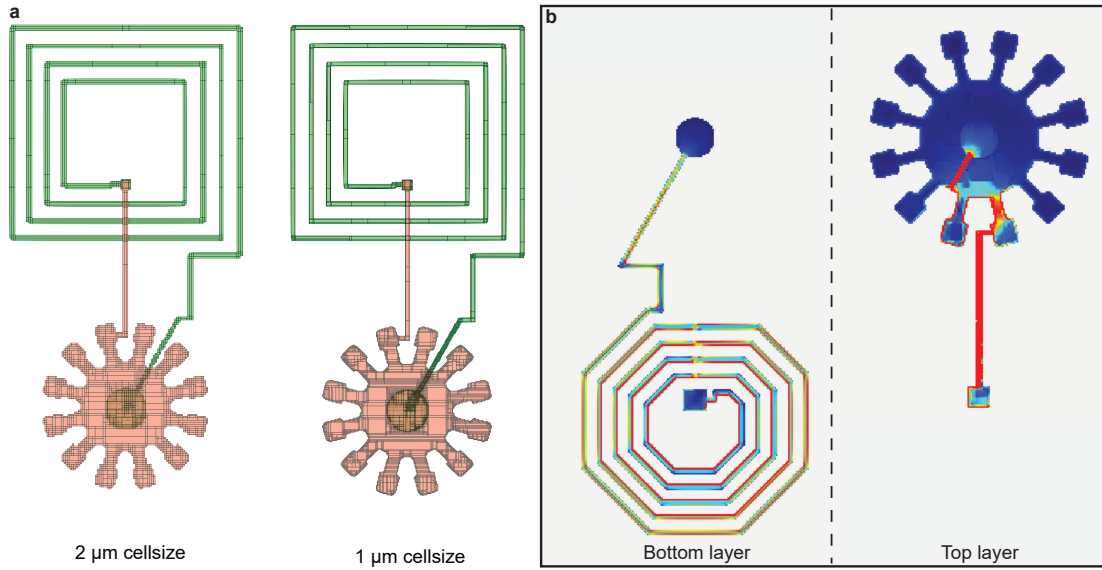


Figure 3.5: **Circuit simulation with Sonnet®**. **a**, Shows the meshed structure of an LC circuit with two different minimum mesh sizes. **b**, Shows the computed on-resonance current density amplitude in both layers.

All the electromagnetic simulations were performed using Sonnet® Suites, which is a 2.5-D simulation software dedicated to RF and microwave IC chip and PCB design. The Sonnet Suites develop precise RF models (S-, Y-, Z-parameters or extracted SPICE model) for planar circuits and antennas. The software requires a physical description of the circuit (in our case GDSII layout and material properties for metal and dielectrics) and employs a rigorous method-of-moments electromagnetic analysis based on Maxwell's equations including parasitic, cross-coupling, and package resonance effects.

The software imports the GDSII design of the circuit in different layers. We can then define material properties for the silicon substrate (assuming  $10^{-5}$  as the loss tangent to have an estimate of the substrate losses) and superconducting aluminum layers (assuming zero resistivity, but  $X_s = 0.02$  pH/sq as kinetic surface inductance). The gap size between the top and bottom aluminum layers can also be tuned and swept. We need to define a grounded box surrounding the design and one or two 50-ohm load-matched ports to calculate the scattering matrix. the ports are normally connected to the waveguide ends. The next step is to select a proper minimum mesh size and type (we typically use  $2\mu\text{m} \times 2\mu\text{m}$  square mesh) and check the connectivity of the elements, specifically the spiral inductor wires. Higher mesh size (Fig. 3.5a) will significantly reduce the size of the mesh matrix and accelerates the simulation but result in less accurate resonance frequencies neglecting the edge effects for example. Sonnet is also capable of calculating the current density amplitude and reporting its map over the circuit (Fig. 3.5b).

as an example, in the topological optomechanical lattices project (Sec. 8.4), We first simulated

the single LC resonator and varied the geometric inductor parameters and bottom capacitor plate diameter (which changes the capacitance) to get the desired resonance frequency around 7 GHz. As detailed in Sec. 3.1.2, when two harmonic modes get coupled together, two hybridized modes appear (Fig. 3.6 a inset). The frequency splitting between such two modes

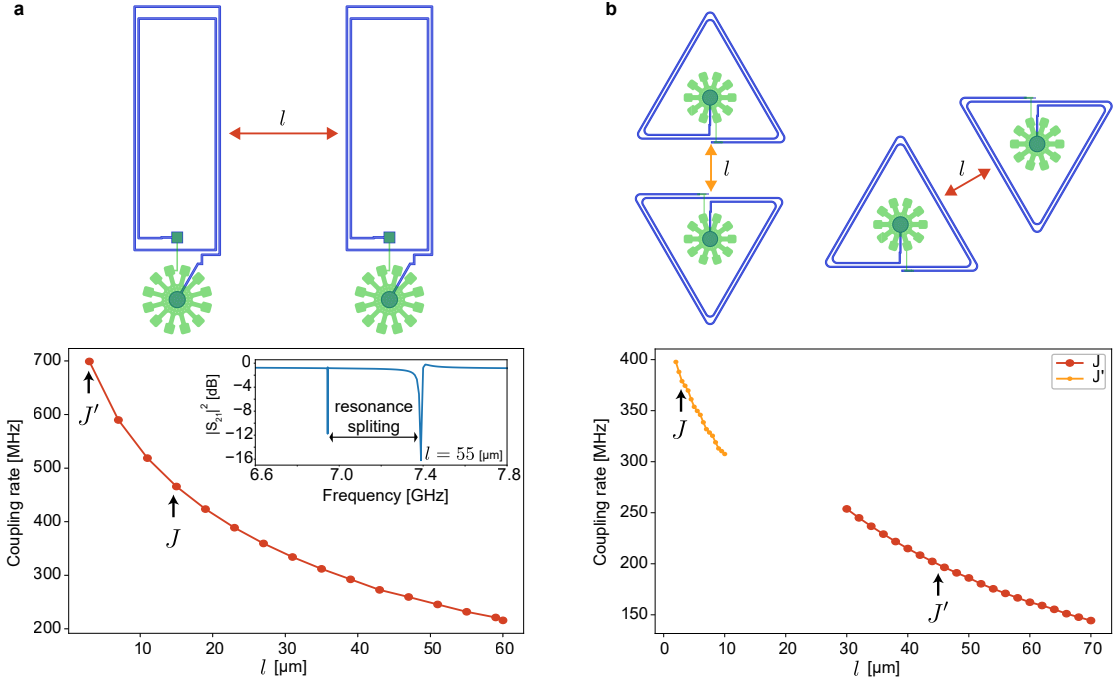


Figure 3.6: **Mutual inductive coupling rate as a function of the distance between two identical sites a**, Unit cells for 1D SSH chain. **b**, Unit cells for 2D strained graphene lattice in different directions. The black arrows show the final designed values. The coupling rates are extracted from the splitting of hybridized modes observed in the FEM simulation with Sonnet as shown in the inset.

is exactly double the coupling rate between them as can be easily seen from Eq. (3.10). In our case, the coupling rate between two neighboring modes is inductive, and its strength can be changed by varying the distance between them. We ran parametrized Sonnet® simulations by varying the distance between them, and for each run we extracted the coupling rate from the resulting frequency splitting. As the distance between the two circuits increases, the coupling rate decreases, as expected. (See Fig. 3.6)

From these simulations, we choose the distances that would result in the coupling strengths that we desired. For the 1D case (Fig. 3.7 a) there is one direction of coupling. In the graph, the chosen values of the inter-cell coupling  $J'$  and intra-cell coupling  $J$  can be seen. From these same simulations, unwanted second and third-order coupling rates can also be extracted, which we used to compute the expected mode shapes (see Sec. 8.5). For the 2D case (Fig. 3.7 b) we ran two different distance sweeps because of the slightly asymmetric shape of the spiral inductor, due to the needed crossover point to connect it to the capacitor plates.

### Chapter 3

Another important aspect is how much the input/output loop couplers are shifting the resonance frequency of the outermost sites. If the loop coupler is too close to the circuit, we get a resonance frequency shift, which will only affect the edges of the array, seriously impairing the hybridization of the modes. To study this effect, after having optimized the dimensions of the loop itself, we swept the distance to a single LC site. In Fig.3.7 the external coupling rate - resonance shift trade-off is shown. We chose a distance that could provide a sufficiently high

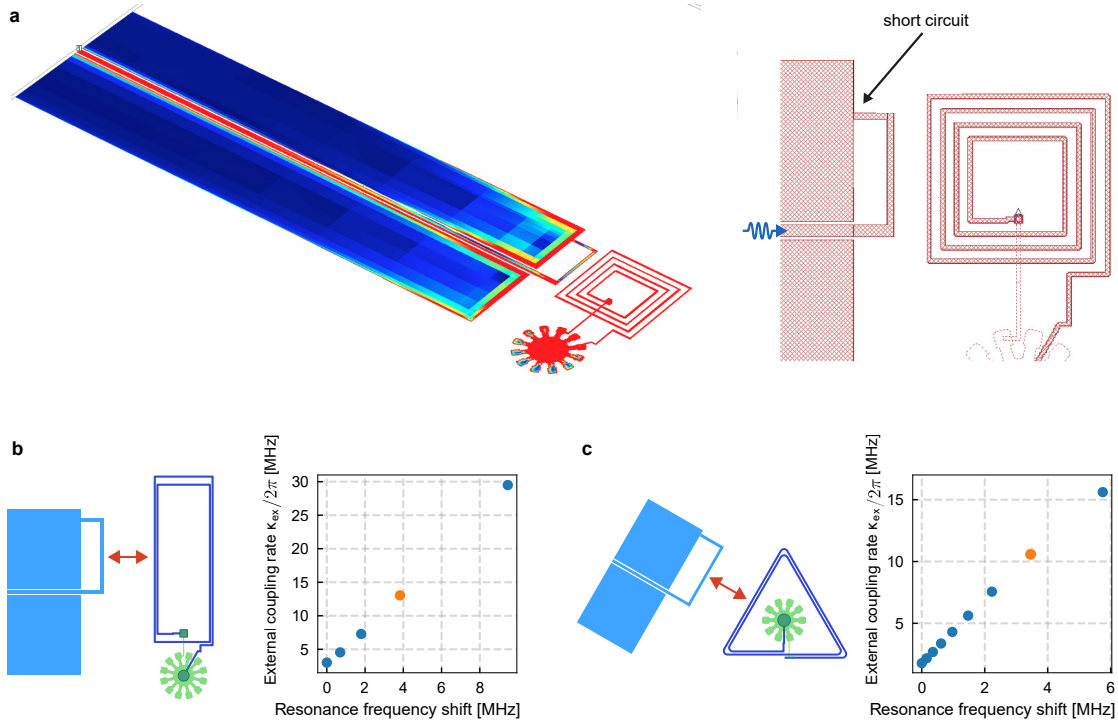


Figure 3.7: **Coupling to the CPW waveguide.** **a**, Sonnet current simulation and meshing of the CPW inductive loop coupler. The CPW is short-ended and the current density is maximum at the end of the waveguide (Bancora, 2021). **b,c**, Sweeping the distance of a single site LC to the loop coupler for the 1D (**b**) and 2D (**c**) design. The external coupling rates, as well as the resonance frequency shift due to probing the system, are extracted. The orange dot corresponds to the distance chosen in the final designs.

coupling rate, but for which the resonance frequency shift was much lower than the coupling rates in the system  $\Delta\omega_c/2\pi \ll J, J'/t$ .

Finally, the whole device can be simulated in Sonnet<sup>®</sup>. The result can be seen in Fig. 3.8. For the 1D case, we directly simulated the mask design used in the fabrication process. For the 2D, given the size of the structure, we substituted the vacuum-gap capacitors with ideal capacitor components to reduce the required memory and speed up the simulation. This should not change the coupling between the sites appreciably because the electromagnetic field of the vacuum-gap capacitor is confined between the plates, and the magnetic field responsible for the coupling of neighboring sites is mostly confined around the spiral lines.

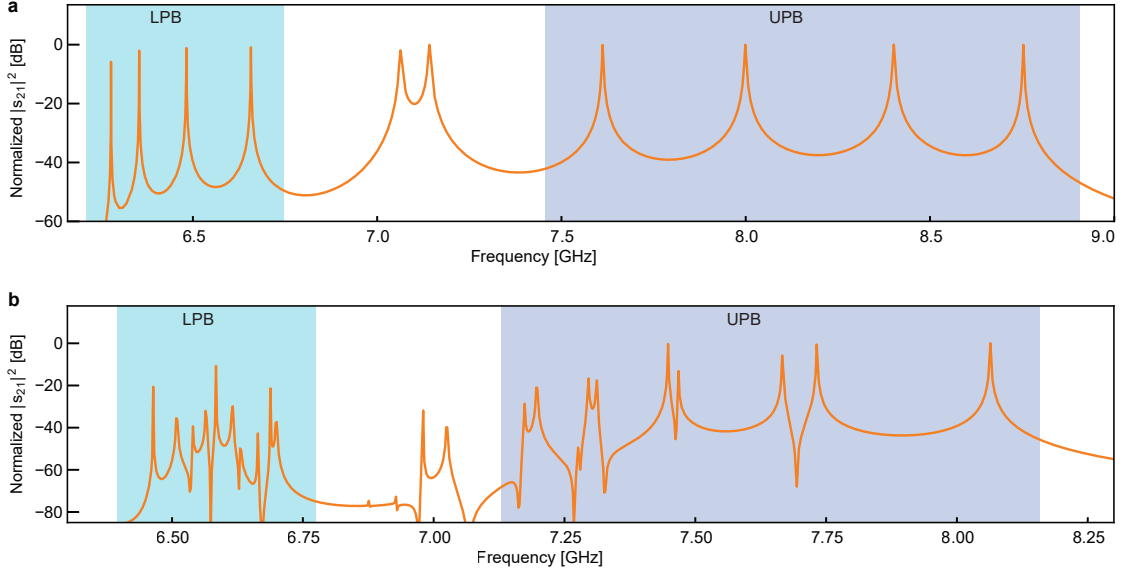


Figure 3.8: **Simulation of the full designs.** Simulated transmission response of the 1D SSH chain and 2D strained graphene lattice used in topological optomechanical array project (Sec. 8.4 and Sec. 8.7). (a) 1D array. (b) 2D lattice. The shades show upper and lower passbands. Isolated edge modes are visible in the middle of the band gap.

### 3.2 Mechanical properties of the drumhead resonator

Here we describe the mechanical properties of a circular drumhead resonator. For sufficiently small deformation of the drumhead, we can approximate the displacement of each element in time as a harmonic oscillation along the vertical axis. The oscillation amplitude of the drum at  $(r, \varphi)$  in polar coordinate is described by  $z(t)u(r, \varphi)$ , where  $z(t)$  with the dimension of length obeys the harmonic oscillation equation:  $\ddot{z} = -\Omega_m^2 z$ , while  $u(r, \varphi)$  is the unit-less mode shape of the drum, normalized such that the amplitude at the origin is 1. For a circular drum with a radius of  $R$ , we have

$$u(r, \varphi) = J_n\left(\frac{\alpha_{n,m}}{R}r\right) \cos(n\varphi),$$

$$\Omega_m^{(n,m)} = \frac{\alpha_{n,m}}{R} \sqrt{\frac{\sigma_m}{\rho}}, \quad (3.17)$$

where  $\alpha_{n,m}$  is the  $m^{\text{th}}$  root of the  $n^{\text{th}}$  order Bessel function of the first kind,  $J_n$ , and  $\sigma_m$  and  $\rho$  are the mechanical stress and density of the material, respectively, in our case aluminum with  $\rho_{\text{Al}} = 2700 \text{ kg/m}^3$ . For the fundamental mode ( $n = 0, m = 1$ ), which we use in this work,  $\alpha_{0,1} \approx 2.4$ . The small holes in the actual device slightly deviate the mode shape from that of a uniform drum. The radius of the drumhead used in the main work is  $R = 75 \mu\text{m}$ . We extracted  $\sigma_{\text{Al}} \approx 350 \text{ MPa}$  tensile stress at cryogenic temperatures by measuring the mechanical frequency of several drums with different radii and matching it with the theory.

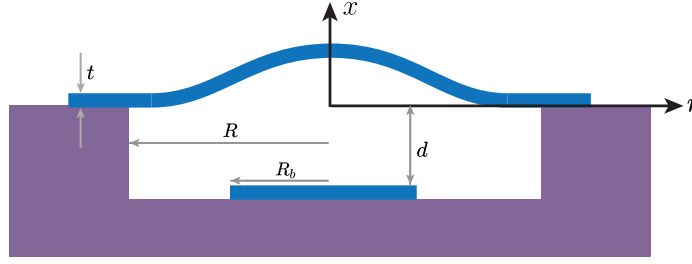


Figure 3.9: **Geometrical parameters of the vacuum-gap capacitor.** The radius of the bottom layer is  $R_b$ , the radius of the drumhead is  $R$ , the thickness of the drumhead is  $t$ , and the distance between the top and bottom layer is  $d$ .

The effective mass of such a mechanical oscillator can be defined as the total kinetic energy over the velocity squared:

$$\begin{aligned} U_{\text{kinetic}} &= \int \frac{1}{2} \rho |\dot{z}(t) u(r, \varphi)|^2 t r dr d\varphi \\ &\equiv \frac{1}{2} m_{\text{eff}} \dot{z}(t)^2, \end{aligned} \quad (3.18)$$

where  $t$  is the thickness of the drumhead resonator. For the fundamental mode of a circular drum, this reduces to

$$\begin{aligned} m_{\text{eff}} &= 2\pi \rho t \int_0^R r |u(r)|^2 dr \\ &= m_{\text{phys}} \xi_{\text{mass}}, \end{aligned} \quad (3.19)$$

where  $m_{\text{phys}}$  is the physical mass of the drum and  $\xi_{\text{mass}}$  is a dimensionless parameter describing the ratio between the effective and physical mass:

$$\begin{aligned} m_{\text{phys}} &= \rho \times \pi R^2 t, \\ \xi_{\text{mass}} &= \frac{2}{R^2} \int_0^R r |u(r)|^2 dr = 2 \int_0^1 \zeta J_0(\alpha_{0,1} \zeta)^2 d\zeta. \end{aligned} \quad (3.20)$$

For the fundamental mode, we have  $\xi_{\text{mass}} \simeq 0.27$ . Having the effective mass and the frequency of the mechanical oscillator, we can find its zero-point fluctuation:

$$x_{\text{ZPF}} = \sqrt{\frac{\hbar}{2m_{\text{eff}} \Omega_m}}. \quad (3.21)$$

For the drumhead used in the ultra-coherent project, the effective mass of the fundamental mode can be calculated as  $m_{\text{eff}} = 2.3 \text{ ng}$  and the zero-point-fluctuation of motion as  $x_{\text{ZPF}} = 1.4 \text{ fm}$ .

Detailed discussion on the aluminum thin film stress at low temperatures is provided in Sec.A.1. To experimentally extract the exact value of the stress we created 16 separate LC



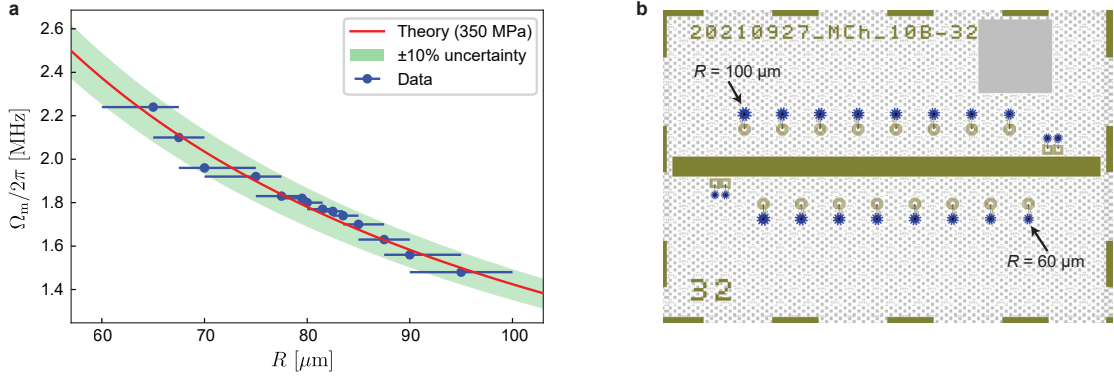


Figure 3.10: **Extraction of the aluminum film stress at low temperatures.** **a**, Measured mechanical frequencies on a chip with 16 separate electromechanical LC resonators. As shown in **b**, in the chip layout the trench radius of drums is swept from 60  $\mu\text{m}$  to 100  $\mu\text{m}$  (The two dimers are separated in the frequency and not used here). Since two LC resonances were inaccessible due to frequency overlap with the JTWPA stopband, we measured 14 resonances and considered an error bar showing the uncertainty in the trench radii. The red line shows the theoretical curve with  $\sigma_{\text{Al}} = 350$  MPa and the green shade shows theory bounds corresponding to  $350\text{MPa} \times (1 \pm 10\%)$  uncertainty.

electromechanical circuits on a chip and swept the radius of the drumhead resonators from 60  $\mu\text{m}$  to 100  $\mu\text{m}$ . By characterizing the mechanical frequencies we can plot them versus trench radius and fit the theoretical formula (Eq.3.17) to extract the stress as  $\sigma_{\text{Al}} = 350(\pm 10\%)$  MPa as shown in Fig.3.10.

### 3.2.1 FEM simulation of the mechanical mode

To precisely calculate the mechanical frequencies of the final design we simulated the drumhead resonator using COMSOL<sup>®</sup> with the finite element method (FEM). FEM simulation allows us to consider geometric nonlinearities and stress relaxation which slightly deviates the actual frequencies from the theory. We use *shell* physics in the structural mechanics library of COMSOL. The shell model reduced the 3D elastic equations into two dimensions considering a constant thickness of the object in the third dimension and is a preferable method for simulating high aspect-ratio structures such as membranes.

Figure 3.11a shows an example of a triangularly meshed drumhead. To be able to precisely calculate mechanical losses (which will be discussed in the following) the mesh needs to be significantly finer on the areas which experience more bending, in our case, the clamps. The simulation is done in two steps stationary stress relaxation and deformation analysis, and the eigenmode solver. The stationary solver, finds the stable solution of the deformation under an initial stress applied on the structure (Fig.3.11b), similar to what happens in practice, when the aluminum film with a uniform stress on the substrate gets released and cooled down. As expected, when we taper the clamps the stress enhances on the edges to satisfy zero total force

Chapter 3

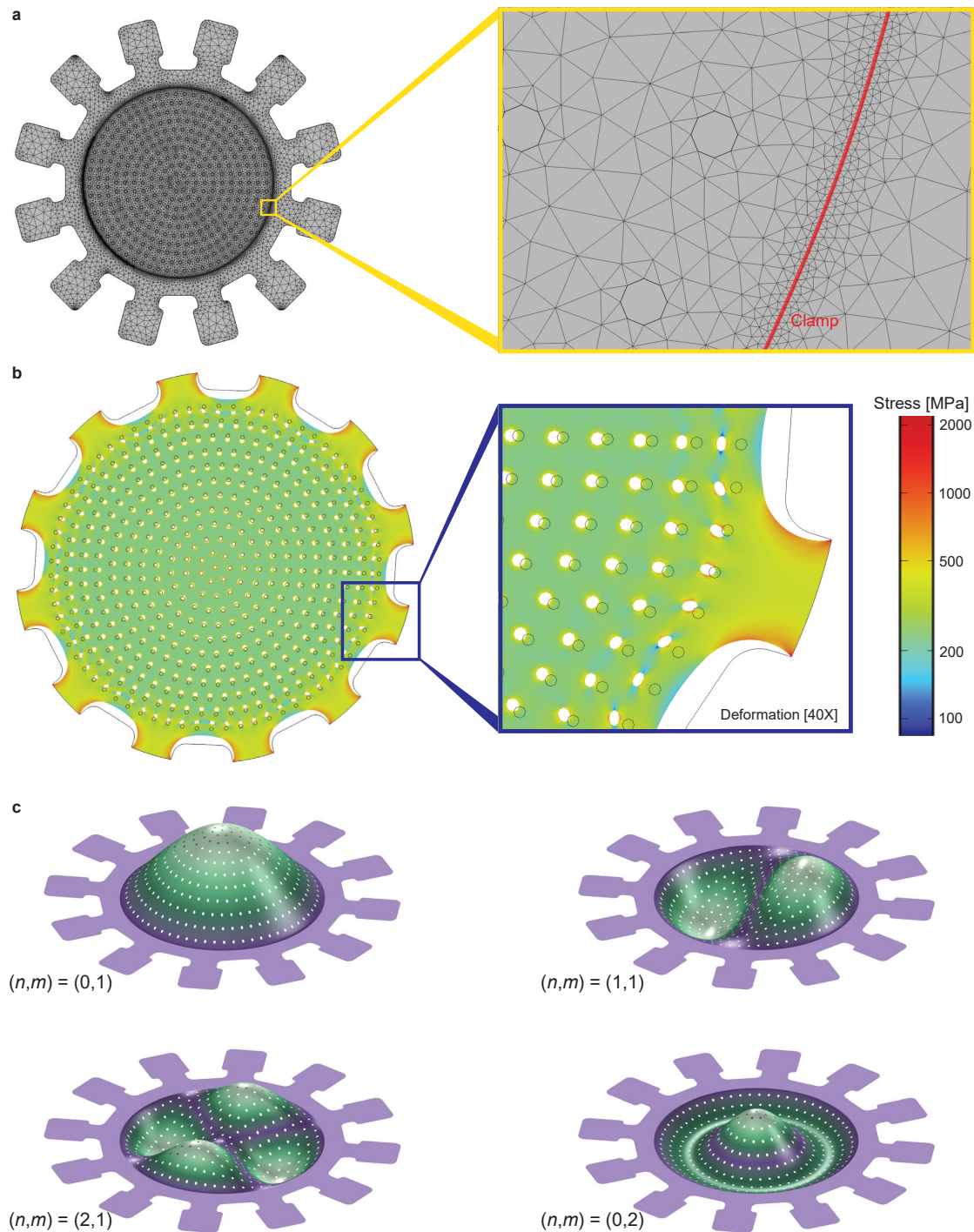


Figure 3.11: **COMSOL® FEM simulation of mechanical modes.** **a**, An example of the triangular meshed drumhead. The mesh size should be finer close to the clamps in order to precisely calculate mechanical losses. Meshing of the clamps which are bounded to the substrate is not needed and only is shown for the sake of visualization. **b**, The solution of the stationary solver showing relaxed stress and magnified deformation of a drumhead considering 350 MPa initial uniform stress. The stress enhances on the tapered clamps as shown in the breakout. **c**, Examples of the first four lower frequency mode shapes as results of the eigenmode solver.

on every arbitrary domain on the drum. Afterward, the eigenmode solver will inherit the initial conditions from the stationary solver and calculates eigenfrequencies and corresponding mode shapes of the structure (Fig.3.11c).

### 3.2.2 Mechanical loss analysis

The loss mechanisms in a macroscopic mechanical oscillator can be separated as intrinsic (bending loss, surface loss, etc.) and extrinsic (gas damping, acoustic radiation, clamp loss, etc.) (S. Fedorov, 2020). The traditional design of drumhead capacitors was resulting in a non-flat geometry of the drumhead, specifically sharp edges at the clamping point. Such a sharp structure can induce mechanical dissipation at the clamping points, i.e. phonon tunneling to the substrate (Cole et al., 2011; Wilson-Rae et al., 2011). The conventional circuit optomechanical devices mainly suffer from such radiative loss, which can be confirmed by the fact that there is a saturation plateau in the temperature dependence of the mechanical damping rate since the clamp loss normally does not have temperature dependence, while the intrinsic mechanical dissipation is expected to decrease for a lower temperature (Cattiaux et al., 2021). The flat geometry in our design may result in smaller clamp losses, as observed in the temperature sweep experiment (see Fig. 6.9) where the mechanical damping rate shows a strong dependency on temperature (while mechanical frequency barely shifts, exhibiting constant stress and Young's modulus in that temperature range).

In the ideal case when there are no extrinsic losses, the mechanical quality factor can reach the maximum bound of the intrinsic quality factor. The intrinsic quality factor in a nanomechanical string or membrane can be described as

$$Q_m = Q_0 \times D_Q, \quad (3.22)$$

where  $Q_0$  is the material's bulk quality factor and  $D_Q$  is the dissipation dilution factor (S. A. Fedorov et al., 2019; S. Fedorov, 2020).  $D_Q = \frac{\langle W_{\text{total}} \rangle}{\langle W_{\text{lossy}} \rangle}$  is defined as the ratio of the dynamic elastic energy averaged over the vibrational period ( $\langle W_{\text{total}} \rangle$ ) over its lossy part ( $\langle W_{\text{lossy}} \rangle$ ). The total energy can be divided into tension energy (corresponding to the elongation of the mode shape and loss-less) and bending energy (corresponding to the bending of the mode shape and lossy). It can be theoretically shown (S. A. Fedorov et al., 2019; S. Fedorov, 2020) that for a thin beam or membrane with a characteristic size of  $R$ ,  $D_Q = (A\lambda + B\lambda^2)^{-1}$ , where  $A$  and  $B$  are unitless geometrical factors and  $\lambda = \frac{t}{2R} \sqrt{\frac{Y}{12\sigma_m}}$  with  $Y$  presenting Young's modulus (for aluminum at low temperatures  $Y \approx 75$  GPa (Ekin, 2006)). Considering system parameters the range of  $\lambda$  parameter for our drumhead resonators is  $\mathcal{O}(10^{-2})$  which validates the approximation of  $D_Q \propto \lambda^{-1}$ . We simulated the drumhead resonator using COMSOL<sup>®</sup> and numerically calculate  $D_Q$  values based on the eigenmodes of resonances. The result shows a good agreement with the theory of loss dilution as shown in Fig. 3.12. The loss dilution factor for the device discussed in the ultra-coherent electromechanics project (chapter 7) is estimated as  $D_Q \approx 100$ . Considering the measured quality factor of  $Q_m = 40 \times 10^6$ , we extract a minimum bound for

## Chapter 3

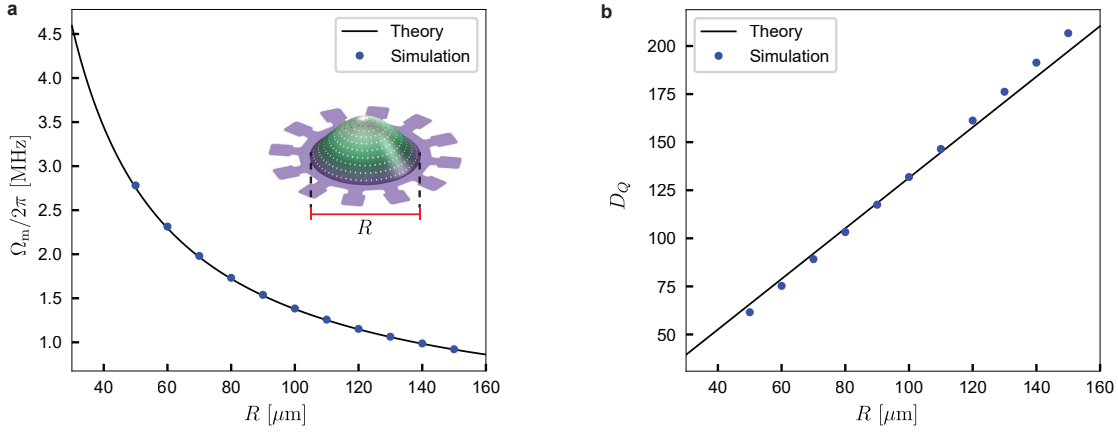


Figure 3.12: **FEM simulation of the loss dilution factor.** **a, b,** Simulated and theoretically calculated mechanical frequency and loss dilution factor versus drum's radius considering  $t = 180$  nm and  $\sigma_{\text{Al}} \approx 350$  MPa.

aluminum's bulk quality factor at 10 mk as  $Q_0 \approx 4 \times 10^5$  for the device we studied.

### 3.3 Single photon optomechanical coupling rate ( $g_0$ )

In this section, we calculate the theoretical value for  $g_0$  based on the physical parameters of the vacuum-gap capacitor (Fig. 3.9). Knowing the displacement function of the top plate (Sec. 3.2) and considering small amplitude oscillations, we can approximate the total capacitance as the sum over differential parallel plate capacitances:

$$\begin{aligned}
 C_{\text{tot}} &= \int \frac{\epsilon_0 r dr d\varphi}{d + z \cdot u(r, \varphi)} + C_{\text{par}} \\
 &= \int_0^{R_b} \frac{\epsilon_0 2\pi r dr}{d + z \cdot u(r)} + C_{\text{par}} \\
 &\simeq \int_0^{R_b} \frac{\epsilon_0 2\pi r dr}{d} \left(1 - \frac{z}{d} u(r)\right) + C_{\text{par}} \\
 &= C_0 - \frac{2\pi\epsilon_0}{d^2} z \int_0^{R_b} r u(r) dr + C_{\text{par}},
 \end{aligned} \tag{3.23}$$

where  $R_b$  is the radius of the bottom plate,  $C_0 = \epsilon_0 \pi R_b^2 / d$  is the unmodulated capacitance of the vacuum-gap, and  $C_{\text{par}}$  is the total parasitic capacitance of the other elements of circuit (wires and spiral inductor). Here, we have considered the mode without angular dependency

and assumed  $z \ll d$ . The frequency of the microwave cavity is then given by

$$\begin{aligned}
 \omega_c(z) &= \frac{1}{\sqrt{LC_{\text{tot}}}} \\
 &= \frac{1}{\sqrt{L(C_0 + C_{\text{par}}) \left(1 - \frac{2\pi\epsilon_0}{d^2(C_0 + C_{\text{par}})} z \int_0^{R_b} r u(r) dr\right)}} \\
 &\approx \frac{1}{\sqrt{L(C_0 + C_{\text{par}})}} \left(1 + \frac{1}{2} \frac{2\pi\epsilon_0/d^2}{C_0 + C_{\text{par}}} z \int_0^{R_b} r u(r) dr\right) \\
 &= \omega_c + \frac{\omega_c}{2d} \xi_{\text{cap}} \xi_{\text{par}} z,
 \end{aligned} \tag{3.24}$$

where

$$\begin{aligned}
 \xi_{\text{cap}} &= \frac{2}{R_b^2} \int_0^{R_b} r u(r) dr = 2 \left(\frac{R}{R_b}\right)^2 \int_0^{\frac{R}{R_b}} \zeta J_n(\alpha_{n,m}\zeta) d\zeta, \\
 \xi_{\text{par}} &= \frac{C_0}{C_0 + C_{\text{par}}}, \\
 \omega_c &= \frac{1}{\sqrt{L(C_0 + C_{\text{par}})}}.
 \end{aligned} \tag{3.25}$$

We can interpret  $\xi_{\text{cap}}$  as the geometrical mode shape contribution factor and  $\xi_{\text{par}}$  as the participation ratio of the modulated capacitor to the total capacitance of the microwave cavity. For the fundamental mode  $u(r) = J_0(\frac{\alpha_{0,1}}{R} r)$ ,  $\xi_{\text{cap}}$  is dependent to the  $R_b/R$ . In our design for the ultra-coherent electromechanics project,  $R_b = 23 \mu\text{m}$  and  $R = 75 \mu\text{m}$ , which results in  $\xi_{\text{cap}} \approx 0.93$ . The participation ratio of the vacuum-gap capacitance to the total capacitance can be extracted in FEM simulations. Simulating our design for the ultra-coherent electromechanics circuit design in SONNET<sup>®</sup> results in  $\xi_{\text{par}} \approx 0.8$ .

The single photon optomechanical coupling rate is then given by  $g_0 = \frac{\partial \omega(x)}{\partial x} x_{\text{ZPF}}$  and we can drive it for our circuit as:

$$g_0 = \frac{\omega_c}{2d} \xi_{\text{cap}} \xi_{\text{par}} x_{\text{ZPF}}, \tag{3.26}$$

where  $x_{\text{ZPF}} = \sqrt{\frac{\hbar}{2m_{\text{eff}}\Omega_m}}$  is the zero point fluctuation, and  $m_{\text{eff}}$  and  $\Omega_m$  were already derived in Sec. 3.2.

The final expression for  $g_0$  based on the system parameters for the fundamental mode then is given by

$$g_0 = 0.37 \sqrt{\hbar} \frac{\omega_c}{2d} (R^2 t^2 \rho \sigma_m)^{-1/4}. \tag{3.27}$$

As it can be seen from the above formula, for a constant microwave cavity frequency  $g_0$  scales with  $d^{-1}$ ,  $R^{-0.5}$ ,  $t^{-0.5}$ ,  $\rho^{-0.25}$ , and  $\sigma_m^{-0.25}$ . The theoretically expected  $g_0$  for the device discussed

## Chapter 3

in the ultra-coherent electromechanics project is calculated  $g_0/2\pi \simeq 14$  Hz, which is in good agreement with the experimentally measured value (Sec. 6.3).

To sum up, we provide a scaling rules table (table 3.1) showing relations between optomechanical properties and physical system parameters.

Table 3.1: Scaling rules in drum-head capacitor based circuit optomechanics.

	$R$	$\sigma_m$	$t$	$d$
$\Omega_m$	$\frac{1}{R}$	$\sqrt{\sigma_m}$	-	-
$\Gamma_m$	$\frac{1}{R^2}$	-	$t$	-
$Q_m, 1/\Gamma_{th}$	$R$	$\sqrt{\sigma_m}$	$t^{-1}$	-
$g_0$	$\frac{1}{\sqrt{R}}$	$\sigma_m^{-\frac{1}{4}}$	$\frac{1}{\sqrt{t}}$	$\frac{1}{d}$
$\mathcal{C}_0 \equiv 4g_0^2/\kappa\Gamma_m$	$R$	$\sigma_m^{-\frac{1}{2}}$	$\frac{1}{t^2}$	$\frac{1}{d^2}$

### 3.4 Mask programming

In order to digitally generate a circuit geometry and transfer it into a lithographically define mask, we developed a Python package to generate GDSII patterns of the chip and wafer layout. GDSII format is a binary database file format which is the industry standard for electronic design automation data exchange of integrated circuit or IC layout artwork. The program is following the same logic as the famous electronic circuit simulation language, SPICE (simulation program with integrated circuit emphasis) (Vladimirescu, 1994). Every circuit element such as a vacuum-gap capacitor, interdigitated capacitor, spiral or meander inductor, etc. is defined as a Python object. The object requires initial arguments defining the size and geometric parameters of the element and generates a set of GDSII polygons (using gdspy library) and paths defining the object, all accumulated in a python list that can be extracted as an object's parameter. We note that a GDSII mask contains several layers corresponding to different fabrication steps. Therefore the extracted GDSII objects also are defined in different layers. In addition, every circuit element object has a list of nodes, containing coordinates of end wires or nodes to be connected to the other circuit elements through wires generated with a dedicated function ('connect()'). Furthermore, we can also define custom parameters for circuit element objects that can be used in the estimation of the electrical parameters of the design. For example, the estimate of the capacitance is calculated by the geometric area and the defined gap size, or the self-inductance of a spiral is calculated by numerical integration of the Neumann formula.

An example of a code generating an LC circuit using our library is shown here:

```

1 import gdspy
2 from circuit tools import vacuum_gap_trampoline, spiral, connect
3 # Defining a GDSII cell

```



```
4     LC_layout = gdspy.Cell('LC_layout')
5
6     # defining geometrical parameters for a vacuum-gap capacitor as a
7     # Python dictionary:
8     C_options = dict(N=12, r_tranch=100, r_bottom=30, wire_width=3,
9     layer_top=5, gap=200e-9, ...[other parameters]...)
10
11     # Calling and defining vacuum-gap object:
12     C = vacuum_gap_trampoline(**C_options)
13
14     # Extracting GDSII list of the capacitor object:
15     C_GDSII_list = C.obj
16
17     # Defining a spiral inductor object
18     L = spiral(**L_options)
19
20     # Connecting L and C with wires. C.node is the list of node
21     # coordinates for the capacitor.
22     wire_1 = connect(C.node[0], L.node[0], wire_width = 3, layer = 5)
23     wire_2 = connect(C.node[1], L.node[1], wire_width = 3, layer = 5)
24
25     # Adding all GDSII objects to the layout and generating the mask:
26     LC_layout = C.obj + L.obj + wire_1 + wire_2
27
28     gdspy.write_gds('LC.gds', cells = LC_layout, unit = 1.0e-6, precision
29     = 1.0e-9)
30
31     # Calculating the estimate of the resonance frequency:
32
33     f_resonance = 1/( 2*n.pi * np.sqrt( L.inductance() * C.capacitance()
34     ))
35     print('Estimated frequency = {} GHz'.format(f_resonance/1e9) )
```

Now that simple elements can be generated using objects and form a close circuit by connecting wires, we can define higher-level functions to generate different kinds of LC circuits, waveguides, and couplers to shape the full design of a chip. The chip designs can be arranged in a grid to fill the whole mask of a round wafer.

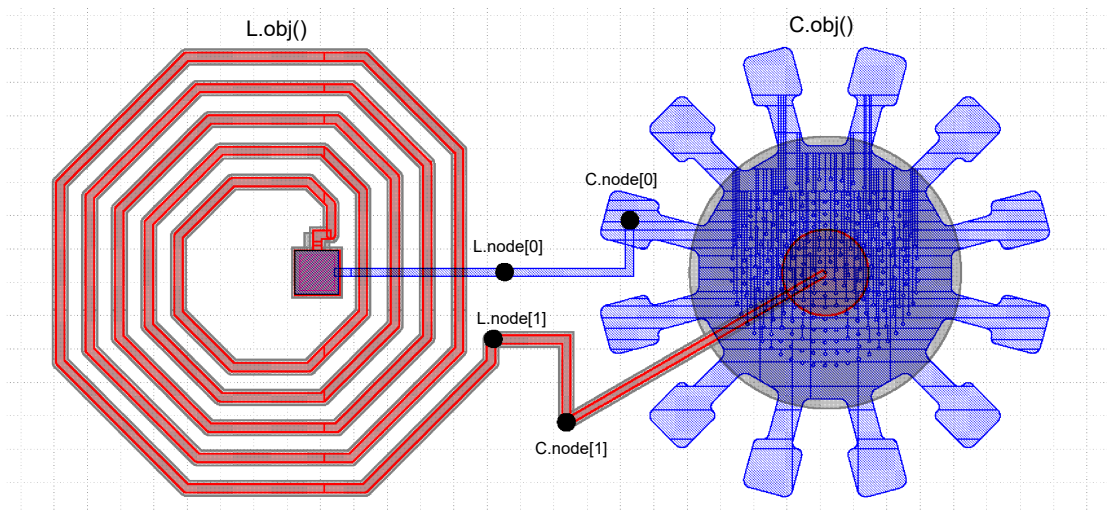


Figure 3.13: **GDSII design programming.** The LC circuit GDSII mask which is generated by the example piece of code provided above. Every element compounds several GDSII polygons in different layers corresponding to fabrication steps. The geometry of each element is controlled by the input argument of its Python object initiator function. Nodes of the elements can automatically be connected by wires.



## 4 Fabrication

In this section, we briefly present the challenge in the conventional nano-fabrication technique for circuit optomechanics, limiting drumhead mechanical resonators' mechanical coherence and reproducibility. Then we introduce the novel fabrication process to overcome such challenges and discuss each step of the process in detail. Finally, we provide more information on a few topics regarding the fabrication of electro-mechanical systems.

### 4.1 History and challenges of the conventional circuit optomechanical platforms

Vacuum-gap capacitors have been studied in the field of superconducting circuit quantum electrodynamics to reduce the losses in microwave resonators by removing the typically lossy dielectric layer of the capacitor and increasing the participation ratio of the electric field in vacuum (Cicak et al., 2010). Naik et al. (2006) was the first work where superconducting vacuum gap capacitors - in the form of high aspect ratio parallel metalized beams hosting MHz range vibrational modes - were used to study the optomechanical interaction in the microwave frequency range in the superconducting circuits platform. The low optomechanical coupling rate and participation ratio (the ratio of vacuum gap capacitance to the total capacitance including the stray capacitance of other circuit's components) in the parallel beam capacitors made this first-generation platform challenging to reach quantum limits in experiments based on such a platform. J. D. Teufel, Donner, Castellanos-Beltran, et al. exploited drumhead parallel-plate vacuum gap capacitors in an optomechanical experiment, realizing ground-state cooling of the mechanical drumhead vibrational mode thanks to the large enough optomechanical coupling and participation ratio in the new platform.

Figure 4.1 shows an overview of circuit optomechanical devices developed in several research groups. Since 2010, when the conventional nano-fabrication process of making superconducting vacuum-gap capacitors was introduced by Cicak et al., the design and process did not have a substantial change, while it was used to implement outstanding quantum experiments in optomechanics, including ground state cooling (J. D. Teufel, Donner, D. Li, et al.,

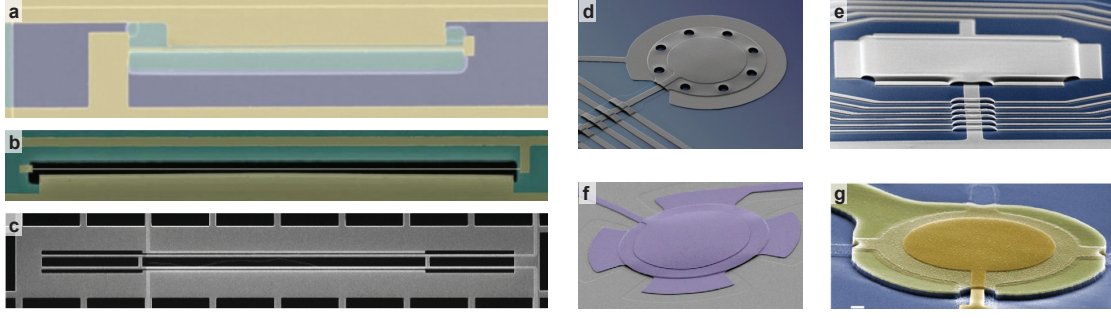


Figure 4.1: **Examples of circuit optomechanical devices.** **a, b, c,** shows the first generation of the electro-mechanical devices using suspended metalized beams developed in EPFL (Zhou et al., 2013) (shown in **a**), NIST/UC Boulder (J. D. Teufel, Donner, Castellanos-Beltran, et al., 2009) (shown in **b**), and IST (Barzanjeh, Redchenko, et al., 2019) (shown in **c**). **d-f** shows the second-generation based on parallel plate vacuum gap capacitors. **d**, NIST/UC Boulder device (J. D. Teufel, Donner, D. Li, et al., 2011). **e**, Caltech device (Wollman et al., 2015). **f**, EPFL device (Toth et al., 2017). **g**, Aalto device (C. Ockeloen-Korppi et al., 2018).

2011), mechanical squeezing (Wollman et al., 2015), and entanglement (Kotler et al., 2021; C. Ockeloen-Korppi et al., 2018) to name a few.

The main steps of the conventional process (Fig. 4.2a) consist of deposition and definition of the bottom plate of the capacitor, deposition of a sacrificial layer covering the bottom layer, deposition and definition of the top capacitor plate, and finally releasing the device by removing (isotropic etching) the sacrificial layer. Following the same principle, several research groups realized circuit optomechanical systems using various sets of sacrificial materials on different substrates such as  $\text{Si}_3\text{N}_4$  on sapphire at NIST (J. D. Teufel, D. Li, et al., 2011), polymer on Si at Caltech (J. Suh et al., 2014),  $\text{SiO}_2$  on quartz at Aalto (Pirkkalainen, Damskäg, et al., 2015), and aSi on sapphire at EPFL (Toth et al., 2017).

Due to the deposition-induced compressive stress in the superconducting thin film (mostly aluminum), the drumhead capacitor buckles up after the release at room temperature, which increases the gap size between two plates up to a few micrometers. Cooling down such devices induces tensile stress in the aluminum film due to the high thermal expansion rate difference with the substrate. Under tensile stress, the drumhead shrinks down and buckles in the opposite direction, resulting in a small ( $\sim 50$  nm), but not accurately predictable, nor reproducible, gap size. This prevents precisely controlling the microwave and mechanical properties of the system at low temperatures and reduces the reproducibility of the design given the high probability of deformations and collapses after the release (Tóth, 2018). In practice, any non-uniformity of the stress distribution in the drumhead after release or asymmetric buckling results in an uncertainty in the final gap size at cryogenic temperatures. This can be in the order of tens of nano-meters, hence limiting the frequency fluctuation in the microwave LC resonator in the order of  $\mathcal{O}(10\%)$ . This was the main barrier to realizing multi-mode optomechanical systems and arrays in superconducting circuit platforms since the microwave and mechanical frequency control is an essential parameter in such systems.

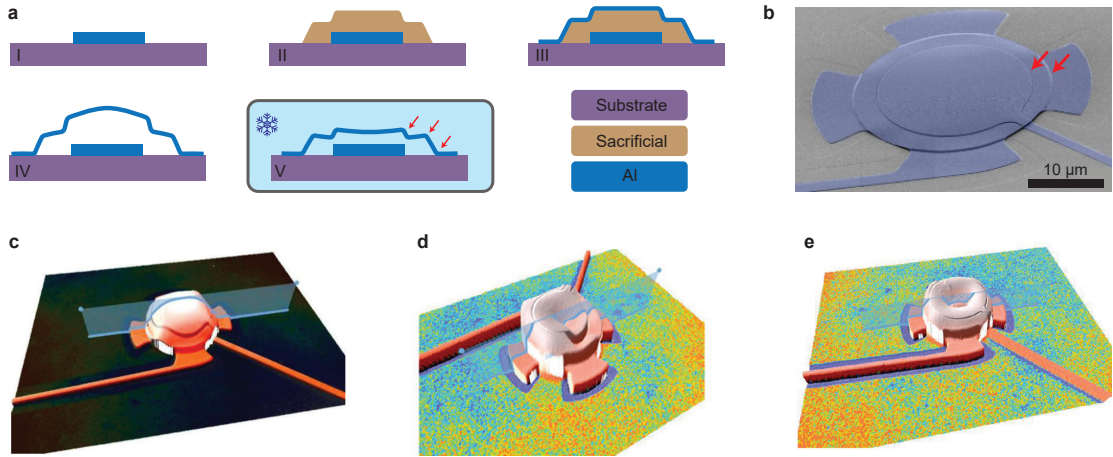


Figure 4.2: **Challenges of the conventional fabrication process for circuit optomechanics.** **a**, The conventional nano-fabrication process used to make mechanically compliant vacuum-gap capacitors: a sacrificial layer (aSi or  $\text{Si}_3\text{N}_4$ ) used to support the top layer. After the release, the capacitor buckles up around  $1\ \mu\text{m}$  due to the compressive stress in the deposited superconducting metal. At low temperatures, the drumhead shrinks resulting in a small but not accurately controllable gap size of  $\sim 50\ \text{nm}$ . Due to the non-flat topography of the sacrificial layer, the suspended plate has several edges close to the clamping point shown by red arrows. **b**, SEM image of a drumhead fabricated with the conventional process at EPFL (Toth et al., 2017; Tóth, 2018) showing the non-flat geometry of the mechanically compliant plate. **c**, Laser profilometry of a successfully released drumhead. **d,e**, Laser profilometry of a deformed and a collapsed drumhead correspondingly.

In addition, the non-flat geometry of the suspended plate -induced by the bottom plate's topography- and the presence of sharp step edges on the clamps increases the mechanical dissipation in such resonators dominated by the phonon tunneling loss (radiation loss) through the substrate (Cattiaux et al., 2021). This limited the mechanical quality factors up to  $Q_m = \mathcal{O}(10^5)$  in such devices.

## 4.2 The new nano-fabrication process for ultra-coherent and reproducible circuit optomechanics

The key idea to solve the existing challenges in circuit optomechanics can be expressed by *flat topography*. In the conventional fabrication process to make vacuum gap capacitors, the shadow pattern of the bottom electrode and sacrificial layer were imprinted on the topography of the suspended vibrating top plate. In contrast, we may imagine a flat topography for the tensioned vibrating plate. This naturally results in lower mechanical loss and prevents thermal-induced deformations, which affects the capacitor gap size. Figure 4.3 b shows a schematic 3D illustration of the vacuum gap capacitor we propose. A flat superconducting trampoline is suspended on top of a so-called *trench* etched in the substrate, containing the bottom electrode. The capacitor gap size is then determined by the depth of the trench minus

the thickness of the bottom electrode and will not be a function of the temperature in case of having tensile stress in the trampoline.

Here we present our novel nano-fabrication process to realize such a device and simultaneously improve the mechanical quality factor, the gap size control, and the process yield.

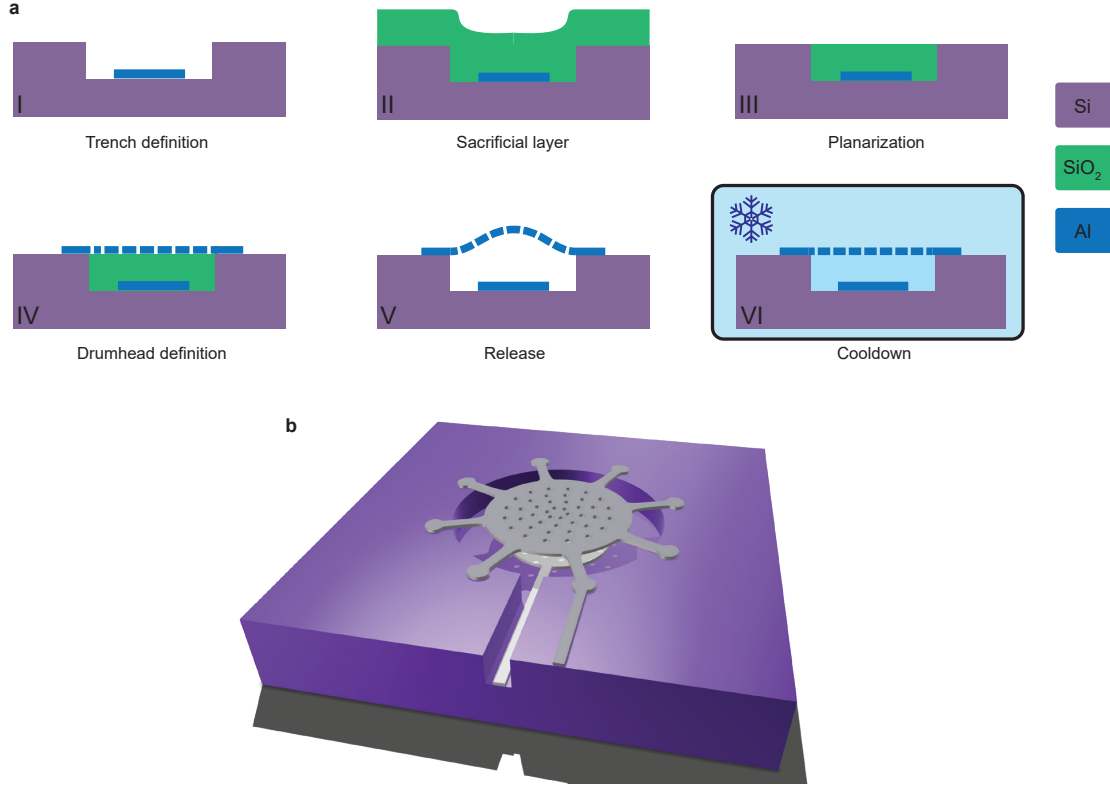


**Figure 4.3: Overview on the fabrication technique for the new generation circuit optomechanics.** **a**, The main steps of the process consists of etching a trench in the substrate followed by deposition of a sacrificial layer, planarization, top layer definition, release, and finally cool down. Due to the compressive stresses, the top plate will buckle up after the release. However, the drumhead shrinks and flattens at cryogenic temperatures, resulting in a controllable gap size. **b**, A schematic 3D model of the final structure. The drumhead parallel plate capacitor is flattened and suspended over the trench.

A brief overview of the developed process is shown in 4.3 a. The main steps of the process are as follows. We first define a trench in a silicon substrate by dry etching. Next, we deposit and pattern the bottom plate of the capacitor inside the trench. The trench is then covered by a thick SiO<sub>2</sub> sacrificial layer, which inherits the same topography of the layer underneath. To remove this topography and obtain a flat surface, we use chemical mechanical polishing (CMP) to planarize the SiO<sub>2</sub> surface. We then etch back the sacrificial layer down to the substrate layer and deposit the top Al plate of the capacitor. The sacrificial layer will be removed by HF vapor isotropic etching to suspend the structure. Although after the release the drumhead

may buckle -depending on the deposition-induced stress- up due to the compressive stress, at cryogenic temperature the high tensile stress ensures the flatness of the top plate. This will guarantee the gap size to be precisely defined by the trench's depth and the bottom plate's thickness. Furthermore, the top plate's flat geometry significantly reduces the drumhead resonator's mechanical dissipation.

The following sections will discuss each step of the process in detail.

### 4.2.1 Material selection

The main idea presented in Fig.4.3b can be implemented using different materials for substrate, superconducting metal, and sacrificial layer. However, process compatibility of materials and their resilience against different etching steps conducts us to choose a specific set of materials for this process.

#### Substrate

The standard options for substrates in superconducting circuits are sapphire, silicon, and quartz. Although sapphire has a low bulk loss tangent ( $\tan(\delta) \approx 10^{-7}$  (Read et al., 2022)) and is generally resilient to Fluorine chemistry etchants as well as acids, it is not the best option for our process. We initially tested sapphire wafers but observed insufficient adhesion of the sacrificial layer to the substrate, which was preventing full planarization (details are provided in Sec. A.3). Also micro-structuring sapphire is challenging since there are not many established processes to etch and manipulate this material. In contrast, silicon wafers show a perfect match to our process due to their processing flexibility -as many nano-fabrication techniques are optimized for silicon wafers at industrial levels- and high-quality wafer suppliers. The loss tangent of the silicon substrate is also low compared to other materials ( $\tan(\delta) \approx 10^{-6}$  (O'Connell et al., 2008)) An important note is to use a high-resistivity float-zone silicon wafer to minimize substrate impurities and losses of the superconducting circuit. Another parameter is the wafer's flatness, uniformity, and bow, which play an essential role in the CMP planarization step. We use a high-resistivity ( $> 20 \text{ k}\Omega\text{cm}$ ), low-bow ( $< 20 \mu\text{m}$ ), low total thickness variation (TTV  $< 5 \mu\text{m}$ ) float-zone intrinsic silicon wafer with 10 cm diameter and 523  $\mu\text{m}$  thickness supplied from Topsil®. It is recommended to do a Piranha (sulfuric acid with peroxide 100°C) cleaning followed by HF cleaning (1% diluted) on the raw wafers before the process.

#### Superconducting metal

Aluminum is a widely used material in the field of superconducting circuits, because of its flexibility in micro-structuring, simple deposition -evaporation or sputtering-, high enough superconducting critical temperature ( $\sim 1.2 \text{ K}$ ), and self-passivating thin oxide layer. For these reasons we also decided to keep aluminum as our superconducting material. This makes future integration of our circuits with conventional superconducting qubits more straightforward. Other materials such as Titanium nitride, Niobium, or Tantalum could also be candidates because of their higher critical temperature, however, they are less compatible

with the release process, form more complex amorphous structures and oxide compounds, and has unknown mechanical properties at low temperatures.

### Sacrificial layer

Amorphous silicon (aSi), silicon nitride ( $\text{Si}_3\text{N}_4$ ), silicon oxide ( $\text{SiO}_2$ ), and polymer photoresists are four candidates for sacrificial layer used in the previous generation of circuit optomechanical devices. Each one needs different isotropic etching as the release process. For example aSi can be removed by  $\text{XeF}_2$ , which is an exothermic pulsed gas etching.  $\text{Si}_3\text{N}_4$  can be etched by  $\text{SF}_6$  plasma, and polymer resists by oxygen plasma. We decided to use  $\text{SiO}_2$  as our sacrificial layer which can be removed with HF vapor, enabling us to release high aspect ratio structures by avoiding plasma or wet etching, therefore increasing the yield and successful release rate of the process. More details will be discussed in the release section (Sec. 4.2.12).

### 4.2.2 Optical lithography

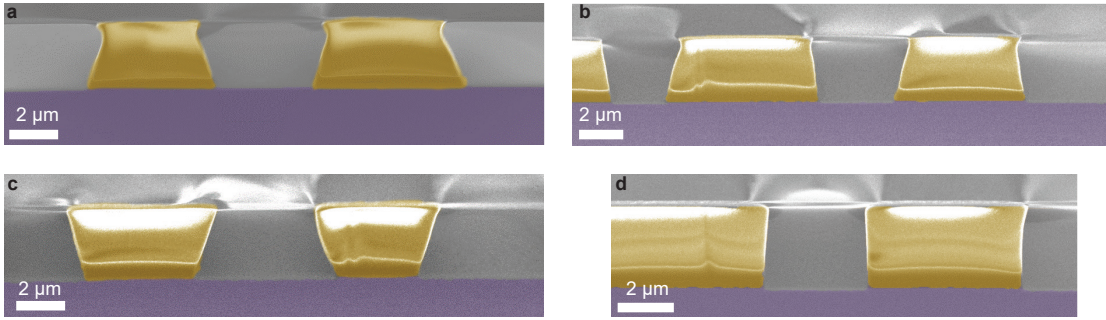


Figure 4.4: **Photo-resists cross section.** The cross-section SEM images show the sidewall angle of different photoresists. This is important for a clean etching of lift-off process. **a**, AZ<sup>®</sup> 1512 positive resist. **b**, AZ<sup>®</sup> ECI 3007 positive resist. **c**, AZ<sup>®</sup> nLof negative resist with high development recipe. **d**, AZ<sup>®</sup> nLof negative resist with low development recipe.

We use optical lithography to transfer patterns on the photoresist. It is performed by direct mask-less optical lithography (Heidelberg<sup>®</sup> MLA 150). We spin coat a  $1\ \mu\text{m}$  thick AZ<sup>®</sup> ECI 3007 positive photoresist after HMDS surface preparation. All photoresist coating and developing steps are processed using automatic coater/developer (Süss<sup>®</sup> ACS200 GEN3). The exposure dose and depth of focus vary based on the tool and need to be calibrated by dose tests, but are typically set to  $\sim 150\ \text{mJ}/\text{cm}^2$ . After the exposure, the resist will be developed, and the wafer will be rinsed in a spin dryer to clean any unwanted contamination. To remove residual photoresist on the surface of exposed areas, we conduct a short (10-20 seconds) oxygen plasma descum at 200 Watts and 200 sccm (Tepla<sup>®</sup> GiGAbatch). After the descum, the wafer is ready for the etching step. Cross-section SEM comparison of a few positive and negative photoresists after exposure and development is shown in Fig. 4.4.

It is worth noting that the perfect exposure dose is different when etching silicon trench or etching aluminum film because of the different reflectivity of the surface. This needs to be



tuned by separate dose tests with and without the aluminum layer. An example of a dose test pattern is shown in Fig. 4.5.

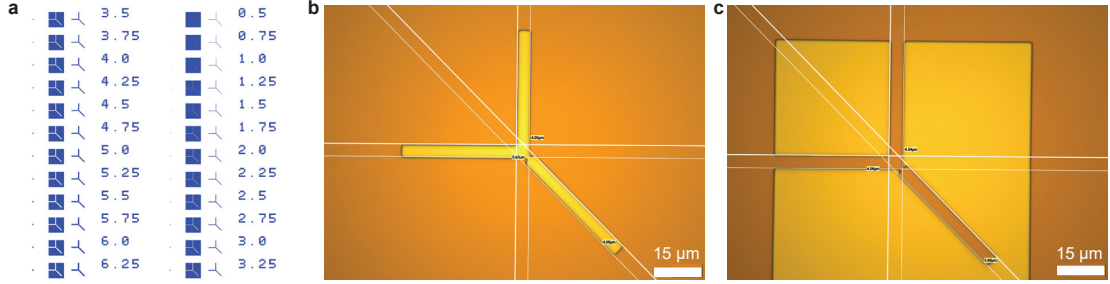


Figure 4.5: **Dose test.** **a**, A dose test pattern containing lines with various angles and widths, both for positive and inverted lithography jobs. The circuit wires are written in the inverted mode using positive resist for aluminum etching, while the trench itself is patterned without inversion. The pattern is written with different doses and depths of focus in direct (mask-less) lithography. We extract the critical dimensions of the wire and trenches using the optimized dose. **b, c**, Examples of positive and inverted patterns after dose test resist development.

The critical dimensions can be achieved by direct laser writing is  $CD \approx 1 \mu m$  minimum thickness of a pattern and pattern size fluctuation of  $\Delta_d \approx 500$  nm. Compared to the sizes of drumhead capacitors and spiral inductors, these CD and SF are sufficiently low resulting in mechanical frequency disorder of  $\frac{\Delta \Omega_m}{\Omega_m} = \frac{\Delta_d}{R} \approx 1\%$  for a trench radius of  $R = 50 \mu m$ . However, when size fluctuation of drums and trenches matter – e.g., to observe collective mechanical phenomena when degenerate mechanical modes are desired – we may consider electron beam lithography ( $\Delta_d \approx 5$  nm) or deep UV lithography ( $\Delta_d \approx 50$  nm). This may result in smaller disorder of mechanical frequencies down to  $\sim 0.01\%$  and  $\sim 0.1\%$  for e-beam and DUV, respectively. Nevertheless, the microwave frequencies are more robust to lateral size fluctuations since the spiral inductor is a relatively large structure with a less concentrated electromagnetic field (compared with meander inductors or interrogated capacitors), and the value of inductance is less sensitive to the thickness disorder of the wire.

After each etching step, the photoresist will be stripped first using UFT remover 1165 wet process, followed by rinse and drying, and 3 minutes 600 Watt and 400 sccm Oxygen plasma (Tepla<sup>®</sup> GiGAbatch). In case the wafer contains not covered aluminum thin-films it is recommended to keep the wafer longer in UFT remover and expose it lower to Oxygen plasma by either reducing power or exposure time to avoid additional oxidation and local heating of the metal, specifically for the vibrating top plate.

#### 4.2.3 Etching trenches in silicon

After lithography, we use deep reactive ion etching (DRIE) to etch the trenches in the silicon substrate. We use  $C_4F_8$  chemistry plasma as etchant (Alcatel<sup>®</sup> AMS200) with a typical etch rate of  $\sim 13$  nm/sec and selectivity of Si:PR  $\sim 10 : 1$ . Since the total depth of etch is tuned by time and the etch rate fluctuates in such a tool, it is recommended to use test wafers with

a similar pattern to calculate the etch rate by removing the resist and measuring the trench depth using mechanical profiler. The total etching depth should be set to  $\sim 30$  nm more than the target capacitor gap size plus the thickness of the bottom electrode to compensate for potential non-uniformity in the CMP planarization step among different chips on a wafer. The excess depth after CMP can be etched back by IBE in the following steps to reach the desired gap size. The roughness of the silicon inside the trenches is measured  $R_a \approx 1.5$  nm with a trench depth uniformity of  $\sim 1\%$ .

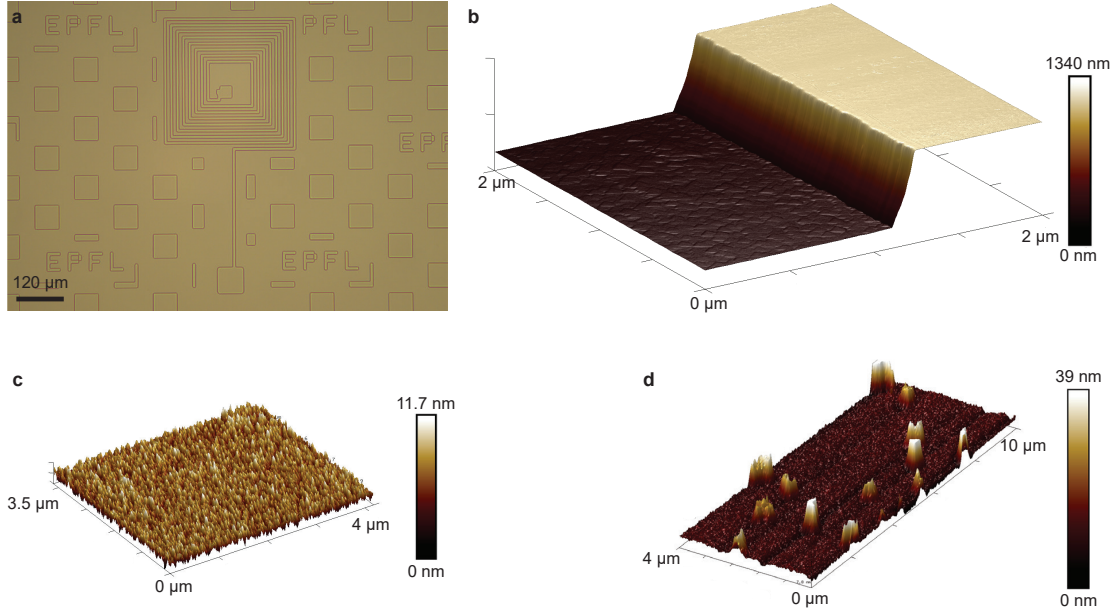


Figure 4.6: **Etching the trench in Silicon.** **a**, Optical microscope image of trenches. **b**, Atomic Force Microscopy of a test trench etched in Si with DRIE. **c**, AFM of the Si surface inside the trench. The average roughness is  $R_a = 1.5$  nm. **d**, An example of a trench etch when the resist descum was not enough. After the etch, the residual photoresist in the trenches results in big hillocks of Si.

#### 4.2.4 Bottom aluminum layer deposition

the bottom layer inside trenches contain the spiral inductor and bottom electrode of the capacitor. Although the spiral inductor can also be located on the top layer, we prefer to keep it in the trench to cover it by sacrificial layer and reduce contamination in the next steps specifically chip dicing. Since the metal-substrate interface has a major effect on the total loss of the superconducting circuit, we clean the wafer after trench etching with Piranha and dip it into HF (1% diluted) for a few minutes to remove the native silicon oxide. Then we abruptly rinse and dry the wafer and immediately transfer it to the deposition tool (less than 3 minutes) and pump down the chamber to avoid re-grow of the native oxide.

Deposition of the bottom aluminum layer can be done by either sputtering or electron beam evaporation. However, evaporation is preferred because of better thickness uniformity and



thickness control compared to sputtering. We typically choose 100 nm thickness for the bottom layer.

#### 4.2.5 Bottom layer patterning and etching

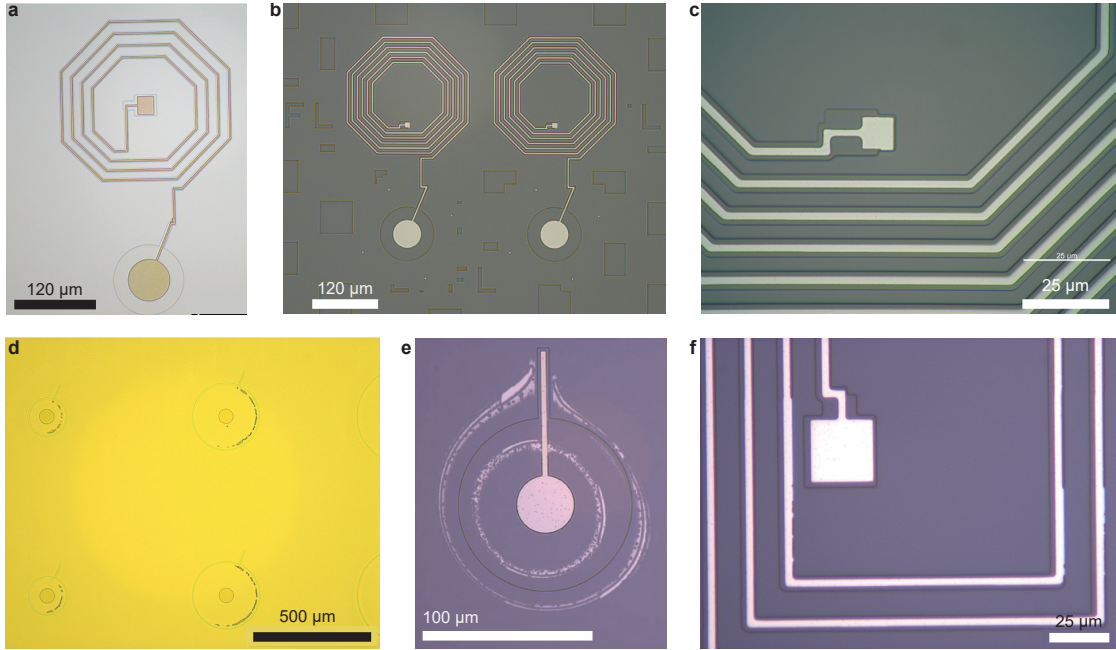


Figure 4.7: **Bottom Aluminum layer patterning.** **a**, Micrograph of a successfully patterned photoresist inside the trench to etch Al. **b**, **c**, Bottom layer circuits after a successful Al etch. **d**, Patterned photoresist after development when the thickness of the resist was not enough. The areas close to edges are under exposed. **e**, Etching result when the photo resist was not thick to compensate the trench topography and gets flattened in spin coating. **f**, When the metal wires pattern are too close to the trench edges, the trench's edge prevents a proper exposure in corners.

After deposition of the aluminum layer, we do a similar lithography as explained earlier (Sec. 4.2.2) to transfer the bottom circuit pattern on the photoresist. The difference is that here most of the aluminum layer will be etched and only the circuit parts will remain, which means the circuit pattern should be covered by resist. For this purpose the circuit pattern should be inverted before exposure of the positive resist. The inversion is done in the exposure tool job setup or by manually defining an inverted layer in GDS file. Another important note in this step is the topography of the surface. We require to perfectly expose both levels on the substrate as well as aluminum inside the trench which is typically  $\sim 300$  nm lower the surface level. Therefore, we increase the thickness of the resist to  $1.2 \mu\text{m}$  to reduce the topography thickness variation after spin coating and increase exposure dose respectively to avoid under-exposure inside the trenches, specifically on areas close to the trench edges (see Fig. 4.7). Due to the scattering effect of trench edges, we recommend a minimum spacing of  $2 \mu\text{m}$  between metal wires and the trench edges. We note that ideally all the metal outside of the design area should

be removed from the wafer, even close to the wafer edges. This helps uniformity of the CMP polishing.

We use wet etching to remove aluminum using the following chemistry at 35°C:  $\text{H}_3\text{PO}_4$  85% +  $\text{CH}_3\text{COOH}$  100% +  $\text{HNO}_3$  70% 83:5.5:5.5. Although the etch rate can be tuned by time, observing the wafer will tell us when the etching is done by an abrupt change of the surface color. After the color change, we keep the wafer  $\sim 10$  seconds more in the etchant and then rinse it. We note that in principle plasma etching of aluminum using chlorine chemistry will also work here, but may result in over etching of the silicon substrate since silicon is not resilient to this etchant. This may destroy the edge sharpness of the trenches and affect the mechanical properties of the drumhead resonator.

#### 4.2.6 Sacrificial layer deposition

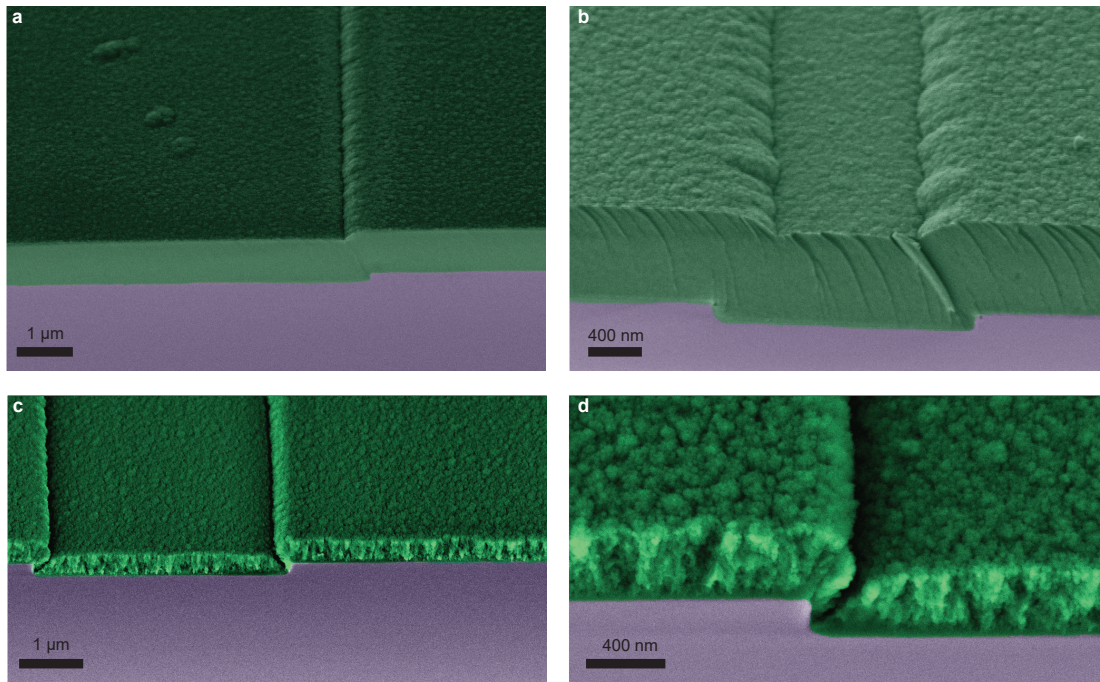


Figure 4.8: **SiO<sub>2</sub> sacrificial layer deposition.** **a, b**, Cross section SEM of low temperature oxide low pressure chemical vapor deposition (LTO LPCVD) of SiO<sub>2</sub> sacrificial layer covering the trenches. The step coverage and gap filling is perfect, the porosity is low, and the oxide layer is dense. **c, d**, Cross section SEM of plasma enhanced chemical vapor deposition (PECVD) of oxide at 200 Celsius. The oxide layer is porous and does not show a good step coverage, forming void areas at the corners of the trench.

Generally there are several methods to deposit/grow SiO<sub>2</sub> such as low pressure chemical vapor deposition (LPCVD), plasma-enhanced chemical vapor deposition (PECVD), low temperature oxide LPCVD (LTO), and sputtering which results in different levels of film quality, porosity, step coverage and adhesion to substrate. The SiO<sub>2</sub> sacrificial layer for our process requires

a few conditions to satisfy: it should be grown at low temperatures (below the melting point of aluminum at 660°C) to minimize aluminum damage, it should have a good step coverage, should not be porous to result in a flat surface after planarization, and should have high enough adhesion to the substrate to avoid delamination or dishing when a big mechanical shear stress is applied to the surface in CMP polishing.

The standard LPCVD normally gives the highest film quality but is operated at temperatures above 1000°C. Sputtering can be done at room temperature but yields a high porosity and soft SiO<sub>2</sub>. PECVD and LTO both can be operated at lower temperatures, 100-250°C and 300-450°C, respectively. We first tried PECVD because of the lower temperature, however, we realized the film quality was not high enough. The softness of the film was causing delamination in CMP, and the porosity was not low enough compared with the roughness of the aluminum top layer resulting in lower quality suspended aluminum film. Then we switched to LTO and found a perfect film quality, a dense oxide, and high adhesion. This can also be observed in CMP, when the etch/polish rate of LTO-grown oxide is measured ~ 30% lower than PECVD oxide. The LTO process is very slow (a few hours of deposition) and gives a very uniform film, often less than 0.5% non-uniformity for 3  $\mu\text{m}$  film around the wafer. We do not observe a tangible increase of the microwave loss in superconducting circuits exposed to the LTO process, as shown by the intrinsic loss ( $\kappa_0 \sim 25$  kHz) of our circuits. However, occasionally and irregularly, we observe small and sparse holes (less than 1  $\mu\text{m}$  diameter) on the bottom aluminum film after LTO. This may be due to contamination in the shared LTO chamber. Nevertheless, we did not observe any impact on the circuits due to this effect. A comparison SEM cross sections of LTO and LPCVD oxides are shown in Fig. 4.8.

The thickness of the grown sacrificial layer should be 4-7 times more than the maximum topography of the wafer, i.e. the trench depth. For example for a 300 nm trench we deposit 2  $\mu\text{m}$  oxide layer. This guarantees enough room to run CMP which simultaneously etches and planarizes the surface.

#### 4.2.7 Chemical-mechanical polishing

CMP is the key step in our process to remove the topography of the trench and bottom layer from the sacrificial layer. The CMP technology is widely used in micro-electronics and integrated circuit industry to planarize copper interconnects and oxide layer (Luo and Dornfeld, 2001). Planarization is a hybrid process of chemical etching and abrasive and corrosive mechanical polishing using liquid slurry nano-particles. As shown in Fig. 4.9, the tool consists of a big rotating polishing pad, a rotating head that holds the wafer, a slurry nozzle, and a conditioning head. The wafer will be fixed upside-down to the head. Then the head will bring the wafer close to the polishing pad and press it on the pad. Both pad and head rotate while the head also laterally moves around the pad. The slurry nozzle pours a little slurry on the pad to facilitate polishing. The conditioning head is separately used to clean and polish the big rotating pad itself after each planarization run. Although the tool often



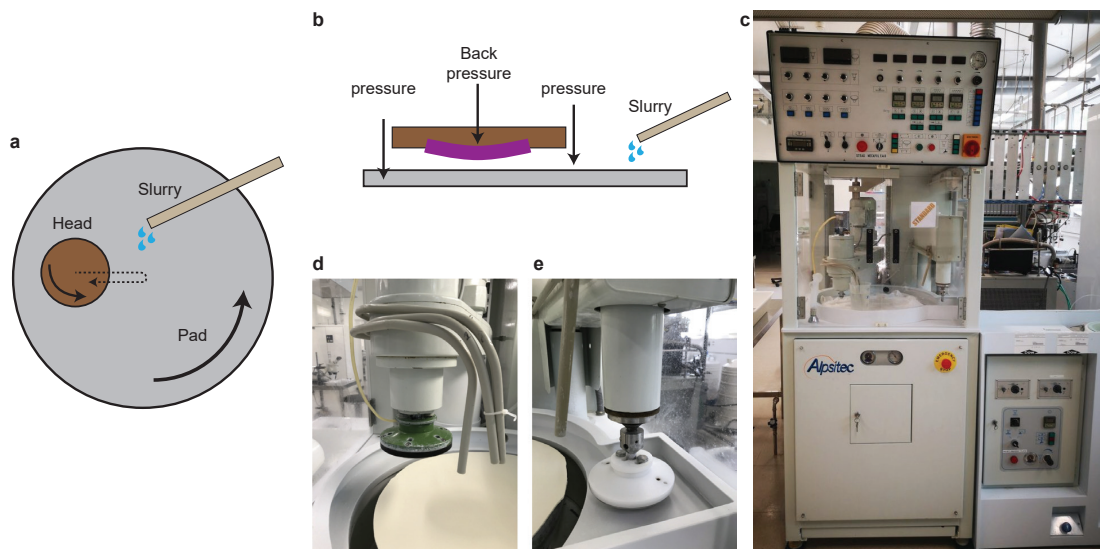


Figure 4.9: **Chemical mechanical polishing tool.** **a**, Top view schematics of CMP tool. A rotating head holding the wafer is moving back and forth to polish the wafer on a big rotating pad with rough surface. The pad is moisturized with a liquid slurry containing abrasive nano-particles. **b**, The side view schematics showing the head pressure and the back pressure used to compensate the wafer's bow. **c**, A photo of the CMP tool used in EPFL CMI cleanroom. **d**, Photo of the polishing head and slurry nozzle. **e**, Photo of the conditioning head used to clean and prepare the polishing pad after each run.

has many knobs to tune different parameters, the most important ones to manipulate for a successful CMP planarization are the pad rotation speed, the head rotation speed, the head pressure on the pad, the back-pressure (for holding the wafer and tune its bow), the slurry rate, and the polishing time. Normally the tool does the polishing in three steps. The first step is surface preparation. The second is the longest step for polishing and the last for cleaning by replacing the slurry with water. After each run, conditioning is required to clean the pad. As mentioned, CMP planarization simultaneously etches the oxide layer and smooths the edges and reduces the topography. The etching rate varies based on the oxide type, pressure, slurry rate, etc. in the range of 100-300 nm/minute, but nonlinear due to the pad softening and heating up (this means that running the CMP two times with a conditioning in between gives a different etch rate of running it once with double of the time). The polishing rate is also depend on parameters and very nonlinear, often higher when topography is deep and lower when it gets shallower (see fig. 4.10). The process is often optimized for 2-3 minutes of polishing time and then will be repeated several times with a conditioning between each cycle. We normally need to remove a thickness of 2-4 times higher than the maximum wafer topography to planarize it, this is the reason that we deposit a thick sacrificial layer in LTO.

There is always a trade-off between uniformity and residual topography when running CMP. Polishing the wafer for longer times and number of cycles will reduce the topography –with a nonlinear trend often saturates by dishing effect– but increases the thickness non-uniformity.

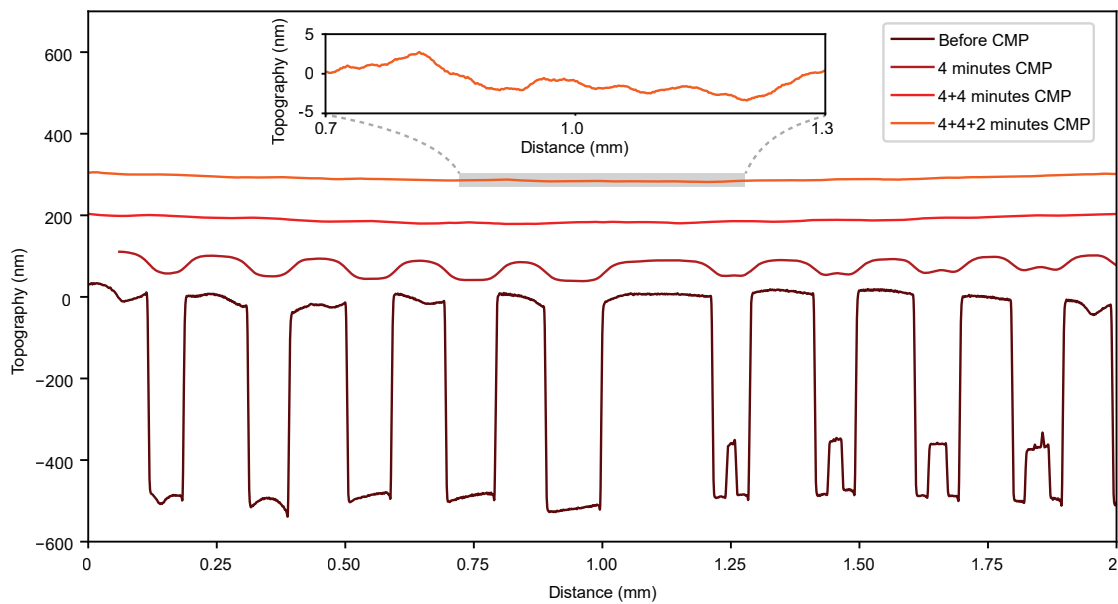


Figure 4.10: **Topography planarization in CMP.** CMP enables us to reduce the surface topography from  $\sim 500$  nm (the trench depth) to below 10 nm. The figure shows the effect of successive CMP runs on the topography measured by a mechanical profilometer. The final global curve in the topography shows the wafer bow. The inset shows magnified final topography.

Therefore it is crucial to optimize the process parameters to get as high as possible uniformity in each cycle, while keeping sufficient planarization. This needs several iterative tests on dummy wafers. The effect of each parameter on the etch rate and polishing is explained in the following. Note that all numbers provided are tuned for the tool we use (ALPSITEC<sup>®</sup> MECAPOL E 460) and may vary for other machines.

- **Pad and head rotation speeds:** higher speed increases both etch rate and polishing rate, normally set around 80 rpm in our case.
- **Slurry rate:** higher rate increases the chemical etching faster than mechanical polishing rate. Normally set to a low rate to just wet the pad. However, very low rate significantly increases the non-uniformity of the polishing due to the high friction.
- **Head pressure:** Increases the polishing rate faster than the etch rate. normally set around 0.5 Bars. Using very high pressures deforms the wafer and increases etching non-uniformity.
- **Back-pressure:** The wafer has a slightly bowed structure causing higher pressure on the edges than it would be on the center, which results in non-uniform polishing. In order to compensate for the wafer bow, back-pressure is applied to the wafer's backside which will equalize the center to edge etch rate difference. This is a crucial parameter to manipulate to reduce the non-uniformity.

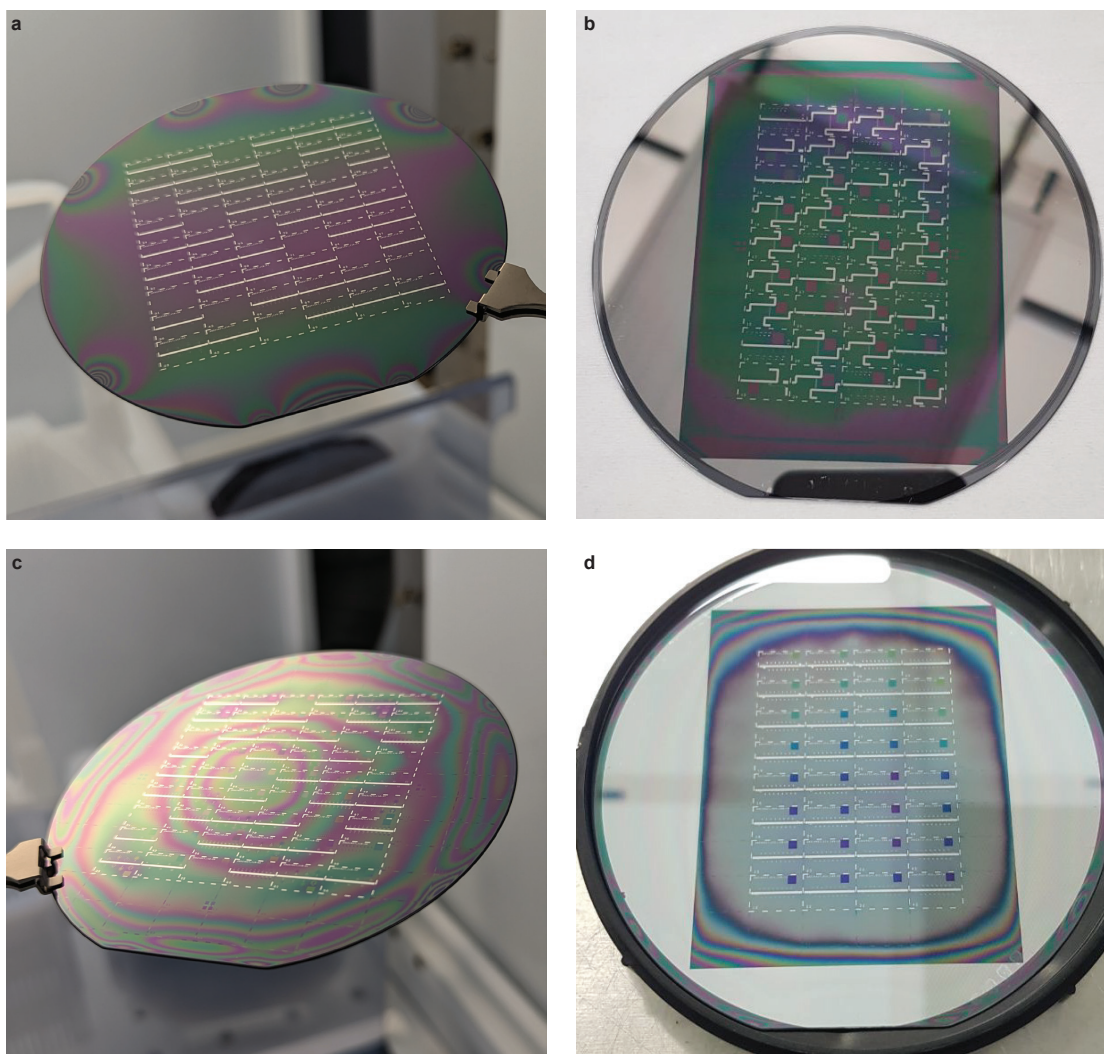


Figure 4.11: **CMP uniformity.** Photos show different wafers after CMP planarization. **a, b,** Showing successful CMP planarization with low non-uniformity around the center of 10 cm wafers. The non-uniformity can be quantitatively measured using optical reflectometer using the big square trenches on every chip. In addition, qualitatively the uniformity can be inspected by color change in fringes forming on the wafer due to the thickness variation of the remaining oxide film. **c,** CMP result when the back-pressure was not properly tuned to compensate the etch rate variation. **d,** It is recommended to remove the excess metal throughout the wafer to increase uniformity. In this wafer, although the uniformity is acceptable at the center, the excess metal imposes thickness variations on the edge chips. the photo is taken after IBE etch-back.

Delamination in CMP happens when sacrificial layer adhesion is not enough, or the thickness of the layer outside of the trench gets very thin. In this case the mechanical shear stress can peel off the sacrificial layer from the trench and creates voids on the corners of the trench (see Fig. 4.12 b-d). For this reason, we always make sure to stop the polishing  $\sim 500$  nm above the substrate level. The remaining oxide layer will be etched back in the next step with IBE.



Dishing effect is generally the final limit for planarization, when the trench's topography gets very smooth and wide over a few hundred microns with a residual depth of  $\sim 5$  nm. In order to minimize dishing and delamination effect, and increase the polishing uniformity, we fill all the empty areas of the wafer and between circuits with *dummy patterns*. These patterns are squares with the size of  $60\mu\text{m}$  with double of this size spacing as shown in Fig. 4.27. This substantially influences the polishing quality. Another helpful tip for a successful CMP is to

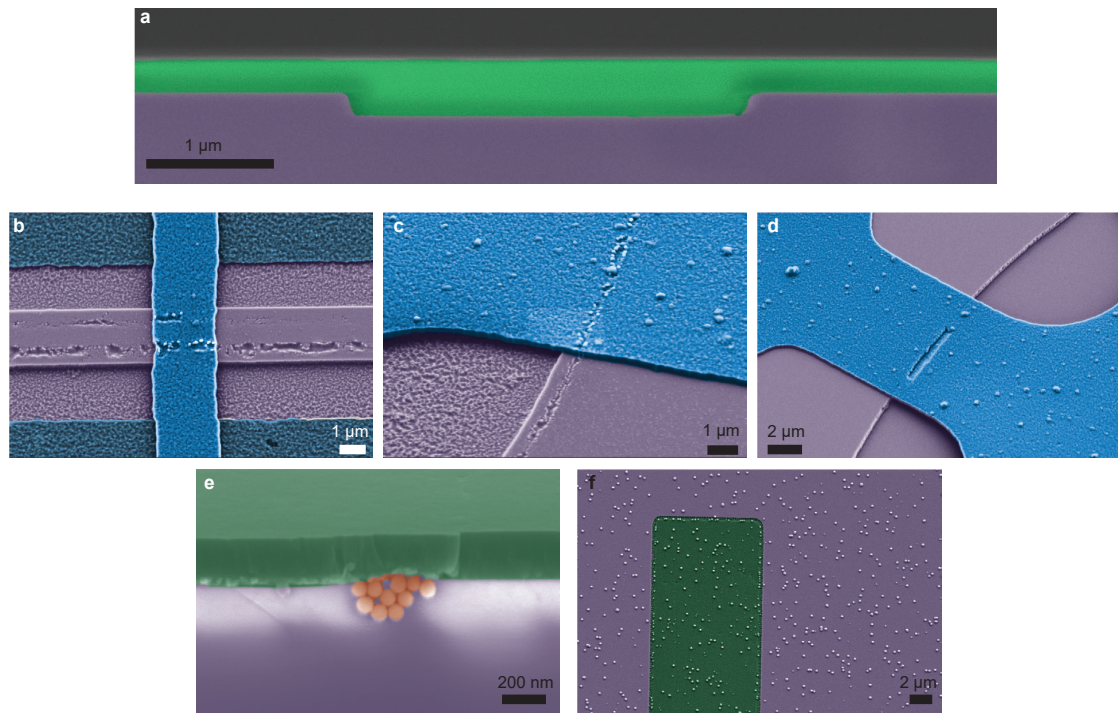


Figure 4.12: **CMP planarization.** **a**, A cross section SEM showing successful CMP planarization of oxide sacrificial layer covering a trench. The remaining oxide will be removed by IBE to prevent delamination. **b-d**, SEM of released final devices where the CMP etched oxide and reached too close to the substrate surface resulting in delamination of the sacrificial layer, creating voids at the edges of the trench and cracks on sidewalls of the trenches. **e, f**, SEM showing the slurry nano-particles after CMP (with PECVD oxide sacrificial layer for these samples). The slurry particles should be cleaned before IBE step using one of the cleaning techniques mentioned in the text.

use a flat wafer, i.e., low bow and low TTV. We usually expect higher quality chips from the half middle of the wafer ( $\pm 2.5$  cm from a 10 cm wafer) and optimize uniformity and polishing for this area. However, it is essential to extend the topography pattern to the edges of the wafer to help a uniform polishing.

The final measurement of the residual topography can be done by mechanical profilometer (KLA<sup>®</sup> Tencor D600). However, the residual thickness of the sacrificial layer (inside or outside of the trench) can not be measured without an optical spectroscopic reflectometer (Nanospec<sup>®</sup> AFT-6100 or FilMetrics<sup>®</sup> F54-XY). to measure the thickness inside the trenches, we always

locate a big dummy trench ( $\sim 0.5 \times 0.5 \text{ mm}^2$ , bigger than the waist diameter of the optical beam) on every chip to be able to individually measure chips and extract a wafer map of the residual thickness.

After the CMP polishing, the remaining slurry particles on the wafer must be removed (see Fig. 4.12 e and f). These particles are a few hundred nano-meter big spheres that can be easily seen under SEM, resulting in surface contamination and, more importantly, topography disorder of the top aluminum plate. The ideal method to remove the slurry is to use a post-CMP cleaning tool (GnP<sup>®</sup> Cleaner 428) immediately after the CMP before the wafer dries out. This tool uses dedicated brushes and sonication to remove these particles completely. However, if such this tool is not available, dipping the wafer in diluted liquid HF (1%) for  $\sim 1$  minute will remove the particles while slowly etching the SiO<sub>2</sub> layer uniformly.

Here we provide a short technical note on the CMP operation procedure we use to polish the wafers:

- We first set up the tool, prepare the slurry (often 30N50, a basic slurry made of colloidal SiO<sub>2</sub> particles for dielectric polishing), and run a 1-minute pad conditioning. We sometimes dilute the slurry with water (1:1) to decrease the etch rate and increase the mechanical polishing effect.
- We start with plain dummy silicon wafers covered with the same oxide layer grown together with the main wafers in LTO. These plain dummy wafers have no pattern and are just used to optimize the etching rate and uniformity of the CMP. We measure their uniformity and average oxide thickness optically and run a single CMP cycle with optimized parameters from our previous experiences. After the run, we simply rinse and dry the plain dummy wafer and measure it again optically. With this, we can extract the average etch rate as well as the non-uniformity of the etch. Depending on these two values, we modify the back pressure (to increase uniformity), head pressure, and slurry rate (to change the etch rate). We then use another clean and plain dummy wafer with the modified parameters and continue this iteration until we reach the minimum possible non-uniformity (usually around 1% non-uniformity after a single CMP run).
- After the uniformity optimization, we use another set of patterned dummy wafers (with exactly the same trench depth and pattern of the trenches we have on the design) to check the planarization rate. We measure the initial topography with a mechanical profilometer. After running an optimized CMP cycle, we measure the topography again to see how much the trench depth is reduced on the sacrificial layer. We continue running CMP cycles to ensure the topography can be reduced to less than 10 nm in a reasonable cycle number (not etching more than 5 times the trench thickness and not reaching closer than 500 nm to the substrate surface to avoid delamination). If the process does not work properly or results in a low planarization rate, we go back to the first step and increase the head pressure or modify the slurry rate and repeat the procedure.



- When all the suitable parameters are achieved, we switch to the main wafers. We run the CMP for several cycles on the wafer, including a 30 s pad conditioning between each cycle until we reach to the residual topography tolerance. After that we immediately run the post-CMP cleaning.
- Finally, we measure the residual thickness of  $\text{SiO}_2$  on the big square trenches we discussed earlier and extract a chip-wise map of thickness over the wafer area.

Table 4.1 shows optimized parameters for a CMP run for our tool.

Table 4.1: Optimized parameters for one cycle of CMP.

Step	Head speed (rpm)	Pad speed (rpm)	Pressure (Bar)	Time (s)
Preparation	40	60	0.2	15
Polishing	78	85	0.4	120
Cleaning	100	100	0.25	30
Slurry	7A5 Gal (pure) or 30N50 (1:1 diluted), both with the flow of 1/10.			
Back pressure	0.25 Bar			

#### 4.2.8 Ion beam etching

After the CMP, we need to etch back the remaining  $\text{SiO}_2$  to reach the Si surface. IBE does this, a physical etching process that uses argon ions also called argon milling. The advantages of using IBE are the extremely uniform etching, slow etch rate, which increases the controllability of the process, and, most importantly, offering almost 1:1 etch selectivity for Si: $\text{SiO}_2$ . The latter is crucial to avoid increasing topography when reaching the wafer's surface. We normally over-etch the surface by  $\sim 20$  nm to make sure all  $\text{SiO}_2$  is removed, and we will have good contact between the top aluminum layer and the Si surface during the HF release process. For this purpose, we have to use a 1:1 selectivity etching process to ensure the sacrificial layer inside the trench will not be etched faster than the Si substrate so that they will be removed together and the flat topography will be maintained. In IBE the wafer rotates during etching (10 rpm in our case) to increase uniformity and it can be exposed to an ion beam with an adjustable angle. This not only modifies the etching rate, but also helps to reduce the re-deposition effect of IBE - when the etched particles get accumulated on the edges of the pattern and create unwanted bumps. In addition doing angled IBE is also a polishing method, since the sharp topographies will be bombarded by ions from different directions and get smoother. The IBE tool we use (Veeco<sup>®</sup> Nexus IBE350) offers different etching powers corresponding to 35 nm/minute (*Low* recipe) and 125 nm/minute (*High* recipe) etching rates for 45 degrees wafer angle. The roughness of the surface will not significantly increase after IBE, and is measured  $R_a \approx 0.75$  nm for Si substrate.

We typically conduct a course IBE with the High recipe until we reach to close to the surface,

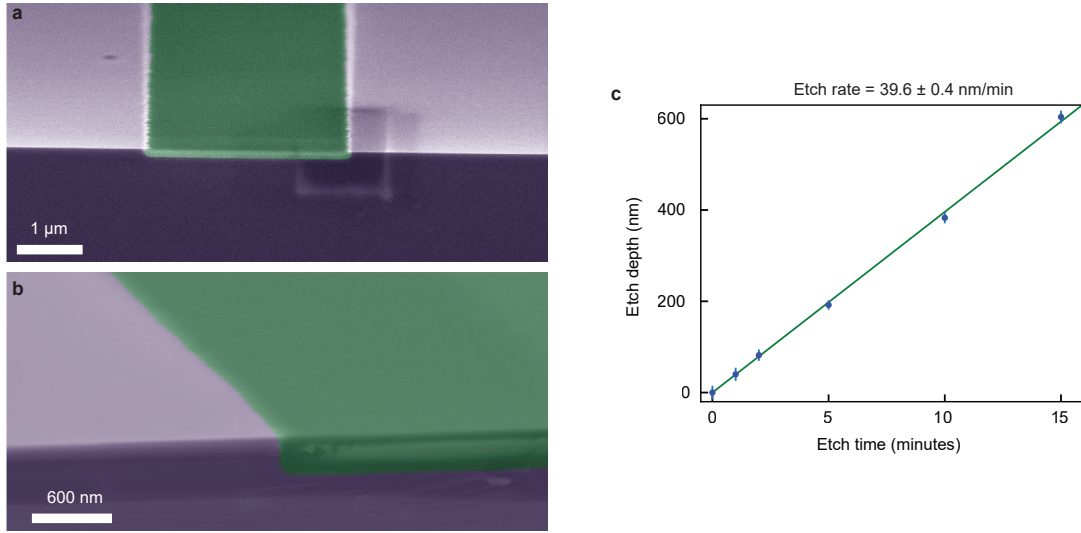


Figure 4.13: **IBE etch-back.** **a**, SEM images showing trenches after planarization and IBE etch-back. The oxide-silicon border is dense and smooth, making a perfect condition for top-layer deposition. **b**, Extracting the etching rate of IBE (Low power recipe). The linear and slow IBE etch rate as well as its 1:1 selectivity for oxide and Si enables us to accurately control the process, land on the Si substrate and over etch it to fine-tune the final gap size.

then we optically measure again the thickness of the sacrificial layer on the trenches (using the big pads discussed earlier) and run a fine IBE with Low recipe and set timing in a way that the Si surface will be over etched with the same amount of tolerance we had added to the trench depth when etching Si to reach to the target gap size.

#### 4.2.9 SiO<sub>2</sub> opening for galvanic connection

Before the deposition of the top aluminum layer, we need to create an opening window in the sacrificial layer to connect the top and bottom circuits galvanically. The galvanic connection can be evaded by making two parallel plate capacitors in series (as shown in Fig. 4.14). In this case, the optomechanical coupling rate will be diluted proportionally to the capacitors' participation ratio. However, we decided not to dilute the coupling and create a direct galvanic contact between the top and bottom layers.

We define square pads of  $\sim 20\mu\text{m}$  size at end of bottom and top wires coming from spiral inductor and capacitor respectively to form the galvanic connection. After IBE we coat the wafer with the normal photoresist and lithographically define an smaller rectangle on top of the SiO<sub>2</sub> layer covering the bottom connection pad. This pattern will be etched to open a window in SiO<sub>2</sub> and let direct galvanic connection during the top Al layer deposition.

Since the thickness of the top aluminum layer is comparable with the height difference between the wafer surface and the bottom layer surface inside the trench, it is essential to

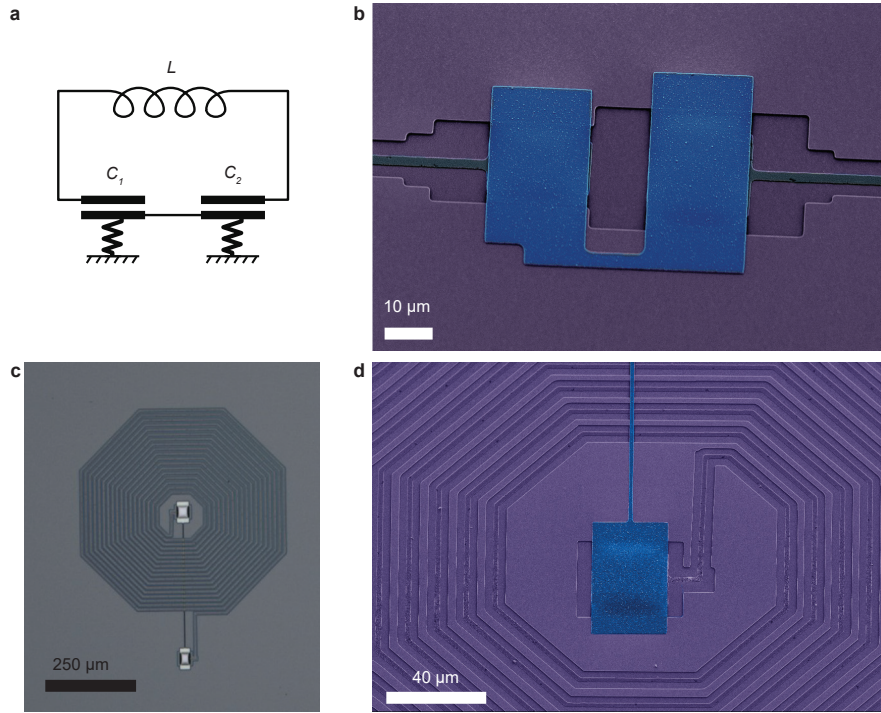


Figure 4.14: **Circuits without galvanic connection.** **a**, Circuit diagram of an electro-mechanical system with two mechanical oscillators which does not require galvanic connection of top to bottom layers. Since two capacitors are in series, the optomechanical coupling for each of them will be reduced proportional with their participation ratio. **b**, SEM of a double-capacitor circuit without galvanic connection. **c**, **d**, Micrograph and SEM of a circuit with spiral inductor and two capacitors inside and outside of the spiral connected through the spiral airbridges.

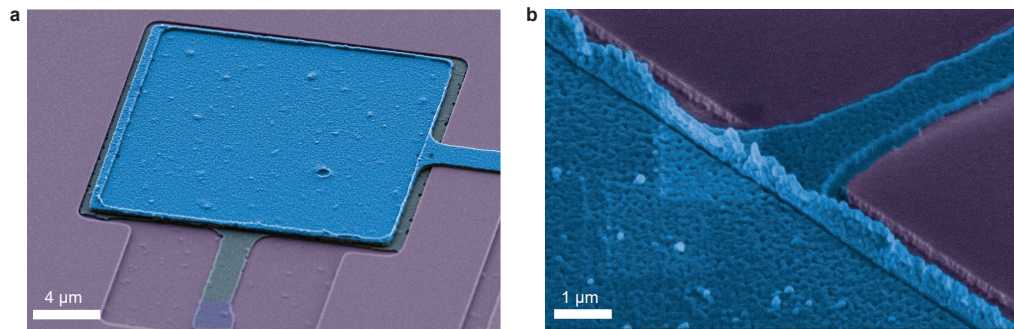
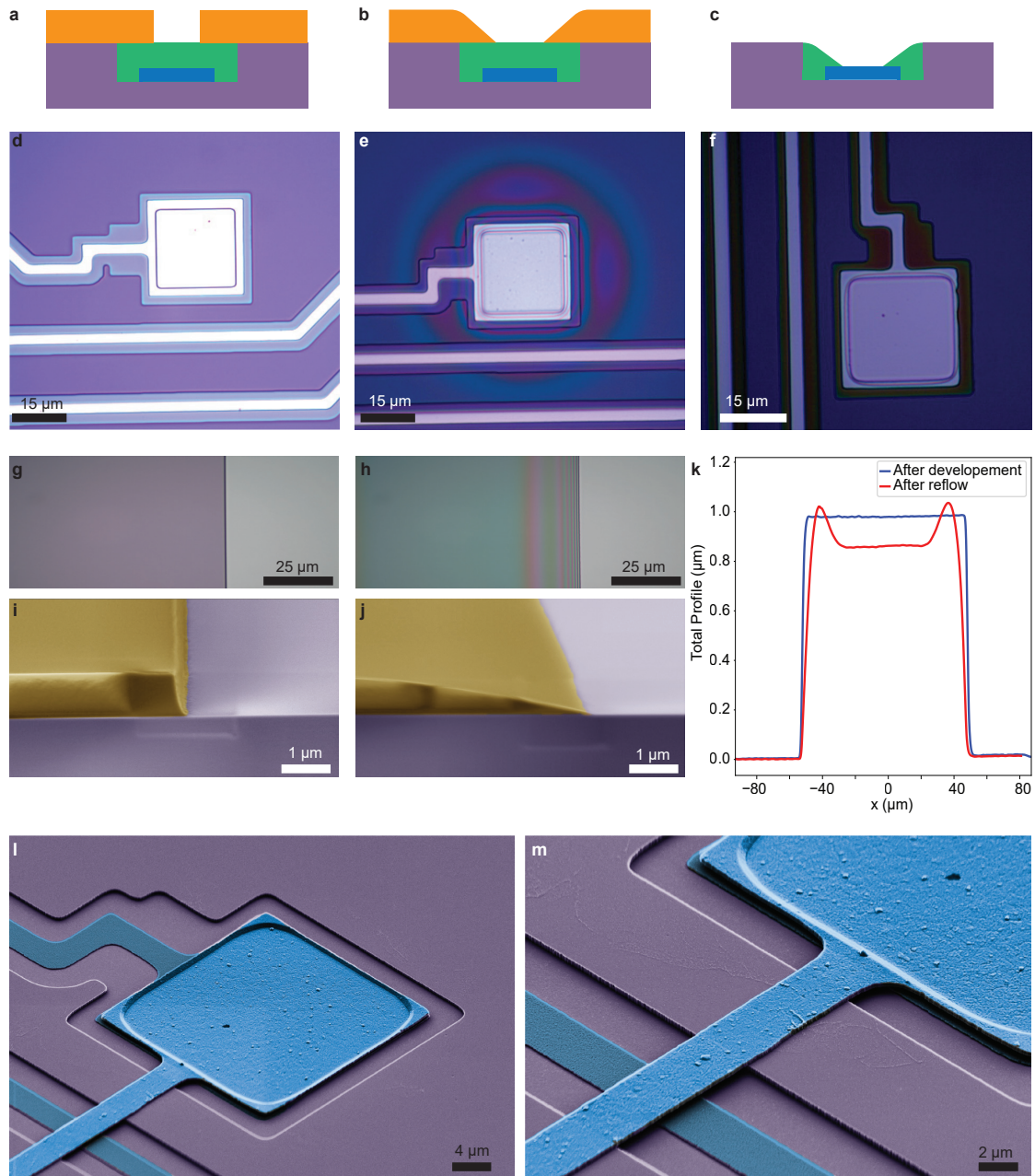


Figure 4.15: **Problem of galvanic connection with sharp edges.** **a**, The galvanic connection on  $\text{SiO}_2$  openings with sharp edges. Due to the local thickness decrease of Al layer on the sharp edges, these circuits show frequency shift when the intracavity photon number -in other words, circulating current- is high. **b**, In addition, the sharp edges of the opening may result in accumulation of Al during the top layer deposition.

smoothly bring down the top wire to avoid sharp thickness reduction. We observed strong high-power nonlinearities in the microwave response of superconducting circuits when we





did not make a smooth top-bottom transition. This may be due to the thin aluminum contact ( $< 50$  nm) on the edges of the galvanic connection, which may not tolerate the high local current densities at high powers (see Fig. 4.15 for examples of galvanic connection without smoothing).

To solve this problem, we reflow the photoresist after development by heating up the wafer to 180 Celsius for 30 seconds using a standard hot plate. This results in smooth and sloped photoresist sidewalls. After the reflow, we do the standard descum to remove resist residues. Afterward, we use DRIE plasma etching (SPTS<sup>®</sup> APS) with  $\text{CHF}_3$  chemistry which offers 1:1 selectivity for  $\text{SiO}_2$ :PR and transfer the photoresist pattern into the oxide. Then the resist will be removed by the standard procedure discussed earlier. Fig. 4.16 shows the steps of the reflow and opening process.

#### 4.2.10 Top aluminum layer deposition

Now the wafer is ready for the top Al layer deposition. The top layer deposition can be done by sputtering or evaporation, which results in different film quality, roughness, and mechanical stress affecting the mechanical properties of the drumhead resonator.

The deposition-induced stress in the Al film is typically compressive in standard deposition methods. This results in the buckling of the drumhead in a dome shape after the release at room temperature. We realized that such a buckling helps a successful release since the gap size will increase more than  $\sim 1\mu\text{m}$ , and HF vapor can penetrate easier to remove the remaining sacrificial layer. On the other side, tensile stress at room temperature will result in higher stress at cryogenic temperatures and prevents significant deformation of the film after the release, which may increase the mechanical quality factor of the resonator. We explored several methods to induce tensile stress in deposition, which are discussed in Sec. A.1.

Now we focus on the evaporation method, which gives us the highest film quality. We use two different evaporators (*Eva*: Alliance-Concept<sup>®</sup> EVA 760, and *Plassys*: Plassys<sup>®</sup> MEB550SL3) for different purposes. *Eva* is a standard electron beam evaporator with 450 mm working distance. a 200 nm Al film grown with 5 nm/s deposition rate in *Eva* results in  $\sim 50$  MPa compressive stress. *Plassys* (as shown in Fig. 4.17b) is an ultra-high vacuum 3-chamber system dedicated for shadow evaporation for Josephson junction fabrication. This system has a separate load-lock chamber equipped with Argon ion milling and can transfer the wafer between the load-lock and the main deposition chamber under a high vacuum. This enables the system to clean or etch the wafer with the embedded IBE immediately before Al deposition without breaking the vacuum and growing the unwanted native oxide on Si or Al. The deposition chamber is relatively smaller than *Eva*'s. An optimized evaporation on 200 nm Al in *Plassys* gives negligibly minor tensile stress in the film.

We typically deposit  $\sim 200$  nm thick Al for the top layer. Although we used *Eva* for the multi-mode optomechanics project and achieved perfect results, *Plassys* offers an essential option

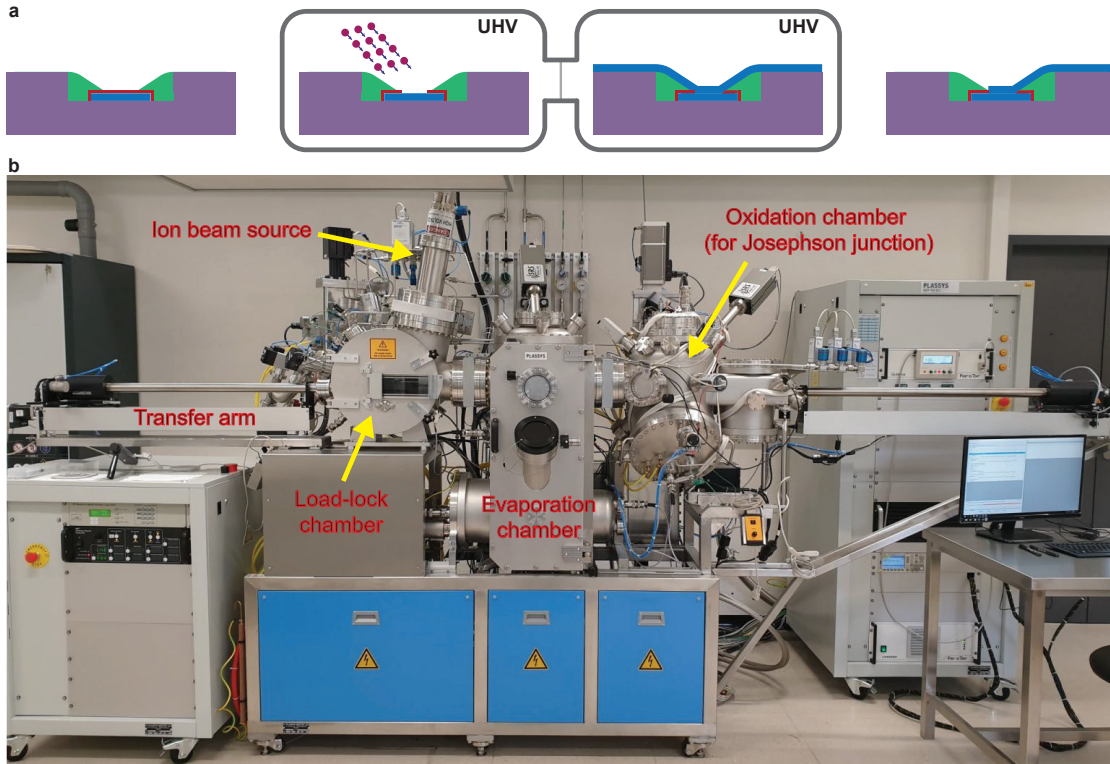


Figure 4.17: **Removing native aluminum oxide in Plassys.** **a**, The schematic fabrication process shows the native  $\text{Al}_2\text{O}_3$  layer in galvanic connection can be removed using Plassys<sup>®</sup> evaporator using argon ion milling. The wafer is then transferred to the evaporation chamber under ultra-high vacuum for the top Al layer deposition. **b**, Shows the Plassys machine we use in EPFL-CMi. The load-lock chamber is equipped with an ion beam source. The transfer arm moves the wafer between different chambers isolated with gates. The oxidation chamber is dedicated for Josephson junction fabrication and not used in this work.

that is crucial for optomechanical systems operated in the quantum regime; The native oxide layer on the aluminum pad in the  $\text{SiO}_2$  opening can be removed by the embedded IBE in Plassys, resulting in a perfect galvanic connection between two layers of the circuit. We discovered that removing such a thin 2-4 nm  $\text{Al}_2\text{O}_3$  layer between the top and bottom superconducting Al layers in the galvanic connection can substantially reduce the microwave cavity heating when pumping the circuit with high power, therefore allowing us to reach lower mechanical occupations in sideband cooling. For this reason, we prefer to use Plassys as we did in the ultra-coherent circuit optomechanics project. We etch 5-10 nm of Si with the Ar milling at 45 degrees incident angle. This is enough to remove the native oxide layer on Al in the opening and Si wafer, which also ensures there will be no remaining native  $\text{SiO}_2$  under the clamps of the Al resonator or the top wire. The etching time can be precisely calibrated and timed using a dummy wafer with  $\text{SiO}_2$  layer. The process is shown in Fig. 4.17a. In Plassys, before taking out the wafer after deposition, we shortly expose it to clean Oxygen flow in the load lock to make sure the native  $\text{Al}_2\text{O}_3$  layer is grown in a clean environment on the drumhead

resonator, and then open the load lock.

After the deposition, we use the standard lithography technique to pattern the top layer and etch it using the same wet process which has mentioned earlier. An interesting tip is that because of the CMP planarization, all the topography information of the wafer is removed, and after covering the wafer with 200 nm reflective aluminum, it will be challenging to find markers for lithography, which are buried below the sacrificial layer and Al. To avoid this problem, we etch big openings on the markers (defined in the trench layer as the first pattern) during SiO<sub>2</sub> opening step to make them visible in the next lithography step.

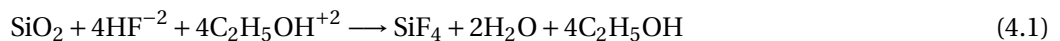
#### 4.2.11 Dicing

Now the wafer is ready to be diced into chips for the last step, the HF release. The size of chips in our design is 9.5 mm×6.5 mm. To dice the wafer, we first spin coat it with a thick resist (15μm AZ<sup>®</sup> 10XT-60) to protect the circuits from Si debris and other contaminations during dicing. We use 100 μm Nickel blade with 35000 rpm rotation speed and 5 mm/s cutting speed (Disco<sup>®</sup> DAD321). On the wafer design, we defined dashed lines in the trench layer and bottom Al layer to as chip border boxes to be used in dicing alignment. After dicing, the chips will be gently detached from the UV tape used for dicing and will be sorted in a teflon chip holder for UFT resist stripping. We keep chips for more than 20 minutes in a UFT clean bath, then rinse and dry them manually (with a pressurized air nozzle). Afterward, we use 600 Watt and 400 sccm oxygen plasma (Tepla<sup>®</sup> GiGAbatch) for a few minutes to clean any remaining resist residue from the chips.

We fabricated a dedicated silicon wafer chip holder by deep etching (Bosch DRIE) a Si wafer pattern 200 μm rectangular pads corresponding to our chip size. We locate chips inside these pads during oxygen plasma and HF release to minimize the risk of chip flipping during chamber pump down.

#### 4.2.12 Release

The last step of the nano-fabrication process is releasing the vacuum gap capacitors by removing all SiO<sub>2</sub> sacrificial layer from trenches. This is done by vapor phase Hydrofluoric acid SiO<sub>2</sub> etching. The vapor HF process uses reduced pressure, gas phase, anhydrous HF and ethanol (C<sub>2</sub>H<sub>5</sub>OH) to etch sacrificial SiO<sub>2</sub> for MEMS release in a non-polluting, vacuum-based system. This produces a clean, residue-free release etch that does not require liquids or supercritical drying. Reaction with the sacrificial SiO<sub>2</sub> on the wafer surface produces silicon tetrafluoride (SiF<sub>4</sub>) gas and water vapor.



Although the liquid HF attacks aluminum, the vapor HF does not deteriorate or degrade Al

films. In addition, the HF vapor offers isotropic etching, as well as the laminar gas flow. The etching process is liquid-free, which is crucial to release structures with high aspect ratios, in our case  $\sim 100\mu\text{m}$  big drums suspended by  $\sim 200\text{ nm}$  gap above another metallic layer. Any water formation will result in the collapse and sticking of two capacitor plates. Combining all mentioned advantages makes HF vapor an ideal process to release vacuum gaps. Examples of successfully released devices are shown in Figs. [4.18](#) and [4.19](#).



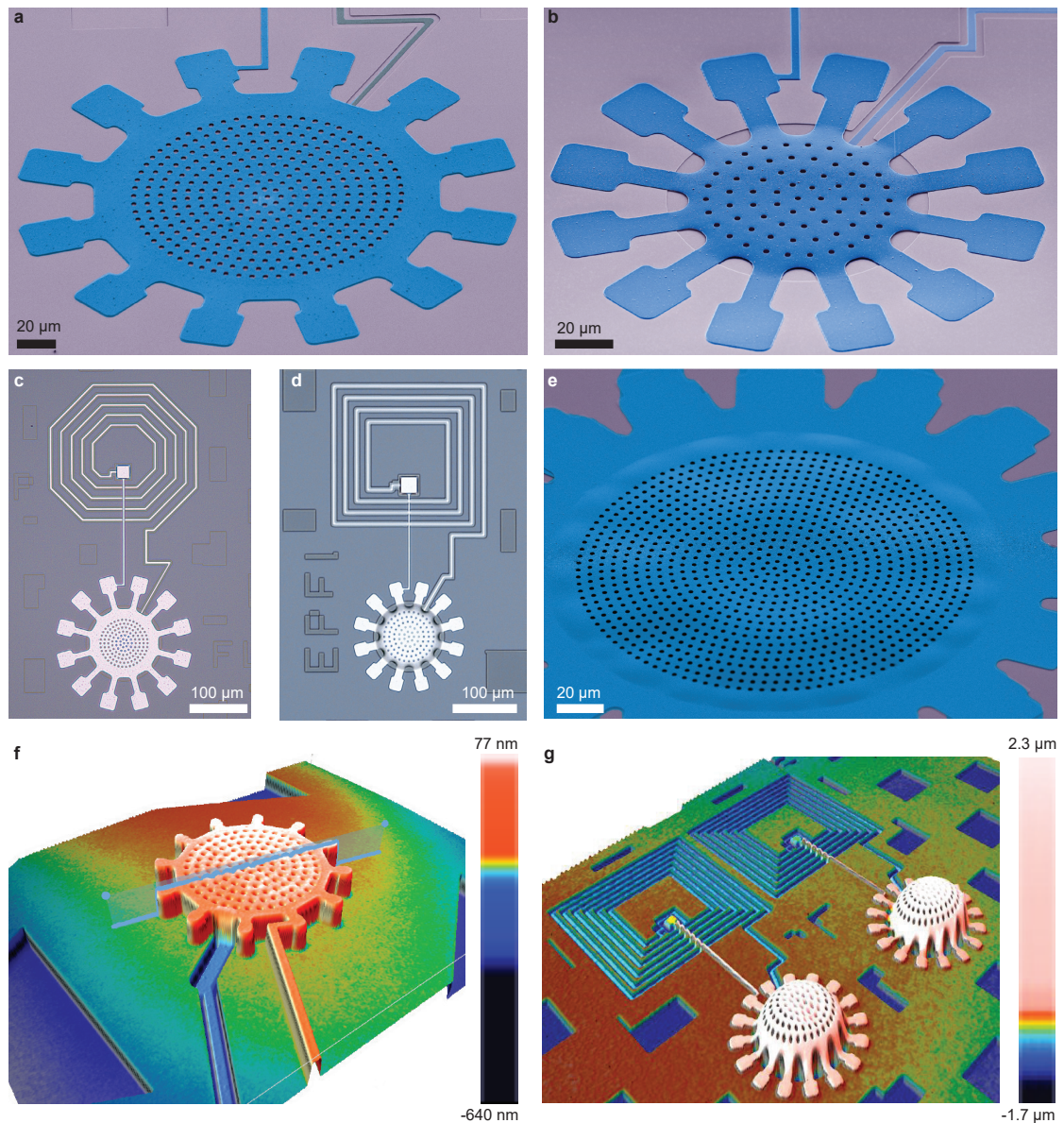
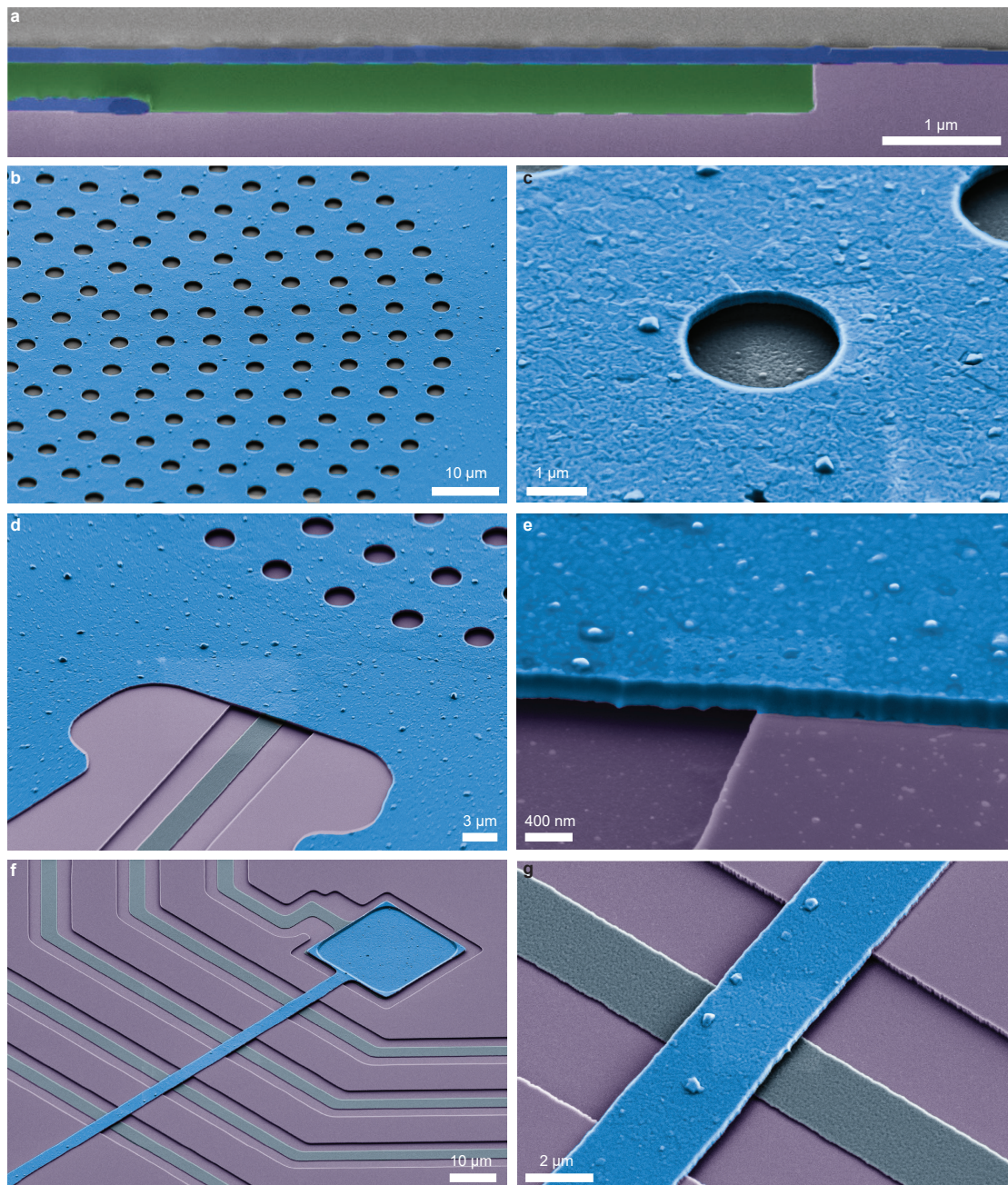


Figure 4.18: **Released devices.** **a, b,** Shows SEM images of released drumhead capacitors for two cases of having zero/tensile (Plassys) and compressive stress (Eva) in the top aluminum layer respectively. **c, d,** Shows microscope images corresponding to each top layer deposition method after the release. Drums with compressive stress clearly buckle up and form a dome shape visible under the microscope. **e,** SEM of a capacitor with clamp ratio of 1 -Drum is totally clamped on the edges of the trench similar to **a**. The compressive stress buckles it up, but in a non-symmetric and wavy shape. **f, g,** Optical profilometry of drums after the release for two two different top layer stresses respectively. In case of compressive stress, the drum may buckles up to  $\sim 2\mu\text{m}$ . However the gap size at cryogenic temperatures goes to the designed value due to the temperature induced tensile stress and consequently flatness of the drum.





**Figure 4.19: Elements of the final device.** **a**, Focused ion beam cross-section of a capacitor before removing the  $\text{SiO}_2$  sacrificial layer (Pt is used as the focused ion beam protective layer). The flatness of the top layer is visible in the image indicating a successful CMP planarization. **b**, SEM image of the perforated released drumhead. The holes facilitate the release process. **c**, Magnified SEM of one release hole. The bottom Al layer is visible from the hole. The small particles seen on the aluminum surface are aluminum hillocks, a well-known accumulation of aluminum in evaporation technique. The size and distribution of hillocks depends on the evaporation rate, and the pressure of the chamber. **d**, Shows the bottom wire going under a drum. **e**, Shows a magnified SEM of a drumhead clamp. **f**, **g**, Show the spiral inductor air bridges and the galvanic connection.

The tool we use (SPTS® uEtch) operates etching in cycles, where each cycle contains stabilizing, etching, and purging of the chamber. This helps the release and reduces the risk of liquid water formation. We use a recipe with 125 Torr pressure and  $\sim 100$  nm/minute etch rate for 900 seconds etching time in every cycle. Since the vapor HF needs to penetrate horizontally between the top Al layer and the trench bottom surface, the total number of cycles needed should be calculated based on the maximum lateral distance between two penetration windows for the gas etchant, considering the pattern of Al covering the trenches. We multiply this number by a factor of four to prevent any residual oxide and ensure the whole structure is released. It is recommended to slowly heat up the chips (sitting on the dedicated wafer we discussed earlier) to 180 Celsius for two minutes right before loading them onto the tool to reduce the risk of water formation.

To facilitate the release, specifically for big drums, we perforate drums by defining small holes with  $1.8\ \mu\text{m}$  diameter and distance of  $\sim 10\ \mu\text{m}$  as shown in Fig. 4.21. These holes let the vapor HP uniformly penetrate underneath, resulting in a more robust release. We could successfully release vacuum gaps with the gap size down to 75 nm, however the success rate of the release was not high for such a low gap size. For gaps above 150 nm, we had almost 100% yield of release. Of course, the success rate depends on the trench size, the thickness of the top plate, and the room temperature stress.

Smaller drums have a lower risk of collapse and can tolerate smaller gap sizes. We usually use 150-200 nm thick Al top layer. Attempts to release thin top layers (50 nm) were not successful (see Fig. 4.22). Also, the compressive stress in the film results in a dome shape buckling and facilitates the release, while having zero or tensile stress increases the risk of collapse.

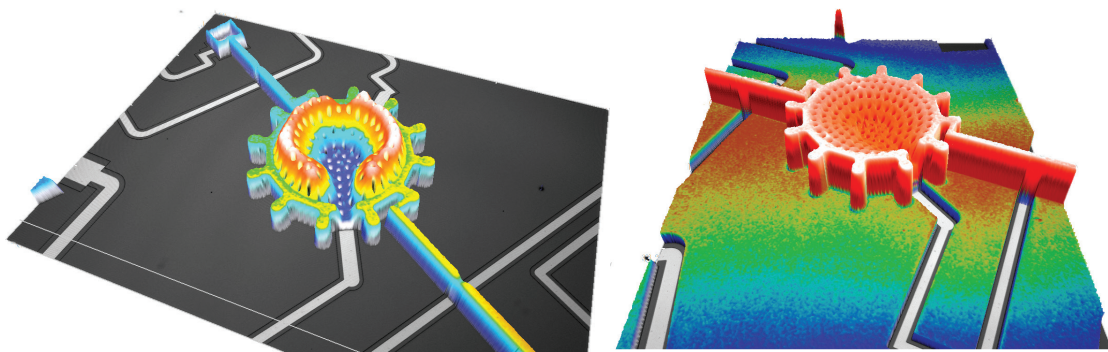


Figure 4.20: **Collapsed drums.** Too small gap size, thin top layer, and the big size of the drumhead can cause collapse of the structure after the release. Nevertheless, the collapse is less stochastic, meaning that defining the mentioned parameters in the proper range will result in high yield fabrication i.e. 100% successful release.



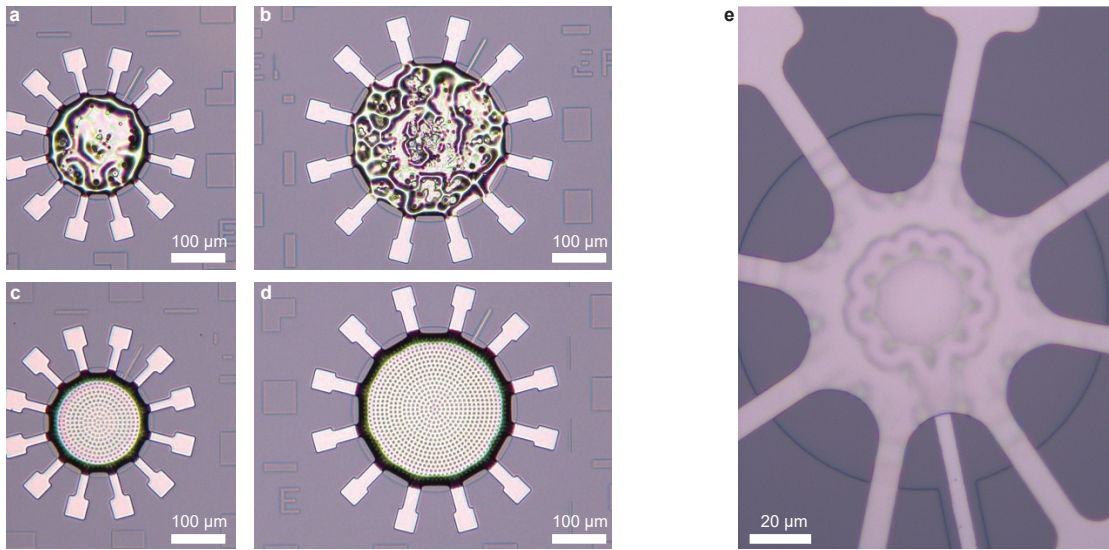


Figure 4.21: **Effect of the release holes.** **a-d**, Shows similar drums on a same chip after release. **a** and **b** shows wrinkled drums without release holes to assist HF vapor penetration under the structure. **c** and **d** shows the effect release holes which result in releasing drumheads in the fundamental symmetric buckling mode. **e**, Shows a drumhead without release holes after a long exposure to HF vapor. The central part which covers the bottom electrode is still not released because of smaller spacing between layers. HF vapor needs longer time to laterally penetrate under the top layer resulting in an incomplete release forming a wavy buckled shape on the released parts.

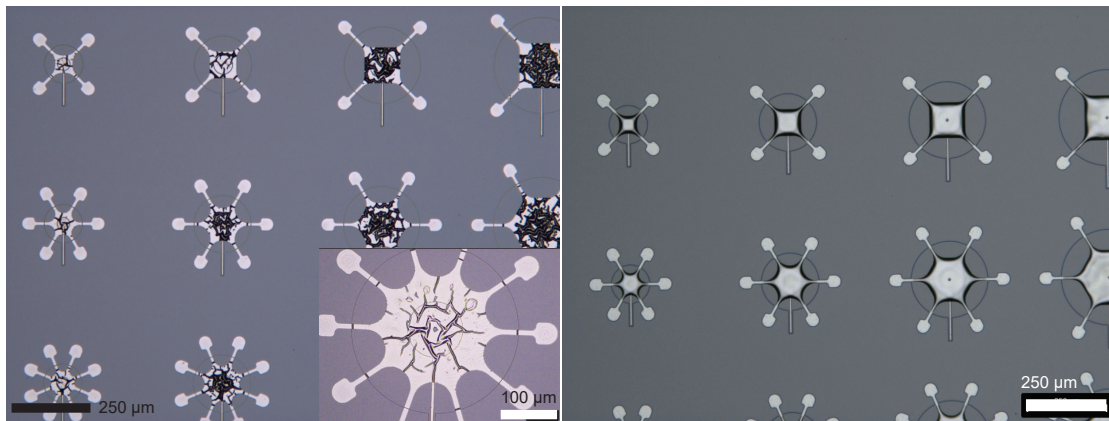
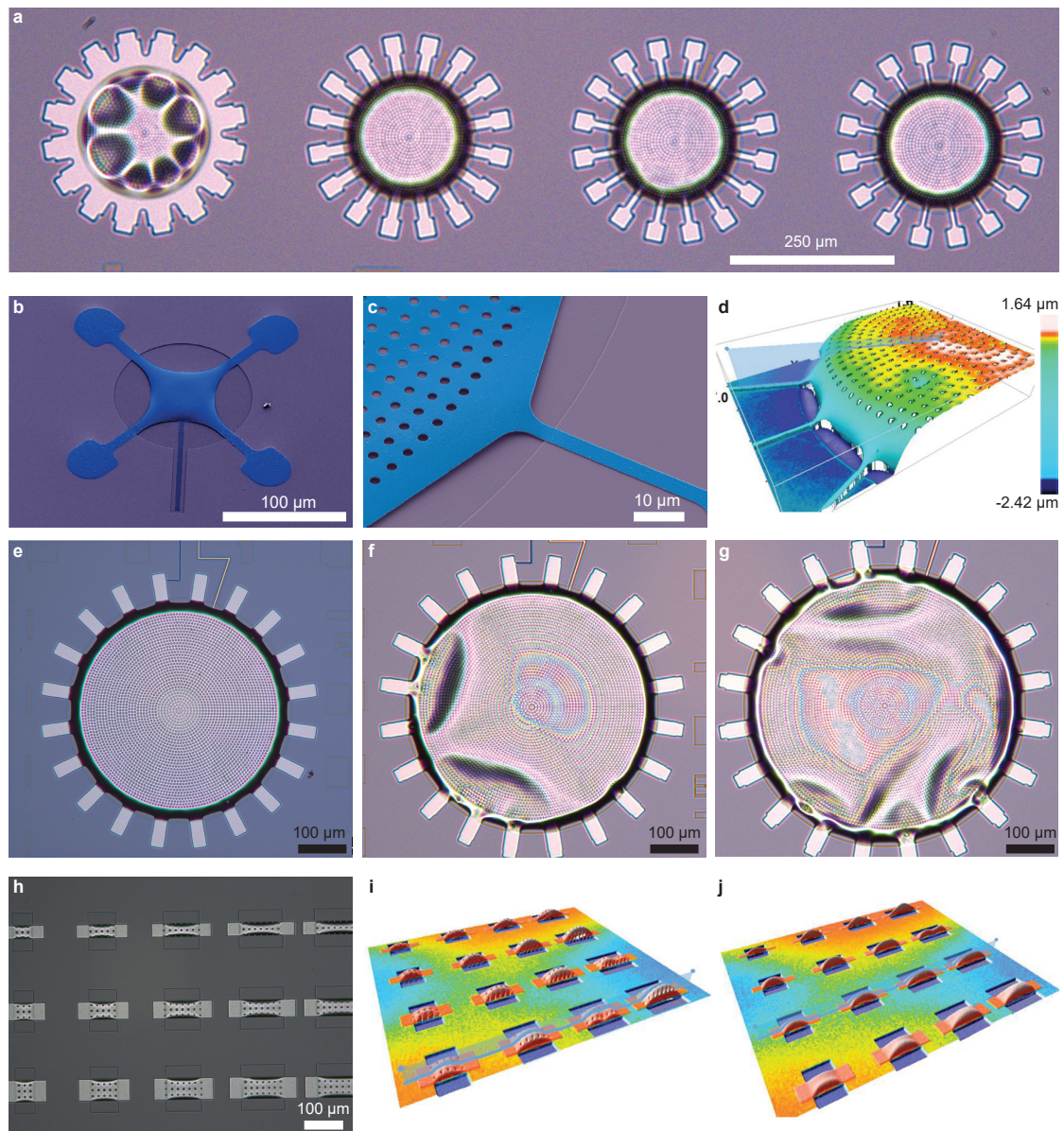


Figure 4.22: **Effect of top layer thickness on the release.** Here we compare two identical designs after release with a same fabrication process but different top aluminum layer thicknesses of 50 nm (left image) and 150 nm (right image) with 200 nm gap size. The thin aluminum wrinkles instead of buckling up.



**Figure 4.23: Effect of clamps, size, and shape on the release.** **a**, Microscope image of drums with same parameters but sweeping the clamp ratio (The ration of the total trench perimeter over the clamps perimeter) from CR=1 (the left drum) to CR=4 (the right drum). Fully clamped drums (CR=1) in the presence of the compressive stress buckles up in a deformed shape, while the rest buckle in the fundamental mode. **b-d**, SEM and optical profilometry of released drums with high CR number. **e-g**, Show the maximum radius of successfully released drums with the gap size of 200 nm (**e**) and the collapse/deformation of bigger drums (**f, g**). **h-j**, Shows other possible geometry as rectangular beams released with and without using release holes.



## 4.2.13 Packaging

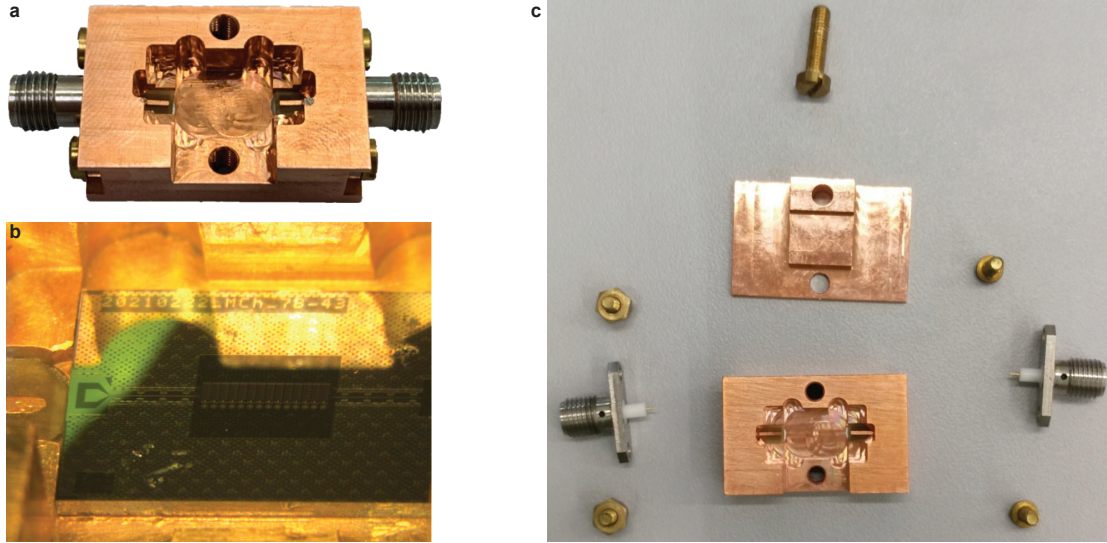


Figure 4.24: **Chip box.** **a**, Photo of the chip box made out of oxygen free high conductivity copper. The box has two SMA coaxial outputs soldered to short micro-strip PCBs glued to the box. **b**, A chip will be glued by conductive silver paint inside the box. **c**, Photo of elements of a sample box before assembling. the lid will be closed to ensure the superconducting sample is light-tight during the experiment.

After the release, the chips are ready for packaging. We need to handle chips carefully to avoid the risk of collapse due to mechanical shocks or electrostatic discharge. The electro-mechanical devices can be inspected using an optical microscope -if we have compressive stress in Al top layer, the dome shape of buckled drums is clearly visible under a 10X microscope aperture. More systematically, we use an optical profilometer (Sensofar<sup>®</sup> S-Neox or Bruker<sup>®</sup> Contour X) to measure the surface topography of the drum (especially when it does not buckle due to stress) and make sure it is successfully released as shown in Fig. 4.18 f and g.

We use a machined copper box as the chip holder made out of oxygen-free high-conductivity copper to ensure good thermal contact at mK temperatures developed by L.D. Toth (Tóth, 2018) and N.R. Bernier (Bernier, 2019). The sample holder has two SMA connectors soldered to a micro-strip line defined on a short piece of printed circuit board which is glued inside the box. The PCBs will be electrically connected to the micro-strip feed line on the chip by wire bonds. The PCBs are permanently glued to the copper box using a conductive epoxy (Epo-Tek<sup>®</sup> H20E). The chip holder can be cleaned using a fiber brush, followed by Isopropanol cleaning. The copper box gets oxidized in the span of time, and can be cleaned by sonication in diluted acetic acid.

We use silver conductive paint (RS<sup>®</sup> Pro) to mount the chip inside the box to make a good thermal connection between the chip and the box and maintain the electrical boundary

condition. Then we use wire bonder (F&S<sup>®</sup> Bondtec 56i or TPT<sup>®</sup> HB10) to connect the feed line on the chip to the PCB using aluminum 25  $\mu\text{m}$  diameter wires. We typically use more than five bonds on each side to ensure the 50-ohm impedance matching connection. Using a smaller number of wires showed impedance mismatch resulting in standing waves for micro-strip feed lines. After wire bonding, the electric connection will be tested by an Ohm-meter (typically shows  $\sim 4$  Ohms between two cores of the SMA connector using micro-strip feed line), and the lid of the box will be closed and tightened by a brass screw, and the device is ready for low-temperature measurements.

Exposing samples to air during the packaging will not degrade them (except for dust contamination on the drums, which can be removed by gently blowing them with pressurized air). However, we recommend avoiding abrupt temperature and humidity changes during the transfer and keeping chips in Nitrogen boxes for long-time storage.

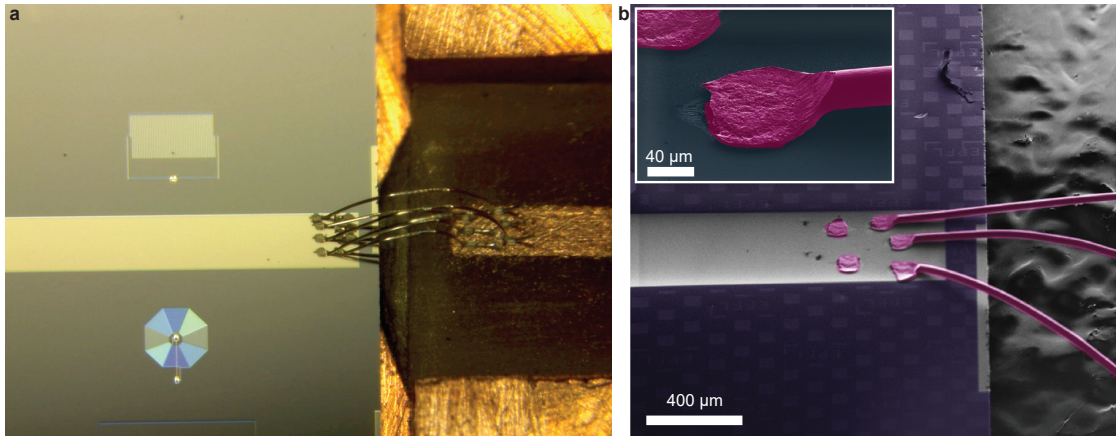


Figure 4.25: **Wire bonds.** **a**, Microscope image of a chip with micro-strip waveguide connected to the copper center of PCB micro-strip waveguide through 35  $\mu\text{m}$  aluminum wire bonds. We normally use more than 5 bonds to ensure the impedance matching between the sample and PCB. **b**, SEM of 35  $\mu\text{m}$  aluminum wire bonds connected to the 100 nm aluminum bottom plate. If the parameters of bonding such as ultra-sonic power, press time, and force are not optimized, the bond will be detached and leaves a  $100 \times 100 \mu\text{m}^2$  footprint on the chip which cannot be used for a second bonding anymore.

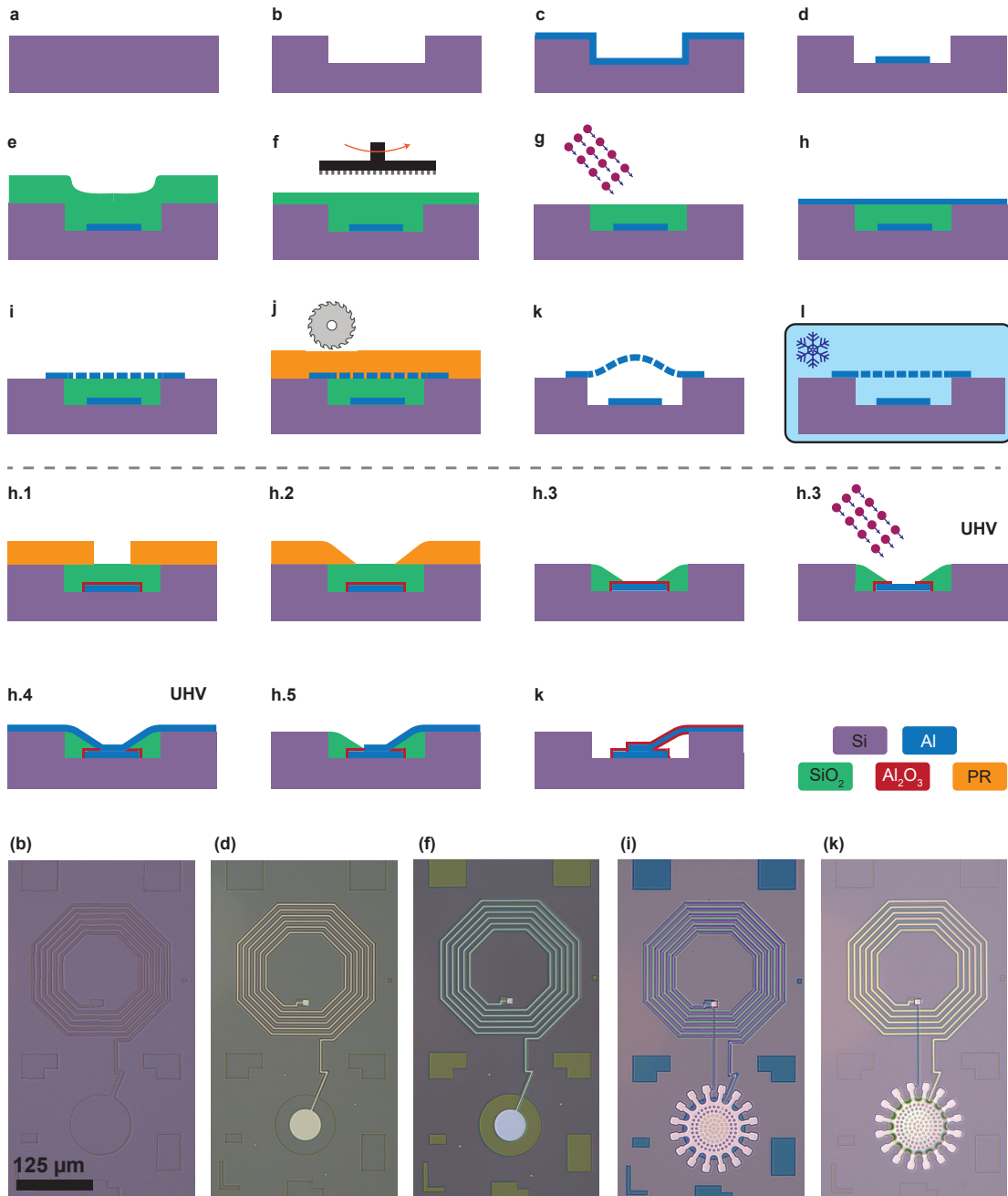
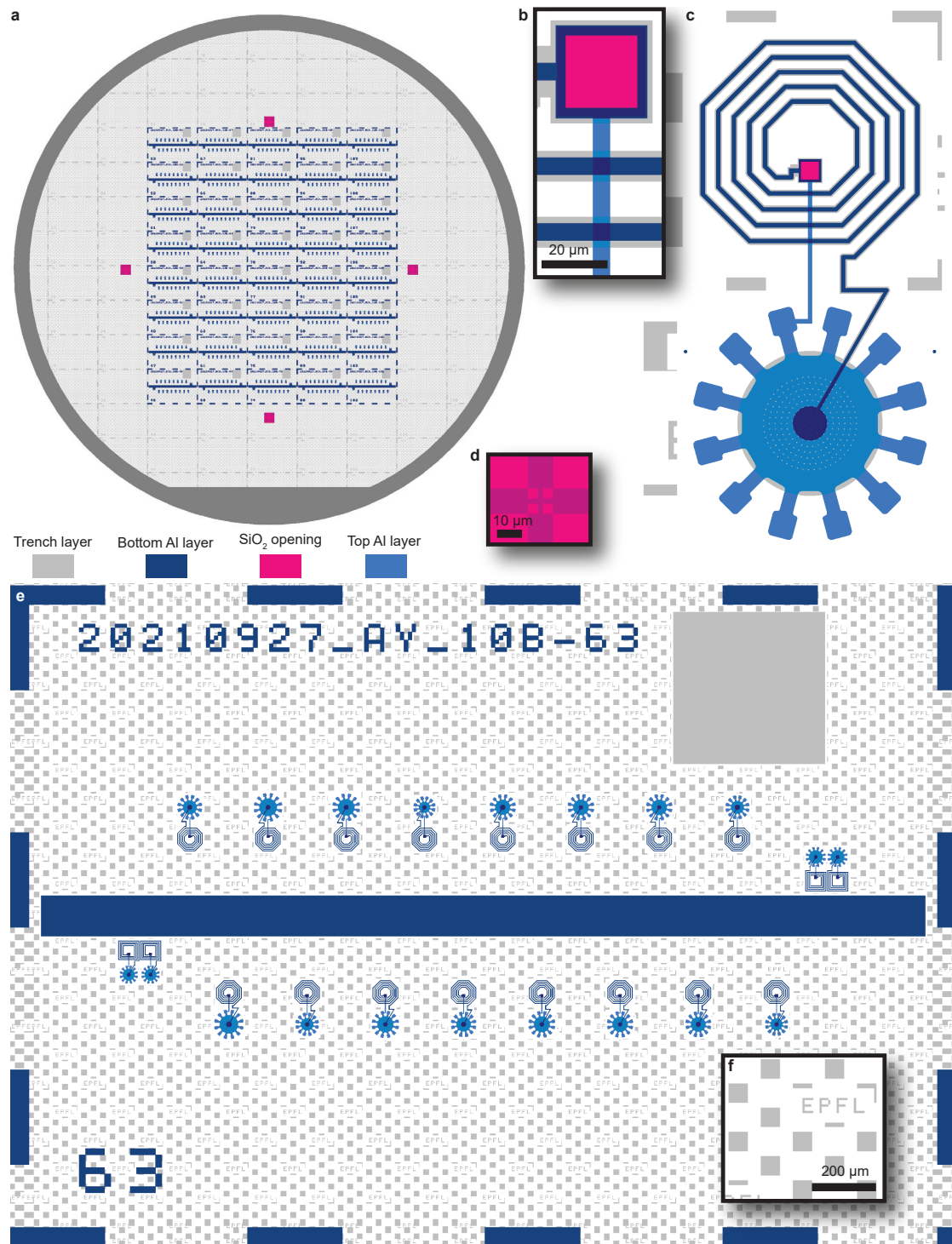


Figure 4.26: **Detail fabrication process flow.** **a**, A high-resistivity silicon wafer is cleaned and used as substrate. **b**, Etching a trench in a silicon wafer (300 nm typical). **c**, Aluminum deposition of the bottom plate (100 nm typical). **d**, Patterning of the bottom Al. **e**,  $\text{SiO}_2$  sacrificial layer deposition ( $2.5 \mu\text{m}$  typical). **f**, CMP planarization. **g**, Etching back and landing on the substrate using IBE. **h**, Aluminum deposition of the top plate (200 nm typical). This step consists of opening the oxide for galvanic connections, removing native  $\text{AlO}_x$ , and deposition, shown in h.1-5. **i**, Patterning the top Al layer. **j**, Dicing the wafer to chips. **k**, Releasing the structure using HF vapor. Depending on the compressive stress of Al top layer, the top plate may buckle up. **l**, At cryogenic temperatures, the drumhead shrinks and flattens. The optical micrographs show examples of selected steps of the process flow.





**Figure 4.27: Example of wafer and chip layout.** **a**, The wafer layout containing chips, alignment markers, and dummy trench patterns filling all the empty area to increase uniformity of the CMP planarization. **b**, the galvanic connection and air bridges of the spiral. **c**, Layout of a LC electro-mechanical resonator. **d**, The alignment markers for direct laser writer. **e**, The full layout of a chip containing several LC resonators (frequency multiplied) inductively coupled to a micro-strip waveguide. The top right rectangular big trench used for optical reflectometer measurement of the remaining  $\text{SiO}_2$  after CMP. **f**, Shows the dummy patterns for CMP.

## 5 Experiment

Perfect devices can never be exploited without a perfect arrangement of the experimental apparatus in the laboratory. This chapter discusses the experimental setups, instruments, and techniques for controlling and measuring superconducting circuit optomechanical devices in the quantum regime. We first introduce dilution refrigerators hosting the devices at cryogenic temperatures and review considerations on wiring the circuit at both low and room temperatures. We discuss microwave measurement instrumentation used in this work and provide information on special components and setups built for quantum-limited measurement and control, such as Josephson traveling wave parametric amplifiers, microwave tone-cancellation setup, and tunable filter cavities. Finally, we review the data acquisition and instrument computer control and programming techniques used in the projects.

### 5.1 Cryogenics

The average photonic or phononic occupation of a harmonic oscillator with the frequency of  $\omega$  in thermal equilibrium with a bath at a temperature of  $T$  is given by the Bose-Einstein statistic,  $\bar{n} = \left( e^{\frac{\hbar\omega}{k_B T}} - 1 \right)^{-1}$ , where  $k_B$  is the Boltzmann constant. For optical cavities ( $2\pi \times \omega \simeq 200 \cdot 10^{12}$  Hz), even at room temperature ( $T \simeq 300$  K), the ratio of thermal fluctuations to the single quanta of energy is negligible, ensuring that the optical cavity is in its ground state. However, for microwave cavities used in the circuit optomechanics with a frequency range of a few Giga-Hertz, this occupation exceeds 1000 quanta, preventing the implementation of any quantum protocol. Although the superconductivity of materials used in circuit optomechanical devices is crucial to reduce cavity losses and can be reached at temperatures below 1 K depending on the material, the above-mentioned thermal occupation enforces operating such systems at much lower temperatures, around 10 mK, where the microwave cavity is ideally at the ground state - without considering noise sources from the higher temperatures.

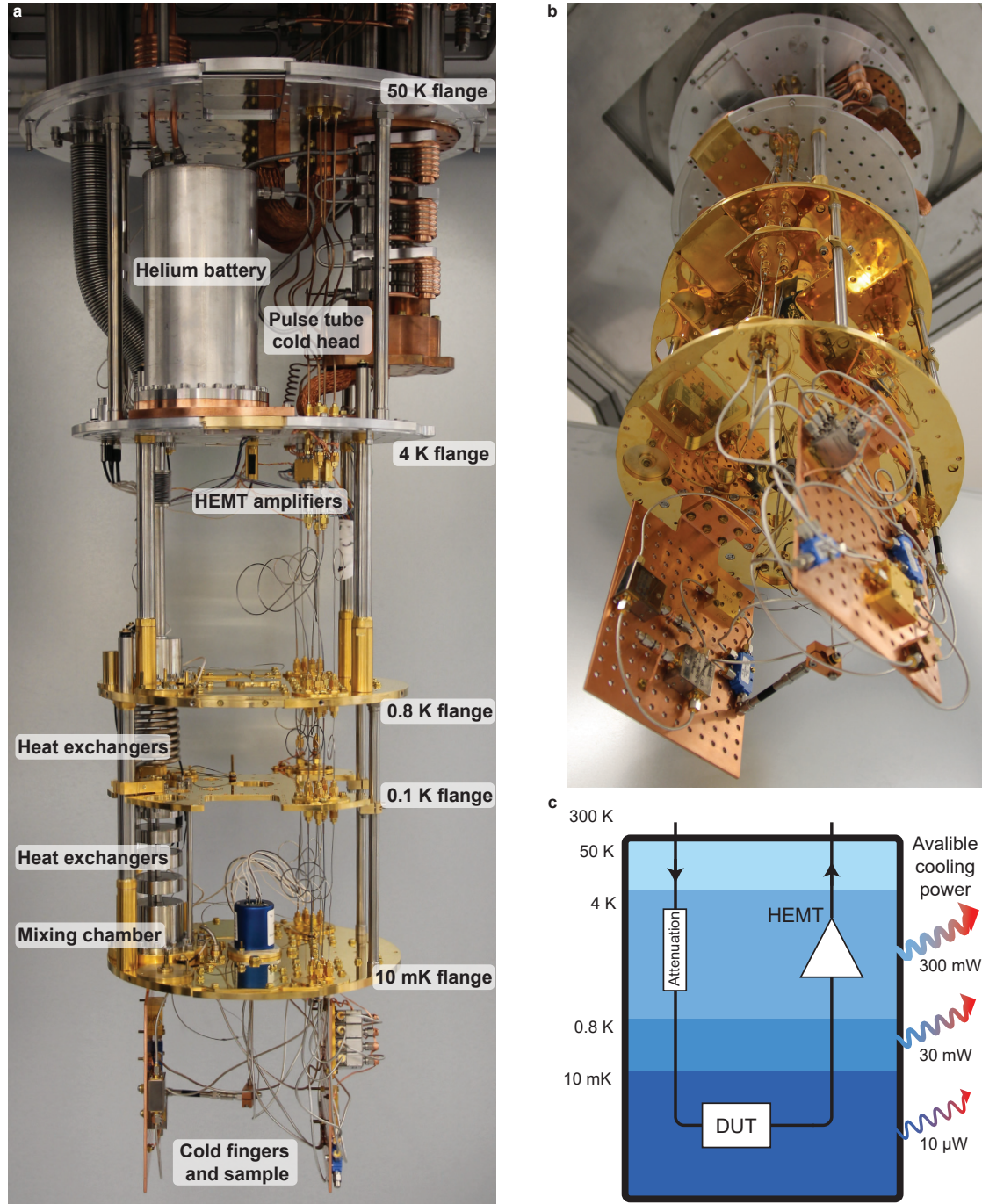


Figure 5.1: **Dilution fridge.** **a, b**, Photo of one of the BlueFors® dilution fridges we use. Flanges and components are marked on the photo. **c**, Schematic of the fridge showing approximate available cooling power at different flanges, i.e. the maximum additional dissipated power before significantly heating up the flange.

### 5.1.1 Dilution refrigerator

Fortunately, these ultra-low temperatures are achievable using the well-established and commercialized technology of dilution refrigeration, where the mixing of two isotopes of helium

(helium-3 and helium-4) as an endothermic process provides continuous cooling power at temperatures below  $\sim 1$  K. In practice, the typical base temperatures that could reach in dilution refrigerators is  $\sim 10$  mK depending on the total heat load in the fridge, the mass, and the design of the fridge.

We use two BlueFors<sup>®</sup> LD-250 dry dilution fridges with similar properties. In dry dilution fridges, the temperature needs to be kept continuously down to 4 K exploiting a pulse-tube cryocooler which uses  $^4\text{He}$  in compression and expansion cycles to extract heat from the system. Dilution fridges have several flanges corresponding to different temperatures, where each flange holds several components, such as heat switches, thermometers, heaters, and dilution process mixture circuits. The dilution fridge has a nested architecture, where each flange has a shield connected to it, covering the other flanges with lower temperatures to prevent thermal radiation to reach the lower stages. These internal shields are not vacuum tight; nevertheless, the whole fridge operates under a high vacuum kept by the exterior room temperature shield, which is vacuum tight. The vacuum is initially prepared by a scroll pump followed by a turbo pump to reach  $\sim 10^{-4}$  mBar. After running the pulse tube to cool down the fridge, all the vacuum pumps will be turned off, and the pressure of the fridge will reach and remain  $\sim 10^{-6}$  mBar due to the fact that the whole body of the fridge acts as a cryo-pump. Of course, at the lower temperature stages, the actual pressure is much smaller, since any gas will be condensed. This enables a dry dilution fridge to run continuously for months and even years without using any vacuum pump and only running the pulse-tube cryo-cooler. The BlueFors<sup>®</sup>-LD fridge consists of the following stages. The room-temperature flange contains all input-output vacuum tight ports for the pulse tube, mixture tubes, electronics wiring and optical feed-throughs if needed. The 50-K flange as a temperature mediator. The 4-K flange connected to the pulse-tube's cold head. The 800-mK flange, also called *still flange*, is connected to the 4-K flange with special He-based heat switches. The 100-mK flange, and finally, the 10-mK flange, which hosts the dilution unit called the mixing chamber where the heat extraction process is happening. Fig. 5.1 shows the dilution fridge when all the shields are removed.

A standard cooling process which typically takes one and half days or less, is as follows:

- **Scroll pumping:** When all the shields are properly closed, and the external shield is tight, a scroll pump starts to evacuate the chamber until the whole fridge reaches pressures below 5 mBar.
- **Turbo pumping:** The turbo pump starts working in series with the scroll pump to evacuate the chamber down to  $\sim 10^{-4}$  mBar.
- **Pulse-tube cooling:** If the pressure drops fast enough with the turbo pump, which is the sign of a successful leak test, the pulse tube starts working to cool down the fridge. Meanwhile, when the temperature reaches a certain level, the turbo pump and scroll pump will be turned off, all valves will be closed, and the pressure keeps going down to  $\sim 10^{-6}$  mBar due to the cryo-pumping effect. The heat switches will be turned on,



increasing the heat conductivity between lower-temperature flanges and the 4-K flange. The process continues for  $\sim 18$  hours depending on the total additional mass and the heat load in the fridge until the 4-K flange reaches close to its nominal temperature while the lower temperature stages get thermalized slower, reaching  $\sim 10$  K.

- **Pule pre-cooling:** In this step, to facilitate thermalization of the low-temperature stages to the 4-K flange, the He mixture gets injected into the dilution unit, passing through all the pipes and heat exchangers and gets evacuated again after a few seconds. This pulsed cycle gets repeated around 100 times until the low-temperature flanges will be thermalized to  $\sim 4$  K.
- **Condensation:** Afterward, the heat switches will be turned off, thermally isolating flanges. A compressor will start to condensate He mixture reaching pressures up to 1.8 Bar to create liquid phase He in the dilution unit and increase the flow of He to  $\sim 1$  mmol/s. This process also starts the cooling of the 10-mK flange and consequently, other flanges to reach close to their nominal temperatures.
- **Normal circulation:** Finally, when all the mixture has been condensed, the compressor stops working, and the turbo pump starts, in series with a scroll pump, circulates the mixture and providing continuous cooling at the base temperature. The total cooling power depends on the flow of the He mixture and the temperature difference between the still flange and the mixing chamber. This can be manipulated by a resistive heater called the still heater installed in the 800-mK flange to slightly heats it up, and increases the pressure and the flow of the mixture in the circuit.

The temperature of the fridge in a standard cooldown cycle is shown in Fig. 5.2.

Thermometry in dilution fridges is usually done by four-port electrical measurement of resistance. Each flange is equipped with a calibrated resistor which can be measured using a low-noise resistance bridge instrument (Lake Shore<sup>®</sup> 370 AC Resistance Bridge or BlueFors<sup>®</sup> built-in system in the newer models). For the base temperature, ruthenium oxide (RuO) is used as the resistance material for the sensor due to its sharp temperature-resistance curve below 100 mK. For the higher stages, germanium sensors can be used.

Although radiation is an important heat transfer channel for higher temperature flanges - which is controlled by the nested shields-, the dominant heat transfer mechanism at temperatures below 4 K is thermal conduction. To ensure uniform thermalization to the 10-mK flange, We tightly mount all the microwave components, including the sample, on a homemade perforated 0.5-cm thick plate made out of high conductivity oxygen-free copper. This plate is tightly screwed under the 10-mK flange. For microwave components such as directional couplers, we brush and remove the insulating paint from one side of their box to increase heat conductivity when mounting them on the copper plate. For components that dissipate power in the base temperature, such as circulators' third ports -which are terminated with 50-ohm - or microwave attenuators, we use copper bundle wires wrapping around them and connected

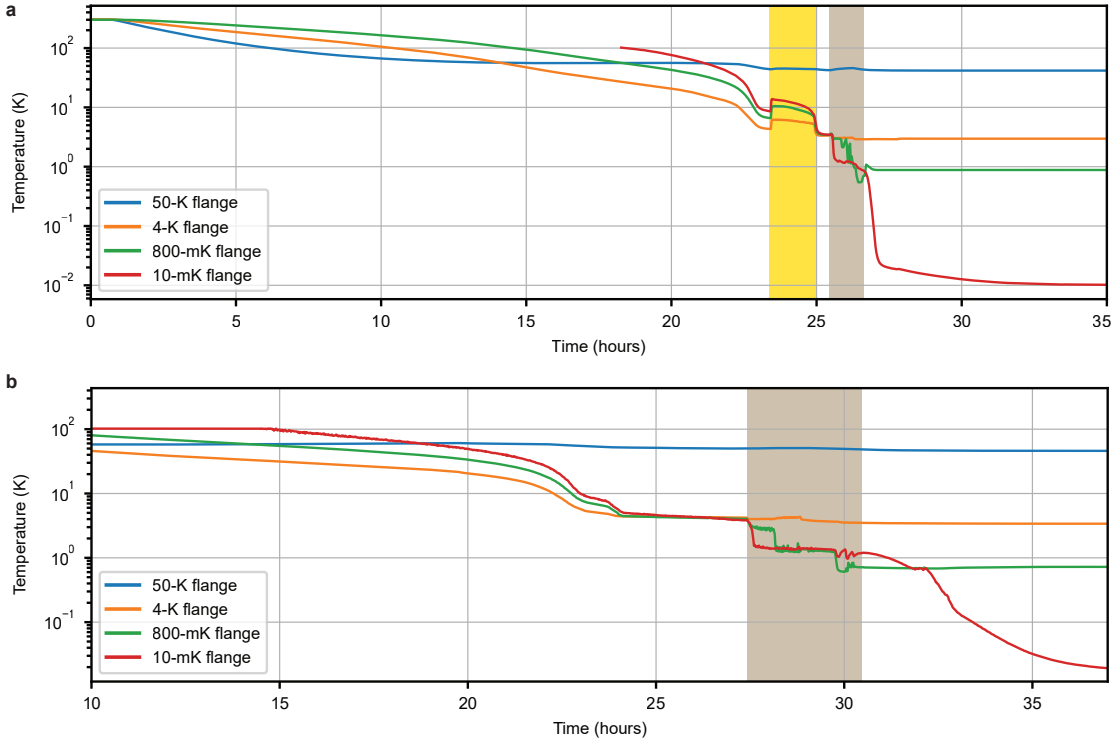


**Figure 5.2: Cooldown of dilution fridge.** **a**, A standard cooldown cycle of the dilution fridge. The yellow shade shows the pulse pre-cooling when injections and extraction of the He mixture facilitate the thermalization of the mixing chamber to the 4-K flange. We observed that the abrupt increase of the 10-mK flange temperature and its fast oscillations during this step may cause significant mechanical quality factor degradation in optomechanical devices which are sensitive to temperature shocks. The Brown shade shows the condensation step. **b**, Example of a cooldown without pulse pre-cooling. The mixing chamber temperature is monotonically decreasing and experiences fewer fluctuations.

to the 10-mK flange. Before a cooldown, we slightly rub off the sample box with a fiber brush to remove the oxide layer or contaminations and improve its thermal contact.

Adding cables or power dissipative components to the fridge will increase the heat load. It must be checked that the additional heat load does not exceed the available cooling power each flange can handle to prevent interruption in the normal circulation conditions. Fig. 5.1c shows available cooling powers at different flanges for our dilution fridge. It is worth noting that the 10-mK flange is equipped with a resistive heater which can be used to intentionally increase the base temperature up to  $\sim 500$  mK without interrupting the normal circulation. This is useful when a temperature sweep is needed in specific characterizations.

It is worth noting that we observed the mechanical quality factor of our drumhead resonators are very sensitive to temperature shocks and thermal cycles, i.e., a fast increase of the fridge's temperature even in a few kelvin range may degrade the mechanical quality factor, even though their mechanical frequencies are not affected. This may be due to the microscopic

crack formation on the clamping points in an abrupt stress shock, as a possible explanation. Because of this issue, we omit the pulse-precooling step in the cooldown process of ultra-coherent samples, which may help maintaining the high quality factors for mechanical devices under test (Fig. 5.2 b). We note that a controlled slow temperature sweep, similar to what is shown in Sec. 6.3, are reproducible and do not reduce the mechanical quality factors.

### 5.1.2 Helium battery

As mentioned earlier, the pulse-tube cooling system is crucial to pre-cool the fridge and provide high cooling power for high-temperature flanges to ensure running the dilution cooling process in proper conditions. In practice, increasing the temperature of the 4-K flange to more than  $\sim 7$  K will heat up the 800-mK flange faster than the available cooling power when the circulation is running and interrupts the normal condition. In these cases, the mixture should be collected, the fridge should reach back to 4 K, and the condensation needs to run again.

In some applications, the weak mechanical vibrations generated by the pulse tube can reach to the sample and disrupt the mechanical state. Each cycle of the pulse tube generates an impulse-like shock with a cycle time of  $\sim 1$  s. Such impulse acoustic shock can travel through the fridge's rigid body and reaches the sample. In some cases, depending on the mechanical frequency of the drumhead resonator, the mounting place and direction, and the total mass of the fridge's body, this shock can excite the mechanical motion with a measurable energy scale. To avoid these shocks in certain experiments, the pulse-tube should be turned off, which results in a fast increase of the 4-K flange temperature in less than two minutes when the mixture is circulating.

A helium battery is an additional option provided by BlueFors® to solve this problem, allowing running the mixture circulation without pulse-tube for a few hours. As shown in Fig. 5.3a, the battery is a container installed on the 4-K flange, which can store liquid  $^4\text{He}$  and let it evaporate at an engineered rate to provide cooling power with evaporation cooling.

The battery should be kept under vacuum until the fridge reaches its standard running conditions. Then we turn off the still heater and let  $^4\text{He}$  gas with a pressure of  $\sim 700$  mBar into the battery. This initially increases the temperature of the 4-K flange -where the battery is installed- to  $\sim 6$  K. Waiting around 15 minutes, the gas in the battery will be thermalized and starts to condensate, and the temperature stabilizes at 4 K. The filling process of the battery takes around 8 hours to condensate around 1000 liters NTP gas  $^4\text{He}$ . When the battery is filled, no matter if the full capacity is used, the  $^4\text{He}$  gas flow can be stopped, and the battery valve can be closed. Although a filled He battery can be kept in the fridge for a long time, it is not recommended to delay between filling and using the battery. The liquid He can explode, turning to the gas phase in case of interruption in the fridge. To operate the fridge with the battery, we start pumping out the battery with the scroll pump and turn off the pulse-tube. He evaporation provides enough cooling power to keep the temperature of the 4-K flange

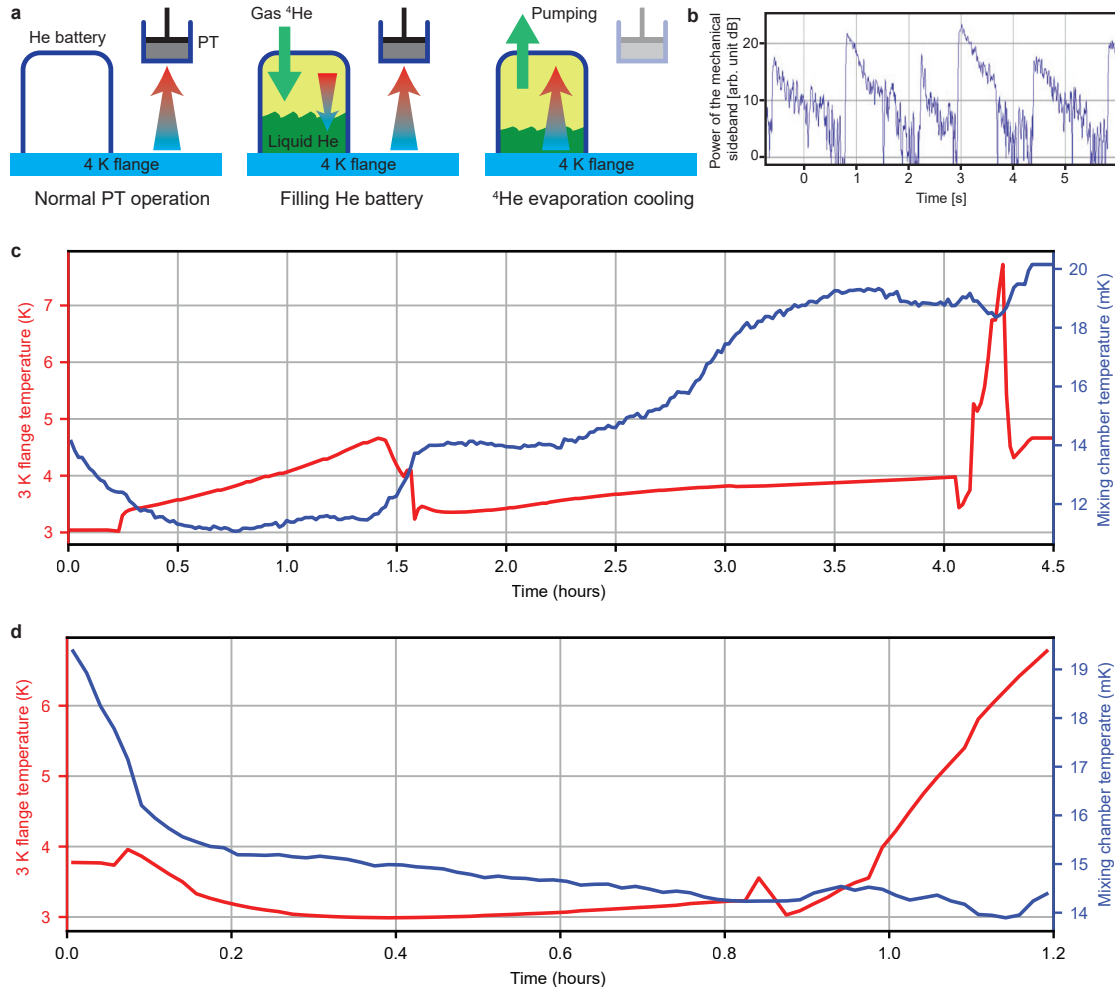


**Figure 5.3: Helium battery.** **a**, Working principle of the  $^4\text{He}$  battery. The 4-K flange is continuously cooled with the pulse tube cold head.  $^4\text{He}$  room temperature gas will be injected into the battery. The  $^4\text{He}$  will slowly be cooled down and condensate into the liquid phase. When the battery is filled, the pulse tube can be turned off while pumping the  $^4\text{He}$  battery. Evaporation of the liquid  $^4\text{He}$  will provide enough cooling power to run the dilution process in the fridge for a few hours. **b**, Example of measured power in an optomechanical sideband of a mechanical oscillator which gets excited by the pulse tube mechanical shocks. **c**, Temperature of the mixing chamber and the 4-K flange when running the  $^4\text{He}$  battery which was filled for about 10 hours. The base temperature remains below 20 mK for up to 3.5 hours. The fast increase of the 4-K flange indicates that the battery is empty and the pulse tube needs to be turned on immediately after the temperature rise. **d**, The same trace for a run with a partially filled battery for only 3 hours of filling.

below 4.5 K, allowing the normal circulation of the mixture for dilution cooling. This can last for maximum 3 hours before the battery gets empty when the pressure of the battery decreases and the temperature of the 4-K flange rises abruptly. Therefore the pulse-tube needs to immediately start cooling the system. Figure 5.3c, and d shows the temperature of the fridge



while running the He battery.

## 5.2 Microwaves and electronics

In this section, we discuss the high-frequency microwave components, instruments, and wiring inside the dilution fridge, as well as the room temperature setup.

### 5.2.1 Cryogenic wiring

Inside the dilution fridge, we use two types of coaxial cables to carry microwave signals in and out of the control and measurement chain. The input lines carrying down the microwave signals from the room temperature setup to the mixing chamber are made out of Copper-nickel (CuNi) alloys satisfying both low thermal conductivity and low microwave loss. At every flange, these cables are thermalized to the nominal temperature. In the base temperature, to route the signal, we use semi-flexible SMA Coaxial cables with 3.5 mm diameter (Pasternack® PE39423), which have 0.9 dB/m loss at room temperature. The output signal, which often carries weak signals in the order of a few quanta/s-Hz, travels through the same cables until it reaches the 10-mK flange, where a set of superconducting niobium-titanium (NbTi) coaxial cables are installed to transfer the output signal with minimal loss to the HEMT amplifier. After the HEMT amplifier avoids signal-to-noise ratio reduction, the signal travels through Cu-Ni cables to reach the room temperature setup. We also use a set of twisted pair phosphor bronze DC wires to feed manual heaters or cold switches at the base temperature.

### 5.2.2 Cold attenuators

Without any attenuation or isolation, the input and output coaxial cables transfer the thermal (Johnson-Nyquist) noise in addition to the main signals from room temperature to the device, which heats up the microwave cavities and is in contradiction with the main reason we operate the experiment at low temperatures. To solve this problem, we need to attenuate the input signal at different temperatures in the fridge to remove and replace the hot thermal noise with the lower energy noise thermalized at lower temperatures.

In quantum mechanics, an attenuator can be modeled as a beam-splitter that takes a fraction  $\eta_{\text{att}}$  of the incoming signal and replaces it with a fraction  $1 - \eta_{\text{att}}$  of the thermal noise. This added noise is necessary to preserve the commutation relations of the traveling mode. For an input signal with a background noise of  $n^{\text{in}} + \frac{1}{2}$ , we can write:

$$n^{\text{out}} + \frac{1}{2} = \eta_{\text{att}} n^{\text{in}} + (1 - \eta_{\text{att}}) n^{\text{th}} + \frac{1}{2}, \quad (5.1)$$

Where  $n^{\text{th}} = \left( e^{\frac{\hbar\omega}{k_B T}} - 1 \right)^{-1}$  is the attenuator's thermal noise. The typical attenuations to remove the 300 K thermal noise from the input signal typically used in our experiments, as well as thermal noises corresponding to different temperatures are shown in table 5.1.

Table 5.1: Cold attenuators arrangement to remove the room temperature thermal noise.

Temperature (K)	300	50	3	0.8	0.1	$10 \times 10^{-3}$
$n^{\text{th}}$ (quanta) at 5 GHz	1250	208	12	2.9	0.1	$10^{-11}$
$\eta$ (dB)	0	0.1	20	10	0.1	20
$n^{\text{out}}$ (quanta) at 5 GHz	1250	1225	24	5.0	4.9	0.03

### 5.2.3 High Electron Mobility Transistor Amplifiers

Cryogenic HEMT amplifiers are essential components in the measurement chain providing a low-noise amplification of microwave signals at 3-K flange to overcome the thermal noise contamination of the warmer stages. We use HEMTs provided by Low Noise Factory<sup>®</sup> (LNF-LNC4-8F) with a typical bandwidth of 4-8 GHz, a gain of  $\sim 40$  dB, and added noise of  $\sim 8$  quanta. The HEMT needs  $\sim 0.7$  V and  $\sim 15$  mA voltage and current applied to the transistor's drain to operate in the low-noise and high-gain regime. This also increases the heat load on the 3-K flange by dissipating  $\sim 1$  mW of power per each operating HEMT.

### 5.2.4 Cryogenic circulators, couplers, and Eccosorb filters

It has been reported that HEMTs emit additional noise back to their input line which can be coupled to the sample at 10-mK and contaminate the signals. For this reason, cryogenic circulators are used to isolate the sample from the backward propagating noise in the output chain. We use LNF<sup>®</sup>-CIC4-8A circulators with typical isolation of 20 dB and insertion loss of  $\sim 0.2$  dB.

Eccosorb microwave filters are also used at the input line in base temperature to protect the sample and JTWPA from high frequency ( $>20$  GHz) and infrared noise radiation.

In circuit optomechanical experiments such as ground state cooling and squeezing often high microwave pump powers are needed in order to reach intracavity photon numbers as large as  $10^6$  quanta. In these cases, the dissipated power of the microwave pump in the 20 dB attenuator at the base temperature can be comparable with the existing cooling power of the mixing chamber stage and result in slight heating of the base temperature. To solve this issue, we normally use a 20 dB directional coupler instead of an attenuator to transfer the 99% residual power through another input line and dissipate it in attenuators installed in higher temperature flanges offering more cooling power. This wiring scheme can simultaneously be used to combine a tone-cancellation tone and generate destructive interference after the

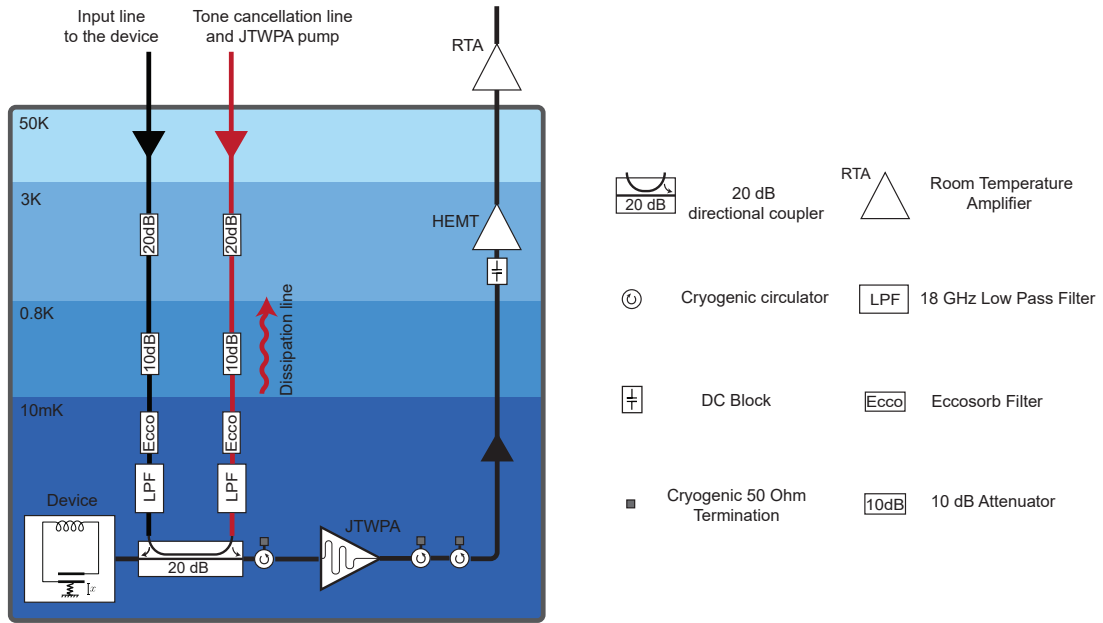


Figure 5.4: **Microwave wiring in the fridge.** The standard microwave wiring used in circuit optomechanical experiments is shown. To reduce power dissipation in the base temperature flange we use directional couplers instead of cold attenuators and redirect the residual high-power optomechanical pump to higher stages to dissipate. The dissipation line simultaneously is used to combine tone cancellation signals to generate destructive interference before JTJWPA. The dissipation line also carries the JTJWPA pump.

coupler output to prevent saturation of the next amplifiers in the measurement chain.

### 5.2.5 Electrical spectrum analyzer

ESA is the final destination of the amplified microwave signals in the measurement chain. Understanding the working principle of ESA helps to optimize the timing and noise level in optomechanical power spectral density measurements.

We use R&S® FSW 26 GHz as our main ESA instrument. In the fast Fourier transform (FFT) mode the signal flow in the spectrum analyzer is described by the following: the microwave input signal to ESA gets mixed with an internal microwave tone to down-convert to an intermediate frequency (IF) range and will be sampled by an analog to digital converter (with 200 MHz sampling clock in our case). The total record length of a single time trace is defined by the resolution bandwidth (RBW), e.g. for  $RBW = 1 \text{ Hz}$  the record length is  $\propto 2/RBW \sim 2 \text{ s}$ . Then the FFT of the digital time trace is numerically calculated, with an arbitrary number of points in the frequency range. The resolution of the frequency spectrum is limited by RBW, i.e. the record length. The truncation of the digital time trace data results in the convolution of the original signal frequency spectrum by a filter (in our case Gaussian) with the linewidth of RBW. A PSD measured with a given resolution bandwidth (RBW) corresponds to the convolution of

an actual PSD  $S(\omega)$  with a Gaussian filter  $f(\omega) = e^{-(\omega/\sqrt{2}\sigma_{\text{RBW}})^2}$ , where  $\sigma_{\text{RBW}} = \text{RBW}/\sqrt{2\pi}$ . This is described as

$$\tilde{S}(\omega) \equiv \int_{-\infty}^{+\infty} S(\omega') \times f(\omega - \omega') d\omega'. \quad (5.2)$$

For a Lorentzian spectrum, the convolution with a Gaussian filter result in a Voigt function:

$$V(\omega; \Gamma, \sigma_{\text{RBW}}) \equiv \int_{-\infty}^{+\infty} \frac{\Gamma}{\pi(\omega'^2 + \Gamma^2)} \times e^{-\frac{(\omega - \omega')^2}{2\sigma_{\text{RBW}}^2}} d\omega' \quad (5.3)$$

The Voigt function is used to numerically fit on PSD of optomechanical sidebands for example. When the linewidth of a sideband signal is smaller or comparable with the RBW, the convolution cannot be negligible for obtaining the sideband power, i.e., the integration of the measured PSD does not give the actual sideband power. Therefore, we fit the measured PSD to a Voigt function with a given RBW and extract the height and linewidth of the Lorentzian PSD to calculate the actual sideband power. ESA is reporting the PSD data in the units of dBm (decibel normalized to 1mW of power) which is the integration of the original PSD with the RBW filter function in time. We can qualitatively consider three different regimes when taking the PSD of a signal with a feature bandwidth of  $W$  using ESA: when  $\text{RBW} \gg W$  We basically lose most of the spectrum information and only observe the Gaussian filter, hence the peak of the Gaussian corresponds to the total power of the signal and ESA acts like a power meter. When  $\text{RBW} \ll W$ , the signal spectrum is resolvable and the measured PSD reflects a good estimate of the main signal spectrum. In this case, the actual PSD of the signal can be inferred by dividing the measured power by the RBW which gives us the PSD in the units of dBm/Hz. When  $\text{RBW} \sim W$ , we have to consider the convolution effect of the RBW Gaussian filter and use fitting or numerical analysis to restore the information of the main signal spectrum.

For example, in the ultra-coherent electromechanical project (chapter 7) the inset of Fig. 7.2h shows the measured PSD of a mechanical sideband, compared with the ideal Gaussian core of the Voigt function ( $\text{RBW} = 1 \text{ Hz} \gg \Gamma_m = 45 \text{ mHz}$ ). The linewidth of the mechanical sideband - which in this case includes any unwanted frequency fluctuation - can be then extracted by fitting a Voigt function to the measured PSD. The noise floor in the PSD of a signal measured with ESA scales with the RBW, since the input white background noise gets integrated in a wider span by increasing RBW. Although reducing RBW increases the signal-to-noise ratio of signals when  $\text{RBW} \gg W$ , it simultaneously increases the measurement time as well. In the regime of  $\text{RBW} \ll W$  however the signal-to-noise ratio remains constant by changing RBW. Due to the stochastic nature of the noises in the real world, averaging the PSD of a stationary signal in ESA reduces the fluctuation of the signal and noise level. Considering a white Gaussian stochastic process for the background noise, the noise fluctuation - i.e. the variation of the measured PSD in frequency compared to the average level of the noise PSD - scales with  $1/\sqrt{N_{\text{avg}}}$ . To properly measure weak signals such as optomechanical sidebands we require that the background noise fluctuation gets smaller than the peak of the signal to be able to reliably fit on the measured PSD.

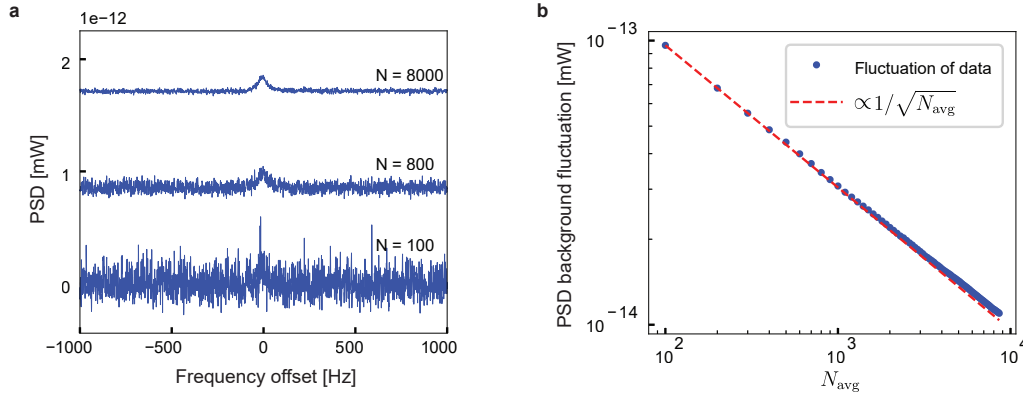


Figure 5.5: **Fluctuation scaling with averages in ESA.** **a**, Shows ESA traces of a weak optomechanical sideband measured with different averages. **b**, The background fluctuation is scaling with  $1/\sqrt{N_{avg}}$  as shown by dashed line. The calculated background standard deviation from the measured traces are shown by blue dots. In order to reliably fit on a data, the background fluctuation needs to be smaller than the signal power. As shown, the slight deviation from the ideal scaling at high averages is mainly due to background ripples of the measurement tool or the measurement line which cannot be eliminated by averaging.

The ESA can be also operated in the zero-span mode, measuring the signal's power in a specific RBW at a fixed frequency versus time. In this mode, the time variation of the signal should be slower than RBW in order to be fully resolvable and not limited by the time response of the filter. Of course, the trade-off between the speed and noise scaling with RBW again exists in this mode. We typically use the zero-span mode for the ring-down measurements (Sec. 6.2.3) to characterize the bare and optomechanically induced mechanical damping rate.

Another useful mode that sometimes comes as an additional option on ESA is the IQ-analyzer. In this mode, the signal gets down-converted around a center frequency to IF domain, gets sampled with A/D converter, and numerically multiplied by numerically generated sine and cosine waves to extract its  $I$  and  $Q$  quadratures versus time in a specific sweep time window and sampling rate. All the numerical processing is done on the internal FPGA of the ESA and the user can directly extract the quadrature data from the tool. This mode is useful when we need more information than average power spectral density and need access to both quadratures of optomechanical sidebands for example to measure the optomechanical sideband quadrature distribution in optomechanical amplification scheme (Sec. 7.4.1). In this mode, the ESA is reporting the quadrature data in Volts versus measurement time.

### 5.2.6 Vector network analyzer

VNA is the standard microwave measurement tool for characterizing scattering matrix parameters,  $S_{ij} = |S_{ij}|e^{i\angle S_{ij}}$ . The tool has two ports, sending a microwave tone from one port to the device and measuring the reflection to the same port and transmission to the other port and extracting the total attenuation/gain as well as the phase shift between the transmitted and

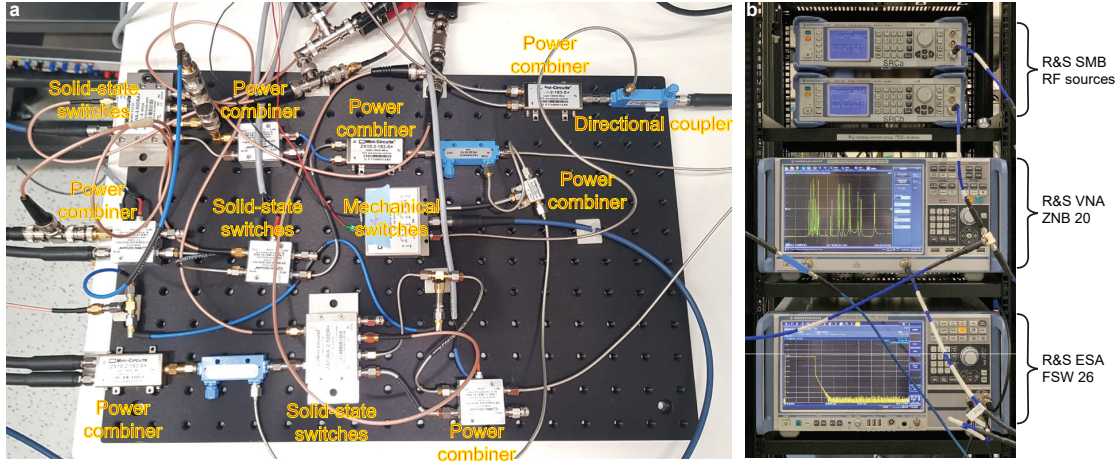


Figure 5.6: **Photo of room temperature components and the measurement instruments.** **a**, An example photo of the room temperature microwave wiring including solid-state switches, couplers, combiners, and mechanical switches for signal routing. The wiring used in the ultra-coherent electromechanics project is slightly different with faster solid-state switches and more components which is schematically shown in Fig. 7.12. **b**, The photo shows ESA in the zero-span mode taking a ringdown trace, the VNA taking the  $S_{21}$  response of a 24-site graphene electromechanical lattice, and two microwave sources. Photo courtesy of **b**: Andrea Bancora.

received signals. By sweeping the frequency of the tone the tool will extract the frequency response of a DUT connected between ports. The received signal is collected through a band-pass filter with adjustable bandwidth, BW. The total sweep time for a trace with a certain frequency span and number of points is given by  $T_{\text{sweep}} \propto \frac{2 \times \text{NOP}}{\text{BW}}$  while the sweep speed of the VNA tone will be  $\frac{2 \times \text{SPAN}}{\text{NOP}} \times \text{BW} \left[ \frac{\text{Hz}}{\text{s}} \right]$ . The span divided by NOP defines the minimum frequency feature that can be resolved by VNA, and should be adjusted considering experiment requirements. For example in OMIT experiment (see Sec. 6.2.2) the feature can be as narrow as the mechanical bare linewidth in the order of 100 mHz when we need many NOP in a small span. BW of the measurement determines the signal-to-noise ratio and in principle decreasing BW is similar to increasing the averages of the trace. Properly choosing BW helps to adjust the sweep speed to avoid the observation of non-stationary effects, e.g. OMIT ripples (see Sec. 6.2.2). We use R&S® ZNB 20 GHz as our main VNA instrument.

### 5.2.7 Other microwave components

To generate high-power microwave pulses (>20 dBm) in the optomechanical amplification experiment we use ultra-fast solid-state switches (Planar Monolithics Industries®, P1T-4G8G-75-R-SFF) with  $\sim 50$  ns rising/falling time. An arbitrary waveform generator (AWG) with two outputs generates short pulses which can activate microwave solid-state switches, and trigger the ESA and microwave sources. We use Tektronix®-AFG3252 as our AWG. Room temperature amplifiers (Mini-Circuits® ZVA-183-S+) are required to increase the HEMT noise floor level



more than the electronic noise of the ESA - but the signal-to-noise ratio will not change significantly due to the high gain of HEMT and JTWPA. We use room-temperature mechanical microwave switches supplied from Mini-circuits® (MSP2T-18XL+) to redirect the VNA tone and microwave sources between different instruments.

### 5.2.8 Phase locking and clock distribution

All microwave measurement instruments and microwave sources need to be phase locked to avoid fluctuations and systematic errors specifically in the long measurements when a sub-milli-Hertz frequency mismatch between instruments can build up errors. The standard procedure in microwave measurements is to generate a very stable reference signal with typically 10 MHz frequency and distribute it between all the instruments as a phase reference. Any other frequencies can be then generated based on the reference clock using frequency doubling schemes. The reference signal can either be generated using an internal Quartz-based clock in instruments such as ESA or VNA, or using a dedicated atomic clock. In our experiment, we decided to use ESA as the reference signal source and use a low-noise signal distributor Oscilloquartz® 5020 to split it into several paths and feed other sources and instruments with it. Microwave sources are using phase-lock loops (PLL) to follow the phase of the reference signal. The bandwidth of the PLL affects the stability of locking and the rate of the phase drift which are crucial parameters for state tomography experiments e.g. mechanical squeezing free evolution experiment (see Sec. 7.5). We operate our sources with PLL bandwidth of 100 Hz and minimum lock-in range of  $\pm 3$  ppm and measure extremely small phase drift using ESA IQ-analyzer less than  $\frac{\pi}{1\text{day}}$  for a GHz range microwave tone.

## 5.3 Josephson traveling wave parametric amplifier

JTWPA is a wide-band and near-quantum-limited amplifier working based on the four-wave-mixing process (Fig. 5.7) in an engineered chain of the nonlinear Josephson junction-based lumped-element resonators forming an effective nonlinear waveguide for microwave signals (Macklin et al., 2015). The first practical realization of JTWPAs dated back to 2015 by MIT Lincoln Laboratory and UC Berkeley. JTWPA offers more than 20 dB loss-compensated gain with less than  $\frac{1}{2} + \frac{1}{2}$  quanta added noise which significantly increases the signal-to-noise ratio compared with the HEMT. JTWPA is usually operated at the base temperature, before the HEMT amplifier. The JTWPA is amplifying the signal in a four-wave mixing process in the presence of a microwave pump, resulting in an amplified signal and idler symmetrically detuned from the pump frequency to satisfy the energy conservation. To overcome the phase-matching condition in the traveling wave amplification process the dispersion of the JTWPA is engineered resulting in a bandgap in the transmission spectrum called the dispersive feature - centered around 6 GHz in our JTWPA. Applying a microwave pump close to the dispersive feature activated the four-wave-mixing process resulting in high gains in the broad bandwidth of 4-8 GHz, excluding the dispersive feature bandwidth. The 1-dB compression point of the

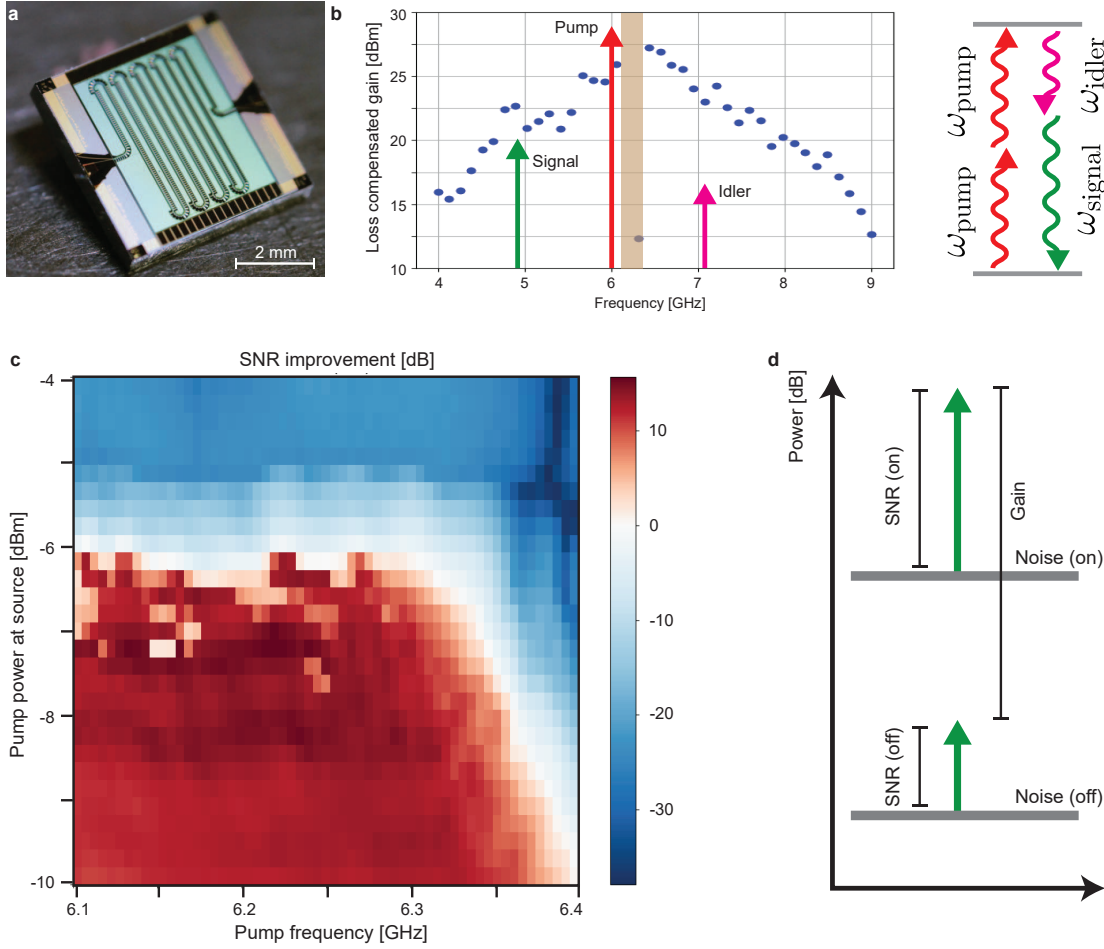


**Figure 5.7: Josephson traveling wave parametric amplifier.** **a**, Photo of a JTWPA device showing a lumped-element waveguide of thousands of nonlinear circuits providing wide-band and low-noise microwave gain fabricated in MIT Lincoln Laboratory (Image courtesy: Macklin, *et.al.* 2015 (Macklin et al., 2015)). **b**, An example of the JTWPA gain profile measured on a device provided by MIT Lincoln Laboratory for our experiment. The brown shade shows the dispersive feature where no gain is expected. The JTWPA needs to be pumped close to the dispersive feature and amplify the signal and idler. To conserve energy conservation in the four-wave mixing process, the signal and idler frequencies are symmetrically detuned from the pump frequency. **c**, To optimize the pump power and frequency we sweep these parameters and measure signal-to-noise ratio improvement when JTWPA is off and on. The higher SNRI corresponds to lower added noise in the amplification process. **d**, Schematics showing SNR and gain when JTWPA is on and off.

JTWPA is reported  $\sim -100$  dBm at the output, therefore any other microwave tone used in the experiments needs to be canceled at the input of the JTWPA to avoid saturation. It is worth noting that JTWPA is extremely sensitive to electrostatic discharges. ESD shocks can destroy junctions in the device which significantly reduce the gain and increases the loss in the device. To avoid ESD damages, we use anti-ESD gloves, and bracelets connected to the common



ground as well as anti-ESD coats.

The quantum efficiency of the measurement chain is strongly dependent on the JTWPA-added noise during amplification. The added noise and gain of the JTWPA are both dependent on the pump frequency and power. To optimize JTWPA and find the best operating points we sweep the pump power and frequency and monitor the signal-to-noise ratio improvement (SNRI) of the JTWPA (Fig. 5.7c, and d). This can be simply measured by introducing a weak microwave tone and measuring its peak power and noise background after and before activating the JTWPA, i.e. turning on the microwave pump.

### 5.3.1 Estimation of the JTWPA added noise using SNRI

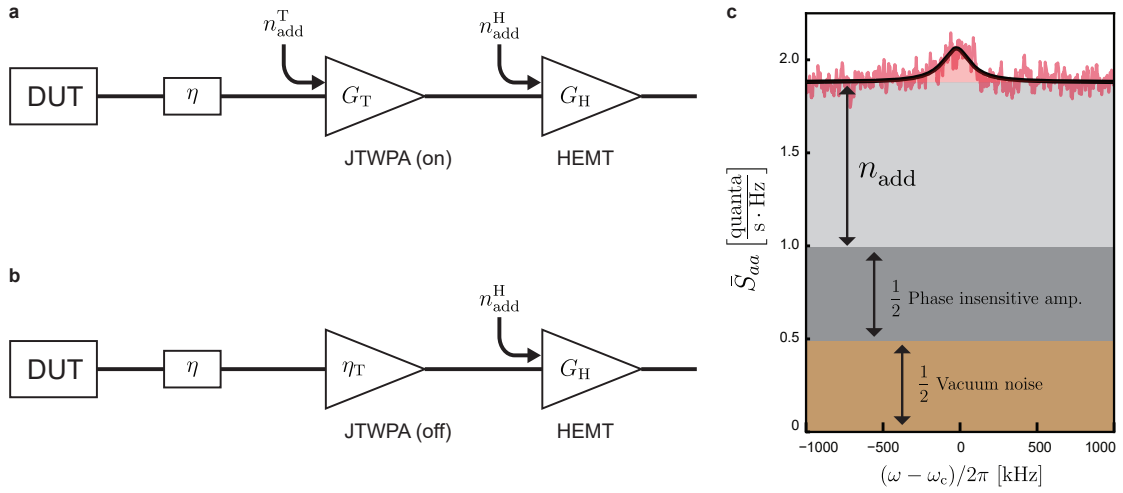


Figure 5.8: **JTWPA SNRI and added noise.** **a,b**, Schematic model of the measurement chain for two cases of JTWPA's pump on (amplification) and off (attenuation). **c**, An example of calibrated PSD of the microwave cavity noise emission. In the ideal phase-insensitive amplification -50% quantum efficiency- a  $\frac{1}{2}$  quanta/s·Hz noise will be added to the vacuum noise level. In practice, the finite quantum efficiency of the measurement chain can be measured and the actual noise background including total added noise referred to the device can be calculated as shown by  $\frac{1}{2} + \frac{1}{2} + n_{\text{add}}$ .

We consider a simplified model for the output chain as shown in Fig. 5.8. The emitted signal from DUT is experiencing a total attenuation of  $\eta$  before reaching JTWPA. When the pump of the JTWPA is off it acts as an attenuator,  $\eta_T$ . When the JTWPA's pump is on, it amplifies the signal by the gain of  $G_T$ , and adds an added noise of  $\frac{1}{2} + n_{\text{add}}^T$  to the signal (referred to the input). The signal is amplified again at 3 K stage by HEMT, with an effective added noise of  $\frac{1}{2} + n_{\text{add}}^H$  (including the attenuation between HEMT and JTWPA) and the gain of  $G_H \sim 40$  dB. Because of the high gain of HEMT, the noise figure of the measurement chain is dominated by HEMT (and JTWPA, if its pump is on), and will not be considerably affected by further attenuation or amplification in the room temperature setup.

We can consider a signal,  $s$ , plus the vacuum noise of  $\frac{1}{2}$  emitted from the DUT. The total output of the HEMT amplifier can be calculated when JTWPA is on or off:

$$\text{JTWPA off: } G_H \left( \frac{1}{2} + n_{\text{add}}^H + \eta_T \left( \eta s + \frac{1}{2} \right) + (1 - \eta_T) \frac{1}{2} \right) = G_H \eta_T \eta \left( s + \frac{1 + n_{\text{add}}^H}{\eta \eta_T} \right), \quad (5.4)$$

$$\text{JTWPA on: } G_H \left( \frac{1}{2} + n_{\text{add}}^H + G_T \left( \frac{1}{2} + n_{\text{add}}^T + \eta s + \frac{1}{2} \right) \right) = G_H G_T \eta \left( s + \frac{1 + n_{\text{add}}^T}{\eta} + \frac{\frac{1}{2} + n_{\text{add}}^H}{\eta G_T} \right). \quad (5.5)$$

In each case, the SNR can be simplified as:

$$\text{SNR}^{\text{off}} = \frac{s}{\frac{1}{\eta \eta_T} (1 + n_{\text{add}}^H)}, \quad (5.6)$$

$$\text{SNR}^{\text{on}} = \frac{s}{\frac{1}{\eta} (1 + n_{\text{add}}^T + \frac{\frac{1}{2} + n_{\text{add}}^H}{G_T})}, \quad (5.7)$$

and the SNRI can be written as:

$$\text{SNRI} = \frac{1 + n_{\text{add}}^H}{(1 + n_{\text{add}}^T) \eta_T + \frac{\eta_T (\frac{1}{2} + n_{\text{add}}^H)}{G_T}}. \quad (5.8)$$

The second term in the denominator can be neglected compared to the first term because of the high gain of JTWPA. Therefore, the JTWPA added noise can be extracted as:

$$n_{\text{add}}^T = \frac{1}{\eta_T} \frac{1 + n_{\text{add}}^H}{\text{SNRI}} - 1. \quad (5.9)$$

With this, the background noise level of the measured signal referred to the DUT,  $1 + n_{\text{add}}$ , can be expressed by:

$$1 + n_{\text{add}} = \frac{1}{\eta \eta_T} \frac{1 + n_{\text{add}}^H}{\text{SNRI}}. \quad (5.10)$$

As an example, in the ground state cooling experiment (Sec. 7.3), we measured SNRI=11.3 dB and a loss compensated gain of  $\frac{G_T}{\eta_T} = 25.7$  dB. The HEMT's added noise is extracted from the datasheet as  $n_{\text{add,nominal}}^H \simeq 6.9$  quanta. The attenuation of the cryogenic circulators is

reported as 0.25 dB at low temperatures based on their datasheet. Considering two circulators between JTWPA and HEMT, 0.5 dB cable loss (1 dB/m flexible coaxial cable loss), and lossless superconducting lines from circulators to the HEMT, the effective HEMT's added noise is assumed  $n_{\text{add}}^{\text{H}} \simeq 8.7$  quanta. The attenuation of the JTWPA is provided by its datasheet as  $\eta_{\text{T}} = 2.5$  dB at 5.5 GHz. The total attenuation between DUT and the JTWPA is composed of: 0.25 dB (cryogenic circulator) + 0.3 dB (directional coupler) + 1.0 dB (1 dB/m flexible coaxial cable loss). This results in the total estimated noise background of  $1 + n_{\text{add}} \simeq 1.9$  quanta/s-Hz, and JTWPA added noise of  $n_{\text{add}}^{\text{T}} \simeq 0.3$  quanta, in agreement with the results from sideband asymmetry calibration discussed in Sec. 7.3.2.

## 5.4 Microwave tone cancellation

To avoid the saturation of the JTWPA by strong optomechanical pumps, we have to cancel the signal before the JTWPA by destructively interfering it with a tone cancellation signal. This is realized by splitting the signal at room temperature into two paths and adding a phase and attenuation to the signal in the tone cancellation path, and combining it with the signal right before the JTWPA. We use digital attenuators and phase shifters for this purpose (Vaunix<sup>®</sup> LDA-602EH and LPS-802), as shown in Fig. 5.9a, and c. In this section, we calculate the guaranteed level of tone cancellation which can be achieved using the digital phase shifters and digital attenuators.

For simplicity, we define the signal after the splitter as  $s_{\text{in}}$  and the signal from the device under test as  $s$  (as shown in Fig. 5.9a). Note that we here consider the case with a balanced splitter, which can be straightforwardly extended to be general. In the ideal case, the attenuator in the cancellation path should add the same total attenuation as the signal in the main path is experiencing, while the phase shifter is adding a  $\pi$  phase shift for the destructive interference. However, our digital attenuator and phase-shifter can only change the attenuation and phase by finite steps of 0.25 dB and  $\frac{\pi}{180}$ , respectively. This limits the maximum guaranteed cancellation that can be achieved in the system. In this case, the residual combined signal can be written as

$$s_{\text{res}} = s + \sqrt{\eta + \Delta\eta} e^{i(\varphi + \Delta\varphi)} s_{\text{in}}, \quad (5.11)$$

where  $\eta$  and  $\varphi$  are the optimal attenuation and phase shift to destructively interfere with the signal, resulting in  $\sqrt{\eta} e^{i\varphi} s_{\text{in}} = -s$ , while  $\Delta\eta$  and  $\Delta\varphi$  are unwanted errors in the tone cancellation elements. An illustration in the complex plane is provided in Fig. 5.9b. Using Taylor expansion, we then approximate the combined signal as

$$s_{\text{res}} \simeq -\left(i\Delta\varphi + \frac{\Delta\eta}{2\eta}\right)s. \quad (5.12)$$

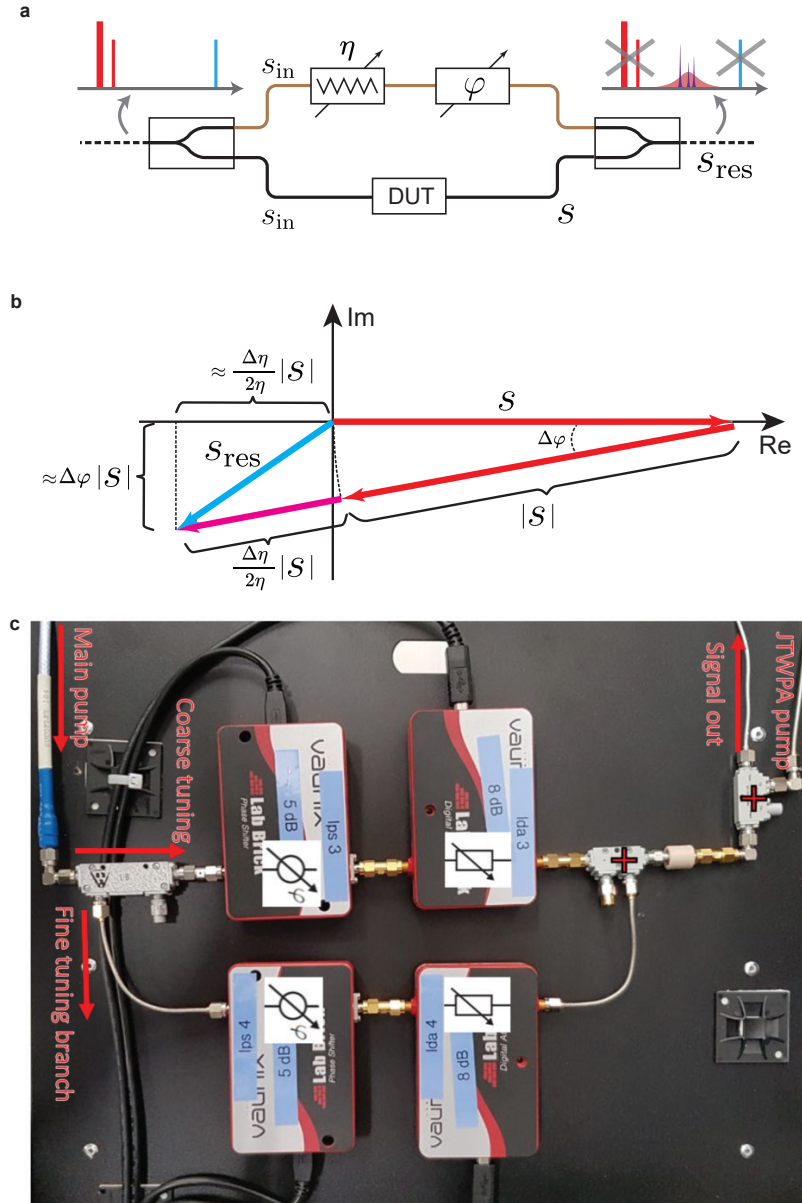


Figure 5.9: **Microwave tone cancellation.** **a**, Splitting a signal into two paths and adding an attenuation and inverse phase using the digital attenuator and phase shifter, results in a destructive interference upon recombining them. This is used to cancel out strong optomechanical pumps to avoid saturation of the JTWPA. **b**, Due to the finite step size of the phase shifter ( $\Delta\varphi$ ) and attenuator ( $\Delta\eta$ ), the combined signal (red vectors plus pink vector) cannot completely vanish. The maximum possible power of the remaining signal (blue vector) determines the guaranteed limit of the tone cancellation. **c**, Photo of the tone cancellation setup showing two coarse and fine-tuning branches of digital attenuators and phase shifters. To reduce the loss in the coarse branch which limits the maximum power of the main pump we use 1:10 directional couplers to split and recombine the fine-tuning branch. The JTWPA pump is normally sent through the tone-cancellation line to avoid unwanted driving of the sample.

Using the relative error in the attenuation, the error in dB is described as

$$\begin{aligned}\Delta(\text{Att.})_{\text{dB}} &= \Delta(-10\log_{10}\eta) \\ &= -10\Delta(\log_{10}\eta) \\ &= \frac{-10}{\ln 10} \frac{\Delta\eta}{\eta}.\end{aligned}\tag{5.13}$$

Hence, the guaranteed tone cancellation in dB can be calculated as

$$10\log_{10}(s_{\text{res}}/s) = 10\log_{10}\left(\Delta\varphi^2 + \left(\frac{\ln 10}{20}\Delta(\text{Att.})_{\text{dB}}\right)^2\right).\tag{5.14}$$

This guaranteed cancellation is independent of absolute values of  $\eta$  and  $\varphi$ . Therefore even in the case of an unbalanced signal splitter, different paths, or unbalanced coupler, where different values of attenuation or phase shift are needed to compensate for the effective path difference between two signals, the residual power will not be changed and only is dependent to the errors of phase shifter and attenuator. Considering the reported values for the Vaunix phase shifter  $\Delta\varphi = \frac{\pi}{2 \times 180}$  and attenuator  $\Delta(\text{Att.})_{\text{dB}} = 0.25/2$  dB (division by 2 in both cases originates from their digital nature), we can achieve at least -35 dB cancellation for every tone cancellation branch. Using several tone cancellation branches multiplies the cancellation level. We use two branches for the optomechanical cooling pump cancellation corresponding to at least -70 dB cancellation. It is worth mentioning that the effective bandwidth of the tone cancellation is inversely proportional to the effective microwave path length ( $L_{\text{path}}$ ):

$$\text{BW}_{\text{TC}} \propto \frac{\pi \nu}{L_{\text{path}}},\tag{5.15}$$

where  $\nu$  is the phase velocity of the signal in the microwave cables. Considering a few meters length of wiring in our setup, this bandwidth is  $\text{BW}_{\text{TC}} = \mathcal{O}(100 \text{ kHz})$  in our setup. For this reason, we use another tone cancellation branch for the blue detuned pumps which are detuned by  $2\Omega_{\text{m}}/2\pi = 3.6 \text{ MHz}$  from the red tone.

## 5.5 Microwave filter cavities

The classical phase noise in a microwave pump for sideband cooling can in principle drive the mechanical resonator and impose a limitation for cooling. The lowest attainable mechanical occupation in the presence of the phase noise (Aspelmeyer, T. J. Kippenberg, and Marquardt, 2014; Rabl et al., 2009) is given by

$$n_{\text{m}}^{(\text{min})} = \sqrt{\frac{\Omega_{\text{m}}^2 n_{\text{m}}^{\text{th}} \Gamma_{\text{m}}}{g_0^2} \bar{S}_{\varphi\varphi}(\Omega_{\text{m}})},\tag{5.16}$$

where  $\bar{S}_{\varphi\varphi}(\Omega_m)$  is the phase noise spectral density at the mechanical frequency in the rotating frame of the pump frequency. To achieve  $n_m^{(\min)} < 1$ , the theoretical limitation requires

$$\bar{S}_{\varphi\varphi}(\Omega_m) < \frac{g_0^2 n_m^{(\min)^2}}{\Omega_m^2 n_m^{\text{th}} \Gamma_m}. \quad (5.17)$$

Considering our system parameters in the ultra-coherent electromechanical project, the theoretical limit to realize  $n_m^{(\min)} < 0.1$  quanta is -137 dBc/Hz at 1.8 MHz detuning from the microwave pump. The measured phase noise for our microwave sources (Rohde & Schwartz, SMA100B) is below -140 dBc/Hz, so it almost fulfills this requirement. However, higher-fidelity ground-state cooling requires a further lower phase noise. This is why we use a microwave filter cavity (Joshi et al., 2021) which is automated, tunable, and narrow-band (Fig. 5.10). It reduces the phase noise within  $\sim 50$  kHz linewidth below -155 dBc/Hz on the microwave cavity frequency, which makes sure that classical phase noise cannot drive the mechanical system.

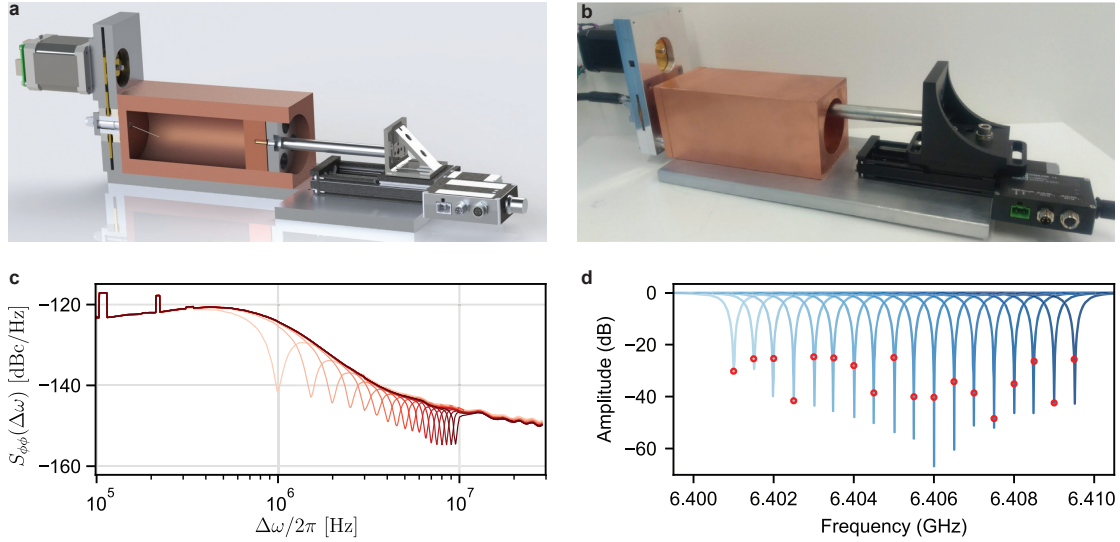


**Figure 5.10: Motorized microwave filter cavity.** **a** The schematic design (cross-section). **b**, The actual device. The frequency of the cavity can be tuned by changing its length using a linear micro-positioner which can be controlled remotely (Image courtesy: Joshi, *et.al.* 2021 (Joshi et al., 2021)). **c**, Phase noise spectrum of a microwave source tone at 6.4 GHz corresponding to different tuning frequencies of the filter cavity (Joshi et al., 2021). **d**,  $|S_{21}|^2$  response of the cavity after an algorithm tune the system at frequencies around 6.4 GHz in steps of 0.5 MHz (corresponding to traces shown in **c**). Red dots indicate the value of the blue curve precisely at the desired frequency (Joshi et al., 2021).

The frequency stability of the filter cavity is essential, especially for the thermal decoherence measurements, where the experiment and calibration process continues for hours. Due to the large size ( $\sim 15$  cm) and high thermal expansion rate of the copper of the filter cavity, we observe a slow frequency drift of the filter cavity frequency. In fact, we estimate 0.5 centigrade

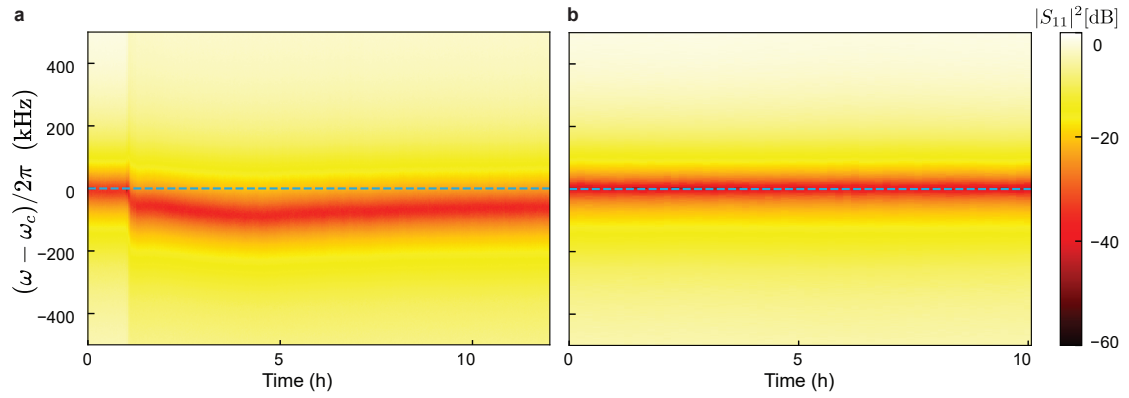


Figure 5.11: **Frequency stability of the motorized filter cavity.** Filter cavity response **a**, without and **b**, with adaptive frequency stabilization. The dashed blue line indicates the target filter frequency. Due to slight environmental temperature changes, the cavity without stabilization can be completely detuned from the target frequency. The issue is solved using an adaptive stabilization technique.

temperature difference can shift the resonance frequency by more than 50 kHz (as shown in Fig. 5.11a). Therefore, we monitor the resonance frequencies of the filter cavities during the experiment by re-routing the VNA signal through them using mechanical switches, and adaptively tune their frequency using a sub-micron accuracy linear positioner. The frequency stability of the cavities with and without the adaptive tuning is shown in Fig. 5.11, where the stabilization process is clearly keeping the cavity resonance on the target frequency. The design and control codes for such cavities are available online and can be found in the supplementary materials of Joshi, *et.al.* (2021) (Joshi et al., 2021).

## 5.6 Instrument control and data acquisition

Conducting an experiment is similar to an orchestra when every instrument needs to be commanded and controlled in a time sequence by a computer program to follow the experiment's logic of initializing devices, sending pulses, measuring the output, and tuning parameters for example. All the instruments in our experiment including the fridge are connected to a local computer network. We can address every instrument by its local IP address and send commands and queries. A measurement computer mediates between instruments and collects the data. QTLab ([QTLab GitHub repository n.d.](https://github.com/qtlab/qtlab)) is a Python package developed at Delft university before 2015 for communication with instruments and running python based measurement scripts. We adopted QTLab and added several features, wrapping codes, and instruments to it and formed a domestic version of this package adapting our new instruments and measurement flow. The structure of our Python-based computer control package can be explained in three levels of Python codes (Fig.5.12).

**1) Instrument control codes:** Every instrument supports dedicated string-based commands



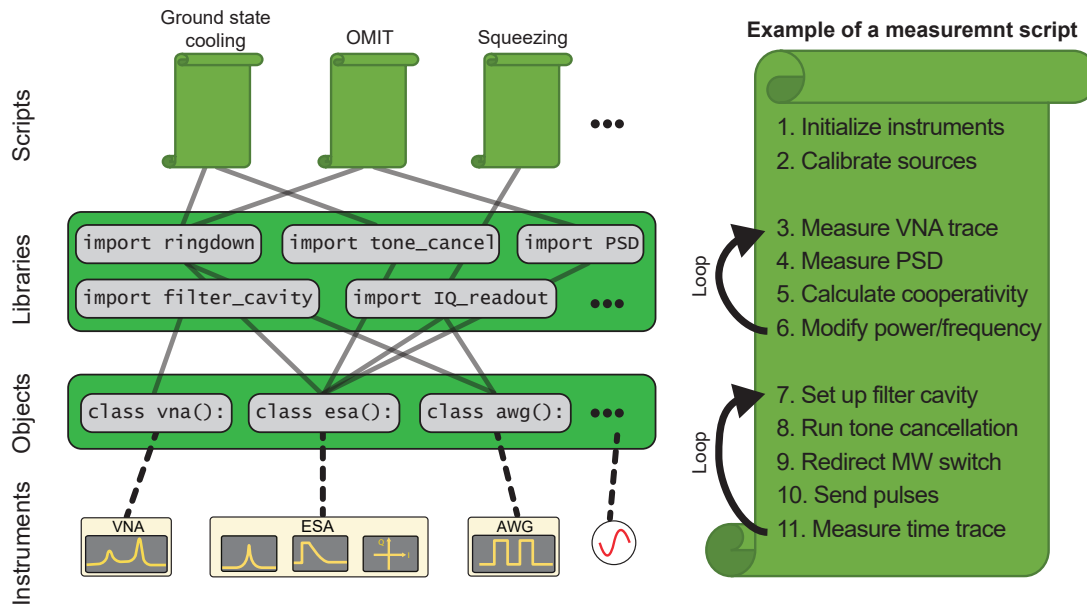


Figure 5.12: **Computer control of the measurement flow.** The figure shows the hierarchy of the measurement control computer program. At the lowest level, Python objects are communicating with instruments through a local network using the PyVisa library. Python objects are used to build libraries containing basic measurement codes to fulfill a single measurement job. At the highest level, a measurement script describes the flow of an experiment using the libraries to sweep and optimize parameters or apply feedback. An example of a measurement script algorithm is shown for the calibration of optomechanical amplifier.

and queries to communicate with developed by its manufacturer. Knowing the IP address of a tool, we can use the PyVisa package to send these commands through LAN cables or USB and receive the tool's response. These low-level commands can change the instrument parameters and modes. By sending queries we can extract information on the parameters of the tool or the raw data of the traces such as measured PSD in ESA or scattering matrix parameters from VNA for example. Here are some examples of the commands and queries:

- 'frequency:span?' : Asks for the frequency span of R&S VNA.
- 'DISP:trac:Y:RLEV?' : Asks for the reference level of the Y axis in R&S ESA.
- 'source1:burst:ncycles 10': Set 10 number of cycles in the burst mode of Tektronics AWG.

To facilitate communication with the instruments, we define a python object for every instrument. The python object contains an initialization function to set up the connection to the instrument using PyVisa. The instrument object has several functions which contain communication codes to instruments to set or get parameters and modes of each tool. Every time a measurement script runs we can define the required instruments as objects at the



beginning of the code and call them when needed. We created these python objects for ESA, VNA, AWG, sources, phase shifters and attenuators, fridges control unit, microwave switches, linear motors, etc. For example for calling VNA object to read the trace data of VNA we simply call `'S = vna.get_tracedata()'` or for setting its bandwidth we send the command `'vna.set_bandwidth(10)'`.

**2) Measurement libraries:** Now that we have access to the instruments through objects, we can form measurement libraries containing Python functions responsible for specific basic measurements requiring one or many instruments. Here we take an example, a ringdown experiment requires one blue-detuned microwave source to excite the mechanics using parametric instability, one red-detuned microwave source to probe the optomechanical sideband, the ESA in the zero-span mode to measure the sideband's power in time, and an AWG to trigger the excitation and readout pulses and also trigger ESA to start the measurement. In this case, we write a library containing a function that asks several arguments such as mechanical and microwave frequencies, and parameters of the ringdown, for example, excitation pulse power and length, readout time, and bandwidth. The function based on the input arguments initializes and sets up the correct parameters in microwave sources and AWG, put ESA in the zero-span mode and initializes it to wait for the trigger, sends the trigger command and waits until the ringdown is complete, and extracts the time trace data from ESA. It can also repeat the cycle and averages the trace if required. Finally, the function generates a folder titled the data and measurement date in a determined data path and saves the trace data and the plot, as well as a setting file containing all the instruments' object parameters at the moment of the measurement. The function can also return the trace data in the code if required. All this process can be run by calling the function from the ringdown library (mrd):

```
'Trace, Times = mrd.ringdown(source1, source2, **options_dict)'
```

Many basic experiments are implemented in such way in Python libraries and can be used as code building blocks in more complicated experiments. This architecture significantly increases the programming flexibility in big projects.

### 3) Experiment scripts:

Although short and quick characterizations can be manually conducted using the measurement functions in the Python console, a complicated and long experiment needs several sweeps and stabilization or feedback during the sweeps which require a programmed script. Let's consider the optomechanical amplification experiment (see Sec. 7.4.1) as an example. In a script, we first need to load and define all the instruments and libraries needed as well as system parameters such as mechanical and microwave frequencies. Then several initialization steps are needed such as calibration of the JTWPA gain, running the tone cancellation optimization function, tuning filter cavities on resonance, and calibrating microwave source powers to name a few. Then a measurement loop starts where we sweep over different cooling pump power to prepare different mechanical occupations close to the ground state. In every iteration of the code, the cavity response with VNA and PSD of the sidebands with ESA needs

to be measured. Then we turn off JTWPA and using ringdown we calibrate the optomechanical damping rate and call the optomechanical amplification function setting up pulses and measuring quadratures of motion using IQ-analyzer in hundreds of iterations. We typically need to average these signals for long times and to stabilize the measurement over days we split these averages into several cycles. In each cycle, we measure the imbalance of the blue and red probes, re-tune filter cavities, re-route the microwave tones using switches in the setup, and run the above-mentioned loop once. All the data corresponding to each measurement is separately saved in a hierarchical structure based on the cycle number, cooling power, and measurement type. In addition, we combine and save the final traces data as well as system parameters in a single Numpy dictionary which can be easily loaded later for post-processing.

Using such a programming structure, we are able to run complicated measurements including several instruments, and precisely control and stabilize the experiment flow over long measuring times.

## 6 Characterization

This chapter reviews the characterization experiments procedure of circuit optomechanical devices and discusses how electrical and mechanical properties can be extracted from those measurements.

### 6.1 Microwave resonance characterization

As discussed in Sec.5.2.6 the microwave response - scattering parameters - of a device under test is measured using a vector network analyzer. Searching for resonance features (as discussed in Sec.3.1.1) in the scattering parameters over a desired frequency span enables us to roughly estimate the center resonance frequencies. The typical linewidth ( $\kappa = \kappa_0 + \kappa_{\text{tot}}$ , including intrinsic loss rate and the external coupling rate) of electromechanical LC circuits is in the range of 5 MHz - 50 kHz depending on the design, and they can be spread over a few GHz of measurable frequency window (typically 4-8 GHz). We developed an automated resonance search protocol to facilitate this initial characterization step. Considering the minimum frequency resolution needed to resolve the finest feature -e.g. a  $2/\kappa^{(\text{max})} = 50$  kHz linewidth resonance- and the maximum number of points of the VNA, the code divides the desired search frequency range into several sub-spans. We typically use 10 kHz frequency spacing and 100 kHz measurement bandwidth for VNA. The measured complex  $S_{21}(\omega)$  contains phase and amplitude response. The phase response reported by VNA is wrapped between 0 to  $2\pi$ . After taking the data, the code unwraps the phase to have a continuous trace,  $\phi(\omega)$ . Then the phase derivative is numerically calculated. The phase derivative of a resonance feature is inversely proportional to the linewidth,  $\frac{d\phi(\omega)}{d\omega} = \frac{2}{\kappa}$ , therefore the peaks higher than a certain value ( $2/\kappa^{(\text{max})}$ ) in the phase gradient response indicate the existence of a resonance feature which can be extracted from the trace. Figure 6.1 shows an example of the measured phase gradient for a chip containing 13 LC circuits.

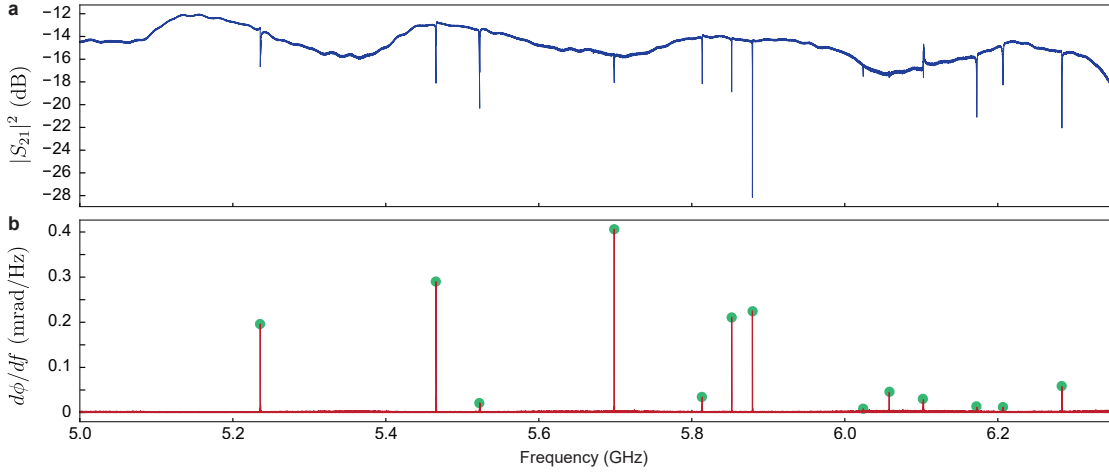


Figure 6.1: **Searching for microwave resonances using phase gradient.** **a**, Shows an example of a  $|S_{21}|^2$  response of a chip measured with VNA. The background wideband ripple indicates a slight impedance mismatch which may result in Fano resonances. **b**, Phase gradient of the measured response. Peak frequencies indicate resonance frequencies and peak heights indicate the inverse of total cavity linewidths.

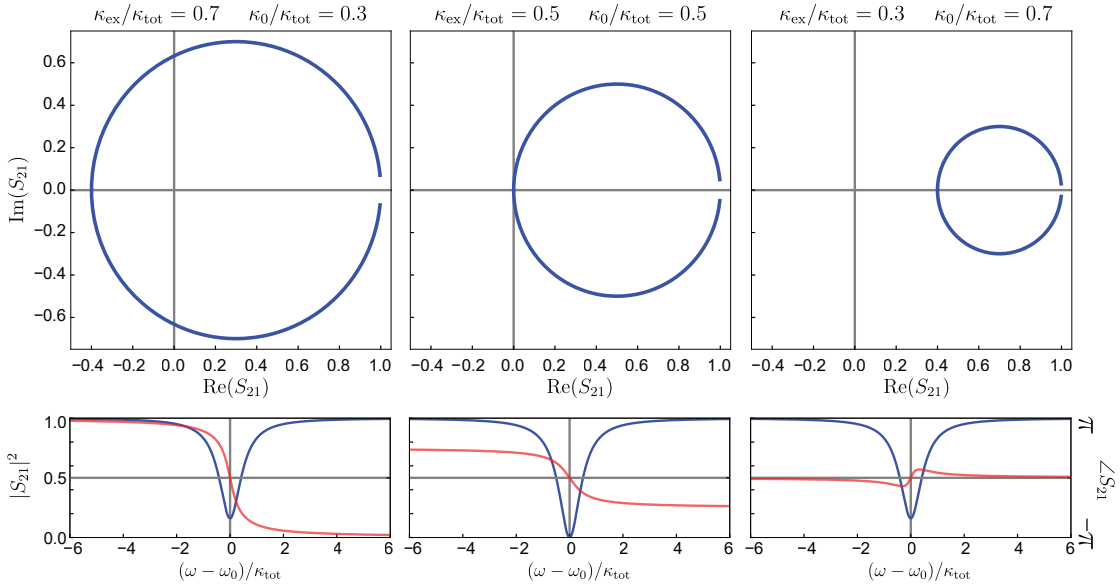


Figure 6.2: **Resonance feature in the complex plain and coupling regimes.** A Lorentzian resonance is corresponding to a circle parametric curve in the complex plain. Depending on the ratio of  $\kappa_{\text{ex}}$  and  $\kappa_0$ , the circle may winds around the origin resulting in a  $2\pi$  phase shift in the response. The three regimes of over-coupling, critical coupling and under-coupling are shown from left to right respectively.

### 6.1.1 Circle fit in the complex plain

Here we consider the short-ended cavity case as an example without losing generality. The reflection coefficient in the ideal model is given by Eq.3.7 ( $S_{11} = \frac{(\kappa_{\text{ex}} - \kappa_0)/2 - i(\omega - \omega_c)}{(\kappa_{\text{ex}} + \kappa_0)/2 + i(\omega - \omega_c)}$ ), and can be

reformatted as:

$$S_{11} = \frac{\kappa_{\text{ex}}}{(\kappa_{\text{ex}} + \kappa_0)/2 - i(\omega - \omega_c)} - 1 = -\frac{\kappa_0}{\kappa} + \frac{\kappa_{\text{ex}}}{\kappa} e^{i2 \tan^{-1}(\frac{\omega - \omega_c}{\kappa/2})}, \quad (6.1)$$

Which corresponds to a circle parametric curve in the complex plain centered at  $-\frac{\kappa_0}{\kappa}$ , with the radius of  $\frac{\kappa_{\text{ex}}}{\kappa}$  as shown in Fig.6.2. This simplified graphical representation shows that for over-coupled resonances ( $\kappa_{\text{ex}} > \kappa_0$ ) a total  $2\pi$  phase shift is expected when passing the resonance frequency since the circular curve winds around the origin of the complex plain, while for the under-coupled resonances ( $\kappa_{\text{ex}} < \kappa_0$ ) this phase shift is zero. A measured microwave

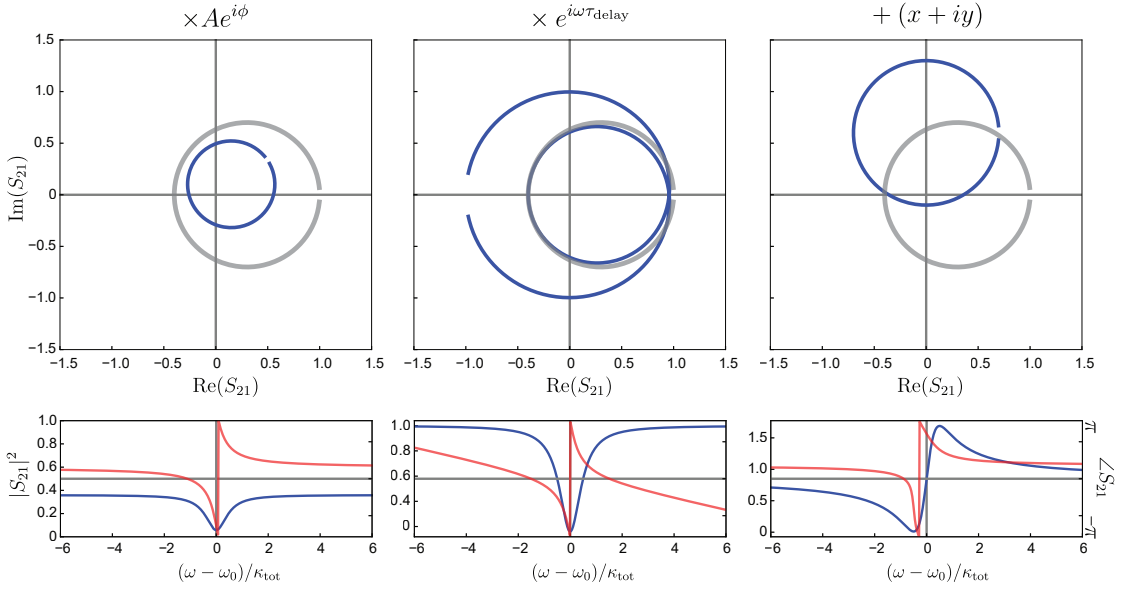


**Figure 6.3: Effect of electric delay and Fanoness on resonance.** The measured resonance deviates from the ideal Lorentzian shape due to measurement line properties and impedance mismatch. The effect of each correction considered in fitting function (Eq.6.2) is shown here: scaling, delay, and Fanoness from left to right respectively.

resonance feature may deviate from the ideal model of Lorentzian shape (Eq.6.1) due to unknown gain and attenuation in the measurement chain, electrical delay, or impedance mismatch (Fig.6.3). In order to extract the resonance properties, we need to expand the model to be able to numerically fit on the measured data:

$$S_{11}^{(\text{meas.})}(\omega) = Ae^{i\phi} \times e^{i\omega\tau_{\text{delay}}} \times \frac{\kappa_{\text{ex}}}{(\kappa_{\text{ex}} + \kappa_0)/2 + i(\omega - \omega_c)} + (x + iy). \quad (6.2)$$

In Eq.6.2,  $Ae^{i\phi}$  is a global constant amplitude and phase shift modeling the loss and gain of the measurement chain,  $e^{i\omega\tau_{\text{delay}}}$  is the electrical delay term modeling the non-negligible length of the measurement chain compared with the wavelength, and  $x + iy$  is modeling the Fano effect. The last term is specifically important to model the unwanted impedance mismatch between the sample and measurement lines (Probst et al., 2015; S. Fan, W. Suh, and

Joannopoulos, 2003; Bernier, 2019). Figure 6.3 shows the effect of each term on the shape of measured the resonance. Applying a fit by numerically minimizing a cost function reflecting the mean square distance of the measured complex dataset of  $S_{21}$  with the parametric curve described by Eq.6.2 will give us resonance parameters (Fig. 6.4).

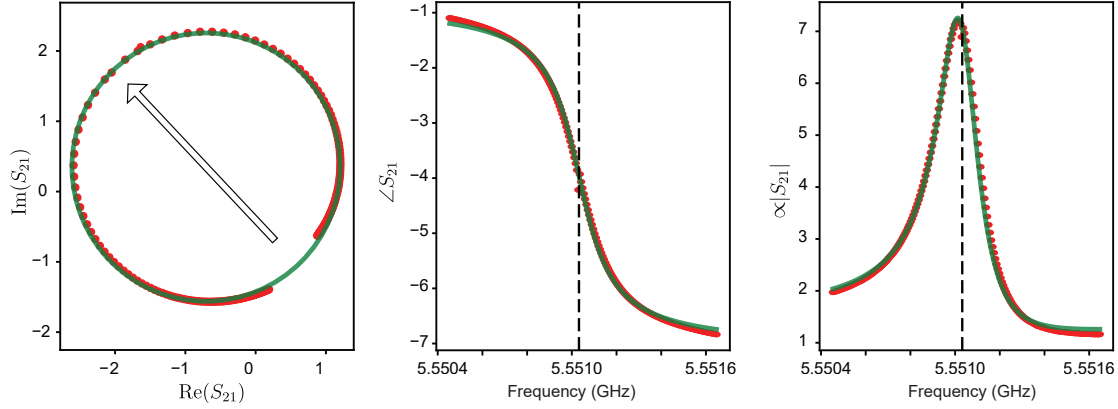


Figure 6.4: **Circle fitting to measured data.** Red dots show the measured dataset after numerical scaling and compensating for the electrical delay. The green curves show the fits to the data set. The fitting is done on the complex dataset and corresponding phase and absolute values are then calculated and sketched respectively.

## 6.2 Mechanical resonator characterization

In this section, we review the routine measurements to characterize mechanical frequencies and damping rates.

### 6.2.1 Optomechanical sidebands

Optomechanical sidebands are the most straightforward signals to be measured for characterizing mechanical frequency. As discussed in the theory chapter (Sec. 2.2), applying a microwave pump to the cavity scatters two optomechanical sidebands separated by the mechanical frequency around the pump. Measuring the PSD of sidebands and calculating the pick frequency minus the frequency of the pump gives us the mechanical resonance frequency. In practice, optomechanical sidebands can be much weaker than the pump itself and at the same level as the measurement chain noise floor. This makes direct detection of the sideband challenging when the cavity is pumped on-resonance ( $\omega_p = \omega_c$ ), and often requires high pump powers, small measurement resolution bandwidth, and many averages to increase the signal-to-noise ratio. Therefore, we often use optomechanical parametric instability (Carmon et al., 2005; T. Kippenberg et al., 2005) to derive the mechanics and easily detect its sidebands. When pumping the cavity blue-detuned ( $\omega_p > \omega_c$ ), optomechanical interaction results in an anti-damping effect on the mechanical resonator, which reduces its



total dissipation rate,  $\Gamma_{\text{tot}} = \Gamma_m - |\Gamma_{\text{opt}}|$ , where  $\Gamma_{\text{opt}}$  is proportional to the pump's intracavity photon number. Moderate blue-detuned pump powers result in negative total damping rates and therefore drive the mechanical state into the high amplitude self-oscillations limited by the system's nonlinearities (Fig. 6.5). In this case, we observe high-power optomechanical sidebands as well as their frequency multiplexed comb-like sidebands which are the results of the higher-order nonlinearities in the system. We often slowly sweep up the frequency of a microwave pump from resonance until the PI feature appears. Then we measure PSD and roughly extract the mechanical frequency, which may vary a few hertz from the exact value due to self-oscillation nonlinearity. Afterward, we pump the system on resonance and focus on the frequency span expected to see the sideband, average a few hundred times with RBW of 1 Hz, and precisely calculate the peak frequency.

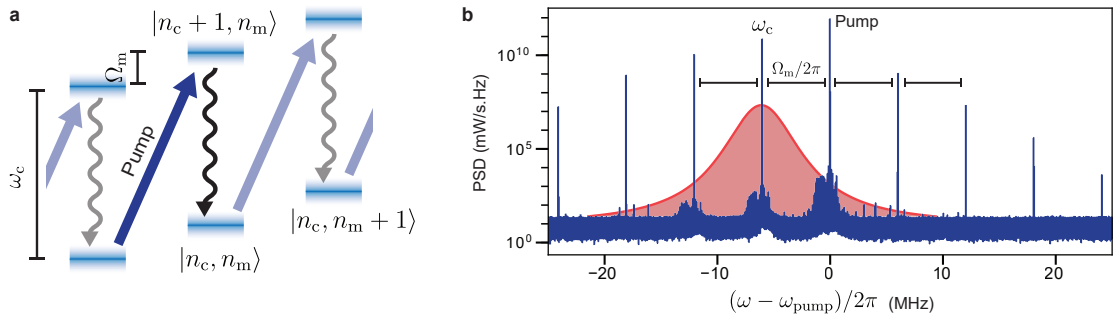
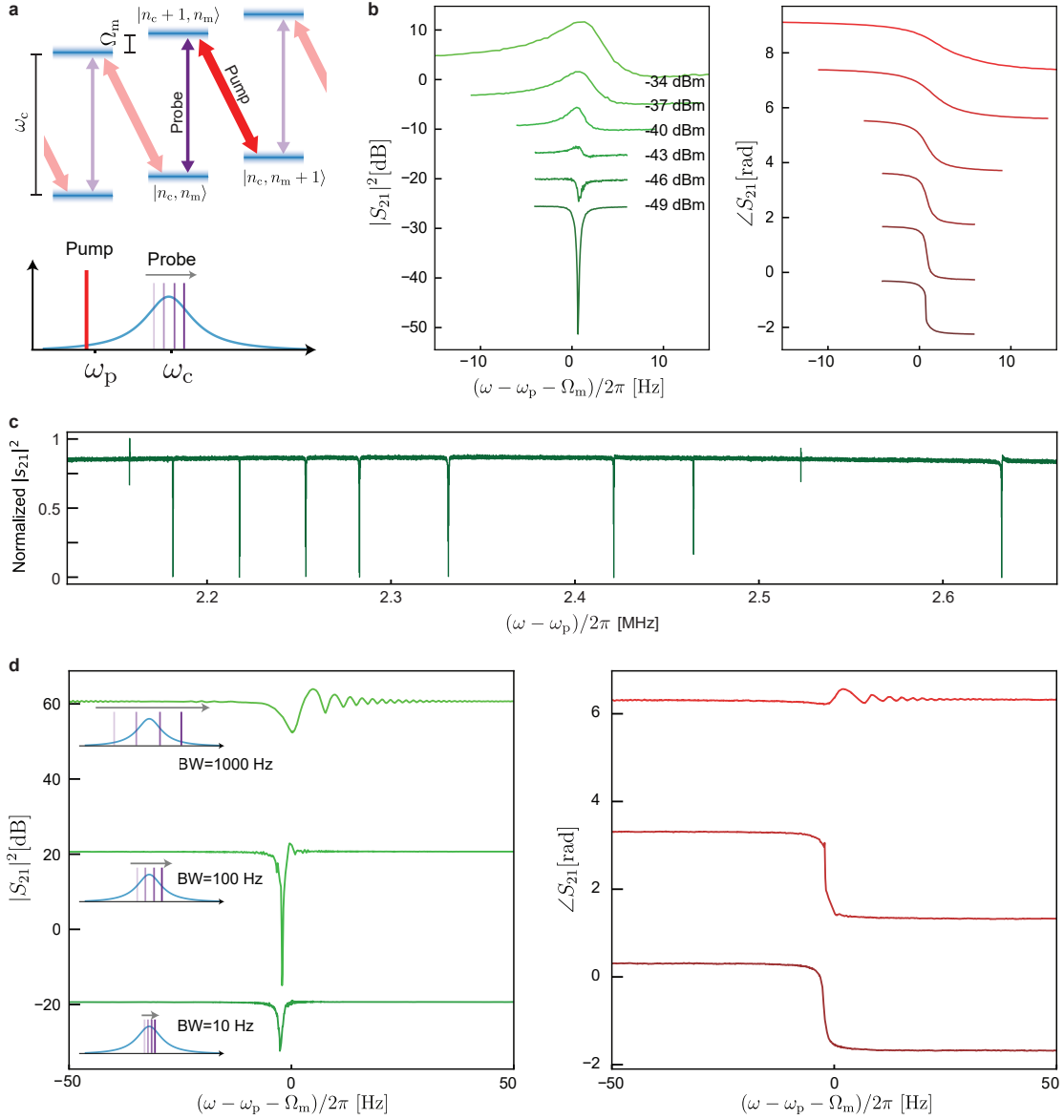


Figure 6.5: **Optomechanical parametric instability.** **a**, Driving an optomechanical system at the frequency of  $\omega_c + \Omega_m$  excites the transition corresponding to photon-phonon generation and amplifies the mechanical occupation. **b**, An example of a measured PI feature when pumping a device blue-detuned. Due to higher-order nonlinearities at high mechanical amplitude oscillations, a train of high-power optomechanical sidebands appears with a spacing of mechanical frequency. This can be used to characterize the mechanical frequency.

### 6.2.2 Optomechanically induced transparency

Optomechanical induced transparency (Weis et al., 2010) is a two-tone spectroscopy measurement when applying a microwave pump on the lower motional sideband (red-detuned by mechanical frequency from the cavity resonance) and sweeping a second weaker probe tone across the resonance (Fig. 6.6a). The strong pump damps the mechanical motion, resulting in a wider effective mechanical linewidth,  $\Gamma_{\text{tot}} = \Gamma_m + |\Gamma_{\text{opt}}|$ , where  $\Gamma_{\text{opt}} = 4g^2/\kappa$ . The microwave pump modifies the cavity response due to the electromechanical coupling, resulting in a transparency window of width  $\Gamma_{\text{tot}}$  that appears on resonance, which will be observed by the probe's transmission or reflection coefficient. Experimentally, This measurement is done using a microwave source as the red-detuned pump and vector network analyzer to sweep the resonance and measure the scattering parameter (Fig. 6.6b). Measuring OMIT window center frequency and linewidth ( $\Gamma_{\text{tot}}$ ) not only reflects the mechanical frequency but more importantly gives us information on the optomechanical coupling rate,  $g$ , as well as the pump's cooperativity,  $\mathcal{C} = 4g^2/\kappa\Gamma_m$ . The latter is specifically important since the total loss



**Figure 6.6: Optomechanical induced transparency.** **a**, Sweeping the microwave cavity with a weak tone while pumping the cavity on the red side and results in an interference feature in the probe's response corresponding to the effective mechanical linewidth. **b**, Example of OMIT response while for different nominal red-detuned pump powers. **c**, OMIT response of an electromechanical system with 10 mechanical resonators. Each feature corresponds to one mechanical mode. **d**, The sweep speed of the microwave probe as well as the bandwidth of the VNA have to be smaller than the effective optomechanical damping rate. Otherwise, the transient mechanical response affects the measured OMIT feature resulting in oscillations in the response. The figure shows an OMIT response measured with three different VNA bandwidths with a 2001 number of points in a 100 Hz span.

from a microwave source to the device is often uncalibrated, therefore knowing  $\Gamma_{\text{tot}}$  enables us to relate the nominal microwave source power with the cooperativity as an important optomechanical parameter.

OMIT is particularly useful compared with sideband PSD measurement in finding mechanical frequencies in a multi-mode optomechanical system. The reason is when pumping such a system on the blue side, nonlinearities often result in high amplitude self-oscillation of only one mechanical mode and the other mechanical frequencies close to the self-oscillated mode do not exhibit PI features. In those cases for example in the optomechanical lattices experiment (chapter 8) we use low cooperativity OMIT features to precisely measure mechanical frequencies (Fig. 6.6c).

The main limitation of OMIT is its slow process of measurement and its limited practical frequency resolution, specifically for characterization of high- $Q_m$  samples when  $\Gamma_m < 1$  Hz. As mentioned in Sec. 5.2.6, the VNA frequency accuracy and step size depend on the instrument model and are typically in the order of a few milli-Hertz which makes sub-Hertz response measurement challenging. More importantly, The transient response time of an optomechanical system is proportional to the lowest dynamic rate in the system which is  $\Gamma_{\text{tot}} = \Gamma_m + \Gamma_{\text{opt}}$ . This means that for the measurement of an OMIT feature with  $\Gamma_{\text{tot}}$  linewidth, for every measurement point in frequency, the VNA needs to wait for more than  $1/\Gamma_{\text{tot}}$  to reach the stationary response and report a true value of the scattering parameter. This forces us to employ small measurement bandwidth which significantly increases the measurement time. Figure 6.6d shows examples of ripple-like artifacts when VNA sweeping speed is comparable to or more than the dynamic rate of the system. decreasing the bandwidth and frequency sweeping speed removes the unwanted oscillations in the response. To overcome this limitation, we use a mechanical ringdown experiment to measure low optomechanical damping rates. Finally, we note that at low cooperativities, far from the strong coupling regime, we can use the standard circle fit (Eq. 6.2) to extract the linewidth and center frequency of an OMIT feature from the measured scattering parameters.

### 6.2.3 Ringdown and ring-up

In order to measure the bare mechanical damping rate,  $\Gamma_m$ , we use a time-domain experiment where we first excite the mechanical oscillator by applying a strong blue-detuned pump, having the system in an optomechanical parametric instability, and then observe the energy decay by measuring the optomechanical sideband scattered from a weak red-detuned probe ( $\mathcal{C}_{\text{probe}} \ll 1$ ) in time, as shown in Figs. 6.7a and b. For higher red-detuned probe powers with cooperativity of  $\mathcal{C}_{\text{probe}}$ , the effective mechanical damping rate is  $\Gamma_{\text{tot}} = \Gamma_m(1 + \mathcal{C}_{\text{probe}})$ . Sweeping the power of the red probe enables us to directly measure  $\Gamma_m$  (Figs. 6.7c and d). In addition, we can accurately calibrate the cooperativity for every pump power, by measuring the effective damping rate in other experiments.

The ringdown experiment requires time control of two blue- and red-detuned pulses which

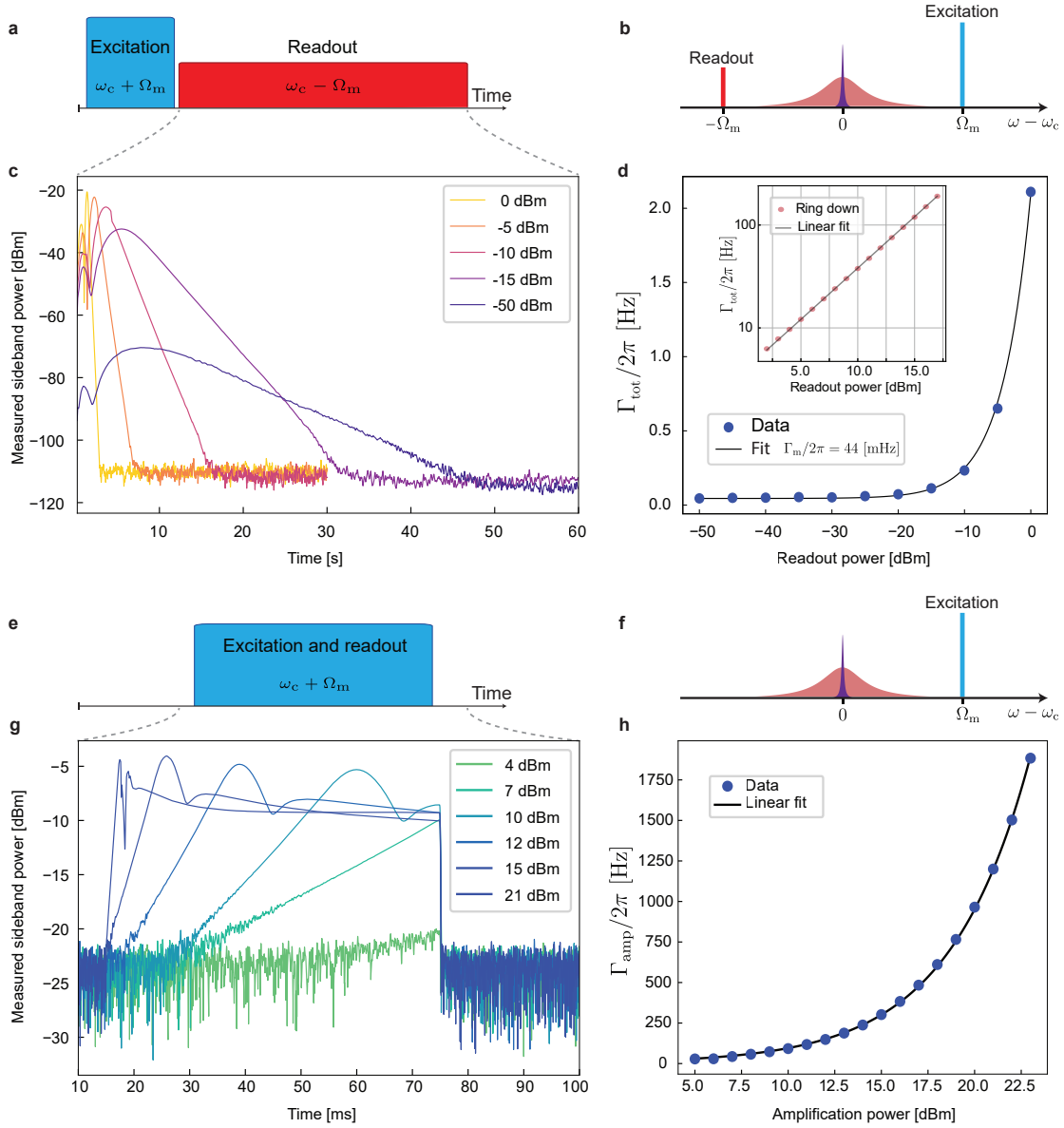


Figure 6.7: **Ringdown and amplification rate measurements.** **a, b** Pulse and frequency scheme of the ringdown measurement. A strong blue detuned pulse is exciting the mechanical oscillator through optomechanical parametric instability. A red-detuned readout pulse generates an optomechanical sideband on resonance. **c**, Example of ringdown traces measured for different readout powers. The initial nonlinear behavior in the ringdown trace may be due to the energy exchange between different mechanical modes of the drumhead at high amplitude vibrations. For the exponential fitting, we only use the low-power linear part of the ring down. **d**, Effective mechanical damping rates versus the readout nominal power at the source. The fit shows a bare mechanical damping rate of  $\Gamma_m/2\pi = 44$  mHz. The inset shows the same for higher pump powers. **e, f** Pulse and frequency scheme of optomechanical amplification rate characterization. **g, h** Optomechanical amplification traces and extracted anti-damping rates measured for different nominal readout powers.

can be controlled by solid-state switches and an AWG (Sec.5.2.7). The time trace is recorded by ESA in the zero-span mode. It is important to check that RBW in ESA is higher than the damping rate,  $\Gamma_{\text{tot}}$ , to be able to resolve the dynamic. It is worth mentioning that mechanical oscillators may experience frequency shifts when driving in the PI, but the frequency of the ESA should be centered at the undriven mechanical frequency to track the low-occupation dynamics of the mechanical oscillator.

We often observe a chirp-like oscillation in the optomechanical sideband power at the beginning of the ringdown when the mechanical oscillator has a very large amplitude after the PI. The origin of such effects is still unknown to us, but we are interested in low-occupation dynamics at many orders of magnitude lower occupations. Because of this effect, we only apply the numerical fitting on the linear part of the ringdown trace. To fit the measured sideband power,  $P_{\text{SB}}(t)$ , we use the simple model of  $P_{\text{SB}}(t) = P_0 e^{-\Gamma_{\text{tot}} t} + n_{\text{floor}}$ , where  $n_{\text{floor}}$  is the constant noise floor or the measurement.

Another crucial characterization is the optomechanical anti-damping rate which needs to be calibrated for the optomechanical amplification experiment (Sec. 7.4.1). When pumping the cavity on the blue sideband, for large enough powers, the total damping rate of the mechanical oscillator will be negative, and an exponential increase in the mechanical occupation and the sideband power is expected. Measuring the transient dynamics of the oscillator when applying the blue-detuned pump from low occupations to the PI self-oscillations enables us to extract the amplification rate and calibrate the nominal blue-detuned microwave source power.

Finally, we note that for multi-mode optomechanical systems, as mentioned earlier (Sec.6.2.2), the PI excitation will not necessarily excite all the mechanical modes and if so, often the ringdown of several modes simultaneously is not desired in the experiment. In these cases, we use another excitation scheme by applying a resonance excitation pump together with a strong red-detuned pump separated by the desired mechanical frequency. The beat note of these two pumps exactly matches only one mechanical mode and drives it into high occupation coherent oscillation. We use this method in the topological optomechanical lattices experiment to read out the collective mode shapes. More discussions will provide in Sec.8.5.

### 6.3 $g_0$ characterization

The single photon optomechanical coupling rate,  $g_0$ , is an important figure of merit for optomechanical systems, which describes the cavity resonance shift induced by the zero-point fluctuation of motion. The method we used for measuring  $g_0$  is based on the PSD measurement of the motional sidebands when pumping the system on-resonance ( $\omega_p = \omega_c$ ) with a relatively weak pump (Bernier, 2019). In this case, two sidebands will appear ( $\omega = \omega_c \pm \Omega_m$ , Fig. 6.10a), where the power in the upper motional sideband when measuring a

short-ended device is given by

$$P_{\text{SB}} = 4g_0^2 n_m \frac{(\kappa_{\text{ex}}/\kappa)^2}{\Omega_m^2 + (\kappa/2)^2} \frac{\omega_c}{\omega_c + \Omega_m} P_{\text{MW}}. \quad (6.3)$$

Here,  $P_{\text{SB}}$  is the scattered sideband power emitted from the device at  $\omega = \omega_c + \Omega_m$ ,  $P_{\text{MW}}$  is the microwave input pump power to the device at  $\omega = \omega_c$ , and  $n_m$  is the mechanical occupation. On resonance pumping does not induce dynamical backaction (i.e. damping or anti-damping) on the mechanics; however, the back action noise can still heat up the mechanical oscillator (Bowen and Milburn, 2015). Here we use microwave powers that result in negligible back-action noise of the microwave pump on the mechanical oscillator,

$$n_{\text{ba}} \equiv \frac{4g_0^2}{\kappa\Gamma_m} \frac{(4\kappa_{\text{ex}}/\kappa^2)P_{\text{MW}}}{1 + (2\Omega_m/\kappa)^2} \ll n_m^{\text{th}}, \quad (6.4)$$

Where  $n_{\text{ba}}$  is the equivalent back-action noise in units of quanta (Bowen and Milburn, 2015). This condition can be simply checked by measuring the effective optomechanical damping rate of the same probe power ( $P_{\text{MW}}$ ) but applied on the red sideband. This can be explained by the fact that the cooperativity of a red-detuned pump with the same microwave power exactly scales the same way that  $n_{\text{ba}}$  scales (Eq.6.4),  $\mathcal{C}_{\text{red}} = \frac{4g_0^2}{\kappa\Gamma_m} \frac{(4\kappa_{\text{ex}}/\kappa^2)P_{\text{MW}}}{1 + (2\Omega_m/\kappa)^2}$ , which can be measured using optomechanical damping rate,  $\mathcal{C}_{\text{red}} = \frac{\Gamma_{\text{opt}}}{\Gamma_m} = \frac{\Gamma_{\text{tot}}}{\Gamma_m} - 1$ .

While it is challenging to directly measure  $P_{\text{MW}}$  and  $P_{\text{SB}}$  at the device, we can measure the sideband at the detector (spectrum analyzer) and the pump power at the microwave source. The pump signal is attenuated with an unknown factor  $\eta_{\text{att}}$  from the source to the device, and the measured sideband is amplified with an unknown factor  $G$  from the device to the detector. Since we need to use the tone cancellation of the pump to avoid the saturation of the JTWPA and also the dynamic range of the ESA is limited, we send an additional weak calibration tone placed at the upper motional sideband frequency with a small detuning ( $\omega = \omega_c + \Omega_m + \delta$ ) that passes through the same input/output lines as the sideband signal, so we can accurately obtain the relative power of the calibration tone to the on-resonance pump. In this case we have

$$\begin{aligned} P_{\text{SB}}^{\text{meas}} &= GP_{\text{SB}} = G \frac{P_{\text{SB}}}{P_{\text{MW}}} \eta_{\text{att}} P_{\text{MW}}^{\text{src}} \\ P_{\text{cal}}^{\text{meas}} &= G\eta_{\text{att}} \frac{\Omega_m^2 + ((\kappa_{\text{ex}} - \kappa_0)/2)^2}{\Omega_m^2 + ((\kappa_{\text{ex}} + \kappa_0)/2)^2} P_{\text{cal}}^{\text{src}}, \end{aligned} \quad (6.5)$$

where  $P_{\text{SB}}^{\text{meas}}$  is the measured sideband at the detector,  $P_{\text{MW}}^{\text{src}}$  is the pump power at the microwave source,  $P_{\text{cal}}^{\text{meas}}$  is the measure calibration pump power at the detector, and  $P_{\text{cal}}^{\text{src}}$  is the calibration tone power at the microwave source. In the above expression, the fraction in the calibration tone comes from its interaction with the microwave cavity.

We can now eliminate the unknown parameter  $G\eta_{\text{att}}$  and reach to:

$$\frac{P_{\text{SB}}^{\text{meas}}}{P_{\text{MW}}^{\text{src}}} \frac{P_{\text{cal}}^{\text{src}}}{P_{\text{cal}}^{\text{meas}}} = 4g_0^2 n_m \frac{(\kappa_{\text{ex}}/\kappa)^2}{\Omega_m^2 + ((\kappa_{\text{ex}} - \kappa_0)/2)^2} \frac{\omega_c}{\omega_c + \Omega_m}. \quad (6.6)$$

If the mechanical oscillator is in a thermal equilibrium with a bath at temperature  $T$ , the mechanical occupation is approximately given by  $n_m \approx n_m^{\text{th}} = k_B T / \hbar \Omega_m$ , where  $k_B$  is the Boltzmann constant, so the measured sideband power is linearly proportional to the temperature. To ensure a proper thermalization we sweep the nominal temperature of the dilution fridge and measure  $P_{\text{SB}}$ .

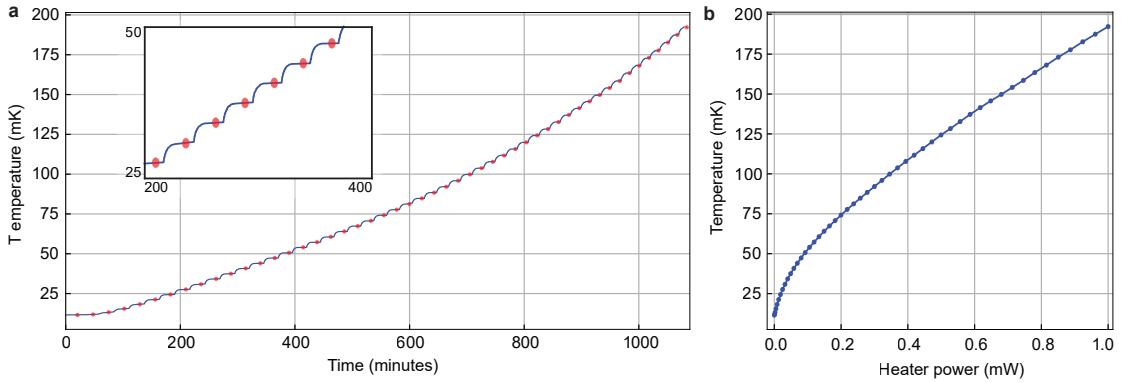


Figure 6.8: **Temperature sweep of the dilution fridge.** **a**, Temperature of the mixing chamber versus time. Measurements are performed when the temperature is stable (red data points). **b**, The stable temperature versus the heater dissipated power at the mixing chamber.

To characterize  $g_0$ , we sweep the mixing chamber temperature using a resistive heater mounted on this flange. To ensure the thermalization of the flange to the nominal temperature, we wait for  $\sim 10$  minutes after each increase in the heater's dissipated power. After the stabilization of the fridge's temperature (Fig. 6.8), the mechanical and microwave parameters, such as  $\kappa$  and  $\omega_c$  are measured by taking a VNA trace (Fig. 6.9), while  $\Gamma_m$  is measured by a ringdown experiment and  $\Omega_m$  is determined as the frequency difference between the optomechanical sideband and the applied microwave pump (Fig. 6.9). Both the mechanical and microwave frequencies slightly vary with temperature (a few parts per million compared to the respective frequencies). Nevertheless, we observe a strong temperature dependence in  $\Gamma_m$ , which indicates that the mechanical dissipation in our drumhead resonator is not dominated by the clamping loss, i.e. phonon tunneling through the substrate (see more discussion in Sec. 3.2.2). We note that the cooperativity of the on-resonance pump needs to be simultaneously checked by measuring ringdown when pumping on the red sideband with the same power to ensure  $\mathcal{C}_{\text{red}} \ll n_m^{\text{th}}$ . The gain and signal-to-noise improvement of JTWPA needs to also be monitored when sweeping the temperature to ensure constant measurement chain properties ( $G$  and  $\eta_{\text{att}}$ ) when reading out the sidebands. Small changes in the JTWPA gain will be compensated on the final measured  $P_{\text{SB}}$ . Finally, we can plot the calibrated sideband power as a function of temperature and use Eq. 6.6 to fit a linear function and extract  $g_0$  as the only free parameter.



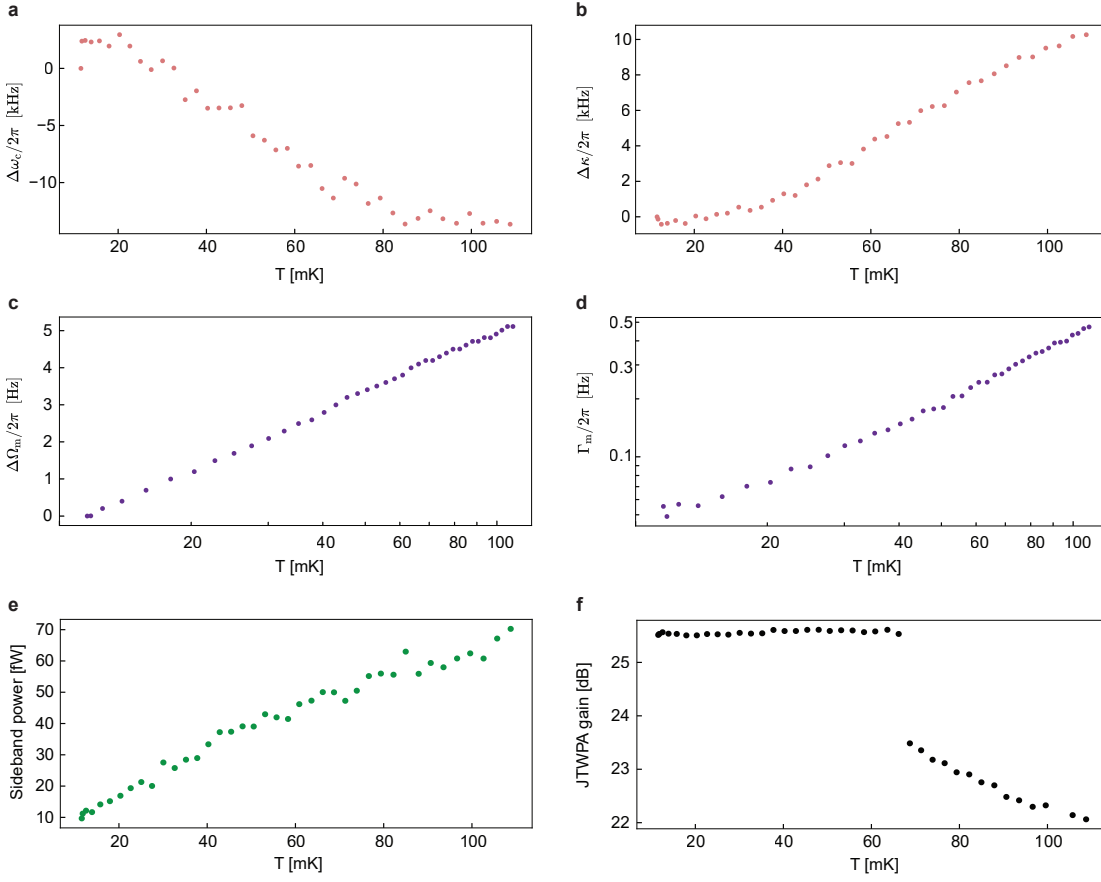


Figure 6.9: **Temperature dependence of system parameters.** **a**, Shift of the microwave cavity frequency and **b**, linewidth versus temperature. **c**, Shift of the mechanical resonance frequency and **d**, linewidth versus temperature. **e**, Measured mechanical sideband power. **f**, JTWPA gain versus temperature. To calibrate  $g_0$ , we only consider the temperature region with the stable gain and compensate for its variation on the measured sideband power.

For example, in the ultra-coherent electromechanics project (chapter 7) the single-photon optomechanical coupling rate is found to be  $g_0/2\pi = 13.4 \pm 0.5$  Hz as shown in Fig. 6.10. The experimentally measured value is in good agreement with the theoretically expected one ( $g_0^{(\text{theory})}/2\pi = 14$  Hz, discussed in Sec. 3.3). As shown in the figure, the linear scaling of the estimated phonon occupation with the temperature at lower temperatures indicates a good sample thermalization and verifies the assumption of  $n_m \approx k_B T / \hbar \Omega_m$ .

It is worth mentioning that in principle higher  $g_0$  values can be achieved by lowering the gap size without sacrificing other optomechanical parameters. However, we did not systematically investigate the samples with lower gaps in this work. More information about the limitations and feasibility of reducing the gap size is provided in the fabrication chapter (Sec. 4.2.12).

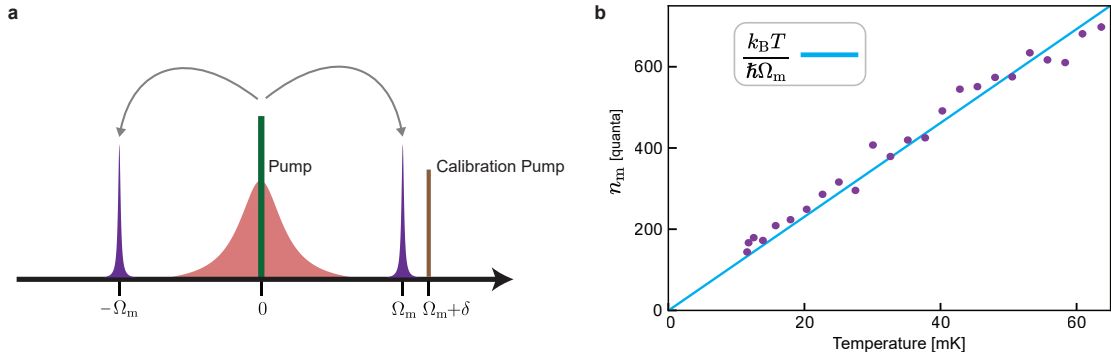
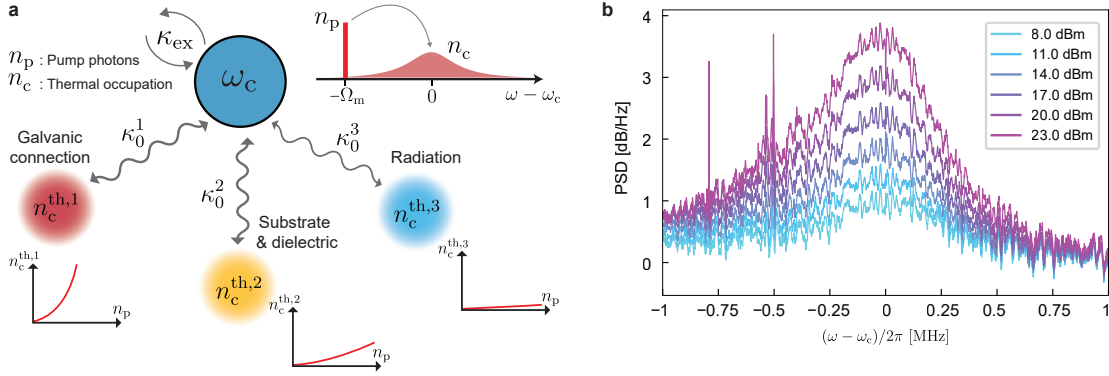


Figure 6.10:  $g_0$  measurement. **a**, Frequency scheme for  $g_0$  measurement experiment. An on-resonance pump (green line) is used to generate two motional sidebands (in purple). A calibration tone (brown) is placed close to the motional sideband to rule out the unknown parameters for the input loss/output gain. **b**, Mechanical occupations (calculated after extracting  $g_0/2\pi = 13.4$  Hz from the measured PSD of the motional sidebands and fitting) versus nominal temperature of the fridge.

## 6.4 Microwave cavity heating

Increasing the intracavity photon number  $n_p$  induced by a pump field enhances the optomechanical coupling rate between a mechanical oscillator and an optical/microwave cavity, as expressed by  $g = \sqrt{n_p} g_0$ . To realize mechanical ground-state cooling in contemporary optomechanical platforms, a large  $n_p$  is required – in the order of  $10^4$  to  $10^7$  photons, depending on the system parameters. Such a large cavity photon number can lead to thermally heating the optical/microwave cavity, resulting in an increase in the effective temperature of the optical/microwave intrinsic bath. In the context of sideband cooling of a mechanical oscillator, the cavity heating effect limits the lowest phonon occupation for most cases (J. D. Teufel, Donner, D. Li, et al., 2011). In this section, we address how to characterize the total thermal photons in the microwave cavity and significantly reduce the cavity heating effect in the circuit optomechanical platform. A microwave cavity can be coupled to several thermal baths through different loss mechanisms such as radiation losses, dielectric losses, substrate losses, galvanic connections, etc. In a phenomenological description, we define a loss rate of  $\kappa_0^i$  for intrinsic bath  $i$  with a thermal bath occupation of  $n_c^{\text{th},i}$  (Fig. 6.11). This results in the effective intrinsic loss rate of  $\kappa_0 = \sum \kappa_0^i$  and the effective thermal bath occupation of  $n_c^{\text{th}} = (\sum \kappa_0^i n_c^{\text{th},i}) / \kappa_0$ . In principle, the thermal bath occupation can be a function of the intracavity photon number, i.e.,  $n_c^{\text{th},i}(n_p)$ , since the absorbed energy from the cavity can be inelastically scattered to the bath and increase its effective temperature. However, the dependency of the bath occupation on  $n_p$  can be different due to the different heat capacity and microscopic loss mechanism of each intrinsic bath. For example, the radiative loss thermal bath is expected to be significantly less sensitive to  $n_p$  compared to the dielectric and substrate losses.

In our platform, the main suspect for the cavity heating was the galvanic connection between the top and bottom aluminum plates of an LC circuit. The native aluminum oxide, which



**Figure 6.11: Microwave cavity heating.** **a**, The mode diagram shows the microwave resonance is coupled to many loss channels corresponding to different physical processes. In the presence of a coherent drive, the effective thermal bath occupation of each loss channel scales differently by the pump's intracavity photon numbers  $n_p$ . The total thermal occupation of the mode is the average of the thermal bath occupations weighted with their loss rates. **b**, An example of the normalized PSD of incoherent noise emission from the microwave cavity when pumping it on the red sideband for different pump powers. .

grows on the bottom layer by a few nanometers, remains when the top layer is deposited without any treatment, leading to a thin resistive layer for the LC circuit. The resistive layer dissipates the intracavity energy and heats up the intrinsic bath, inducing a finite cavity thermal photon. To address the heating effect, we perform argon milling to remove the aluminum oxide layer, followed by the deposition of the top aluminum layer. Importantly, note that these two processes are performed successively under the ultra-high vacuum (see more detail in Sec. 4.2.10).

To characterize the cavity heating effect, i.e., the cavity thermal photon number induced by one or more microwave drive fields, we measure the cavity thermal emission by using the JTWPA as a nearly quantum-limited amplifier. As shown in Eq. 2.21, the noise power spectral density of the cavity emission is given by  $\tilde{S}_c(\omega)$ . Note that the expression is general regardless of the number of microwave drive fields. By integrating the power spectral density and normalizing it by the external coupling rate with  $2\pi$ , we obtain the cavity thermal photons as

$$n_c = \frac{\int d\omega \tilde{S}_c(\omega)}{2\pi\kappa_{\text{ex}}}. \quad (6.7)$$

In Fig. 6.12, the cavity thermal photon number induced by a strong pump is extracted for two samples with and without the native oxide resistive layer, respectively. By employing the Ar milling to remove the oxide layer, we could reduce the cavity heating effect by a factor of  $\sim 30$ , resulting in a vast improvement in the ground-state cooling of the mechanical oscillator, since the final phonon occupation is usually limited by the cavity heating. We finally note that in cavity heating measurement the background (off-resonance) noise level remains

unchanged even at very high pumping powers. This indicates that the temperature increase in microwave attenuators in the input coaxial lines is negligible and the microwave lines' effective temperature, i.e. the input noise, can be safely considered constant and close to the vacuum noise.

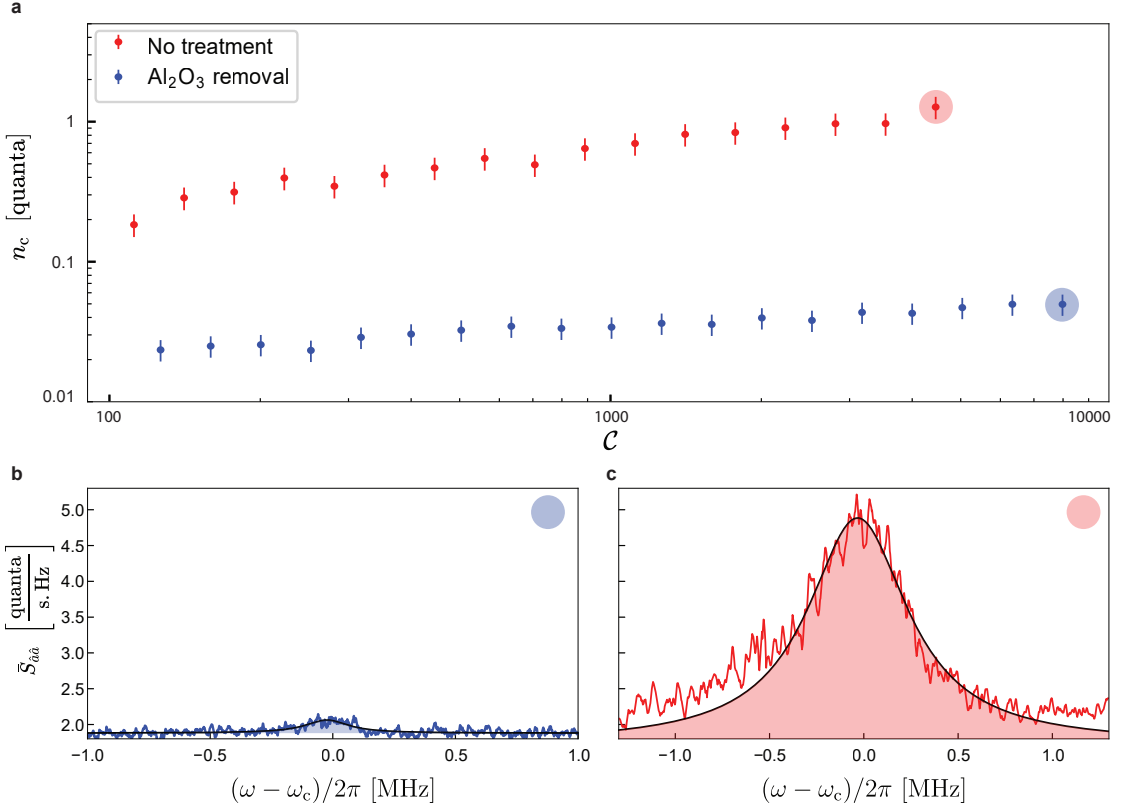


Figure 6.12: **Cavity heating treatment.** **a**, Cavity thermal photon number as a function of cooling pump cooperativity for two samples with (blue) and without (red) the Argon milling treatment to remove the aluminum oxide layer. The shaded circles correspond to the noise power spectra respectively, shown in **b** and **c**. **b**, **c**, Noise power spectrum of the cavity thermal emission with a red pump applied to the samples with (b) and without (c) the Argon milling treatment, respectively. Both resonances are over-coupled, resulting in the fact that the peaks correspond to  $4n_c$ .

## 6.5 HEMT added noise

HEMT-added noise is a reference level often used to calibrate measured PSD of signals. If JTWP is not used in an experiment, the noise floor of the measured PSD is considered as the effective HEMT added noise as it will be the dominant added noise of the measurement chain because of the HEMT's high gain. Although in experiments such as ground-state cooling or squeezing, we use an out-of-loop and calibration-free technique to extract the mechanical occupations which do not rely on the added noise calibration (see Sec. 7.3.1), it is still useful to

characterize HEMT for rough estimations of the output spectra and signal powers.

The HEMT added noise is calibrated by a temperature sweep. The measured power spectral density at the output of the measurement chain  $S$  can be written as

$$S = \alpha G^H (n^T + n_{\text{add}}^H), \quad (6.8)$$

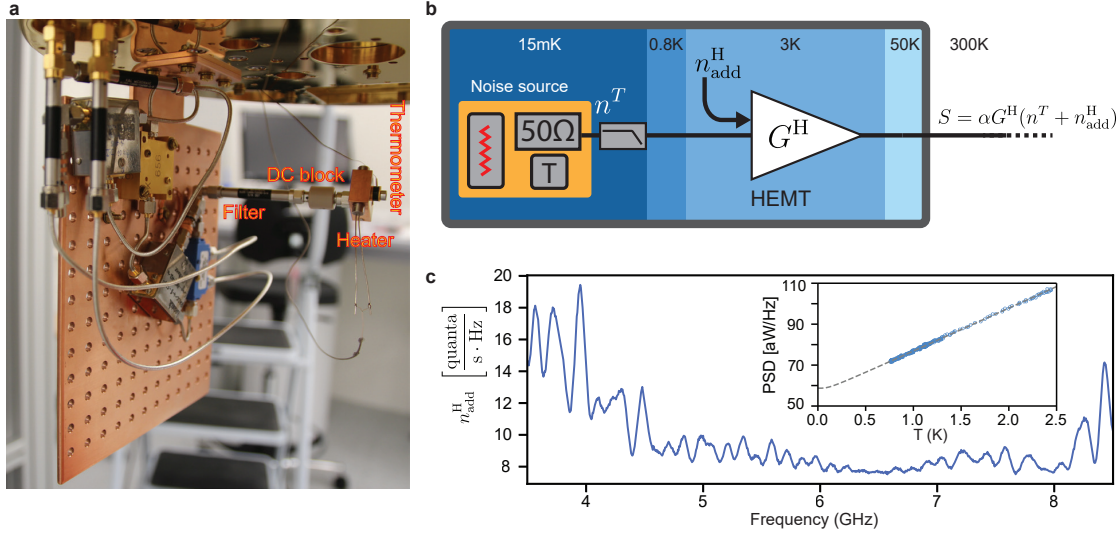


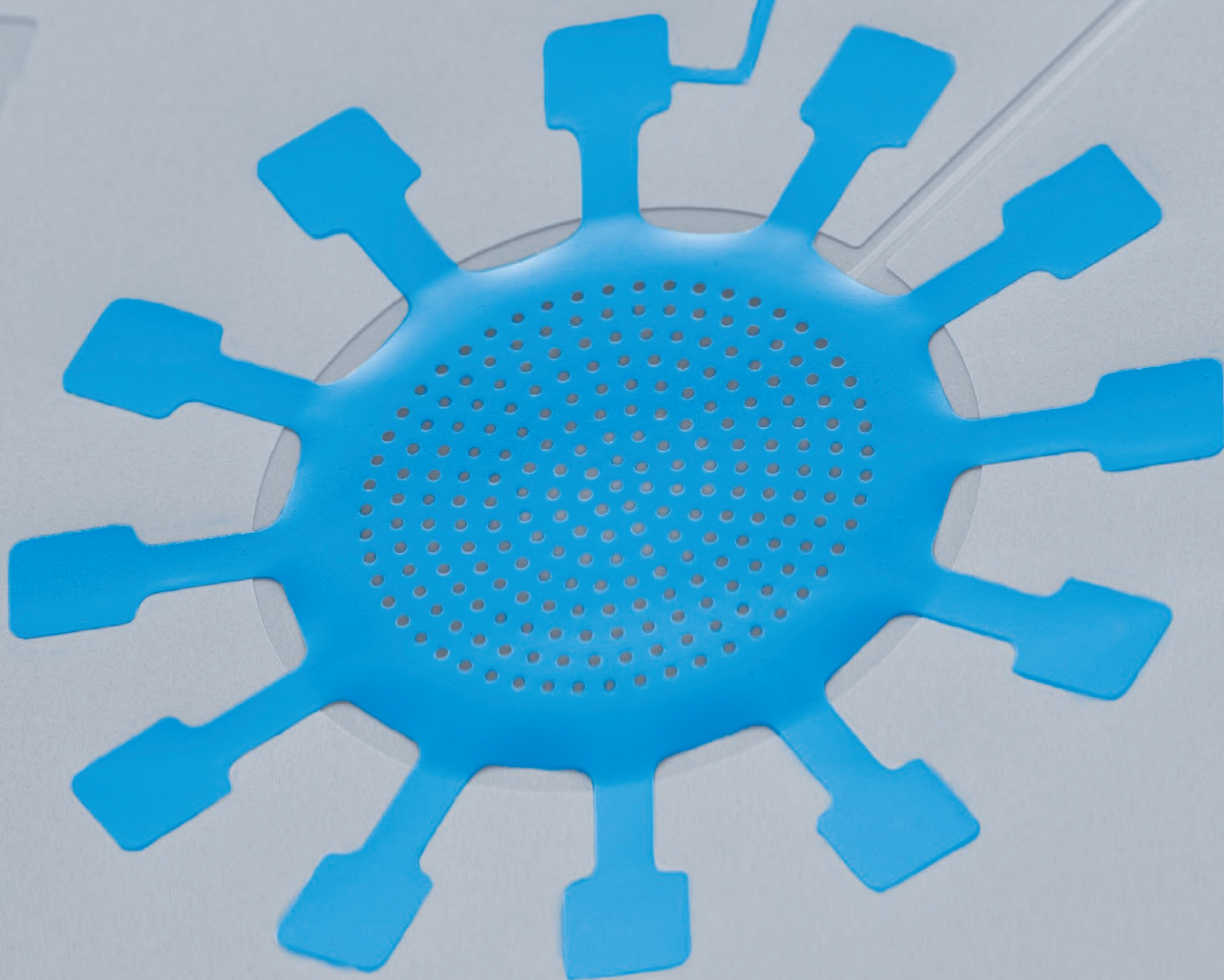
**Figure 6.13: HEMT noise characterization.** **a, b,** Experimental setup and schematic signal flow for HEMT noise characterization. A noise source thermalized at temperature  $T$  feeds the HEMT with Johnson noise. The measured power spectral density is proportional to the noise from the source plus the HEMT's added noise. The noise source is a thermally isolated copper block containing a cryogenic resistive heater, a thermometer, and a  $50\text{--}\Omega$  load. The noise source is connected to a ceramic DC block and 12 GHz low-pass filter. **b,** The added noise of the HEMT versus frequency. Inset: An example of the measured average power spectral density of HEMT background noise at 6 GHz vs.  $T$ . The dashed line is the fit based on Eq. (6.8).

Where  $\alpha$  is the total loss factor of the measurement chain after the HEMT and  $n^T = 1/(e^{\hbar\omega/k_B T} - 1)$  is the spectral density of the Johnson noise generated by a cryogenic 50-Ohm load thermalized at temperature  $T$ . By sweeping  $T$ , we can extract  $n_{\text{add}}^H$  at different frequencies and use this value as a reference level for further calibrations.  $n_{\text{add}}^H$  is the effective added noise referred to the device, which includes the internal noise of the HEMT plus any thermal contribution at the input of the HEMT divided by the attenuation factor between the DUT and HEMT. The noise source consists of a cryogenic resistive heater, a thermometer, and a 50-Ohm load, all plugged into a small copper block, to ensure proper thermalization (Fig. 6.13). The copper block is suspended from the 10 mK stage by a 12 GHz low-pass filter (K&L 6L250-1200/T26000-0/0, insertion loss  $< 1$  dB at room temperature) that thermally isolates it from the stage while allowing microwave propagation. The thermal isolation allows the operation of the noise source up to 3 K while keeping the mixing chamber temperature below 100 mK. After the low-pass filter, we use the exact same cables to the HEMT (NbTi superconducting coaxial

lines) as in the other experiments. We note that the measured ESA noise floor drops by 15 dB when turning HEMT off, verifying that the noise floor in the output chain is dominated by the HEMT with negligible contribution from the room temperature amplifier.

Figure 6.13 shows an example of the measured HEMT added noise within its 4-8 GHz nominal bandwidth. At each frequency, the measured average PSD is fitted versus the temperature of the Johnson noise source and the added noise is extracted as shown in the figure inset. The ripples in the added noise versus frequency indicate a slight impedance mismatch between the noise sources and the HEMT.





**A superconducting vacuum-gap capacitor  
hosting longlife mecahnical quantum states**



## 7 A squeezed mechanical oscillator with milli-second quantum decoherence

Quantum control and measurement of mechanical oscillators has applications ranging from quantum metrology (Aasi et al., 2013; Mason et al., 2019; Whittle et al., 2021) and quantum computing (Pechal, Arrangoiz-Arriola, and Safavi-Naeini, 2018; Wallucks et al., 2020), to fundamental test of quantum mechanics itself (Fiaschi et al., 2021; Marinković et al., 2018) or searches for dark matter (Carney et al., 2021; Manley et al., 2021). This has been achieved by coupling mechanical oscillators to auxiliary degrees of freedom in the form of optical or microwave cavities (Aspelmeyer, T. J. Kippenberg, and Marquardt, 2014), or superconducting qubits (A. Clerk et al., 2020; Chu and Gröblacher, 2020), allowing numerous advances such as mechanical squeezing (Wollman et al., 2015; Pirkkalainen, Damskäg, et al., 2015; Lecocq, Clark, et al., 2015), quantum state transfer (A. Reed et al., 2017; Chu, Kharel, et al., 2018), quantum transduction (Mirhosseini, Sipahigil, et al., 2020b; Andrews et al., 2014), or teleportation (Fiaschi et al., 2021). An enduring challenge in constructing such hybrid systems is the dichotomy of engineered coupling to an auxiliary degree of freedom, while being mechanically well isolated from the environment, that is, low quantum decoherence – which consists of both thermal decoherence and dephasing. Although Hertz-level thermal decoherence has been achieved in optomechanical crystals at mK temperature (MacCabe et al., 2020), such systems suffer from large dephasing. Currently employed opto- and electro-mechanical (M. Rossi et al., 2018; Palomaki, Harlow, et al., 2013; Magrini et al., 2021) as well as qubit-coupled mechanical systems (Chu, Kharel, et al., 2018; Wollack et al., 2022; Satzinger et al., 2018) have significantly higher thermal decoherence.

In this chapter, we show how to overcome this challenge by introducing a superconducting circuit optomechanical platform which exhibits an ultra-low quantum decoherence while having a large optomechanical coupling to prepare with high fidelity the quantum ground and squeezed states of motion. We directly measure a thermal decoherence rate of only 20.5 Hz (corresponding to  $T_1 = 7.7$  ms) as well as a pure dephasing rate of 0.09 Hz, on par with and better than, respectively, the motional degree of freedom of trapped ion systems in high vacuum (Gaebler et al., 2016; Leibfried et al., 2003), and 100-fold improvement of quantum-state lifetime compared to the prior optomechanical systems (M. Rossi et al., 2018;

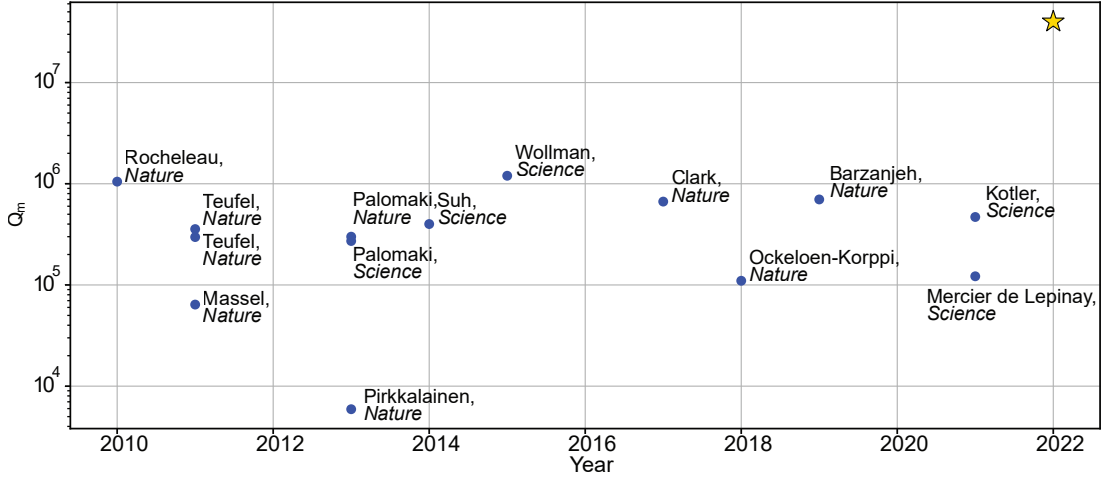


Figure 7.1: **Mechanical quality factors in circuit optomechanics platforms since 2010.** A summary of published works on circuit optomechanics in Nature and Science since 2010. No improvements have been realized in the mechanical quality factors -and consequently phonon lifetime - in the recent decade. The star shows our platform enhancing the mechanical coherence by almost two orders of magnitude.

MacCabe et al., 2020; A. Reed et al., 2017). This enables us to reach to 0.07 quanta motional ground state occupation (93% fidelity) and realize mechanical squeezing of -2.7 dB below zero-point-fluctuation. To directly measure the quantum-state lifetime, we observe the free evolution of the phase-sensitive squeezed state for the first time, preserving its non-classical nature over milli-second timescales. Such ultra-low quantum decoherence not only increases the fidelity of quantum control and measurement of macroscopic mechanical systems, but may equally benefit interfacing with qubits (Gely and G. A. Steele, 2021a; Pechal, Arrangoiz-Arriola, and Safavi-Naeini, 2018), and places the system in a parameter regime suitable for tests of quantum gravity (Gely and G. A. Steele, 2021b; Y. Liu, Mummery, et al., 2021).

## 7.1 Quantum decoherence

The decoherence of a mechanical oscillator induced by the interaction with its environment conceals macroscopic quantum phenomena and limits the realization of mechanical oscillator-based quantum protocols (Marinković et al., 2018; Fiaschi et al., 2021; Wallucks et al., 2020; Kotler et al., 2021; M. Rossi et al., 2018; R. D. Delaney et al., 2019; Mirhosseini, Sipahigil, et al., 2020b). The quantum decoherence can be characterized with two independent rates: the thermal decoherence rate ( $\Gamma_{\text{th}} = (n_{\text{m}}^{\text{th}} + 1)\Gamma_{\text{m}}$ , where  $n_{\text{m}}^{\text{th}}$  is the thermal bath occupation and  $\Gamma_{\text{m}}$  is the bare damping rate), which describes the rate at which phonons are exchanged with the thermal bath, and the pure dephasing rate ( $\Gamma_{\varphi}$ ), caused by the mechanical frequency fluctuations, i.e. phonon-number conserving interactions with the environment (Gardiner, Zoller, and Zoller, 2004).

Table 7.1: The comparison of the longest measured mechanical quantum state lifetime in various platforms.

Platform	Thermal decoherence	Dephasing	Quantum state lifetime
Optomechanical crystals (MacCabe, Science 2020)	0.1 Hz	4 kHz	130 $\mu$ s
Dissipation-diluted Si <sub>3</sub> N <sub>4</sub> membranes (Rossi, Nature 2018)	220 Hz	Not measured	<0.7 ms
Levitated particles (Reported in several works)	$\sim$ 1 kHz	Not measured	<100 $\mu$ s
Circuit optomechanics (Reed, Nature Physics 2017)	1 kHz	Not measured	140 $\mu$ s
HBAR-Qubit (von Lüpke, Nature Physics 2022)	2 kHz	$\sim$ 1 kHz	$\sim$ 100 $\mu$ s
<b>This work</b>	20 Hz	0.09 Hz	<b>7.7 ms</b>

Even though the lowest thermal decoherence has been achieved in optomechanical crystals at mK temperature ( $\Gamma_{\text{th}}/2\pi \simeq 0.1$  Hz), such systems experience a large dephasing ( $\Gamma_{\varphi}/2\pi \simeq 4$  kHz), limiting their quantum coherence (MacCabe et al., 2020). Soft clamped dissipation diluted Si<sub>3</sub>N<sub>4</sub> membranes (M. Rossi et al., 2018) and levitated particles (Magrini et al., 2021; Tebbenjohanns et al., 2021) are other examples of optomechanical platforms interfacing with light, which achieved thermal decoherence rates of  $\mathcal{O}(1$  kHz), but support limited optomechanical protocols as they operate in the non-resolved-sideband or cavity-free regimes, or suffer from optical heating (Delić et al., 2020; Piotrowski et al., 2023).

One of the most widely and successfully used optomechanical platforms is microwave superconducting circuit optomechanics (J. D. Teufel, Donner, D. Li, et al., 2011), which exhibits large optomechanical coupling in the resolved-sideband regime, and can be integrated with superconducting qubits (A. Reed et al., 2017; A. Clerk et al., 2020). These circuits have been used for numerous advances including mechanical squeezing (Wollman et al., 2015; Pirkkalainen, Damskägg, et al., 2015; Lecocq, Clark, et al., 2015), entanglement (Kotler et al., 2021; C. Ockeloen-Korppi et al., 2018; Palomaki, J. Teufel, et al., 2013), non-classical state storage (A. Reed et al., 2017; Palomaki, Harlow, et al., 2013), and non-reciprocal circuits (Bernier et al., 2017). However, it has been a challenge to achieve a high quantum coherence in this platform - state-of-the-art decoherence rates are  $\mathcal{O}(1$  kHz) (Palomaki, Harlow, et al., 2013). Enhancing the quantum coherence in such systems improves the fidelity of quantum optomechanical protocols (Wallucks et al., 2020; Pechal, Arrangoiz-Arriola, and Safavi-Naeini, 2018; Gely and

G. A. Steele, 2021a) and may equally benefit future tests of quantum mechanics (Fiaschi et al., 2021; Marinković et al., 2018; Gely and G. A. Steele, 2021b; Y. Liu, Mummery, et al., 2021). While some attempts (Seis et al., 2022; Y. Liu, Q. Liu, et al., 2021) have been made to integrate ultra-coherent soft clamped  $\text{Si}_3\text{N}_4$  membranes (Tsaturyan et al., 2017) with superconducting circuits, these hybrid systems have been compounded by insufficient optomechanical coupling, resulting in unwanted cavity heating.

Here we demonstrate a circuit optomechanical platform which simultaneously realizes an ultra-low quantum decoherence, i.e. both thermal decoherence and dephasing, while exhibiting an efficient optomechanical coupling for quantum control and measurement. By observing free evolution of the prepared ground state as well as squeezed state we report a thermal decoherence rate of 20.5 Hz (corresponding to 130 quanta/sec motional heating rate) and a pure dephasing rate of 0.09 Hz, showing the quantum decoherence is dominated by the thermal decoherence, comparable with motional decoherences achieved in trapped ion systems in high vacuum (Leibfried et al., 2003), where the thermal decoherence is typically  $\mathcal{O}(10 \text{ Hz})$ , while the dephasing rate reaches  $\mathcal{O}(100 \text{ Hz})$  (Gaebler et al., 2016).

## 7.2 Ultra-coherent circuit optomechanical platform

We develop a nanofabrication process based on a silicon-etched trench (see chapter 4), which enables us to significantly enhance the mechanical quality factor,  $Q_m$ . Figure 7.2a shows a vacuum gap capacitor with a top plate suspended on a circular trench with a gap size of 180 nm. The capacitor is shunted by a spiral inductor (Figs. 7.2b and c), forming a microwave LC resonator with a frequency of  $\omega_c/2\pi = 5.55 \text{ GHz}$  and a total decay rate of  $\kappa/2\pi = 250 \text{ kHz}$  which is inductively coupled to a waveguide (Fig. 7.2f). This superconducting circuit is operated in a dilution fridge with  $\sim 11 \text{ mK}$  base temperature. The flat geometry of the top plate (Figs. 7.2d and e) ensures minimal clamp and radiative mechanical losses, as well as stress relaxation in the aluminum thin-film. A mechanical ring-down measurement (Fig. 7.2h) clearly exhibits the extremely low dissipation rate of  $\Gamma_m/2\pi = 45 \text{ mHz}$  for the fundamental drumhead mode with a frequency of  $\Omega_m/2\pi = 1.8 \text{ MHz}$ , corresponding to  $Q_m = 40 \times 10^6$ . This can be explained by the loss dilution factor (Schmid et al., 2011) estimated to be  $D_Q \simeq 100$  from finite element method (FEM) simulation for such a flat drumhead as shown in Fig. 7.2h top inset (see Sec.3.2.1 for detailed information). The single-photon optomechanical coupling rate is measured to be  $g_0/2\pi = 13.4 \pm 0.5 \text{ Hz}$  (see Sec.6.3). We note that lower gap sizes lead to higher  $g_0$  values, but not implemented in this work. Furthermore, the frequency fluctuation is observed below 0.1 Hz - inferred as an upper bound for dephasing- by measuring the power spectral density (PSD) of a thermomechanical sideband averaged over more than an hour and subtracting a measurement resolution bandwidth of 1 Hz (Fig. 7.2h bottom inset, see Sec.5.2.5 for more information).

The summary of system parameters characterized or measured in this experiment is shown in table 7.2.

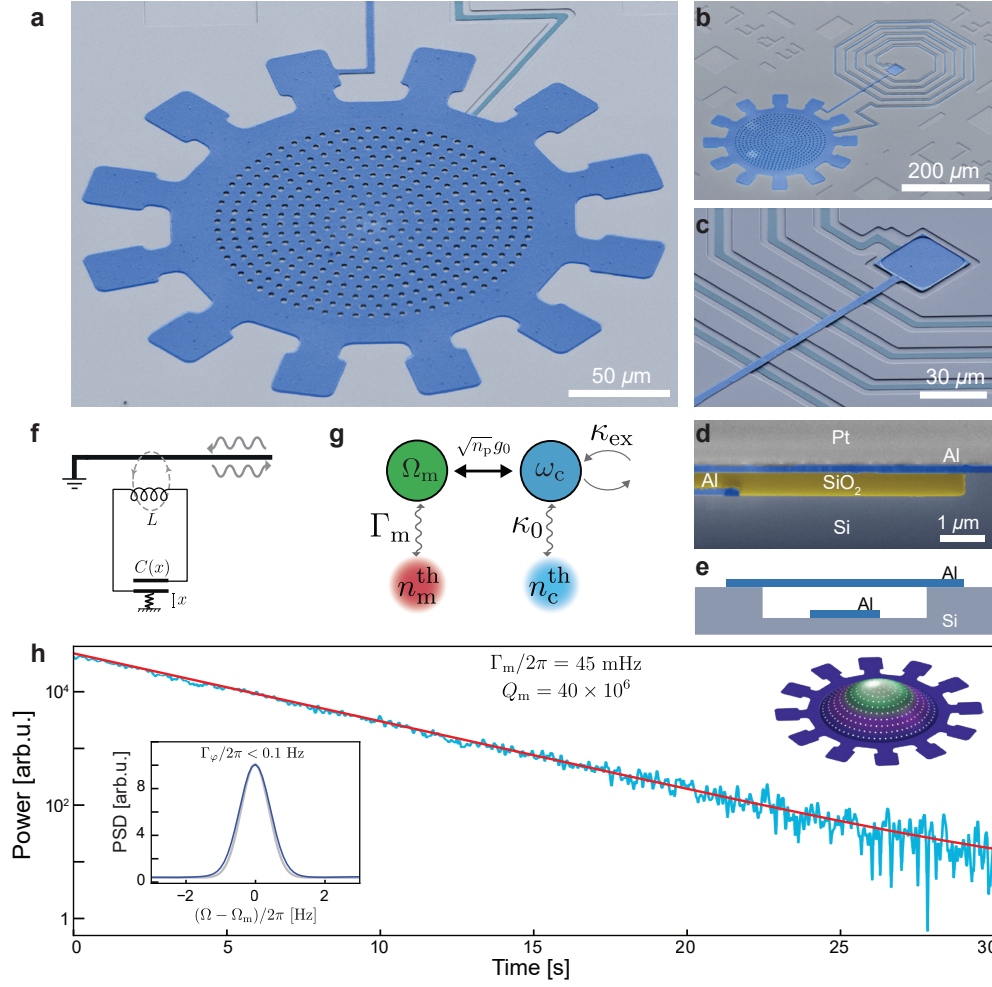


Figure 7.2: **Ultra-coherent circuit optomechanics.** **a**, False colored SEM image of a mechanically compliant parallel plate capacitor. **b**, A microwave superconducting LC resonator consisting of the capacitor shunted by a spiral inductor. **c**, Magnified image showing a silicon-etched trench, inductor air-bridges, and the galvanic connection. **d**, Focused ion beam cross-section of a test capacitor –with a higher gap size than the main device– before removing a  $\text{SiO}_2$  sacrificial layer, where Pt is used as the FIB protective layer. **e**, Schematic cross-section of the suspended capacitor over the trench. **f**, Mode diagram of an optomechanical system.  $\kappa_0$  and  $\kappa_{\text{ex}}$  are internal loss and external coupling rates of the cavity respectively. **(g)**, Equivalent circuit diagram of the system. **h**, Ring-down trace, showing the energy decay of the mechanical oscillator with a rate of  $\Gamma_m/2\pi = 45$  mHz. The red line is the exponential fit. The top inset shows the FEM simulation of the fundamental mechanical mode of the drum. The blue line in the bottom inset shows the averaged PSD of the mechanics with 1 Hz measurement resolution bandwidth (gray line), indicating the frequency instability of less than 0.1 Hz.

### 7.2.1 Fabrication technique

A comprehensive discussion on the nanofabrication process we developed for circuit optomechanics can be found in chapter 4. In summary, We define a trench in the substrate containing

Table 7.2: System parameters

Parameter	Symbol	Value
Microwave cavity frequency	$\omega_c$	$2\pi \cdot 5.5 \text{ GHz}$
Microwave cavity linewidth ( $\kappa_{\text{ex}} + \kappa_0$ )	$\kappa$	$2\pi \cdot 250 \text{ kHz}$
Microwave cavity external coupling rate	$\kappa_{\text{ex}}$	$\sim 2\pi \cdot 200 \text{ kHz}$
Microwave cavity internal loss rate	$\kappa_0$	$\sim 2\pi \cdot 50 \text{ kHz}$
Mechanical frequency	$\Omega_m$	$2\pi \cdot 1.8 \text{ MHz}$
Mechanical bare damping rate	$\Gamma_m$	$2\pi \cdot 45 \text{ mHz}$
Mechanical quality factor	$Q_m$	$40 \times 10^6$
Single-photon optomechanical coupling rate	$g_0$	$2\pi \cdot 13.4 \text{ Hz}$
Thermal decoherence rate of mechanical oscillator	$\Gamma_{\text{th}}$	$2\pi \cdot 20.5 \text{ Hz}$
Pure dephasing rate of mechanical oscillator	$\Gamma_\varphi$	$2\pi \cdot 0.09 \text{ Hz}$

the bottom plate of the capacitor. The trench is then covered by a thick  $\text{SiO}_2$  sacrificial layer, which inherits the same topography as the layer underneath. To remove this topography and obtain a flat surface, we use chemical mechanical polishing to planarize the  $\text{SiO}_2$  surface. We then etch back the sacrificial layer down to the substrate layer and deposit the top Al plate of the capacitor. We release the structure by Hydrofluoric acid vapor etching of  $\text{SiO}_2$ . At cryogenic temperatures, the high tensile stress ensures the flatness of the top plate. This will guarantee that the gap size is precisely defined by the depth of the trench and the thickness of the bottom plate and reduces the clamp losses in the mechanical oscillator.

We note that we did not systematically investigate the minimum gap size that can be achieved using this process, but observed a lower successful release rate (in the HF vapor etching step) for gap sizes below 100 nm most probably due to the van der Waals force between two plates or water formation during the release step. Increasing the thickness of the top layer, reducing the radius, and decreasing the HF release etch rate (lowering the pressure and increasing the etching time) may help to increase the release success rate. In addition, the compressive room temperature stress of the top layer of the aluminum thin film helps the buckling of the drumhead and facilitates the release. This thermally induced deposition stress can be controlled by evaporation rate and temperature. Optimizing the release process using the methods mentioned above combined with enhancing the CMP planarization may allow us to achieve much lower effective gap sizes down to the ultimate limit of the roughness of the top and bottom aluminum films (in the order of a few nanometers). It is worth mentioning that the fabrication-induced disorder in identically designed LC circuits using optical direct laser lithography is measured below 1% for mechanical frequencies and 0.5% for microwave frequencies (Youssefi et al., 2022).



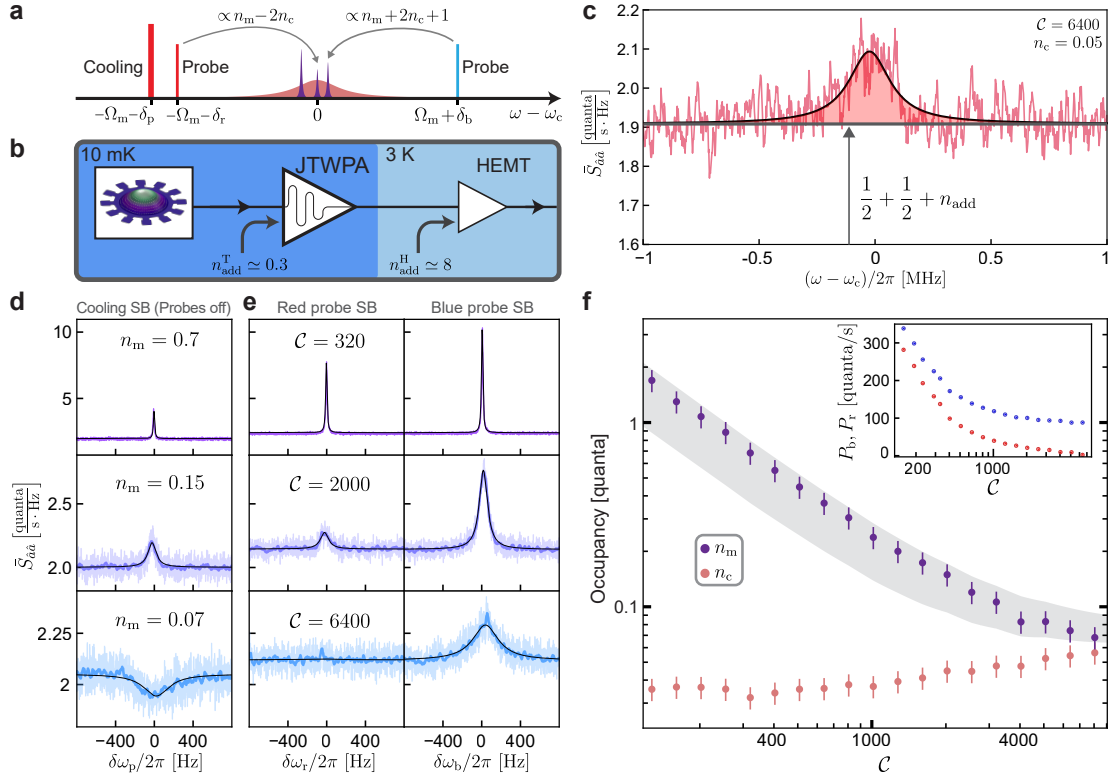


**Figure 7.3: High-fidelity optomechanical ground-state cooling.** **a**, Frequency landscape for optomechanical cooling and sideband asymmetry measurement. The Stokes and anti-Stokes sideband powers are proportional to  $n_m + 2n_c + 1$  and  $n_m - 2n_c$  respectively. **b**, Simplified experimental setup for optomechanical cooling. **c**, An example of the PSD of the microwave cavity thermal emission measured at  $\mathcal{C} = 6400$  on top of the noise floor of  $1 + n_{\text{add}}$ . **d**, PSD of optomechanical sidebands scattered from the cooling pump when two probes are off. The black line shows the Lorentzian fit. **e** PSD of optomechanical sidebands scattered from red and blue probes. **f**, Measured occupation of the mechanical (violet dots) and microwave (red dots) modes as a function of the cooperativity when the two probes are off. The shaded area shows theoretically expected phonon occupation in the range of system parameters errors. The inset shows the measured powers of the Stokes (blue) and anti-Stokes (red) sidebands generated,  $P_b$  and  $P_r$ , by the probes, exhibiting high quantum efficiency of the readout chain.

### 7.3 High-fidelity optomechanical ground state cooling

The extremely high mechanical quality factor, together with the sufficient optomechanical coupling, enables us to perform an effective optomechanical sideband cooling (J. D. Teufel, Donner, D. Li, et al., 2011) to prepare the mechanical oscillators in its quantum ground state with high fidelity. As schematically shown in Fig. 7.2g, in the resolved-sideband regime, where the quantum back-action does not influence the final phonon occupation (Aspelmeyer, T. J. Kippenberg, and Marquardt, 2014), i.e.,  $(\kappa/4\Omega_m)^2 = 0.001 \ll 1$  in our case, the phonon occupation of the mechanical oscillator in the presence of a cooling pump red-detuned by



$\Omega_m$  from the cavity frequency is given by

$$n_m = \frac{n_m^{\text{th}}}{1 + \mathcal{C}} + \frac{\mathcal{C}}{1 + \mathcal{C}} n_c, \quad (7.1)$$

where  $\mathcal{C} = 4n_p g_0^2 / (\kappa \Gamma_m)$  is the optomechanical cooperativity with the intracavity pump photon number  $n_p$  and  $n_c = \kappa_0 n_c^{\text{th}} / \kappa$  is the cavity thermal photon number induced by a finite loss rate of  $\kappa_0$  to an intrinsic photon bath with  $n_c^{\text{th}}$ . The strong cooling pump may heat up the intrinsic photon bath occupation and consequently  $n_c$ , which normally imposes the minimal achievable phonon occupancy in the large cooperativity limit, i.e.,  $\mathcal{C} \gg 1$  (J. D. Teufel, Donner, D. Li, et al., 2011). We discovered that the thin native oxide layer in the galvanic connection between top and bottom layers (shown in Fig. 7.2c) is the dominant source of such cavity heating, which has been ubiquitous in all microwave optomechanical experiments. We significantly reduced the heating by removing the oxide to achieve  $n_c \sim 0.05$  quanta at high cooperativities (see Sec. 6.4 for details of the characterization procedure and Sec. 4.2.10 for fabrication details).

To reliably characterize the phonon occupation close to the ground state, we use optomechanical sideband asymmetry (Weinstein et al., 2014) as an out-of-loop calibration. As shown in Fig. 7.3a, we apply a strong cooling pump, and two weak, blue- and red-detuned, probes with balanced powers to generate Stokes and anti-Stokes optomechanical sidebands, respectively, on the cavity resonance with a few kHz spacing to individually measure them. Figure 7.3b shows the simplified experimental setup, where a Josephson traveling wave parametric amplifier (JTWPA) (Macklin et al., 2015) is used to amplify microwave signals with an added noise of  $\frac{1}{2} + n_{\text{add}}^{\text{T}} \simeq \frac{1}{2} + 0.3$  quanta and sufficient gain of  $G_{\text{T}} = 25$  dB to suppress the classical noise dominated by the HEMT amplifier ( $n_{\text{add}}^{\text{H}} \simeq 8$ ), enabling a nearly quantum-limited measurement of thermomechanical noise spectrum with an effective added noise of  $\frac{1}{2} + n_{\text{add}} \simeq \frac{1}{2} + 0.9$  (see the calibrated noise floor in Fig. 7.3c). Figures 7.3c and e show the measured thermomechanical noise spectrum of the cavity thermal emission, as well as the Stokes and anti-Stokes sidebands, which used for obtaining their powers, expressed by  $P_c$ ,  $P_b$ , and  $P_r$ , respectively, by fitting a Lorentzian to the PSD of the sidebands. While the sideband asymmetry may allow us to perform the calibration-free measurement of  $n_m$ , a finite cavity heating distorts the asymmetry, i.e.,  $P_b \not\propto n_m + 1$  and  $P_r \not\propto n_m$ , preventing us from extracting  $n_m$  without the prior knowledge of  $n_c$  (Weinstein et al., 2014). Nevertheless, we are able to simultaneously extract both  $n_c$  and  $n_m$  without any calibration of the measurement chain by analytically obtaining them from the two sideband powers normalized by the cavity thermal emission power, expressed by

$$\frac{P_b}{P_c} = \frac{\Gamma_b}{\kappa} \frac{n_m + 1 + 2n_c}{n_c} \quad \text{and} \quad \frac{P_r}{P_c} = \frac{\Gamma_r}{\kappa} \frac{n_m - 2n_c}{n_c}, \quad (7.2)$$

where  $\Gamma_r(\Gamma_b)$  is the optomechanical (anti-)damping rate of the red (blue) probe. Importantly, this analysis enables us to calibrate the scaling factor between the actual occupations and the measured powers, which can be used to directly extract  $n_c$  and  $n_m$  independently from the cavity thermal emission and the sideband induced by the cooling pump, even when the two probes are off – therefore avoiding the quantum back-action induced by the blue probe and

an additional cavity heating (see Sec. 2.2 for theoretical details).

Using the PSDs of the thermomechanical sideband from the cooling pump (Fig. 7.3d) and the cavity thermal emission when two probes are off, we thus extract  $n_c$  and  $n_m$  as a function of the cooling pump cooperativity, as shown in Fig. 7.3f. The result shows a high-fidelity ground state cooling down to  $n_m^{(\min)} = 6.8(\pm 0.9) \times 10^{-2}$  quanta (93% ground state occupation which is  $-8.7$  dB of the zero-point energy), mainly limited by the cavity heating.

### 7.3.1 Detailed discussion on the sideband asymmetry calibration

To characterize the phonon occupation cooled by a red-detuned pump in a continuous-wave measurement, we use the sideband asymmetry measurement (Weinstein et al., 2014) as an out-of-loop calibration, where two balanced probes red- and blue-detuned by the mechanical frequency are applied, and the thermomechanical sideband signals are measured (Fig. 7.4a). This scheme requires quantum measurement of the noise power spectrum density of the output signals from the cavity. Pre-amplifying the weak signals in a quantum-limited manner at the cryogenic temperature allows us to realize such a quantum measurement. Therefore, we amplify the output signals using a JTWPA operated in a nearly quantum-limited phase-insensitive manner and measure them classically at room temperature (see Sec. 7.6.1 for the detailed experimental setup). The total microwave measurement chain, including propagation losses, the gain and added noise for each amplifier, and the detection noise, can be characterized by only two parameters, an effective added noise ( $n_{\text{add}}$ ) and a scaling factor ( $G$ ). Using these two parameters, the measured noise power spectrum density is described as

$$\tilde{S}'(\omega) = G \left[ \tilde{S}(\omega) + \frac{1}{2} + n_{\text{add}} \right], \quad (7.3)$$

where  $\tilde{S}(\omega)$  is the noise power spectrum density from the device, which is described in Eqs. (2.21)–(2.27). Note that the  $1/2$  quanta added noise is inevitable even with an ideal phase-insensitive amplification process, and is distinguished from  $n_{\text{add}}$  that may be induced by any kinds of imperfections, such as propagation losses and amplification noises. Namely, the ideal measurement of the noise power spectral density is realized by  $n_{\text{add}} = 0$  in our definition. In the sideband asymmetry measurement with a cooling pump, there are three thermomechanical sideband peaks and one thermal cavity emission peak in the full noise power spectrum density. By integrating each Lorentzian noise peak after subtraction of the corresponding noise floor, we can obtain the photon flux for the respective peak, which is

analytically given by

$$P_p = G\eta_\kappa \left[ 2\pi I_{\text{opt}}^p (n_m - 2n_c) \right], \quad (7.4)$$

$$P_r = G\eta_\kappa \left[ 2\pi I_{\text{opt}}^r (n_m - 2n_c) \right], \quad (7.5)$$

$$P_b = G\eta_\kappa \left[ 2\pi I_{\text{opt}}^b (n_m + 1 + 2n_c) \right], \quad (7.6)$$

$$P_c = G\eta_\kappa [2\pi\kappa n_c], \quad (7.7)$$

where  $P_p$ ,  $P_r$ , and  $P_b$  are the noise photon fluxes of the sidebands induced by the cooling pump and the red- and blue-detuned probes respectively, and  $P_c$  is the noise photon flux from the cavity. Here, the collection efficiency of the cavity is defined as  $\eta_\kappa = \kappa_{\text{ex}}/\kappa$ . For convenience, we normalize the photon fluxes by the corresponding rates and define the scaled phonon and photon numbers as

$$N_p = P_p / (2\pi I_{\text{opt}}^p) = G\eta_\kappa (n_m - 2n_c), \quad (7.8)$$

$$N_r = P_r / (2\pi I_{\text{opt}}^r) = G\eta_\kappa (n_m - 2n_c), \quad (7.9)$$

$$N_b = P_b / (2\pi I_{\text{opt}}^b) = G\eta_\kappa (n_m + 1 + 2n_c), \quad (7.10)$$

$$N_c = P_c / (2\pi\kappa) = G\eta_\kappa n_c. \quad (7.11)$$

Note that  $I_{\text{opt}}^p$ ,  $I_{\text{opt}}^r$ ,  $I_{\text{opt}}^b$ , and  $\kappa$  can be determined from independent experiments, allowing us to experimentally obtain all the scaled occupation,  $N_p$ ,  $N_r$ ,  $N_b$ , and  $N_c$ . Furthermore, we can obtain the noise floor of the power spectrum density, which is described as

$$N_{\text{floor}} = G(1 + n_{\text{add}}). \quad (7.12)$$

Here, our task is to extract the four unknown parameters,  $n_m$ ,  $n_c$ ,  $G$ , and  $n_{\text{add}}$  from Eqs. (7.8)–(7.12) including the experimentally accessible parameters,  $N_p$ ,  $N_r$ ,  $N_b$ ,  $N_c$ , and  $N_{\text{floor}}$ . Given the fact that  $N_p$  and  $N_r$  are equivalent, we have four independent equations and four unknown parameters, enabling us to analytically obtain the solutions for the four unknown parameters. This shows that the sideband asymmetry measurement is useful even when there is a squashing (or a fake asymmetry) in the thermomechanical sideband signals induced by the cavity heating, i.e., when  $n_c > 0$ .

For our experiment, there is a Fano effect in the cavity reflection spectrum, preventing us from reliably determining the collection efficiency  $\eta_\kappa$ . Nevertheless, we find that it is still possible to extract the three unknown parameters  $n_m$ ,  $n_c$ , and the effective scaling factor  $G\eta_\kappa$  from the three equations, Eqs. (7.10), (7.11) and (7.9). This is because the collection efficiency effectively modifies only the scaling factor in the measurement chain for all the signals emitted from the cavity [see Eqs. (7.8)–(7.11)]. By using Eqs. (7.9), (7.10), and (7.11), we have the analytical

solutions described as

$$n_m = \frac{R_I(N_r + N_b) + 2(R_N + R_I)N_p}{(R_N - R_I)(N_r + N_b) - 4(R_N + R_I)N_p} \quad (7.13)$$

$$n_c = \frac{R_N n_m - R_I(n_m + 1)}{2(R_N + R_I)} \quad (7.14)$$

$$G\eta_\kappa = \frac{(N_r + N_b)/2}{n_m + 1/2}, \quad (7.15)$$

where we define  $R_N = N_b/N_r$  and  $R_I = I_{\text{opt}}^b/I_{\text{opt}}^r$ . Note that we use  $N_p$  instead of  $N_r$  in our analysis since  $N_p$  can be obtained with a higher signal-to-noise ratio for a high cooling pump power.

It is known that there is a quantum-backaction induced by the blue-detuned probe that may dominantly heat the mechanical oscillator in the sideband asymmetry measurement even when the red- and blue- detuned probes are perfectly balanced (see Eq. (2.17)). Also, the two probes may induce an additional heating effect on the cavity, which limits the lowest phonon occupancy achievable by sideband cooling.

Here we propose to characterize the phonon occupation cooled by a cooling pump without using the two probes used for the sideband asymmetry measurement. In this case, the measured noise power spectral density contains the thermomechanical sideband induced by the cooling pump and the cavity thermal emission. Thus, the photon fluxes of the sideband and the cavity emission,  $P_p$  and  $P_c$ , can be obtained independently by integrating each peak. Then, we obtain the scaled phonon and photon numbers by normalizing the photon fluxes by the corresponding emission rates, which are analytically described as

$$N_p = P_p / (2\pi I_{\text{opt}}^p) = G\eta_\kappa (n_m - 2n_c) \quad (7.16)$$

$$N_c = P_c / (2\pi\kappa) = G\eta_\kappa n_c. \quad (7.17)$$

The key idea is that we use the effective scaling factor,  $G\eta_\kappa$ , which has already been calibrated in a reliable way based on the sideband asymmetry measurement. Importantly, note that we can experimentally confirm that the effective scaling factor does not depend on how strong total power is applied to the device in our measurement. With  $G\eta_\kappa$ , we can first obtain the thermal cavity photon number as

$$n_c = \frac{N_c}{G\eta_\kappa}. \quad (7.18)$$

Using  $n_c$ , we then obtain the phonon occupation as

$$n_m = \frac{N_p}{G\eta_\kappa} + 2n_c. \quad (7.19)$$

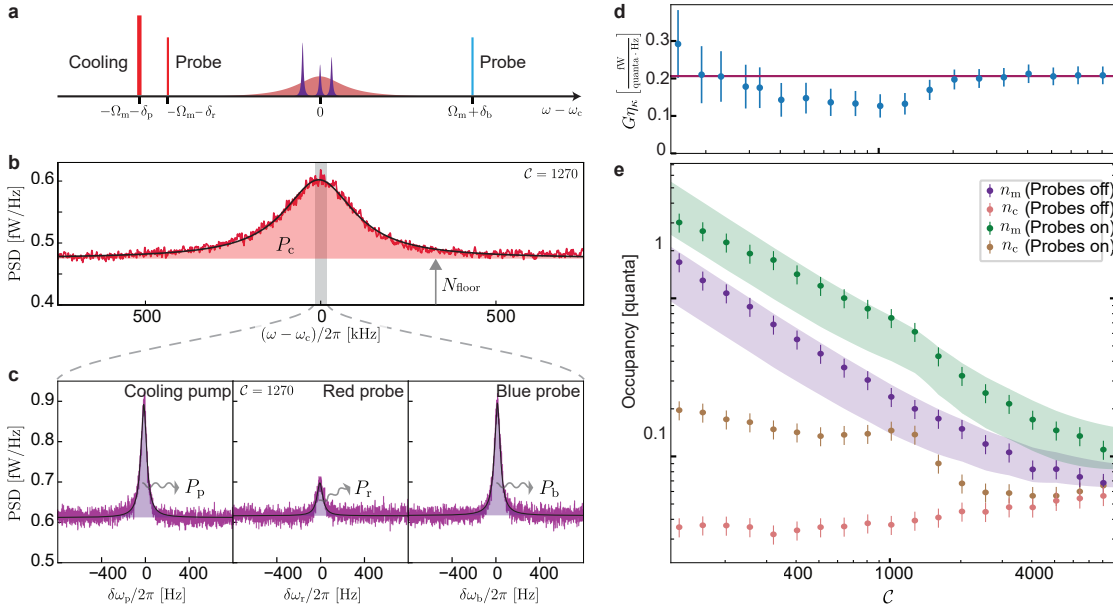


Figure 7.4: **Sideband asymmetry experiment** **a**, Frequency scheme of the sideband asymmetry experiment. **b**, **c**, An example of cavity emission and optomechanical sidebands measured for  $\mathcal{C} = 1270$ . The power of each signal is extracted by Voigt function fitting as shown by black lines. **d**, Calculated values of  $G\eta_k$  for different cooling cooperativities. The solid line shows the average of the flat part of the plot which is used as the global calibration factor. This value is in good agreement with the calibration method based on SNR improvement of JTWPA. Error bars are corresponding to standard deviations. **e**, Calibrated photon and phonon occupations of the cavity and mechanics respectively for both cases of probes on and off. Error bars are corresponding to standard deviations. The shaded area shows theoretically expected occupations in the range of system parameters errors.

### 7.3.2 Experimental details of the sideband asymmetry measurement

In the experiment, we set the optomechanical damping and anti-damping rates of the balanced probes to  $\Gamma_{\text{opt}}^r/2\pi = \Gamma_{\text{opt}}^b/2\pi = 12.9$  Hz, inducing sidebands with frequency detuning of  $\delta_r/2\pi = 0$  and  $\delta_b/2\pi = 10$  kHz at the cavity frequency. The cooling pump is applied to cool down the mechanical oscillator and generate the sideband with  $\delta_p/2\pi = 25$  kHz, and its power is swept up to the maximum output power of the microwave source, corresponding to cooperativity of  $\mathcal{C} = 8000$ .

For the calibration based on the sideband asymmetry measurement, we apply the cooling pump together with the red- and blue-detuned balanced probes. Figures 7.4b and c show the measured noise power spectrum density of the cavity thermal emission and the respective optomechanical sidebands. The power of the cavity thermal emission is obtained as the area of a Lorentzian fitted to the measured spectrum density, while the power of each optomechanical sideband is obtained by fitting a Voigt function (a convolution of a Lorentzian with a Gaussian filter with a 1 Hz resolution bandwidth) to the spectrum density and extracting the area of the

Lorentzian. Note that the residual imbalance of the probe powers (less than 2%) is directly measured and compensated in the data analysis. Using the obtained powers together with Eqs. (7.13)–(7.15), we obtain and show the scaling factor  $G\eta_k$  as a function of the cooling cooperativity in Fig. 7.4d. We find that there is an unknown heating effect on the cavity (see the cavity occupation with the two probes in Fig. 7.4e) when the cooling pump is nearly balanced with the blue probe, which distorts the scaling factor  $G\eta_k$ . Nevertheless, we reliably obtain the scaling factor to be  $G\eta_k = 0.21(\pm 0.03)$  [fW/quanta·Hz], shown with the red line in Fig. 7.4d, by using a cooperativity region where the heating effect disappears when the cooling pump is sufficiently large ( $\mathcal{C} > 2000$ ).

We use ringdown in the optomechanical cooling experiment to verify that the dynamical back-actions of the balanced probes are negligible compared to the cooling pump. This is confirmed by comparing the linewidth of the measured PSD of optomechanical sidebands when probes are on and off with the values from the ringdown experiment. As shown in Fig. 7.5e, the agreement between these three values of the total damping rate ensures that the two probes are well balanced. Moreover, we can also confirm that the optomechanical coupling still behaves linearly for higher cooling cooperativities.

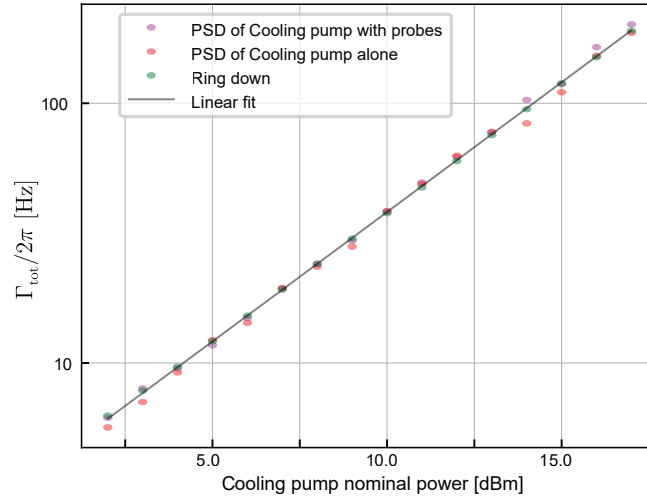


**Figure 7.5: Comparing mechanical linewidth from ringdown and PSD.** Effective mechanical damping rates versus nominal source powers in the optomechanical cooling experiment (measured in different room temperature setup). Mechanical linewidth is measured directly by ringdown (green) and by fitting to the measured PSD of the cooling pump’s sideband when sideband asymmetry probes are on (magenta) and off (red). The fact that extracted linewidths are the same in three experiments verifies that the effective dynamical back action of balanced probes is negligible compared to the cooling pump.

We ensure sufficient attenuation in the input line, therefore we can assume that the input noise from the waveguide corresponds to the vacuum noise, regardless of the amount of input pump power (This assumption is used in the theoretical derivations in Sec.2.2). This can be experimentally confirmed by the fact that there is no significant dip on the noise floor of the

power spectral density at the cavity frequency, showing that the effective temperature of the external bath is equal to the intrinsic bath temperature that can be safely assumed to be zero when a strong pump field is not applied. Furthermore, there is no significant increase in the noise floor even when stronger pump fields are applied.

We experimentally confirm that the gain and SNR improvement of the JTWPA for a weak coherent tone is not varying for different cooling powers, with and without the two probes, ensuring the scaling factor  $G\eta_\kappa$  is constant for the entire measurements. Using the well-calibrated  $G\eta_\kappa$ , we can therefore directly extract the microwave and mechanical occupations from the cavity thermal emission and the optomechanical sideband induced by the cooling pump respectively by using Eqs. (7.18) and (7.19). Figure 7.4e shows both the extracted occupations when probes are on and off. Due to additional heating effects induced by the two probes, the cavity occupation with the probes is higher than that without the probes, which limits the minimum phonon occupation that can be achieved by sideband cooling. Here, we obtain the minimal phonon occupation to be  $n_m = 6.8(\pm 0.9) \times 10^{-2}$  quanta when the probes are switched off, which is approaching the limitation imposed by the cavity heating effect.

It is worth mentioning that the power spectral density of sidebands scattered from the red probe or the cooling pump can show a dip, instead of a peak, when  $n_m - 2n_c < 0$ . As shown in Fig. 7.6d, a Lorentzian dip of the cooling pump sideband is indeed observed for  $\mathcal{C} = 6400$ , implying that the mechanical occupation is reaching the minimum limit imposed by the cavity heating.

Furthermore, using Eq. (7.12), we determine the effective added noise of the microwave measurement chain to be  $n_{\text{add}} = 0.9(\pm 0.2)$  quanta in agreement with the independently calibrated added noise using the SNR improvement of the JTWPA discussed in Sec. 5.3.

## 7.4 Measurement of motional heating rate

After preparing a high-fidelity ground state with optomechanical cooling, we directly measure the thermal decoherence by recording the thermalization of the mechanical oscillator out of the ground state using a time-domain protocol (Fig. 7.6b), where we first prepare the ground state, and leave the system to freely evolve for a certain time of  $\tau_{\text{ev}}$ . Using optomechanical amplification technique with a blue-detuned pump (Palomaki, J. Teufel, et al., 2013; R. D. Delaney et al., 2019), we intrinsically amplify the mechanical motion by  $\sim 50$  dB with a minimal added noise, and measure both quadratures of motion encoded in a generated optomechanical sideband signal (Fig. 7.6a). Repeating this pulse sequence allows us to capture the quadrature distribution of the mechanical state, realizing quantum-state tomography (Fig. 7.6d). As shown in Fig. 7.6c, we are able to precisely calibrate the amplification process using different phonon occupations as an input state, which are well-calibrated by the sideband asymmetry measurement, resulting in  $n_{\text{add}}^{\text{opt}} = 0.80 \pm 0.09$  quanta.

Figure 7.6d shows examples of the measured quadrature distributions at different evolution



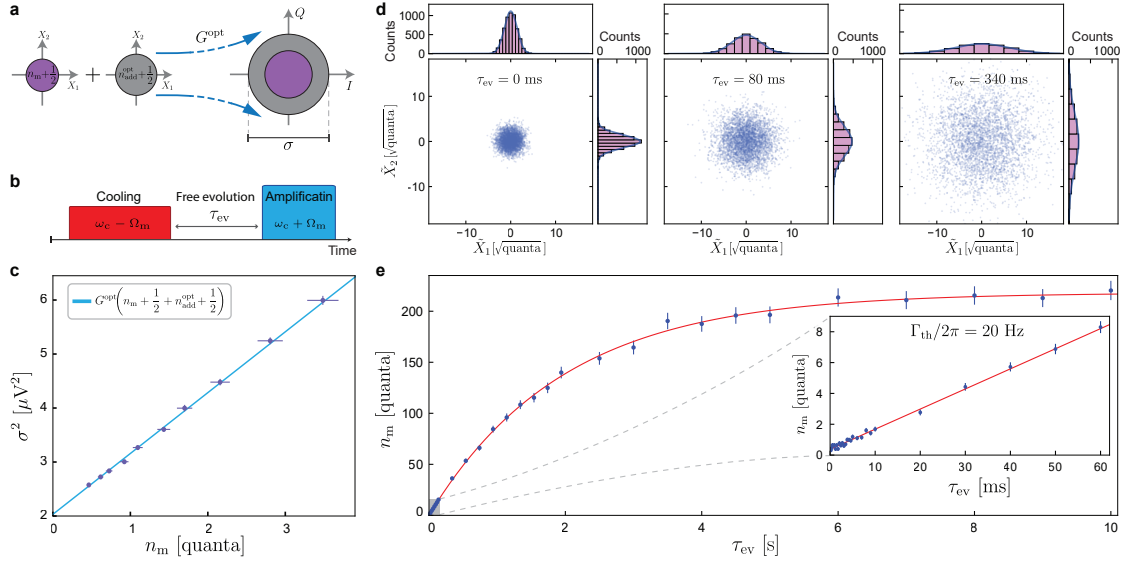


**Figure 7.6: Recording the motional heating rate out of the quantum ground state.** **a**, Schematic diagram showing optomechanical amplification process, where an initial mechanical state is amplified by  $G^{\text{opt}}$  with an added noise of  $\frac{1}{2} + n_{\text{add}}^{\text{opt}}$  referred to input. **b**, Pulse sequence for observing the thermalization of the ground state. **c**, Quadrature variance of the optomechanical sideband signal,  $\sigma^2$ , as a function of the prepared phonon occupation that is calibrated by the sideband asymmetry measurement, enabling us to reliably determine  $G^{\text{opt}}$  and  $n_{\text{add}}^{\text{opt}}$ . **d**, Scatter plots of the measured quadratures of motion normalized by  $\sqrt{G^{\text{opt}}}$  for different evolution times. The marginal histogram for each quadrature is shown by purple bars. A Gaussian curve with the calculated variance is shown by thick blue lines, reproducing each histogram. **e**, Extracted mechanical occupations as a function of the free evolution time. The blue dots are experimental data with error bars while the red line is the exponential fit. The right inset shows the same experiment for a short evolution time range, exhibiting a thermal decoherence rate of  $\Gamma_{\text{th}}/2\pi = 20.5 \pm 0.6$  Hz obtained from the linear fit.

times in units of  $[\sqrt{\text{quanta}}]$ . Figure 7.6e shows the free evolution from the ground state to the thermal equilibrium. The exponential fit results in a bare dissipation rate of  $\Gamma_{\text{m}}/2\pi = 80$  mHz in the low phonon occupation regime, close to the value measured from the ring-down experiment with  $n_{\text{m}} > 10^7$  (Fig. 7.2h). The right inset of the Fig. 7.6 e shows the thermalization in shorter evolution times, where the thermal decoherence rate is directly measured as  $\Gamma_{\text{th}}/2\pi = 20.5 \pm 0.6$  Hz, corresponding to a phonon lifetime of  $T_1 = 7.7$  ms.

#### 7.4.1 Optomechanical amplification measurement and calibration

To observe the thermal decoherence rate of our mechanical oscillator, we use a time-domain protocol, where we first prepare the mechanical oscillator to either a vacuum state or a squeezed state, let it freely evolve for a certain time ( $\tau_{\text{ev}}$ ), and then measure the mechanical quadrature by using the optomechanical amplification process induced by a blue-detuned pump (A. Reed et al., 2017; R. D. Delaney et al., 2019) (see Sec. 2.3). We measure the optome-

chanical induced amplification sideband signal and obtain the phase-insensitive amplified mechanical quadratures. Repeating such a time domain protocol and collecting the measured output microwave quadrature data (a pair of  $I$  and  $Q$  electrical quadratures in units of  $\mu\text{V}$  extracted from each recorded time trace) allow us to construct the quadrature probability density function (PDF) of the measured state and calculate its standard deviations, which in case of a thermal (symmetric Gaussian) state are equal to each other  $\sigma^2 = \langle I^2 \rangle = \langle Q^2 \rangle$ . Using this intrinsic optomechanical amplifier, we achieve  $G^{\text{opt}} = \exp(+\tau_{\text{amp}}\Gamma_{\text{amp}}) \approx 50$  dB gain in the microwave optomechanical sideband signal where  $\tau_{\text{amp}} = 22$  ms and  $\Gamma_{\text{amp}} = 2\pi \times 85$  Hz are the blue pulse length and total optomechanical anti-damping rates, respectively. It is worth to note that in each cycle, the length of the preparation (cooling or squeezing) pulse should be long enough to damp the mechanics which was amplified in the previous amplification sequence ( $\Gamma_{\text{prep}}\tau_{\text{prep}} \gg \Gamma_{\text{amp}}\tau_{\text{amp}}$ ) to avoid instability of the time domain protocol. We set the  $\tau_{\text{prep}} > 100$  ms to ensure  $\sim 50$  dB higher cooling rate than the amplification rate in the sequence. After each sequence, we turn off all pulses for 10 ms to collect the traces from the measurement device, which is also sufficient to thermalize the cavity and microwave thermal bath to their initial states in the absence of pumps. The total repetition rate is around 5 sequences per second in our experiment, slightly varying based on the preparation time needed for different cooling rates.

As discussed in the theory section (Sec. 2.3), the original mechanical state is added with an effective noise referred to input,  $n_{\text{add}}^{\text{opt}}$ , in the amplification process. The measured PDF normalized with  $\sqrt{G^{\text{opt}}}$  shows the convolution of the quadrature PDF of the original state (thermal or squeezed state) with the added noise of a Gaussian PDF. By calculating the average of the standard deviations of both the mechanical quadratures, we can obtain the scaled phonon occupation including the vacuum noises and the input-referred added noise in the optomechanical amplification process. For a thermal state, the measured phonon occupation is described by

$$\sigma^2 = \frac{\langle I^2 \rangle + \langle Q^2 \rangle}{2} = G^{\text{opt}} \left( n_{\text{m}} + \frac{1}{2} + n_{\text{add}}^{\text{opt}} + \frac{1}{2} \right), \quad (7.20)$$

where  $n_{\text{m}} \geq 0$  is the thermal phonon occupation of the prepared state,  $G^{\text{opt}}$  and  $n_{\text{add}}^{\text{opt}}$  are the conversion factor and the added noise in the optomechanical phase-insensitive amplification, respectively. Note that the 1 quanta is the sum of the vacuum noise of the mechanical oscillator and the added noise of the ideal phase-insensitive amplification. To precisely calibrate the conversion factor and added noise of the amplification process, we prepare several different thermal states which are independently calibrated with the sideband asymmetry experiment based on continuous waves, and measure them through the optomechanical readout. Then, we can relate the measured microwave variances,  $\sigma^2$ , to the actual phonon occupation of the prepared state,  $n_{\text{m}}$ , by fitting a linear function to the variance as a function of the phonon occupation (as shown in Fig. 7.6d). With this, we are able to determine the added noise to be  $n_{\text{add}}^{\text{opt}} = 0.80(\pm 0.09)$  quanta and the conversion factor to be  $G^{\text{opt}} = 1.13 \pm (0.04)$  [ $\mu\text{V}^2/\text{quanta}$ ], respectively.

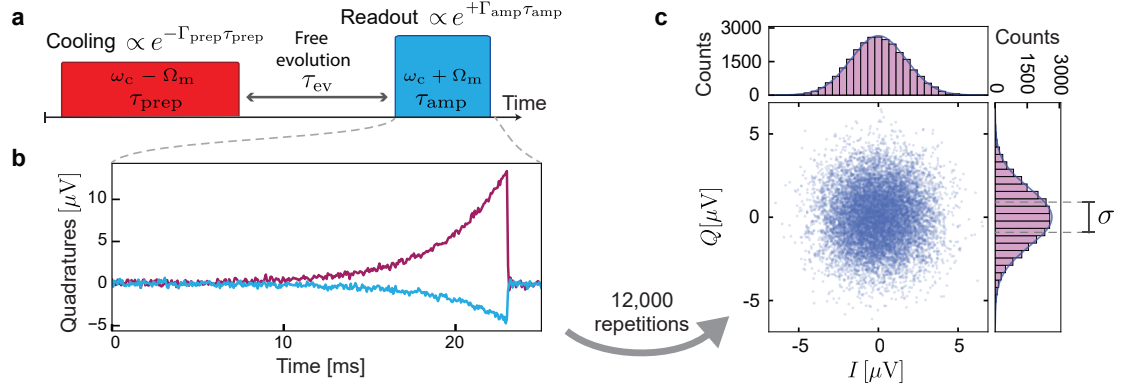
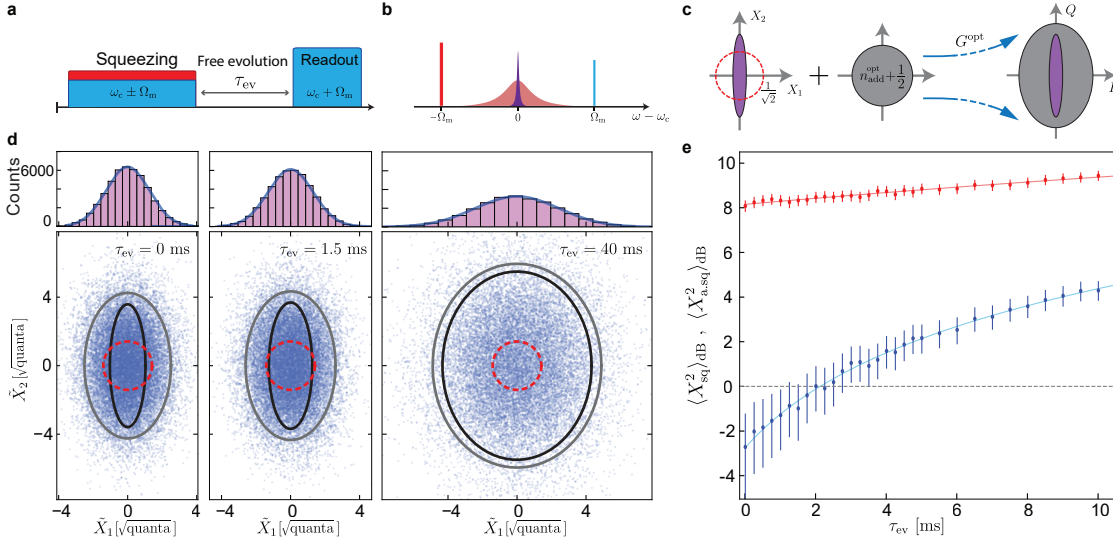


Figure 7.7: **Optomechanical amplification.** **a**, The pulse sequence of optomechanical cooling and amplification. A red-detuned pulse prepares the mechanical oscillator in its ground-state. After leaving the state to freely evolve for  $\tau_{\text{ev}}$ , a blue-detuned pulse amplifies the thermalized mechanical state to allow low-noise measurement of quadratures of motion. The sequence is repeated ( $\sim 12,000$  times) to extract the quadrature scatter plots. **b**, an example of the time trace collected during the optomechanical amplification process. Both quadratures of the microwave field corresponding to the optomechanical sidebands are exponentially growing and being simultaneously recorded. One pair of  $I$  and  $Q$  is extracted from each trace. **c**, An example of the scatter plot of measured quadratures. Marginal histograms verify the Gaussian distribution.

## 7.5 Recording thermalization of squeezed mechanical state

Finally, we generate a quantum-squeezed state of our oscillator. Since the squeezed state is a phase-sensitive quantum state, its free evolution is subject to the dephasing in the system. Tracking its time evolution enables us to directly measure the quantum-state lifetime and verify minimal dephasing in our mechanical oscillator. The ability to squeeze the mechanical oscillator critically relies on the residual thermal occupation upon cooling, which in our case is below 0.1 quanta, implying that strong squeezing below zero-point fluctuation is possible. We use optomechanical dissipative squeezing technique (Kronwald, Marquardt, and A. A. Clerk, 2013; Wollman et al., 2015; Pirkkalainen, Damskagg, et al., 2015; Lecocq, Clark, et al., 2015) by simultaneously applying two red- and blue-detuned pumps symmetrically with respect to the cavity frequency (Fig. 7.8b), and achieve  $\langle X_{\text{sq}}^2 \rangle / \frac{1}{2} = -2.7^{+1.4}_{-2.3}$  dB squeezing in one quadrature of motion below the vacuum fluctuation and  $\langle X_{\text{a.sq}}^2 \rangle / \frac{1}{2} = 8.1^{+0.3}_{-0.3}$  dB anti-squeezing in the other quadrature. These are obtained by subtracting the accurately calibrated  $n_{\text{add}}^{\text{opt}}$  in the optomechanical amplification (Figs. 7.8 a and c).

Figure 7.8d shows measured quadrature scatter plots of the prepared squeezed state and its time evolution. We are able to record the free evolution of a prepared squeezed state (Fig. 7.8d) and observe the decoherence of both the quadratures to the thermal equilibrium (Fig. 7.8e). A slight difference is observed in the decoherence rates of the two quadratures,  $(I^{\text{sq}} - I^{\text{a.sq}})/2\pi = 1.1(\pm 0.6)$  Hz. Comparing it with a numerical simulation allows us to characterize the dephasing rate of  $\Gamma_{\varphi}/2\pi = 0.09(\pm 0.05)$  Hz in our platform (see sec.7.5.2), in



**Figure 7.8: Tracking the free evolution of a mechanical squeezed state.** **a**, Pulse sequence for recording the free evolution of a squeezed state. **b**, Frequency landscape of optomechanical dissipative squeezing. **c**, Schematic diagram showing optomechanical amplification process of an initially prepared squeezed state. **d**, The measured quadrature scatter plots for the initially prepared squeezed state and its time evolution. The gray and black ellipses represent standard deviation contours scaled by a factor of 2 (for better visualization) of the Gaussian density function before (measured state) and after (inferred squeezed state) noise subtraction. Dashed red circles indicate the same for the zero-point fluctuation (ideal ground state). **e**, Variance of the squeezed (blue) and anti-squeezed (red) quadratures, relative to the zero-point fluctuation, as a function of the free evolution time. The initial state shows  $-2.7^{+1.4}_{-2.3}$  dB squeezing and  $8.1^{+0.3}_{-0.3}$  dB anti-squeezing. The blue and red solid lines are the linear fits, revealing a slight difference in decoherence rates of two quadratures, corresponding to a pure dephasing rate of  $\Gamma_\varphi/2\pi = 0.09(\pm 0.05)$  Hz.

agreement with the measured frequency fluctuation discussed earlier. We observe that the variance of the squeezed quadrature remains below the zero-point fluctuation up to 2 ms, demonstrating a significantly long quantum state storage time in a macroscopic mechanical oscillator.

### 7.5.1 Generation and calibration of mechanical squeezed states

We use optomechanical dissipative squeezing technique to squeeze one quadrature of motion below the zero-point-fluctuation (Kronwald, Marquardt, and A. A. Clerk, 2013; Wollman et al., 2015; Pirkkalainen, Damskäg, et al., 2015). As shown in Fig. 7.9 a inset, simultaneously applying two symmetrically red- and blue-detuned pumps from the microwave frequency with optomechanical damping and anti-damping rates of  $\Gamma_{\text{opt}}^r$  and  $\Gamma_{\text{opt}}^b$  respectively results in a beam-splitter interaction Hamiltonian:

$$\hat{H}_{\text{int}} = -\hbar g \hat{a}^\dagger \hat{b} + \text{H.c.}, \quad (7.21)$$

where  $\hat{\beta} = \sqrt{\frac{\Gamma_{\text{opt}}^{\text{r}}}{\Gamma_{\text{opt}}^{\text{r}} - \Gamma_{\text{opt}}^{\text{b}}}} \hat{b} + \sqrt{\frac{\Gamma_{\text{opt}}^{\text{b}}}{\Gamma_{\text{opt}}^{\text{r}} - \Gamma_{\text{opt}}^{\text{b}}}} \hat{b}^{\dagger}$  is the Bogoliubov's mode annihilation operator and  $\mathcal{G} = \sqrt{\kappa/4} \sqrt{\Gamma_{\text{opt}}^{\text{r}} - \Gamma_{\text{opt}}^{\text{b}}}$  is the coupling rate. This beam-splitter Hamiltonian allows us to reach the ground state of the Bogoliubov operator, which is a squeezed state of motion with

$$\langle \hat{X}_{\text{sq}}^2 \rangle = \frac{1}{2} e^{-2r}, \quad \langle \hat{X}_{\text{a.sq}}^2 \rangle = \frac{1}{2} e^{+2r}, \quad (7.22)$$

where  $\tanh(r) = \sqrt{\Gamma_{\text{opt}}^{\text{b}}/\Gamma_{\text{opt}}^{\text{r}}}$ . In practice, the non-zero occupation of the thermal bath prevents us from reaching to such a pure squeezed state. A more comprehensive analytical derivation on the purity of optomechanical squeezing is discussed by Kronwald *et.al.* (2013) (Kronwald, Marquardt, and A. A. Clerk, 2013).

We use optomechanical amplification to measure quadrature PDF of the amplified state ( $\tilde{X}_1 = I/\sqrt{G^{\text{opt}}}$ ,  $\tilde{X}_2 = Q/\sqrt{G^{\text{opt}}}$  scaled to  $[\sqrt{\text{quanta}}]$  unit) as a convolution of the initial state with the precisely calibrated Gaussian added noise during amplification as shown in Fig. 7.10a. Subtracting the added noise from the variance of the scaled quadrature PDF results in the squeezed and anti-squeezed quadrature variances of the input mechanical state for the optomechanical amplification:

$$\langle \hat{X}_{\text{sq,a.sq}}^2 \rangle = \langle \hat{X}_{1,2}^2 \rangle - n_{\text{add}}^{\text{opt}} - \frac{1}{2}. \quad (7.23)$$

Figures 7.9a and b show the measured phonon occupation and quadratures of the generated squeezed state prepared with different blue pump powers. We used a damping rate of  $\Gamma_{\text{opt}}^{\text{r}}/2\pi = 75$  Hz. The optimal power of the blue pump for the thermalization of the squeezed state is found 5 dB below the red pump, where the maximum quadrature squeezing is achieved, as shown in Fig. 7.9b. Increasing the relative power of the blue pump results in optomechanical heating. In particular, when the power of pumps close to the balanced condition, optomechanical instabilities, such as two-tone instability, will occur in the presence of a slight frequency detuning (Shomroni, Youssefi, et al., 2019). With the optimal pump powers, we obtain  $\langle X_{\text{sq}}^2 \rangle_{\text{dB}} = 10 \log_{10} \left( \langle X_{\text{sq}}^2 \rangle / \frac{1}{2} \right) = -2.7_{-2.3}^{+1.4}$  dB squeezing of one quadrature of motion below the vacuum fluctuation and  $\langle X_{\text{a.sq}}^2 \rangle_{\text{dB}} = 8.1_{-0.3}^{+0.3}$  dB anti-squeezing in the other quadrature, as shown in Fig. 7.10b. The achieved squeezing value is close to the theoretical squeezing limit, corresponding to  $2\langle \hat{X}_{\text{sq}}^2 \rangle = \sqrt{(1 + 2n_{\text{m}}^{\text{th}})/\mathcal{C}} = -3.5$  dB (Kronwald, Marquardt, and A. A. Clerk, 2013).

Afterward, we record the free evolution of the prepared squeezed state, as shown in Fig. 7.10c. The marginal PDF of both the measured quadratures, as well as the noise-subtracted squeezed and anti-squeezed mechanical quadratures are shown for different evolution times. One quadrature of motion remains below the zero-point fluctuation up to 2 ms. At the longer evolution times, the state is thermalized to an isotropic thermal state (Fig. 7.10d).

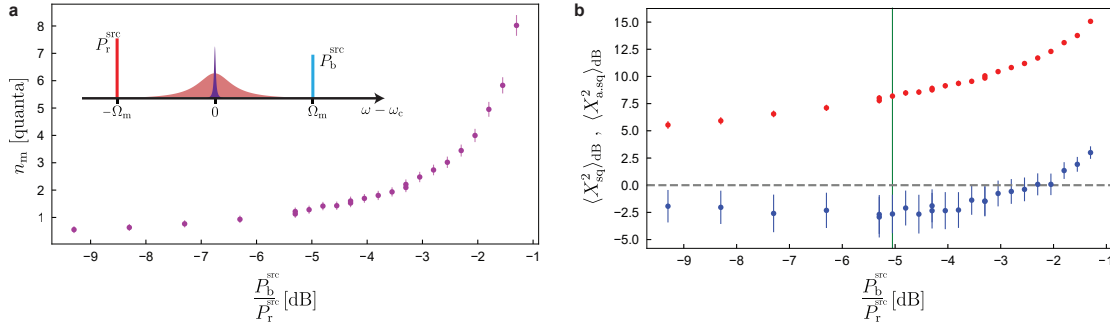


Figure 7.9: **Optomechanical squeezing.** **a** (inset), Frequency landscape for optomechanical squeezing. two symmetrically detuned blue and red pumps with nominal powers of  $P_b^{\text{src}}$ ,  $P_r^{\text{src}}$  are applied to the cavity. **a**, Measured total phonon occupation versus the ratio between blue and red pump powers. While the blue pump power increases, The system will be closer to the optomechanical instability threshold. Error bars are corresponding to standard deviations. **b**, Measured squeezed and anti-squeezed quadratures of motion versus the blue pump relative power. The optimally selected squeezing point for the thermalization experiment is shown by the green line. Error bars are corresponding to standard deviations.

### 7.5.2 Dephasing effect on thermalization of squeezed states

A mechanical squeezed state has a phase coherence between the Fock states, resulting in the sensitivity to the pure dephasing. By observing the free evolution of such a phase-sensitive state, we can characterize the pure dephasing rate of our mechanical oscillator. When the mechanical state is initialized in an isotropic Gaussian state, such as the vacuum or thermal states, the decoherence rates for the quadrature variances in all phases are identical regardless of the amount of the pure dephasing. However, when the mechanical state is initialized in a squeezed state, the decoherence rate of the quadrature variance in the squeezed axis is greater than that in the anti-squeezed axis if the pure dephasing rate is finite. Thus, we can use this property to extract the pure dephasing rate of the mechanical oscillator.

In the large phonon bath occupation limit ( $n_m^{\text{th}} \gg 1$ ), which is the case for our experiment, the free evolution of a mechanical oscillator with a pure dephasing is described by a master equation,

$$\frac{d\hat{\rho}}{dt} = \Gamma_{\text{th}}\mathcal{D}[\hat{b}]\hat{\rho} + \Gamma_{\text{th}}\mathcal{D}[\hat{b}^\dagger]\hat{\rho} + 2\Gamma_\varphi\mathcal{D}[\hat{b}^\dagger\hat{b}]\hat{\rho}, \quad (7.24)$$

where  $\Gamma_\varphi$  is the pure dephasing rate,  $\hat{\rho}$  is the density matrix, and  $\mathcal{D}[\hat{O}]\rho = \hat{O}\hat{\rho}\hat{O}^\dagger - (\hat{O}^\dagger\hat{O}\hat{\rho} + \hat{\rho}\hat{O}^\dagger\hat{O})/2$  is the Lindblad dissipator. By calculating the time evolution of the density matrix, we can numerically obtain (using the Python QuTiP package (Johansson, Nation, and Nori, 2012)) the time evolution of the quadrature variances and the phonon occupation as  $\langle \hat{X}_1(t)^2 \rangle = \text{Tr}[\rho(t)\hat{X}_1^2]$ ,  $\langle \hat{X}_2(t)^2 \rangle = \text{Tr}[\rho(t)\hat{X}_2^2]$ , and  $n_m = \langle \hat{b}^\dagger\hat{b} \rangle$ , respectively. Note that we here consider only a mechanical state with  $\text{Tr}[\rho\hat{X}_1] = \text{Tr}[\rho\hat{X}_2] = 0$ , e.g. a vacuum, thermal, and squeezed states.

The blue and red circles in Fig. 7.11a show the experimental results of the quadrature variances,

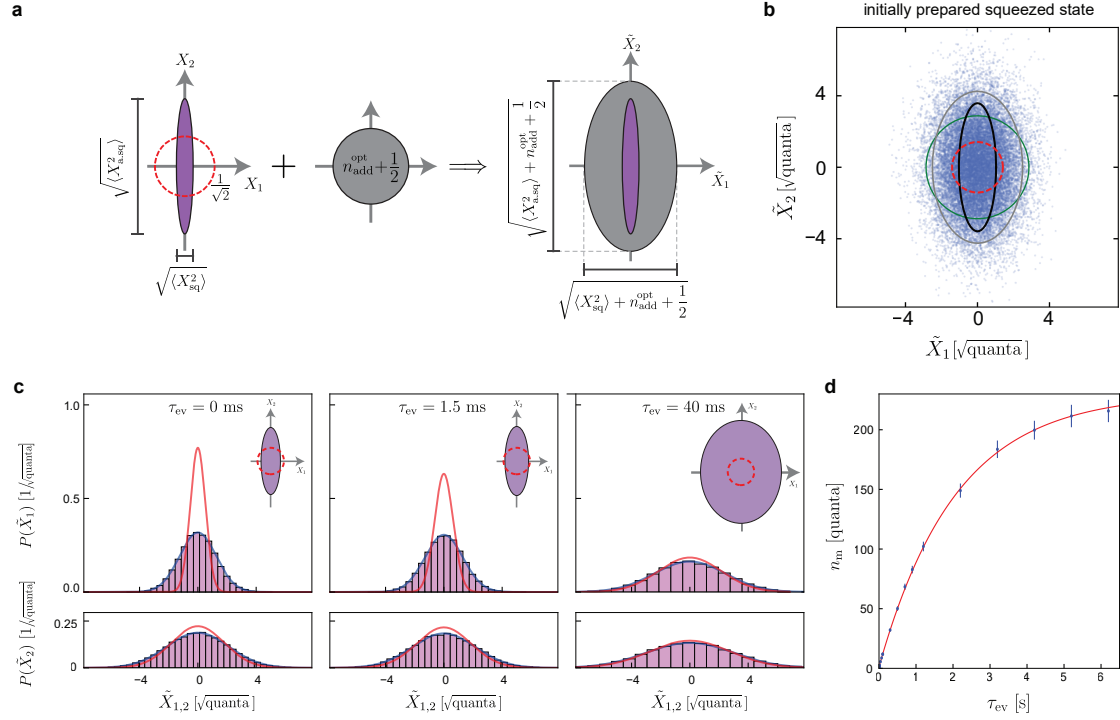


**Figure 7.10: Measurement of squeezing.** **a**, Schematic diagram showing the prepared squeezed state added with the input-referred noise of the amplification process. The measured state has a quadrature density function proportional to the convolution of the initial state with the added noise. Precise calibration of the Gaussian added noise allows us to extract the initial state quadrature variances. **b**, Quadrature scatter plot for the initially prepared squeezed state. The gray ellipse represents standard deviation contours scaled by a factor of 2 (for better visualization) of the Gaussian density function. The green circle shows the same for the measured ground state. The black ellipse shows the same for the noise-subtracted state demonstrating the initial squeezing. The red dashed line shows the same for the zero-point fluctuation (ideal ground state). **c**, Quadrature marginal histograms are shown by purple bars and calculated Gaussian marginal density functions by thick blue lines verifying measurement of Gaussian squeezed state. The red lines show the added noise-subtracted density functions of the initial squeezed state. Insets depict the extracted squeezed state versus the zero-point fluctuation. **d**, Phonon occupation of the squeezed state evolution in long time scales. The red line shows the exponential fit. Error bars are corresponding to standard deviations.

$\langle X_{\text{sq}}^2 \rangle$  in the squeezed axis and  $\langle X_{\text{a.sq}}^2 \rangle$  in the anti-squeezed axis as a function of the free-evolution time respectively, while the purple circles show the time evolution of the phonon occupation,  $n_m = (\langle X_{\text{sq}}^2 \rangle + \langle X_{\text{a.sq}}^2 \rangle) / 2 - 1/2$ . Here, we define the decoherence rate as a slope of the time evolution, i.e.,  $\Gamma^{\text{sq}} = \frac{d\langle X_{\text{sq}}^2 \rangle}{dt}$ ,  $\Gamma^{\text{a.sq}} = \frac{d\langle X_{\text{a.sq}}^2 \rangle}{dt}$ , and  $\Gamma_{\text{th}} = \frac{dn_m}{dt}$ . By linearly fitting the results (see the black dotted lines in Fig. 7.11a), the decoherence rates are found to be  $\Gamma^{\text{sq}}/2\pi = 17.7 \pm 0.7$  Hz,  $\Gamma^{\text{a.sq}}/2\pi = 16.5 \pm 0.6$  Hz, and  $\Gamma_{\text{th}}/2\pi = 17.1 \pm 0.6$  Hz. Furthermore, the difference between the decoherence rates in the squeezed and anti-squeezed axes is obtained as  $(\Gamma^{\text{sq}} - \Gamma^{\text{a.sq}})/2\pi = 1.1 \pm 0.6$  Hz. Importantly note that the thermal decoherence rate can be obtained by observing



the thermalization of a squeezed state, instead of the vacuum state, i.e.,  $\Gamma_{\text{th}} = (I^{\text{sq}} + I^{\text{a.sq}})/2$ , enabling us to determine the pure dephasing rate from the difference between the decoherence rates in the squeezed and anti-squeezed axes.

The sensitivity of a squeezed state to the pure dephasing depends on its squeezing level. To accurately extract the pure dephasing rate, we therefore need to numerically determine the initial squeezed state using the experimentally obtained quadrature variances, i.e.,  $\langle X_{\text{sq}}^2 \rangle = 0.27 \pm 0.1$  and  $\langle X_{\text{a.sq}}^2 \rangle = 3.27 \pm 0.2$ . We can consider the prepared squeezed state as a squeezed thermal state, which is defined as  $S\rho_{\text{th}}S^\dagger$ , where  $S = \exp[\frac{r}{2}(\hat{b}^2 - \hat{b}^{\dagger 2})]$  is a squeezing operator with a squeezing parameter of  $r$  and  $\rho_{\text{th}}$  is a thermal state with an average phonon number of  $n_{\text{th}}$ . We can extract the thermal phonon number and the squeezing parameter as  $n_{\text{th}} = \sqrt{\langle X_{\text{sq}}^2 \rangle \langle X_{\text{a.sq}}^2 \rangle} - 1/2 = 0.4 \pm 0.2$  and  $r = -\frac{1}{4} \log(\langle X_{\text{sq}}^2 \rangle / \langle X_{\text{a.sq}}^2 \rangle) = 0.6 \pm 0.1$ .

Using the initial squeezed state, we calculate the time evolution of the quadrature variances for different pure dephasing rates and obtain the difference between the thermal decoherence rates of the squeezed and anti-squeezed variances. The green line in Fig. 7.11b shows the numerical results of the thermal decoherence rate difference. As the dephasing rate increases, the difference becomes larger. We compare the numerical results with the experimentally obtained value, which are shown with the blue line. From this, we find that the pure dephasing rate of our mechanical oscillator is found to be  $\Gamma_\varphi/2\pi = 0.09 \pm 0.05$  Hz.

Finally, we show the numerical results of the time evolution of the quadrature variances and the phonon occupation with a dephasing rate of  $\Gamma_\varphi/2\pi = 0.09$  Hz in Fig. 7.11a (see the green lines). The numerical results reproduce well the experimental ones.

## 7.6 Technical information on the experiment

### 7.6.1 Experimental setup and wiring

The experimental setup, including room temperature (RT) and cryogenic, can be seen in Fig. 7.12. For the sideband cooling experiment, four sources are required: one for pumping JTWPA near its stopband (Rohde & Schwartz, SGS100A) to activate a 4-wave mixing amplification process, one strong pump for optomechanical sideband cooling (Rohde & Schwartz, SMA100B), which is red detuned from the cavity, and two weak probes (Keysight, N518313) to generate Stokes and anti-Stokes sidebands for sideband asymmetry calibration. All signals from sources first go through a microwave filter cavity to remove the phase noise around the cavity frequency (see Sec. 5.5). The reflected signal from the filter cavity will be divided in two paths: one goes to the device in the fridge and the other one goes to a tone cancellation line, which consists of a variable digital phase shifter (Vaunix, LPS-802) and attenuator (Vaunix, LDA-602EH). The signal from the tone cancellation line will be combined with the TWPA input line to realize a destructive interference and suppress strong optomechanical drives that saturate the JTWPA (see Sec. 5.4). A coherent signal from the Vector Network Analyzer (VNA: Rohde & Schwartz, ZND) is also combined with the input line to measure the microwave frequency

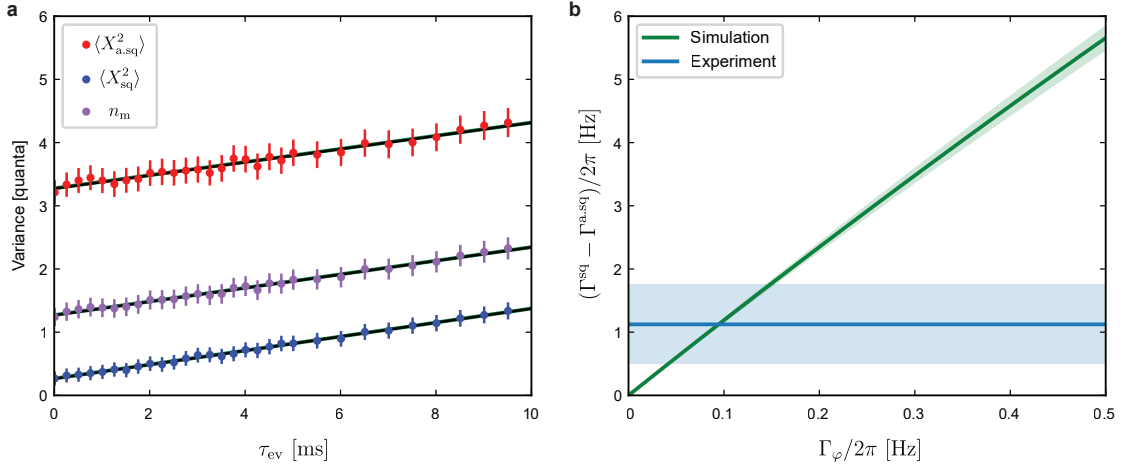


Figure 7.11: **Dephasing effect on the free evolution of a mechanical squeezed state.** **a**, Quadrature variances and average phonon number of a squeezed state as a function of the free-evolution time. The blue, red and purple circles are the data for the quadrature variances in the squeezed and anti-squeezed axes, and the average phonon number, respectively. The black dotted lines are linear fits, while the green lines are the numerical simulation results. Error bars are corresponding to standard deviations. **b**, The difference of the thermal decoherence rates for the quadrature variances in the squeezed and anti-squeezed axes as a function of the pure dephasing rate. The green line shows the numerical simulation results, while the blue line is the experimentally obtained value. The shaded regions showing the errors, respectively.

response of the device. Using mechanical microwave switches (Mini-Circuits, MSP2T-18XL+), we can redirect the main signal path to directly observe the frequency response of the filter cavities and accurately tune them.

In time-domain experiments, where we observe the thermalization of the vacuum and squeezed states, we use an additional microwave source, as a blue-detuned pump for optomechanical amplification (Rohde & Schwartz, SMA100B). The cooling pump and blue probe are also used for generating thermal states or squeezed states. All microwave pulses are generated using ultra-fast solid state switches (Planar Monolithics Industries, P1T-4G8G-75-R-SFF) with  $\sim 50$  ns rising/falling time, and are controlled with an arbitrary wave generator (AWG: Tektronix, AFG325230). The output signal from the fridge divides in two parts using a hybrid coupler: one part goes to the second port of the VNA to measure scattering parameters, and the other part goes to the Electronic Spectrum Analyzer (ESA: Rohde & Schwartz, FSW). Depending on purposes, we use different modes of ESA: for measuring PSD, e.g. in the sideband asymmetry experiment, we use frequency domain mode, for measuring signals in the time domain e.g. optomechanical amplification experiment, we use I-Q analyzer mode, and for measuring the ringdown of the mechanical oscillator, we use the zero span PSD measurement mode. In the time domain experiments, the ESA is triggered by the AWG.

The device is mounted in the mixing chamber of the dilution refrigerator (BLUEFORS, LD250). In the refrigerator, for both the input line to the device and the tone cancellation line, we use

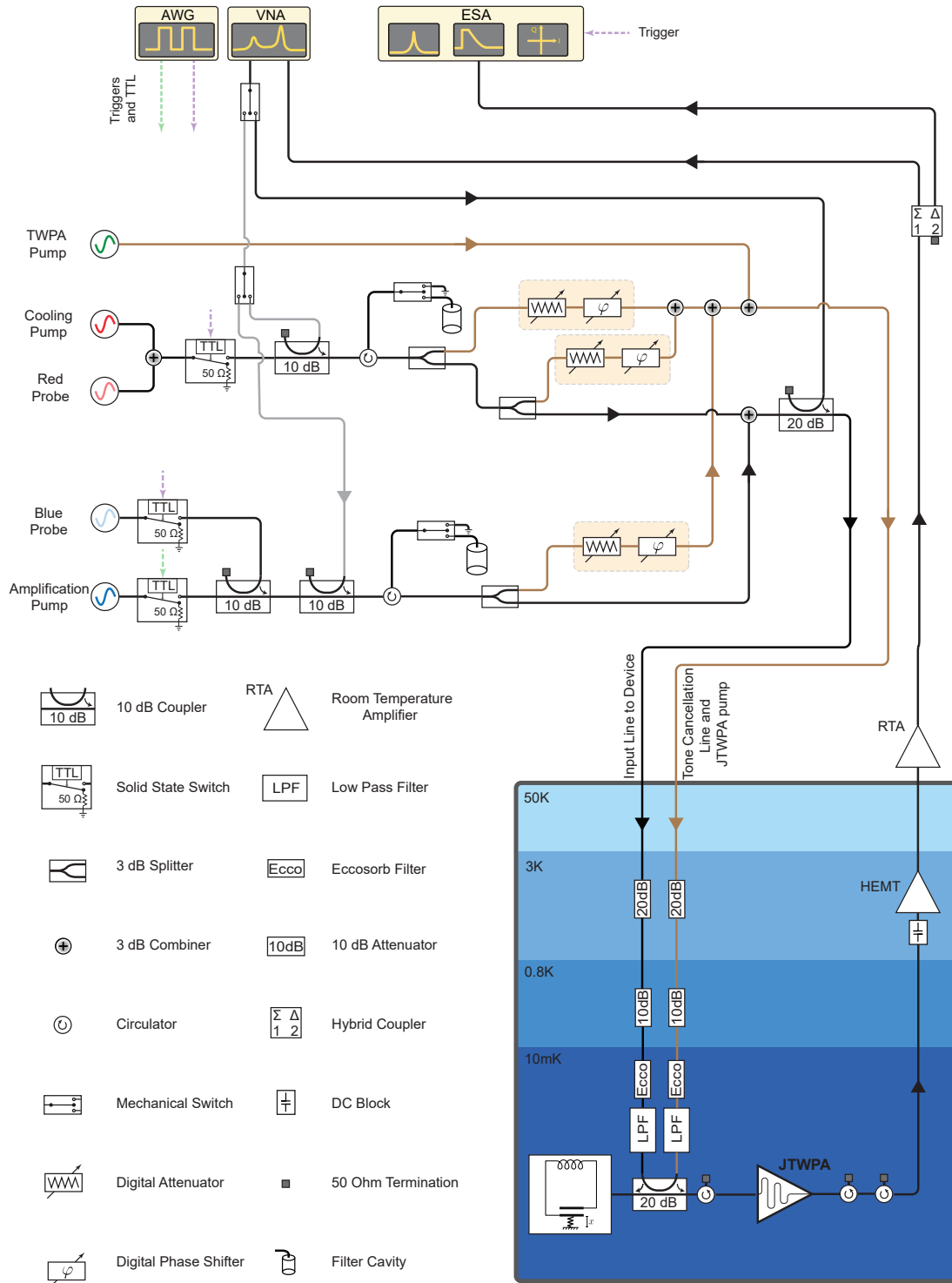


Figure 7.12: **Detailed experimental setup.** The black lines show the main signal path of the control and readout. The brown lines show the tone cancellation and JTWPA pump path. The gray lines show auxiliary paths used for filter cavity tuning. The solid-state switches are only used in the time domain experiments.

cryogenic attenuators, Eccosorb filters, and 18-GHz low pass filters. The reflected signal from the device which is combined with the tone cancellation signal is amplified using a JTWPA (provided by MIT Lincoln Lab), which is a nearly quantum-limited amplifier (Macklin et al., 2015). Before the JTWPA, we use a cryogenic circulator (Low Noise Factory, LNF-CIC4-12A) to remove reflections from JTWPA back to the device. We also use circulators after the JTWPA to remove hot noise penetrating down from the higher temperature stages to the JTWPA. The signal is then amplified using a High-Electron-Mobility Transistor (HEMT: Low Noise Factory, LNF-LNC4-8C) at 4 Kelvin, followed by a Room Temperature Amplifier (RTA: Mini-Circuits, ZVA-183-S+)

### 7.6.2 Full data of chip characterization

The circuit optomechanical device studied in this work is one of the 16 separate electromechanical LC circuits fabricated on a 9.5 mm×6.5 mm chip (Fig.7.13). Those 16 LC resonators follow the same design principle as shown earlier, but frequencies were multiplexed in a chip in the range of 5-7 GHz and 1.5-2.5 MHz for both microwave and mechanical frequencies respectively. This was done by changing the trench radius for mechanical frequency tuning, and the capacitor bottom plate radius for microwave frequency tuning. All 16 LC circuits were magnetically coupled to a micro-strip waveguide.

In Table 7.3, we provide the system parameters for all 14 independent electromechanical LC resonators in a chip - we did not observe two LC resonators, most probably due to overlapping their frequencies with the JTWPA stop-band. More than 50% of the resonators exhibit more than  $20 \times 10^6$  mechanical quality factor, which demonstrates a high yield in our new fabrication process.

The total linewidth, intrinsic loss, and external coupling rates of each microwave cavity are obtained by taking the VNA trace and applying a circle fit in the complex plane. For a few microwave cavities, we could not reliably obtain the internal and external coupling rates due to the Fano effect, which may be originated from the impedance mismatch. The microwave cavity used in the main work (No. 2) is strongly over-coupled, while it suffers from the Fano effect. Nevertheless, the total linewidth can be reliably determined by the circle fit even in the presence of the Fano effect. Importantly note that all the calibration methods used in the main work (e.g. sideband asymmetry experiment, optomechanical amplification and squeezing) are independent of the absolute values of  $\kappa_0$  and  $\kappa_{ex}$ , since our calibration method is based on the total coupling rate ( $\kappa$ ). As all the microwave cavities in the same chip are fabricated together, we do not expect to observe a significant statistical deviation of the intrinsic loss rates among them. Therefore, we can assume that the internal coupling rate of our device is  $\kappa_0/2\pi = 47 \pm 17$  kHz, which is the average and the standard deviation of all the extracted internal coupling rates.

Table 7.3: Full characterization data of different resonances in a chip.

	$\omega_c/2\pi$ (GHz)	$\kappa/2\pi$ (kHz)	$\kappa_{\text{ex}}/2\pi$ (kHz)	$\kappa_0/2\pi$ (kHz)	$\Omega_m/2\pi$ (MHz)	$\Gamma_m/2\pi$ (Hz)	$Q_m$ ( $10^6$ )
1	5.30	610	-	-	1.48	0.056	<b>26.4</b>
2*	5.55	250	-	-	1.80	0.045	<b>40.0</b>
3	5.70	76	46	30	2.10	6.6	<b>0.3</b>
4	5.74	81	36	45	1.82	0.076	<b>23.9</b>
5	5.80	264	192	72	1.56	0.079	<b>19.7</b>
6	5.81	179	157	22	1.92	0.058	<b>33.1</b>
7	5.86	342	-	-	1.63	0.040	<b>40.8</b>
8	5.92	125	91	34	1.96	0.085	<b>23.1</b>
9	6.09	288	232	56	1.70	5.88	<b>0.3</b>
10	6.12	528	456	72	1.74	0.07	<b>24.9</b>
11	6.20	221	162	59	1.77	0.05	<b>35.4</b>
12	6.25	137	103	34	2.24	0.30	<b>7.5</b>
13	6.36	360	-	-	1.76	13.2	<b>0.1</b>
14	6.43	256	-	-	1.83	31.0	<b>0.1</b>

\* This resonator is used for all measurements in the main work.

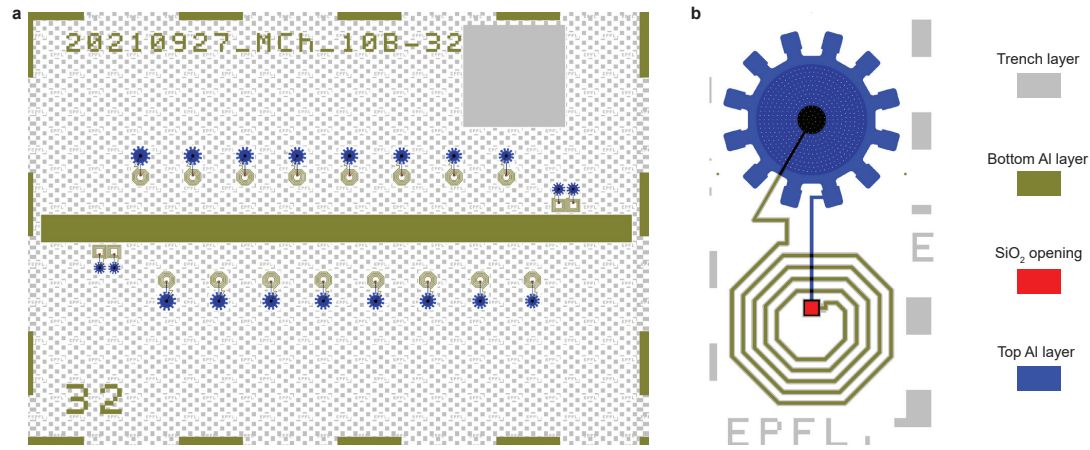
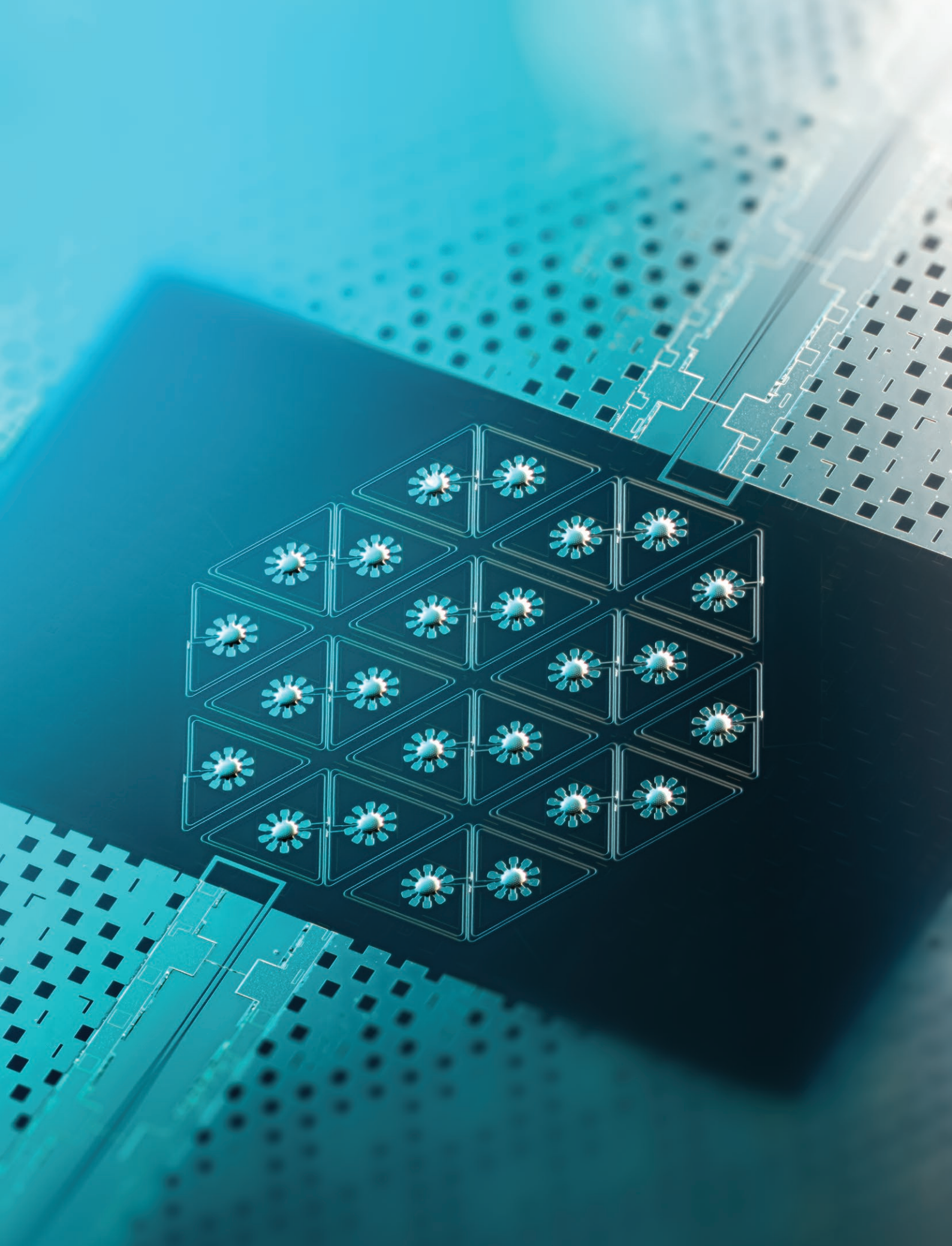


Figure 7.13: **Chip layout of for the ultra-coherent electromechanical samples.** **a**, The designed layout of the chip used in the experiment. Each chip includes 16 separate frequency multiplexed LC resonators as well as two dimer LCs which are not studied in this work. **b**, magnification of the layout of one LC resonator. The color code explains different lithography layers.





A superconducting circuit optomechanical graphene flake (Photo by A. Bancora)

## 8 Topological lattices realized in superconducting circuit optomechanics

Cavity optomechanics enables controlling mechanical motion via radiation pressure interaction (Aspelmeyer, T. J. Kippenberg, and Marquardt, 2014), and has contributed to the quantum control of engineered mechanical systems ranging from kg scale LIGO mirrors to nano-mechanical systems, enabling ground-state preparation (J. D. Teufel, Donner, D. Li, et al., 2011; Chan, Alegre, et al., 2011), entanglement (Kotler et al., 2021; C. Ockeloen-Korppi et al., 2018), squeezing of mechanical objects (Wollman et al., 2015), position measurements at the standard quantum limit (J. D. Teufel, Donner, Castellanos-Beltran, et al., 2009), and quantum transduction (Andrews et al., 2014). Yet, nearly all prior schemes have employed single- or few-mode optomechanical systems. In contrast, novel dynamics and applications are expected when utilizing optomechanical lattices (Peano et al., 2015), which enable to synthesize non-trivial band structures, and have been actively studied in the field of circuit QED (Carusotto et al., 2020). Superconducting microwave optomechanical circuits (J. D. Teufel, Donner, D. Li, et al., 2011) are a promising platform to implement such lattices, but have been compounded by strict scaling limitations. In this chapter, we show how to overcome this challenge and demonstrate topological microwave modes in 1D circuit optomechanical chains realizing the Su-Schrieffer-Heeger (SSH) model (Asbóth, Oroszlány, and Pályi, 2016; Ozawa et al., 2019). Furthermore, we realize the strained graphene model (Pereira, Neto, and Peres, 2009; Naumis et al., 2017) in a 2D optomechanical honeycomb lattice. Exploiting the embedded optomechanical interaction, we show that it is possible to directly measure the mode functions of the hybridized modes without using any local probe (Underwood et al., 2016; H. Wang et al., 2019). This enables us to reconstruct the full underlying lattice Hamiltonian and directly measure the existing residual disorder. Such optomechanical lattices, accompanied by the measurement techniques introduced, offers an avenue to explore collective (G. Heinrich et al., 2011; Xuereb, Genes, and Dantan, 2012), quantum many-body (Ludwig and Marquardt, 2013), and quench (Raeisi and Marquardt, 2020) dynamics, topological properties (Peano et al., 2015; Zangeneh-Nejad and Fleury, 2020) and more broadly, emergent nonlinear dynamics in complex optomechanical systems with a large number of degrees of freedoms (Akram et al., 2012; Sanavio, Peano, and Xuereb, 2020; Tomadin et al., 2012).



## 8.1 challenges of realizing multi-mode optomechanical systems

The majority of optomechanical systems, which have probed classical as well as quantum properties and dynamics, have utilized few-mode optomechanics, i.e., systems that employ a small number of optomechanical degrees of freedom. Pioneering theoretical works have predicted that significantly richer and novel dynamics can be accessed in optomechanical lattices including topological phases of light and sound (Peano et al., 2015), collective (G. Heinrich et al., 2011; Xuereb, Genes, and Dantan, 2012; Roque et al., 2017) and quench (Raeisi and Marquardt, 2020) dynamics, quantum many-body dynamics (Ludwig and Marquardt, 2013) and entanglement (Akram et al., 2012), non-reciprocity (Sanavio, Peano, and Xuereb, 2020), reservoir engineering (Tomadin et al., 2012), and topological phonon transport (Ren et al., 2020). To date, such optomechanical lattices have only been realized via mechanically mediated coupling (Safavi-Naeini, Hill, et al., 2014) - similar to studies that employ mechanical meta-materials (Yang et al., 2015). Indeed, while the coupling of mechanical oscillators for acoustic metamaterials has been successfully achieved (Huber, 2016; Surjadi et al., 2019), implementing optomechanical lattices has been a long-lasting challenge. Topological phonon transport has recently been reported in optomechanical crystals (Ren et al., 2020), consisting of coupled mechanical oscillators. However, site-by-site engineerable optomechanical lattices have not yet been realized due to the stringent requirements on identical individual optomechanical sites. To realize optomechanical lattices that include photon transport, it is imperative that the disorder in the optical (or microwave) cavity is sufficiently small to enable building lattice models.

Superconducting circuit optomechanical systems based on vacuum-gap capacitors (Cicak et al., 2010) are a very promising platform to realize such lattices, and have been employed in a wide range of experiments, including ground-state cooling (J. D. Teufel, Donner, D. Li, et al., 2011), mechanical squeezing (Wollman et al., 2015), entanglement (C. Ockeloen-Korppi et al., 2018; Kotler et al., 2021; Lépinay, C. F. Ockeloen-Korppi, et al., 2021) of mechanical motion, dissipative quantum reservoir engineering (Toth et al., 2017), the realization of hybrid qubit-mechanical systems (Palomaki, Harlow, et al., 2013; Pirkkalainen, Cho, et al., 2013; A. Reed et al., 2017), as well as non-reciprocal microwave devices (Bernier et al., 2017). While microwave planar resonators have been coupled and been used to create topological waveguides (Mirhosseini, Kim, et al., 2018; Kim et al., 2021), it has to date not been possible to realize optomechanical lattices in a similar fashion due to the technical challenge of reliably fabricating multiple vacuum-gap capacitors, with identical mechanical and microwave properties. Here we overcome this challenge and demonstrate circuit optomechanical lattices. We use them to implement a 1D chain with a topological band structure exhibiting topologically protected edge states (Asbóth, Oroszlány, and Pályi, 2016; Ozawa et al., 2019), as well as a 2D honeycomb lattice realizing the strained graphene model with edge states (Pereira, Neto, and Peres, 2009; Naumis et al., 2017; Ni et al., 2008; Rechtsman et al., 2013; Delplace, Ullmo, and Montambaux, 2011). Using the on-site optomechanical interactions, we are able to perform a direct measurement of the collective microwave modeshapes and reconstruct the full

Hamiltonian of such a multimode system, addressing an experimental challenge in large-scale multimode superconducting circuits where only indirect approaches were performed by near field scanning probes (Underwood et al., 2016), laser scanning microscopy (H. Wang et al., 2019; Morvan et al., 2021), or dispersive coupling to qubits (Kim et al., 2021).

## 8.2 Multimode optomechanics in lattices

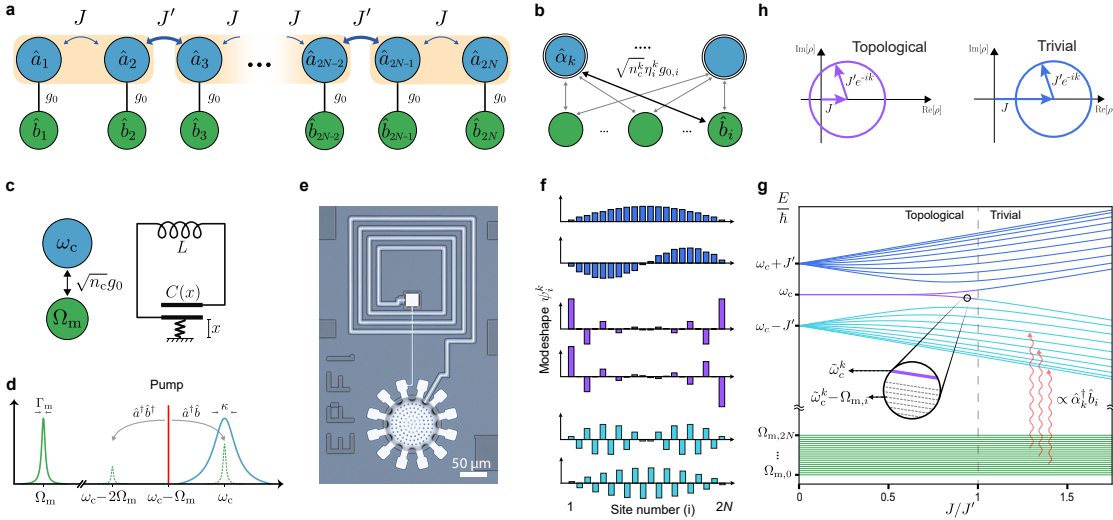


**Figure 8.1: Optomechanical lattices composed of superconducting circuit optomechanical systems.** **a**, Mode diagram of an optomechanical array with staggered mutual couplings demonstrating the Su-Schrieffer-Heeger model. Electromagnetic and mechanical modes are shown by blue and green circles correspondingly. **b**, Equivalent mode diagram in the collective electromagnetic basis. The collective electromagnetic modes are coupled to all the mechanical resonators by the effective optomechanical coupling rates which are proportional to their energy participation ratio,  $\eta_i^k$ . **c**, The equivalent circuit representation of an optomechanical site. **d**, Red-detuned pumping on the lower sideband, generating thermomechanical sidebands **e**, Microscope image of an optomechanical circuit with a mechanically compliant capacitor. **f,g**, Modeshapes and energy levels of a 1D SSH chain versus mutual coupling rates ratio. The optomechanical damping of mechanical oscillator  $i$  can be induced by sideband driving collective electromagnetic mode  $k$ . Collective electromagnetic modeshape examples of the two highest and lowest frequency modes as well as topological edge states shown in **f** are calculated for  $J/J' = 0.5$ . **h**, Off-diagonal element  $\rho(k)$  of the bulk Hamiltonian for the SSH model in the cases of the topological and trivial phases, respectively.

As shown in Fig. 8.1a, we first theoretically consider an arbitrary lattice composed of optomechanical systems, whereby electromagnetic modes are mutually coupled with coupling rates  $J_{ij}$ . Each optomechanical system consists of a mechanical oscillator with a frequency  $\Omega_{m,i}$  and an electromagnetic mode with a frequency  $\omega_{c,i}$ , coupled via radiation-pressure force with a single-photon optomechanical coupling rate  $g_{0,i}$ , where the photon-phonon interaction can be induced by pumping the electromagnetic mode, leading to the effective optomechanical

coupling rate  $g = \sqrt{n_c} g_0$  (Aspelmeyer, T. J. Kippenberg, and Marquardt, 2014), enhanced by the mean intracavity photon number  $n_c$  (see Figs. 8.1c and d). Figure 8.1e shows the physical realization of the optomechanical site in the microwave superconducting circuit platform, consisting of an LC circuit with a mechanically compliant vacuum-gap capacitor (J. D. Teufel, Donner, D. Li, et al., 2011). The Hamiltonian of such a lattice is described by

$$\begin{aligned} \hat{H}/\hbar = & \sum_i \left( \omega_{c,i} \hat{a}_i^\dagger \hat{a}_i + \Omega_{m,i} \hat{b}_i^\dagger \hat{b}_i + g_{0,i} \hat{a}_i^\dagger \hat{a}_i (\hat{b}_i^\dagger + \hat{b}_i) \right) \\ & + \sum_{i \neq j} \left( J_{ij} \hat{a}_i^\dagger \hat{a}_j + J_{ji} \hat{a}_j^\dagger \hat{a}_i \right), \end{aligned} \quad (8.1)$$

where  $\hat{a}_i$  and  $\hat{b}_i$  are the annihilation operators for the electromagnetic and mechanical modes at site  $i$ , respectively. In the weak optomechanical coupling regime, the Hamiltonian of the microwave subsystem is diagonalized by collective microwave modes, described as  $\hat{\alpha}_k = \sum_i \psi_i^k \hat{a}_i$ , where  $\psi_i^k$  is the normalized modeshape of collective microwave mode  $k$  at site  $i$ . Using the collective mode basis, the total Hamiltonian is given by

$$\begin{aligned} \hat{H}/\hbar = & \sum_k \tilde{\omega}_c^k \hat{\alpha}_k^\dagger \hat{\alpha}_k + \sum_i \Omega_{m,i} \hat{b}_i^\dagger \hat{b}_i \\ & + \sum_{k,i} \left( g_{0,i} \cdot \eta_i^k \right) \cdot \hat{\alpha}_k^\dagger \hat{\alpha}_k (\hat{b}_i^\dagger + \hat{b}_i), \end{aligned} \quad (8.2)$$

where  $\tilde{\omega}_c^k$  is the eigenfrequency of collective microwave mode  $k$  and  $\eta_i^k = |\psi_i^k|^2$  is the energy participation ratio of collective microwave mode  $k$  at site  $i$ . As schematically shown in Fig. 8.1b, each collective microwave mode is parametrically coupled to all the mechanical oscillators with the weight of the corresponding participation ratio. Since each mechanical oscillator is locally coupled to the collective microwave modes, the optomechanical interaction can be used as a local probe to perform a microwave modeshape measurement.

When the coupling strengths are designed to be alternating along a 1D chain, the microwave subsystem corresponds to a bosonic SSH chain (Asbóth, Oroszlány, and Pályi, 2016; Ozawa et al., 2019). As shown in Fig. 8.1a, each unit cell consists of two optomechanical building blocks with an intra-cell electromagnetic coupling rate of  $J$ , and is connected with an inter-cell coupling rate of  $J'$ . Solving the two-band Bulk Hamiltonian of an infinite-size SSH chain yields upper and lower passbands (UPB and LPB). There are two topologically distinct phases, for which the transition occurs when the band gap closes at  $J/J' = 1$  (see Fig. 8.1g). For  $J < J'$ , the phase is *topological*, with two *zero-energy* modes emerging in the band gap when the SSH chain is truncated to be a finite system. The zero-energy modes are spatially localized at the edges of the chain, and are hybridized at both the edges for a disorder-free system. Figure 8.1f shows examples of the modeshapes for a few modes from the UPB and LPB, and the two zero-energy modes in the topological phase. The bulk-edge correspondence identifies the two phases by the winding number, which is topologically protected (Asbóth, Oroszlány, and Pályi, 2016; Ozawa et al., 2019). The winding number is a bulk property, defined as the number of times that the off-diagonal element  $\rho(k)$  of the two-band bulk Hamiltonian winds around the

origin of the complex plane, i.e., a chain with a non-zero winding number is in the topological phase, exhibiting the edge states (see Fig. 8.1h and more details in the following section).

### 8.3 Review on SSH model in a 1D bosonic chain

To demonstrate a topological property, we realize the 1D SSH model in our multimode optomechanical system. Here, we report the analysis of J. K. Asbóth, *et al.* (2011) (Asbóth, Oroszlány, and Pályi, 2016) and discuss the topological aspects of the SSH model.

#### 8.3.1 Band structure

The SSH model is constructed by a 1D chain of unit cells individually consisting of two sites ( $A$  and  $B$ ). The two sites in a unit cell are coupled to each other with a coupling strength of  $J$ , while a unit cell is connected to adjacent cells with a strength of  $J'$ , as shown in Fig. 8.2a. To analyze the band structure, we consider a 1D SSH chain with a total cell number of  $N$  and impose a periodic boundary condition on the chain. The Hamiltonian of such a chain is given by

$$\hat{H} = \sum_n (J|n, B\rangle\langle n, A| + J'|n+1, A\rangle\langle n, B| + \text{h.c.}), \quad (8.3)$$

where  $|n, A\rangle$  and  $|n, B\rangle$  denote a state vector at site  $A$  and  $B$  of unit cell  $n$ , respectively. For convenience, the Hamiltonian is described by a tensor product of the intra-cell and inter-cell subsystems, i.e.,

$$\hat{H} = \sum_n (J|n\rangle\langle n| \otimes \hat{\sigma}_+ + J'|n+1\rangle\langle n| \otimes \hat{\sigma}_- + \text{h.c.}), \quad (8.4)$$

where  $|n\rangle$  is a state vector of the inter-cell subsystem and  $\hat{\sigma}_+ = |B\rangle\langle A|$  ( $\hat{\sigma}_- = |A\rangle\langle B|$ ) is a ladder operator describing the intra-cell coupling. Based on Bloch's theorem, we can diagonalize the Hamiltonian of the inter-cell subsystem using a wavenumber basis, which is defined as

$$|k\rangle = \frac{1}{\sqrt{N}} \sum_n e^{ikn} |n\rangle, \quad (8.5)$$

where  $k = 2\pi\nu/N$  ( $\nu = 1, 2, \dots, N$ ) is the wavenumber. Thus, the Hamiltonian can be rewritten as

$$\hat{H} = \sum_k |k\rangle\langle k| \otimes \left[ J\hat{\sigma}_x + J' \left( \hat{\sigma}_+ e^{ik} + \hat{\sigma}_- e^{-ik} \right) \right]. \quad (8.6)$$

Then, the band structure of the 1D chain is obtained as the eigenenergy of the so-called 'bulk Hamiltonian' related to the intra-cell subsystem:

$$\hat{H}(k) = \langle k | \hat{H} | k \rangle \quad (8.7)$$

$$= J\hat{\sigma}_x + J' \left( \hat{\sigma}_+ e^{ik} + \hat{\sigma}_- e^{-ik} \right) \quad (8.8)$$

$$= \begin{pmatrix} 0 & \rho(k) \\ \rho^*(k) & 0 \end{pmatrix}, \quad (8.9)$$

where  $\hat{\sigma}_x$  is the Pauli- $x$  matrix of the intra-cell system. Here, the off-diagonal element  $\rho(k)$  of the bulk Hamiltonian is defined as

$$\rho(k) = J + J' e^{-ik} \equiv |\rho(k)| e^{-i\phi(k)}. \quad (8.10)$$

From the  $2 \times 2$  matrix, the eigen-energy for each wavenumber is obtained as

$$E(k) = \pm |\rho(k)| = \pm \sqrt{J^2 + J'^2 + 2JJ' \cos k} \quad (8.11)$$

with eigenvectors (Bloch wave function) of

$$|u_{k,\pm}\rangle = \frac{1}{\sqrt{2}} \begin{pmatrix} e^{-i\phi(k)} \\ \pm 1 \end{pmatrix}. \quad (8.12)$$

In the thermodynamic limit of  $N \rightarrow \infty$ , the band structure shows upper and lower bands when  $J \neq J'$ , while the two bands are closed at the phase transition point of  $J = J'$  (see the Fig. 8.2b).

### 8.3.2 Bulk-edge correspondence

The bulk-edge correspondence (Delplace, Ullmo, and Montambaux, 2011) reveals the existence of edge states of a truncated 1D SSH chain from the bulk properties of the corresponding infinite chain. More specifically, we can predict the existence from the Zak phase, which is calculated using the eigenvectors of Eq. (8.12) as

$$\mathcal{Z} = i \oint dk \langle u_{k,\pm} | \partial_k | u_{k,\pm} \rangle = \frac{1}{2} \oint dk \partial_k \phi(k), \quad (8.13)$$

where the integration is performed over the first Brillouin zone. Note that the Zak phase is a bulk property, which can be defined in the infinite size limit. The chiral symmetry confirms that the Zak phase is discretized to be  $\pi$  multiplied by an integer. As we will see in the following section, when  $\mathcal{Z} = 0$ , the chain is in the trivial phase, where the truncated chain does not show edge states. On the other hand, when  $\mathcal{Z} = \pi$ , the chain is in the nontrivial topological phase, showing two edge states when the chain is truncated to be a finite system. For the 1D SSH model,  $\mathcal{Z} = 0$  when  $J > J'$  while  $\mathcal{Z} = \pi$  when  $J < J'$ .

Furthermore, the Zak phase can be graphically obtained from the winding number of  $\rho(k)$ . As

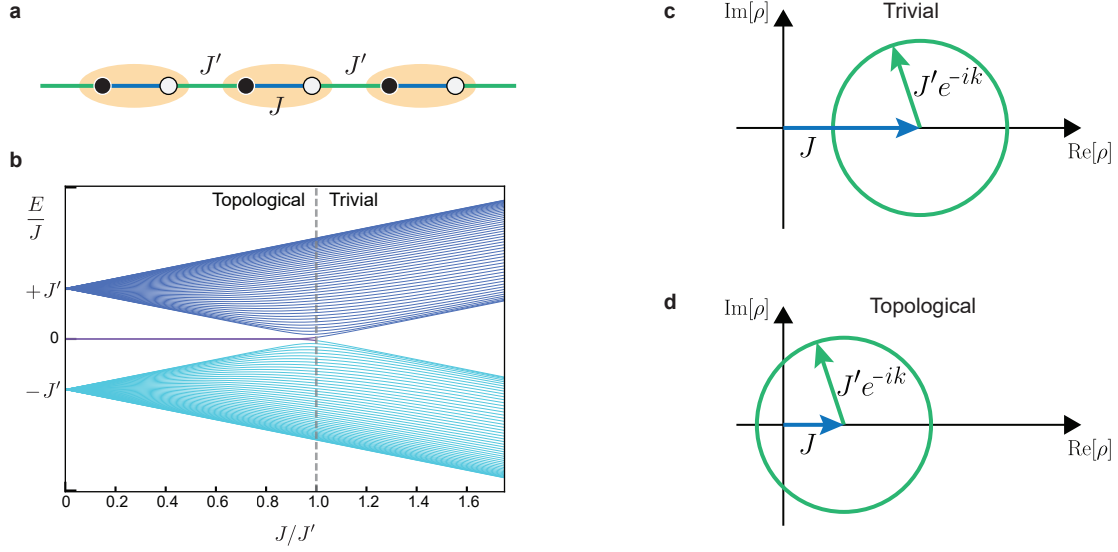


Figure 8.2: **1D SSH model.** **a**, Schematic of a 1D SSH chain. The black and white circles describe sites  $A$  and  $B$ , respectively. **b**, Band structure as a function of the coupling ratio  $J/J'$ . **c,d**, off-diagonal element  $\rho(k)$  in the bulk Hamiltonian in the trivial and topological phase, respectively.

shown in Figs. 8.2c and d, the off-diagonal element  $\rho(k)$  of the bulk Hamiltonian for the trivial and topological cases is described by a closed curve in the complex plane, respectively. The Zak phase is obtained as the product of  $\pi$  and the winding number of the closed curve around the origin. Namely, the existence of edge states is simply determined by whether the closed curve winds around the origin or not for the 1D SSH model.

### 8.3.3 Finite-size effect

Here, we report the analysis presented and introduced by Delplace, *et al.* (2011) (Delplace, Ullmo, and Montambaux, 2011), explaining how the Zak phase can predict the existence of edge states in the 1D SSH model. Then, we discuss the finite-size effects on the prediction. Importantly, the following analysis can be extended to a generalized 1D SSH model, where a 1D chain is constructed by a chain of 2-site unit cells with arbitrary inter-cell couplings that do not break the translational symmetry. Furthermore, the analysis can be valid as long as the inter-cell couplings do not induce the Pauli- $z$  component in the bulk Hamiltonian. This is the case for our 1D SSH model including the second and third nearest-neighbor couplings, as well as a wavenumber-resolved 1D model reduced from a strained graphene ribbon.

When an open boundary condition is imposed on a 1D SSH chain, an eigenstate of the full Hamiltonian can be described by a superposition of two degenerate plane waves. Using Bloch's

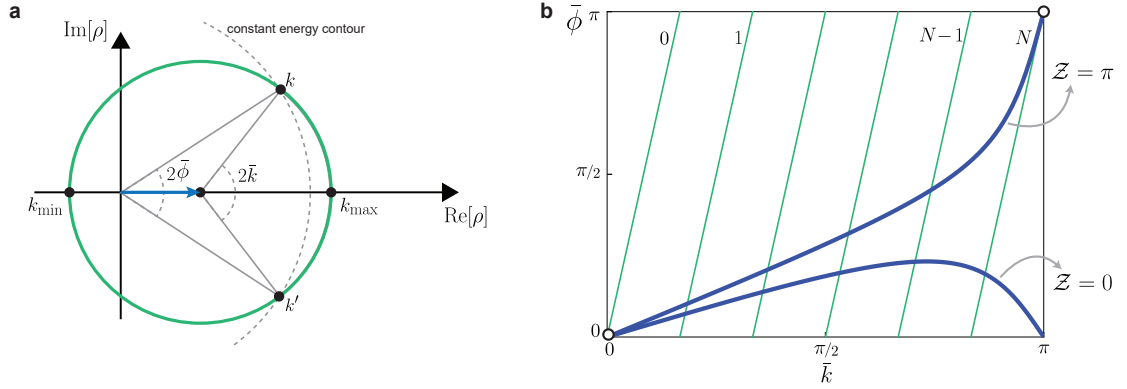


Figure 8.3: **finite-size effect in 1D SSH model.** **a**, off-diagonal element  $\rho(k)$  in the complex plane. Its value corresponding to the maximum and minimum absolute values of the eigen-energy are shown at wavenumbers  $k_{\max}$  and  $k_{\min}$ . The wavenumber  $k$  and  $k'$  that satisfy the degeneracy constraint are found by the two intersections between  $\rho(k)$  and the constant energy contour. **b**,  $(N+1)\bar{k} - \pi j$  (green lines for  $j = 0, 1, \dots, N$ ) and  $\bar{\phi}(\bar{k})$  (blue lines for the cases in the trivial and topological phases, respectively) as a function of  $\bar{k}$ .

theorem, a state vector of a plane wave with an eigen-energy of  $E(k) = \pm|\rho(k)|$  is described by

$$|\psi_k, \pm\rangle = \frac{1}{\sqrt{2N}} \sum_n e^{ikn} \begin{pmatrix} e^{-i\phi(k)} \\ \pm 1 \end{pmatrix} (|n, A\rangle |n, B\rangle). \quad (8.14)$$

Note that there are two degenerate plane waves, except for the maximum and minimum absolute values of eigen-energy. Thus, a trial eigenstate of bulk modes is given by a superposition of  $|\psi_k, \pm\rangle$  and  $|\psi_{k'}, \pm\rangle$  with the constraint of the degeneracy, i.e.,  $E(k) = E(k')$ .

To satisfy the open boundary condition, the trial eigenstate should vanish at the nearest site outside of the chain, that is, at site  $B$  for  $n = 0$  and at site  $A$  for  $n = N + 1$ . These conditions determine a possible wavenumber for bulk modes. The condition at site  $B$  for  $n = 0$  is straightforwardly satisfied by superposing the two plane waves such that  $(|\psi_k, \pm\rangle - |\psi_{k'}, \pm\rangle)/\sqrt{2}$ . Then, the other condition at site  $A$  for  $n = N + 1$  imposes

$$[k(N+1) - \phi(k)] - [k'(N+1) - \phi(k')] = 2\pi j, \quad (8.15)$$

where  $j$  is an integer. By defining  $\bar{k} = \frac{k-k'}{2}$  and  $\bar{\phi}(\bar{k}) = \frac{\phi(k) - \phi(k')}{2}$ , Eq. (8.15) is rewritten as

$$(N+1)\bar{k} - \pi j = \bar{\phi}(\bar{k}). \quad (8.16)$$

Thus, counting the number of the solutions, which is the number of the possible bulk modes, corresponds to counting the number of intersections between  $(N+1)\bar{k} - \pi j$  and  $\bar{\phi}(\bar{k})$  in the range of  $0 < \bar{k} < \pi$ .

For simplicity, we assume that the phase references are determined by the plane wave with the highest absolute value of the eigen-energy such that  $\bar{k} \rightarrow 0$  and  $\bar{\phi}(\bar{k}) \rightarrow 0$  when  $k \rightarrow k_{\max}$ ,



where  $k_{\max}$  is the wavenumber associated with the maximum absolute value of the eigen-energy (see Fig. 8.3a). Moreover, without loss of generality, we can define  $\bar{k}$  to be a positive number. With these conditions,  $\bar{k}$  depends on only  $k$  due to the constraint of  $E(k) = E(k')$ . Then, we systematically find solutions from the wavenumber with the highest absolute value of the eigen-energy ( $\bar{k} = 0$ ) to one with the lowest absolute value of the eigen-energy ( $\bar{k} = \pi$ ) by plotting  $(N + 1)\bar{k} - \pi j$  and  $\bar{\phi}(\bar{k})$ , as shown with an example of the standard 1D SSH case in Fig. 8.3b. While  $\bar{\phi}(0) = 0$  by definition,  $\bar{\phi}(\pi)$  depends on the Zak phase, i.e., while  $\bar{\phi}(\pi) = 0$  if  $\mathcal{Z} = 0$ ,  $\bar{\phi}(\pi) = \pi$  if  $\mathcal{Z} = 1$  (see Fig. 8.3a for the topological case). As shown in Fig. 8.3b, we can always find  $N$  solutions in the range of  $0 < \bar{k} < \pi$  when in the trivial phase ( $\mathcal{Z} = 0$ ), confirming that all the solutions are found in the bulk modes and there are no edge states. On the other hand, when in the nontrivial topological phase ( $\mathcal{Z} = \pi$ ), the function of  $(N + 1)\bar{k} - \pi j$  for  $j = 1, 2, \dots, N - 1$  have an intersection with  $\bar{\phi}(\bar{k})$ , but not for  $j = N$  in the range of  $0 < \bar{k} < \pi$ , for sufficiently large  $N$ . Thus, there are only  $N - 1$  solutions for bulk modes, implying that there is one another mode that is not described by the plane waves, corresponding to an edge state (Delplace, Ullmo, and Montambaux, 2011). Since we can independently apply the same analysis to both the upper and lower bands, there are two edge states in total when  $\mathcal{Z} = \pi$ .

When the system size is large enough, the Zak phase calculation accurately predicts the existence of edge states. However, when the system becomes smaller, the number of solutions of Eq. (8.16) may change. More precisely, even though the condition of  $\mathcal{Z} = \pi$  is satisfied, we can find an intersection between  $(N + 1)\bar{k} - \pi j$  for  $j = N$  and  $\bar{\phi}(\bar{k})$  in the range of  $0 < \bar{k} < \pi$  when the slope of  $\bar{\phi}(\bar{k})$  at  $\bar{k}$  is steeper than  $N + 1$ . Therefore, the slope condition for the existence of edge states is mathematically described as

$$\left| \frac{\partial \bar{\phi}(\bar{k})}{\partial \bar{k}} \right|_{\bar{k}=\pi} < N + 1, \quad (8.17)$$

which is actually satisfied in the example shown in Fig. 8.3b for the case in the topological phase. Furthermore, Eq. (8.17) can be simplified as

$$\left| \frac{\partial \phi(k)}{\partial k} \right|_{k=k_{\min}} < N + 1, \quad (8.18)$$

where we use  $\frac{\partial \phi(k)}{\partial k} = -\frac{\partial \phi(k')}{\partial k'}$  for  $k, k' \rightarrow k_{\min}$ . Here,  $k_{\min}$  is the wavenumber associated with the minimum absolute value of the eigen-energy. Therefore, in order to possess edge states, a 1D SSH chain needs to satisfy two conditions: the condition for the Zak phase ( $\mathcal{Z} = \pi$ ) and the slope condition for  $\phi(k)$  at  $k = k_{\min}$ , described by Eq. (8.18). Note that the slope condition is automatically satisfied in the limit of infinite size ( $N \rightarrow \infty$ ), implying the Zak phase calculation accurately predicts the existence of edge states for a large-size system.

### 8.3.4 Effect of parasitic couplings

In most physical implementations of the SSH model in lattices, parasitic couplings between distanced sites are unavoidable and deviate the actual response of the devices from the

ideal model. In our case, the parasitic couplings arise from the mutual inductance between distanced spiral inductors of LC circuits. The parasitic coupling rate decreased with  $J_{\text{par.}} \propto \frac{1}{l^3}$ , where  $l$  is the effective distance between two spirals. The effect of these higher-order couplings on the band structure, modeshapes, and topological properties of the SSH chains has been studied in several works (L. Li, Z. Xu, and S. Chen, 2014; Pérez-González et al., 2018; Pérez-González et al., 2019). Here we summarize these results and calculate the band structure of the designed devices in the presence of the parasitic coupling.

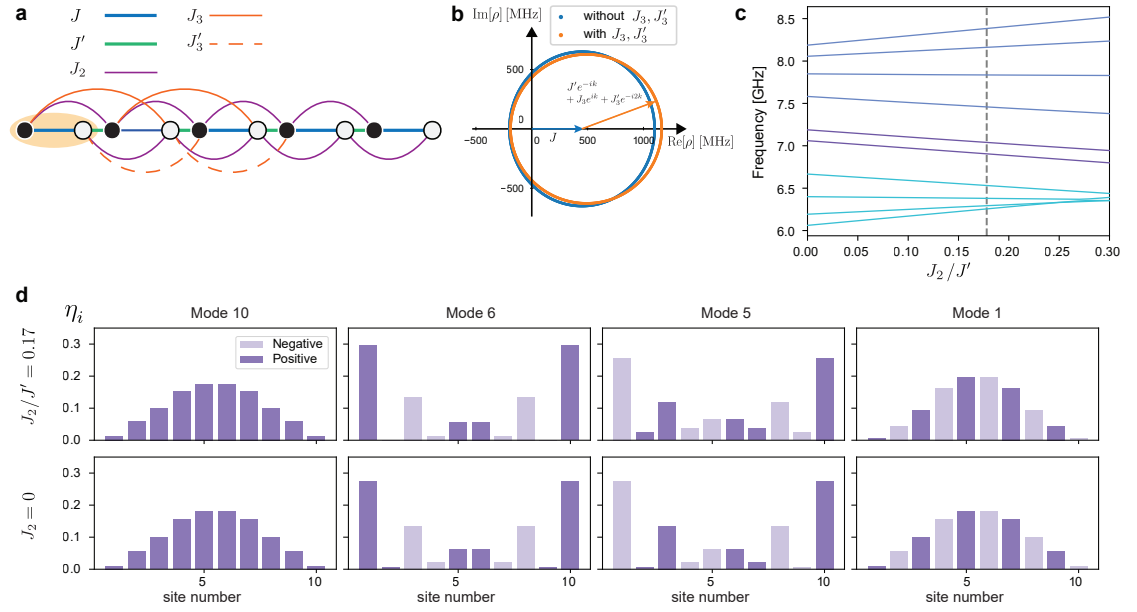


**Figure 8.4: Effect of parasitic couplings on the 1D SSH model.** **a**, Mode diagram of a 1D SSH chain including second and third nearest-neighbor couplings. The black and white circles describe sites  $A$  and  $B$ , respectively. **b**, Off-diagonal element  $\rho(k)$  in the complex plane with and without taking into account the third nearest-neighbor couplings. We use the system parameters of the 1D device presented in Sec. 8.4. **c**, The energy levels (eigenfrequencies) as a function of the relative second nearest-neighbor coupling strength for the 1D SSH chain. The dashed line shows the value of the second nearest-neighbor coupling of the actual devices discussed in Sec. 8.4. Color coding denotes the LPB, edge states and UPB. **d**, Comparison of the modeshapes between an ideal 10-site SSH chain and a chain with the second nearest-neighbor couplings, showing a minor change in the modeshapes.

Figure 8.4a shows the mode diagram including the second and third nearest-neighbor couplings  $J_2$ ,  $J_3$  and  $J'_3$ . In our 1D optomechanical system, the second and third nearest-neighbor couplings are found to be approximately  $J_2/2\pi = 100$  MHz,  $J'_3/2\pi = 37$  MHz and  $J_3/2\pi = 27$  MHz respectively, while the alternating nearest-neighbor couplings are found to be  $J/2\pi = 470$  MHz and  $J'/2\pi = 700$  MHz. Importantly, we can safely assume that the two different second nearest-neighbor couplings are strictly identical due to the geometry of our 1D system. The Hamilto-

nian of a 1D SSH chain including such parasitic couplings is given by

$$\begin{aligned}\hat{H} = \sum_n [ & J|n, B\rangle\langle n, A| + J'|n+1, A\rangle\langle n, B| \\ & J_2|n+1, A\rangle\langle n, A| + J_2|n+1, B\rangle\langle n, B| \\ & J_3|n+1, B\rangle\langle n, A| + J'_3|n+2, A\rangle\langle n, B| \\ & + \text{h.c.}].\end{aligned}\quad (8.19)$$

Since the parasitic couplings does not distort the translational symmetry, we can apply Bloch's theorem using the wavenumber basis defined as Eq. (8.5), and obtain the bulk Hamiltonian as

$$\hat{H}(k) = \begin{pmatrix} \epsilon(k) & \rho(k) \\ \rho^*(k) & \epsilon(k) \end{pmatrix}, \quad (8.20)$$

where

$$\rho(k) = J + J'e^{-ik} + J_3e^{ik} + J'_3e^{-i2k} \equiv |\rho(k)|e^{-i\phi(k)} \quad (8.21)$$

and

$$\epsilon(k) = J_2 \cos(k). \quad (8.22)$$

The second nearest-neighbor couplings modify the diagonal elements of the bulk Hamiltonian, not inducing a component of the Pauli- $z$  matrix but only the identity matrix. This is because the two different second nearest-neighbor couplings, which, in general, may differ, are identical in our 1D system. As a result, we can diagonalize the Bulk Hamiltonian with eigenvectors in the same form as Eq. (8.12) and apply the same analysis as the ideal 1D SSH model in order to predict the existence of edges states. On the other hand, the third nearest-neighbor couplings modify the off-diagonal element  $\rho(k)$ .

In Fig. 8.4b, we plot  $\rho(k)$  in the complex plane, using the experimentally obtained coupling strengths with and without taking into account the third nearest-neighbor couplings. Since the third nearest-neighbor couplings are negligible in our 1D optomechanical system, the winding number is found to be 1 for both the cases. As long as it shows a well-defined band gap ( $J_2 < J'/2$ ), the 1D SSH chain with the non-trivial winding number possess edges modes (Pérez-González et al., 2018). This is the case for the 1D optomechanical chain presented in Sec.8.4.

Furthermore, we numerically study the effect of parasitic couplings on the eigen-energies and modes in the SSH model. For simplicity, we here neglect the third nearest-neighbor couplings. Figure 8.4c shows the energy levels as a function of the relative second nearest-neighbor coupling strength for our 1D SSH chain. The second nearest-neighbor coupling breaks the symmetry of the band structure resulting in a wider UPB and narrower LPB (Pérez-González et al., 2018), while the edge states splitting and the band gap is barely affected. Figure 8.4e shows the modes of an ideal 10-site SSH chain and a chain with the second nearest-neighbor couplings, respectively. The second nearest neighbor couplings of our 1D

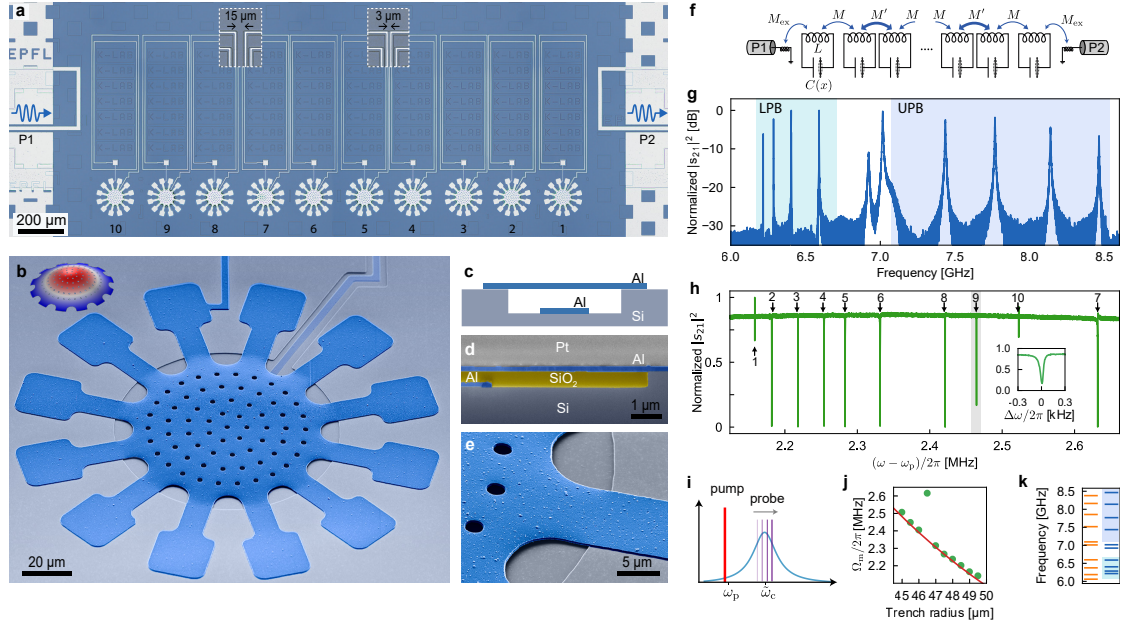


Figure 8.5: **Superconducting circuit optomechanical chain realizing the 1D SSH model.** **a**, Microscope image of a 10-site circuit optomechanical chain. The mutual coupling is controlled by the spacing between adjacent spiral inductors (see insets). The chain is inductively coupled at both edges to co-planar waveguides. **b**, SEM of a mechanically compliant vacuum-gap capacitor. The inset shows the FEM simulation of the fundamental mechanical mode of the vibrating plate. **c**, Schematic cross-section of the capacitor. **d**, Focused ion beam cross-section of a capacitor before removing the SiO<sub>2</sub> sacrificial layer (Pt is used as the FIB protective layer). **e**, SEM of a suspended clamp over the trench. **f**, Equivalent circuit diagram of the SSH chain. **g**, Transmission spectrum of the device shown in **a**. Two topological edge modes are observed in the gap of the two bands (shaded regions), which are numerically calculated for the corresponding infinite SSH chain including parasitic couplings (see Sec. 8.3.4). **h**, Optomechanical induced transparency (OMIT) response of the highest frequency collective microwave mode. Each OMIT feature is associated to one of the drumhead capacitors along the chain, identified by the mechanical frequency. **i**, Frequency scheme for the OMIT measurement. **j**, Measured mechanical frequencies versus the trench radius (green dots). The solid line shows the inverse linear fit. One mechanical resonance is off due to an unusual deformation of the capacitor after the release. **k**, Microwave resonance frequencies of the device, design targets (orange), and measured values (blue).

device do not significantly change the modeshapes.

## 8.4 Circuit optomechanical lattices

The main challenge of implementing such circuit optomechanical lattices is the low reproducibility of the gap size of vacuum-gap capacitors. The non-flat geometry of the movable capacitor plate (Cicak et al., 2010) prevents accurate control of the gap size and consequently

the mechanical and microwave frequencies, as well as their coupling strength.

To overcome this challenge, we developed a nanofabrication process that significantly improves reproducibility and controllability over the gap size. We realize a flat aluminum membrane as the movable capacitor plate suspended over a trench (Figs. 8.5b, c, and d). In brief, we first etch a trench in a silicon substrate and cover it with a  $\text{SiO}_2$  sacrificial layer. We then planarize the oxide layer to remove the topography and deposit the flat top plate of the capacitor. Finally, by removing the sacrificial layer, the top plate is suspended (see Figs. 8.5b and e). Cooling down of the device induces a tensile stress in the Al thin film, which guarantees the flatness and consequently the gap size to be controlled by the trench depth (see chapter 4 for details). This high-yield process allows us to control microwave and mechanical resonance frequencies with fluctuations of less than 0.5% and 1% respectively (see Sec.8.5 for details). Moreover the approach benefits from low mechanical dissipation  $\Gamma_m/2\pi \sim \mathcal{O}(1 - 10)$  Hz (see Sec.8.10.3 for the full characterizations).

To realize a circuit optomechanical 1D SSH chain in the topological phase (Fig. 8.1a), we fabricated a 10-site chain of mechanically compliant LC resonators with alternating mutual inductive coupling controlled by their physical distance (Figs.8.5a, and f). The gap size is fabricated to be 245 nm, which results in a microwave frequency of  $\omega_c/2\pi = 7.12$  GHz and a single-photon optomechanical coupling rate of  $g_0/2\pi = 10$  Hz for all sites. The microwave coupling rates are designed to be  $J/2\pi = 470$  MHz and  $J'/2\pi = 700$  MHz to achieve the non-trivial topological phase.

Figure 8.5g shows the microwave transmission spectrum of the chain, the UPB and LPB are highlighted by the shaded areas, and two topological edge modes can be observed in the middle of the band gap. The transmission response is in good agreement with the calculated eigenfrequencies of the desired design (Fig. 8.5k), which indicates reliable control over the system parameters in the fabrication process. The linewidth of the modes varies from 7 MHz for the edge modes to 80 kHz for the first LPB mode depending on the collective modeshape. The asymmetry of the band structure in the transmission spectrum originates from the small parasitic mutual inductive coupling between sites beyond the nearest neighbor (see Sec.8.3.4) and does not change the topological properties of the chain (L. Li, Z. Xu, and S. Chen, 2014).

In order to identify each site by its mechanical frequency, we gradually increment the trench radius by 500 nm along the chain to distinguish them in the further measurements (see Figs. 8.5b inset). The mechanical frequencies can be measured using optomechanically induced transparency (OMIT) (Weis et al., 2010) by applying a microwave pump red-detuned from a collective microwave mode while sweeping a weak probe tone across the resonance, as shown in Fig. 8.5i. Figure 8.5h shows the OMIT response of the highest bulk mode. We observe ten OMIT features indicating mechanical frequencies, matching the inverse trench radius relationship (Fig. 8.5j).

### 8.4.1 Device design considerations

The mechanical frequency of the first fundamental mode of a drumhead resonator can be approximated as  $\Omega_m \simeq \frac{2.4}{R} \sqrt{\frac{\sigma^{\text{Al}}}{\rho^{\text{Al}}}}$  where  $R$  is the radius of the drumhead (radius of the circular trench as fixed mechanical boundary condition) and  $\sigma^{\text{Al}}$ ,  $\rho^{\text{Al}}$  are the stress and the density of the Al thin film (refer to Sec. 3.2 for comprehensive discussion on the drumhead mechanical mode). In the device, we gradually change the trench radius of different sites by 500 nm (1%) to distinguish them in the mode-shape measurement experiment by their mechanical frequency. It is important to mention that the mechanical frequency disorder in the fabrication process should be smaller than the mechanical frequency shift introduced by incrementing trench radius in order to keep them in the correct designed order. This can be verified by comparing the measured mechanical frequencies from OMIT response and the theoretical  $\Omega_{m,i} \propto \frac{1}{R_i}$  relation from the design, as shown in Fig. 8.5j and Fig. 8.14d. We note that this slight variation on the trench radius does not have a significant effect on the electrical boundary conditions of the capacitor, given that the bottom plate of the capacitor only sees  $\approx 20\%$  of the center top plate's area and thus does not perturb the microwave resonance frequencies of the LC circuits,  $\omega_c = 1/\sqrt{LC}$ .

To probe the system, the two ends of the chain are inductively coupled to coplanar waveguides using two short-circuited inductive loop couplers. The external coupling rate to the outermost sites is designed to be comparably smaller than internal microwave couplings in the chain to avoid deviation from the ideal SSH model (See Fig. 3.6).

### 8.4.2 Device fabrication

A detailed description of each step can be found in chapter 4. To briefly summarize the process here we mention important steps. We define a trench in the substrate containing the bottom plate of the capacitor. The trench then is covered by a thick  $\text{SiO}_2$  sacrificial layer, which inherits the same topography of the layer underneath. To remove this topography and obtain a flat surface, we use chemical mechanical polishing (CMP) to planarize the  $\text{SiO}_2$  surface. We then etch back the sacrificial layer down to the substrate layer Using ion beam etching. We create openings in the sacrificial layer for the top-bottom galvanic connection and then deposit the top Al plate of the capacitor. Although after the release of the structure by HF vapor etching of  $\text{SiO}_2$  the drumhead will buckle up due to the compressive stress, at cryogenic temperatures the high tensile stress ensures the flatness of the top plate. This will guarantee the gap size is precisely defined by the depth of the trench and the thickness of the bottom plate.

## 8.5 Optomechanical modeshape measurement

Next, we exploit mechanical oscillators as embedded probes to directly and non-perturbatively measure the collective microwave modeshapes. We use the optomechanical damping ef-



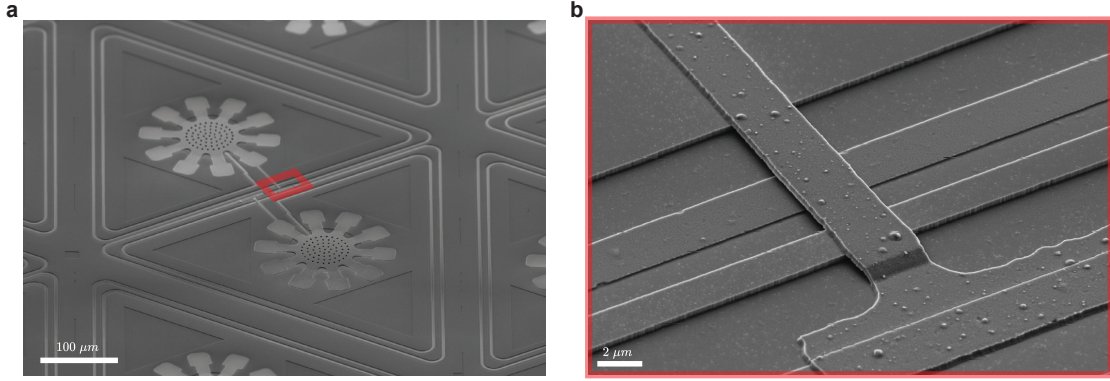


Figure 8.6: **Example of a honeycomb lattice and the galvanic connection in the circuit.** **a**, SEM micrograph of the triangular building blocks of the honeycomb lattice. **b**, The galvanic connection of top and bottom Al layers and the crossovers of the spiral inductor.

fect (Aspelmeyer, T. J. Kippenberg, and Marquardt, 2014) to deduce the modeshape information ( $\eta_i^k$ ) from the mechanical oscillator's dynamics. In the sideband resolved regime ( $\kappa_{\text{tot}}^k \ll \Omega_{m,i}$ ), the effective damping rate of mechanical mode  $i$ , in the presence of a pump on the lower sideband for collective microwave mode  $k$ , is given by

$$\Gamma_{\text{eff},i}^k = \Gamma_{m,i} + n_c^k \frac{4(\eta_i^k \cdot g_{0,i})^2}{\kappa_{\text{tot}}^k}, \quad (8.23)$$

where  $\Gamma_{m,i}$  is the bare mechanical damping rate,  $n_c^k$  and  $\kappa_{\text{tot}}^k$  are the photon number and the linewidth of the collective mode, respectively. In a time-domain protocol, we apply an excitation pulse on resonance to generate a beat note with a pump red detuned by  $\Omega_{m,i}$  (Fig. 8.7b) and selectively excite mechanical mode  $i$  (the disorder in  $\Omega_{m,i}$  from the designed value is smaller than the mechanical frequency increment to ensure correct identification of sites in the lattice). We then measure the ringdown signal of the optomechanical sideband in the presence of the red-detuned pump. The slope of  $\Gamma_{\text{eff},i}^k$  as a function of the pump power is proportional to  $(\eta_i^k)^2$ , as shown in Eq. 8.23. Figure 8.7c shows the ringdown data sets for a few mechanical modes in the chain measured on the highest UPB mode. By measuring the effective damping rate of every site in the chain, the full modeshape can be extracted for the corresponding microwave mode. Although it is challenging to independently obtain several parameters in Eq. 8.23, such as  $g_{0,i}$  and  $n_c^k$ , we can extract  $\eta_i^k$  from all the slopes of  $\Gamma_{\text{eff},i}^k$  by using the normalization condition of the modeshapes, i.e.,  $\sum_k \eta_i^k = \sum_i \eta_i^k = 1$  (see Sec. 8.5.2 for details). Figure 8.7e shows the full result of the modeshape characterization on the 10-site chain compared with the theoretical values with the design parameters. The data is in excellent agreement with the theoretical predictions, demonstrating bulk modes in UPB, LPB, and topologically protected edge modes.

In prior experimental realizations of the SSH model, non-hybridized topological edge states were observed (Kim et al., 2021; St-Jean et al., 2017) (localized on only one side of the chain).



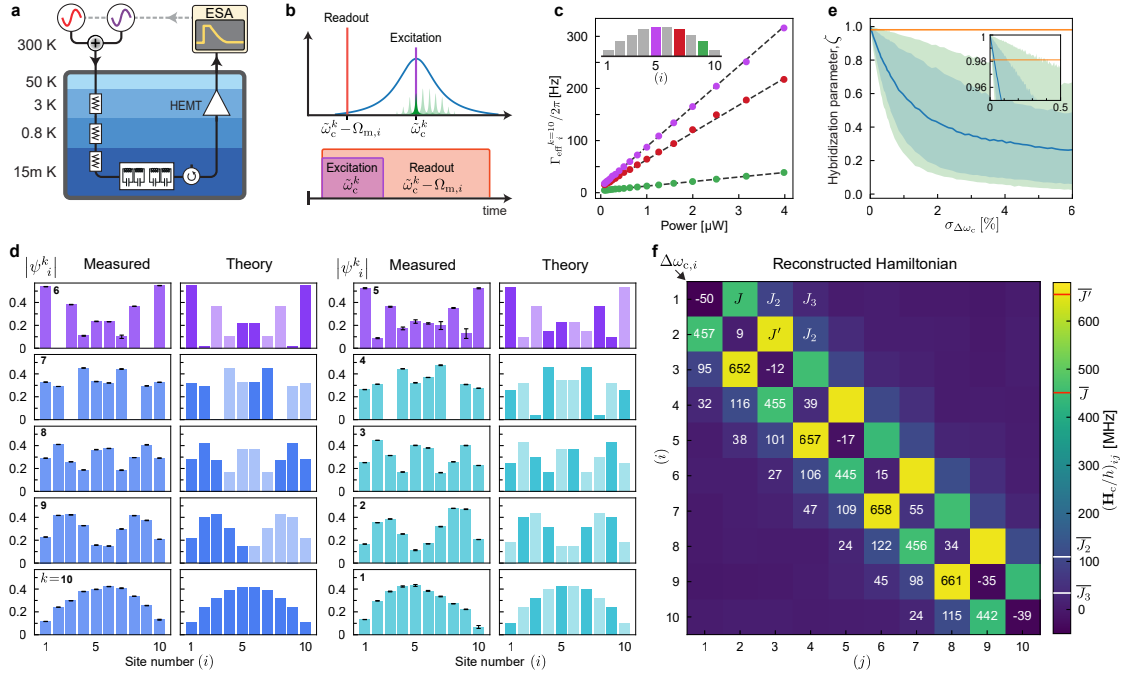


Figure 8.7: **Optomechanical modeshape measurement and Hamiltonian reconstruction of a topological SSH chain.** **a**, Experimental setup for the modeshape measurement. **b**, Frequency and pulsing scheme: each mechanical mode is selectively excited by a resonant cavity drive while a readout pump on the lower sideband is on. **c**, Effective mechanical damping rate of the specific sites shown in the inset while driving the highest UPB mode. The slope of the linear fits depends on the collective modeshape. **d**, Measured and corresponding theoretical modeshapes of UPB, topological edge states, and LPB. Error bars are shown in black. In the theory plots, the sign of the phases is represented by different brightness. **e**, Stochastic analysis of the cavity frequency disorder effect on edge state hybridization, quantified by  $\zeta$ . The blue line shows the expected value, blue and green shades reflect 70% and 90% certainty ranges, and the orange line shows the measured value. **f**, Reconstructed Hamiltonian matrix of the microwave subsystem in the rotating frame of the averaged cavity frequency. The diagonal elements show the cavity frequency disorder, and off-diagonal ones show the nearest-neighbor couplings ( $J, J'$ ) as well as the parasitic couplings between distanced sites ( $J_2, J_3$ , etc.).

The edge state hybridization strongly depends on the disorder in the system parameters. Here, in contrast, we observe fully hybridized topological edge states, indicating minimal frequency disorder in the fabrication process. We perform numerical stochastic analysis to study the effect of disorder in the bare cavity frequency on the hybridization of the edge modes, quantified by  $\zeta$  (see the definition in Sec. 8.6). Figure 8.7e shows the expected value of  $\zeta$  versus the standard deviation of the disorder  $\sigma_{\Delta\omega}$ , indicating less than 0.3% disorder in the experimentally realized chain (see Sec. 8.6 for details).

Finally, considering the knowledge of all the eigenvectors ( $\psi_i^k$ , modeshapes) and eigenvalues ( $\bar{\omega}_c^k$ , collective microwave frequencies) of the system, we can reconstruct the actual Hamiltonian

nian of the microwave subsystem in the basis of the physical sites:

$$\mathbf{H}_c / \hbar = \mathbf{U}_\psi^\dagger \begin{bmatrix} \tilde{\omega}_c^1 & & 0 \\ & \ddots & \\ 0 & & \tilde{\omega}_c^{2N} \end{bmatrix} \mathbf{U}_\psi \quad (8.24)$$

where  $[\mathbf{U}_\psi]_{k,i} = \psi_i^k$  is a unitary matrix obtained from the measured participation ratios. Since our measurement protocol does not retrieve the phase of the eigenvectors, we infer it from the theoretically calculated ones. To more accurately reconstruct the Hamiltonian, we correct the unitary matrix by further imposing the orthogonality condition (see Sec. 8.5.3 for details). Figure 8.7f shows the reconstructed Hamiltonian of the 1D SSH device. The diagonal elements represent the cavity frequency disorder of each site ( $\sigma \Delta_\omega = 0.5\%$  corresponds to a 2 nm gap size variation), while off-diagonal elements show the alternating microwave couplings as designed for the SSH model and parasitic second and third nearest neighbor couplings between distanced sites.

### 8.5.1 Extraction of participation ratio from optomechanical damping rate

As discussed earlier, we introduce a new technique to characterize the participation ratio  $\eta_i^k$  and consequently the microwave collective modes by measuring the optomechanical damping rate of mechanical mode  $i$  coupled to collective mode  $k$ . From Eqs. (2.63), the optomechanical damping rate (Aspelmeyer, T. J. Kippenberg, and Marquardt, 2014) is given by

$$\Gamma_{\text{opt},i}^k = n_{c,i}^k \left( \eta_i^k g_{0,i} \right)^2 \left( \frac{\kappa_{\text{tot}}^k}{\left( \Omega_{m,i} - \Delta_i^k \right)^2 + \kappa_{\text{tot}}^k / 4} - \frac{\kappa_{\text{tot}}^k}{\left( \Omega_{m,i} + \Delta_i^k \right)^2 + \kappa_{\text{tot}}^k / 4} \right), \quad (8.25)$$

where

$$n_{c,i}^k = |\langle \hat{a}_k \rangle|^2 = \frac{\dot{n}_d^k \kappa_1^k}{\Delta_i^{k2} + \kappa_{\text{tot}}^k / 4}$$

is the average photon number in collective mode  $k$ , where  $\dot{n}_d^k$  is the on-chip photon flux. This yields the total effective damping rate of mechanical mode  $i$ :

$$\Gamma_{\text{eff},i}^k = \Gamma_{m,i} + \Gamma_{\text{opt},i}^k. \quad (8.26)$$

To extract the optomechanical damping effect, we can linearly change the drive power generated by a microwave source. Here, we define the transmittance between the microwave source at room temperature and the device as  $R^k = \dot{n}_d^k / \dot{n}_d$ , where  $\dot{n}_d$  is the photon flux at the output of the microwave source. The frequency dependence of the input wiring and components is weak and we assume that the transmittance depends only on  $k$ , but not on  $i$ . Then, we obtain

$\partial \Gamma_{\text{eff},i}^k / \partial n_d$ , the slope of the total damping rate with respect to the photon flux  $\dot{n}_d$ .

From Eq. (8.25), the slope of the total mechanical damping rate is analytically obtained as

$$\frac{\partial \Gamma_{\text{eff},i}^k}{\partial n_d} = \frac{\kappa_1^k R^k (\eta_i^k g_{0,i})^2}{\Delta_i^{k^2} + \kappa_{\text{tot}}^{k^2} / 4} \left( \frac{\kappa_{\text{tot}}^k}{(\Omega_{m,i} - \Delta_i^k)^2 + \kappa_{\text{tot}}^{k^2} / 4} - \frac{\kappa_{\text{tot}}^k}{(\Omega_{m,i} + \Delta_i^k)^2 + \kappa_{\text{tot}}^{k^2} / 4} \right). \quad (8.27)$$

From this equation, we experimentally obtain the un-normalized participation ratio  $(\sum_k \text{or } i \widetilde{\eta}_i^k \neq 1)$  as

$$\widetilde{\eta}_i^k = \sqrt{\frac{\partial \Gamma_{\text{eff},i}^k}{\partial n_d} (\Delta_i^{k^2} + \kappa_{\text{tot}}^{k^2} / 4) \left( \frac{\kappa_{\text{tot}}^k}{(\Omega_{m,i} - \Delta_i^k)^2 + \kappa_{\text{tot}}^{k^2} / 4} - \frac{\kappa_{\text{tot}}^k}{(\Omega_{m,i} + \Delta_i^k)^2 + \kappa_{\text{tot}}^{k^2} / 4} \right)^{-1}}. \quad (8.28)$$

By definitions in Eqs. (8.27) and (8.28), the relation between the normalized and un-normalized participation ratios is described as

$$\widetilde{\eta}_i^k = g_{0,i} \eta_i^k \sqrt{\kappa_1^k R^k}. \quad (8.29)$$

### 8.5.2 Iterative normalization

In principle, the participation ratio  $\eta_i^k$  can be determined by normalizing Eq. (8.29) with  $g_{0,i}$ ,  $\kappa_1^k$  and  $R^k$  that would be obtained independently. However, the local optomechanical coupling  $g_{0,i}$  can not be straightforwardly measured in such a multimode optomechanical system. Furthermore, it is also not trivial to determine  $\kappa_1^k$  and  $R^k$  using the conventional microwave setups in the transmission configuration, since it is difficult to differentiate the input contribution to the output one.

Nevertheless, we can determine  $\eta_i^k$  from experimentally-obtainable  $\widetilde{\eta}_i^k$  based on the normalization conditions of the unitary transformation (Eqs. (2.55) and (2.56)). Here, we apply an iterative normalization method for  $\widetilde{\eta}_i^k$  as follows. We first define the initial un-normalized participation ratio as

$$\widetilde{\eta}_{i(0)}^k = \widetilde{\eta}_i^k. \quad (8.30)$$

Then, we iterate the normalization process in the row and column axes alternatively. Namely, the un-normalized participation ratio  $\widetilde{\eta}_{i(n)}^k$  at step  $n$  is updated in each normalization step to  $\widetilde{\eta}_{i(n+1)}^k$  as

$$\widetilde{\eta}_{i(n+1)}^k = \frac{\widetilde{\eta}_{i(n)}^k}{\sum_i \widetilde{\eta}_{i(n)}^k} \quad (\forall k, \text{ if } n \text{ is even}) \quad (8.31)$$

or

$$\widetilde{\eta}_{i(n+1)}^k = \frac{\widetilde{\eta}_{i(n)}^k}{\sum_k \widetilde{\eta}_{i(n)}^k} \quad (\forall i, \text{ if } n \text{ is odd}). \quad (8.32)$$

In the iterative normalization method, the un-normalized participation ratio at step  $n$  can be always described as

$$\widetilde{\eta}_{i(n)}^k = C_{i(n)} \eta_i^k D_{k(n)}, \quad (8.33)$$

where  $C_{i(n)}$  and  $D_{k(n)}$  are coefficients depending only on either  $i$  or  $k$ , respectively. Importantly, each normalization process updates only the coefficients  $C_{i(n)}$  and  $D_{k(n)}$  without any changes in  $\eta_i^k$ . This can be easily confirmed from Eqs. (8.31) and (8.32).

Here, we numerically confirm that both  $C_{i(n)}$  and  $D_{k(n)}$  converge to 1, i.e.,  $\widetilde{\eta}_{i(n)}^k \rightarrow \eta_i^k$  with an sufficiently large number of the iteration. For this purpose, we prepare a random  $N \times N$  unitary matrix  $\mathbf{U}$  and obtain the participation ratio as  $\eta_i^k = |[\mathbf{U}]_{k,i}|^2$ . In addition, we prepare random coefficients  $0 < C_i < 1$  and  $0 < D_k < 1$  and artificially generate the un-normalized participation ratio as  $\widetilde{\eta}_i^k = C_i \eta_i^k D_k$  to simulate the un-normalized participation ratio. The task is to deduce  $\eta_i^k$  from  $\widetilde{\eta}_i^k$ . We apply the iterative normalization method to the un-normalized participation ratio. As an evaluation function, we define the averaged relative error of the un-normalized participation ratio at  $n$  step compared with the original one as

$$\varepsilon = \frac{\sum_{i,k} |\widetilde{\eta}_{i(n)}^k - \eta_i^k| / \eta_i^k}{N^2}. \quad (8.34)$$

In Fig. 8.8, we plot the averaged relative error  $\varepsilon$  at each iteration step for 1000 different data sets. From these results, we confirm that the un-normalized participation ratio converges to the original one, i.e.  $\widetilde{\eta}_{i(n)}^k \rightarrow \eta_i^k$  when the number of the iteration is sufficiently large.

### 8.5.3 Orthogonalization of modeshapes

Our measurement scheme does not retrieve the sign of the modeshapes of the collective microwave modes to fully determine the unitary matrix  $\mathbf{U}_\psi$ , which is necessary for the Hamiltonian reconstruction. By inferring the phase information from the theoretical modeshapes, we can construct the “unitary” matrix  $\tilde{\mathbf{U}}_\psi$  from  $\eta_i^k$  as

$$[\tilde{\mathbf{U}}_\psi]_{k,i} = +\sqrt{\eta_i^k} \quad \text{or} \quad -\sqrt{\eta_i^k}. \quad (8.35)$$

While it satisfies the normalization conditions, the obtained matrix does not satisfy the orthogonalization condition due to the finite measurement error. To more accurately reconstruct the Hamiltonian, we further correct  $\tilde{\mathbf{U}}_\psi$  to satisfy both the normalization and orthogonalization

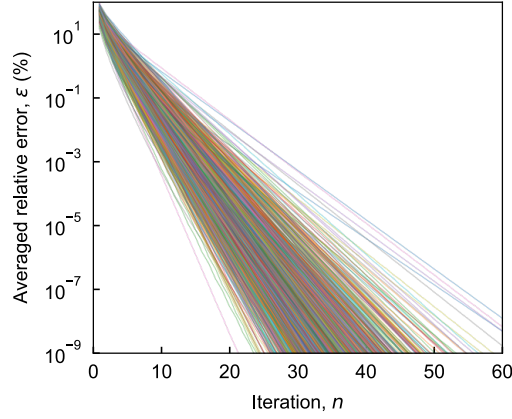


Figure 8.8: **Numerical justification of iterative normalization method.** The averaged relative error of the un-normalized participation ratio compared with the original participation ratio as a function of step  $n$  of the iterative normalization. Each different-colored line corresponds to a different dataset. The system size is chosen to be  $N = 10$ .

conditions. We first numerically calculate the generator of  $\tilde{\mathbf{U}}_\psi$  as

$$\mathbf{G} = \log(\tilde{\mathbf{U}}_\psi). \quad (8.36)$$

In general, the generator can be decomposed into a Hermitian matrix  $\mathbf{H}$  and anti-Hermitian matrix  $\tilde{\mathbf{H}}$  as

$$\mathbf{G} = \mathbf{H} + \tilde{\mathbf{H}}, \quad (8.37)$$

where  $\mathbf{H} = (\mathbf{G} + \mathbf{G}^\dagger)/2$  and  $\tilde{\mathbf{H}} = (\mathbf{G} - \mathbf{G}^\dagger)/2$ . Although the generator of a unitary matrix only contains an anti-Hermitian matrix, the experimentally obtained  $\mathbf{G}$  contains the finite Hermitian component. By neglecting the Hermitian component, the corrected unitary matrix can be obtained as

$$\mathbf{U}_\psi = \exp(\tilde{\mathbf{H}}), \quad (8.38)$$

which is used for the Hamiltonian reconstruction.

#### 8.5.4 Modeshape extraction methods comparison

As explained in section 8.5.1, to extract the modeshapes we have to go through at least one normalization step.

$$\widetilde{\eta}_i^k \rightarrow \frac{\widetilde{\eta}_i^k}{\sum_i \widetilde{\eta}_i^k} \quad \forall k$$

This step is very intuitive as we are summing over all sites ( $i$ ) in a given collective mode ( $k$ ): the total input power gets distributed along the sites according to their participation ratio  $\eta_i^k$ , and all the participation ratios in a given collective mode must sum up to 1.

Next, we make use of the normalization conditions of the unitary matrix, and perform the iterative normalization process described in section 8.5.1. These are the modeshapes presented in Figs. 8.7 and 8.14.

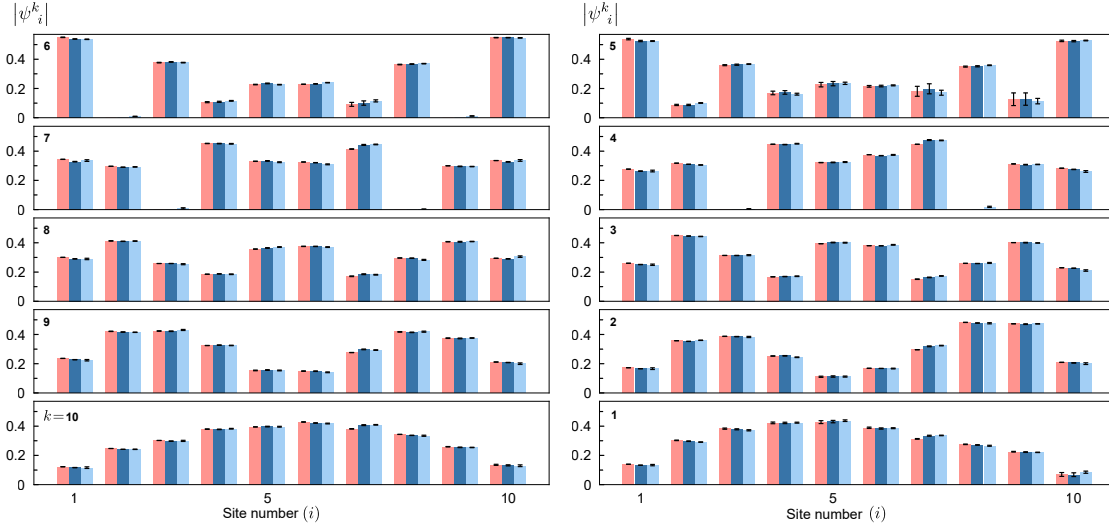


Figure 8.9: **Three different modeshape extraction methods comparison.** The red bars are with the single-step normalization for each collective mode. The dark blue bars are with the iterative normalization method (presented in Sec.8.5.2). The light blue bars are modeshapes corrected based on the orthogonalization property of the unitary matrix.

As described in Sec. 8.5.3, in order to accurately reconstruct the Hamiltonian shown in Fig. 8.7, the modeshapes obtained from the iterative normalization method are further corrected based on the orthogonalization property of the unitary matrix, providing the modeshapes satisfying both the normalization and orthogonalization conditions. In Fig. 8.9 we present the evolution of the modeshapes along these three steps.

Collective mode, $i$	10	9	8	7	6	5	4	3	2	1
$1 - F(\psi_i^R, \psi_i^N) [\times 10^{-3}]$	0.8	0.6	0.4	1.2	0.3	0.5	1.2	0.3	0.6	0.6
$1 - F(\psi_i^N, \psi_i^{N,O}) [\times 10^{-3}]$	0.06	0.3	0.5	0.4	0.7	1.3	0.7	0.4	0.2	0.5

Table 8.1: Infidelities between different subsequent normalization methods

To verify that our iterative normalization method does not perturb the modeshapes we compute the infidelities  $1 - F(\psi_i, \psi_i')$ , where  $F(\psi_i, \psi_i') = |\langle \psi_i | \psi_i' \rangle|^2$ , between the same mode with different normalization methods. Table 8.1 shows the comparison between a one-step (site-wise) normalization as the raw data,  $\psi_i^R$ , and the iterative normalization process,  $\psi_i^N$ . It also shows the comparison between the iterative normalization method,  $\psi_i^N$ , and the modeshapes

computed from the orthogonalization after iterative normalization,  $\psi_i^{N,O}$ , (introduced in the Sec.8.5.3). The small infidelities calculated demonstrates the minimal disorder in the system parameters.

Collective mode	10	9	8	7	6	5	4	3	2	1
$1 - F(\psi_i^N, \psi_i^{th}) [\times 10^{-3}]$	2.1	2.2	1.5	0.3	1.4	4.6	5.4	4.2	17	17

Table 8.2: Infidelities between the measured modes and the theoretical ones

For completeness, in table 8.2 we also report the infidelities between the experimental modes (iterative normalization,  $\psi_i^N$ ) and the theoretical ones,  $\psi_i^{th}$ , presented in Fig. 8.9.

### 8.5.5 Statistical analysis of orthogonality and measurement error

We discussed the optomechanical modeshape measurement technique in Sec.8.5 to directly extract the eigenmodes (eigenvectors of the system Hamiltonian). In Sec.8.5.2, we explained the iterative normalization method used to extract the modes without the need to measure some hardly-accessible parameters of our system. To check the accuracy of our measurements and quantitatively verify the orthogonality of the modes as eigenstates of the system, we show the inner product of every pair of modes,  $|\sum_i \psi_i^{*k} \psi_i^l|$  in Fig. 8.10a,b for 10 site 1D chain as well as 24 site honeycomb lattice. Since the measurement does not retrieve the phase in the modes (i.e. positive or negative signs because such a system always results in real eigenvector and eigenvalues), we inferred the phases from the theoretical modeshape estimates. As it is shown in the figure, the 1D dataset manifests high orthogonality with a maximum  $\sim 3\%$  inner product. The 2D dataset also shows small values except for a single mode (mode 17) which has a non-zero product with a few other modes. As a figure-of-merit, the average value of all inner products,  $\frac{\sum_{k \neq l} \langle \psi^k | \psi^l \rangle}{2N \times (2N-1)}$ , is 1.2% for the 1D chain and 5% for the 2D lattice.

To estimate the average error induced by the measurement process on the extracted eigenstates, we performed a simple numerical stochastic analysis. In a  $2N$ -dimensional space, one can consider an ideal orthonormal set of vectors,  $\{\mathbf{e}_k\}$ , and add a  $2N$ -dimensional Gaussian random variable with a standard deviation of  $\sigma$  to every element in order to create a disturbed set of  $\{\mathbf{e}'_k\}$ . Figure 8.10c shows the stochastic expected value and the 90% certainty range of the average inner product of the disturbed set,  $\frac{\sum_{k \neq l} \mathbf{e}'_k \cdot \mathbf{e}'_l}{2N \times (2N-1)}$  for  $2N = 10$  (1D) and  $2N = 24$  (2D). Considering the measured average inner products, we conclude  $\sigma \simeq 1\%$  for 1D and  $\sigma \simeq 5\%$  for 2D devices.

## 8.6 Disorder effect and edge state hybridization in SSH chains

Here we discuss the effect of disorder in the finite SSH chains. In any realized system, disorder and fluctuations can distort the system's parameters and consequently deviate the response from the ideal model. There are two possible types of disorder in the coupled circuit



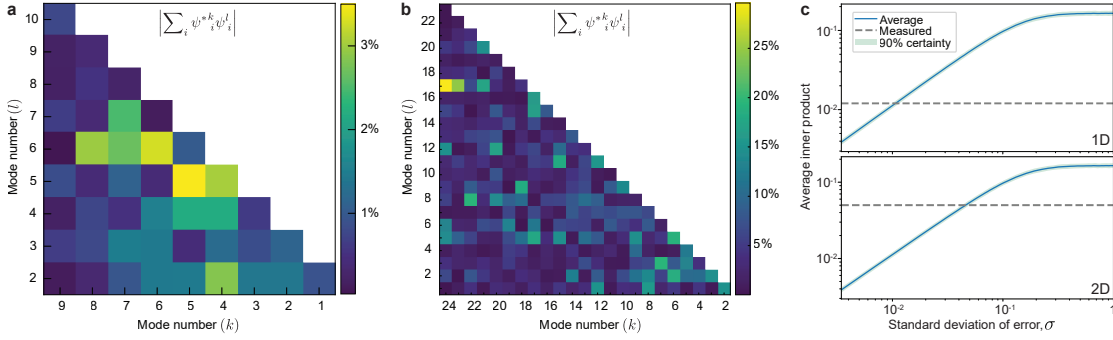


**Figure 8.10: Inner products of the measured eigenstates as an indicator for measurement accuracy.** **a, b**, Scalar products between the measured mode functions after iterative normalization (introduced in the theory section) for 1D and 2D devices correspondingly. The inner products are a quantitative orthogonality verification of the measured modes (eigenvectors) in those systems. **c** The stochastic analysis of the standard deviation of the equivalent Gaussian noise ( $\sigma$ ) induced in the measurement on the eigenmodes. The expected value of the average inner products in a 10 (1D), and 24 (2D) dimensional space is shown versus  $\sigma$ . The grey lines indicate the measured average inner product.

chains: cavity frequency fluctuation and mutual coupling rate fluctuation. In the case of electromechanical arrays introduced in this work, the coupling rate fluctuation is related to the -lithographically defined- self and mutual inductances disorder. In contrast to capacitive coupling where the coupling rate depends on the local electric field between closely spaced electrodes, here the coupling rate depends on the longer-range magnetic field generated by spirals and is more robust to the geometry distortions that arise from the lithographic accuracy ( $\sim 500$  nm). The dominant source of disorder is the capacitor's gap size fluctuation, which is strongly depending on CMP planarization uniformity as well as the etched trench depth variation. The gap size fluctuation was observed up to 1% using mechanical profilometry (which corresponds to 0.5% cavity frequency fluctuation), hence  $g_0$  variations are small.

To study the effect of disorder on the energy spectrum and mode structure of the SSH chains, here we consider a stochastic error on the cavity frequencies with normal distribution:

$$\omega_{c,i} = \omega_c (1 + \mathcal{N}(0, \sigma_{\Delta\omega})) \quad (8.39)$$

Where  $\mathcal{N}$  is a Gaussian random variable with zero mean and standard deviation  $\sigma_{\Delta\omega}$  expressing the relative cavity frequency error. Assuming coupling rates and resonance frequencies same as the 10 cell SSH chain discussed in Sec. 8.4, we numerically calculate the energy spectrum and modes for various relative disorder standard deviations,  $\sigma_{\Delta\omega}$ . Figure 8.11a shows the result for frequency disorder up to 6%, averaged over 4000 random distributions for each standard deviation. The uncertainty ( $\pm$  standard deviation) in energies increases with the disorder as shown with shaded areas in Fig. 8.11a and leads to the regime that two eigenmodes are not distinguishable anymore, as they overlap. As mentioned in Sec. 8.3, the ideal SSH model in finite chains always results in two topological edge states, both with co-localized

modeshapes on two edges regardless of the size of the chain (See Fig. 8.1h). In contrast to eigen energies that are robust against disorder, the topological modeshapes hybridization will break down sooner due to disorder and result in two edge states each one only localized on one end of the chain. To quantitatively describe this effect, we defined the edge states hybridization factor,  $\zeta$ , defined by:

$$\zeta = \frac{1}{2} \left( \frac{\min\{\eta_1^N, \eta_{2N}^N\}}{\max\{\eta_1^N, \eta_{2N}^N\}} + \frac{\min\{\eta_1^{N+1}, \eta_{2N}^{N+1}\}}{\max\{\eta_1^{N+1}, \eta_{2N}^{N+1}\}} \right) \quad (8.40)$$

where again  $\eta_i^k$  is the energy participation ratio of site  $i$  to the collective microwave mode  $k$ , hence  $\eta_i^N$  and  $\eta_i^{N+1}$  are the energy participation ratios of the topological edge modes in a  $2N$  cell SSH chain. For a fully co-localized topological modeshape  $\zeta = 1$ , while it reduces to 0 for the fully non-hybridized (single side-localized) case (Fig. 8.11b). We calculated the average and standard deviation of  $\zeta$  over the statistical pool for various  $\sigma_{\Delta\omega}$ . Figure 8.11c shows that hybridization is dramatically affected by disorder. Based on the modeshape measurement data presented in Sec.8.5, the hybridization factor for the 10 cell SSH device is  $\zeta^{\text{meas}} = 0.98$  which corresponds to the stochastic frequency disorder in the range of  $\sigma_{\Delta\omega} = (0.01\%, 0.38\%)$  with 90% certainty. This indicates small relative disorder in the gap size ( $\sigma_{\Delta\text{gap}} = \frac{1}{2}\sigma_{\Delta\omega}$ ). It's worth mentioning that hybridization is also strongly affected by the length of the SSH chain, where for an example of 20 cell chain with the same parameters as the 10 cell case, the hybridization factor reduces sharply at smaller  $\sigma_{\Delta\omega}$  as shown in Fig. 8.12.

### 8.6.1 Observation of edge state localization

As explained in Section 8.6, in order to observe well-hybridized edge states instead of localized ones, the disorder in the cavity frequencies needs to be low enough. The physical quantity to compare the disorder to is the coupling rates  $J, J'$  between the array sites. We say that the disorder is low enough when it's negligible compared to the coupling rates. The device shown in Sec.8.4 belongs to a second-generation design. The first generation design, visible in Fig. 8.13a featured a different inductor design and the coupling rates were lower:  $J'/2\pi = 127$  MHz,  $J/2\pi = 260$  MHz by fitting the hybridized modes' frequencies with an SSH model. The superconducting optomechanical array was also inductively coupled to input-output waveguides, albeit with a different, microstrip, geometry. In Fig. 8.13 we show a 12-site topological realization of this generation of devices. Thanks to the use of two circulators on the two input/output ports of the chip this device could be measured either in transmission or in reflection from both sides. Firstly, we see in the transmission spectrum (8.13b-c) that the edge modes have abnormally low transmission, even though their current density at the edges should be very big, resulting in a great external coupling rate. This is because the edge states are actually localized at one of the edges each. This can be seen in the reflection measurements in Fig. 8.13d where when we look at the reflection from one side we see only one of the topological peaks, and the other one is only visible at the opposite side of the array.

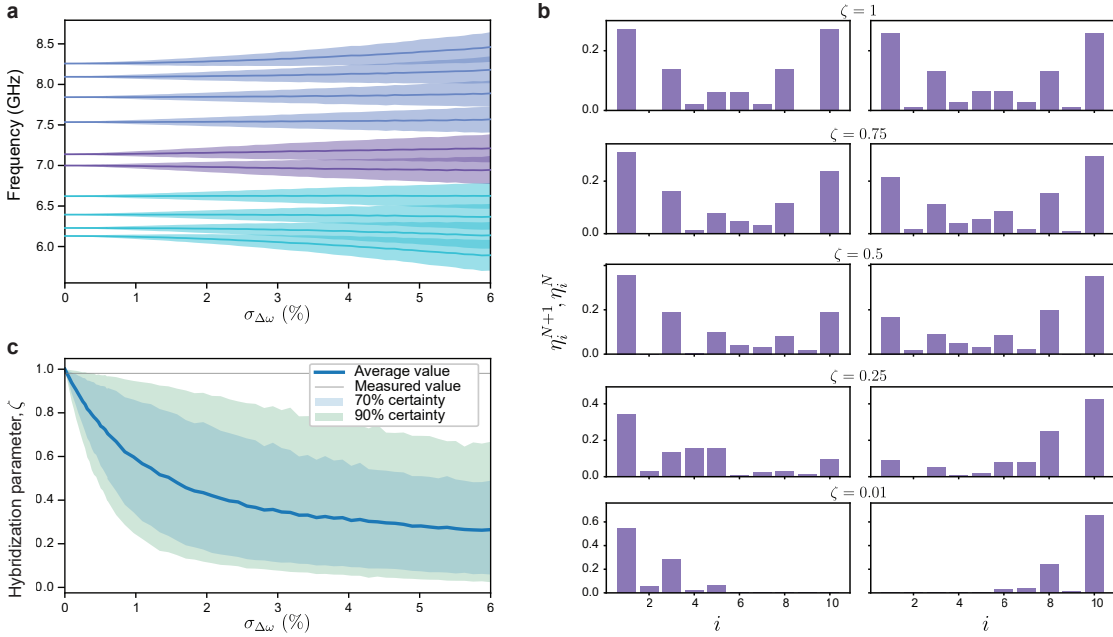


Figure 8.11: **Disorder effect in SSH chains.** **a**, Effect of cavity frequency disorder on the mode spectrum of a 10 cell SSH chain considering the same parameters as the device discussed in the main device. For every relative frequency disorder standard deviation,  $\sigma_{\Delta\omega}$ , 4000 random cases were generated. The solid lines show the average mode frequency. The shades show the statistical standard deviation of mode frequencies. **b**, Example of disordered topological edge states with different hybridization factors,  $\zeta$ . **c**, Plot of hybridization factor versus frequency disorder standard deviation. The solid blue line shows the statistical average over 4000 random points for each error percentage. The shades show bonds for 70% and 90% statistical certainty. The gray line identifies the measured hybridization factor in the 1D chain discussed earlier.

The horizontal axis in subpanels c and d are the same.

## 8.7 2D circuit optomechanical lattice

The circuit optomechanical platform introduced here can be straightforwardly extended to 2D structures. As a proof-of-concept experiment, we realize a 2D optomechanical honeycomb lattice. To demonstrate the coupling tunability, we alternate the mutual microwave couplings ( $J$  and  $J'$ ) along the vertical axis (see Fig. 8.14b), which is known as the strained graphene model (Pereira, Neto, and Peres, 2009; Naumis et al., 2017). For strain-free graphene ( $J = J'$ ), the band structure is gapless, and the upper and lower bands are connected to each other, forming Dirac cones. When applying strain in a certain orientation and decreasing the ratio of  $J'/J$ , a phase transition occurs at  $J'/J = 0.5$ , and a band gap appears. For a finite-size graphene sheet, a set of edge modes can emerge depending on the structure of the edges and the strength of a strain (Nakada et al., 1996; Delplace, Ullmo, and Montambaux, 2011).

Figures 8.14a and b show a 24-site circuit optomechanical system and its mode diagram

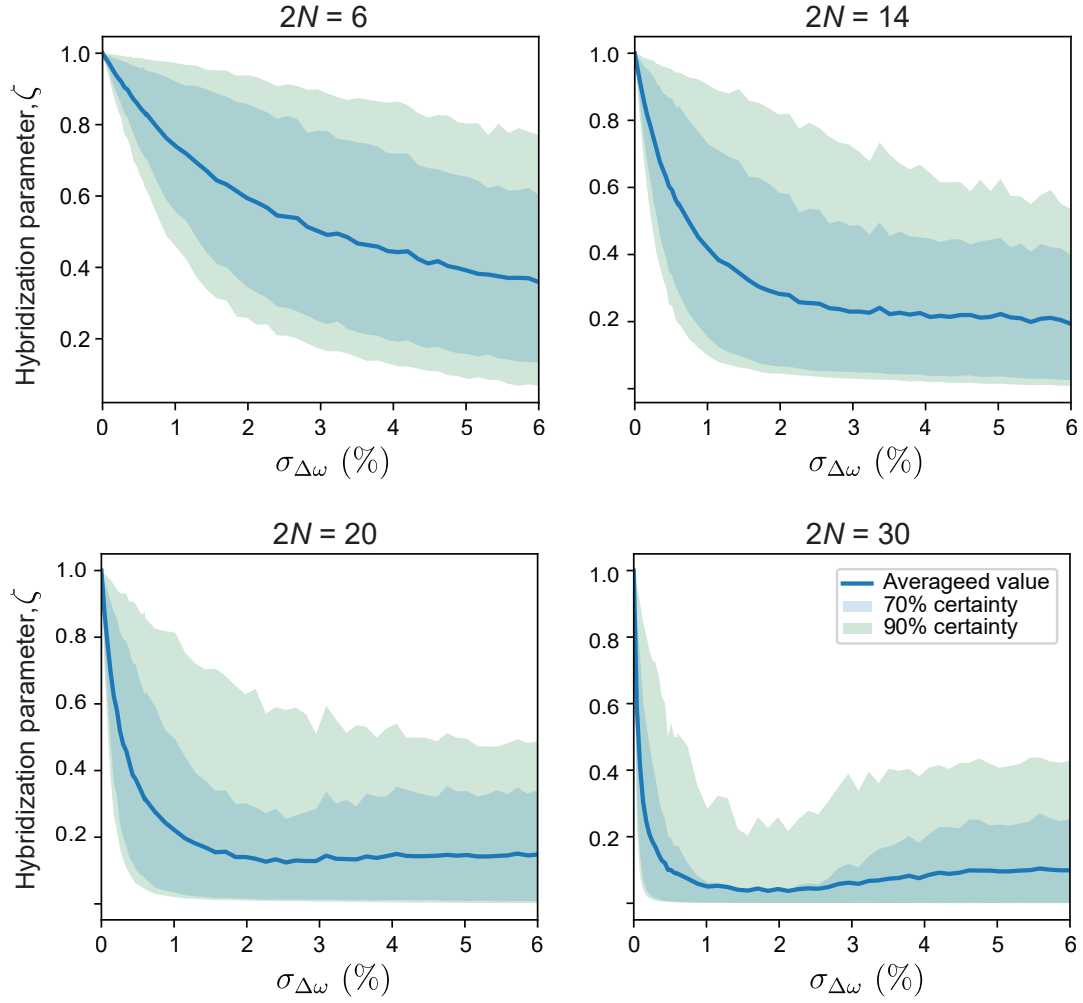


Figure 8.12: **Disorder effect on hybridization for different chain lengths.** The hybridization factor  $\zeta$  in relation to the frequency disorder is shown for several chain lengths with same the parameters. In longer chains, the hybridization is more sensitive to disorder.

respectively, realizing a strained graphene flake, where the triangular spiral inductor in each site is inductively coupled to its three neighbors. The system is designed on the border of the phase transition  $J'/J \approx 0.5$  (see Sec. 8.8.1 for details). Figures 8.14c and d show all the microwave collective modes in the transmission spectrum and all the mechanical frequencies as a function of the trench radius, respectively.

Next, to gain insight into the properties of edge states and their topological origin, we consider our 24-site graphene flake as a truncated strained graphene ribbon, where the existence of edge states can be predicted using the bulk-edge correspondence (Delplace, Ullmo, and Montambaux, 2011). Figures 8.14e and f, and figures in Sec. 8.8.3 show all 6 possible orientations for the ribbon. Given a parallel wavenumber  $k_{\parallel}$ , which is a good quantum number for the ribbon Hamiltonian, the graphene ribbon can be reduced to a wavenumber-resolved 1D

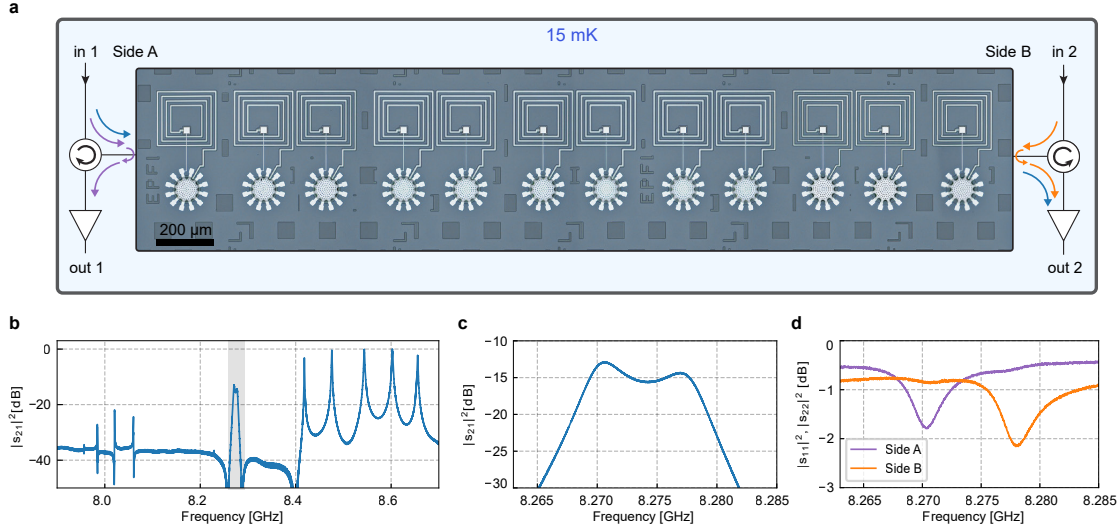


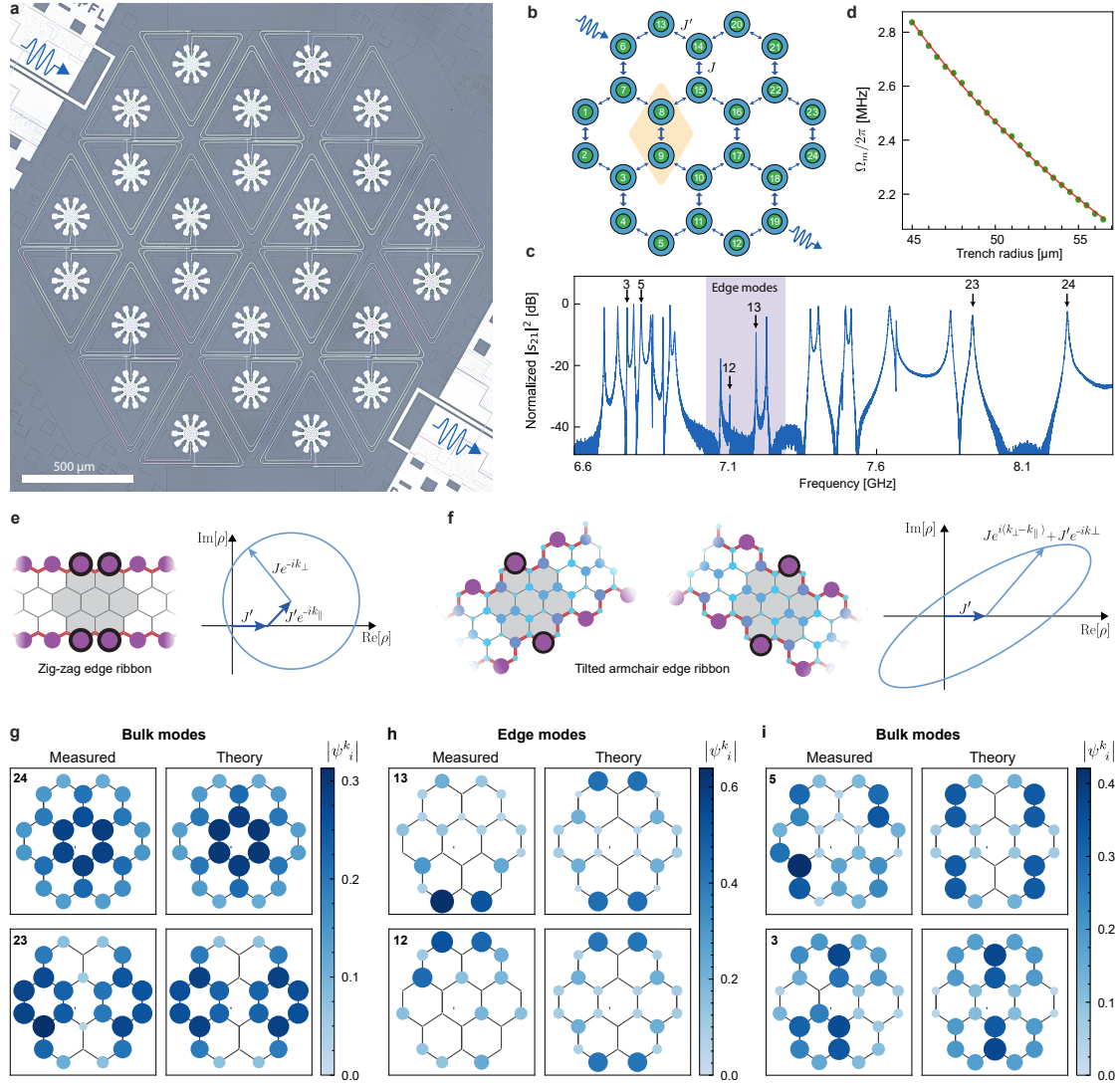
Figure 8.13: **Experimental evidence of edge state localization.** **a**, First generation 12-site topological SSH array measured with reflection capabilities from both sides. **b,c**, VNA  $S_{21}$  transmission measurement of the device. **d**, VNA  $S_{11}$  measurements from both sides of the device. The horizontal axis is the same as in **c**.

model in the perpendicular direction. In a similar manner to the two-band model for the standard 1D SSH chain, the off-diagonal element  $\rho(k_{\perp}|k_{\parallel})$  of the corresponding bulk Hamiltonian can be obtained by introducing a perpendicular wavenumber  $k_{\perp}$ . If  $\rho(k_{\perp}|k_{\parallel})$  winds around the origin in the complex plane, the ribbon with the  $k_{\parallel}$  is in the nontrivial topological phase, possessing edge states. As shown in Figs. 8.14 e and f, we find that only a “zig-zag” edge ribbon with  $\rho(k_{\perp}|k_{\parallel}) = J' + J'e^{-ik_{\parallel}} + Je^{-ik_{\perp}}$  and two “tilted armchair” edge ribbons with  $\rho(k_{\perp}|k_{\parallel}) = J' + Je^{i(k_{\perp}-k_{\parallel})} + J'e^{-ik_{\perp}}$  can possess edge states, while not for the other orientations. Both the two sites on the top and bottom edges of the flake overlap with edge modes seen in either the zig-zag or tilted armchair edge ribbons, enabling one to predict the existence of edge states on these 4 sites (see Sec.8.9.1 for details).

We perform a full modeshape measurement on the 2D lattice, revealing close agreement with the theoretical calculations. A few examples of the modeshapes are shown in Figs. 8.14e–h (the full results can be found in Fig. 8.17). We find that there are four collective microwave modes whose modeshapes are localized in the two sites on either the top or bottom edges, as the topological analysis predicts.

### 8.7.1 Extended data for 2D lattice

The full OMIT response of the 24-site optomechanical system in the 2D honeycomb lattice is shown in Fig. 8.15a measured on the highest frequency collective microwave mode. We extract all the mechanical frequencies by fitting each OMIT resonance, shown in Fig. 8.14d. The minimum and maximum trench radius used in the device is highlighted in the figure.



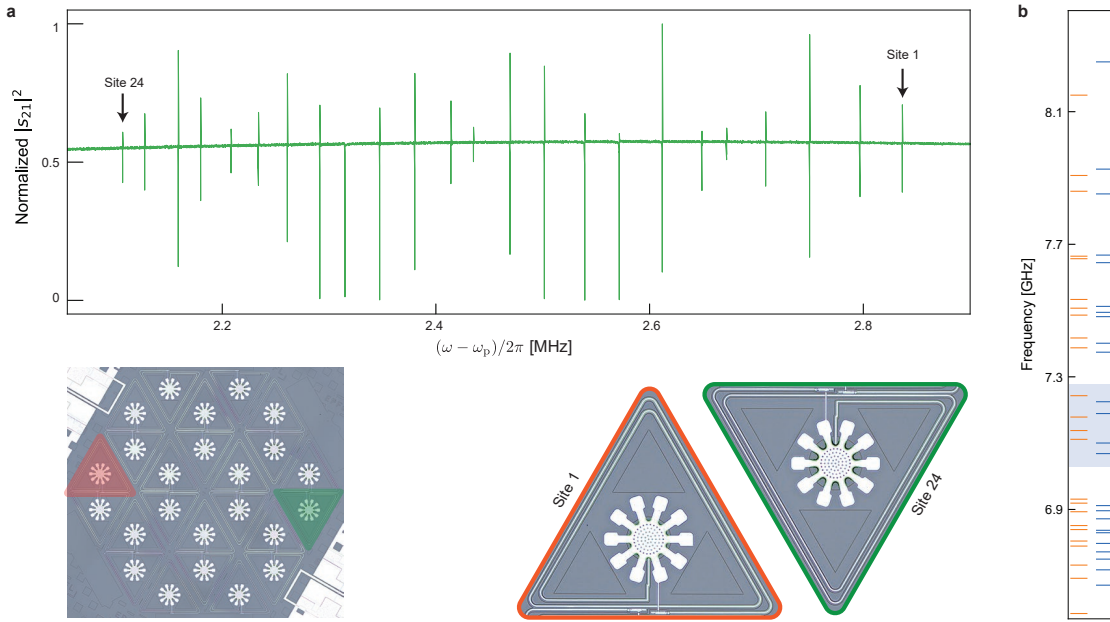
**Figure 8.14: Two-dimensional superconducting circuit optomechanical honeycomb lattice realizing the strained graphene model.** **a**, Microscope image of a 24-site optomechanical honeycomb lattice (strained graphene flake) with alternating couplings. **b**, Mode diagram of the device shown in **a**. **c**, Transmission spectrum of the 2D lattice. Four edge modes are observed in the band gap. **d**, Measured mechanical frequencies versus trench radius and the inverse linear fit. **e,f**, 24-site flake (gray-shaded region) as a truncated strained graphene ribbon in the zig-zag or tilted armchair orientations, respectively. The numerically simulated modeshapes of edge states are shown in amplitude, where the sites hosting the edge modes in the flake are identified by black circles. The off-diagonal element  $\rho(k_{\perp}|k_{\parallel})$  of the corresponding bulk Hamiltonian for a fixed wavenumber  $k_{\parallel}$  is shown in the case of the topological phase, respectively. **g-i**, Examples of measured modeshapes of the 2D lattice in the upper and lower bulk modes, and edge modes, respectively. The observed edge modes are overlapping with the sites hosting the edge states in the analogous graphene ribbons in **e** and **f**. The modeshape information in amplitude is reflected on the color and area of each circle.



Fig. 8.15b shows the design target collective microwave frequencies versus the measured values.

All the modeshapes of the 2D device obtained by the iterative normalization method are shown in Fig. 8.17. For some of them, we don't see good agreements as we observed in the 1D case. This is because, given the much higher number of microwave modes, the effect of frequency disorder plays a more important role. Where the dots are completely missing it means that the experimental power participation ratio  $\eta_i^k$  of site  $i$  to the collective microwave mode  $k$  was not high enough to produce a detectable signal.

Using the extracted modeshapes of the 2D device, we reconstruct the Hamiltonian of the microwave subsystem. Fig. 8.16 shows the reconstructed Hamiltonian matrix in the rotating frame of the average microwave frequency and the ideal designed Hamiltonian including the second-nearest neighbor couplings. Due to the higher frequency disorder in the measured modeshapes of the 2D device, the unitary matrix and consequently Hamiltonian are slightly more disturbed compared to the 1D case, however, they still, show good agreement with the design and theoretical predictions.



**Figure 8.15: Characterization of 24-site 2D honeycomb lattice.** **a**, Optomechanically-induced transparency (OMIT) response of the 2D device measured on the highest microwave bulk mode. Increasing the trench radius results in a slight shift of the mechanical frequencies. **b**, Microwave resonance frequencies of the device, design targets (orange), and measured values (blue).



## 8.8 Strained graphene model

To demonstrate the extendability of our scheme to a 2D structure, we realize the strained graphene model in our optomechanical system, as shown in Sec. 8.7. Here, we explain the basic concepts of the graphene model (Ni et al., 2008; Naumis et al., 2017; Pereira, Neto, and Peres, 2009), including the band structure of an infinite-size system, the bulk-edge correspondence, and the numerically-simulated results for a finite-size system. These will give us a good intuition about the modeshapes of our 24-site 2D optomechanical system.

### 8.8.1 Band structure

To label every site in a honeycomb lattice, we define two lattice vectors, as denoted with  $\mathbf{a}_1$  and  $\mathbf{a}_2$  in Fig. 8.18a, where the coordinate is chosen to have lattice vectors defined as  $\mathbf{a}_1, \mathbf{a}_2 = (\pm \frac{\sqrt{3}}{2}, \frac{3}{2})$ . In addition, one unit cell, enclosed in the green shaded area, consists of two sites. As shown with lines at different angles, connecting sites in Fig. 8.18a, three unique couplings ( $J_a$ ,  $J_b$ , and  $J_c$ ) exist in the honeycomb lattice.

The Hamiltonian of such a 2D multimode system can be formally written as

$$\hat{H} = \sum_{\mathbf{i}-\mathbf{j}=\mathbf{a}_1} J_a |\mathbf{i}, A\rangle \langle \mathbf{j}, B| + \sum_{\mathbf{i}-\mathbf{j}=\mathbf{a}_2} J_b |\mathbf{i}, A\rangle \langle \mathbf{j}, B| + \sum_{\mathbf{i}} J_c |\mathbf{i}, B\rangle \langle \mathbf{i}, A| + \text{h.c.}, \quad (8.41)$$

where  $|\mathbf{i}, A\rangle$  and  $|\mathbf{i}, B\rangle$  denotes a state vector at site  $A$  and  $B$  of unit cell  $\mathbf{i} = m\mathbf{a}_1 + n\mathbf{a}_2$ , respectively.

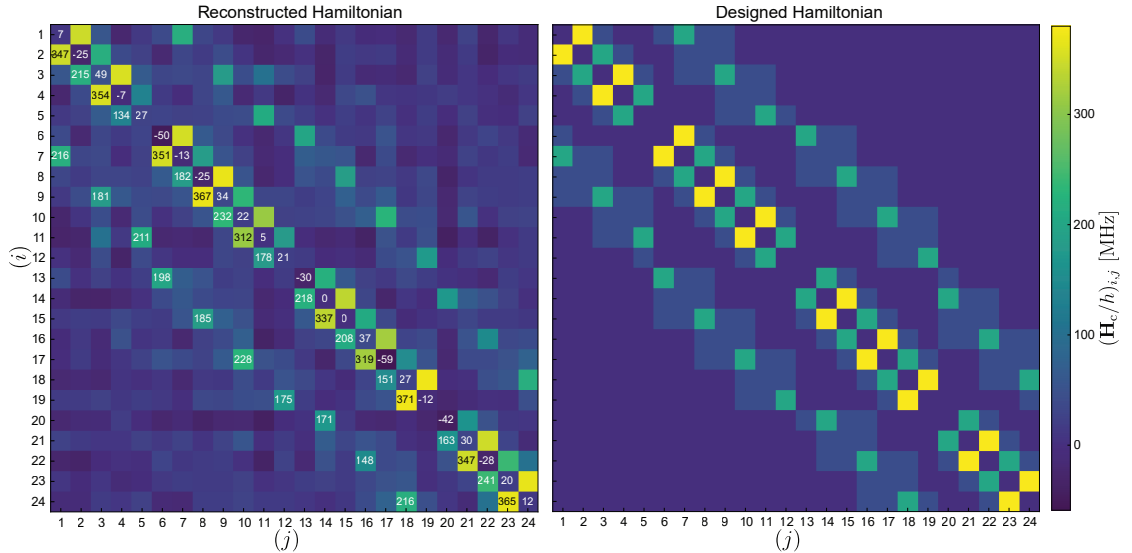


Figure 8.16: **Hamiltonian reconstruction of 24-site 2D honeycomb lattice.** The reconstructed Hamiltonian of 24-site 2D honeycomb device (left) and the designed Hamiltonian including second nearest-neighbor couplings (right). The diagonal elements represent the individual site's resonance frequency deviation from the average bare cavity frequency.

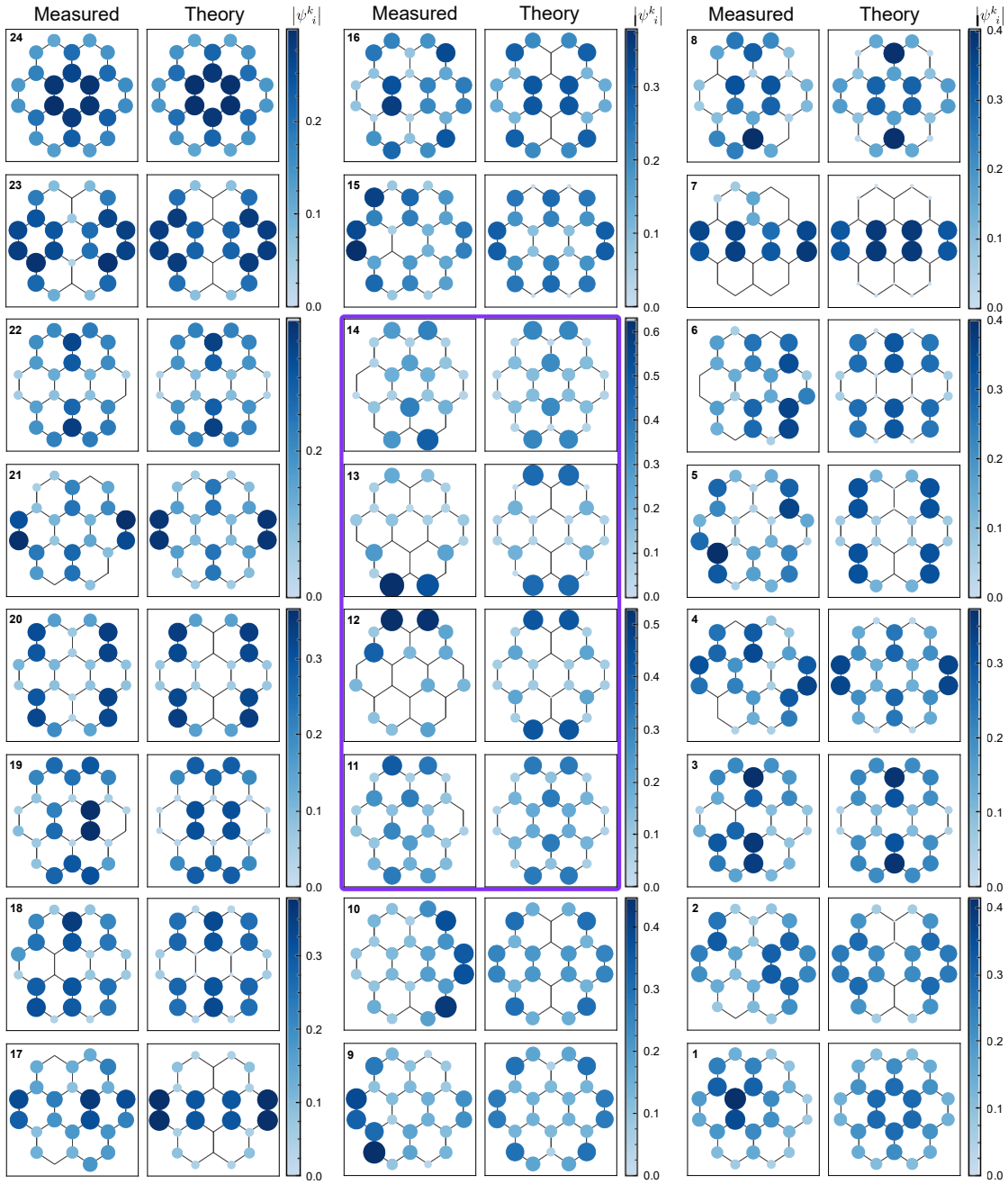


Figure 8.17: **Modeshapes of 24-site 2D honeycomb lattice.** The amplitude of the modeshape  $|\psi_i^k|$  is encoded in the area of the circles. Only for modes that share the same colorbar, the size and color of the circles can be compared. Highlighted in purple are the four edge modes.

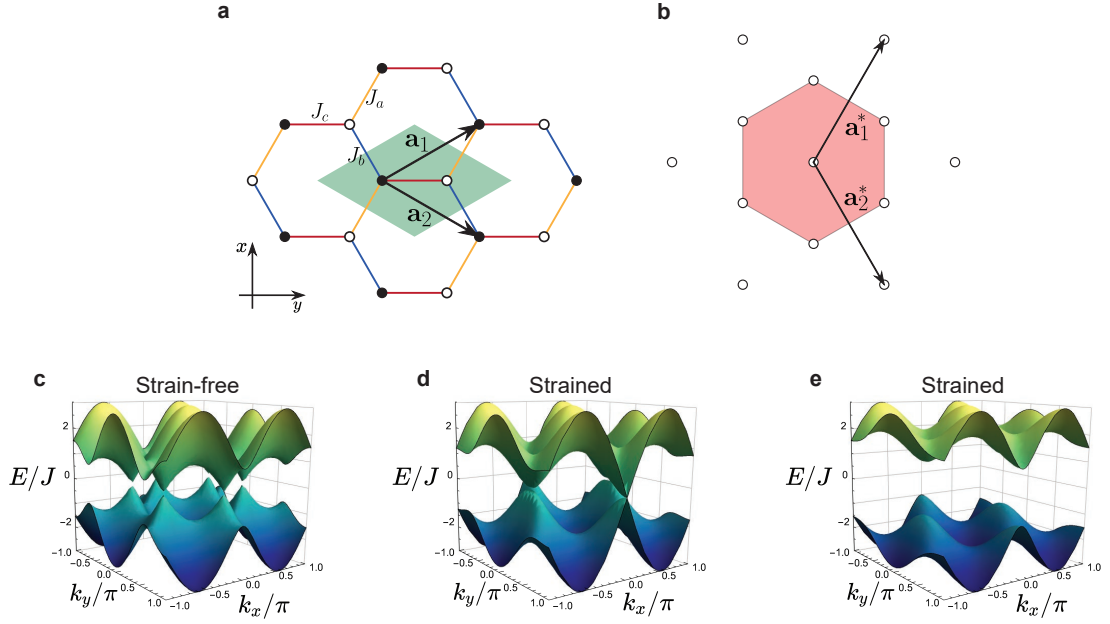


Figure 8.18: **Honeycomb lattice for a graphene of infinite size.** **a**, Multimode system in a honeycomb lattice with a unit cell (green region) and two lattice vectors ( $\mathbf{a}_1$  and  $\mathbf{a}_2$ ). Three coupling strengths ( $J_a$ ,  $J_b$ , and  $J_c$ ) in different orientations are shown with lines of different colors, respectively. The black and white circles describe sites  $A$  and  $B$ , respectively. **b**, Reciprocal honeycomb lattice with two reciprocal lattice vectors ( $\mathbf{a}_1^*$  and  $\mathbf{a}_2^*$ ), where the first Brillouin zone is highlighted. **c–e**, Band structure of a strain-free and strained graphene for  $J'/J = 1$ ,  $J'/J = 0.5$ , and  $J'/J = 0.25$ , respectively.

In a similar way to the 1D SSH model, we first consider the Hamiltonian of an infinite-size honeycomb lattice with periodic conditions in the two translational-symmetry directions (thermodynamical limit of  $N \rightarrow \infty$ ). Using Bloch's theorem, we can diagonalize the Hamiltonian of the inter-cell subsystem by using a wavenumber basis, which is defined as

$$|\mathbf{k}\rangle = \frac{1}{\sqrt{N}} \sum_{\mathbf{i}} e^{i\mathbf{i}\cdot\mathbf{k}} |\mathbf{i}\rangle, \quad (8.42)$$

where  $\mathbf{i}$  denotes a lattice point and  $\mathbf{k}$  is the wave vector, shown with red in Fig. 8.18b, together with the reciprocal lattice. The two reciprocal lattice vectors are  $\mathbf{a}_1^*, \mathbf{a}_2^* = 2\pi(\pm \frac{\sqrt{3}}{3}, \frac{1}{3})$  in the coordinate we choose, following the convention  $\mathbf{i} \cdot \mathbf{j}^* = 2\pi\delta_{ij}$  ( $i, j \in \{\mathbf{a}, \mathbf{b}\}$ ). Thus, the wavenumber-resolved intra-cell Hamiltonian, called bulk Hamiltonian, is obtained as

$$\hat{H}(\mathbf{k}) = \langle \mathbf{k} | \hat{H} | \mathbf{k} \rangle \quad (8.43)$$

$$= \begin{pmatrix} 0 & \rho(\mathbf{k}) \\ \rho^*(\mathbf{k}) & 0 \end{pmatrix}, \quad (8.44)$$

where

$$\rho(\mathbf{k}) = J_c + J_a e^{-i\mathbf{a}\cdot\mathbf{k}} + J_b e^{-i\mathbf{b}\cdot\mathbf{k}} \equiv |\rho(\mathbf{k})| e^{-i\phi(\mathbf{k})}. \quad (8.45)$$

By diagonalizing the bulk Hamiltonian, the band structure can be obtained as  $E(\mathbf{k}) = \pm|\rho(\mathbf{k})|$ . The upper and lower bands for strain-free graphene of infinite size ( $J_a = J_b = J_c$ ) are shown in Fig. 8.18c, where the upper and lower bands are connected at the Dirac points. A strain applied to the lattice will introduce non-equal couplings for different angles, depending on the orientation of the strain. For the threshold  $J_i + J_j = J_k$  ( $i, j, k \in \{a, b, c\}$ ), pairs of Dirac points will merge (see Fig. 8.18d), while the upper and lower bands become gapped for further anisotropy (see Fig. 8.18e). For the model presented in Sec. 8.7, two of the couplings are equal ( $J_a = J_b = J$ ) while the other is different from them ( $J_c = J'$ ). In this case, the infinite 2D honeycomb lattice shows a phase transition at  $J'/J = 0.5$ , where the band structure will be gapped for  $J'/J < 0.5$ .

### 8.8.2 Graphene ribbon

The 2D optomechanical lattice presented in Sec. 8.7 can be interpreted as a truncated graphene ribbons with different orientations of the boundaries, as shown in Fig. 8.21a. It is well known that the existence of edge states depends on the edge structure of a graphene ribbon (Nakada et al., 1996; Kohmoto and Hasegawa, 2007; S. Wang et al., 2016; Hatsugai, 2009; Rechtsman et al., 2013; Plotnik et al., 2014) and can be predicted from the bulk structure of the corresponding graphene model of infinite size. This is known as the bulk-edge correspondence. One of the examples of such edge states appears on the so-called zig-zag edges of a graphene ribbon (Nakada et al., 1996) and has been experimentally observed in 2D materials (S. Wang et al., 2016; Plotnik et al., 2014) as well as photonic (Rechtsman et al., 2013) and microwave (Bellec et al., 2013; Bellec et al., 2014) structures. To predict the existence of edge states for our 2D optomechanical lattice, we follow the method formalized by Delplace, *et al.* (2011) (Delplace, Ullmo, and Montambaux, 2011). Here, we explain how a graphene ribbon with different orientations of boundaries can be described to predict the existence of edge states using the bulk-edge correspondence.

A graphene ribbon is modeled by a multimode system in a honeycomb lattice, where the periodic boundary condition is imposed on the ribbon direction while the open boundary condition is imposed on the width direction that is parallel to a lattice vector defining the ribbon width. The translational symmetry in the ribbon direction ensures that the wavenumber in the ribbon direction is well defined. Therefore, given a certain wavenumber in the ribbon direction, the 2D lattice can be reduced to a 1D chain in the width direction, enabling us to predict the existence of edge states of the ribbon by using a similar analysis to the 1D SSH model (Delplace, Ullmo, and Montambaux, 2011). Note that a different wavenumber in the ribbon direction gives a different result on the prediction of the existence of edge states.

The choice of a unit cell and two lattice vectors is naturally determined by the boundary

structure of a graphene ribbon to be considered. This is crucial to predicting the edge states on the boundary using the bulk-edge correspondence. Since our 2D optomechanical system can be considered to have either so-called zig-zag or armchair edges, we describe the Hamiltonian with two different choices of a unit cell and two lattice vectors.

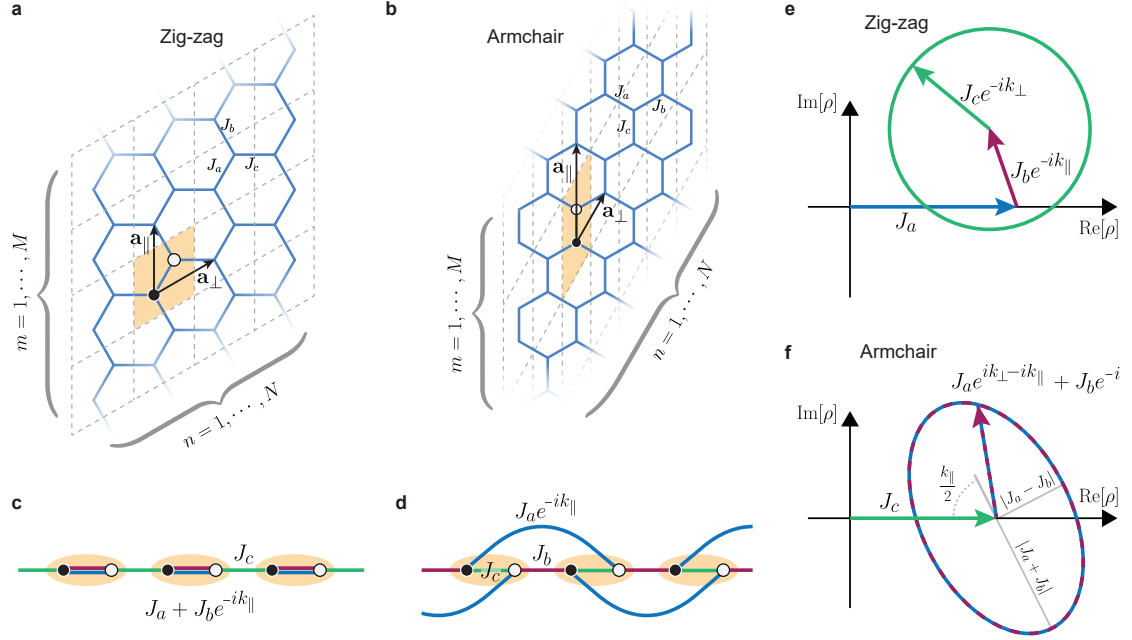


Figure 8.19: **Graphene ribbon.** **a**, Zig-zag edge graphene ribbon. **b** Armchair edge graphene ribbon. **c,d**, Schematic of wavenumber-resolved generalized 1D SSH chains for zig-zag and armchair edges, respectively. The black and white circles describe sites  $A$  and  $B$ , respectively. **e,f**,  $\rho(k_{\perp} | k_{\parallel})$  as a function of  $k_{\perp}$  in the complex plane for zig-zag and armchair edges, respectively.

The zig-zag edges of a graphene ribbon can be described by using a unit cell and two lattice vectors of  $\mathbf{a}_{\parallel}$  and  $\mathbf{a}_{\perp}$  that are shown in Fig. 8.19a. The direction of  $\mathbf{a}_{\parallel}$  is parallel to the ribbon direction, while the size of  $\mathbf{a}_{\perp}$  defines the width of the ribbon. More precisely, a graphene ribbon with zig-zag edges can be defined by imposing an open boundary condition on the basis of  $\mathbf{a}_{\perp}$  while a periodic boundary condition is imposed on the basis of  $\mathbf{a}_{\parallel}$ . The Hamiltonian of such a graphene ribbon is given by

$$\hat{H} = \sum_{n,m} [J_a |m, n\rangle \langle m, n| \otimes \hat{\sigma}_- + J_b |n, m+1\rangle \langle m, n| \otimes \hat{\sigma}_- + J_c |m, n+1\rangle \langle m, n| \otimes \hat{\sigma}_- + \text{h.c.}], \quad (8.46)$$

where  $|m, n\rangle$  for  $n = 1, 2, \dots, N$  and  $m = 1, 2, \dots, M$  is a state vector at unit cell  $(m, n)$  of the lattice. By using the translation symmetry in the ribbon direction ( $\mathbf{a}_{\parallel}$ ), the Hamiltonian is partially diagonalized as

$$\hat{H} = \sum_{k_{\parallel}} |k_{\parallel}\rangle \langle k_{\parallel}| \otimes \sum_m \left[ (J_a + J_b e^{-ik_{\parallel}}) |n\rangle \langle n| \hat{\sigma}_- + J_c |n+1\rangle \langle n| \hat{\sigma}_- + \text{h.c.} \right], \quad (8.47)$$

where the wavenumber basis in the ribbon direction is defined as

$$|k_{\parallel}\rangle = \frac{1}{\sqrt{M}} \sum_m e^{ik_{\parallel}m} |m\rangle \quad (8.48)$$

with the wavenumber  $k_{\parallel} = 2\pi\mu/M$  ( $\mu = 1, 2, \dots, M$ ). By projecting the full Hamiltonian onto a certain wavenumber subspace with  $k_{\parallel}$ , we obtain the Hamiltonian for a wavenumber-resolved 1D chain:

$$\hat{H}(k_{\parallel}) = \langle k_{\parallel} | \hat{H} | k_{\parallel} \rangle = \sum_n \left[ (J_a + J_b e^{-ik_{\parallel}}) |n\rangle \langle n| \hat{\sigma}_- + J_c |n+1\rangle \langle n| \hat{\sigma}_- + \text{h.c.} \right]. \quad (8.49)$$

As schematically shown in Fig. 8.19c, the 1D chain is considered as a generalized 1D SSH chain, where unit cells, individually consisting of two sites, are connected to each other in a chain. Here, an intra-cell coupling coefficient is a complex number and depends on wavenumber  $k_{\parallel}$ .

To predict the existence of edges states in the reduced 1D chain with the given wavenumber of  $k_{\parallel}$ , or edge states on the boundaries of the graphene ribbon, we here use a similar analysis to the 1D SSH model, explained in Sec. 8.3. By imposing a periodic boundary condition on the chain, we can diagonalize the Hamiltonian using a well-defined wavenumber basis, that is given by

$$|k_{\perp}\rangle = \frac{1}{\sqrt{N}} \sum_n e^{ik_{\perp}n} |n\rangle, \quad (8.50)$$

where  $k_{\perp} = 2\pi\nu/N$  ( $\nu = 1, 2, \dots, N$ ). Then, we have the bulk Hamiltonian:

$$\hat{H}(k_{\perp}|k_{\parallel}) = \langle k_{\perp} | \hat{H}(k_{\parallel}) | k_{\perp} \rangle \quad (8.51)$$

$$= \begin{pmatrix} 0 & \rho(k_{\perp}|k_{\parallel}) \\ \rho^*(k_{\perp}|k_{\parallel}) & 0 \end{pmatrix}, \quad (8.52)$$

where

$$\rho(k_{\perp}|k_{\parallel}) = J_a + J_b e^{-ik_{\parallel}} + J_c e^{-ik_{\perp}} \equiv |\rho(k_{\perp}|k_{\parallel})| e^{-i\phi(k_{\perp}|k_{\parallel})}. \quad (8.53)$$

Using the wavenumber-resolved bulk Hamiltonian in the thermodynamic limit ( $N \rightarrow \infty$ ), we can predict the existence of edge states by the following discussions. Note that the thermodynamic limit in the ribbon direction ( $M \rightarrow \infty$ ) is not necessarily required as long as the periodic boundary condition is imposed. For a finite-length ribbon, the wavenumber  $k_{\parallel}$  is discretized depending on the size  $M$ .

With a graphical approach, we plot the closed curve of the off-diagonal element  $\rho(k_{\perp}|k_{\parallel})$  of the bulk Hamiltonian for a given  $k_{\parallel}$  and varying  $k_{\perp}$ , in the complex plane, as shown in Fig. 8.19e. When the winding number of the closed curve around the origin is one, the wavenumber-resolved 1D chain is in the nontrivial topological phase, supporting two edge states on the zig-zag edges for the given  $k_{\parallel}$ . On the other hand, when the winding number is zero, the chain

is in the trivial phase, showing no edge states.

Alternatively, we can also predict the existence of edge states by calculating the wavenumber-resolved Zak phase, given by

$$\mathcal{Z}(k_{\parallel}) = i \oint dk_{\perp} \langle u_{k_{\perp}|k_{\parallel}, \pm} | \partial_{k_{\perp}} | u_{k_{\perp}|k_{\parallel}, \pm} \rangle = \frac{1}{2} \oint dk_{\perp} \partial_{k_{\perp}} \phi(k_{\perp}|k_{\parallel}), \quad (8.54)$$

where  $|u_{k_{\perp}|k_{\parallel}, \pm}\rangle = 1/\sqrt{2}(e^{-i\phi(k_{\perp}|k_{\parallel})}, \pm 1)^T$  is an eigenvector (Bloch wave function), diagonalizing the two-band bulk Hamiltonian of Eq. (8.52). The wavenumber-resolved generalized 1D SSH chain is in the topological phase when  $\mathcal{Z}(k_{\parallel}) = \pi$ , while the chain is in the trivial phase when  $\mathcal{Z}(k_{\parallel}) = 0$ .

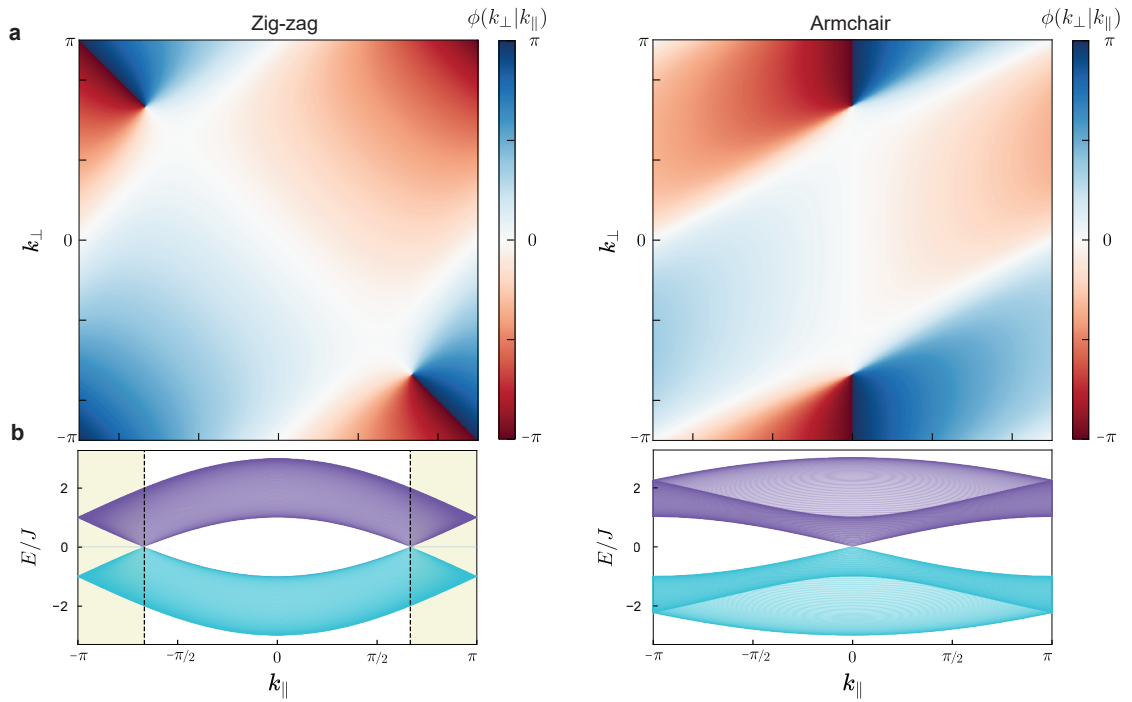


Figure 8.20: **Strain-free graphene ribbons.** **a**, Phase  $\phi(k_{\perp}|k_{\parallel})$  for zig-zag and armchair edge graphene ribbons, respectively. The discontinuities of the phase are located at the boundary between the red region ( $\phi = -\pi$ ) and the blue region ( $\phi = \pi$ ). **b**, Band structure as a function of  $k_{\parallel}$  for zig-zag and armchair edge graphene ribbons with an approximately 100-cell width, respectively. The regions of  $k_{\parallel}$  satisfying  $\mathcal{Z} = \pm\pi$  are highlighted.

In the same manner, we can predict the existence of edge states in a graphene ribbon with armchair edges. An armchair-edge graphene ribbon is defined by a unit cell and two lattice vectors that are shown in Fig. 8.19b. According to the connectivity among the unit cells, the full Hamiltonian of the graphene ribbon is given by

$$\hat{H} = \sum_{n,m} (J_c |m, n\rangle \langle m, n| \otimes \hat{\sigma}_- + J_b |m, n+1\rangle \langle m, n| \otimes \hat{\sigma}_- + J_a |m+1, n-1\rangle \langle m, n| \otimes \hat{\sigma}_- + \text{h.c.}). \quad (8.55)$$



Importantly, the connectivity is different from the Hamiltonian for the zig-zag edges [see Eq. (8.46)], which results in a different prediction of the existence of edge states. By diagonalizing the full Hamiltonian with the wavenumber basis in the ribbon direction ( $k_{\parallel}$ ), we have the Hamiltonian of a wavenumber-resolved generalized 1D SSH chain:

$$\hat{H}(k_{\parallel}) = \langle k_{\parallel} | \hat{H} | k_{\parallel} \rangle = \sum_n \left( J_c |n\rangle \langle n| \otimes \hat{\sigma}_- + J_b |n\rangle \langle n+1| \otimes \hat{\sigma}_- + J_a e^{-ik_{\parallel}} |n-1\rangle \langle n| \otimes \hat{\sigma}_- + \text{h.c.} \right). \quad (8.56)$$

As schematically shown in Fig. 8.19d, the wavenumber-resolved 1D chain can be considered as a generalized 1D SSH chain. By introducing the wavenumber basis in the width direction ( $k_{\perp}$ ), the bulk Hamiltonian is obtained as Eq. (8.52), where the off-diagonal element is modified as

$$\begin{aligned} \rho(k_{\perp} | k_{\parallel}) &= J_c + J_b e^{-ik_{\perp}} + J_a e^{-ik_{\parallel} + ik_{\perp}} \\ &= J_c + e^{-ik_{\parallel}/2} \left[ (J_a + J_b) \cos(k_{\perp} - k_{\parallel}/2) + i(J_a - J_b) \sin(k_{\perp} - k_{\parallel}/2) \right]. \end{aligned} \quad (8.57)$$

In this case, the closed curve of  $\rho(k_{\perp} | k_{\parallel})$  is an ellipse in the complex plane, as shown in Fig. 8.19f. However, we can apply the same analysis to the armchair-edge graphene ribbon in order to predict the existence of edge states, as in the case of the zig-zag edges. Namely, if the closed curve winds up the origin, the armchair-edge graphene ribbon shows edge states for the given  $k_{\parallel}$ .

As examples, we analyze strain-free graphene ribbons with zig-zag and armchair edges, for which  $J_a = J_b = J_c$ . In Fig. 8.20a, the phase  $\phi(k_{\perp} | k_{\parallel})$  for the zig-zag and armchair edge graphene ribbons are shown as a function of  $k_{\parallel}$  and  $k_{\perp}$ , respectively, as introduced by Delplace (Delplace, Ullmo, and Montambaux, 2011). The phase is restricted to the interval  $[-\pi, \pi]$  to be a single-valued function. The two singularity points, corresponding to the Dirac points, are shown in each plot. With a fixed  $k_{\parallel}$ , the phase of  $\phi(k_{\perp} | k_{\parallel})$  along  $k_{\perp}$  gives the wavenumber-resolved Zak phase to predict the existence of edge states. More simply, the discontinuities of  $\phi(k_{\perp} | k_{\parallel})$  are useful to determine the discretized Zak phase ( $\mathcal{Z} = 0$  or  $\pi$ ) since a path along  $k_{\perp}$  necessarily goes across a discontinuity to give a non-zero Zak phase.

In Fig. 8.20b, we numerically calculate the band structure of graphene ribbons with zig-zag and armchair edges for different  $k_{\parallel}$ , respectively. The ribbon width is set to be on the order of 100 to avoid the finite-size effect. Since the ribbon width is sufficiently wide, edge states are found to be zero-energy states in the band gap. The regimes of  $\mathcal{Z}(k_{\parallel}) = \pi$  are highlighted in Fig 8.20b. As the Zak phase predicts, there are edge states in the zig-zag edge ribbon for  $|k_{\parallel}| > 2\pi/3$ , while not in the armchair edge ribbon for all  $k_{\parallel}$ .

### 8.8.3 Strained graphene ribbon

In our 2D optomechanical lattice, only one of the couplings in three different orientations is different, where the coupling strength is denoted by  $J$  while the other two coupling strengths are denoted by  $J'$ . This corresponds to applying a strain to a graphene ribbon in a direction

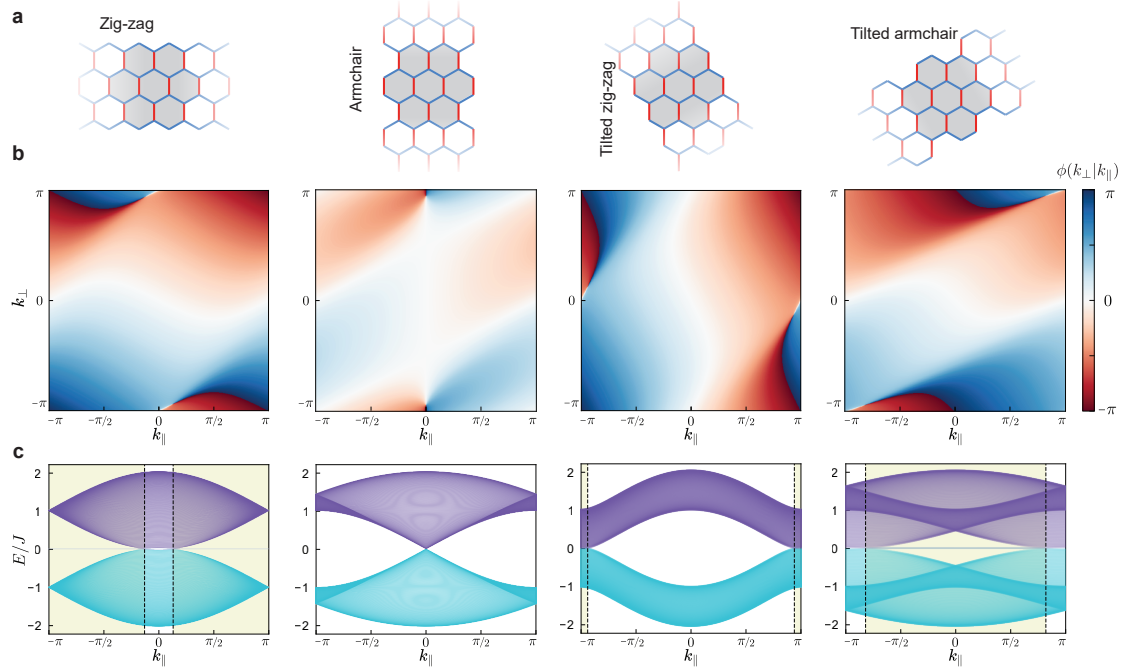


Figure 8.21: **Strained graphene ribbons.** **a**, Four different interpretations of our 2D lattice as a truncated strained graphene ribbon: zig-zag, armchair, tilted armchair, and tilted zig-zag edge. **b**, The phase  $\phi(k_{\perp}|k_{\parallel})$  for the four different orientations. The discontinuities of the phase are located at the boundary between the blue region ( $\phi = -\pi$ ) and the red region ( $\phi = \pi$ ). **c**, Band structure as a function of  $k_{\parallel}$  for the four different graphene ribbons with an approximately 100-cell width, respectively. The region of  $k_{\parallel}$  satisfying  $\mathcal{L} = \pm\pi$  are highlighted.

parallel or perpendicular to the direction of coupling  $J$ . As shown in Fig. 8.21a, our 2D lattice is interpreted as a truncated strained graphene ribbon with zig-zag or armchair edges. More precisely, there are four different possible orientations for the ribbon: zig-zag edges perpendicular to the direction of coupling  $J$  (zig-zag ribbon), armchair edges parallel to the direction of coupling  $J$  (armchair ribbon), zig-zag edges tilted with respect to the direction of coupling  $J$  (tilted zig-zag ribbon), and armchair edges tilted with respect to the direction of coupling  $J$  (tilted armchair). Note that due to the reflection symmetry, there are two orientations of strained graphene ribbons with tilted zig-zag and tilted armchair edges, respectively, that are not shown in Fig. 8.21a to avoid redundancy.

We plot the phase  $\phi(k_{\perp}|k_{\parallel})$  for the four different orientations of the ribbon. To describe a zig-zag strained graphene ribbon, we set  $J_c = J$  and  $J_a = J_b = J'$  in the Hamiltonian of Eq. (8.46), while we set  $J = J_a$  and  $J_b = J_c = J'$  (or  $J = J_b$  and  $J_a = J_c = J'$ ) for a tilted zig-zag ribbon. To describe an armchair strained graphene ribbon, we set  $J_c = J$  and  $J_a = J_b = J'$  in the Hamiltonian of Eq. (8.55), while we set  $J_a = J$  and  $J_b = J_c = J'$  (or  $J = J_b$  and  $J_a = J_c = J'$ ) for a tilted armchair ribbon. We note that due to the reflection symmetry, the phase for the two tilted zig-zag ribbons can be converted by replacing  $J$  and  $J'$ , resulting in identical phase trajectories in the complex plane. The same argument is valid for the two tilted armchair

orientations.

For our specific setting with  $J'/J = 0.51$ , the phase  $\phi(k_\perp|k_\parallel)$  is plotted as a function of  $k_\parallel$  and  $k_\perp$  in Fig. 8.21b. The two Dirac points almost merge since the coupling ratio is close to the transition point of 0.5. In the same way as the cases without a strain, we can determine for which  $k_\parallel$  edge states exist from the phase  $\phi(k_\perp|k_\parallel)$  in the path along  $k_\perp$ . To confirm that the prediction of the existence of edge states from the Zak phase is correct, we numerically simulate the band structure of strained graphene ribbons of approximately 100-cell width, as shown in Fig. 8.21c, where the regions of  $\mathcal{Z} = \pi$  are highlighted. Edge states appear as zero-energy modes in the band gap (Kohmoto and Hasegawa, 2007; Delplace, Ullmo, and Montambaux, 2011). The analytical calculation of the Zak phase accurately predicts the existence of edge states. Importantly, for our specific setting with  $J'/J = 0.51$ , the zig-zag ribbon and the tilted armchair ribbon show edge states for almost all  $k_\parallel$ .

#### 8.8.4 Finite-width effect on graphene ribbon

Depending on the boundary structures, the width of the graphene ribbon is found to be  $N = 4$  for the zig-zag edges and  $N = 7$  for the armchair edges (see Fig. 8.22a). As discussed in Sec. 8.3, the finite-size effect modifies the prediction of the existence of edge states. Since the wavenumber-resolved 1D chain reduced from a graphene ribbon can be considered as a generalized 1D SSH chain, we can apply the same discussions as for the standard 1D SSH model to predict the existence of edge states of a graphene ribbon in the presence of the finite-width effect. Namely, edge states appear when both  $\mathcal{Z} = \pi$  and the slope condition are satisfied simultaneously. Here, the slope condition for the wavenumber-resolved 1D chain is described as

$$\left| \frac{\partial \phi(k_\perp|k_\parallel)}{\partial k_\perp} \right|_{k_\perp=k_{\perp,\min}} < N + 1, \quad (8.58)$$

where  $k_{\perp,\min}$  is the wavenumber associated with the minimum absolute value of the eigenenergy for the given  $k_\parallel$ .

As shown in Fig. 8.22b, we numerically simulate the energy levels as a function of  $k_\parallel$  for the four different ribbons with the same width as our 24-site lattice. We find that for specific ranges of  $k_\parallel$ , there are zero-energy modes, corresponding to edge states, in the band gap, only for the zig-zag and tilted armchair edge ribbons. This is consistent with the prediction. However, due to the finite width of the ribbons, the edge states are hybridized, showing an energy splitting. For further study, the band structure as a function of the coupling ratio of  $J'/J$  is shown in Fig. 8.22c. As expected, zero-energy states appear when  $J'/J \rightarrow 0$  only for the case with the zig-zag edges and the tilted armchair edges.

Using the Zak phase condition ( $\mathcal{Z} = \pi$ ) and the slope condition, we can predict the existence of the edges states. In Fig. 8.22b, the regions of  $k_\parallel$  that satisfy both the conditions are highlighted, while the transition points that are predicted from the Zak phase calculation are shown with

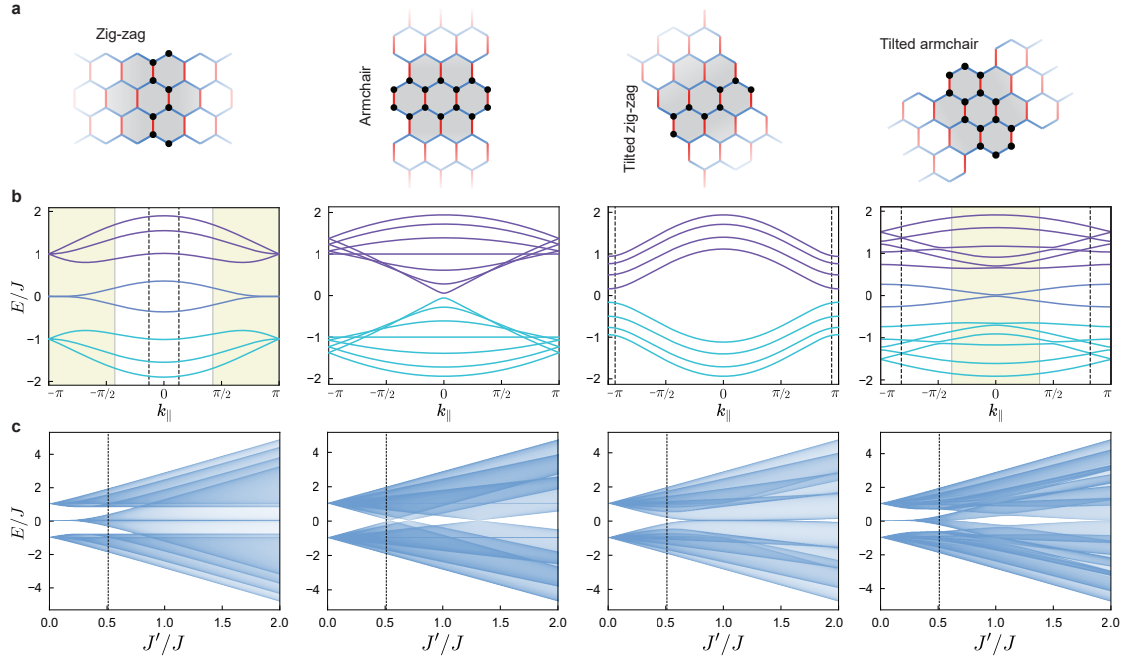


**Figure 8.22: Strained graphene ribbons of finite width.** **a**, Four different interpretations of our 2D lattice as a truncated strained graphene ribbon: zig-zag, armchair, tilted zig-zag, and tilted armchair edges. The black dots denote the unit cell used for the calculation of the band structure based on Bloch's theorem. **b**, Band structure as a function of  $k_{\parallel}$  for the four different orientations. The coupling ratio is set to be  $J'/J = 0.51$  and the width is the same as our 24-site lattice. The number of the energy levels corresponds to the number of sites in the unit cell (black dots in **a**). The regions of  $k_{\parallel}$  satisfying both  $\mathcal{Z} = \pi$  and the slope condition are highlighted while the transition points calculated only from the Zak phase are shown with the black dashed lines. **c**, Band structure of the corresponding graphene ribbons as a function of  $J'/J$ . The dashed line points out  $J'/J = 0.51$ , our design value.

the black dashed lines. We find that the region of  $k_{\parallel}$  showing edge states are decreased from the case with an infinite width due to the finite-width effect. Importantly, edge states exist only in either the zig-zag edge ribbon or the tilted armchair edge ribbon.

## 8.9 24-site honeycomb lattice

### 8.9.1 Band structure and modes shapes

The 24-site multimode optomechanical system in a honeycomb lattice presented in the Sec. 8.7 is designed to be close to the transition point for strained graphene ( $J'/J = 0.5$ ). From the discussions for strained graphene ribbons, we could expect that edge states appear on both the two sites of the top and bottom edges of the flake. This is because the two sites overlap the edge states seen in the zig-zag and tilted armchair edge ribbons with the same width as our 24-site lattice, as shown in Fig. 8.23 (see Sec. 8.8.4). However, the prediction can be

precise only when a periodic boundary condition is imposed in the ribbon direction. Our 24-site lattice could be obtained by truncating the corresponding strained graphene ribbon and imposing an open boundary condition in the ribbon direction. Therefore, it is not trivial and beyond the scope of this work and still an open question how to precisely predict the existence of edge states in such a small flake of strained graphene, since the finite-size effects in both the two lattice directions could be mixed up.

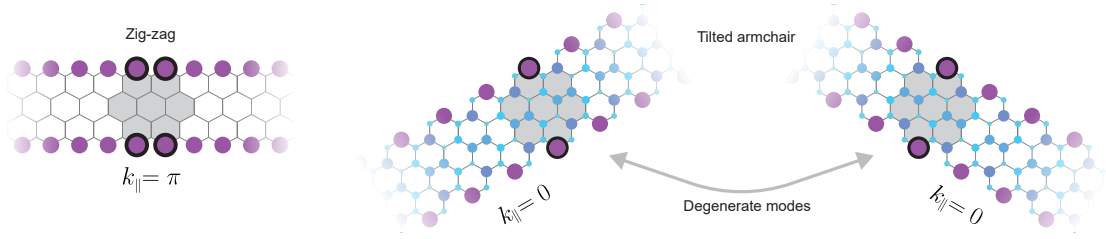


Figure 8.23: **Edge states of graphene ribbons overlapping the flake structure.** Examples of numerically simulated modeshapes of edge states in zig-zag and tilted armchair edge graphene ribbons, overlapping both the two sites on the top and bottom edges of the 24-site flake. The tilted armchair orientation has a reflection symmetry resulting in two degenerate mode shapes.

Nevertheless, we can numerically simulate the band structure and the modeshapes of the 24-site multimode system. In Fig. 8.24a, we show the energy levels of the 24-site system as a function of  $J'/J$ . In the small coupling ratio limit ( $J'/J \rightarrow 0$ ), four zero-energy modes appear in the band gap. Figures 8.24b and c show several examples of modeshapes of two of the upper bulk modes, all the zero-energy states, and two of the lower bulk modes for  $J'/J = 0.15$  and  $J'/J = 0.51$  (design values), respectively. As expected, the four zero-energy modes are localized at the four sites of the top and bottom edges. This is consistent with the topological prediction of the existence of edge states from strained graphene ribbons, discussed in Sec. 8.8.4.

### 8.9.2 Effect of parasitic couplings

The ideal nearest neighbor coupling in the honeycomb lattice is realized by mutual inductance between adjacent triangular spirals with shared edges in the circuit shown in Fig. 8.14. Beyond this, there are parasitic mutual inductances between distanced spirals in the realized lattice. Based on the electromagnetic FEM simulations, we expect that parasitic mutual inductance between triangles which have a shared vertex (as shown in Fig. 8.25a) resulting in approximately identical parasitic coupling rates, while the parasitic coupling is an order of magnitude smaller than the nearest neighbor coupling rate. Figure 8.25b shows the numerically calculated energy levels including the parasitic couplings for the 24-site graphene flake versus the relative second nearest-neighbor coupling rate. This can explain the asymmetry in the band structure of the 24-site flake which was experimentally measured and presented in Sec. 8.7.

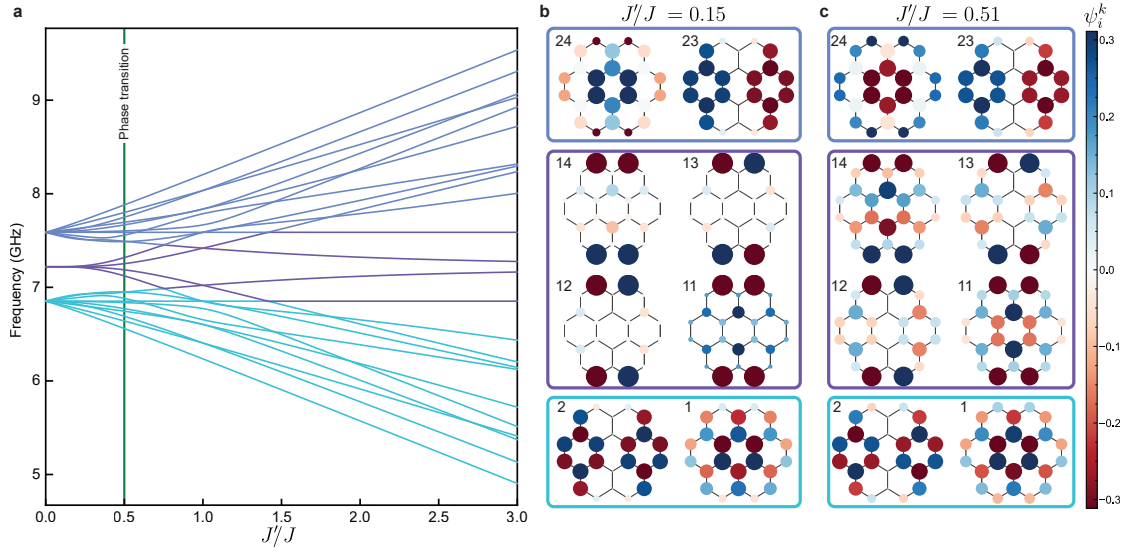


Figure 8.24: **24-site honeycomb lattice designed bands.** **a**, Energy levels of the 24-site honeycomb lattice as a function of  $J'/J$ . The green line shows the phase transition for a graphene flake of infinite size. **b,c**, Examples of the mode shapes in two of the upper bulk modes, all the edge states, and two of the lower bulk modes for  $J'/J = 0.15$  and  $J'/J = 0.51$  (design values), respectively.

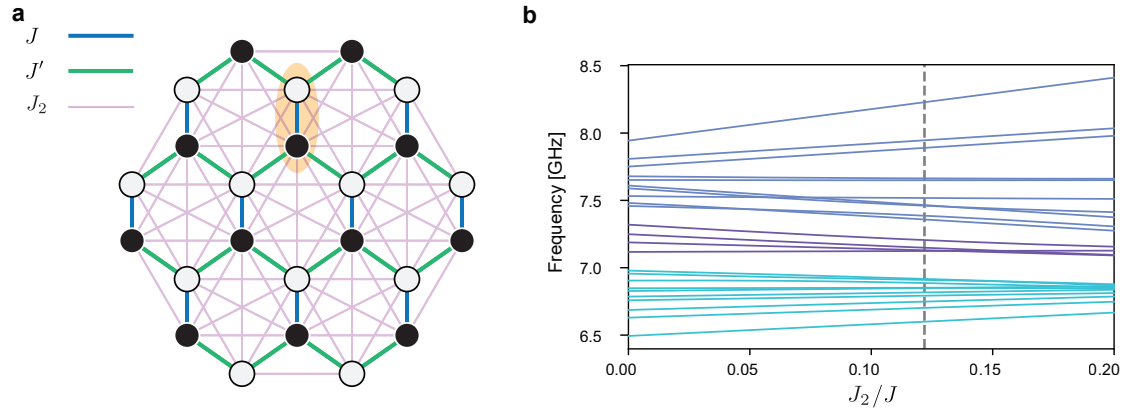


Figure 8.25: **Effect of parasitic coupling on the 2D honeycomb lattice.** **a**, Mode diagram of the 24-site 2D honeycomb lattice including second nearest-neighbor couplings. **b**, Energy levels as a function of the relative second nearest-neighbor coupling rate for the 2D case. The dashed line shows the values of the actual device discussed in Sec.8.7. Color coding denotes the LPB, edge states and UPB.

## 8.10 Experimental setup and measurement techniques

### 8.10.1 Full experimental setup

The full experimental setup (Fig.8.26a) consists of a room-temperature (RT) and a cryogenic section. At RT, two Rohde & Schwartz (R&S) SMB 100A analog microwave sources generate



the cooling/probe and excitation pumps, a R&S ZNB20 Vector Network Analyzer (VNA) and a R&S FSW 26 Electronic Spectrum Analyzer (ESA) are used for the measurement itself. The

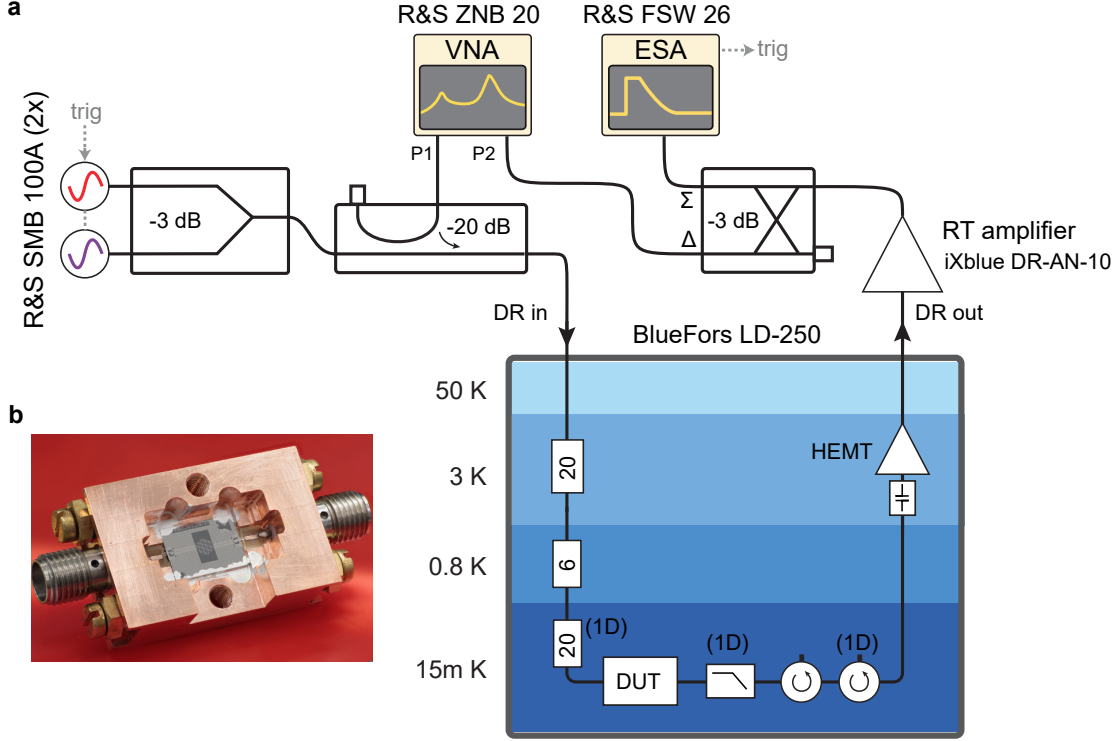


Figure 8.26: **Experimental setup for optomechanical lattices experiment.** **a**, Full experimental setup used for the chips' characterization. Some elements of the input line (inside round brackets) are specific only to the 1D sample. **b**, Packaged chip inside the copper sample holder.

VNA measures the coherent response of the devices, in our case the transmission scattering parameter  $S_{21}(\omega)$ . The ESA is not used in its usual frequency-domain mode, instead, for our experiment we use it in the so-called 'zero-span'. In this mode the instrument demodulates at a fixed CW frequency and effectively implements a time-domain power measurement over a large dynamic range, which is typical of spectrum analyzers. The ESA is able to trigger the microwave sources to start the time-domain sequence, which is programmed in the sources. All the instruments are locked together and to an SRS FS725 Rubidium Frequency Standard to achieve reliable frequency stability and accuracy. The two microwave sources are combined at RT through a 3dB microstrip coupler. The VNA is then directionally coupled with 20dB of insertion loss and all the signals are finally sent to the Dilution Refrigerator (DR).

A series of cryogenic attenuators are used at the different flanges to thermally anchor the input wiring and more importantly to remove the room temperature noise from the input signal. For the 1D sample a total of 46 dB of nominal attenuation were used. For the 2D samples a total of 26 dB of nominal attenuation were used. In this experiment we are not interested to probe the devices at the single photon level, hence the not-so-high attenuation values. We are more interested in being able to reach the regime where the effective mechanical damping



rate greatly exceeds the intrinsic one  $\Gamma_{\text{eff}} \gg \Gamma_{\text{m}}$  through optomechanical sideband cooling, which requires high on-chip powers ( $\mathcal{O}(-30 \text{ dBm})$ ). For the 1D chip an additional K&F 18GHz lowpass filter and circulator were used.

The output signal from the chips is firstly amplified with a cryogenic High Electron Mobility Transistor (HEMT) amplifier at the 4K flange of the DR. The HEMTs were both from Low-Noise-Factory, model numbers are LNF-LNC4\_8C and LNF-LNC1\_12A for the 1D and 2D samples respectively. The typical gain is 40 dB. The circulators placed after the chips are crucial in preventing the back-propagating high-amplitude signals of the HEMT amplifier from reaching the chip. A room temperature amplifier, model number iXblue DR-AN-10 is placed as close to the fridge as possible to further amplify the signal and make it robust against injected noise along the cables until they reach the measurement equipment. This signal is then split with a 180-hybrid coupler and sent back to port 2 of the VNA and the ESA.

The chip holder (Fig. 8.26b) is mounted at the MXC flange of the DR, which has a temperature of  $T \approx 15 \text{ mK}$ . The chip holder is constructed with Oxygen-free copper. The CPW signal lines are wire bonded, as well as the ground plane close to them, while the perimeter ground plane has been contacted using conductive silver glue.

### 8.10.2 Ringdown data analysis and cavity shifts

We fit the ringdown data, an example data set of which can be seen in Fig. 8.27a, with an exponential profile  $P(t) = P_0 \exp(-\Gamma_{\text{eff}}/2\pi) + N$  and extract  $\Gamma_{\text{eff}}$  from such fit.

Given the very large amount of ringdown traces ( $\# \text{ powers} \times \# \text{ sites} \times \# \text{ collective modes} = (5, 100 \text{ for the 1D and } 29, 236 \text{ for the 2D sample})$ ), a robust automated fitting algorithm has been advised to reliably find good initial parameters for the fits. Another challenge arises because, due to the large variation of  $\eta_i^k$  across the different modes and sites, there can be more than 2 orders of magnitude in the exponential decay rate of the measured signal, as can be seen in Fig. 8.27b. This makes it difficult to have a one-for-all starting condition for the fits. Moreover, the initial decay of a highly-excited mechanical oscillator can exhibit non-linear behaviour due to the high-amplitude oscillations and it should not be included in the exponential fit. Finally, since for the optomechanical damping effect the relative detuning between the cavity and mechanical frequency is relevant, we measured the collective modes' resonance frequency shift with the cooling powers used for the experiment. Figure 8.27c shows an example of such analysis for mode  $k = 15$  which has a linewidth closest the average among all the modes. We can see that for this mode the cavity shift is negligible compared to the linewidth. This might not be the case for the modes with the lowest linewidths, and it could justify restricting the fitting to a lower-power range. This effect can also be taken into account by plugging in the correct  $\tilde{\omega}_c^k$  and  $\kappa_{\text{tot}}^k$  into the optomechanical damping rate equation (8.25).

### 8.10.3 Samples parameters

The hybridized modes frequencies  $\omega_c$  and line-widths  $\kappa$  (Tab. 8.3 and 8.5) were measured at the VNA then fitted with a complex  $S_{21}^{\text{exp}}(\omega) = S_{21}^{\text{Lor}}(\omega) + x + iy$  expression that also takes into account any non-ideal Fano effect.  $S_{21}^{\text{Lor}}(\omega)$  is a Lorentzian lineshape and  $x + iy$  is a complex displacement that even though it doesn't physically interpret the origin of the 'Fanoness', it enables us to model it. For the cavity and mechanical resonance frequencies, the uncertainty in the values is many orders of magnitude smaller than the least significant reported digit.

The mechanical frequencies (Tab. 8.4 and 8.6) were measured in a similar way, doing and OMIT measurement, and fitting the VNA trace with an  $S_{11}^{\text{exp}}(\omega)$  reflection Lorentzian experimental profile. The bare mechanical damping rates  $\Gamma_m$  were extracted by taking the intercept of the  $\Gamma_{\text{eff}}$  fits versus power. For a fixed mechanical site, more than one independent value of  $\Gamma_m$  was extracted by looking at the different hybridized modes. What we are reporting here is the

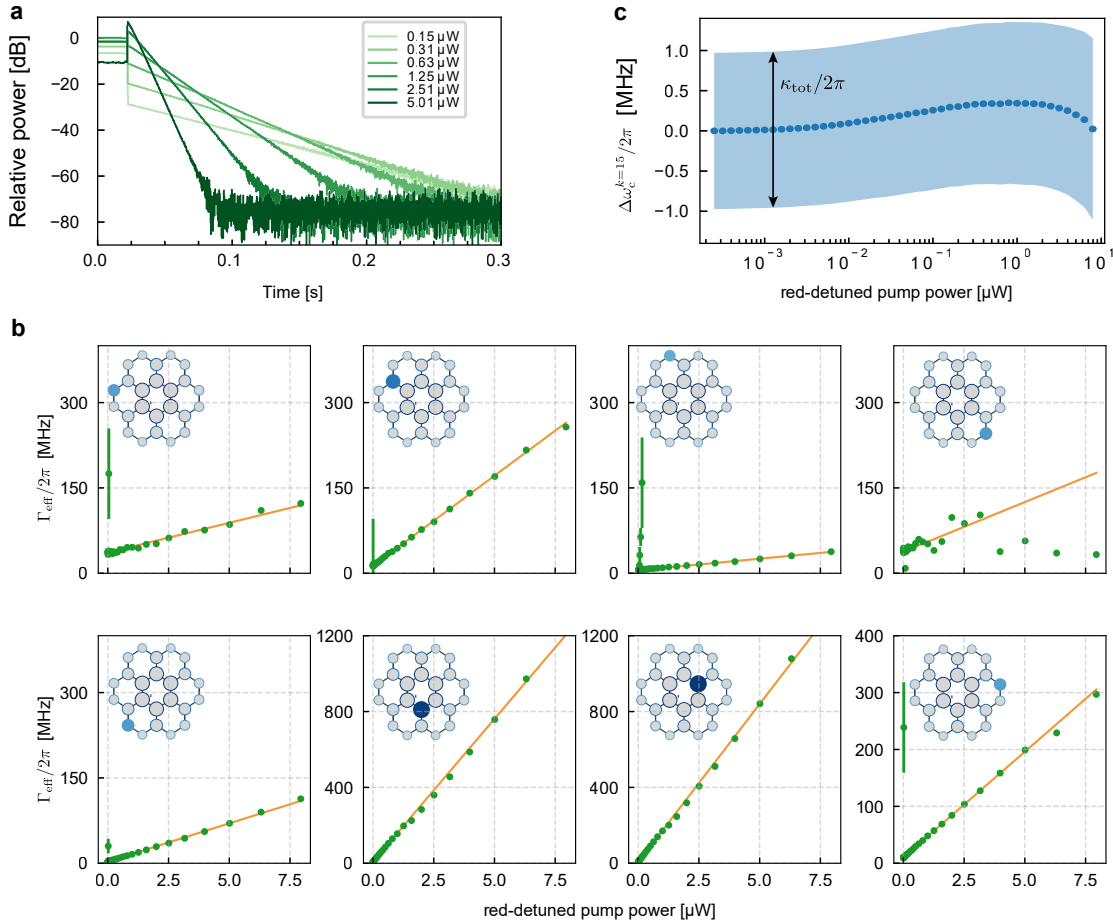


**Figure 8.27: Data analysis.** **a**, Example raw data set of ringdowns with increasing cooling power. **b**,  $\Gamma_{\text{eff}}$  vs cooling power data for some sites of the  $k=24$  collective mode of the 2D sample. **c**, Collective mode resonance frequency shift versus cooling power for the average-linewidth mode with  $\kappa/2\pi = 2$  MHz. The shaded area indicates the mode's linewidth.

weighted average of such values. The error in these measurements is of the same order of magnitude of the digit in round brackets.

Hybridized mode	10	9	8	7	6
$\omega_c/2\pi$ [GHz]	8.463	8.139	7.767	7.435	7.016
$\kappa/2\pi$ [MHz]	3.904	4.556	4.176	4.668	4.964
Hybridized mode	5	4	3	2	1
$\omega_c/2\pi$ [GHz]	6.922	6.590	6.404	6.285	6.216
$\kappa/2\pi$ [MHz]	7.09	0.696	0.384	0.239	0.080

Table 8.3: 1D hybridized cavity modes parameters

Site number	1	2	3	4	5
$\Omega_m/2\pi$ [MHz]	2.142	2.165	2.202	2.238	2.267
$\Gamma_m/2\pi$ [Hz]	4.3(3)	4.2(3)	12.(1)	11.(1)	15.(4)
Site number	6	7	8	9	10
$\Omega_m/2\pi$ [MHz]	2.315	2.616	2.405	2.448	2.506
$\Gamma_m/2\pi$ [Hz]	12.(2)	15.(2)	8.(0)	16.(6)	10.6(3)

Table 8.4: 1D mechanical modes parameters

Hybridized mode	24	23	22	21	20	19	18	17
$\omega_c/2\pi$ [GHz]	8.250	7.926	7.851	7.667	7.644	7.512	7.494	7.481
$\kappa/2\pi$ [MHz]	6.468	2.165	2.504	1.027	3.31	2.002	0.349	0.362
Hybridized mode	16	15	14	13	12	11	10	9
$\omega_c/2\pi$ [GHz]	7.401	7.374	7.224	7.189	7.100	7.068	6.911	6.896
$\kappa/2\pi$ [MHz]	4.79	4.601	4.485	1.09	0.265	0.766	4.36	1.121
Hybridized mode	8	7	6	5	4	3	2	1
$\omega_c/2\pi$ [GHz]	6.871	6.837	6.829	6.797	6.772	6.750	6.717	6.671
$\kappa/2\pi$ [MHz]	0.241	0.174	2.635	1.603	1.261	0.532	1.308	0.456

Table 8.5: 2D hybridized cavity modes parameters

Site number	1	2	3	4	5	6	7	8
$\Omega_m/2\pi$ [MHz]	2.106	2.127	2.158	2.179	2.208	2.233	2.260	2.291
$\Gamma_m/2\pi$ [Hz]	43.(7)	9.(0)	6.(9)	4.(1)	15.(6)	12.(6)	14.(1)	6.0(9)
Site number	9	10	11	12	13	14	15	16
$\Omega_m/2\pi$ [MHz]	2.314	2.347	2.380	2.413	2.435	2.469	2.501	2.539
$\Gamma_m/2\pi$ [Hz]	29.(8)	8.(1)	20.(5)	3.2(7)	5.(5)	10.(8)	6.7(7)	6.(4)
Site number	17	18	19	20	21	22	23	24
$\Omega_m/2\pi$ [MHz]	2.571	2.611	2.648	2.672	2.708	2.749	2.796	2.836
$\Gamma_m/2\pi$ [Hz]	16.(3)	9.(8)	39.(0)	20.(5)	18.(6)	10.(3)	8.(9)	18.(1)

Table 8.6: 2D mechanical modes parameters

#### 8.10.4 Measurement of optomechanical coupling rate

In order to measure  $\eta_i^k g_{0,i}$ , the effective optomechanical coupling rate between collective microwave mode  $k$  and mechanical oscillator  $i$ , we characterize the mechanical sideband induced by a resonant microwave drive. In contrast to the measurement of the optomechanical damping rate, we set the drive power so that the cooperativity can be about 1 to minimize the measurement backaction on the phonon occupation. We measure the power spectrum density (PSD) of the upper sideband signal and integrate the PSD to obtain the total power. From Eq. (2.63), the sideband power (Toth et al., 2017) scaled to photon flux is given by

$$n_{\text{sb}} = G^k \frac{\kappa_2^k}{\kappa_{\text{tot}}^k} \frac{\kappa_{\text{tot}}^k (\eta_i^k g_{0,i})^2 n_c^k}{\Omega_{m,i}^2 + \kappa_{\text{tot}}^k / 4} n_{m,i}, \quad (8.59)$$

where  $G^k$  is the gain of the full measurement chain from the device,  $\kappa_2^k$  is the external coupling rate to the output line, and  $n_{m,i}$  is the phonon occupation of mechanical oscillator  $i$ . The intracavity photon number with the resonant drive is explicitly described as

$$n_c^k = \frac{4\kappa_1^k}{\kappa_{\text{tot}}^k} R^k n_{\text{d,in}}, \quad (8.60)$$

where  $R^k$  is the transmittance between the device and a microwave source used for the drive,  $\kappa_1^k$  is the external coupling rate to the input line, and  $n_{\text{d,in}}$  is the drive power scaled to photon flux at the output of the microwave source. From the scattering parameters based on the input-output formalism (A. A. Clerk et al., 2010), the transmitted drive power scaled to photon flux is given by

$$n_{\text{d,out}} = G^k \frac{4\kappa_1^k \kappa_2^k}{\kappa_{\text{tot}}^k} R^k n_{\text{d,in}}, \quad (8.61)$$

where we assume that the gain  $G^k$  and transmittance  $R^k$  does not have frequency dependence between the drive and the mechanical sideband. Using Eqs. (8.59), (8.60), and (8.61), we obtain

$$\frac{n_{\text{sb}}}{n_{\text{d,out}}} = \frac{(\eta_i^k g_{0,i})^2}{\Omega_{m,i}^2 + \kappa_{\text{tot}}^k / 4} n_{m,i}. \quad (8.62)$$

Note that all the parameters that would be challenging to obtain experimentally, except for the effective optomechanical coupling rate  $\eta_i^k g_{0,i}$ , are canceled out in this expression, enabling us to determine the coupling rate.

We calibrate the phonon occupation  $n_{m,i}$  by increasing the temperature of the environment for the device so that the mechanical oscillator can be thermalized, i.e.  $n_{m,i} \approx k_B T / \hbar \Omega_{m,i}$ , where  $T$  is the base temperature of the dilution refrigerator. Figure 8.28a shows the PSD of the mechanical sideband of mechanical mode  $i = 6$  induced by the resonant drive to collective

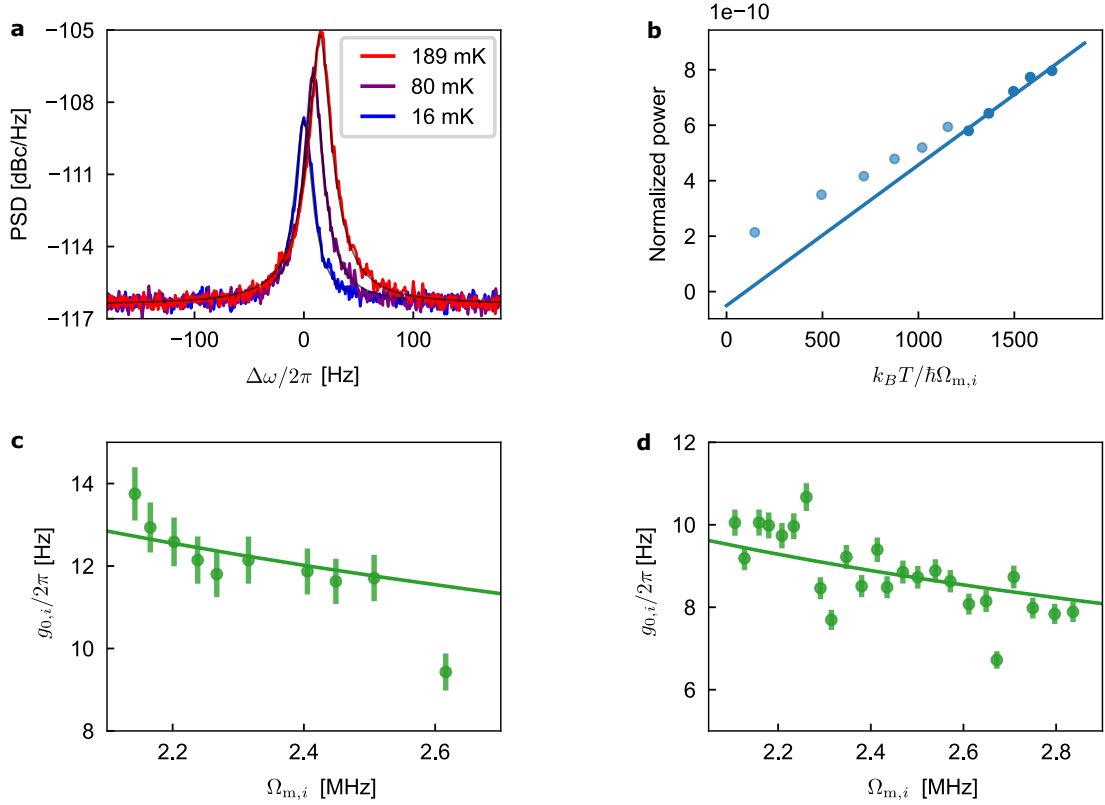


Figure 8.28: **Measurement of optomechanical coupling rate.** **a**, Power spectrum density (PSD) of the upper mechanical sideband with the different base temperatures of the dilution refrigerator. The black lines are the Voigt function fits to extract the total power of the sideband. **b**, Normalized total power of the mechanical sideband as a function of the nominal phonon occupation, calculated from the base temperature. The dots are the experimental results and the line is the linear fit to the data in the higher temperature region (dark blue). **c,d** Single-photon optomechanical coupling rate at site  $i$  for the 1D chain and 2D lattice, respectively. The lines are inverse square root fits.

microwave mode  $k = 10$  of the 1D chain. Since the minimum resolution bandwidth of the spectrum analyzer is comparable with the mechanical linewidth, we extract the total power of the mechanical Lorentzian peak by fitting the PSD with a Voigt function with the Gaussian bandwidth corresponding to the resolution bandwidth. Figure 8.28b shows the sideband power normalized by the transmitted drive power as a function of the nominal phonon occupation calculated by  $k_B T / \hbar \Omega_{m,i}$ . In the region of the higher temperature, the normalized sideband power follows linearly the nominal phonon occupation, so that we can assume it is thermalized. By fitting the slope in this region, the effective optomechanical coupling rate can be extracted as

$$(\eta_i^k g_{0,i})^2 = \frac{\partial(n_{\text{sb}}/n_{\text{d,out}})}{\partial n_{m,i}} \left( \Omega_{m,i}^2 + \kappa_{\text{tot}}^2 / 4 \right), \quad (8.63)$$

where all the remaining parameters are determined from independent measurements. Using the data shown in Fig. 8.28b, the optomechanical coupling rate between the collective microwave mode and the mechanical oscillator is found to be  $(\eta_i^k g_{0,i})/2\pi = 2.2$  Hz for  $k = 10$  and  $i = 6$ . Using the known participation ratio  $\eta_i^k$ , the optomechanical coupling rate at site  $i$  is found to be  $g_{0,i}/2\pi = 12$  Hz for  $i = 6$ .

Since all the participation ratio  $\eta_i^k$  are determined as discussed in Sec. 8.5.1, all the optomechanical coupling rate  $g_{0,i}$  are determined as follows. From the optomechanical damping rate, the unnormalized participation ratio  $\widetilde{\eta}_i^k$  is experimentally obtained by Eq. (8.28). Using the relation described in Eq. (8.29), the relative optomechanical coupling rate at site  $i$  can be determined as

$$\bar{g}_{0,i} = \frac{g_{0,i}}{\sum_i g_{0,i}} = \frac{(\widetilde{\eta}_i^k / \eta_i^k)}{\sum_i (\widetilde{\eta}_i^k / \eta_i^k)}. \quad (8.64)$$

We obtain the relative coupling rate using the modeshapes for  $k = 10$  of the 1D chain. From the mechanical sideband measurement, we have already known one of the optomechanical coupling rate, i.e.  $g_{0,i'}$  for  $i' = 6$  in our case. Thus, the optomechanical coupling rate at site  $i$  is determined as

$$g_{0,i} = \frac{\bar{g}_{0,i}}{\bar{g}_{0,i'}} g_{0,i'}. \quad (8.65)$$

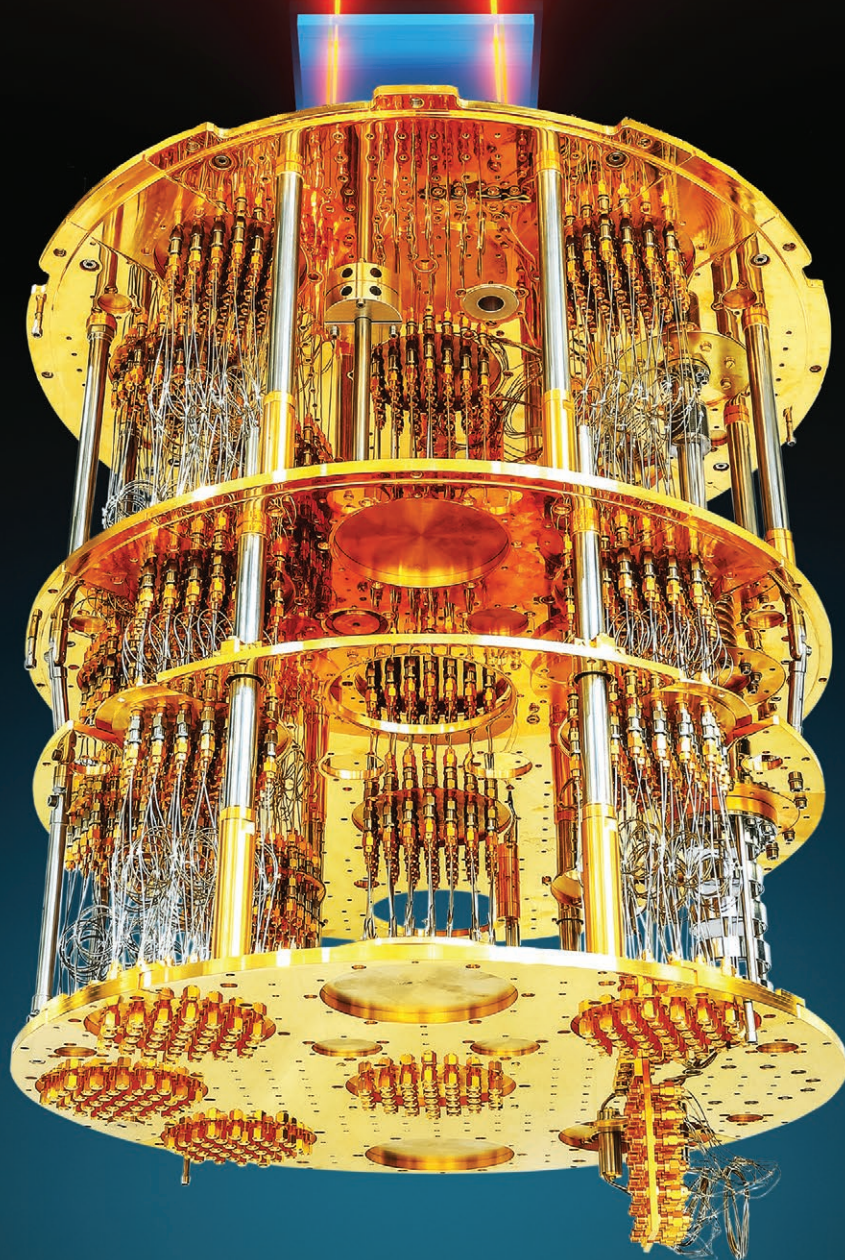
Figure 8.28c shows all the optomechanical coupling rate between the bare microwave mode and the mechanical oscillator at site  $i$  of the 1D chain. We apply the same measurement and analysis for the 2D lattice. All the optomechanical coupling rates in the 2D lattice are determined as shown in Fig. 8.28d.

As shown in Figs. 8.28c and d, the single-photon optomechanical coupling rates are fitted well to the inverse of the square root of the mechanical frequency. This can be interpreted by the fact that the zero-point fluctuation of motion of a mechanical oscillator is proportional to the inverse of the square root of the mechanical frequency, i.e.  $x_{\text{ZPF}} = \sqrt{\hbar/(2m_{\text{eff}}\Omega_m)}$ , where  $m_{\text{eff}}$  is the effective mass (Aspelmeyer, T. J. Kippenberg, and Marquardt, 2014).



# nature electronics

Getting a read of superconducting  
devices with light



Nature Electronics cover page of the May 2021 issue  
highlighting our work on cryogenic electro-optical interconnects



## 9 Cryogenic electro-optic interconnect for superconducting devices

The encoding of information onto optical fields via electro-optical modulation is the backbone of modern telecommunication networks (Winzer, Neilson, and Chraplyvy, 2018). The approach is based on optical fibers and offers vast bandwidth and low-loss transport. As a result, optical fibers are now replacing electrical cables in short-range communications within data centers (Kachris and Tomkos, 2012; Q. Cheng et al., 2018; Blumenthal et al., 2000). Optical interconnects based on silicon photonics have, in particular, been developed to address the high power consumption of electrical interconnects (Thomson et al., 2016), and these interconnects could also potentially be used for on-board chip-to-chip communication (Sun et al., 2015; Miller, 2000). Similar challenges exist in the development of superconducting quantum circuits (Devoret and R. J. Schoelkopf, 2013; Martinis, Devoret, and Clarke, 2020; Blais, Girvin, and Oliver, 2020), where the electrical connections required to interface with qubits introduce heat load, limiting the scaling of superconducting qubit technology (Arute et al., 2019). As the number of qubits is scaled up (Krinner et al., 2019), it will be necessary to increase the number of microwave control and readout lines, while preserving the base temperature and protecting the qubits from thermal noise.

In contrast to coaxial cables, optical fibers have superior thermal insulation, reducing the heat load per line by two orders of magnitude (Fig. 9.1c). Optical fibers additionally exhibit ultra-low signal losses (of about 0.2 dB/km), compared to the losses of coaxial cables at GHz frequencies (about 3 dB/m). Furthermore, thermal noise is completely negligible at optical frequencies. Optical fibers could therefore provide a solution to scaling the number of lines without the concomitant heating.

For such an approach, transducers that can convert input microwave signals to the optical domain at low temperatures and with low-noise are required, and quantum-coherent interfaces between the microwave and optical domains are being developed (Lauk et al., 2020; Lecocq, Quinlan, et al., 2020). To date, quantum coherent conversion schemes based on piezo-electromechanical (Jiang, Patel, et al., 2019; Jiang, Sarabalis, et al., 2019), magneto-optical (Bartholomew et al., 2019), and optomechanical (Higginbotham et al., 2018; Forsch et al., 2020; Arnold et al., 2020; Andrews et al., 2014; Chu and Gröblacher, 2020; Mirhosseini,

Sipahigil, et al., 2020a) coupling have been developed. In addition, schemes based on cavity electro-optics (Tsang, 2010) have been demonstrated using bulk (Rueda, Sedlmeir, Collodo, et al., 2016; Rueda, Sedlmeir, Kumari, et al., 2019; Hease et al., 2020) or integrated (L. Fan et al., 2018; McKenna et al., 2020; Holzgrafe et al., 2020) microwave cavities coupled via the Pockels effect to an optical cavity mode. However, all these schemes can only transduce narrow-band microwave signals to the optical domain and cannot replace current cryogenic semiconductor amplifiers, which are based on high electron mobility transistors (HEMTs) and used for the readout of GHz microwave signals. Optical interconnects based on broadband electro-optical modulation could potentially be an attractive alternative to cryogenic semiconductor amplifiers for superconducting quantum circuits (Devoret and R. J. Schoelkopf, 2013; Martinis, Devoret, and Clarke, 2020; Blais, Girvin, and Oliver, 2020) and hybrid superconducting devices (A. Clerk et al., 2020). While this approach may yield lower conversion efficiency compared to systems employing narrow-band resonant cavities, continued improvements in design, and new material systems, can render it competitive, especially given its relative simplicity. However, little is known about optical modulation at cryogenic temperatures.

Here, we report a cryogenic electro-optical interconnect based on a commercial titanium-doped lithium niobate ( $\text{Ti:LiNbO}_3$ ) optical phase modulator (Wooten et al., 2000) and detect microwave signals from a cryogenic circuit. We show that such modulators are compatible with operation down to 800 mK—below the typical 3 K operation temperature of conventional microwave amplifiers based on HEMTs (Pospieszalski et al., 1988; Duh et al., 1988)—and maintain their room temperature Pockels coefficient.

To demonstrate electro-optical read-out, we perform spectroscopy on a superconducting circuit optomechanical system and measure optomechanically induced transparency (OMIT) (Weis et al., 2010; Safavi-Naeini, Alegre, et al., 2011; J. D. Teufel, D. Li, et al., 2011). Furthermore, we encode thermomechanical sidebands from the microwave domain onto an optical signal processed at room temperature.

Although our optical readout currently has significantly higher noise, +60 dB compared to the output of a typical HEMT, substantial noise reduction should be attainable by harnessing recent advances in integrated modulators (C. Wang et al., 2018; He et al., 2019; Thiele et al., 2020; Chakraborty et al., 2020), such as by increasing the modulator length, or by using materials with a higher electro-optic coefficient (Abel et al., 2019; Eltes et al., 2019).

Our work highlights the potential of electro-optical modulators for massively parallel readout for emerging quantum computing (Devoret and R. J. Schoelkopf, 2013; Martinis, Devoret, and Clarke, 2020; Blais, Girvin, and Oliver, 2020; A. Clerk et al., 2020) or cryogenic classical computing (A. I. Braginski, 2019) platforms.

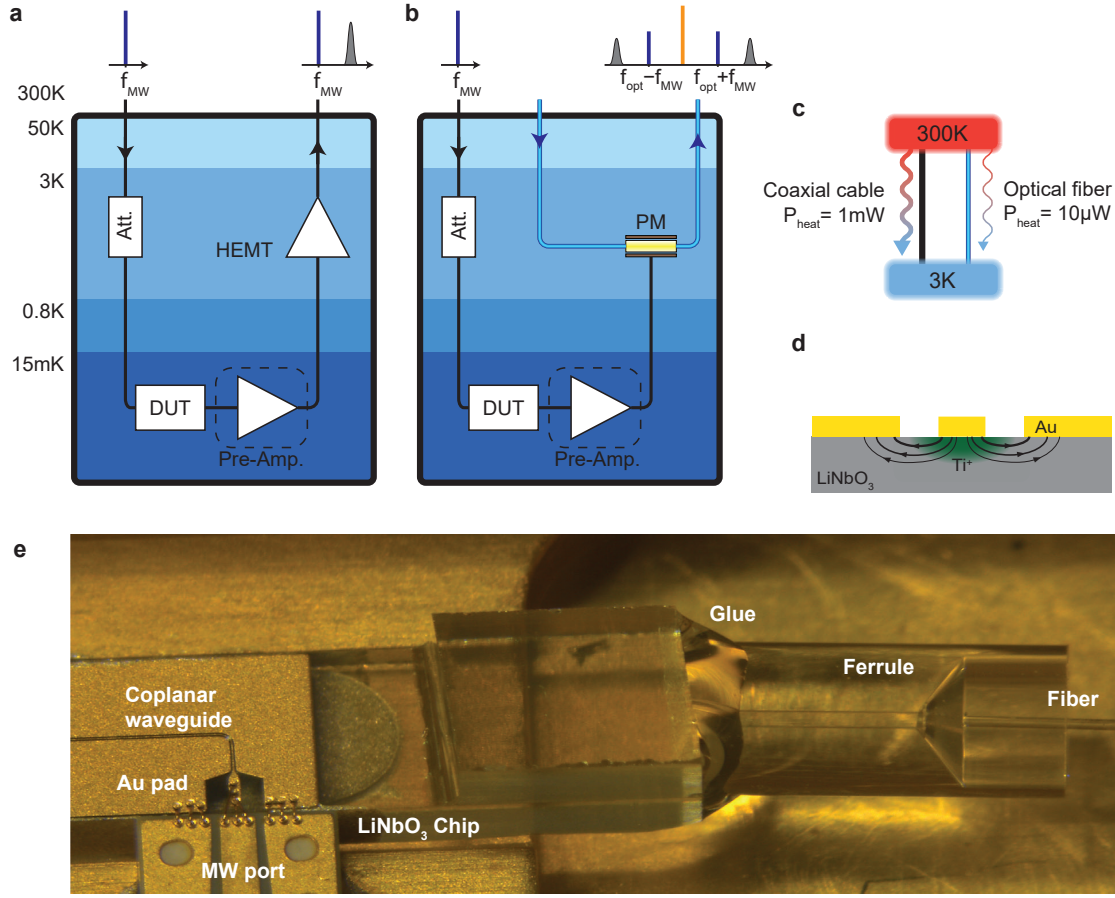


**Figure 9.1: Principle of a cryogenic electro-optic interconnect for readout of superconducting devices.** **a**, Simplified schematic of a conventional readout of a device under test (DUT) in a dilution fridge using a cryogenic HEMT amplifier. The dashed box indicates an optional quantum-limited pre-amplifier not used in this work. The devices are interrogated by input microwave signals that are attenuated to reduce thermal noise, and amplified using an HEMT amplifier at 3 K. **b**, Principle of a cryogenic electro-optic readout scheme using an electro-optic phase modulator. The DUT is interrogated using the same microwave input line, but the microwave signals are converted to the optical domain at 3 K, reducing thermal load. **c**, Conducted heat through a typical cryogenic coaxial cable and optical fiber, between room temperature and 3 K. **d**, Schematic cross-section of a z-cut LiNbO<sub>3</sub> electro-optic phase modulator. **e**, Microscope photo of the commercial phase modulator used in the experiment, showing the coupling region between fiber and LiNbO<sub>3</sub> chip.

## 9.1 Principle of Operation of electro-optical transducer

A prototypical measurement setup for a single superconducting device-under-test (DUT) that operates at the 15 mK stage of a dilution refrigerator is shown in Fig. 9.1a. Coaxial cables are used to transmit output signals to the room temperature, as well as to send control signals to the cold stages of the fridge. To read out GHz microwave signals, a HEMT amplifier that operates at the 3 K stage and has low-added-noise, expressed as  $n_{add} \sim 10 \text{ quanta}/(\text{s} \cdot \text{Hz})$ , is

typically used to amplify the DUT output signal for further processing outside the cryostat. The HEMT amplification also compensates for losses in the cables. HEMTs are not quantum-limited (Pospieszalski et al., 1988; Duh et al., 1988), therefore Josephson junction-based pre-amplifiers (Macklin et al., 2015; Siddiqi et al., 2004) that operate at the 15 mK stage can be employed for near-quantum-limited microwave amplification (shown in Fig. 9.1). The presence of the coaxial cables introduces additional heat load from room temperature into the cold stages of the refrigerator, which poses a significant barrier to the scalability of such systems (Krinner et al., 2019).

We replace the HEMT amplifier with a LiNbO<sub>3</sub>-based optical phase modulator—the workhorse of modulator technology—to directly transduce the DUT microwave output signal onto sidebands around the optical carrier field (Fig. 9.1b), detectable using standard homodyne or heterodyne detection schemes at ambient temperatures. To illustrate the principle of the readout, we consider the operating principle of a PM. Optical PMs are based on the Pockels effect (Fig. 9.1d) and induce a phase shift on the input optical field  $E_{\text{in}}(t)$ , proportional to the voltage  $V(t)$  applied on the input microwave port of the device,

$$E_{\text{out}}(t) = E_{\text{in}}(t) e^{-i\pi V(t)/V_\pi} \approx E_{\text{in}}(t) [1 - i\pi V(t)/V_\pi], \quad (9.1)$$

where the half-wave voltage  $V_\pi$  is the voltage at which the phase shift is  $\pi$ , and typical  $V(t) \ll V_\pi$  is assumed. The relation between microwave (field operator  $\hat{b}$ ) and optical (field operator  $\hat{a}$ ) photon flux spectral densities (A. A. Clerk et al., 2010),  $\mathcal{J}_{bb}$  and  $\mathcal{J}_{aa}$  respectively, can be written as (see Sec. 9.1.1 and Appendix B)

$$\bar{\mathcal{J}}_{aa}[\omega_{\text{opt}} \pm \omega_{\text{MW}}] = G \times (\bar{\mathcal{J}}_{bb}[\omega_{\text{MW}}] + n_{\text{add}}) \quad (9.2)$$

where  $\omega_{\text{MW}}$  and  $\omega_{\text{opt}}$  are the microwave signal and optical carrier frequencies,  $n_{\text{add}}$  is the added noise of the transducer (referred to the input), and the transduction gain  $G$  is the number of transduced optical photons per microwave input photon, given by (see Sec. 9.1.1):

$$G = P_{\text{opt}} \frac{\omega_{\text{MW}}}{\omega_{\text{opt}}} \frac{\pi^2 Z_0}{2V_\pi^2} \quad (9.3)$$

where  $P_{\text{opt}}$  is the power of the optical carrier at the output of the PM, and  $Z_0$  its input microwave impedance. In this experiment, we employ a commercial (Thorlabs LN65S-FC), *z*-cut traveling wave Ti-doped LiNbO<sub>3</sub> PM with specified bandwidth of 10 GHz and  $V_\pi = 7.5$  V at 10 GHz (Fig. 9.1e). We use a 1555 nm fiber laser as the optical source. The typical incident optical power on the PM is 15 mW. The optical transmission of the PM was reduced during the first cooldown, and measured at 23%. Additional details on the cryogenic optical setup are given in Sec. 9.5.2.

Previous works investigated the temperature dependence of the electro-optic coefficient and refractive index of congruent LiNbO<sub>3</sub> at low frequencies down to 7 K (Herzog, Poberaj, and Günter, 2008). Commercial *x*-cut LN modulators were also tested down to 10 K, showing a

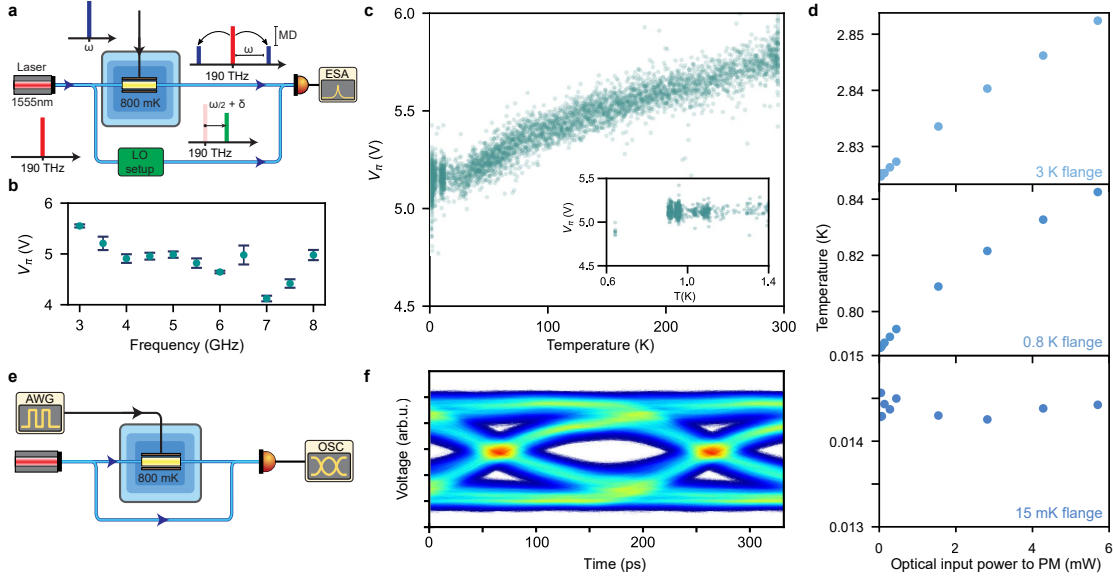


Figure 9.2: **Cryogenic characterization of a LiNbO<sub>3</sub> phase modulator.** **a**, Experimental setup for low-temperature characterization of the phase modulator. **b**, plot of  $V_\pi$  vs. frequency at 800 mK. **c**, Characterization of  $V_\pi$  at 5 GHz vs. temperature from room temperature to 800 mK. **d**, Measurement of heating due to optical dissipation when the phase modulator is mounted on the 800 mK flange. Plot of the steady state temperature vs. input laser power of the 3 K, 800 mK, and 15 mK flanges. **e**, Experimental setup for phase shift keying detection. RF signal from the waveform generator is directly applied on a phase modulator. After homodyne detection the electrical signal is recorded on a fast oscilloscope. **f**, Eye-diagram of an optical signal phase-modulated at a rate of 5 Gbaud, the bit error ratio is  $5 \times 10^{-5}$ .

slight change in  $V_\pi$  from its room temperature value (Morse et al., 1994; C. McConaghy et al., 1996). Ref. (Yoshida, Kanda, and Kohjiro, 1999) discusses the behavior of LiNbO<sub>3</sub> modulators with superconducting electrodes down to 4 K. To date, however, such modulators have not been used in a dilution refrigerator to directly read out a superconducting device.

### 9.1.1 Quantum mechanical model for a phase modulator.

In the following, we derive a simple quantum description of the phase modulator to establish the quantum limits in transducing the input microwaves. A more detailed discussion is also provided in Appendix B. The central assumption is that the linear regime stays valid, for sufficiently low input microwave powers. As such, the scattering equations linking inputs to output should be identical in both quantum and classical cases. We can use the known classical regime as a starting point, with the output optical field amplitude  $\hat{a}_{\text{out}}$  expressed as a function of the input optical field  $\hat{a}_{\text{in}}$  as

$$\hat{a}_{\text{out}} = e^{-i\pi V/V_\pi} \hat{a}_{\text{in}} \approx (1 - i\pi V/V_\pi) \hat{a}_{\text{in}}, \quad (9.4)$$

where  $V$  is the classical voltage applied at the input and the half-wave voltage  $V_\pi$  is the voltage at which the phase modulator applies a phase shift of  $\pi$ . For the quantum model, the classical fields are replaced by their quantum equivalent. The microwave input becomes  $\hat{V} = \sqrt{\hbar\omega_{\text{MW}}Z_0}(\hat{b} + \hat{b}^\dagger)/\sqrt{2}$  with  $\hat{b}$  the annihilation operator for the microwave field at frequency  $\omega_{\text{MW}}$  traveling on a transmission line of impedance  $Z_0$ . The optical input is  $\hat{a}_{\text{in}} = \alpha e^{-i\omega_{\text{opt}}t} + \delta\hat{a}_{\text{in}}$ , where  $\alpha$  is the amplitude of the coherent carrier field of frequency  $\omega_{\text{opt}}$ , with  $|\alpha|^2 = P_{\text{opt}}/\hbar\omega_{\text{opt}}$ , and  $\delta\hat{a}_{\text{in}}$  carries the quantum fluctuations of the input optical field. Inserting the expressions in Eq. (9.4), we can compute  $\delta\hat{a}_{\text{out}} = \hat{a}_{\text{out}} - \alpha e^{-i\omega_{\text{opt}}t}$ , the quantum fluctuations of the output optical field, given by

$$\delta\hat{a}_{\text{out}} = \delta\hat{a}_{\text{in}} - i\sqrt{G}e^{-i\omega_{\text{opt}}t}(\hat{b} + \hat{b}^\dagger) \quad (9.5)$$

with the transduction gain  $G$  given by Eq. (9.3).

To understand the implications of Eq. (9.5) for the quantum noise in the transduction, we compute the power spectral density of the output optical field,

$$\mathcal{S}_{\delta\hat{a}^\dagger\delta\hat{a}}^{\text{out}}[\omega_{\text{opt}} + \omega_{\text{MW}}] = \mathcal{S}_{\delta\hat{a}^\dagger\delta\hat{a}}^{\text{in}}[\omega_{\text{opt}} + \omega_{\text{MW}}] + G(\mathcal{S}_{b^\dagger b}[\omega_{\text{MW}}] + \mathcal{S}_{bb^\dagger}[-\omega_{\text{MW}}]). \quad (9.6)$$

The first term corresponds to the *added* quantum noise due to the input optical field. The second term contains contributions from the microwave frequency  $\omega_{\text{MW}}$ , including both the signal and noise. The third term contains *added* microwave noise at frequency  $-\omega_{\text{MW}}$ , composed of thermal and quantum noise components, respectively  $n_{\text{th}}^{\text{MW}} + 1/2$ .

Thus Eq. (9.6) can be simplified to

$$\mathcal{S}_{\delta\hat{a}^\dagger\delta\hat{a}}^{\text{out}}[\omega_{\text{opt}} + \omega_{\text{MW}}] = G\mathcal{S}_{b^\dagger b}[\omega_{\text{MW}}] + G\left(n_{\text{th}}^{\text{MW}} + \frac{1}{2}\right) + \frac{1}{2}. \quad (9.7)$$

We emphasize two limiting cases. When  $G \ll 1$ , as in our experiment, the added noise is dominated by the input optical quantum noise, the last term in Eq. (9.7). In the opposite limit,  $G \gg 1$ , the added noise is dominated by the microwave input noise, and the signal-to-noise ratio is independent of  $G$ . In any case, the added noise referred to the input is given by Eq. (9.9).

## 9.2 Cryogenic Characterization of the optical modulator

To characterize the electro-optic behavior of the device at cryogenic temperatures, we mount the PM on the 800 mK flange of the dilution fridge. We directly drive the microwave port of the PM at frequency  $\omega_{\text{MW}}$  using a microwave source outside the fridge, generating sidebands around the optical carrier frequency (Fig. 9.2a). The half-wave voltage  $V_\pi$  is determined from the modulation depth MD, defined as the ratio of the power in one of the sidebands to the



power in the carrier,

$$V_\pi = \pi \sqrt{\frac{Z_0 P_{\text{MW}}}{2 \text{MD}}}, \quad (9.8)$$

where  $P_{\text{MW}}$  is the power at the microwave input port of the PM. We measure MD by beating the output optical signal with a local oscillator (LO) with frequency  $\omega_{\text{opt}} + \omega_{\text{MW}}/2 + \delta$ , generating two closely-spaced beatnotes at  $\omega_{\text{MW}}/2 \pm \delta$ , due to the carrier and the high-frequency sideband. Using Eq. (9.8) we extract  $V_\pi$  by sweeping the microwave power and measuring MD. Figure 9.2c shows  $V_\pi$  at 5 GHz monitored as the fridge is cooled down from room temperature to 800 mK, and Fig. 9.2b shows  $V_\pi$  at different frequencies at 800 mK. Importantly,  $V_\pi$  does not change substantially from the room temperature value.

To investigate the effect of heating caused by optical dissipation in the PM, we measured the steady state temperature of different flanges of the dilution fridge when the PM is mounted on the 800 mK flange. The results are shown in Fig. 9.2d. In Sec. 9.5.2, by comparing to a calibrated heater, we show that these temperature increases can be attributed to optical power loss within the PM package (and not, e.g. light leakage into the fridge volume). This allows quantitative comparison with, e.g., heat dissipation due to a HEMT, and suggests reduced heat load in high optical transmission devices.

To further assess the performance of the PM at 800 mK, we also performed a basic telecommunication experiment shown in Fig. 9.2e. An arbitrary waveform generator (AWG) directly drives the PM with a pseudo-random bit sequence at a rate of 5 GBaud. We beat the optical phase-modulated carrier output with its reference arm, effectively forming a Mach-Zehnder interferometer whose average transmission is tuned to the quadrature point by adjusting the laser frequency, and detect the electrical signal on the oscilloscope. Figure 9.2f shows an eye diagram obtained from  $8 \times 10^5$  samples. The open eye diagram features no error bits, hence the upper bound on the bit error ratio is limited by the total amount of measured samples and can be estimated to be  $5 \times 10^{-5}$  with 95% confidence level (Keysight, 2018). These measurements clearly demonstrate that the cryogenic modulator still functions at 800 mK.

### 9.3 Optical readout of coherent microwave spectroscopy

Having established the cryogenic modulation properties, we next carry out a cryogenic interconnect experiment, where the microwave output of a DUT is read out optically. As an example system, we employ a superconducting electromechanical device in the form of a mechanically-compliant vacuum gap capacitor parametrically coupled to a superconducting microwave resonator (Fig. 9.3a–e). These devices have been employed in a range of quantum electromechanical experiments, such as cooling the mechanical resonator to its quantum ground state (J. D. Teufel, Donner, D. Li, et al., 2011), strong coupling between mechanical and microwave modes (J. D. Teufel, D. Li, et al., 2011), squeezing of mechanical motion (Wallucks et al., 2020), and demonstration of the quantum entanglement in the

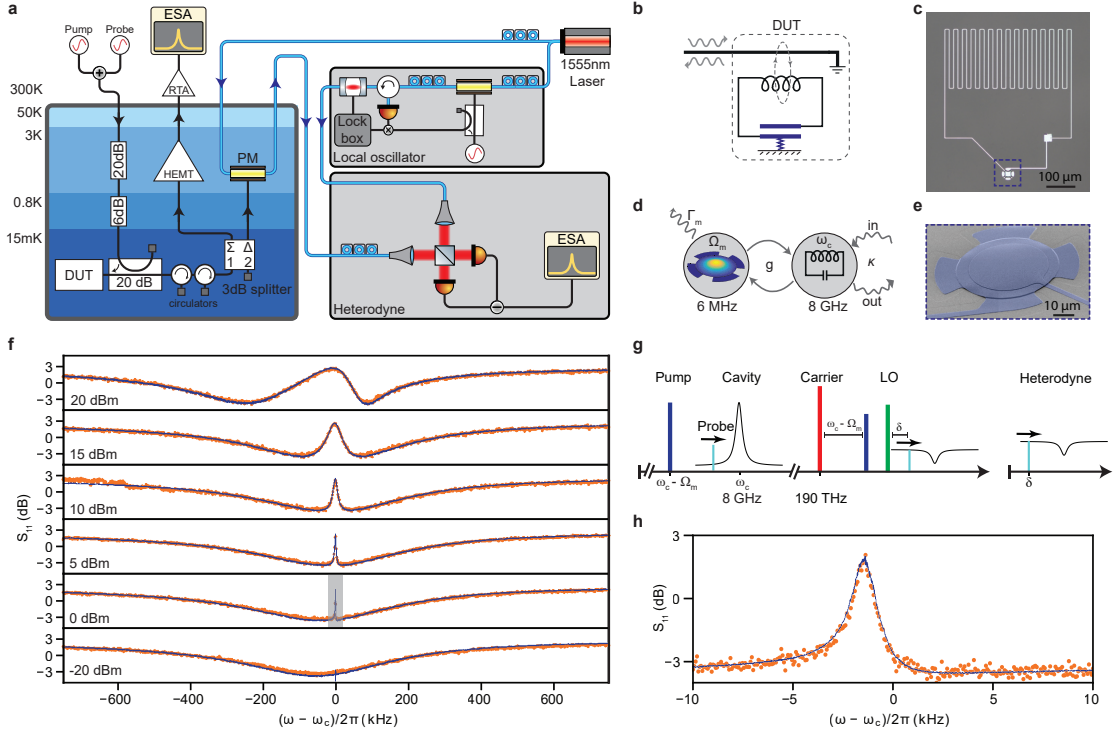


**Figure 9.3: Electro-optic readout of a coherent microwave spectrum of a superconducting electromechanical system.** **a**, Experimental setup. Left: dilution fridge, right: optical setup. (ESA: electrical spectrum analyzer, DUT: device under test, RTA: room temperature amplifier) **b**, Electromechanical system used as a DUT. **c**, Optical micrograph of the *LC* resonator. **d**, Modal diagram of the electromechanical system. **e**, Scanning electron micrograph of the mechanically compliant capacitor. **f**, Coherent measurement of the electromechanical resonance for increasing microwave pump powers of (−20, 0, 5, 10, 15, 20) dBm at the source, from bottom to top respectively. The probe power is −20 dBm at the source. The estimated total attenuation from the source to DUT is −70 dB. Each trace is normalized to its leftmost, off-resonance data point. By increasing the pump power, the optomechanically induced transparency window emerges, and at stronger pump powers the modes get strongly coupled, leading to an avoided crossing effect. Blue lines correspond to HEMT readout and orange dots to optical readout. **g**, the frequency scheme for microwave tones, optical tones, and measured signal after heterodyning. **h**, high resolution measurement of the transparency window highlighted in **f** with the gray box.

mechanical motion (C. Ockeloen-Korppi et al., 2018), as well as implementing mechanically mediated tunable microwave non-reciprocity (Bernier et al., 2017) and quantum reservoir engineering (Toth et al., 2017). The microwave resonance (frequency  $\omega_c \approx 2\pi \times 8.2$  GHz and linewidth  $\kappa \approx 2\pi \times 3$  MHz) is coupled to the mechanical resonance (frequency  $\Omega_m \approx 2\pi \times 6$  MHz and linewidth  $\Gamma_m \approx 2\pi \times 10$  Hz) of the capacitor via electromechanical coupling (Aspelmeyer, T. J. Kippenberg, and Marquardt, 2014) (Fig. 9.3d). The electromechanical coupling rate is  $g = g_0 \sqrt{\bar{n}_{\text{cav}}}$ , where  $g_0 \approx 2\pi \times 150$  Hz is independently characterized (Bernier, 2019) and  $\bar{n}_{\text{cav}}$  is intracavity microwave photon number, proportional to the microwave pump power. The

system is inductively coupled to a microwave feed-line, enabling us to pump and read out the microwave mode in reflection.

To demonstrate the electro-optical readout technique, we perform two-tone spectroscopy and measure optomechanically induced transparency (OMIT) (Weis et al., 2010; Safavi-Naeini, Alegre, et al., 2011) on the electromechanical sample, by applying a microwave pump tone on the lower motional sideband (red-detuned by  $\Omega_m$  from the cavity resonance) and sweeping a second probe tone across the resonance. The strong pump damps the mechanical motion, resulting in a wider effective mechanical linewidth,  $\Gamma_{\text{eff}} = \Gamma_m + 4g^2/\kappa$ . The microwave pump modifies the cavity response due to the electromechanical coupling, resulting in a transparency window of width  $\Gamma_{\text{eff}}$  that appears on resonance, which we observe by the probe (Fig. 9.3g). We performed an OMIT experiment for different pump powers and observed the mechanical resonance via the transparency feature. In order to electro-optically read out the coherent response, the optical output is detected in a balanced heterodyne detector, using a frequency-shifted local oscillator (Fig. 9.3g). Note that the local oscillator phase is locked to the optical signal, which enables reading out a microwave feature narrower than the laser linewidth (Fig. 9.3h). To compare the optical and HEMT readouts, the reflected signal is split and measured simultaneously using both techniques (Fig. 9.3a). Figure 9.3f shows the OMIT results, with excellent agreement between the optical and HEMT readouts. At high pump powers, when  $g \sim \kappa$ , we observe mode splitting as a result of strong coupling and mode-hybridization between the mechanical and microwave modes (J. D. Teufel, D. Li, et al., 2011).

## 9.4 Optical readout of an incoherent microwave spectrum

Next, we employ our scheme to directly read out optically the power spectral density of a microwave signal emitted by the DUT. For this, we drive the mechanical oscillator into self-oscillation by pumping the system on its upper motional sideband,  $\omega_{\text{pump}} = \omega_c + \Omega_m$ , inducing a parametric instability (Aspelmeyer, T. J. Kippenberg, and Marquardt, 2014; Marquardt, Harris, and Girvin, 2006; Carmon et al., 2005). The output microwave spectrum features strong sidebands around the microwave pump, at integer multiples of the mechanical frequency (Fig. 9.4a).

Figure 9.4c shows these mechanical signals obtained simultaneously using both our optical readout and the HEMT amplifier. We use the known properties of the HEMT to estimate the transduction gain  $G$  [Eq. (9.2)] of our optical readout. The blue trace in Fig. 9.4c shows the HEMT output referred back to its input using its known added noise,  $n_{\text{add}}^{\text{HEMT}} \simeq 8 \text{ quanta}/(\text{s} \cdot \text{Hz})$ , characterized independently (See Sec. 6.5). This calibration yields the HEMT input signal  $S$ , which is also equal to the PM microwave input. The noise in the optically detected spectrum, referred to the optical output of the PM, is dominated by the optical shot noise,  $1 \text{ quanta}/(\text{s} \cdot \text{Hz})$ , for our  $G \ll 1$ . In this calibration, we can obtain  $G$  from the optical spectrum containing the transduced microwave signal  $GS$ . The orange trace in Fig. 9.4c shows the

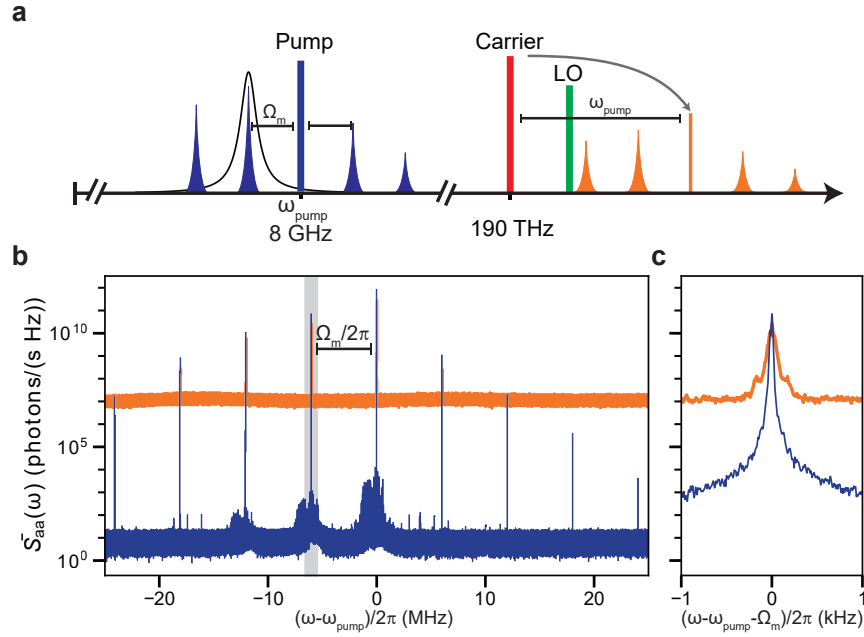


Figure 9.4: **Electro-optic readout of an incoherent microwave spectrum of a superconducting electromechanical system.** **a**, Frequency-domain picture: a microwave tone pumps the electromechanical system on the upper motional sideband, inducing a parametric instability and generating mechanical sidebands equally spaced around the tone by the mechanical resonance frequency  $\Omega_m$ . The phase modulator transfers the microwave spectrum on the optical signal, which is subsequently mixed with a local oscillator (LO) and detected via heterodyne detection. **b**, Measured power spectral densities of the microwave pump (central peak) and mechanical sidebands detected by the HEMT (blue) and optical (orange) readouts. **c**, Enlargement of the gray-shaded area in **b**, showing the power spectral densities of the on-resonance mechanical sideband.

optical noise spectrum referred to the microwave input, and Fig. 9.4d shows a zoom-in of a single sideband. In this calibration, the signal areas in both measurements are equal to  $S$ . Further explanation of this calibration is given in Sec. 9.5.1. This yields  $G \sim 10^{-7}$ , in good agreement with the theoretical value  $G^{\text{theory}} = 3.5 \times 10^{-7}$  obtained from Eq. (9.3) using the measured output optical power,  $P_{\text{opt}} = 1.1 \text{ mW}$  (optical efficiency of 5%, including losses in fiber connectors and heterodyne detection setup). We note that the frequency widening of the optically detected sidebands, observed in Fig. 9.4d, is due to fluctuations in the LO frequency, caused by the limited bandwidth of the locking setup in conjunction with using a minimal resolution bandwidth (RBW) of 1 Hz in the spectrum measurement. The integrated sideband power, however, is conserved. Improving the LO locking setup can reduce this effect.

The added noise in the transduction process is (see Sec. 9.5.1)

$$n_{\text{add}} = \frac{1}{2G} + n_{\text{th}}^{\text{MW}} + \frac{1}{2}, \quad (9.9)$$

where  $n_{\text{th}}^{\text{MW}}$  is the average occupation of the thermal photonic bath due to the microwave fields. This gives  $n_{\text{add}} \approx 6 \times 10^6$ . The noise floor of the optical measurement in Fig. 9.4c is 60 dB above the HEMT readout. This is due to the very small gain  $G$ , caused by the large  $V_\pi$  and the limited optical power. However, there is much room for improvement in these parameters. Ref. (Abel et al., 2019) reported a  $V_\pi$ -length product of 0.45 V cm in a BaTiO<sub>3</sub>-based modulator, thus  $V_\pi \sim 50$  mV can be realized in a  $\sim 10$  cm device, possibly using low-loss superconducting electrodes (Yoshida, Kanda, and Kohjiro, 1999; Holzgrafe et al., 2020). The optical power can be increased arbitrarily in principle, however, one needs to consider optical losses (mainly at the fiber-to-chip interfaces) that lead to heating. Considering a device with an improved optical transmission of 66% and incident power of 15 mW, yields  $P_{\text{opt}} \sim 10$  mW (commercial PMs with typical insertion loss  $< 2$  dB, ( $> 63\%$  transmission), at room temperature are already available).

This scenario achieves  $G \sim 5 \times 10^{-2}$  [Eq. (9.3)], with  $n_{\text{add}} \approx 20$  at 3 K and 8 GHz. Together with a heat load of  $\sim 5$  mW, this is comparable to the performance of a typical cryogenic HEMT. However, while improvements to HEMT power consumption have been reported recently (Cha et al., 2020a; Cha et al., 2020b; Wong et al., 2020), these devices still admit *passive* heat load due to the thermally-conducting coaxial cables. In contrast, an important advantage of the electro-optic approach is the ultra-low passive heat load [ $10 \mu\text{W}$  per fiber, see Fig. 9.1(c)]. This allows scaling the number of transducers, in conjunction with time-division multiplexing of the laser pumps, without incurring additional heat load (Lecocq, Quinlan, et al., 2020).

It is worth mentioning that many experiments utilize a near-quantum-limited pre-amplifier at the 15 mK stage (Fig. 9.1a,b). In this case, the noise added in the second amplification stage, referred to the input, is  $\sim (G_{\text{PA}} G)^{-1}$  (see Sec. 9.5.1), where  $G_{\text{PA}} \sim 10^2$  is the pre-amplifier gain (Macklin et al., 2015; Siddiqi et al., 2004). Thus,  $G > G_{\text{PA}}^{-1}$  suffices to preserve near-quantum-limited amplification.

## 9.5 Experimental details and characterization

### 9.5.1 Calibration of the transduction gain

Figure 9.5 illustrates the procedure of experimentally characterizing the transduction gain of our electro-optic transducer. The microwave signal is split equally into two parts  $S$ , fed to the HEMT amplifier and the PM respectively (Fig. 9.5a). The HEMT added noise is characterized independently to be  $n_{\text{add}}^{\text{HEMT}} = 8$  quanta/(s · Hz). We infer  $S$  from the spectrum of the HEMT amplified signal, referring the noise floor to  $n_{\text{add}}^{\text{HEMT}}$  (Fig. 9.5b). In the PM branch, the added noise of the transduction is given by Eq. (9.9). The spectrum is detected using a balanced heterodyne detector, which adds  $1/2$  quanta/(s · Hz) of noise (Fig. 9.5c). We can safely neglect  $G(n_{\text{th}}^{\text{MW}} + 1/2)$  and consider the noise floor of the spectrum referred to the input of the heterodyne detector, i.e. 1 quanta/(s · Hz). This allows us to calculate  $GS$ , and finally obtain  $G$  with knowledge of  $S$  from the HEMT measurement.

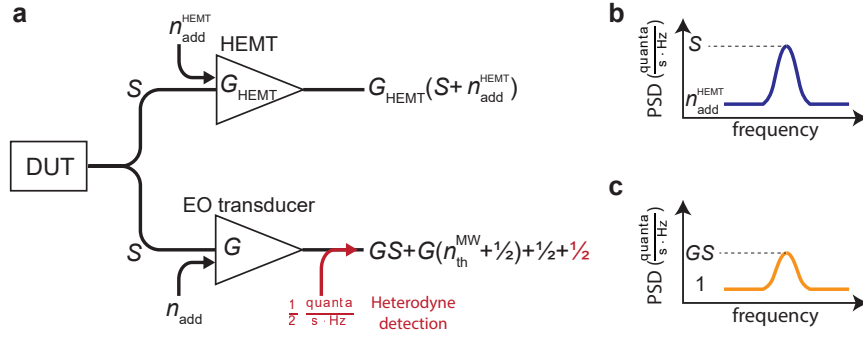


Figure 9.5: **Illustration of the gain characterization procedure.** **a**, Propagation of the DUT signal through the system. **b**, Power spectral density of the HEMT output. **c**, Power spectral density of the optical heterodyne detector.

When using a quantum-limited pre-amplifiers before the electro-optical transducer (not done in our experiment), we can model the readout chain as shown in Fig. 9.6b. The total added noise of the readout chain is

$$n_{\text{add}}^{\text{total}} = n_{\text{add}}^{\text{PA}} + \frac{n_{\text{add}}}{G_{\text{PA}}} \approx n_{\text{add}}^{\text{PA}} + \frac{1}{2G_{\text{PA}}G} \quad (9.10)$$

Therefore when  $G \approx 1/G_{\text{PA}}$ , the total added noise will be dominated by  $n_{\text{add}}^{\text{PA}} \sim 1 \text{ quanta}/(\text{s} \cdot \text{Hz})$  (Macklin et al., 2015; Siddiqi et al., 2004) and the readout will be near-quantum-limited.

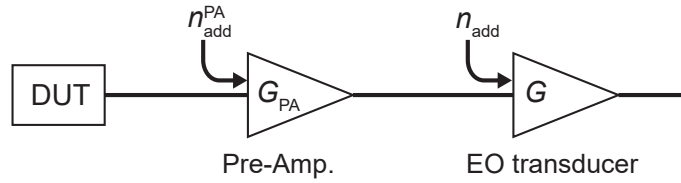


Figure 9.6: **Schematic signal flow when pre-amplifier is used.**

### 9.5.2 Experimental details and heating measurements.

We use a fiber-coupled lithium niobate PM from Thorlabs, model LN65S, used as-is with no modifications. Note that the minimum specified operating temperature is  $0^\circ\text{C}$ . The device sustained several cooldown-warmup cycles with reversible behavior in its optical transmission. We measured 25% reduction in the optical transmission at cryogenic relative to room temperature. The PM metallic box was tightly clamped to the flange of the 800 mK or 3 K stage. We use a Bluefors LD-250 dilution refrigerator. The approximate *available* cooling powers of the {15 mK, 800 mK, 3 K} stages are {12  $\mu\text{W}$ , 30 mW, 300 mW}.

Figure 9.2c shows the variation of  $V_\pi$  from room temperature to 800 mK, obtained during a cooldown of the dilution fridge and measured using the default thermometer on the 800 mK flange, located next to the heat exchanger, about 10 cm from the PM. In order to rule out



possible temperature gradients, we mounted a calibrated thermometer next to the PM and monitored both thermometer readings during cooldown. Figure 9.7a shows the measured relative temperature difference, which is less than  $\sim 5\%$  throughout the cooldown. Note that this excludes pulse precooling and mixture condensation period when the temperature is unstable (shown for completeness in Fig. 9.7a).

Figure 9.2d shows the temperature increase of the 15 mK, 800 mK, and 3 mK stages of the dilution fridge as a function of the optical power incident on the PM, which is mounted on the 800 mK stage. We performed a simple measurement to verify that this temperature increase can be ascribed to light absorbed in the PM body (and not, e.g, light leakage into the fridge volume), corresponding to the optical transmission (insertion loss) of the PM. We used the calibrated  $120\ \Omega$  still heater built in the 800 mK stage to apply heat directly, we then repeated the measurement using optical input to the PM as the heating source (as in Fig. 9.2d). Figure 9.7a,b compares the results of this measurement, showing temperature increase in the 3 K and 800 mK stages (the latter recorded with the two separated thermometers) vs. dissipated power. In the case of optical heating, the dissipated power is computed directly from the incident power on the PM and its measured transmission of 23%.

Figure 9.7b,c shows the result of this measurement. The optical heating shows a temperature increase of 13.3 mK/mW (6.5 mK/mW) at the 800 mK (3 K) stage (Fig. 9.7a), while the resistive heating shows a temperature increase of 14.1 mK/mW (8.3 mK/mW) at the 800 mK (3 K) stage (Fig. 9.7b). Thus heating due to the operation of the electro-optic interconnect is very similar to localized, resistive heating.

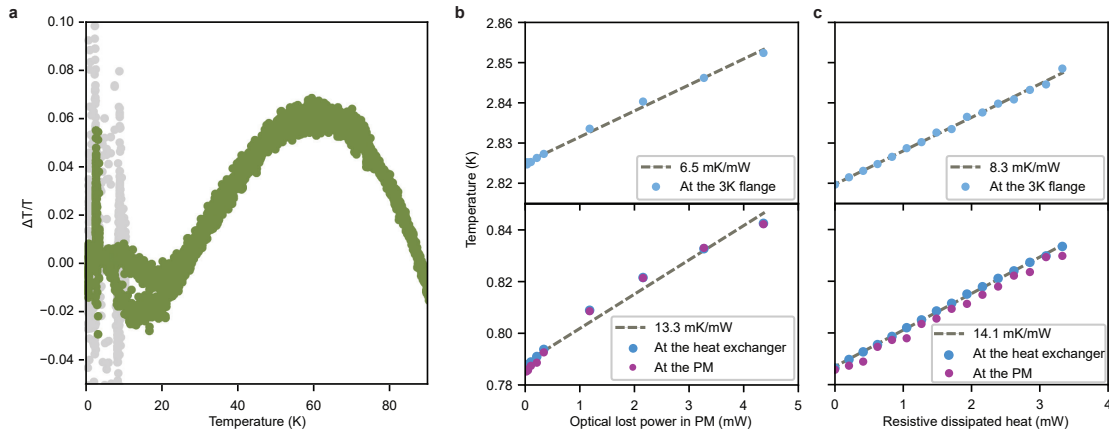


**Figure 9.7: Heat dissipation and temperature gradients.** **a**, Relative temperature difference between PM box and heat exchanger, on 800 mK flange during a cooldown. The gray data points correspond to specific periods of pulse precooling and mixture condensation, where the temperature is unstable. **b**, Measurement of heating due to optical dissipation when the phase modulator is mounted on the 800 mK flange. **c**, Measurement of heating using a calibrated resistive heater mounted on the 800 mK flange.

## 10 Conclusion and outlook

In this thesis, we introduced a new platform for superconducting circuit optomechanics that allows us to create and store high-fidelity quantum states of mechanical oscillators, significantly enhance the mechanical quantum coherence, scale up the number of mechanical and microwave modes to create lattices of optomechanical systems, explore multi-mode and collective effects in such lattices, and exploit optomechanical interaction as intrinsic probes to measure collective mode shapes in large-scale superconducting circuits.

The ultra-coherent electromechanical system can be exploited in quantum sensing applications (B.-B. Li et al., 2021). The expected on-resonance force sensitivity of our device can be estimated as  $\sqrt{S_{FF}} = \sqrt{4k_B T m_{\text{eff}} \Gamma_m} = 240 \times 10^{-21} \left[ \frac{\text{N}}{\sqrt{\text{Hz}}} \right]$  which is considerably low compared with several other optomechanical platforms thanks to the high mechanical quality factor and the low operating temperature of the device.

The high-fidelity quantum control and measurement of mechanical oscillators with such extremely low thermal decoherence and pure dephasing rates will benefit the implementation of qubit-mechanics interfaces (A. Reed et al., 2017), generation of mechanical non-classical states (Gely and G. A. Steele, 2021a), and can realize long life-time memories for quantum computation and communication (Wallucks et al., 2020; Pechal, Arrangoiz-Arriola, and Safavi-Naeini, 2018). Furthermore, such a low quantum decoherence sets the stage to perform fundamental tests of quantum mechanics in macroscopic scales such as quantum gravity tests (Y. Liu, Mummery, et al., 2021; Gely and G. A. Steele, 2021b), as well as high fidelity Bell tests (Marinković et al., 2018; Hong et al., 2017), quantum teleportation (Fiaschi et al., 2021), or even the search for Dark matter (Carney et al., 2021; Manley et al., 2021).

Particularly, the Diósi-Penrose effect (Penrose, 1996; Diosi, 1987) -as an example of the broader class of quantum collapse models (Bassi et al., 2013)- is expected to be experimentally resolvable in massive and quantum coherent optomechanical systems. In the proposal by Gely (Gely and G. A. Steele, 2021b), an estimated time scale to observe a general relativity-induced quantum state decoherence in a mechanical object prepared in a superposition state is  $T_{\text{GR}} \simeq \frac{1}{m_{\text{eff}}} \times 3 \times 10^{-15} \text{ [kg}\cdot\text{s]}$ . In order to observe such GR-induced state decoherence the

oscillator should be able to maintain the quantum from thermal decoherence and dephasing for much longer times, i.e.  $T_{\text{dec}} \gg T_{\text{GR}}$  or in other words  $\Gamma_{\text{th}}^{-1}, \Gamma_{\phi}^{-1} \gg T_{\text{GR}}$ . Assuming the numbers, among all optomechanical platforms to date, our superconducting circuit-based system is one of the best candidates to satisfy this condition as we have  $T_{\text{GR}} \simeq 1$  ms and  $T_{\text{dec}} \simeq 8$  ms considering 2.3 ng effective mass (see Sec. 3.2). This was not the case for the conventional circuit electromechanical systems when the decoherence times were substantially shorter.

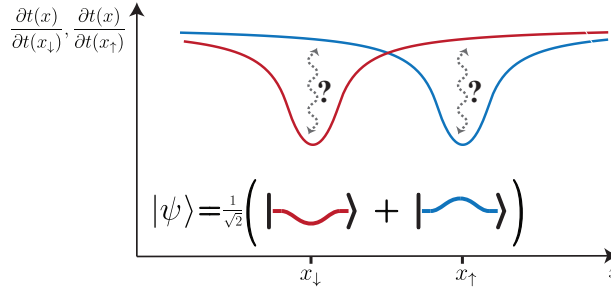
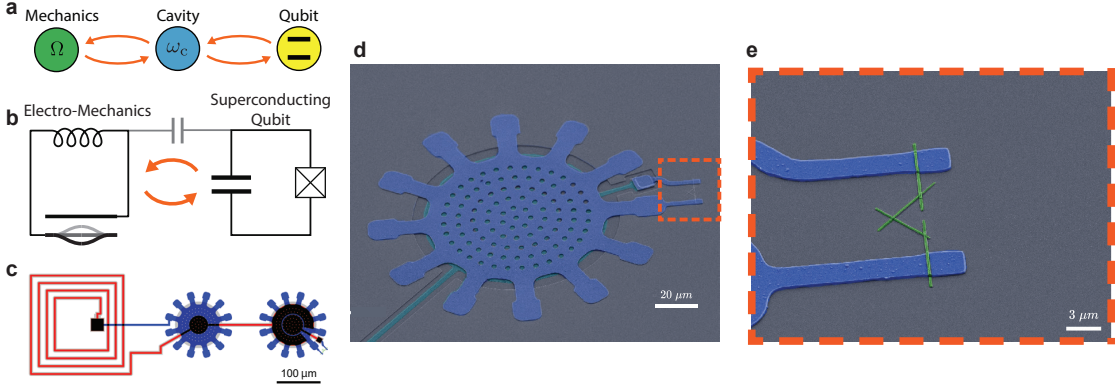


Figure 10.1: **Gravitational induced time-shift ambiguity in massive mechanical superposition states.** We can imagine a drumhead capacitor -or any other massive mesoscopic mechanical resonators- prepared in a superposition state of  $|x_{\downarrow}\rangle$  and  $|x_{\uparrow}\rangle$ . There will be an ambiguity in time definition at one position depending on the mass distribution of the mechanical resonator if we assume a superposition state. this time ambiguity can lead to energy uncertainty and consequently quantum decoherence of the superposition state (Gely and G. A. Steele, 2021b).

Another clear path to continue is to integrate the ultra-coherent electromechanical device with superconducting qubits. A superconducting qubit is known as a low-dissipation microwave circuit with the nonlinearity brought by Josephson junctions. The Josephson nonlinearity enables us to generate a nontrivial quantum state in a microwave field, a fundamental source of quantum information processing. The strong coupling to microwave fields and the flexibility in circuit design have enabled the field of superconducting qubits to revolutionize quantum information science, providing not only a promising experimental platform for large-scale quantum information processing (Barends et al., 2014), but also the possibility to generate a nonclassical quantum state in a microwave cavity (Vlastakis et al., 2013). The availability of quantum control of microwave photons together with a theoretical breakthrough about a hardware-efficient quantum error correction (Leghtas et al., 2013) has provided a new platform of quantum information processing based on microwave cavities. To realize a large-scale quantum computation, however, there still remains a challenge in scaling up microwave cavities because of their bulky structures (Reagor et al., 2016).

Various experimental achievements on microwave optomechanical systems have brought a lot of attention to realizing a quantum memory based on a mechanical oscillator to help quantum information processing with superconducting quantum circuits (Pechal, Arrangoiz-Arriola, and Safavi-Naeini, 2018). The main advantage of mechanical oscillators as a quantum memory against microwave cavities is that the thermal decoherence rate of a mechanical oscillator is



**Figure 10.2: Integration of electromechanical device with superconducting qubits.** **a**, The mode diagram of the qubit-mechanics hybrid system is shown as well as the equivalent circuit **(b)** and proposed design **(c)**, where a vacuum-gap transmon qubit is coupled to mechanics. **d** and **e**, False colored SEM of a proof-of-concept qubit-electromechanics integration attempt. The Josephson junction shunted with the parallel plate capacitor is shown by green. Photo credit: Mahdi Chegnizadeh.

smaller than that of a microwave cavity, enabling us to store a quantum state for a longer time. By applying elastic strain engineering and soft clamping to a mechanically compliant vacuum capacitor, the mechanical  $Q$  factor is expected to be enhanced even more. Moreover, the size of a mechanical oscillator is much smaller than that of a microwave cavity, enabling us to save footprints for a large-scale quantum system.

One of the first milestones in this direction is to demonstrate a high- $Q$  superconducting qubit formed by a vacuum gap capacitor shunted by a Josephson junction. This will not only prove that the fabrication process of electromechanical systems is compatible with that for superconducting qubits, but also demonstrate the availability of a vacuum gap capacitor for the field of superconducting quantum circuits. This will provide a smaller footprint, less crosstalk, and a lower dielectric loss in the qubit capacitor for a scalable quantum information processor based on superconducting qubits.

Demonstration of the first engineerable optomechanical lattice with exceptionally low disorder was another topic discussed in this thesis. Looking forward, such optomechanical lattices offer a path to realize proposals exploring the rich physics in multimode optomechanics, ranging from quench (Raeisi and Marquardt, 2020) and collective (G. Heinrich et al., 2011) dynamics, to reservoir engineering (Tomadin et al., 2012; Yanay and A. A. Clerk, 2020; Zippilli and Vitali, 2021). Specifically, by using degenerate mechanical oscillators it is possible to create collective long-range interactions and observe strong cooperative effects on mechanical motion (Xuereb, Genes, and Dantan, 2012). Moreover, our system may enable the generation of highly entangled mechanical states (Akram et al., 2012), and viewed more broadly, it can be used to explore quantum correlations in topological optomechanical lattices (Peano et al., 2015; Zangeneh-Nejad and Fleury, 2020; Ludwig and Marquardt, 2013).

More specifically, the extremely low disorder achieved in our platform allows us to study the collective dynamics in multiple nearly degenerate mechanical oscillators optomechanically coupled to a shared microwave resonator. It can be shown that the mechanical oscillators undergo a transition from individual to collective dynamics as their optomechanical interactions are enhanced (Scigliuzzo et al., 2023). Particularly, the sideband cooling of multimode mechanical systems can be achieved, where one collective mechanical mode is efficiently cooled down while the individual modes retain the large phonon occupations. By optimizing the circuit optomechanical platform, we may reduce even more the disorder among mechanical oscillator frequencies, less than 0.1%, and observe the transition from the individual ones to the collective mechanical mode, and, even further, the strong coupling of the collective mechanical mode and the microwave resonator. With the high-quality factor of the mechanical oscillators, we may be able cool the collective mode close to the quantum ground state. This system is envisioned to enable the study of the entanglement among multiple macroscopic mechanical oscillators as well.

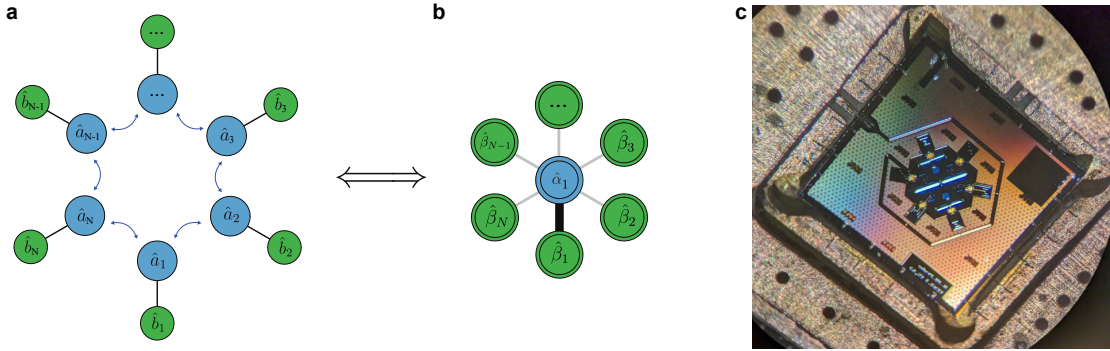


**Figure 10.3: Collective dynamics in superconducting circuit optomechanical chains.** **a**, The mode diagram of an optomechanical chain with degenerate mechanical modes. **b**, At high cooperativities when driving one of the microwave collective modes, the cross-talk between degenerate mechanical modes result in forming a collective mechanical mode strongly coupled to the driven microwave with the same modeshape, while the other microwave modes are well optomechanically decoupled from the collective microwave mode. **c**, Photo of a prototype optomechanical chain with six modes in a chain. Photo credit: Mahdi Chegnizadeh and Marco Scigliuzzo.

The last but not the least, We believe that our first proof of concept cryogenic electro-optical interconnect experiment demonstrates unambiguously the major potential that fiber optical communication paired with efficient electro-optical modulators have for solving the superconducting interconnect scaling problem. Fiber optical interconnects, as in the case of data-center interconnect, could provide a viable route to a new generation of readout techniques -that so far, had received little attention. Furthermore, we quantified the gap between conventional microwave amplifiers and our electro-optical approach. Although our optical readout scheme results in higher noise compared to the output of a typical HEMT, significant noise improvements should be feasible by using improved devices with lower  $V_\pi$ , resulting

in a near-quantum-limited broadband microwave-to-optical interconnect. The emergence of new materials such as BaTiO<sub>3</sub> (Eltes et al., 2019; Ortmann et al., 2019), BaSrTiO<sub>3</sub>, KNbO<sub>3</sub>, and organic polymers (Dalton, Sullivan, and Bale, 2010) with significantly higher Pockels coefficients than LiNbO<sub>3</sub> may lead to a substantial increase in transduction efficiencies. developing novel nano-fabrication techniques, exploiting new electro-optic materials specifically for low temperatures, and improving the design of microwave circuitry to increase the mode overlap for ultra-efficient integrated electro-optical transducers, reducing their noise figure below the conventional electrical amplifiers. Realizing such devices also allows the efficient generation of microwave-optical entangled photons for communication applications (Rueda, Hease, et al., 2019).

## Supplementary discussions on nano-fabrication

### A.1 Aluminum thin films

As expected, the quality, stress, and roughness of the aluminum thin film used for the top layer influences both the release step and the low-temperature mechanical quality factor of drum-heads. Here discuss the effect of deposition and post-deposition techniques to manipulate such parameters.

#### A.1.1 Deposition method

Aluminum can be deposited by either electron beam evaporation or sputtering techniques as physical depositions. The evaporation is done under high vacuum ( $10^{-6} - 10^{-8}$  mBar), where an electron beam is hitting a crucible to emit Al atoms. The deposition rate is controlled by the electron-beam power and the distance of the wafer to the crucible. In sputtering, a crucible of aluminum will be bombarded by plasma Argon ions. The detached Al atoms will be sputtered on the wafer. Sputtering normally gives better step coverage compared to evaporation. The deposition rate and film properties can be controlled by argon flow and the source power. The pressure of the chamber in sputtering is typically around  $10^{-3}$  mBar, depending on the argon flow.

#### A.1.2 Low-temperature stress of aluminum films

Although the aluminum thin film can have compressive stress at room temperature, the significant difference between the thermal expansion rate of Al and Si results in the shrinking of Al films faster than Si and induces tensile stress at cryogenic temperatures. The following relation can estimate the final low-temperature stress of the film:

$$\sigma_{\text{Al}} = \sigma_{\text{Al}}^{\text{RT}} + \int_{10 \text{ mK}}^{300 \text{ K}} Y_{(T)}^{\text{Al}} (\alpha_{(T)}^{\text{Al}} - \alpha_{(T)}^{\text{Si}}) dT \approx 300 \text{ MPa} + \sigma_{\text{Al}}^{\text{RT}}, \quad (\text{A.1})$$



Where  $Y^{\text{Al}}$  is Young's modulus of aluminum and  $\alpha$  is the thermal expansion rate of Al or Si, respectively. The relatively big difference between two expansion rates ( $\alpha_{(20\text{K})}^{\text{Al}} = 23.1 \times 10^{-6}/^{\circ}\text{C}$  and  $\alpha_{(20\text{K})}^{\text{Si}} = 2.6 \times 10^{-6}/^{\circ}\text{C}$ ) results in considerable stress change at lower temperatures as well as high sensitivity of deposition induced initial stress to the deposition temperature and thermalization. The initial room temperature stress,  $\sigma_{\text{Al}}^{\text{RT}}$ , varies depending on the deposition conditions. The stress of a thin film can be calculated by measuring the change of the wafer's bow - i.e., the curvature of the wafer - before and after deposition using the following relation:

$$\sigma_{\text{film}} = -\frac{Y_{\text{sub}}}{6(1-\nu_{\text{sub}})} \frac{t_{\text{sub}}^2}{t_{\text{film}}} \left( \frac{1}{R_{\text{sub+film}}} - \frac{1}{R_{\text{sub}}} \right), \quad (\text{A.2})$$

Where  $\nu$  shows the Poisson's ratio,  $t$  is the thickness, and  $R$  is the wafer's bow. The wafer's bow can be measured optically by sweeping a laser on the wafer in stress measurement tool (Toho Technology<sup>®</sup> FLX 2320-S).

### A.1.3 High temperature aluminum deposition

We explored high temperature evaporation and sputtering of Al to reach to tensile stress at room temperature. Both evaporator and sputtering tools can deposit at higher temperatures up to 350 Celsius. We tested deposition of 250 nm Al on Si wafer at 200°C with both methods. Although both methods resulted in tensile stress of  $\sim 30$  MPa at room temperature, sputtering showed an acceptable film quality with  $R_a = 7$  nm while the high temperature evaporation resulted in color change of the material to white and increasing of the grain size and roughness to  $R_a = 50$  nm, which indicates compound formation between Al and Si.

### A.1.4 High temperature sputtering and surface roughness

We deposited Al at different temperatures with the sputtering tool (Pfeiffer<sup>®</sup> SPIDER 600) and measured stress and roughness. Although the film stress increases by temperature, the roughness and grain size also increases which reduces the quality of the film.

Table A.1: High temperature aluminum sputtering.

T (Celsius)	20	100	200	250	350
$\sigma_{\text{Al}}$ (MPa)	-53	35	41	47	61
$R_a$ (nm)	2	10	15	17	20

### A.1.5 Effect of evaporation rate on surface roughness

We measured the film roughness in the three conditions of room temperature Al evaporation mentioned below and realized EVA 760 gives us the best film quality. We note that for the ground state cooling experiment we need to remove the galvanic connection and have to

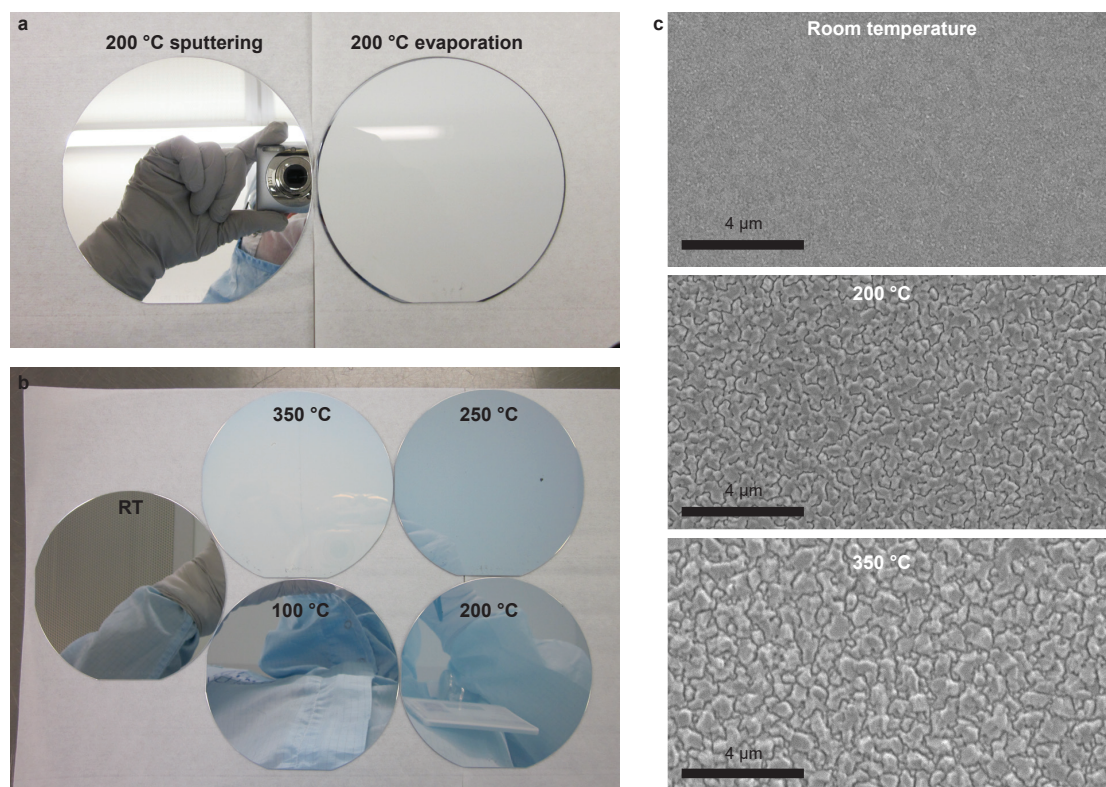


Figure A.1: **High temperature aluminum deposition.** **a**, Comparison between 200°C sputtering and evaporation. **b**, Aluminum sputtering at high temperatures. **c**, SEM of high temperature aluminum sputtering showing significant increase of grain size by temperature.

deposit the top layer with Plassys<sup>®</sup> UHV evaporator with  $10^{-8}$  mBar vacuum which also demonstrated high mechanical quality factors.

- Alliance-Concept<sup>®</sup> EVA 760 with  $10^{-6}$  mBar pressure, 45 cm working distance, and 5 Å/s deposition rate. Film roughness:  $R_a = 2.1$  nm
- Leybold Optics<sup>®</sup> LAB 600H with  $1.8 \times 10^{-6}$  mBar pressure, 100 cm working distance, and 4 Å/s deposition rate. Film roughness:  $R_a = 3.5$  nm
- Leybold Optics<sup>®</sup> LAB 600H with  $1.8 \times 10^{-6}$  mBar pressure, 100 cm working distance, and 1 Å/s deposition rate. Film roughness:  $R_a = 8$  nm

#### A.1.6 Effect of annealing cycle on the stress

The effect of thermal annealing on the aluminum thin film stress has been studied in Gardner et al. (Gardner and Flinn, 1990). It has been demonstrated that the slow annealing cycle of the Al-1%Si film with 640 nm thickness after deposition by heating it up to  $\sim 200^\circ\text{C}$  and cooling it down shows a hysteresis behavior in the stress resulting in higher tensile stress at the

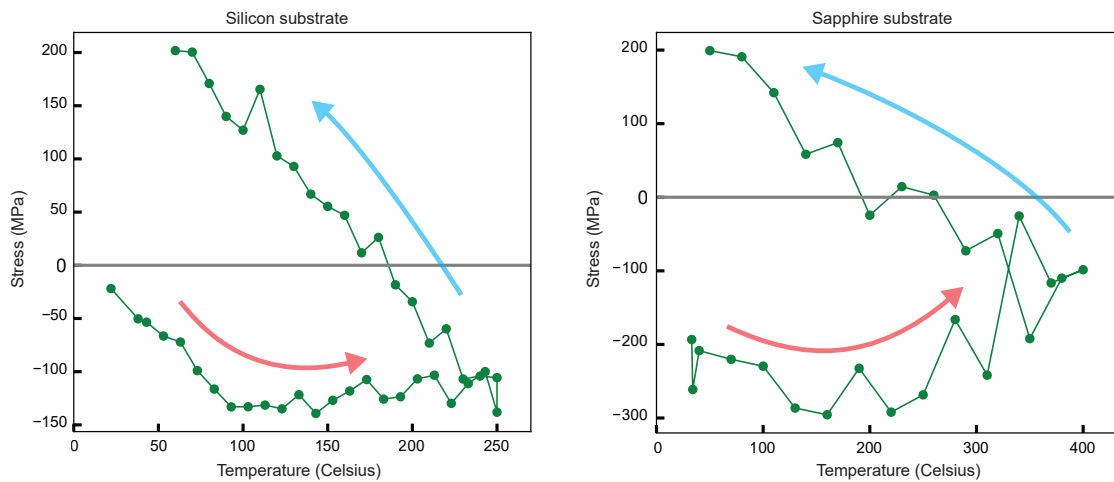


Figure A.2: **Effect of annealing on the aluminum stress.** Annealing aluminum thin film and cooling it down adiabatically changes the stress to tensile. 150 nm Al is evaporated on silicon and sapphire substrates and annealing for about two hours cycle up to 250°C and 400°C respectively showed stress enhancement to 200 MPa at room temperature. One has to be careful to run annealing under vacuum to avoid oxidation of the film.

same initial temperature. We investigated this behavior on the pure Al with 150 nm thickness evaporated by 4 Å/s rate. The result confirmed the same behavior where we could change the stress of the film deposited on Si or Sapphire wafers from initial compressive stress to ~ 200 MPa tensile. While this can be a useful technique to engineer the stress after deposition, we did not manage to use it for the final high- $Q_m$  and reproducible devices because of concerns about the compound formation and oxidation on the Al film. We did not investigate further the change of roughness and grain size after annealing. However, we qualitatively did not observe any color change, severe roughness, or reduced transparency of the film after annealing. It is worth noting that annealing under a weak vacuum to 200°C is often used in the traditional fabrication process of drumhead capacitors to relax and uniform stress in such drums before the release (Tóth, 2018).

### A.1.7 Yield stress of aluminum films

The stress-strain relation in materials generally has a linear behavior for small strains, which is called an elastic regime. By increasing the strain, in some cases, the stress does not scale linearly anymore, and the material goes to the plastic regime. Increasing the strain further results in buckling or cracking of the film. The stress which the elastic regime goes to plastic is called the *yield stress*. Although the bulk yield stress can be theoretically calculated for some materials, the experimental values are often lower than the theoretical expectations (Courtney, 2005). The bulk yield stress of Al is calculated ~ 900 MPa however, the measured values for the bulk aluminum and its alloys are between 200 – 400 MPa (Courtney, 2005). These values also depend on temperature. The low-temperature data on the mechanical properties of bulk

Al and its alloys can also be found in (Ekin, 2006). It is known that the yield stress in thin films or nano-structures can be higher than the bulk values approaching the theoretical limit depending on the thickness and grain size (Richter et al., 2009; Steinwall and Johnson, 1990). We did not find a systematic study on the yield stress of the sub-micron thin aluminum films at low temperatures.

Tapering the clamps of the drumhead increases the local stress on the clamps and is expected to decrease mechanical bending losses (Bereyhi et al., 2019). This enhanced stress should be below the yield stress to avoid breaking the legs or going to the plastic regime. To observe the ultimate limit of stress enhancement, we can achieve we made a sweep over the clamping ratio ( $CR \equiv$  the total perimeter of the trench divided by the total perimeter of the clamps) and cooled down these devices. After warming them up again, we observed drums with  $CR > 4$  are cracked, meaning that the maximum tolerable stress in our design at low temperatures should be below 1 GPa.

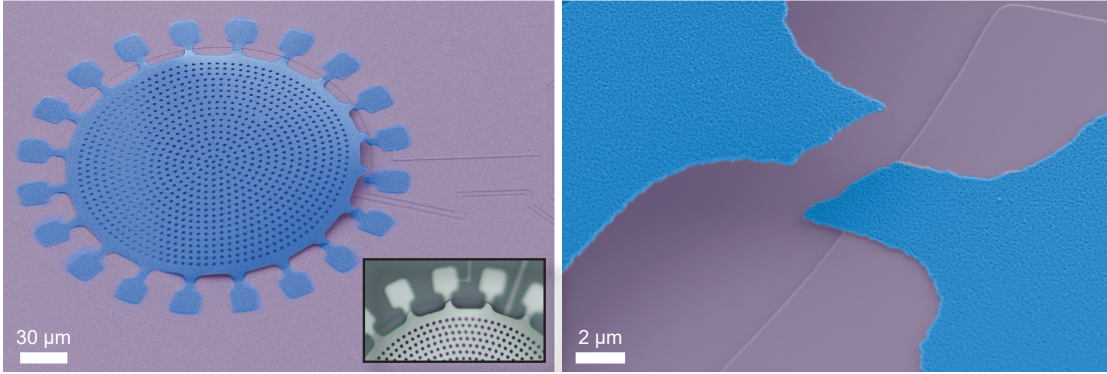


Figure A.3: **Broken clamps and yield stress.** SEM and microscope images show an example of devices after cool down with high clamp ratio ( $CR=7$  for the device shown in the figure). Due to clamp tapering, the stress increases reaching to the yield stress of the thin film which results in the crack of the clamp.

## A.2 Non-uniformity tolerance

In many applications, we need to design arrays and lattices of coupled identical LC electro-mechanical circuits. Studying the disorder tolerance in such systems is crucial to understand the fabrication technique's limits and to improve it. In the LC circuits with the spiral inductor and vacuum gap capacitor, the dominant frequency disorder mechanism is the gap size imperfection which is directly defined by the total non-uniformity of the trench depth and bottom aluminum layer thickness at the end of the fabrication process. The frequency disorder between two identical circuits with a central frequency of  $\omega_c$  and target gap size of  $d$  can be written as:

$$\frac{\Delta\omega_c}{\omega_c} = \frac{\Delta d}{2d}. \quad (\text{A.3})$$

For example, this results in  $15 \frac{\text{MHz}}{\text{nm}}$  shift of the cavity for a 6 GHz central cavity resonance frequency and 200 nm gap size. The total non-uniformity tolerance ( $\epsilon \equiv$  gap size variation divided by the lateral distance) is proportional to the maximum frequency tolerance of the circuit,  $\Delta\omega_c$ , and the maximum lateral distance between two vacuum gap capacitors in the design,  $l$ , expressed by:

$$\epsilon = \frac{2d\Delta\omega_c}{l\omega_c}. \quad (\text{A.4})$$

The frequency tolerance is normally defined by the desired mutual coupling between the identical LCs which is typically designed greater than 100 MHz in our designs. Considering one of the designs for the topological lattice project as an example, we required 50 MHz minimum coupling rate for a 2 mm lattice which results in maximum non-uniformity tolerance of  $\epsilon \simeq 2 \frac{\text{nm}}{\text{mm}}$ .

Each step of the fabrication process can in principle, induces non-uniformity. The total non-uniformity on the final device can be expressed based on the individual step's non-uniformity as  $\epsilon_{\text{tot}} = \sqrt{\sum \epsilon_i^2}$ . Considering our process flow, the main non-uniformity origins are silicon plasma etching ( $\epsilon < 0.5 \frac{\text{nm}}{\text{mm}}$ ), bottom layer aluminum evaporation ( $\epsilon \simeq 0.1 \frac{\text{nm}}{\text{mm}}$ , for sputtering it is higher value), LTO SiO<sub>2</sub> deposition ( $\epsilon \simeq 0.2 \frac{\text{nm}}{\text{mm}}$ ), IBE etch-back ( $\epsilon < 0.1 \frac{\text{nm}}{\text{mm}}$ ), and most importantly CMP,  $\epsilon_{\text{CMP}}$ . Considering the above-mentioned example of the topological lattice, the maximum tolerated CMP non-uniformity should be  $\epsilon_{\text{CMP}} < \sqrt{\epsilon_{\text{tot}}^2 - \sum_{i \neq \text{CMP}} \epsilon_i^2} = 1.9 \frac{\text{nm}}{\text{mm}}$ . This value can be easily achieved in CMP by optimizing the polishing parameters as discussed in Sec. 4.2.7.

### A.3 Sapphire substrate processing

In the early stage of our process development, we investigated implementing the idea of etching trenches on sapphire substrate, using amorphous Si as a sacrificial layer and planarizing it with CMP and releasing the drumhead with XeF<sub>2</sub> which is an isotropic gas etching, inspired by the traditional electro-mechanical platform were developed in LPQM-EPFL (Tóth, 2018). The advantage of sapphire at first sight was that it is a very resilient material to etchants, has high Young's modulus, low thermal expansion rate, and, most importantly, known to have less bulk dielectric loss for microwave circuits (Read et al., 2022). However, the other side of the coin was that micro-machining of sapphire is not trivial since it does not react with standard etchants. We realized that a few chlorine chemistries could be used to plasma-etch sapphire (Jeong et al., 2002). Among the possible options we tried 20%Cl<sub>2</sub>-80%BCl<sub>3</sub> argon plasma etching (STS® Multiplex ICP). Although the achieved etch rate was low (37 nm/min) and selectivity was below one (sapphire:PR ~ 1:3.5), we managed to etch a few hundred nano-meter depth trenches with acceptable sidewall angle for our purpose and roughness of  $R_a = 1.2$  nm inside the trenches.

After making the trench and deposition of the aSi sacrificial layer (sputtering with a good



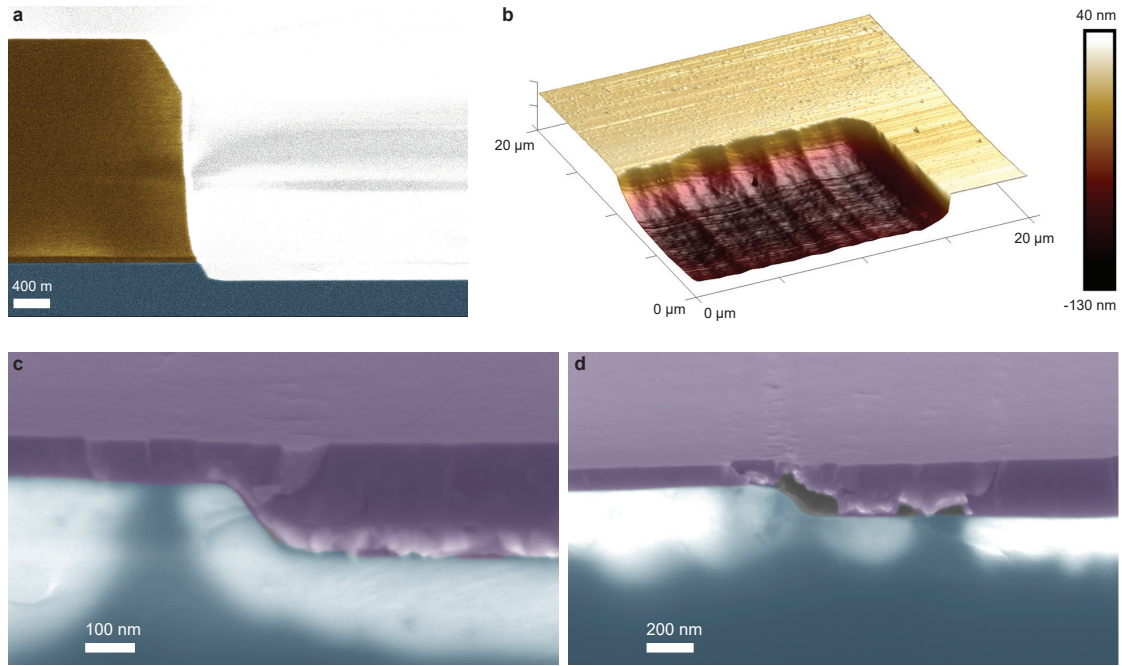


Figure A.4: **Sapphire substrate processing.** **a**, Cross section SEM of plasma etched trench in sapphire substrate. The orange color shows the photo resist. **b**, The AFM topography of a trench in sapphire. **c, d**, Cross section SEM of a sapphire trench covered by amorphous silicon sacrificial layer after CMP planarization. Due to the low adhesion of the aSi to the substrate, the sacrificial layer delaminates in the CMP.

step coverage), we tried using CMP to planarize the topography. In this step, we realized two important challenges. First, because of the hardness of the sapphire wafer, the bow compensation with the back pressure was challenging, resulting in low uniformity after the CMP. The second problem was the low adhesion of aSi to the sapphire substrate, which resulted in the delamination of the sacrificial layer even when we stopped polishing above the wafer level. Considering such issues, we decided to switch to the high resistivity silicon substrate, which supports a wide range of standardized micro-machining processes.

## Appendix B

# Linear quantum model for electro-optical phase modulators

In this appendix, we describe the optical output of a phase modulator, taking into account the quantum aspects of the microwave input. Dr. Nathan Bernier had a substantial contribution to the development of the theoretical framework described here.

### B.1 Quantum model description

We note that only the optical output is relevant in the description, since most low- $V_\pi$  modulators are implemented with a matched load for the microwave input port, such that all microwaves are absorbed into the device.

The central assumption in the description is that the linear regime is valid for the optical modulation, which is always the case for sufficiently weak input microwave powers. At the classical level, we can write the output optical field amplitude  $\hat{a}_{\text{out}}$  as a function of the input optical field  $\hat{a}_{\text{in}}$  as

$$\hat{a}_{\text{out}} = e^{-i\pi V(t)/V_\pi} \hat{a}_{\text{in}} \approx \left[ 1 - i\pi \frac{V(t)}{V_\pi} \right] \hat{a}_{\text{in}}, \quad (\text{B.1})$$

where  $V$  is the classical voltage applied at the input and  $V_\pi$  is the voltage at which the phase modulator applies a phase shift of  $\pi$ .

For the quantum description, we will simply insert quantum operators instead of classical fields in [B.1](#). This simple swap is valid in the linear picture as nothing changes in the equation of motion of the system. For linear systems, the quantum aspects are only relevant as they set the minimum of random noise in the system. Otherwise, the dynamics transduces input to output with no distinction for quantum or classical signals. The voltage is described quantum mechanically as

$$V = \frac{V_{\text{zp}}}{\sqrt{2}} (\hat{b} + \hat{b}^\dagger) \quad (\text{B.2})$$



with  $\hat{b}$  the annihilation operator for the traveling microwave field and  $V_{zp}$  the “zero-point voltage”. Note that since  $\hat{b}$  represents a traveling field, it is not unitless and  $\langle \hat{b}^\dagger \hat{b} \rangle$  has units of number of photons per second and the commutation relations are

$$[\hat{b}(t), \hat{b}^\dagger(t')] = \delta(t - t'). \quad (\text{B.3})$$

This means that  $V_{zp}$  actually has units of voltage per  $\sqrt{(\text{photon/s})}$ . In Sec.B.2, we show that it corresponds to the RMS amplitude of the voltage of a wave for a unit photon rate. The optical field is described by

$$\hat{a}_{\text{in}} = \alpha e^{-i\omega_c t} + \delta \hat{a}_{\text{in}} \quad (\text{B.4})$$

where  $\alpha$  is the amplitude of the coherent carrier field in the optical input at frequency  $\omega_c$  and  $\delta \hat{a}_{\text{in}}$  carries the quantum fluctuations of the input optical field. Inserting the expressions of Eq.B.4 in Eq.B.1, we get

$$\delta \hat{a}_{\text{out}} = \hat{a}_{\text{out}} - \alpha e^{-i\omega_c t} = \delta \hat{a}_{\text{in}} - i\sqrt{G}e^{-i\omega_c t}(\hat{b} + \hat{b}^\dagger) \quad (\text{B.5})$$

with the microwave-to-optical transduction “gain”

$$\sqrt{G} = \frac{\pi \alpha V_{zp}}{\sqrt{2} V_\pi}. \quad (\text{B.6})$$

In order to compare the signals in the input to the output, we should compute the quantum spectral densities of the fields. As a reminder, the spectral densities of a field  $\delta \hat{a}$  that contains only thermal noise with the equivalent occupation  $\bar{n}_{\text{th}}$  are defined as

$$\begin{aligned} \mathcal{S}_{\delta \hat{a}^\dagger \delta \hat{a}}^{\text{in}}[\omega] &= \int_{-\infty}^{\infty} dt e^{-i\omega t} \langle \delta \hat{a}_{\text{in}}^\dagger(t) \delta \hat{a}_{\text{in}}(0) \rangle = \bar{n}_{\text{th}}, \\ \mathcal{S}_{\delta \hat{a} \delta \hat{a}^\dagger}^{\text{in}}[\omega] &= \int_{-\infty}^{\infty} dt e^{-i\omega t} \langle \delta \hat{a}_{\text{in}}(0) \delta \hat{a}_{\text{in}}^\dagger(t) \rangle = \bar{n}_{\text{th}} + 1, \\ \bar{\mathcal{S}}_{\delta \hat{a}^\dagger \delta \hat{a}}^{\text{in}}[\omega] &= \frac{1}{2} \int_{-\infty}^{\infty} dt e^{-i\omega t} \left( \langle \delta \hat{a}_{\text{in}}^\dagger(t) \delta \hat{a}_{\text{in}}(0) \rangle + \langle \delta \hat{a}_{\text{in}}(0) \delta \hat{a}_{\text{in}}^\dagger(t) \rangle \right) \\ &= \frac{1}{2} \left( \mathcal{S}_{\delta \hat{a}^\dagger \delta \hat{a}}^{\text{in}}[\omega] + \mathcal{S}_{\delta \hat{a} \delta \hat{a}^\dagger}^{\text{in}}[\omega] \right) = \bar{n}_{\text{th}} + \frac{1}{2} \end{aligned} \quad (\text{B.7})$$

where  $\mathcal{S}$  is the standard spectral density and  $\bar{\mathcal{S}}$  is the symmetrized spectral density. As intermediary computations, we obtain

$$\langle \delta \hat{a}_{\text{out}}^\dagger(t) \delta \hat{a}_{\text{out}}(0) \rangle = \langle \delta \hat{a}_{\text{in}}^\dagger(t) \delta \hat{a}_{\text{in}}(0) \rangle + G e^{i\omega_c t} \left( \langle \hat{b}^\dagger(t) \hat{b}(0) \rangle + \langle \hat{b}(t) \hat{b}^\dagger(0) \rangle \right), \quad (\text{B.8})$$

$$\langle \delta \hat{a}_{\text{out}}(0) \delta \hat{a}_{\text{out}}^\dagger(t) \rangle = \langle \delta \hat{a}_{\text{in}}(0) \delta \hat{a}_{\text{in}}^\dagger(t) \rangle + G e^{i\omega_c t} \left( \langle \hat{b}^\dagger(0) \hat{b}(t) \rangle + \langle \hat{b}(0) \hat{b}^\dagger(t) \rangle \right). \quad (\text{B.9})$$

Note first that the fields  $\delta \hat{a}$  and  $\hat{b}$  are not correlated such that all terms of the form  $\langle \delta \hat{a}^\dagger \hat{b} \rangle$  cancel, and second that we are neglecting the terms of the form  $\langle \hat{b}^\dagger \hat{b}^\dagger \rangle$  and  $\langle \hat{b} \hat{b} \rangle$  that in principle give rise to cyclostationary noise, which normally lies outside the frequency range of

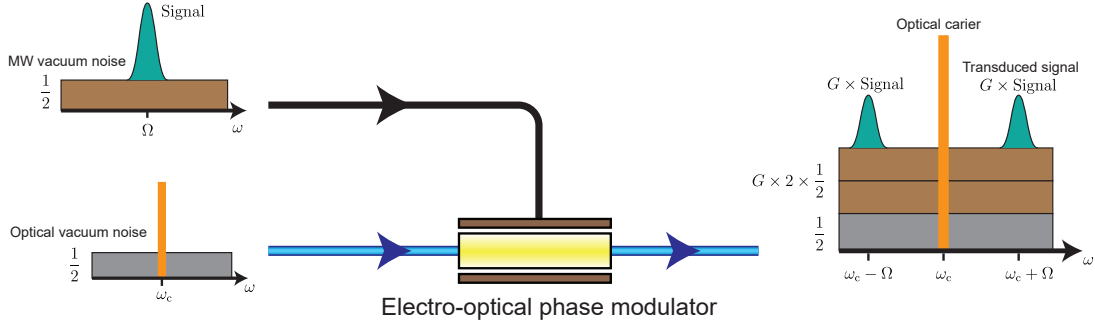


Figure B.1: **Added noise in electro-optic phase modulation.** The microwave input signal has a vacuum noise of  $1/2$ . The output optical field  $\delta \hat{a}_{\text{out}}$  is shown on the right. The input signal is amplified by a gain  $G$  in two sidebands. The input microwave noise is doubled and amplified by the same gain. The optical vacuum noise of  $1/2$  is kept from the input field  $\delta \hat{a}_{\text{in}}$ .

interest.

The symmetrized spectral density of the output can be computed as

$$\bar{\mathcal{S}}_{\delta \hat{a}_{\text{out}}^\dagger \delta \hat{a}_{\text{out}}}[\omega] = \bar{\mathcal{S}}_{\delta \hat{a}_{\text{in}}^\dagger \delta \hat{a}_{\text{in}}}[\omega] + G \left( \bar{\mathcal{S}}_{\hat{b}^\dagger \hat{b}}[\omega - \omega_c] + \bar{\mathcal{S}}_{\hat{b}^\dagger \hat{b}}[-(\omega - \omega_c)] \right) \quad (\text{B.10})$$

If we have a microwave signal at frequency  $\Omega$  such that  $\bar{\mathcal{S}}_{\hat{b}^\dagger \hat{b}}[\Omega]$  is non-trivial, it will be transduced at frequency  $\omega_c + \Omega$  as

$$\bar{\mathcal{S}}_{\delta \hat{a}_{\text{out}}^\dagger \delta \hat{a}_{\text{out}}}[\omega_c + \Omega] = \bar{\mathcal{S}}_{\delta \hat{a}_{\text{in}}^\dagger \delta \hat{a}_{\text{in}}}[\omega_c + \Omega] + G \left( \bar{\mathcal{S}}_{\hat{b}^\dagger \hat{b}}[\Omega] + \bar{\mathcal{S}}_{\hat{b}^\dagger \hat{b}}[-\Omega] \right). \quad (\text{B.11})$$

The term  $\bar{\mathcal{S}}_{\hat{b}^\dagger \hat{b}}[-\Omega]$  should in general contain no signal but increases the noise (in effect doubling the microwave noise). Note that the definition of the symmetrized density spectrum in Eq. B.7 does not imply that  $\bar{\mathcal{S}}[\omega] = \bar{\mathcal{S}}[-\omega]$ . We can compute the added noise as

$$n_{\text{added}} = \frac{1}{G} \left( \bar{n}_{\text{th}}^{\text{opt}} + \frac{1}{2} \right) + \bar{n}_{\text{th}}^{\text{MW}} + \frac{1}{2}. \quad (\text{B.12})$$

In our experiment, we are performing a heterodyne measurement of the optical output field  $\delta \hat{a}_{\text{out}}$ . A heterodyne measurement rather measures the unsymmetrized spectral density

$$\mathcal{S}_{\delta \hat{a}_{\text{out}}^\dagger \delta \hat{a}_{\text{out}}}[\omega_c + \Omega] = \mathcal{S}_{\delta \hat{a}_{\text{in}}^\dagger \delta \hat{a}_{\text{in}}}[\omega_c + \Omega] + G \left( \mathcal{S}_{\hat{b}^\dagger \hat{b}}[\Omega] + \mathcal{S}_{\hat{b}^\dagger \hat{b}}[-\Omega] \right). \quad (\text{B.13})$$

In terms of the quantum noise, this is equivalent to the expression with the symmetrized spectrum density in B.11. The added noise is represented visually in B.1.

## B.2 Computing $V_{zp}$ and $G$

In order to compute  $V_{zp}$  and  $G$ , we will anchor the quantum model with the classical model. We assume the microwave input to contain a single Fourier frequency with a voltage

$$V_{in}(t) = V_0 \cos(\Omega t) \quad (B.14)$$

where  $\Omega$  is the microwave frequency of interest and  $V_0$  is the amplitude of the voltage oscillations. Along the polarization axis of interest, the input optical field of amplitude  $E_0$  and optical frequency  $\omega_c$  changes phase such that the optical output is given by

$$E_{out}(t) = E_0 e^{-i\omega_c t} e^{-i\pi \frac{V_0}{V_\pi} \cos(\Omega t)} \quad (B.15)$$

$$\approx E_0 e^{-i\omega_c t} \left( 1 - i \frac{\pi}{2} \frac{V_0}{V_\pi} (e^{i\Omega t} + e^{-i\Omega t}) \right) \quad (B.16)$$

where  $V_\pi$  is the voltage for which the optical field is phase-delayed by a shift of  $\pi$ . The approximation for a weak amplitude  $V_0 \ll V_\pi$  is to expand the exponential of the phase delay to the first order, which results in two sidebands detuned from the carrier by  $\pm\Omega$ .

If we only consider the signal of a single sideband, it can be interpreted as a transduction of the original microwave signal, of power

$$P_{MW} = \frac{V_0^2}{2Z_0}, \quad (B.17)$$

where  $Z_0$  is the characteristic impedance of the input line, which has been converted to an optical signal of power

$$P_{opt}^{out} = \frac{\pi^2}{4} \frac{V_0^2}{V_\pi^2} P_{opt}^{in} \quad (B.18)$$

where  $P_{opt}^{in}$  is the power of the input optical field, proportional to  $E_0^2$ .

The gain  $G$  is this conversion rate from microwave to optical field, expressed in number of photons per second as

$$G = \frac{P_{opt}^{out}/(\hbar\omega)}{P_{MW}/(\hbar\Omega)} = \frac{\pi^2}{4} \frac{\Omega}{\omega} \left( P_{opt}^{in} / \left( \frac{V_\pi^2}{2Z_0} \right) \right). \quad (B.19)$$

By comparison with [B.6](#), we find that

$$V_{zp}^2 = \hbar\Omega Z_0 \quad (B.20)$$

using  $P_{opt}^{in} = \hbar\omega|\alpha|^2$ . The squared “zero-point voltage”  $V_{zp}^2$  multiplied by a photon rate and divided by the transmission line impedance  $Z_0$  gives the power of the traveling wave; it is the squared RMS voltage divided by the photon rate.

# Bibliography

- Aasi, J. et al. (2013). “Enhanced sensitivity of the LIGO gravitational wave detector by using squeezed states of light”. In: *Nature Photonics* 7 (8), pp. 613–619.
- Abel, S. et al. (2019). “Large Pockels effect in micro- and nanostructured barium titanate integrated on silicon”. In: *Nature Materials* 18 (1), pp. 42–47.
- Akram, U. et al. (2012). “Photon-phonon entanglement in coupled optomechanical arrays”. In: *Physical Review A* 86 (4), p. 042306.
- Andrews, R. W. et al. (2014). “Bidirectional and efficient conversion between microwave and optical light”. In: *Nature Physics* 10 (4), pp. 321–326.
- Arnold, G. et al. (2020). “Converting microwave and telecom photons with a silicon photonic nanomechanical interface”. In: *arXiv preprint arXiv:2002.11628*.
- Arute, F. et al. (Oct. 2019). “Quantum supremacy using a programmable superconducting processor”. In: *Nature* 574 (7779), pp. 505–510.
- Asbóth, J. K., L. Oroszlány, and A. Pályi (2016). “A short course on topological insulators”. In: *Lecture notes in physics* 919, pp. 997–1000.
- Ashkin, A. (1997). “Optical trapping and manipulation of neutral particles using lasers”. In: *Proceedings of the National Academy of Sciences* 94 (10), pp. 4853–4860.
- Aspelmeyer, M., T. J. Kippenberg, and F. Marquardt (2014). “Cavity optomechanics”. In: *Reviews of Modern Physics* 86 (4), p. 1391.
- Bancora, A. (2021). *Master thesis: Multimode superconducting circuit optomechanics*. Tech. rep. Università degli Studi di Milano.
- Barends, R. et al. (2014). “Superconducting quantum circuits at the surface code threshold for fault tolerance”. In: *Nature* 508 (7497), pp. 500–503.
- Bartholomew, J. G. et al. (2019). “On-chip coherent microwave-to-optical transduction mediated by ytterbium in YVO<sub>4</sub>”. In: *arXiv preprint arXiv:1912.03671*.
- Barzanjeh, S., E. Redchenko, et al. (2019). “Stationary entangled radiation from micromechanical motion”. In: *Nature* 570 (7762), pp. 480–483.
- Barzanjeh, S., M. Wulf, et al. (2017). “Mechanical on-chip microwave circulator”. In: *Nature communications* 8 (1), pp. 1–7.
- Barzanjeh, S., A. Xuereb, et al. (2022). “Optomechanics for quantum technologies”. In: *Nature Physics* 18 (1), pp. 15–24.
- Bassi, A. et al. (2013). “Models of wave-function collapse, underlying theories, and experimental tests”. In: *Reviews of Modern Physics* 85 (2), p. 471.

- Bellec, M. et al. (2013). “Topological transition of Dirac points in a microwave experiment”. In: *Physical review letters* 110 (3), p. 033902.
- Bellec, M. et al. (2014). “Manipulation of edge states in microwave artificial graphene”. In: *New Journal of Physics* 16 (11), p. 113023.
- Bereyhi, M. J. et al. (2019). “Clamp-tapering increases the quality factor of stressed nanobeams”. In: *Nano letters* 19 (4), pp. 2329–2333.
- Bernier, N. R. et al. (2017). “Nonreciprocal reconfigurable microwave optomechanical circuit”. In: *Nature Communications* 8 (1).
- Bernier, N. R. (2019). *Multimode microwave circuit optomechanics as a platform to study coupled quantum harmonic oscillators*. Tech. rep. EPFL.
- Beth, R. A. (1936). “Mechanical detection and measurement of the angular momentum of light”. In: *Physical Review* 50 (2), p. 115.
- Blais, A., S. M. Girvin, and W. D. Oliver (Mar. 2020). “Quantum information processing and quantum optics with circuit quantum electrodynamics”. In: *Nature Physics* 16 (3), pp. 247–256.
- Blumenthal, D. J. et al. (2000). “All-optical label swapping networks and technologies”. In: *Journal of Lightwave Technology* 18 (12), p. 2058.
- Bowen, W. P. and G. J. Milburn (2015). *Quantum optomechanics*. CRC press.
- Braginski, A. I. (Jan. 2019). “Superconductor Electronics: Status and Outlook”. In: *Journal of Superconductivity and Novel Magnetism* 32 (1), pp. 23–44.
- Braginski, V. and A. Manukin (1967). “Ponderomotive effects of electromagnetic radiation”. In: *Sov. Phys. JETP* 25 (4), pp. 653–655.
- Braginskii, V. B. and A. B. Manukin (1977). “Measurement of weak forces in physics experiments”. In: *Chicago*.
- Braginsky, V. B., V. Borisovich, and F. Y. Khalili (1995). *Quantum measurement*. Cambridge University Press.
- Carmon, T. et al. (2005). “Temporal behavior of radiation-pressure-induced vibrations of an optical microcavity phonon mode”. In: *Physical Review Letters* 94 (22), p. 223902.
- Carney, D. et al. (2021). “Mechanical quantum sensing in the search for dark matter”. In: *Quantum Science and Technology* 6 (2), p. 024002.
- Carusotto, I. et al. (2020). “Photonic materials in circuit quantum electrodynamics”. In: *Nature Physics* 16 (3), pp. 268–279.
- Cattiaux, D. et al. (2021). “A macroscopic object passively cooled into its quantum ground state of motion beyond single-mode cooling”. In: *Nature communications* 12 (1), pp. 1–6.
- Cha, E. et al. (2020a). “A 300- $\mu$ W Cryogenic HEMT LNA for Quantum Computing”. In: pp. 1299–1302.
- Cha, E. et al. (2020b). “InP HEMTs for Sub-mW Cryogenic Low-Noise Amplifiers”. In: *IEEE Electron Device Letters* 41 (7), pp. 1005–1008.
- Chakraborty, U. et al. (2020). “Cryogenic operation of silicon photonic modulators based on DC Kerr effect”. In: *arXiv preprint arXiv:2007.03395*.
- Chan, J., T. M. Alegre, et al. (2011). “Laser cooling of a nanomechanical oscillator into its quantum ground state”. In: *Nature* 478 (7367), pp. 89–92.

## BIBLIOGRAPHY

---

- Chan, J., A. H. Safavi-Naeini, et al. (2012). “Optimized optomechanical crystal cavity with acoustic radiation shield”. In: *Applied Physics Letters* 101 (8).
- Cheng, Q. et al. (Nov. 2018). “Recent advances in optical technologies for data centers: a review”. In: *Optica* 5 (11), pp. 1354–1370.
- Chu, Y. and S. Gröblacher (2020). “A perspective on hybrid quantum opto-and electromechanical systems”. In: *Applied Physics Letters* 117 (15), p. 150503.
- Chu, Y., P. Kharel, et al. (2018). “Creation and control of multi-phonon Fock states in a bulk acoustic-wave resonator”. In: *Nature* 563 (7733), pp. 666–670.
- Cicak, K. et al. (2010). “Low-loss superconducting resonant circuits using vacuum-gap-based microwave components”. In: *Applied Physics Letters* 96 (9), p. 093502.
- Clerk, A. et al. (2020). “Hybrid quantum systems with circuit quantum electrodynamics”. In: *Nature Physics* 16 (3), pp. 257–267.
- Clerk, A. A. et al. (2010). “Introduction to quantum noise, measurement, and amplification”. In: *Reviews of Modern Physics* 82 (2), p. 1155.
- Cohadon, P.-F., A. Heidmann, and M. Pinard (1999). “Cooling of a mirror by radiation pressure”. In: *Physical Review Letters* 83 (16), p. 3174.
- Cole, G. D. et al. (2011). “Phonon-tunnelling dissipation in mechanical resonators”. In: *Nature communications* 2 (1), pp. 1–8.
- Courtney, T. H. (2005). *Mechanical behavior of materials*. Waveland Press.
- Dalton, L. R., P. A. Sullivan, and D. H. Bale (2010). “Electric field poled organic electro-optic materials: state of the art and future prospects”. In: *Chemical reviews* 110 (1), pp. 25–55.
- Delaney, R. et al. (2022). “Superconducting-qubit readout via low-backaction electro-optic transduction”. In: *Nature* 606 (7914), pp. 489–493.
- Delaney, R. D. et al. (2019). “Measurement of motion beyond the quantum limit by transient amplification”. In: *Physical review letters* 123 (18), p. 183603.
- Delić, U. et al. (2020). “Cooling of a levitated nanoparticle to the motional quantum ground state”. In: *Science* 367 (6480), pp. 892–895.
- Delplace, P., D. Ullmo, and G. Montambaux (2011). “Zak phase and the existence of edge states in graphene”. In: *Physical Review B* 84 (19), p. 195452.
- Devoret, M. H. and R. J. Schoelkopf (2013). “Superconducting Circuits for Quantum Information: An Outlook”. In: *Science* 339 (6124), pp. 1169–1174.
- Diosi, L. (1987). “A universal master equation for the gravitational violation of quantum mechanics”. In: *Physics letters A* 120 (8), pp. 377–381.
- Duh, K. G. et al. (1988). “Ultra-low-noise cryogenic high-electron-mobility transistors”. In: *IEEE transactions on electron devices* 35 (3), pp. 249–256.
- Ekin, J. (2006). *Experimental techniques for low-temperature measurements: cryostat design, material properties and superconductor critical-current testing*. Oxford university press.
- Eltes, F. et al. (2019). “An integrated cryogenic optical modulator”. In: *arXiv:1904.10902 [physics]*. arXiv: 1904.10902.
- Fabre, C. et al. (1994). “Quantum-noise reduction using a cavity with a movable mirror”. In: *Physical Review A* 49 (2), p. 1337.



- Fan, L. et al. (2018). “Superconducting cavity electro-optics: A platform for coherent photon conversion between superconducting and photonic circuits”. In: *Science Advances* 4 (8).
- Fan, S., W. Suh, and J. D. Joannopoulos (2003). “Temporal coupled-mode theory for the Fano resonance in optical resonators”. In: *JOSA A* 20 (3), pp. 569–572.
- Fedorov, S. (2020). *Mechanical resonators with high dissipation dilution in precision and quantum measurements*. Tech. rep. EPFL.
- Fedorov, S. A. et al. (2019). “Generalized dissipation dilution in strained mechanical resonators”. In: *Physical Review B* 99 (5), p. 054107.
- Fiaschi, N. et al. (2021). “Optomechanical quantum teleportation”. In: *Nature Photonics* 15 (11), pp. 817–821.
- Forsch, M. et al. (2020). “Microwave-to-optics conversion using a mechanical oscillator in its quantum ground state”. In: *Nature Physics* 16 (1), pp. 69–74.
- Gaebler, J. P. et al. (2016). “High-fidelity universal gate set for be 9+ ion qubits”. In: *Physical review letters* 117 (6), p. 060505.
- Gan, J.-H. et al. (2016). “Solitons in optomechanical arrays”. In: *Optics letters* 41 (12), pp. 2676–2679.
- Gardiner, C., P. Zoller, and P. Zoller (2004). *Quantum noise: a handbook of Markovian and non-Markovian quantum stochastic methods with applications to quantum optics*. Springer Science & Business Media.
- Gardner, D. S. and P. A. Flinn (1990). “Mechanical stress as a function of temperature for aluminum alloy films”. In: *Journal of Applied Physics* 67 (4), pp. 1831–1844.
- Gely, M. F. and G. A. Steele (2021a). “Phonon-number resolution of voltage-biased mechanical oscillators with weakly anharmonic superconducting circuits”. In: *Physical Review A* 104 (5), p. 053509.
- Gely, M. F. and G. A. Steele (2021b). “Superconducting electro-mechanics to test Diósi–Penrose effects of general relativity in massive superpositions”. In: *AVS Quantum Science* 3 (3), p. 035601.
- Hänsch, T. W. and A. L. Schawlow (1975). “Cooling of gases by laser radiation”. In: *Optics Communications* 13 (1), pp. 68–69.
- Hatsugai, Y. (2009). “Bulk-edge correspondence in graphene with/without magnetic field: Chiral symmetry, Dirac fermions and edge states”. In: *Solid state communications* 149 (27–28), pp. 1061–1067.
- He, Y. et al. (2019). “Self-starting bi-chromatic LiNbO<sub>3</sub> soliton microcomb”. In: *Optica* 6 (9), pp. 1138–1144.
- Hease, W. et al. (May 2020). “Cavity quantum electro-optics: Microwave-telecom conversion in the quantum ground state”. In: *arXiv:2005.12763 [physics, physics:quant-ph]*.
- Heinrich, G. et al. (2011). “Collective dynamics in optomechanical arrays”. In: *Physical review letters* 107 (4), p. 043603.
- Herzog, C., G. Poberaj, and P. Günter (2008). “Electro-optic behavior of lithium niobate at cryogenic temperatures”. In: *Optics Communications* 281 (4), pp. 793–796.
- Higginbotham, A. P. et al. (2018). “Harnessing electro-optic correlations in an efficient mechanical converter”. In: *Nature Physics* 14 (10), pp. 1038–1042.

## BIBLIOGRAPHY

---

- Hofheinz, M. et al. (2009). “Synthesizing arbitrary quantum states in a superconducting resonator”. In: *Nature* 459 (7246), pp. 546–549.
- Holzgrafe, J. et al. (2020). “Cavity electro-optics in thin-film lithium niobate for efficient microwave-to-optical transduction”. In: *arXiv:2005.00939 [physics, physics:quant-ph]*.
- Hong, S. et al. (2017). “Hanbury Brown and Twiss interferometry of single phonons from an optomechanical resonator”. In: *Science* 358 (6360), pp. 203–206.
- Huber, S. D. (2016). “Topological mechanics”. In: *Nature Physics* 12 (7), pp. 621–623.
- Jacobs, K. et al. (1994). “Quantum-nondemolition measurement of photon number using radiation pressure”. In: *Physical Review A* 49 (3), p. 1961.
- St-Jean, P. et al. (2017). “Lasing in topological edge states of a one-dimensional lattice”. In: *Nature Photonics* 11 (10), pp. 651–656.
- Jeong, C. H. et al. (2002). “A study of sapphire etching characteristics using BCl<sub>3</sub>-based inductively coupled plasmas”. In: *Japanese journal of applied physics* 41 (10R), p. 6206.
- Jiang, W., R. N. Patel, et al. (2019). “Lithium niobate piezo-optomechanical crystals”. In: *Optica* 6 (7), pp. 845–853.
- Jiang, W., C. J. Sarabalis, et al. (2019). “Efficient bidirectional piezo-optomechanical transduction between microwave and optical frequency”. In: *arXiv preprint arXiv:1909.04627*.
- Johansson, J. R., P. D. Nation, and F. Nori (2012). “QuTiP: An open-source Python framework for the dynamics of open quantum systems”. In: *Computer Physics Communications* 183 (8), pp. 1760–1772.
- Jones, N. et al. (2018). “How to stop data centres from gobbling up the world’s electricity”. In: *Nature* 561 (7722), pp. 163–166.
- Joshi, Y. J. et al. (2021). “Automated wide-ranged finely tunable microwave cavity for narrow-band phase noise filtering”. In: *Review of Scientific Instruments* 92 (3), p. 034710.
- Kachris, C. and I. Tomkos (2012). “A Survey on Optical Interconnects for Data Centers”. In: *IEEE Communications Surveys Tutorials* 14 (4), pp. 1021–1036.
- Keysight (2018). “How to measure BER”. In: *www.keysight.com*.
- Kim, E. et al. (2021). “Quantum electrodynamics in a topological waveguide”. In: *Physical Review X* 11 (1), p. 011015.
- Kippenberg, T. et al. (2005). “Analysis of radiation-pressure induced mechanical oscillation of an optical microcavity”. In: *Physical Review Letters* 95 (3), p. 033901.
- Kohmoto, M. and Y. Hasegawa (2007). “Zero modes and edge states of the honeycomb lattice”. In: *Physical Review B* 76 (20), p. 205402.
- Kono, S. et al. (2023). “Mechanically Induced Correlated Errors on Superconducting Qubits with Relaxation Times Exceeding 0.4 Milliseconds”. In: *arXiv preprint arXiv:2305.02591*.
- Kotler, S. et al. (2021). “Direct observation of deterministic macroscopic entanglement”. In: *Science* 372 (6542), pp. 622–625.
- Krinner, S. et al. (2019). “Engineering cryogenic setups for 100-qubit scale superconducting circuit systems”. In: *EPJ Quantum Technology* 6 (1), pp. 1–29.
- Kronwald, A., F. Marquardt, and A. A. Clerk (2013). “Arbitrarily large steady-state bosonic squeezing via dissipation”. In: *Physical Review A* 88 (6), p. 063833.

- Lauk, N. et al. (2020). “[Perspectives on quantum transduction](#)”. In: *Quantum Science and Technology* 5 (2), p. 020501.
- Lecocq, F., F. Quinlan, et al. (2020). “[Control and readout of a superconducting qubit using a photonic link](#)”. In: *arXiv preprint arXiv:2009.01167*.
- Lecocq, F., J. B. Clark, et al. (2015). “[Quantum nondemolition measurement of a nonclassical state of a massive object](#)”. In: *Physical Review X* 5 (4), p. 041037.
- Leghtas, Z. et al. (2013). “[Hardware-efficient autonomous quantum memory protection](#)”. In: *Physical Review Letters* 111 (12), p. 120501.
- Leibfried, D. et al. (2003). “[Quantum dynamics of single trapped ions](#)”. In: *Reviews of Modern Physics* 75 (1), p. 281.
- Lépinay, L. M. de, E. Damskägg, et al. (2019). “[Realization of directional amplification in a microwave optomechanical device](#)”. In: *Physical Review Applied* 11 (3), p. 034027.
- Lépinay, L. M. de, C. F. Ockeloen-Korppi, et al. (2021). “[Quantum mechanics-free subsystem with mechanical oscillators](#)”. In: *Science* 372 (6542), pp. 625–629.
- Li, B.-B. et al. (2021). “[Cavity optomechanical sensing](#)”. In: *Nanophotonics* 10 (11), pp. 2799–2832.
- Li, L., Z. Xu, and S. Chen (2014). “[Topological phases of generalized Su-Schrieffer-Heeger models](#)”. In: *Physical Review B* 89 (8), p. 085111.
- Liu, Y., Q. Liu, et al. (2021). “[Optomechanical Anti-Lasing with Infinite Group Delay at a Phase Singularity](#)”. In: *Physical Review Letters* 127 (27), p. 273603.
- Liu, Y., J. Mummery, et al. (2021). “[Gravitational forces between nonclassical mechanical oscillators](#)”. In: *Physical Review Applied* 15 (3), p. 034004.
- Ludwig, M. and F. Marquardt (2013). “[Quantum many-body dynamics in optomechanical arrays](#)”. In: *Physical review letters* 111 (7), p. 073603.
- Luo, J. and D. A. Dornfeld (2001). “[Material removal mechanism in chemical mechanical polishing: theory and modeling](#)”. In: *IEEE transactions on semiconductor manufacturing* 14 (2), pp. 112–133.
- MacCabe, G. S. et al. (2020). “[Nano-acoustic resonator with ultralong phonon lifetime](#)”. In: *Science* 370 (6518), pp. 840–843.
- Macklin, C. et al. (2015). “[A near-quantum-limited Josephson traveling-wave parametric amplifier](#)”. In: *Science* 350 (6258), pp. 307–310.
- Magrini, L. et al. (2021). “[Real-time optimal quantum control of mechanical motion at room temperature](#)”. In: *Nature* 595 (7867), pp. 373–377.
- Mancini, S. and P. Tombesi (1994). “[Quantum noise reduction by radiation pressure](#)”. In: *Physical Review A* 49 (5), p. 4055.
- Mancini, S., D. Vitali, and P. Tombesi (1998). “[Optomechanical cooling of a macroscopic oscillator by homodyne feedback](#)”. In: *Physical Review Letters* 80 (4), p. 688.
- Manley, J. et al. (2021). “[Searching for vector dark matter with an optomechanical accelerometer](#)”. In: *Physical review letters* 126 (6), p. 061301.
- Marinković, I. et al. (2018). “[Optomechanical bell test](#)”. In: *Physical review letters* 121 (22), p. 220404.

## BIBLIOGRAPHY

---

- Marquardt, E., J. Harris, and S. M. Girvin (2006). “Dynamical multistability induced by radiation pressure in high-finesse micromechanical optical cavities”. In: *Physical Review Letters* 96 (10), p. 103901.
- Martinis, J. M., M. H. Devoret, and J. Clarke (2020). “Quantum Josephson junction circuits and the dawn of artificial atoms”. In: *Nature Physics* 16 (3), pp. 234–237.
- Mason, D. et al. (2019). “Continuous force and displacement measurement below the standard quantum limit”. In: *Nature Physics* 15 (8), pp. 745–749.
- McConaghy, C. et al. (1996). “The performance of pigtailed annealed proton exchange LiNbO<sub>3</sub> modulators at cryogenic temperatures”. In: *IEEE Photonics Technology Letters* 8 (11), pp. 1480–1482.
- McKenna, T. P. et al. (2020). “Cryogenic microwave-to-optical conversion using a triply-resonant lithium niobate on sapphire transducer”. In: *arXiv:2005.00897 [physics, physics:quant-ph]*.
- Miller, D. A. (2000). “Optical interconnects to silicon”. In: *IEEE Journal of Selected Topics in Quantum Electronics* 6 (6), pp. 1312–1317.
- Mirhosseini, M., E. Kim, et al. (2018). “Superconducting metamaterials for waveguide quantum electrodynamics”. In: *Nature communications* 9 (1), pp. 1–7.
- Mirhosseini, M., A. Sipahigil, et al. (2020a). “Quantum transduction of optical photons from a superconducting qubit”. In: *arXiv preprint arXiv:2004.04838*.
- Mirhosseini, M., A. Sipahigil, et al. (2020b). “Superconducting qubit to optical photon transduction”. In: *Nature* 588 (7839), pp. 599–603.
- Morse, J. D. et al. (1994). “Characterization of lithium niobate electro-optic modulators at cryogenic temperatures”. In: 2150. Ed. by M. N. Armenise, pp. 283–291.
- Morvan, A. et al. (2021). “Bulk properties of honeycomb lattices of superconducting microwave resonators”. In: *arXiv preprint arXiv:2103.09428*.
- Naik, A. et al. (2006). “Cooling a nanomechanical resonator with quantum back-action”. In: *Nature* 443 (7108), pp. 193–196.
- Nakada, K. et al. (1996). “Edge state in graphene ribbons: Nanometer size effect and edge shape dependence”. In: *Physical Review B* 54 (24), p. 17954.
- Naumis, G. G. et al. (2017). “Electronic and optical properties of strained graphene and other strained 2D materials: a review”. In: *Reports on Progress in Physics* 80 (9), p. 096501.
- Ni, Z. H. et al. (2008). “Uniaxial strain on graphene: Raman spectroscopy study and band-gap opening”. In: *ACS nano* 2 (11), pp. 2301–2305.
- O’Connell, A. D. et al. (2008). “Microwave dielectric loss at single photon energies and millikelvin temperatures”. In: *Applied Physics Letters* 92 (11), p. 112903.
- Ockeloen-Korppi, C. et al. (2018). “Stabilized entanglement of massive mechanical oscillators”. In: *Nature* 556 (7702), pp. 478–482.
- Ortmann, J. E. et al. (2019). “Ultra-Low-Power Tuning in Hybrid Barium Titanate–Silicon Nitride Electro-Optic Devices on Silicon”. In: *ACS Photonics* 6 (11), pp. 2677–2684.
- Ozawa, T. et al. (2019). “Topological photonics”. In: *Reviews of Modern Physics* 91 (1), p. 015006.
- Palomaki, T., J. Harlow, et al. (2013). “Coherent state transfer between itinerant microwave fields and a mechanical oscillator”. In: *Nature* 495 (7440), pp. 210–214.

- Palomaki, T., J. Teufel, et al. (2013). "Entangling mechanical motion with microwave fields". In: *Science* 342 (6159), pp. 710–713.
- Peano, V. et al. (2015). "Topological phases of sound and light". In: *Physical Review X* 5 (3), p. 031011.
- Pechal, M., P. Arrangoiz-Arriola, and A. H. Safavi-Naeini (2018). "Superconducting circuit quantum computing with nanomechanical resonators as storage". In: *Quantum Science and Technology* 4 (1), p. 015006.
- Penrose, R. (1996). "On gravity's role in quantum state reduction". In: *General relativity and gravitation* 28, pp. 581–600.
- Pereira, V. M., A. C. Neto, and N. Peres (2009). "Tight-binding approach to uniaxial strain in graphene". In: *Physical Review B* 80 (4), p. 045401.
- Pérez-González, B. et al. (2018). "SSH model with long-range hoppings: topology, driving and disorder". In: *arXiv preprint arXiv:1802.03973*.
- Pérez-González, B. et al. (2019). "Interplay between long-range hopping and disorder in topological systems". In: *Physical Review B* 99 (3), p. 035146.
- Peterson, C. W. et al. (2018). "A quantized microwave quadrupole insulator with topologically protected corner states". In: *Nature* 555 (7696), pp. 346–350.
- Piotrowski, J. et al. (2023). "Simultaneous ground-state cooling of two mechanical modes of a levitated nanoparticle". In: *Nature Physics*, pp. 1–5.
- Pirkkalainen, J.-M., S. Cho, et al. (2013). "Hybrid circuit cavity quantum electrodynamics with a micromechanical resonator". In: *Nature* 494 (7436), pp. 211–215.
- Pirkkalainen, J.-M., E. Damskägg, et al. (2015). "Squeezing of quantum noise of motion in a micromechanical resonator". In: *Physical Review Letters* 115 (24), p. 243601.
- Plotnik, Y. et al. (2014). "Observation of unconventional edge states in 'photonic graphene'". In: *Nature materials* 13 (1), pp. 57–62.
- Pospieszalski, M. W. et al. (1988). "FETs and HEMTs at cryogenic temperatures-their properties and use in low-noise amplifiers". In: *IEEE transactions on microwave theory and techniques* 36 (3), pp. 552–560.
- Pozar, D. M. (2011). *Microwave engineering*. John Wiley & sons.
- Probst, S. et al. (2015). "Efficient and robust analysis of complex scattering data under noise in microwave resonators". In: *Review of Scientific Instruments* 86 (2), p. 024706.
- Purdy, T. P. et al. (2013). "Strong optomechanical squeezing of light". In: *Physical Review X* 3 (3), p. 031012.
- QTLab GitHub repository (n.d.). <https://github.com/heeres/qtlab.git>. Accessed: 2023-03-30.
- Rabl, P. et al. (2009). "Phase-noise induced limitations on cooling and coherent evolution in optomechanical systems". In: *Physical Review A* 80 (6), p. 063819.
- Raeisi, S. and F. Marquardt (2020). "Quench dynamics in one-dimensional optomechanical arrays". In: *Physical Review A* 101 (2), p. 023814.
- Read, A. P. et al. (2022). "Precision measurement of the microwave dielectric loss of sapphire in the quantum regime with parts-per-billion sensitivity". In: *arXiv preprint arXiv:2206.14334*.
- Reagor, M. et al. (2016). "Quantum memory with millisecond coherence in circuit QED". In: *Physical Review B* 94 (1), p. 014506.



## BIBLIOGRAPHY

---

- Rechtsman, M. C. et al. (2013). “Topological creation and destruction of edge states in photonic graphene”. In: *Physical review letters* 111 (10), p. 103901.
- Reed, A. et al. (2017). “Faithful conversion of propagating quantum information to mechanical motion”. In: *Nature Physics* 13 (12), pp. 1163–1167.
- Ren, H. et al. (2020). “Topological phonon transport in an optomechanical system”. In: *arXiv*.
- Richter, G. et al. (2009). “Ultrahigh strength single crystalline nanowhiskers grown by physical vapor deposition”. In: *Nano Letters* 9 (8), pp. 3048–3052.
- Riedinger, R. et al. (2018). “Remote quantum entanglement between two micromechanical oscillators”. In: *Nature* 556 (7702), pp. 473–477.
- Rodrigues, I., D. Bothner, and G. Steele (2019). “Coupling microwave photons to a mechanical resonator using quantum interference”. In: *Nature communications* 10 (1), p. 5359.
- Roos, A. K. et al. (2023). “Kinetic inductive mechano-electric transduction for nano-scale force sensing”. In: *arXiv preprint arXiv:2301.11055*.
- Roque, T. F. et al. (2017). “Anderson localization of composite excitations in disordered optomechanical arrays”. In: *New Journal of Physics* 19 (1), p. 013006.
- Rossi, M. et al. (2018). “Measurement-based quantum control of mechanical motion”. In: *Nature* 563 (7729), pp. 53–58.
- Rueda, A., W. Hease, et al. (2019). “Electro-optic entanglement source for microwave to telecom quantum state transfer”. In: *npj Quantum Information* 5 (1), p. 108.
- Rueda, A., F. Sedlmeir, M. C. Collodo, et al. (2016). “Efficient microwave to optical photon conversion: an electro-optical realization”. In: *Optica* 3 (6), pp. 597–604.
- Rueda, A., F. Sedlmeir, M. Kumari, et al. (2019). “Resonant electro-optic frequency comb”. In: *Nature* 568 (7752), pp. 378–381.
- Safavi-Naeini, A. H., T. M. Alegre, et al. (2011). “Electromagnetically induced transparency and slow light with optomechanics”. In: *Nature* 472 (7341), pp. 69–73.
- Safavi-Naeini, A. H., J. T. Hill, et al. (2014). “Two-dimensional phononic-photonic band gap optomechanical crystal cavity”. In: *Physical Review Letters* 112 (15), p. 153603.
- Sanavio, C., V. Peano, and A. Xuereb (2020). “Nonreciprocal topological phononics in optomechanical arrays”. In: *Physical Review B* 101 (8), p. 085108.
- Satzinger, K. J. et al. (2018). “Quantum control of surface acoustic-wave phonons”. In: *Nature* 563 (7733), pp. 661–665.
- Schliesser, A. et al. (2006). “Radiation pressure cooling of a micromechanical oscillator using dynamical backaction”. In: *Physical Review Letters* 97 (24), p. 243905.
- Schmid, S. et al. (2011). “Damping mechanisms in high-Q micro and nanomechanical string resonators”. In: *Physical Review B* 84 (16), p. 165307.
- Schuster, D. et al. (2007). “Resolving photon number states in a superconducting circuit”. In: *Nature* 445 (7127), pp. 515–518.
- Scigliuzzo, M. et al. (2023). “Collective dynamics in circuit optomechanical systems”. In: *Bulletin of the American Physical Society*.
- Seis, Y. et al. (2022). “Ground state cooling of an ultracoherent electromechanical system”. In: *Nature communications* 13 (1), pp. 1–7.



- Shomroni, I., L. Qiu, et al. (2019). “Optical backaction-evading measurement of a mechanical oscillator”. In: *Nature communications* 10 (1), p. 2086.
- Shomroni, I., A. Youssefi, et al. (2019). “Two-tone optomechanical instability and its fundamental implications for backaction-evading measurements”. In: *Physical Review X* 9 (4), p. 041022.
- Siddiqi, I. et al. (2004). “RF-driven Josephson bifurcation amplifier for quantum measurement”. In: *Physical review letters* 93 (20), p. 207002.
- Steinwall, J. E. and H. Johnson (1990). “Mechanical properties of thin film aluminum fibers: Grain size effects”. In: *MRS Online Proceedings Library (OPL)* 188.
- Suh, J. et al. (2014). “Mechanically detecting and avoiding the quantum fluctuations of a microwave field”. In: *Science* 344 (6189), pp. 1262–1265.
- Sun, C. et al. (2015). “Single-chip microprocessor that communicates directly using light”. In: *Nature* 528 (7583), pp. 534–538.
- Surjadi, J. U. et al. (2019). “Mechanical metamaterials and their engineering applications”. In: *Advanced Engineering Materials* 21 (3), p. 1800864.
- Tebbenjohanns, F. et al. (2021). “Quantum control of a nanoparticle optically levitated in cryogenic free space”. In: *Nature* 595 (7867), pp. 378–382.
- Teufel, J. D., T. Donner, M. Castellanos-Beltran, et al. (2009). “Nanomechanical motion measured with an imprecision below that at the standard quantum limit”. In: *Nature nanotechnology* 4 (12), pp. 820–823.
- Teufel, J. D., T. Donner, D. Li, et al. (2011). “Sideband cooling of micromechanical motion to the quantum ground state”. In: *Nature* 475 (7356), pp. 359–363.
- Teufel, J. D., D. Li, et al. (2011). “Circuit cavity electromechanics in the strong-coupling regime”. In: *Nature* 471 (7337), pp. 204–208.
- Thiele, F. et al. (2020). “Cryogenic Electro-Optic Polarisation Conversion in Titanium indiffused Lithium Niobate Waveguides”. In: *arXiv:2006.12078 [physics, physics:quant-ph]*.
- Thomson, D. et al. (June 2016). “Roadmap on silicon photonics”. In: *Journal of Optics* 18 (7), p. 073003.
- Tomadin, A. et al. (2012). “Reservoir engineering and dynamical phase transitions in optomechanical arrays”. In: *Physical Review A* 86 (3), p. 033821.
- Toth, L. D. et al. (2017). “A dissipative quantum reservoir for microwave light using a mechanical oscillator”. In: *Nature Physics* 13 (8), pp. 787–793.
- Tóth, L. D. (2018). *Dissipation as a resource in circuit quantum electromechanics*. Tech. rep. EPFL.
- Tsang, M. (2010). “Cavity quantum electro-optics”. In: *Physical Review A* 81 (6), p. 063837.
- Tsaturyan, Y. et al. (2017). “Ultracoherent nanomechanical resonators via soft clamping and dissipation dilution”. In: *Nature nanotechnology* 12 (8), pp. 776–783.
- Underwood, D. et al. (2016). “Imaging photon lattice states by scanning defect microscopy”. In: *Physical Review X* 6 (2), p. 021044.
- Vladimirescu, A. (1994). *The SPICE book*. Wiley New York.
- Vlastakis, B. et al. (2013). “Deterministically encoding quantum information using 100-photon Schrödinger cat states”. In: *Science* 342 (6158), pp. 607–610.

## BIBLIOGRAPHY

---

- Wallucks, A. et al. (2020). “A quantum memory at telecom wavelengths”. In: *Nature Physics* 16 (7), pp. 772–777.
- Wang, C. et al. (2018). “Integrated lithium niobate electro-optic modulators operating at CMOS-compatible voltages”. In: *Nature* 562 (7725), pp. 101–104.
- Wang, H. et al. (2019). “Mode structure in superconducting metamaterial transmission-line resonators”. In: *Physical Review Applied* 11 (5), p. 054062.
- Wang, S. et al. (2016). “Giant edge state splitting at atomically precise graphene zigzag edges”. In: *Nature communications* 7 (1), pp. 1–6.
- Weinstein, A. et al. (2014). “Observation and interpretation of motional sideband asymmetry in a quantum electromechanical device”. In: *Physical Review X* 4 (4), p. 041003.
- Weis, S. et al. (2010). “Optomechanically induced transparency”. In: *Science* 330 (6010), pp. 1520–1523.
- Whittle, C. et al. (2021). “Approaching the motional ground state of a 10-kg object”. In: *Science* 372 (6548), pp. 1333–1336.
- Wilson-Rae, I. et al. (2011). “High-Q nanomechanics via destructive interference of elastic waves”. In: *Physical review letters* 106 (4), p. 047205.
- Wineland, D. J. and W. M. Itano (1979). “Laser cooling of atoms”. In: *Physical Review A* 20 (4), p. 1521.
- Winzer, P. J., D. T. Neilson, and A. R. Chraplyvy (2018). “Fiber-optic transmission and networking: the previous 20 and the next 20 years”. In: *Optics express* 26 (18), pp. 24190–24239.
- Wollack, E. A. et al. (2022). “Quantum state preparation and tomography of entangled mechanical resonators”. In: *Nature* 604 (7906), pp. 463–467.
- Wollman, E. E. et al. (2015). “Quantum squeezing of motion in a mechanical resonator”. In: *Science* 349 (6251), pp. 952–955.
- Wong, W.-T. et al. (2020). “A 1 mW Cryogenic LNA Exploiting Optimized SiGe HBTs to Achieve an Average Noise Temperature of 3.2 K from 4–8 GHz”. In: pp. 181–184.
- Wooten, E. L. et al. (2000). “A review of lithium niobate modulators for fiber-optic communications systems”. In: *IEEE Journal of selected topics in Quantum Electronics* 6 (1), pp. 69–82.
- Xuereb, A., C. Genes, and A. Dantan (2012). “Strong coupling and long-range collective interactions in optomechanical arrays”. In: *Physical review letters* 109 (22), p. 223601.
- Yanay, Y. and A. A. Clerk (2020). “Reservoir engineering with localized dissipation: Dynamics and prethermalization”. In: *Physical Review Research* 2 (2), p. 023177.
- Yang, Z. et al. (2015). “Topological acoustics”. In: *Physical review letters* 114 (11), p. 114301.
- Yoshida, K., Y. Kanda, and S. Kohjiro (1999). “A traveling-wave-type LiNbO<sub>3</sub> optical modulator with superconducting electrodes”. In: *IEEE Transactions on Microwave Theory and Techniques* 47 (7), pp. 1201–1205.
- Youssefi, A. et al. (2022). “Topological lattices realized in superconducting circuit optomechanics”. In: *Nature* 612 (7941), pp. 666–672.
- Zangeneh-Nejad, F. and R. Fleury (2020). “Topological optomechanically induced transparency”. In: *Optics Letters* 45 (21), pp. 5966–5969.

- Zhang, M. et al. (2019). “Broadband electro-optic frequency comb generation in a lithium niobate microring resonator”. In: *Nature* 568 (7752), pp. 373–377.
- Zhou, X. et al. (2013). “Slowing, advancing and switching of microwave signals using circuit nanoelectromechanics”. In: *Nature Physics* 9 (3), pp. 179–184.
- Zippilli, S. and D. Vitali (2021). “Dissipative engineering of Gaussian entangled states in harmonic lattices with a single-site squeezed reservoir”. In: *Physical Review Letters* 126 (2), p. 020402.



# AMIR YOUSSEFI

[amir.youssefi@epfl.ch](mailto:amir.youssefi@epfl.ch)

[youssefi.16@gmail.com](mailto:youssefi.16@gmail.com)

[Google scholar/ Amir Youssefi](#)

[Linkedin/ Amir Youssefi](#)

## ABOUT ME

I am an Electrical engineer (Ph.D.) and physicist, eager to find creative solutions and develop novel devices for cutting-edge technologies. My expertise in opto- and electro-mechanical devices design, simulation, and nano-fabrication, combined with knowledge of microwave design, cryogenics, superconducting circuit, and multi-physics systems helps me to unlock challenges in contemporary technologies and science.

## EDUCATION

<b>Ph.D. in Electrical Engineering</b> Laboratory of Photonic and Quantum Measurement <a href="#">↗</a> , Swiss Federal Institute of Technology in Lausanne (EPFL) Advisor: Prof. Tobias J. Kippenberg	2017 – 2023 Switzerland
<b>B.Sc. in Physics</b> Sharif University of Technology	2013 – 2017 Iran
<b>B.Sc. in Electrical Engineering</b> Sharif University of Technology	2012 – 2017 Iran

## RESEARCH INTERESTS

Hybrid Quantum Systems, Cavity Opto-Mechanics, Quantum sensing, Microwave Quantum Optics, Superconducting Circuits and Devices, Electro-Optical Transducers, Nano Photonics

## SELECTED CONTRIBUTIONS TO SCIENCE AND DISCOVERIES

- Demonstration of the longest quantum-state lifetime has ever been achieved in a macroscopic mechanical oscillator ( $T_1, T_2 > 8$  milli-seconds, a 100-fold enhancement) for quantum information storage applications.  
**A. Youssefi**, S. Kono, M. Chegnizadeh, & T. J. Kippenberg, “A squeezed mechanical oscillator with milli-second quantum decoherence”, **Nature Physics** (2023) [↗](#)
- Overcoming the scaling challenge in optomechanics, and demonstration of the first large-scale engineerable optomechanical lattice simulating topological phenomena in condensed matter models.  
**A. Youssefi**, S. Kono, A. Bancora, M. Chegnizadeh, J. Pan, T. Vovk, & T. J. Kippenberg, “Topological lattices realized in superconducting circuit optomechanics”, **Nature** 612 (2022) [↗](#)
- The first optical readout of superconducting devices, addressing the scalability challenge in future quantum computers exploiting cryogenic electro-optical transducers and optical fibers.  
**A. Youssefi**, I. Shomroni, Y. J. Joshi, N. R. Bernier, A. Lukashchuk, P. Uhrich, L. Qiu, & T. J. Kippenberg, “A cryogenic electro-optic interconnect for superconducting devices”, **Nature Electronics** 4 (2021) [↗](#)
- Discovery of an instability process limiting the tolerance of quantum non-demolition measurements in optomechanical systems.  
I. Shomroni, **A. Youssefi**, N. Sauerwein, L. Qiu, P. Seidler, D. Malz, A. Nunnenkamp, & T. J. Kippenberg, “Two-Tone Optomechanical Instability and Its Fundamental Implications for Backaction-Evading Measurements”, **Physical Review X** 9 (2019) [↗](#)

- Invention of the new technique of "Brewster Differentiator" for optical analog computing which is widely used in contemporary experiments in the field.  
A. Youssefi, F. Zangeneh-Nejad, S. Abdollahramezani, & A. Khavasi, "Analog computing by Brewster effect", **Optics letters** 41 (2016) [↗](#)
- Realization of ultra-coherent superconducting qubits with a world-record  $T_1 > 400\mu\text{s}$  and discovery of mechanically induced correlated errors in superconducting qubits.  
S. Kono, J. Pan, M. Chegnizadeh, X. Wang, A. Youssefi, M. Scigliuzzo, & T. J. Kippenberg, "Mechanically Induced Correlated Errors on Superconducting Qubits with Relaxation Times Exceeding 0.4 Milliseconds", **arXiv (Under review in Nature Comm.)** (2023) [↗](#)
- Realization of many-body quantum collective dynamics and distributed entanglement in optomechanical lattices. (APS March meeting 2023, Manuscript under preparation)

## HONORS AND AWARDS

<b>Swiss Nanotechnology Ph.D. Award, Switzerland</b> The Swiss Micro- and Nanotechnology Network <a href="#">↗</a>	2023
<b>Best Poster Award in MCQST, Germany</b> Munich Conference on Quantum Science and Technology	2022
<b>Highlighted on the Cover Page of Nature Electronics</b> For the first optical readout of superconducting devices <a href="#">↗</a>	2021
<b>Ranked 1<sup>st</sup> and Gold Medalist of the SOUS, Iran</b> the 21 <sup>st</sup> Physics National Scientific Olympiad For University Students	2016
<b>Silver Medalist of the 43<sup>th</sup> International Physics Olympiad (IPHO), Estonia</b> <a href="#">↗</a>	2012
<b>Gold Medalist of the 24<sup>th</sup> National Physics Olympiad, Iran</b>	2011

## CONFERENCES AND TALKS

- Emergent Quantum Technologies Conference 2023, "Superconducting circuit optomechanics: from milli-second quantum decoherence to topological lattices ", *Iran* (Invited speaker)
- APS March Meeting 2023, "Topological lattices in superconducting circuit optomechanics: strained graphene model", *Los Vegas* (Contributed talk)
- International Workshop on Nanomechanical Sensing 2022, "A new generation of superconducting circuit optomechanics: from high Q resonators to topological lattices ", *Online* (Plenary speaker, on behalf of T.J.K.)
- bigQ symposium on Quantum Information Science 2022, "A new generation of superconducting circuit optomechanics: from high Q resonators to topological lattices ", *Copenhagen* (Keynote speaker, on behalf of T.J.K.)
- British Optomechanical Research Network 2022, "Topological superconducting circuit optomechanical lattices", *online* (Invited speaker)
- APS March Meeting 2022, "A squeezed mechanical oscillator with milli-second quantum decoherence", *online* (Contributed talk)
- APS March Meeting 2021, "A reproducible design for multi-mode high-Q superconducting quantum electromechanics", *online* (Contributed talk)

## TEACHING EXPERIENCE

<b>Quantum Electromagnetics and Quantum Optics</b> Course Coordinator and Teaching Assistant, EPFL	2019–2021 Switzerland
<b>Statistical Physics IV</b> Course Coordinator and Teaching Assistant, EPFL	2018–2021 Switzerland
<b>Optics Laboratory</b> Microwave photonics experiments responsible, EPFL	2018 Switzerland
<b>Electromagnetics course in EE department</b> Course Coordinator and Teaching Assistant, Sharif University of Technology	2014–2017 Iran
<b>Member of the National Physics Olympiad Committee</b> Teaching to the selected national team, and designing national Olympiad exams.	2014–2016 Iran
<b>Teaching Physics Olympiad</b> Special courses preparing students for national and international physics Olympiad. Several top high schools in Tehran, Mashhad, Semnan, and other cities.	2011–2017 Iran

## OTHER PROFESSIONAL ACTIVITIES

---

- **Reviewer for Scientific Journals**, including Science Advances, Physical Review Letters, and Optics Letters.
- **Student Supervision:**
  - i Mahdi Chegnizadeh, “Long-lived mechanical quantum memory”, Ph.D., EPFL (2020 – present).
  - ii Jiahe Pan, “Topological phenomena in optomechanical arrays”, Ph.D., EPFL (2021 – 2022).
  - iii Andrea Bancora, “Multimode circuit optomechanics”, Master, EPFL (2020 – 2022), Currently in Deeplight ®.
  - iv Navid Akbari, “Collective dynamics in optomechanical arrays”, Master, EPFL (2020).
  - v Yash J. Joshi, “Cryogenic optical readout”, Master, EPFL (2018 – 2020), Currently in University of Chicago.
  - vi Tatiana Vovk, “Fabrication of superconducting vacuum-gap capacitors”, Master, EPFL (2018 – 2020), Currently in University of Innsbruck.
  - vii Philipp Uhrich, “Tunable and High-Q microwave filter cavities”, Ph.D., EPFL (2018 – 2019), Currently in University of Trento.
- **Contribution in Proposals and Reports for Research Projects:**
  - i Swiss National Science Foundation cavity quantum electro-optomechanics grant (2021 – present).
  - ii European Research Council (ERC) extremely coherent mechanical oscillators and circuit cavity electro-optics grant (2019 – present).
  - iii Swiss National Science Foundation NCCR-QSIT quantum sensing program (2018 – 2022).
  - iv EU H2020 research and innovation program, hybrid optomechanical technologies grant (2018 – 2021).
  - v European Microkelvin Platform (EMP) project on “Ringdown measurements of aluminum nanomechanical drums below 1 mK” (2023, project PI: A.Y., 30 k€ grant for collaboration with Néel institute).
- **Laboratory Management Experiences:**
  - i 2019-2021: Responsible for proposal writing, publishing a public tender, and purchasing and installation process of an ultra-high vacuum shadow evaporator for Josephson junction-based quantum circuits fabrication (850,000 CHF budget) [↗](#).
  - ii 2020-2022: Responsible for proposal writing, publishing a public tender, and purchasing and installation process of a dilution fridge cryogenic system (450,000 CHF budget) [↗](#).
  - iii 2019-present: Manager of the superconducting circuit laboratory of Prof. Kippenberg’s group.

## SCIENTIFIC OUTREACH AND PRESS RELEASES

---

- “A macroscopic oscillator goes and stays quantum”, *Nature Physics News & Views* (2023) [↗](#)
- “2D Optomechanical Lattice Mimics Graphene Physics”, *Optics & Photonics News* (2022) [↗](#)
- “A photonic link for quantum circuits”, *Nature Electronics News & Views* (2021) [↗](#)
- “EPFL Reports Electro-optical Readout of a Superconducting Circuit”, *Superconductor Week newsletter* (2021) [↗](#)
- “Optical links help superconducting quantum computers keep their cool”, *Physics World* (2021) [↗](#)
- “Evading Heisenberg isn’t easy”, *EPFL News* (2019) [↗](#)

## PERSONAL INFORMATION

---

I was born on 06.06.1994 in Tehran, Iran. I am married and Muslim. I am a citizen of the Islamic Republic of Iran and a residence of Canton of Vaud, Swiss Confederation (2017-present).

**Languages:** English (Proficient), Persian (Native), Arabic Al-Fusha (Intermediate), French (Elementary)



﴿دَعُواهُمْ فِيهَا سُبْحَانَكَ اللَّهُمَّ وَتَحْنِيتُهُمْ فِيهَا سَلَامٌ﴾

وَأَخِرُ دَعْوَاهُمْ أَنِ الْحَمْدُ لِلَّهِ رَبِّ الْعَالَمِينَ ﴿يونس ١٠﴾